Alexander Epp

Multiphysical Models and Optimization for Conceptual Design of High-Voltage Battery Systems

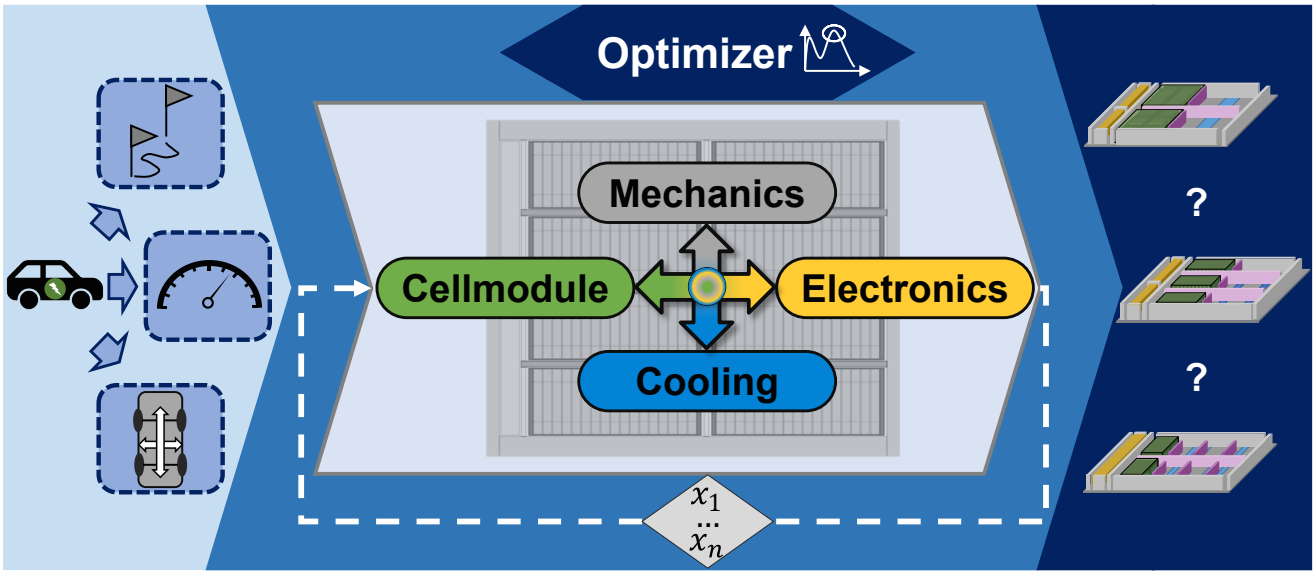

Aachener Beiträge des ISEA Band 176

Multiphysical Models and Optimization for Conceptual Design of High-Voltage Battery Systems

Von der Fakultät für Elektrotechnik und Informationstechnik
der Rheinisch-Westfälischen Technischen Hochschule Aachen
zur Erlangung des akademischen Grades eines Doktors der
Ingenieurwissenschaften genehmigte Dissertation

vorgelegt von
Alexander Epp, M. Sc.
aus Lübbecke

Berichter:
Univ.-Prof. Dr. rer. nat. Dirk Uwe Sauer
Univ.-Prof. Dr.-Ing. Christoph Herrmann, TU Braunschweig

Tag der mündlichen Prüfung: 19. Dezember 2023

AACHENER BEITRÄGE DES ISEA
Vol. 176

Editor:
Univ.-Prof. Dr. ir. Dr. h. c. Rik W. De Doncker
Director of the Institute for Power Electronics and Electrical Drives (ISEA)
RWTH Aachen University

ISSN 1437-675X

Institute for Power Electronics and Electrical Drives (ISEA), RWTH Aachen University
Campus-Boulevard 89 • 52074 Aachen • Germany
Tel: +49 (0)241 80-96920
Fax: +49 (0)241 80-92203
post@isea.rwth-aachen.de

Vorwort

Die vorliegende Dissertation ist während meiner Tätigkeit als Doktorand bei der Volkswagen AG in der Technischen Entwicklung in Wolfsburg entstanden. Für das Gelingen der Arbeit möchte ich mich bedanken:

An erster Stelle gilt mein Dank Professor Dirk Uwe Sauer für die Möglichkeit der Promotion sowie das Vertrauen zur Übernahme und Betreuung meiner Dissertation. Zudem danke ich Professor Christoph Herrmann für die Übernahme des Korreferats.

Bedanken möchte ich mich auch beim Institut für Stromrichtertechnik und Elektrische Antriebe (ISEA) sowie speziell bei der Abteilung BST, in welcher ich bereits meine Bachelorarbeit und Masterarbeit geschrieben habe. Besonders Philipp Dechent möchte ich dafür danken, mich für die Welt der Batterien und Batteriesysteme begeistert zu haben und mich auch über die Institutsaktivitäten hinaus zu unterstützen.

Vielen Dank an meine direkten Kolleginnen und Kollegen der Volkswagen AG, die mich herzlichst aufgenommen und jederzeit unterstützt haben. Ganz besonders Robert Wendland, der die Arbeit fachlich mitbetreut hat, möchte ich danken.

Das allergrößte Dankeschön gilt meiner Familie: Meiner Mama Claudia, meinem Papa Waldemar und meiner Omi Hannelore möchte ich für die Möglichkeit zum Studium in Aachen und der kindlichen Prägung zum Nachfragen, zum Erkunden und zur technischen Affinität danken. Meinem Bruder Philipp und meiner Schwester Franziska danke ich für die Motivation und den Rückhalt in jeder Phase.

Abschließend möchte ich mich bei meiner Freundin Marei bedanken: Deine unendliche Unterstützung war und ist die Essenz - Danke für … *einfach alles*.

Wolfsburg, Januar 2024

Alexander Epp

Disclaimer

The results, opinions, and conclusions expressed in this thesis are not necessarily those of Volkswagen Aktiengesellschaft.

Abstract

The lithium-ion battery is the most expensive and weight-intensive component in electric vehicles (EVs). Therefore, in the development of new EVs, the battery is often the focus of optimization. In addition to the actual battery cell design, the serial and parallel cell connection, the cooling capability, the battery's mechanical integration in the pack, and the electronics play a decisive role in a battery system. There are also major direct dependencies between the optimal battery system and the necessary EV requirements regarding energy, power, and system voltage. Moreover, fundamental guidelines with regard to durability, safety, and general lifetime must be met and thus taken into account in the battery system package design.

This thesis aims to combine the multitude of interfaces within battery system development using a multiphysical framework capable of holistically evaluating, comparing, and optimizing battery system concepts. The framework consists of interconnected simulation models representing each major component group within the battery system design.

The fundament is a generic cellmodule model capable of interdependently optimizing cell and cellmodule geometries. The model is based on pooled data to geometrically describe the entire integration pathway from the cell and its subcomponents to the packaging specifications and the finalized module. The cellmodule model was extended by electrical, thermal, and mechanical properties to be integrated within the battery system simulation framework, consisting of additional parametrized models for cooling, mechanics, and electronics design. Several interfaces between different components were derived and defined in an interconnected submodel-concept. The modular structure of this concept allows simple extension or decoupling of the individual models for future developments. The resulting interconnectivity provides an in-depth understanding of battery system design dependencies that are not observable by standalone models. Machine learning optimization is used to derivate globally optimized battery system design concepts. The optimization combines methods of Gaussian process regression and classifications. Thereby, the solution space is divided into multiple areas in which area-targeted search criteria are used.

Finally, analyses regarding optimized cell formats, beneficial system geometries, or spot-on designed battery systems are conducted. Thereby, novel EV battery-related issues are discussed from the cell to the module to the system level. Findings underline the imperative need for component-coupled simulation models when evaluating battery system designs.

Contents

1 Introduction

1.1 Motivation and objective

With the Paris Climate Agreement, nearly every country commits itself to work towards limiting the increase of the global average temperature to significantly below 2 °C (shortening to 1.5 °C) compared to the level of the pre-industrial era. Significant reductions in greenhouse gas (GHG) emissions across all emitting sectors are needed to achieve this goal. The most relevant greenhouse gas is CO_2 [1]. Therefore, other greenhouse gases like methane are often converted into CO_2-equivalents to make the effect comparable. The share of total emissions is often divided into several sectors like energy, industry, transport, buildings, or agriculture. The transport sector is usually placed as the second or third most significant greenhouse gas emitting sector. Depending on the calculation method, approach, and location, different emission distributions result for Germany [2–6], the EU [7–10], and the global earth [11–14]. The transport sector thus accounts for a GHG emission share of about 19% - 23%. Within the transport sector, 72% - 96% of GHG emissions can be attributed to road transport. Of these, 60% - 66% come from passenger cars and motorcycles. Figure 1.1 shows the distribution of GHG emissions in more detail.

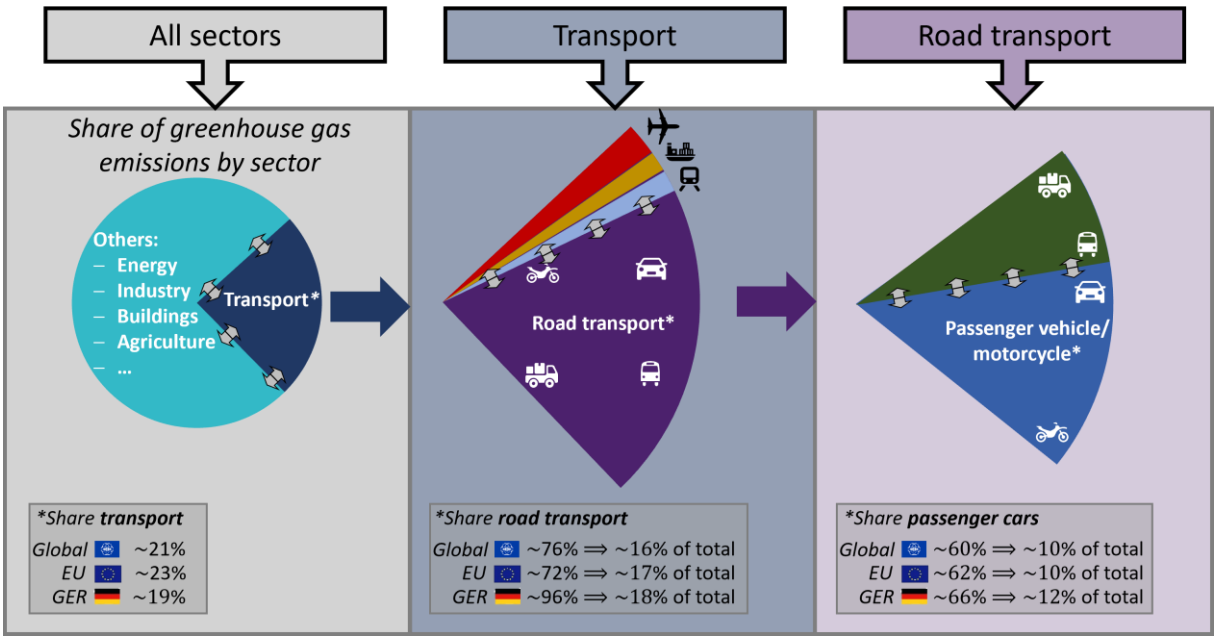

Figure 1.1: Greenhouse gas emissions by sectors.

The shares of total emissions underline the significance of green mobility, especially for road transport. However, while other sectors in Germany, such as industry or buildings, have already achieved major savings in recent years, CO_2-emissions in the transport sector have remained essentially unchanged since 1990 [15, 16]. While the energy efficiency of vehicles has primarily improved, the trend towards larger, heavier, and generally higher traffic volume compensates for the savings given by higher efficiencies [17].

In order to further drastically reduce the CO_2-emissions of passenger and commercial vehicles, vehicles powered by renewable energies are needed. While hydrogen

production for vehicles is still not efficient enough, considering the still scarce renewable energies, most car manufacturers are focusing on battery electric vehicles (EVs). The battery electric vehicle represents a market-ready technology that can reduce greenhouse gas emissions from the transport sector in the short term. The effect grows with the share of renewable energies in the electricity mix [18, 19].

A battery system stores energy to operate the electric motors in battery-electric vehicles. The system generally consists of several battery modules in which the individual battery cells are stacked. To date, the batteries used in electric vehicles are almost exclusively lithium-ion battery (LIB) cells. To ensure long-lasting and safe operation, the battery cells are usually actively cooled by thermal management systems and safely operated by an electronic unit. The battery system's outer frame encloses the cells and all related components, providing safety in the event of a crash [20–22].

In the complex development of battery systems, several physical aspects have to be combined to meet the multitude of often conflicting requirements. Demands of durability, safety, ecology, and economy must be addressed by conceiving the battery system’s design from a holistic perspective. Additionally, novel approaches to battery system design require detailed predictions already in the early stages of development. In this context, the functional integration of individual battery cells in cell to pack methods aims to integrate the cells deeper into the overall system structure [23–25].

In order to meet these challenges and ultimately satisfy the multitude of requirements for each component of battery systems, prediction models with great accuracy and reliability have to be developed. Simulation models (for this thesis, this term includes also physical computation models and other approaches that use already executed results from simulation models) offer cheap and fast evaluations to support the battery system development process, especially in the early development stages. Standalone models can represent individual components in great detail. Albeit, to make the best overall design decisions for future battery systems, individual simulation models representing each major battery system component must be coupled with each other. Coupled simulations (for this thesis, this term defines interconnected or reciprocal models, which exchange model parameters with each other) are often particularly complex since multiple interfaces must be addressed, and the individual generic models must be created based on the interfaces with sufficient accuracy for all components. Within an optimization, the simulations must also take relatively low computation time in order to be able to provide a wide range of supportive information in the early development phase of the battery systems and thus derive otherwise unrecognizable potentials.

This thesis aims to:

- Derive the challenges and opportunities in battery system design considering the geometric properties of the cell, module, and system.

- Develop a design space parameterization for battery systems and elaborate a methodology for different coupled simulation models for all main component groups for battery system design.

- Propose a nonlinear machine learning optimization framework using combined Gaussian process regression and classification methods to ensure the interchangeability of the variable simulation models.

- Utilize the developed battery system optimization tool to derive and holistically evaluate battery system designs from the system to cell level based on various EV requirements.

1.2 Structure

The structure of the work is shown in Figure 1.2.

Chapter 2 briefly describes the fundamentals with regard to battery system engineering and optimization relevant to this work. In particular, the structure of battery systems and the relevant components will be presented. Furthermore, the basics of machine learning optimization using Gaussian process regression methods are given. Finally, the development process of battery systems is classified within the product development process for passenger cars. Thereby, the role of simulation in the early development stages is explained.

Chapter 3 stresses packaging differences and resulting utilization rates between different battery cell formats used within a cellmodule. Subsequently, a generic cellmodule model is derived and conditioned based on a literature review. This cellmodule model enables to optimize both the module as well as the cell geometry. The objective function is varied to investigate the cost and energy perspectives.

In Chapter 4, a battery system optimization tool is developed based on different simulation models for all main component groups. A cell model, which is resolved down to the electrode stack level, is added to the cellmodule model developed in Chapter 3. Additional models for cooling, mechanical system design, and electronics are added to the framework. A novel parametrization of battery system space allocation defines design space for each main component group, within which each component is optimized. Different battery system concepts can be compared by varying the space allocation between the components. In addition to electrical, thermal, or mechanical comparisons, detailed weight and cost breakdowns can also be used to perform quantitative comparisons of system designs.

In Chapter 5, a mixed integer optimization methodology is developed, combining Gaussian process regression and Gaussian process classification methods. The optimization framework evaluates iteratively changing battery system designs to ultimately find a globally optimized battery system concept. A black-box approach within the optimization framework is used, which enables individual simulation models to be interchanged or replaced.

In Chapter 6, the optimization framework from Chapter 5 is coupled with the battery system design simulation models described in Chapter 4. The holistic battery system optimization tool is used to address battery system-related issues from the system level down to the cell level. Different usage scenarios for the battery system optimization tool are then presented. Optimizations of the total installation space, the cell format, the cell geometry, the system geometry, and other variables are carried out. The optimizations are based on different EV requirements in terms of energy,

power, charging capability, and other sizes. An evaluation of battery system designs with different cell integration levels quantitatively predicts the potential of the novel cell to pack approaches.

Chapter 7 presents the conclusion and outlook of this thesis.

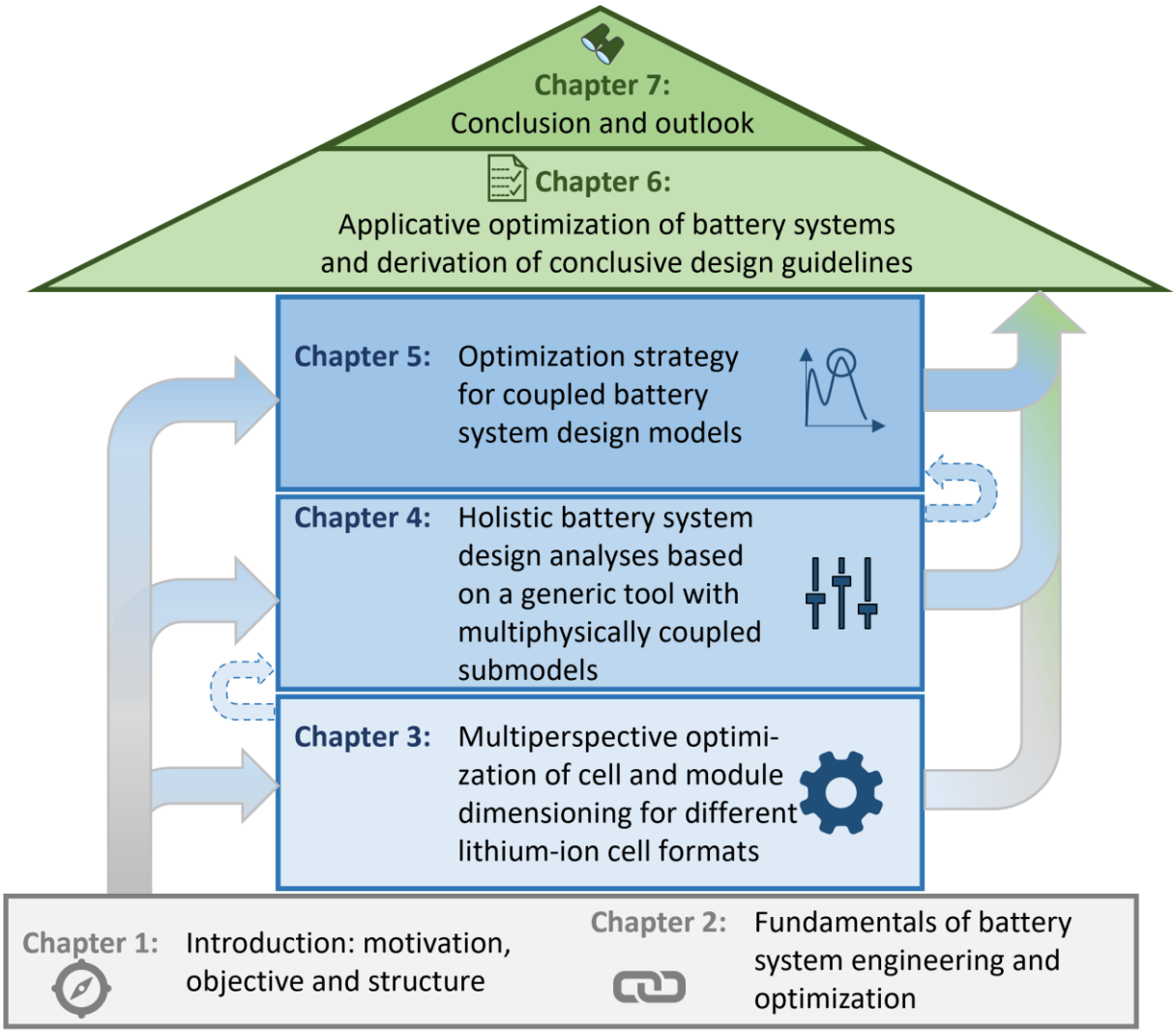

Figure 1.2: Structure of the thesis.

2 Fundamentals of battery system engineering and optimization

This chapter covers essential fundamentals for this thesis. First, the role of battery system development within electromobility is introduced. Then, the electric vehicle's traction battery is presented as an overall system. Afterward, the different individual component groups, cellmodule, cooling, mechanics, and electronics will be explained. The component groups' physical principles and their interaction within the battery system will be briefly described. Subsequently, optimization principles, particularly machine learning methods, are classified. Finally, the thesis will be thematically integrated into the product development process of automotive manufacturers.

2.1 Electromobility and electrified vehicles

An electric car can generally be described as an automobile with an electric drivetrain. The first development of electric cars dates back to earlier than 1900, but while internal combustion engines for cars initially prevailed at that time, the development and production of electric cars increased again, primarily due to the industrialization of the lithium-ion battery at the beginning of the 21st century. EVs can be divided into hybrid electric vehicles (HEV), plug-in hybrid electric vehicles (PHEV), and battery electric vehicles (BEVs). Next to the battery-electric supply, hydrogen-based supplies of the electric drivetrain are also used [26]. However, these fuel cell vehicles (FCV) will not be discussed further in this thesis. In 2021, roughly 6.75 million electric passenger vehicles, light trucks, and light commercial vehicles were registered. This represents more than 100% growth compared to 2020 and almost 200% compared to 2019 [27]. Two phenomena mainly explain this growth. First, the global demand for individual mobility, like passenger vehicles, has been growing for decades [28]. Second, commitments such as the Paris Climate Agreement require countries to reduce global CO_2-emissions significantly [29]. Hereby, the mobility sector plays a crucial role. Many governments around the world are subsidizing the purchase and use of electric cars. These subsidies are often necessary to compensate for the price differences between electric and equivalent combustion variants [29]. Other government measures include tax breaks, special free parking spaces, free charging options, and many more [30, 31].

Although the prediction of a general vehicle service life is difficult due to the multiple interdependencies, it is assumed that a standard mid-range vehicle should achieve an average lifetime of 150000 to 250000 km. For EVs, this lifetime is expected to be higher as less maintenance effort and lower maintenance intervals are needed for the electric motor and the transmission [32]. In order to also reach a satisfactory battery lifetime, special consideration must be given to the design of the traction battery. As the by far most expensive component in the overall electric car, particular emphasis is placed on the longevity and fail-safety of the battery. Therefore, different battery-related components have to be well-matched to each other. Most car manufacturers additionally guarantee battery functionality with a warranty period. Thus, the interest in an optimized traction battery is crucial for both the consumer as well as the manufacturer. The California Air Resources Board (CARB) plans to extend current standard manufacturer battery lifetime guarantees by defining new rules for EV battery lifetime. The CARB suggests that by 2026, every EV battery has to maintain 80% of its certified range for 15 years or 240000 km [33].

Given the premise of safety and durability, environmental reusability also plays a role in traction battery design. Car manufacturers are planning return programs to reuse the valuable materials from the battery. If batteries are to be recycled, it is of particular importance that they can be disassembled in the best possible way. This approach is partly opposite to the deep integration of battery cells within the vehicle with novel integration methods such as cell to pack and cell to car [25]. In order to balance this trade-off and further develop cost- and weight-optimized battery systems, competitive advantages must be explored by synchronously optimizing major component groups within battery systems.

2.2 High-voltage battery systems for battery electric vehicles

The design of high-voltage (HV) battery systems is directly dependent on the individual vehicle requirements for which it is designed. Fundamental differences result from the design of the energy storage system. While battery systems for hybrid electric vehicles often require small, powerful battery storage units, pure electric vehicles usually place more emphasis on the amount of energy available. Differences can also be found in the space available for the battery system.

Figure 2.1 schematically depicts the packaging for the drive system of a battery-electric vehicle. The main components of any battery system are the battery cells in the corresponding module structure. The cells are the energy and power carriers and, at the same time, represent the highest cost and weight component of the overall system. The electronics consist of control units like the battery management system and application units like the switch box, which is responsible for the inherent safety of the battery system. A cooling system is installed in the battery system to ensure optimal operating conditions of the battery cells to maximize their lifetime and power output. All system components are embedded in the outer frame, ensuring external safety for severe weather conditions or crash events.

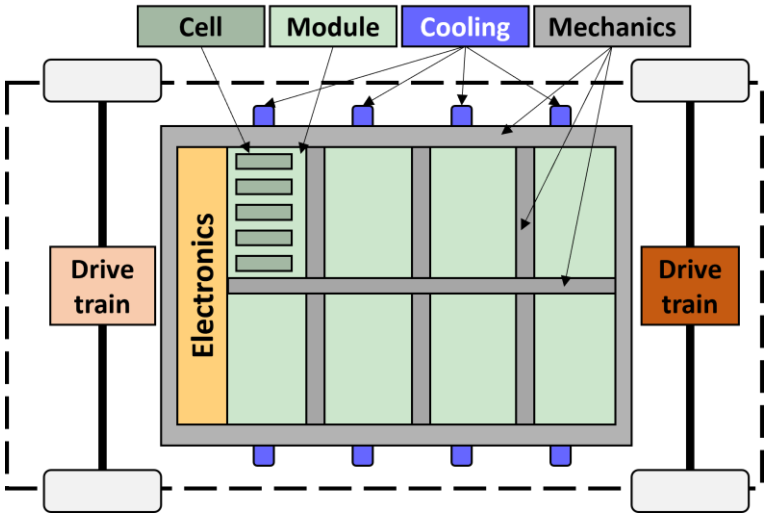

Figure 2.1: Schematic battery and drivetrain structure for an electric vehicle.

As energy and power supply, battery systems require a significantly larger amount of total vehicle installation space than the liquid or hydrogen fuel tank in combustion-powered vehicles. While battery systems can achieve volumetric energy densities of 200 Wh/l – 400 Wh/l [34], diesel or gasoline has an energy density of about 25 – 50

times higher, at about 10 kWh/l [35]. This difference is narrowed if the energy use efficiencies are put in perspective. In addition, fewer components (e.g., gearbox) are used to power the EV, which frees up additional installation space that can be used for the battery. In battery-powered vehicles, this needed battery space is typically located in the underbody of the vehicle, which often results in slightly heightened vehicles. Figure 2.2 shows a schematic of three battery system geometries integrated into the vehicle's underbody. Depending on the specific EV requirements and the other components' design, each battery system geometry can be vehicle-type-specific optimal. From the battery system view, a rather wide geometric design can lead to an overall sizeable high installation space volume. However, battery cells must be exceedingly well protected in a side crash due to the resulting short path of possible energy absorption. A rather long design may require additional cross beams for mechanical stiffness, adding weight to the system. A trade-off between the two can generally lead to a smaller battery system leading to fewer battery cells for energy and power supply. Every design geometry can furthermore directly influence the cellmodule geometry, the cooling system, or the mechanical structure.

The functions of the individual component groups within the battery system are consolidated in the following chapters.

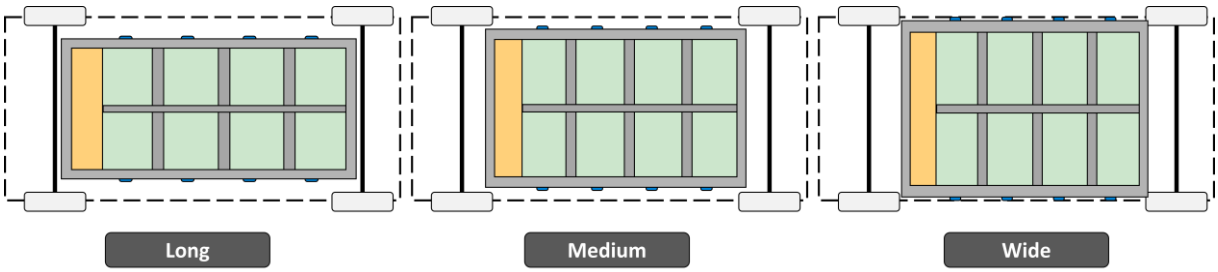

Figure 2.2: Schematic of differently shaped battery systems.

2.2.1 Structure of cellmodules and overview of lithium-ion batteries

Several battery cells must be used to meet the electric vehicle's energy and performance requirements. Individual cells are usually combined as a unit to form a cellmodule. A schematic of a cellmodule, consisting of 12 battery cells in two cellstacks, is shown in Figure 2.3. The module housing protects the individual battery cells from external influences and the mechanical expansion of the cells.

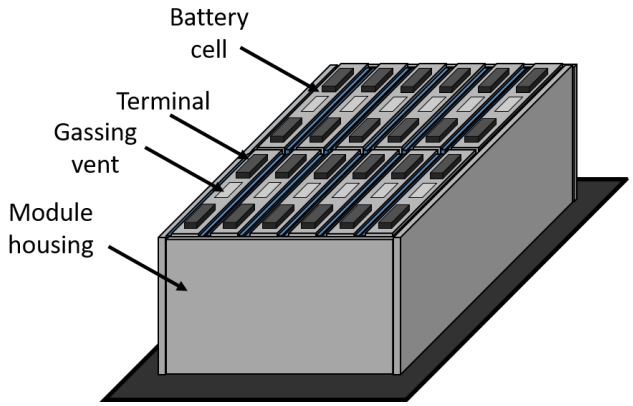

Figure 2.3: Schematic structure of a battery cellmodule with prismatic cells.

Several identically constructed cellmodules are usually used within a battery system. Cellmodule-based battery system design enables to benefit from modularity, economies of scale, easier maintainability, and reparability. The cellmodules thus represent one of the main components of each battery system design.

2.2.1.1 Interconnection of battery cells

The battery cells within the cellmodule are electrically connected. While the cellmodules are usually purely connected in series, the individual cells within the cellmodules are connected in both series or parallel. The used interconnection is a complex design decision associated with multiple dependencies [36]. Thereby, the requirements of the battery system voltage play an essential role. The battery system's power can be nominally described using $P_{\mathrm{system}} = U_{\mathrm{system}} \cdot I_{\mathrm{system}}$. The system voltage can be increased by connecting more cells in series. The permissible total system current on the other side can be increased by the parallel connection. However, omic heating losses occurring, e.g. in the battery junction box or wires, according to $P = I_{\mathrm{system}}^2 \cdot R_{\mathrm{system}}$, and thus change quadratically to the current. Therefore, high voltages and the associated high number of series connections are often favored over parallel connections. Typical battery system voltages are around 400 V. Some manufacturers also offer and plan vehicles with up to 800 V [37]. On the negative side, higher voltages also have disadvantages due to more expensive components in the junction box and can furthermore increase the risk in the event of a failure. Aghabali et al. reviewed the benefits and challenges of 800 V systems in detail [38]. Purely serially connected battery systems are also more susceptible to cell defects [39] and lead to larger inhomogeneities in operation [40–42]. This results from the fact that the worst cell in a serial row of cells determines the behavior of the complete cell string. Furthermore, a defect in one cell can lead to a complete failure of the entire battery system. Therefore, the parallel connection of cells generally enhances the system's lifetime and increases homogenous behavior. Self-balancing between parallel connected cells increases the system's overall homogeneity [43, 44]. In real-world EV applications, battery systems are often built using combinations of serial and parallel connections [45]. Thus, the advantages of both series and parallel connections can be combined [40]. Cell connection, often mentioned as topology, is usually described using 'x_{s}s x_{p}p' with x_{s} being the number of cells connected in series and x_{p} the number of cells connected in parallel. Table 2.1 shows some exemplary interconnections for different EVs. The examples emphasize that no globally optimal solution for the best interconnection exists. Rather, the optimal solution correlates with the specific vehicle, cell type and system architecture.

Electric vehicle	Battery system topology
Volkswagen ID.3 58 kWh [46]	Nine modules serial connected with 12s2p
Mitsubishi i-MiEV [47]	Ten modules serial connected with 8s1p Two modules serial connected with 4s1p
Smart Fortwo Electric Drive [47]	90 cells connected in 90s1p
VW e-Up [47]	17 modules serial connected with 6s2p
Tesla Model-S 85 kWh [47, 48]	16 modules serial connected with 6s74p
BMW i3 [48]	Eight modules serial connected with 12s1p

Table 2.1: Exemplary battery system topologies for different electric vehicles.

2.2.1.2 Overview of battery cell formats

Different battery cell formats are used in electromobility applications. The cell formats can be classified as cylindrical, prismatic, and pouch. While in recent years, many manufacturers used different cell formats for their battery system platforms, a number of manufacturers are recently aiming to focus exclusively on one format. However, it is difficult to make a reliable statement about the development potential of cell formats due to the associated complexity and application specificity. Therefore, considerations and analyses of cell formats must be made from the cell to the module and to the system level [49]. This aspect will be extensively discussed in Chapter 3.

Depending on the cell format, the inner electrode stack is inserted differently into the cell housing [50]. While cylindrical cells have wound electrode layer structures, the electrode layers are usually stacked for pouch cells. Prismatic cells can be produced with either wound or stacked electrode layers [51]. The winding process has the greatest possible speed in production since electrode layers need to be cut less frequently [52]. The resulting smaller capacity of cylindrical cells leads to a large number of cells in EV applications. This can lead to more difficult cell monitoring for the battery management system. In addition, the utilization rate at the module or system level is often higher for the pouch and prismatic cells [53, 54].

2.2.1.3 Lithium-ion battery: overview and function principle

Today's electric vehicles almost exclusively use lithium-ion battery technology. Lithium-ion batteries offer higher energy and power densities than other battery technologies, enabling large amounts of stored electrical energy to be provided in a small space and with low weight at high power levels. Comparative ragone plots can underline their superiority over other electrical energy sources [55]. The broader spread in energy and power density emphasizes the flexible usage possibilities for various applications. The possibility of designing the cells as high energy or high performance cells also enables flexible use for various applications, especially in the field of electrification. This aspect will be further stressed in Chapter 2.2.1.5.

In the following, the functional principle of the lithium-ion battery is explained. For this purpose, Figure 2.4 shows an example of the schematic structure of a lithium-ion cell. The positive electrode is shown on the left, and the negative electrode is on the right. A separator in the middle isolates the two electrodes from each other. The separator is a porous membrane and prevents a short circuit between the two electrodes. An ion-conductive electrolyte lies between the two electrodes and within their pores [56]. A wide range of different materials is used in both electrodes. This will be further stressed in Chapter 2.2.1.4. The positive electrode is equipped with a current aluminum collector. As aluminum can react with lithium ions at high battery voltages, the current collector on the negative side is usually made of copper [57].

The small and highly mobile lithium ions are the active part of the lithium-ion battery. During charging, electrons flow to the anode through the external circuit. As a result, lithium ions migrate from the metal oxide layer, with the help of the electrolyte, through the separator to the opposite graphite electrode and are deposited in intercalation compounds between the large graphite molecules. During discharging, this process is reversed. As the lithium ions migrate back to the cathode, the electrons are released through the external circuit and can thus be used as electrical energy (rocking chair

principle). While anode and cathode generally change their designation depending on the electrochemical reaction (charging or discharging process), the convention for lithium-ion cells is to determine the designation during the discharge process [58].

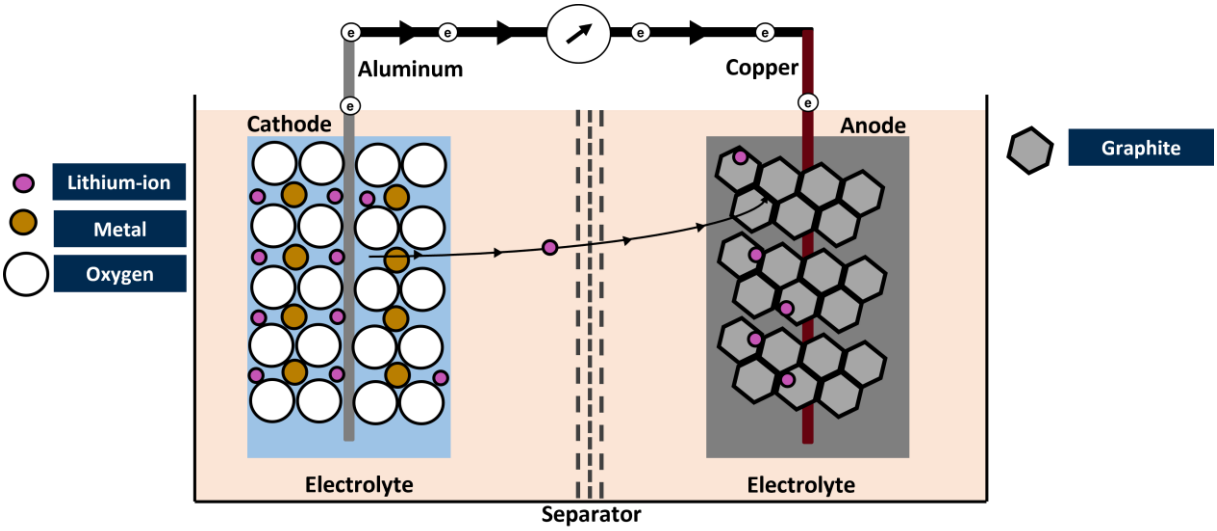

Figure 2.4: Schematic structure of a lithium-ion battery cell (charging direction).

2.2.1.4 Lithium-ion battery: materials, naming, voltage levels

Lithium-ion batteries gain some of their advantageous properties in particular from their naming element lithium. Through the usage of lithium, some lithium-ion cell chemistries can reach voltages above 4 V [56]. Generally, the voltage of a cell is significantly influenced by the used electrode materials. A large difference between the anode and cathode potentials increases the voltage and, thus, energy and power density of a cell. Furthermore, material usage can also influence power capability, low or high-temperature performance, and aging. This results in different advantages and disadvantages depending on the material combination. The most commonly used anode material is graphite. It has a low redox potential versus Li/Li^+ and gains low volume expansion when lithium ions are intercalated. The downside of the low potential is the risk that lithium can form metallic deposits on the electrode under certain conditions. This effect of loss is called lithium plating (further aging phenomena are described in Chapter 2.2.1.6). Another common anode material is titanium oxide ($Li_4Ti_5O_{12}$ or LTO) [59]. Its potential versus Li/Li^+ is higher. Due to its high potential, the use of the material is inherently safer than graphite. However, it is rarely used in the automotive sector because of the resulting low energy storage capability. Other novel materials like silicon-based alloys promise the potential to increase energy density but need special provisions to control the volume expansion during cyclic usage [60]. The review by Feng et al. highlights the advantages and the state of research on silicon alloy anodes [61].

An even greater variety of materials is given for the cathode. Cathode materials generally aim for high redox potentials versus Li/Li^+ [59]. During the market launch, lithium cobalt oxide cathodes were almost exclusively used. $LiCoO_2$ has good electrochemical properties, such as high specific heat capacity, low self-discharge, and high voltage, with good cyclic aging performance. However, the material is expensive and environmentally harmful. These and other reasons have led to research into new material combinations. Nowadays, mixed materials such as nickel-manganese-cobalt

oxides ($LiNiMnCoO_2$ or NMC) or nickel-cobalt-aluminum oxides ($LiNiCoAlO_2$ or NCA) are primarily used. Another cathode material used is lithium iron phosphate ($LiFePO_4$ or LFP). Due to the lower redox potential versus Li/Li^+, battery cells with LFP cathodes have lower energy density than cells with NMC or NCA cathodes [62].

The naming for different lithium-ion cell technologies is not consistent and can vary between the cathode and anode material used. The NMC-Type cell represents a cell with the eponymous cathode-side material combination of nickel-manganese-cobalt oxide. Graphite is often used on the anode. NMC-Type cells have high voltages of up to 4.3 V and can reach energy densities of 600 Wh/l and more. Individual properties of the cell chemistry can be designed by the proportions of the materials nickel, manganese, and cobalt leading to nickel-rich NMC cathodes having, e.g., larger gravimetric capacities [63]. Closely related is the NCA cell. Usually, the nickel content in this chemistry is more than 80%.

LFP is often considered a low-cost cell chemistry. The lithium iron phosphate cathode gives the name to this cell type [62]. Due to the low potential versus Li/Li^+, graphite is used in the anode [64]. LFP cells reach voltages of up to 3.6 V. Their open-circuit voltage is characterized by a particularly flat course over almost the entire SOC range. This course is schematically depicted in Figure 2.5.

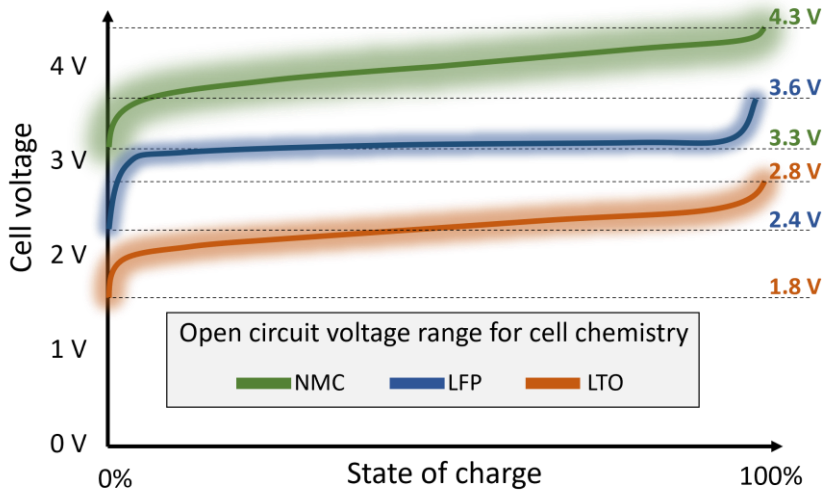

Figure 2.5: Exemplary open circuit voltage ranges for different cell chemistries.

The LTO cell has its name based on to anode material titanium oxide. On the cathode side, an NMC material combination is often used [59, 65]. LTO cells reach voltages of up to 2.8 V.

New material combinations are continuously being worked on to complement advantages and ultimately generate application-specific optimal cell chemistries. A novel example is the LiMnFePO (LMFP) chemistry, which is expected to combine the high safety of LFP with higher energy densities of NMC-Type battery cells [66].

2.2.1.5 Lithium-ion battery: high power and high energy electrode design

LIBs and other rocking chair batteries can vary widely in terms of power and energy density. Different material combinations can change the properties of a cell significantly. However, equally large changes can be made by the structure of the used

electrodes. This leads to an often opposing trade-off between power and energy in cell design.

Electrodes for high power applications are usually designed with thinner electrode layers [67]. This makes it easier for the lithium ions to move between the electrodes because the diffusion path lengths are minimized. As a result, the internal cell resistance decreases. The work in [68] concludes that high power cells use lower coat weights are areal capacities as well as smaller active particles, and higher cathode porosities.

Conversely, the cell's electrodes are usually designed thicker for high energy applications. While thicker electrodes generally increase the cell's energy density, production costs can often be simultaneously decreased [69]. The work by Kuan et al. [70] provides a wide-ranging overview of the principles, opportunities, and challenges with regard to thick electrodes.

2.2.1.6 Lithium-ion battery: aging phenomena and aging effects

The usability of lithium-ion batteries deteriorates with time and use of the cell due to changes in the electrochemical components, which leads to capacity and performance degradation. Both phenomena are collectively named aging in the battery. Aging is linked to multiple coupled aging mechanisms, which depend on various, often correlated, factors, such as battery chemistry, cell design, as well as environmental and operating conditions [71]. The point at which a battery no longer meets the energy or power requirements needed for its specific application is generally referred to as the end of life (EOL). Accordingly, the EOL is not firmly defined but is often fixed in the literature at 80% relative remaining capacity [72, 73]. More dynamic approaches use degradation "knee-points" as an indicator for estimating EOL [74, 75]. A widely used and accepted subdivision of aging in the literature is divided into the loss of free lithium ions (Loss of Lithium Inventory: LLI), the loss of active material (LAM), and the increase in internal resistance [76].

The load-free calendar aging considers aging mechanisms that do not depend on the cell's power output. The main influencing factors are the state of charge (SOC) and the temperature at which the cell is stored. At high SOCs, only a few lithium ions are located in the active material of the cathode. This increases the chemical affinity for unwanted reactions with the electrolyte. High temperatures can accelerate these reactions.

Cyclic aging occurs during the use of the battery cell. Thereby, the main factors are the average charge or discharge voltage, the temperature and the cycle's depth of discharge (DOD), and the cell's charge or discharge current rates. Due to repeated reactions in the cell, the condition quality of the internal materials continuously decreases. The review by Barré et al. [77] summarizes these and other aging phenomena. To prevent or decelerate some of the mentioned aging mechanisms, EV manufacturers often restrict the usable SOC range [78]:

$$\mathrm{SOC}_{\mathrm{cell,lower\,lim.}} \leq \mathrm{SOC}_{\mathrm{usable,lower\,lim.}} < \mathrm{SOC}_{\mathrm{usable,upper\,lim.}} \leq \mathrm{SOC}_{\mathrm{cell,upper\,lim.}}. \qquad (2.1)$$

A particular challenge in the automotive sector arises from the increasing demand for fast charging (also named quick charging) times. During fast charging, high

overpotentials and lithium ion concentrations can occur. This can lead to a metallic deposition of the lithium on the graphite anode. Lithium plating belongs to the LLI. In extreme cases, lithium plating can short-circuit the cell, causing oxidation of the electrolyte and dangerous thermal runaway [79, 80]. Thermal runaway describes the exothermic reaction of LIB in which different stages lead to massive energy release, which can destroy other cells within a cellstack. The cascading reaction is then called thermal propagation. In-depth literature on thermal runaway and thermal propagation can be found in [81–83]. Due to its low reversibility, lithium plating also leads to short-term efficiency losses. Careful cell design and highly accurate predictive methods must be used to operate the battery cells at specific operating point-dependent current and voltage limits so that plating does not occur [84]. Further expositions of aging phenomena and diagnosis methods for automotive applications are described in [85].

In addition, reversible aging effects are often mentioned in the literature. These include, for example, the effect of the anode protrusion [86] and local inhomogeneities in the distribution of the lithium ions [87].

2.2.1.7 Lithium-ion battery: swelling and cellstack compression

Significant volume changes can occur in lithium-ion cells. Reversible volume changes of roughly 10% have been reported in lithiated graphite [88]. Even larger volume changes come with the usage of silicon anodes [89]. Depending on the nickel content, volume changes of the cathode were also proposed in the literature [90]. In addition, various aging mechanisms (growth of solid electrolyte interface (SEI), lithium plating) lead to irreversible swelling of the cell. Moreover, gas evolution in LIB can lead to significant cell swelling, especially in prismatic and pouch cells [91, 92]. In order to manage these cell volume changes, counter pressure plays a vital role in cellstack packaging. Different preload pressures can influence the cell’s aging behavior differently [93]. Literature shows the existence of a cell- and stack-dependent optimized pressure. Insufficient pressure can lead to the delamination of electrode layers and separator deformation [94]. Mussa et al. [95] show that cyclic lithium losses are reduced at optimum pressure.

In addition to reduced aging, the thermal behavior of battery cells can also be pressure-dependent influenced. Steinhardt et al. [96] measured a roughly 12% increased through-plane thermal conductivity for prismatic cells with compression pressure between 37.1 kPa and 74.2 kPa. Since the battery cell must also expand during its lifetime, cell stress must also be considered throughout the life of the battery [97]. Different cushion pads offer the possibility to keep the pressure on the cells well during their lifetime. The range of possible material combinations is broad, as the pads are often used additionally to prevent thermal propagation [94].

2.2.1.8 Lithium-ion battery: load operation and heat losses

Heat losses occur in battery cells due to charging or discharging. Cell-specific properties like cell format and cell chemistry can greatly influence the thermal behavior of the cell. Generally, heat generation can be divided into reversible and irreversible parts. The reversible parts result from entropy changes during the intercalation and deintercalation of the lithium ions. The irreversible parts are, in particular, the occurring resistive (joule) heating. Further, at the system level often negligible parts occur from

intracellular side reactions. Derivations and methods to determine different heat losses can be found in [98, 99].

In order to describe heat release as a transient function of power or current, electrical equivalent circuit models (ECM) are often used. With ECMs, the electrical behavior of LIBs can be described in sufficient detail for numerous applications. Additionally, ECMs are useful electrical surrogate models in large simulation models because of their short computation time.

Multiple RC circuits can be used to electrically describe the battery cells and their dynamic behavior in a simplified way. Figure 2.6 illustrates a 2-RC model with a corresponding schematic voltage drop for a pulse current. Cell-specific electrochemical impedance spectroscopy (EIS) is used to condition these RC models. Several measurements with dependencies in SOC and temperature are performed for model generation. Further recent investigations and general comparisons about different RC models and EIS measurements can be found in [100–102].

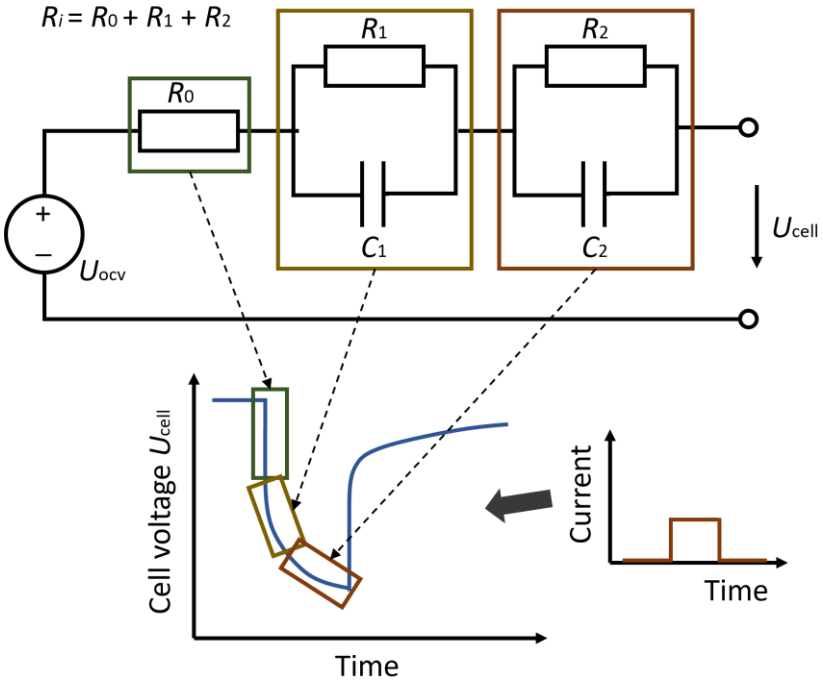

Figure 2.6: Schematic of 2-RC-Model for a lithium-ion battery cell and corresponding cell voltage diagram for a current pulse.

2.2.2 Thermomanagement in battery system engineering

In order to ensure optimized performance and the longevity of the battery system, the battery cells must be optimally tempered. In EVs, a battery thermal management system (BTMS) is therefore used to control the temperatures [103]. For most types of LIBs, an operating temperature range of -20 °C to 60 °C applies. Outside these limits, the risk of severe aging or even destruction of the battery cell due to thermal propagation increases drastically. A smaller temperature range is usually recommended to ensure optimal performance [104]. In order to additionally ensure temperature homogeneity of the individual cells within a module or system, minimizing

cell temperature differences should also be taken into account when designing the cooling system. The literature recommends average temperature differences within one operating cellmodule to be kept below 5 °C [105]. However, this difference can be significantly increased while fast charging [98].

When evaluating heat generation within the battery, a distinction can be made between profiles describing real vehicle cycles and intensive charging processes using fast-charge profiles. In recent developments, fast charging is often considered particularly challenging for temperature homogeneity and total cell load [106]. This makes fast-charging capability one of the core design premises for the cooling circuit.

In order to effectively transport the heat release from the cell, module, and battery system, a number of design criteria have to be considered for the design of the BTMS. Air, coolant, refrigerant, or combinations of fluids can be used to transport the heat losses from the cell to the ambient [107]. While air cooling is an inexpensive and practicable approach, it is significantly less effective than liquid-cooled systems [98]. Due to the increasing demand for higher energy and power densities, a powerful cooling system is becoming more and more important. Therefore, liquid cooling systems are the most commonly used cooling methods in today's EVs (e. g. Chevrolet Bolt, Tesla Model S, BMW i3, and BMW i8) [108]. Exemplary liquid flows for different battery systems can be observed in the work of White et al. in [109].

Nevertheless, the choice of fluid also directly influences the connection options of the cells to the cooling fluid. A distinction can generally be made between direct and indirect cooling connections. In direct cooling systems, the fluid is directly in contact with the cellmodule. Examples of direct cooling are air cooling or liquid immersion cooling systems. The advantage of the method is its high effectiveness in heat transport. Indirect cooling systems use cooling plates in which the fluid flows. The cooling plates are thermally connected to the cell or cellmodule using different gap fillers or gap pads. The advantage of indirect cooling is the distinct separation of wet and dry battery system areas. When designing an optimized cooling plate, the following interdependent design criteria must be taken in particular into account [110–114]:

- Pressure loss-dependent cooling plate design: Optimal cooling channel routing and geometry of the cooling tubes determine the necessary fluid volume flow rate. A suitable water pump must be selected based on the corresponding cooling plate design. Additionally, the orientation of the cooling channel depends on the module geometry. Furthermore, other production-specific requirements, such as minimal tube-to-tube distances, must also be considered.

- The flow routing of the cooling channels describes how the cooling channels are distributed to the individual battery modules. A distinction is often made between different flow paths (parallel, perpendicular).

- The number of passes of each cooling tube along one cellmodule can be modified.

- The cooling channel geometry depends on the available installation space and is also subject to production constraints.

- Different thicknesses and types of gap fillers are used to optimize the thermal connection from the cooling plate to the cellmodule.

Figure 2.7 shows a schematic diagram of a cooling system with indirect active liquid cooling.

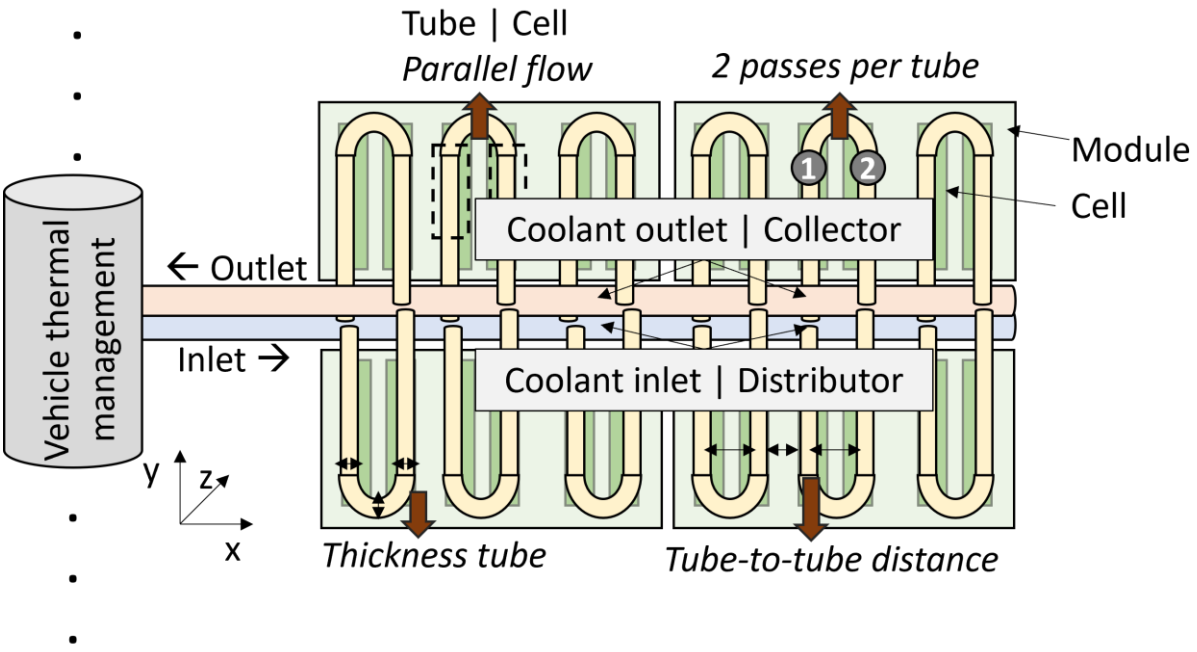

Figure 2.7: Exemplary cooling plate with different design parameters and construction sizes.

BTMS concepts with water/glycol-based coolant offer various integration options within the vehicle. Often, a combination of two circuits is used. On the one hand, the coolant temperature can be lowered to lower ambient temperatures using the low-temperature cooler circuit. On the other hand, the coolant temperature can be adjusted by the vehicle refrigerant using a chiller. Using the vehicle's air conditioning circuit is particularly important at high ambient temperatures to ensure a low inlet temperature of the coolant in the battery system. If battery heating is required, the coolant can also be heated using, for example, a positive temperature coefficient (PTC) heater [115, 116].

In addition to the combination of coolant and refrigerant circuits, a direct refrigerant cooling circuit can also be used. Thereby, the refrigerant evaporates inside the cooling channels to transport the heat from the battery system. Refrigerant cooling is used in the BYD Dolphin [117].

Compilations, advantages, and disadvantages of different cooling configurations are summarized in the work of Deng et al. [115] and Xia et al. [118].

Various numerical model approaches can be used to evaluate thermal behavior. Examples are computationally expensive 3D thermal models or simplified lumped parameter models. The general advantage of lumped mass models lies in lower computation times and simple coupling with further electrical or electrochemical models [119, 120].

2.2.3 Mechanics in battery system engineering

The safety of vehicle occupants plays a special role in the design of vehicles and also in the design of the battery system, which is additionally protected by legal framework conditions. The safety measures can be divided into two large groups. One is active safety, and the other is passive safety. Avoiding collisions before they take place refers to active safety systems, whereas passive safety systems are used to minimize the impact of an accident during a crash. These include airbags, safety belts, and the crumple zone [121]. In the ideal design, two fundamentally contradictory requirements apply to the passenger compartment. Rigid structures are needed for the passenger cell to protect the occupant, while flexible structures like the crumple zone are used to dissipate the crash energy via plastic deformation [122]. The battery system of battery electric vehicles is usually installed in the underbody of the vehicle and thus represents a direct part of the vehicle mechanics. For this reason, the battery system must be matched to the vehicle's mechanical requirements.

When a metallic structure is deformed by an impact or collision event, kinetic energy is converted into internal energy. The deformation of the structure can be divided into two different mechanisms. Elastic deformation is reversible, and after reaching the state of maximum deformation, springback occurs in which the elastic deformation regresses. Plastic deformation, on the other hand, is irreversible and occurs in metallic structures due to a migration of dislocations at the atomic level. During this process, the energy required for plastic deformation is converted into thermal energy [21].

An exemplary force and displacement curve is depicted in Figure 2.8. The maximum force $F_{\mathrm{max.}}$ is reached early. Afterward, the force is nearly constant until the maximum deformation of $x_{\mathrm{max.}}$ is reached. Elastic deformation lowers the absolute displacement afterward. The integral within the curve can be described as the energy absorption of the structure [123].

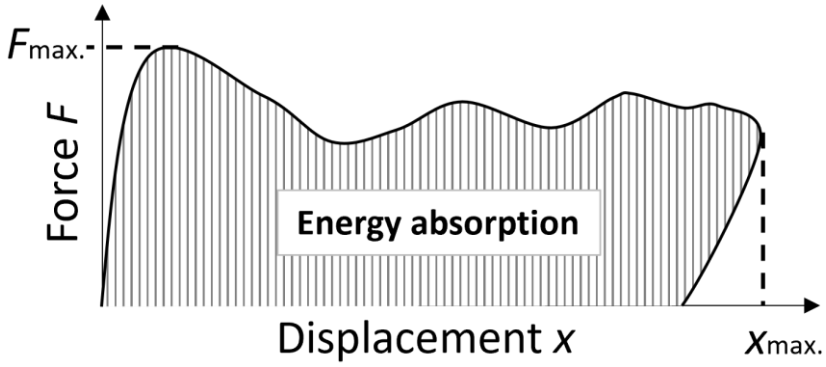

Figure 2.8: Basic force-displacement curve for a deforming structure.

The maximum force that a crash structure can generally withstand is limited, for example, by the fact that exceeding a critical force will damage other structures of the vehicle or connection technology, such as welding points. In addition, forces suffered by the vehicle or crash structures are directly related to the acceleration or deceleration of the occupants, which should be as low as possible in the event of an accident. The maximum deformation path, on the other hand, is limited by the available deformation and installation space. Automotive manufacturers use a number of load cases to design individual crash structures and complete vehicles according to passive safety

aspects: e.g., front and side crash, crush, rollover, and vibration [123]. More details and country-specific crash lists can be found in [124].

In order to test the load cases for a defined structure, finite element methods (FEM) are often used. In a FEM model, various mechanical relationships, which can be mathematically calculated using numerous differential equations, are solved coherently. For this purpose, the component is discretized into finite elements. Generally, the number of elements influences the result's accuracy potential. Nevertheless, FEM is always an approximation method. The individual elements are interconnected at nodes, where, e.g., forces are transferred. During the calculation process, the node displacements and rotations are determined. The resulting stresses due to external forces are calculated using kinematic relationships and material laws. Afterward, interpolation with neighboring elements is used [125–127].

Different unique parts have to be interdependently optimized to design the mechanics framework for the battery system. Next to the top and bottom cover plate, design optimization can be performed explicitly regarding the thicknesses and shape of the outer battery frame profile. Additionally, cross and side members are used to increase the system's stiffness. The resulting box-shaped space is used for the cellmodules or the electronics within the battery system.

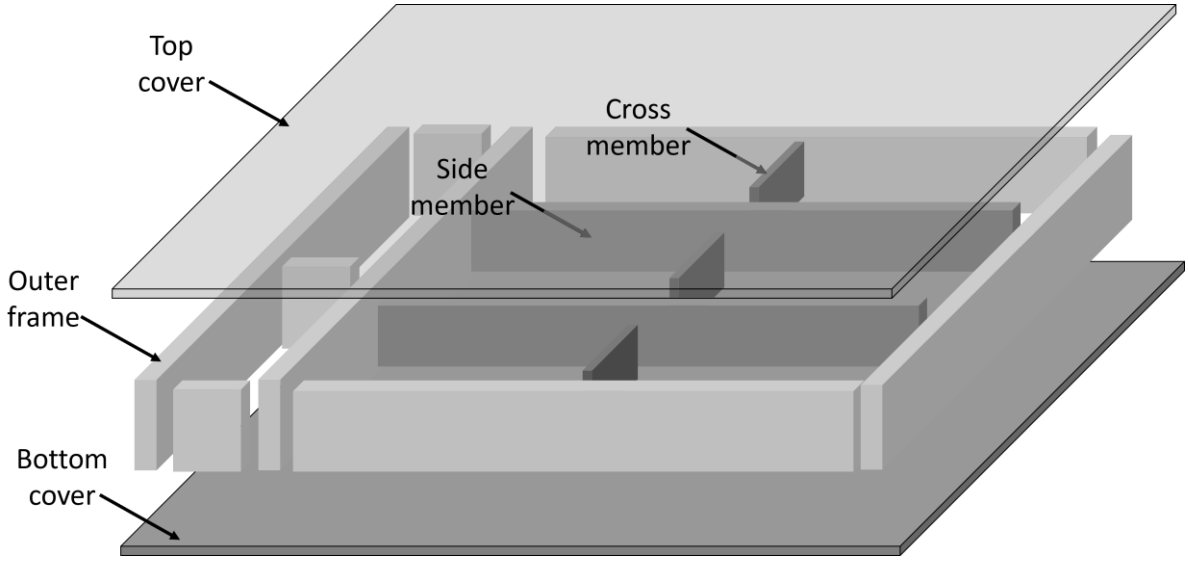

Figure 2.9: Basic mechanical components for a battery system.

Another important role for reliability and robustness is the material choice for the mechanical parts of the battery system. Aluminum is widely used as a lightweight metal and is especially popular due to its rigidity and low cost. Furthermore, high temperatures can be managed well from the metal case and even facilitate efficient cooling of the battery modules and cells. Table 2.2 presents examples of the materials used for battery housing in different vehicles.

Electric vehicle	**Main material used for battery system housing**
Tesla Model S	Aluminium
Honda Fit EV	Steel
Chevrolet Volt	Steel
BMW i3	Aluminium

Table 2.2: Overview of the main material used for the battery system housing in different commercial cars. Data from [21].

Recent developments show that mechanical stability can be further increased by integrating the battery cells as a mechanical unit. Examples are the Blade battery system with the blade cell from BYD [128] or the cell to pack Qilin battery from CATL [129]. Cell to pack, cell to chassis, or cell to car systems require direct integration of the battery cells into the battery system or even the underbody of the vehicle. The cell's mechanical behavior must be precisely known when using the battery cell as a mechanical unit. Thereby, module housing structures can be made narrower or even omitted. These measures can save weight and costs [24, 25, 130, 131]. One obvious measure to integrate the cell within the battery pack is to glue it directly into the battery housing. However, this makes disassembly almost impossible and thus effectively precludes a replacement or partial repair of the battery cells or stacks. In the future, an EU regulation will specify the level to which a traction battery must be replaceable and thus also repairable and recyclable [132].

2.2.4 Electronics in battery system engineering

The electronics for the EV’s traction battery play an important role in the proper and efficient operation of the battery system. Intelligent and optimized operation of the traction battery increases reliability, safety, and the ecology of the battery system. Furthermore, it is responsible for the safety and monitoring of the individual cells within the battery system.

In particular, in the event of an error, for example, from a crash, the battery must be switched off quickly to protect the vehicle occupants and enable any necessary rescue. This task is usually performed by a battery junction box (BJB). The BJB is often also named battery disconnect unit or E-Box. The main passive components are contactors (relays), fuses, current sensors (shunt or hall sensors), capacitors for load shedding, and a pre-charging circuit (consisting of a resistor and contactor). Additional interfaces in the form of connector strips provide the connection between BJB and the battery [133]. The overall package also requires a good seal and an easily accessible cover to minimize susceptibility to faults and ensure good repairability. In some cases, the BJB also has a cooling concept that is separate from the battery system.

The electronic control unit is the battery management system (BMS). The BMS is subdivided into cell management controller (CMC), module management controller (MMC), and battery management controller (BMC). Due to the hierarchical structure, individual variables can be combined and monitored at different levels. Therefore, the BMS monitors temperatures, currents, and voltages within the entire battery system and initiates any necessary switching operations of the passive components described above. Furthermore, necessary cell balancing is operated by charge and discharge control between individual cells. In addition, the SOC of the cells can be used to evaluate the expected remaining vehicle range. Together with the passive components, the BMS represents the electronic control unit of the entire battery system [50, 134].

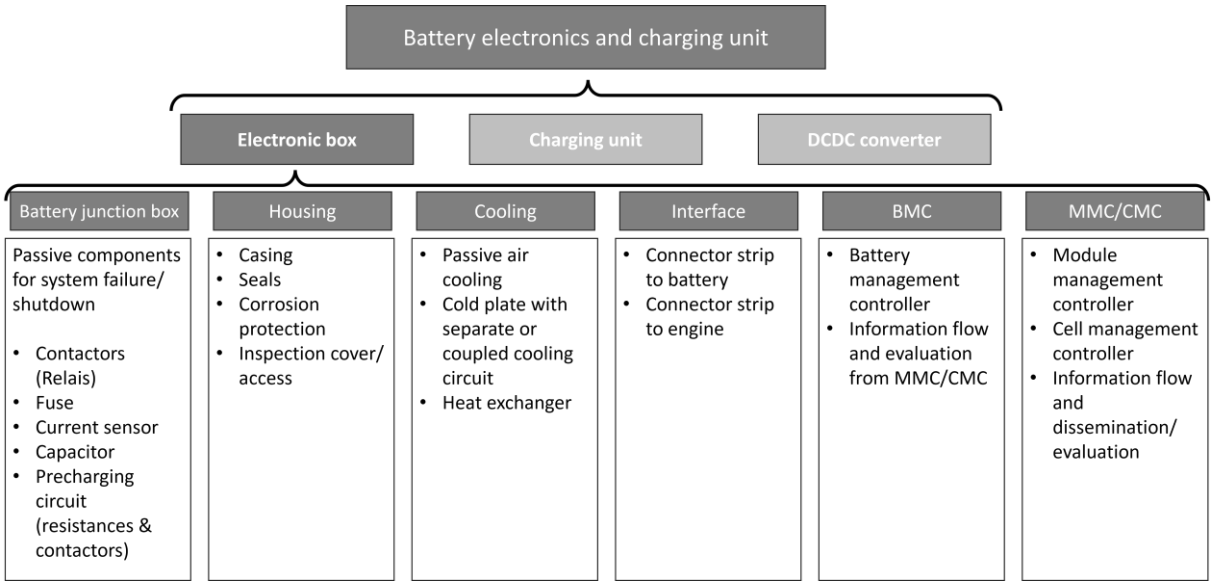

Figure 2.10: Breakdown of battery electronics in EV battery systems.

2.3 Optimization methods

The terminology optimization describes the search for the best result of an objective function with the help of mathematical procedures, heuristics, or other algorithm-based methods. An essential challenge for the realization of optimization is to firmly define the optimization problem with the help of the objective function and often multiple constraints. The problem must be written mathematically in such a way that, on the one hand, the technical problem to be examined is suitably represented and that, on the other hand, the best solution exists which can be solved in a computing time appropriate to the technical problem [135, 136].

Optimization problems can be classified by the types of variables used to describe the initial problem. A distinction is made between integer, continuous, and mixed integer optimizations. In general, an optimization problem can be described by some function

$$\begin{gathered} f: V \to \mathbb{R}: \\ \underset{x}{\text{minimize}}\, f(x) \\ \text{subject to } g_i(x) \leq 0, i = 1, \ldots, n \\ \text{with } x \in V. \end{gathered} \tag{2.2}$$

In addition, a distinction is made between different classes of optimizations. Linear optimizations are characterized by a linear objective function and the linear representation of the constraints for a system. A widely used solution methodology for linear problems is the simplex method.

Much more common in science and engineering and, at the same time, more difficult is handling nonlinear optimization problems, where the objective function, constraints, or both are nonlinear. Examples can be typical cost or weight optimization of parts,

components, or systems. Nonlinear influences of different parameters or constraints on the decision variables lead to nonlinear optimization. Solving nonlinear optimization problems is generally associated with significantly more challenges [137, 138]. For this purpose, different evolutionary or gradient-based algorithms can be used, but also machine learning provides promising possibilities [139]. The applied methods often use an iterative approach to converge to the optimal solution. A general iterative optimization procedure is illustrated in Figure 2.11. One common solution method for nonlinear problems is based on dividing the total solution space into several subdomains. If the individual subdomains are differentiable and convex, a local minimum can be found using gradient-based methods. Local minima of the other subdomains can then be compared to each other. Uncertainties and challenges can be found, for example, in the quality of the search for the local minima as well as in the computation time-adjusted partitioning of the subdomains. Machine learning algorithms can help to evaluate and subdivide the solution space by previously considered points [140].

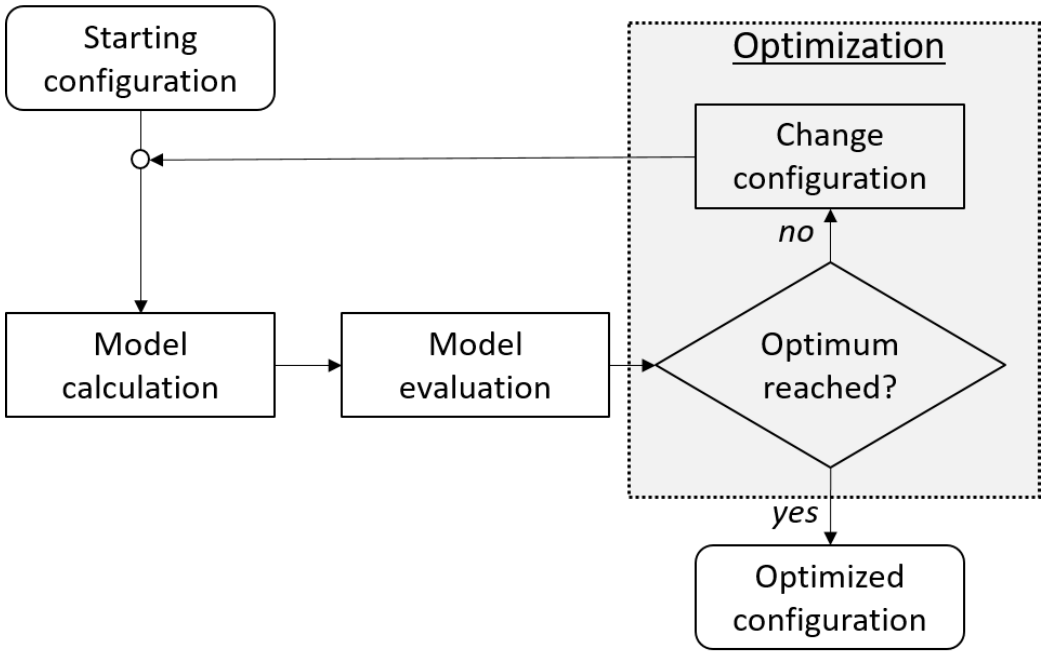

Figure 2.11: Schematic flowchart of iterative optimization.

2.3.1 Machine learning

Artificial intelligence as a terminology was first defined in 1956 by McCarthy, Minsky, Rochester, and Shannon at the Dartmouth Conference [141]. The term describes machines, robots, or software systems that take on complex tasks independently, without being given each individual step. Machine learning is a subfield of artificial intelligence and has been recognized for decades as an established field of research with rapid growth.

In general, machine learning terminology encompasses all methods that use defined learning processes to identify relationships in existing data sets to make predictions for further data points [142]. The areas of application for machine learning continue to grow. Machine learning models aim to make future-relevant conclusions or predictions based on self-learning effects with previously existing data without having to be

explicitly specified. The algorithm can therefore adapt and improve itself based on the input data. The data can be of different types, e.g., continuous, integer, or binary. Generally, machine learning is divided into the following three categories: supervised, unsupervised learning, and reinforced learning [143].

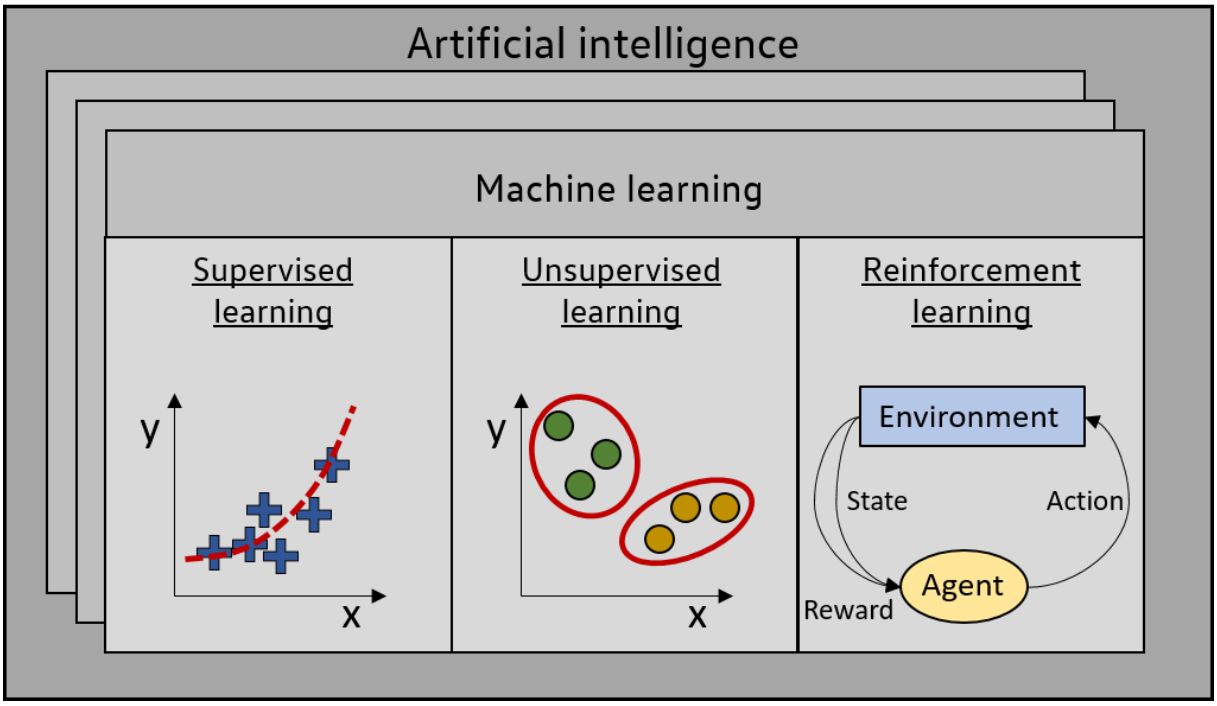

Figure 2.12: Overview of the sub-areas of machine learning.

Unsupervised learning refers to the method of machine learning in which the algorithm learns to recognize patterns and relationships in the given data independently and without supervision. The input data has no predetermined target variable, which means the desired output data is not predetermined. Unsupervised learning helps detect unknown patterns or categorizations in any data type [139, 143].

Reinforcement learning finds solutions and strategies to complex problems based on a trial-and-error process and rewards received for specific actions performed. Unlike the other learning methods, no initial data is required to train the learning system (agent). The knowledge is thus created during multiple different optimization iterations. The algorithms aim to maximize the rewards received. The individual actions are not predefined but are determined by the utility generated from the rewards received. Reinforcement learning is similar to human learning and uses, for example, artificial neural networks [143].

The goal of the supervised learning procedure is to predict the output value with as high an accuracy as possible using the available input values. In order to validate the model parameters on previously unknown data, the entire data set is divided into a training set and a test set. The actual learning process for predicting the target variable is based on the training set, whereas the evaluation of this trained model is performed using the test data set. This ensures that the evaluation variables, such as accuracy and error rate, are determined with data from the test set that is unknown to the model. Furthermore, hyperparameters can be used to adjust the learning algorithm to increase the model's goodness [139, 143, 144].

2.3.1.1 Bayesian optimization with Gaussian process regression

A common supervised learning method is the interpolation method based on a Gaussian process controlled by prior covariances. This procedure, called Kriging, is also known as Gaussian process regression (GPR) and is often used within Bayesian optimization. For unknown objective or model functions, Gaussian process regression can approximate the objective function by interpolation, extrapolation, or smoothing. Bayesian optimization is commonly used when evaluating the objective function is time-consuming, leading to only a limited number of possible function evaluations. Based on the approximated GP-based model, the point selection within an iterative optimization can be determined [145]. The iterative Bayesian optimization procedure is shown schematically in Figure 2.13.

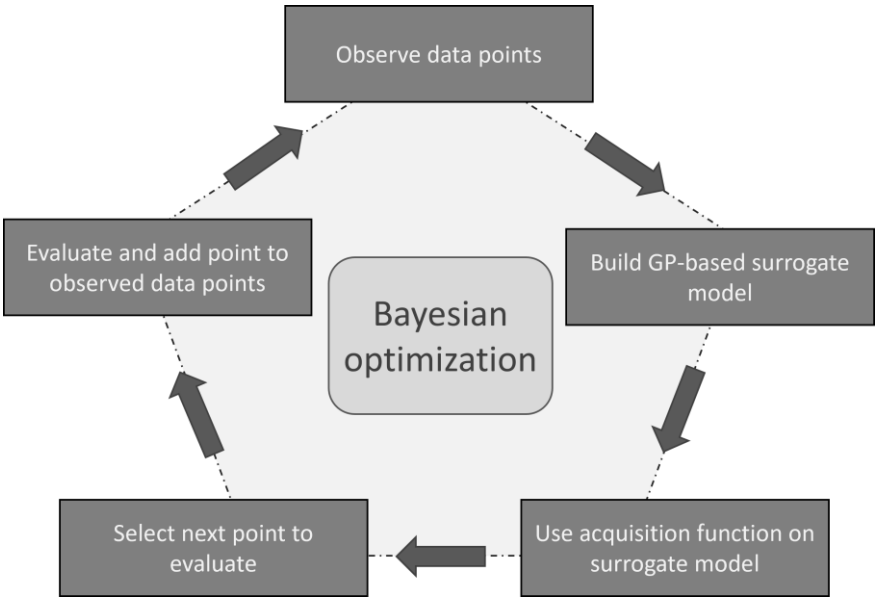

Figure 2.13: Procedure of Bayesian optimization with Gaussian process regression.

GPR methodology is based on Gaussian processes (GP) that are controlled by the covariance function. The GP model represents a probability distribution of the possible interpolation functions that can be used to derive the solution with the highest probability. The following steps describe the basic working principle of the Gaussian process regression model [146]:

- By forming the a priori expected value function, the regression problem is first estimated. A trend or offset of the total data known in advance can be determined.

- The a priori covariance function, also called the kernel function, is set property-specifically according to the nature of the optimization problem. By hyperparameter tuning, the parameters of the covariance function can be specifically adapted to the optimization problem.

- The already evaluated points of the unknown objective function are used to determine the conditional a-posteriori Gaussian process for new points from the a priori Gaussian process to subsequently determine the expected value as well as the location-dependent variance for each point.

If the estimated GP model of the total solution area is available, the next step in Bayesian optimization is to select the next query point to be evaluated. However, since the actual objective function is unknown and only the approximation based on a covariance function is available, the next query point must be selected based on the expected value and location-dependent variance. An example of this is shown in Figure 2.14.

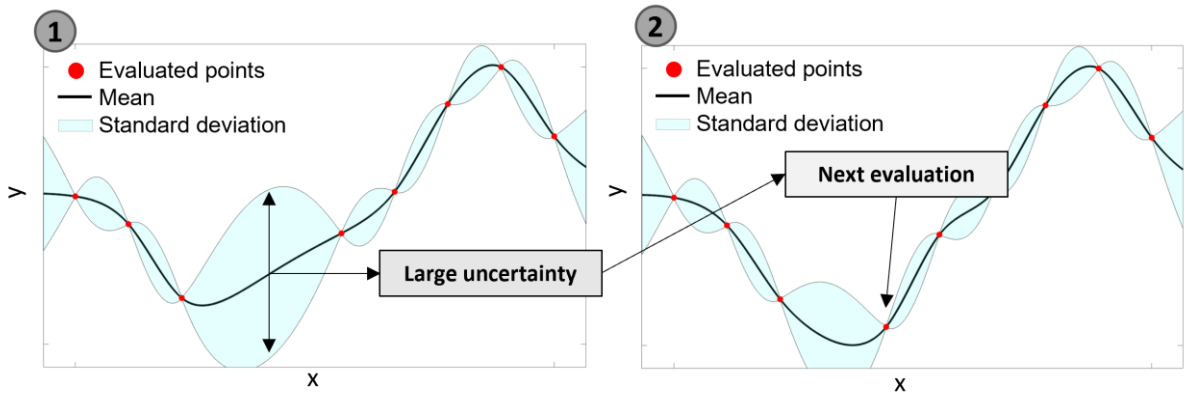

Figure 2.14: Query point selection for an exemplary GPR model.

Different procedures, named acquisition functions, for the query point selection are frequently used in the literature [147]:

- Selecting the lowest expected value.
- Selection of highest standard deviation (upper confidence bound, lower confidence bound).
- Combination of the expected value and the standard deviation (Expected Improvement, Probability of Improvement).
- Selection of highest differential entropy (see, e.g., [148]).

The various acquisition functions must be selected problem-specific, as they pursue different goals and can be associated with higher computation times. Here, the trade-off between exploration and exploitation plays a decisive role, which is shown schematically in Figure 2.15. While exploration allows a better search of the overall solution space and the identification of promising solution regions, exploitation scans smaller solution spaces in great detail [145].

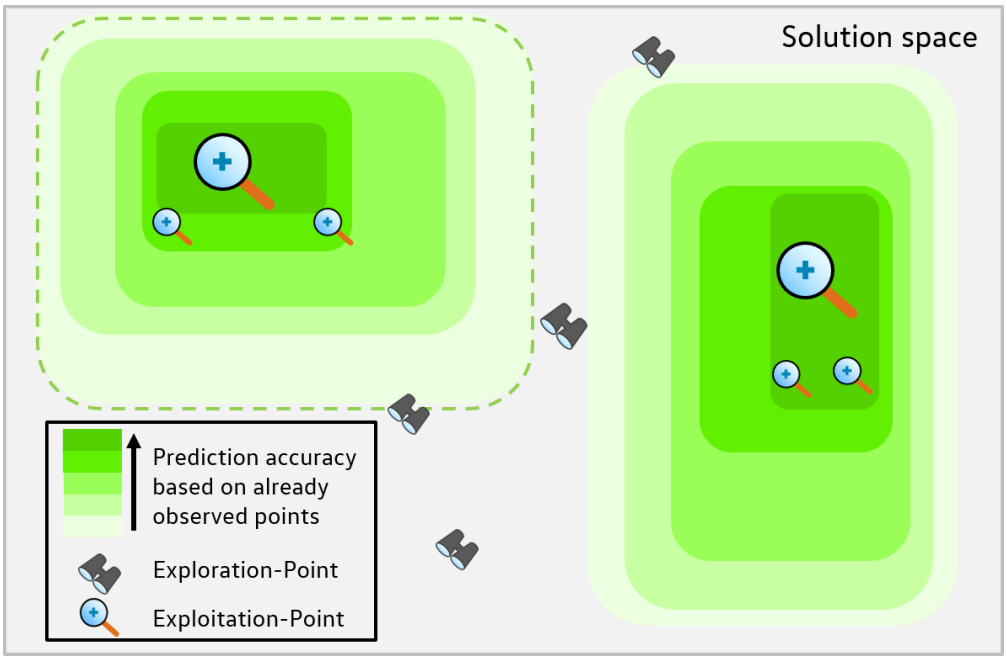

Figure 2.15: Basics of exploration and exploitation in optimization algorithms.

Different acquisition functions can be useful at different times in the optimization, for example, to scan the overall solution space first and search deeper in certain attractive solution areas later in the optimization.

A more detailed derivation and description of Gaussian process regression and various acquisition functions can be found in [145].

2.3.2 Parallelization

In order to carry out optimizations even more efficiently, several data points can be evaluated in parallel in the program instead of the continuous evaluation of one data point. Often, one execution of the initial model is performed on each logical core of a computer. The main goal of parallel optimization is to obtain more target function evaluations per time unit and, thus, more knowledge gain per time unit [149]. The basic parallelization principle is illustrated in Figure 2.16.

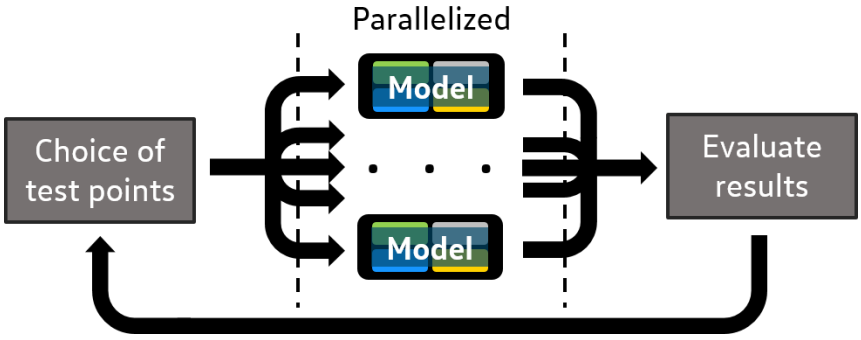

Figure 2.16: Basics of parallel computing.

The necessary steps in direct comparison to the non-parallel approach are, in particular, the setup of the parallelization process, which can be divided into three major areas:

- Definition of the points to be tested in parallel. It must be ensured that no redundant points are evaluated.
- Performing the parallel objective function evaluation.
- Merging and evaluation of the individual results.

In order to make parallelization efficient, the parallelization process must be designed optimally [150]. Figure 2.17 gives a schematic example to emphasize occurring problems in non-efficient parallelization. A detailed review of parallel computational optimization can be found in [151].

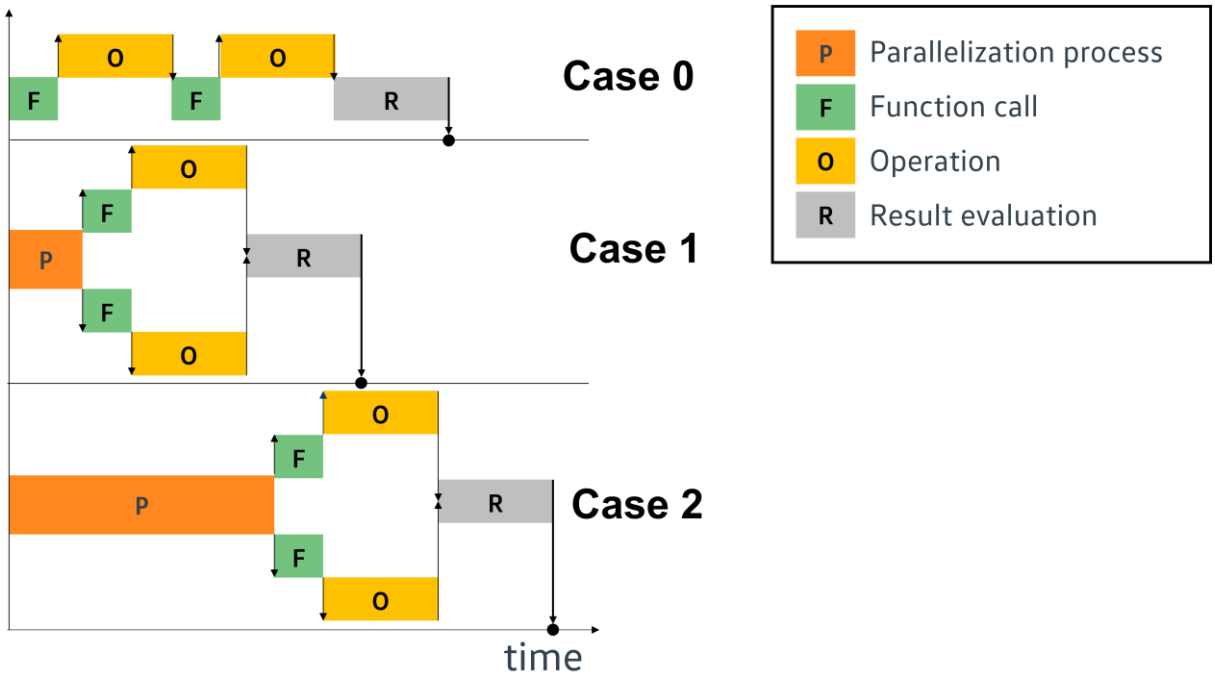

Figure 2.17: Schematic comparison for serial computation (Case 0), beneficial parallelization (Case 1), and non-beneficial parallelization (Case 2).

2.4 Integration of battery system concept development within the vehicle product development process

In this chapter, the contents of this thesis are to be placed in the overall development process of automobiles. The basis is the concept of a product development process (PDP) commonly used in the automotive industry.

The product development of new automobiles is a highly complex balance between innovation, cost-reduction, and development speed. The main objective of the process is to develop a vehicle that is attractive to customers at the time of completion. Thereby, the product's attractiveness must be so high that customers are willing to pay a price for the vehicle that overcompensates for the previous development and production

process costs [152]. This complex process involves a large number of participants with many different competencies. The PDP includes a milestone plan that can be broken down into the phases: product planning, concept phase, series development, and production (see Figure 2.18).

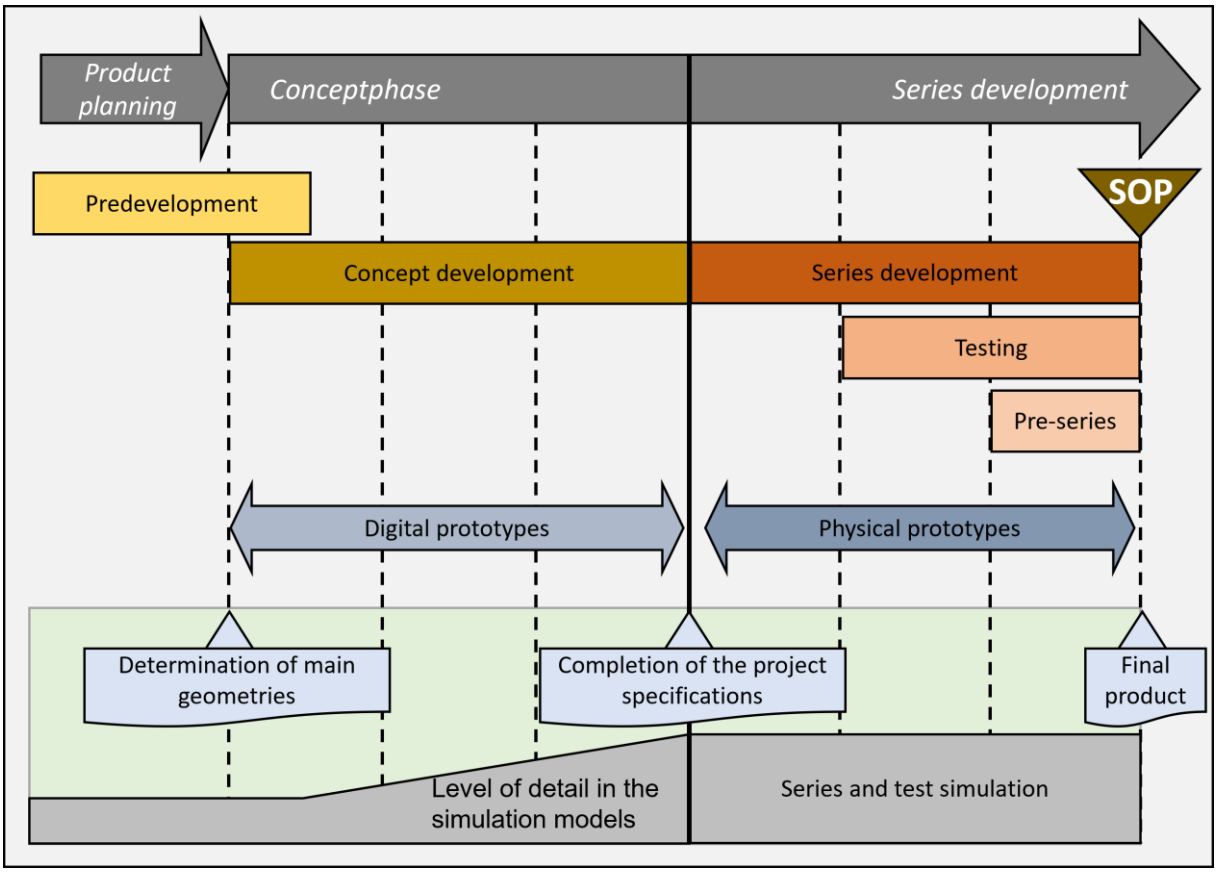

Figure 2.18: Schematic representation of development phases in the product development process with different project phases to start of production (SOP). Own graphic, adapted from [153] and [154].

In the product planning phase, the essential features and requirements of the end product are defined on the basis of various market analyses together with the development team involved [155]. In the subsequent concept phase, the first evaluations on concept implementations are pursued. Hereby, the main task is to work out a concept based on the previously defined requirements and to prove the feasibility of this concept. This process is time-critical, as requirements can quickly change if there is a delay within the development process. Findings from predevelopment, e.g., simulation models, can be used to support the development of the concept. Virtual prototypes can additionally verify the feasibility of concept stages. The concept phase ends with the decision and definition for a final concept with fully defined product specifications. Subsequent concept changes can often only be implemented at high technical risk and with an additional financial expense. Therefore, high-quality product specifications from the concept phase are crucially necessary.

For this reason, targeted tool development for evaluating and illustrating concepts is of particular importance for the early phase and can generate a strategic competitive advantage. Tools to be used must be generically adaptable in order to be able to evaluate development changes quickly. Simulation models can be used to derive

changes in space allocation, resulting geometry changes, and their influence on the physical properties of affected components within a short period of time [156].

After the concept phase, the series development optimizes the fully defined concept into a finished product with the help of several sample stages. Physical prototypes can additionally ensure feasibility. With the start of production (SOP), the ramp-up of series production starts. Further literature on the automotive PDP can be found in [157].

An additional way to accelerate the development process is to standardize individual components that have already been developed and can be used again in the new vehicle project. Different individually designed hats are used to provide a vehicle portfolio based on just one platform. This allows individual platforms to serve entire vehicle families and thus significantly reduce vehicle development costs [158]. In addition, the concept of carry-over-parts (COPs) allows the adoption of, e.g., large parts of the powertrain directly into the new vehicle. COPs eliminate the need for new developments and can also enhance brand recognition through, e.g., interior elements or brand-specific driving dynamics [159, 160].

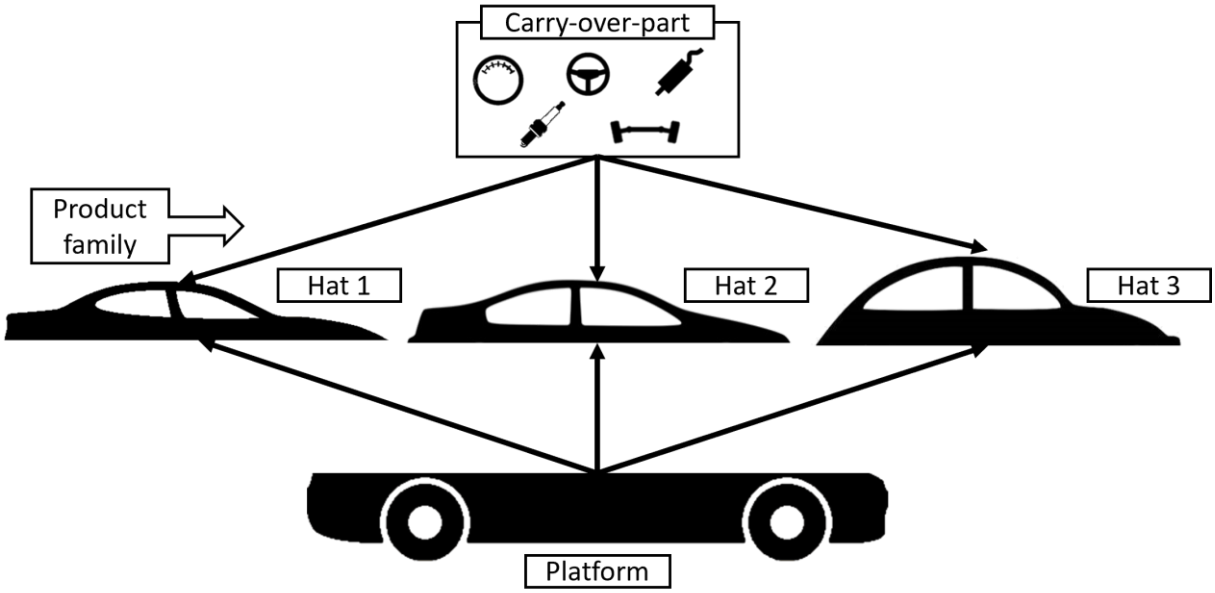

Figure 2.19: Relation between automotive platforms, hats, and carry-over-parts.

3 Multiperspective optimization of cell and module dimensioning for different lithium-ion cell formats

Parts of this chapter are published in a journal article [161] as part of this thesis. This chapter contains minor modifications and extensions with respect to the original publication. The use of the article content, including illustrations, is permitted with the consent of Wiley-VCH.

The main challenge in developing electric and electrified vehicles is the drivetrain with the associated battery system. Within the battery system, individual modules consisting of multiple interconnected battery cells provide the engine with power and energy. A crucial part of developing the electric vehicle's battery is the optimized dimensioning of modules and cells. Therefore, designing a unified cell format may be a competitive advantage for original equipment manufacturers (OEMs) in rapidly changing market situations. Different constraints, such as peculiarities of different battery formats, module sizes, or required module voltages, must be evaluated for optimized battery cell dimensioning.

This chapter provides a holistic cellmodule optimization based on geometric and generic assumptions. The presented model considers various factors like cell format-dependent geometries and their limits, cell-size specific cell-to-cell stacking distances, as well as module geometries and voltage requirements. An application-dependent energy and cost perspective analysis is provided that results in a user-defined weighting model to optimize the cell format and its corresponding dimensions. Furthermore, the optimized module dimensioning for prior-specified cells is introduced. Pareto-optimal results within this analysis are discussed and enable the generic cellmodule optimization to be used in higher integrated battery system optimization models.

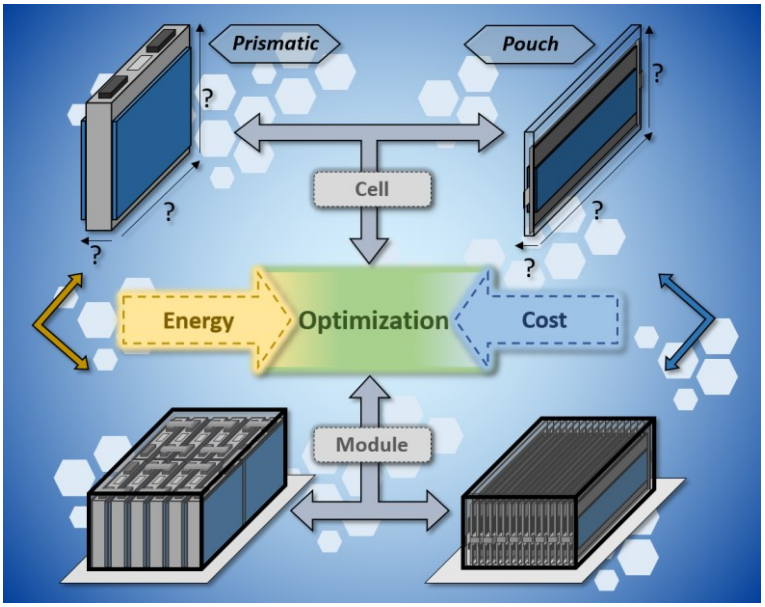

Figure 3.1: Graphical abstract of cellmodule optimization framework.

3.1 Introduction and scientific integration

Electric vehicles are an essential part of bringing the mobility CO_2-emission to lower levels and ultimately reaching the Paris Climate Agreement [162, 163]. In recent years, EVs received considerable attention leading to car manufacturers announcing new electric platforms and cars among all the different car classifications from A- to F-segment. Already, EVs have achieved annual record sales for the last few years [28, 164–167]. Yet, they are still relatively expensive, leading to different states subsidizing electrified cars to make them more attractive to customers [31]. One major reason for EVs being more expensive than the alternative combustion engine version is the still expensive battery system. Thus, the “e-version” of a car can cost up to 75% more than its combustion engine alternative, like the Opel Mokka and Mokka-e [168]. Although cell costs have massively decreased over the past years, individual battery cell costs still play a significant role within the battery system’s summarized cost [167].

As the lithium-ion battery has continuously improved over the last years, it is often already considered a quite mature developed product. While improvements have mostly been made at the component level, huge cost reduction still lies in the system engineering process when integrating multiple cells in bigger applications like EVs [23]. In general, cell integration has to address a variety of challenges, from mechanical, electrical, and thermal engineering [169–171]. Whereas high power and energy are still one of the most important claims of customers, car manufacturers set goals on reducing passive components within the battery system to reduce its weight and general environmental impact while increasing its energy and power density [172, 173]. As the next evolution of the LIB with the solid-state battery is not yet ready for market entry, car manufacturers like Tesla [174] and Volkswagen [175] recently started announcing extensive provisions to increase range, power, and safety while still reducing the costs of their EVs. One major emphasis lies on promising unified cell formats, with which it may be possible to equip a wide set of EVs within the manufacturer’s car portfolio. Through a firmly defined unified cell, manufacturing equipment can be set at optimal cost, and new EVs with different specifications can be designed around this cell. However, to enable this competitive advantage, the unified cell must be tailored to the manufacturer’s requirements and meet the balancing act between energy density, cost, and external specifications, such as the required voltage level within the cellmodules. At least three different types of LIB cells can be identified in the automotive industry [20, 173]. First, the often rather small solid-housed cylindrical cells, usually in a standard format of 18650, 21700, or Tesla’s newly announced 4680. Second and third, larger-format cells like the soft-housed pouch cells as well as solid-housed prismatic cells. In contrast to the cylindrical cell format, no standardized pouch or prismatic cell geometry is defined. Yet, the standards ISO/PAS 16,898:2012 and DIN 91,252:2016–11 define some general regulations [20, 176]. Differences between utilization rates, dimensions, mechanical structures, and costs are summed up in Table 3.1.

Category	Pouch Cell	Prismatic Cell	Cylindrical Cell
Utilization rate [22, 34, 177–181]	Medium energy density on cell level; Medium packaging efficiency on module and pack level	Lower energy density on cell level; Higher packaging efficiency on module and pack level	Higher energy density on cell level; Lower packaging efficiency on module and pack level

Dimension possibilities [182, 183]	No standardized but usually thin cell size; Often large-format cells	No standardized cell size; Often large-format cells	Most common: 18650, 21700, 4680; Often small-format cells
Mechanical structure [22, 184]	Low mechanical stability; Thermal propagation difficult to control due to often missing gassing vent	High mechanical stability and stiffness; Flexible gassing vent positioning	Highest mechanical stability; Robust to high internal pressures
Cell costs [185–188]	Medium	Often higher, especially for small cells	Often lower, especially for large cells

Table 3.1: Comparison of the three mainly used cell formats in different categories.

Battery systems are usually built from numerous individual battery modules. The battery modules contain the battery cells that serve the EV's engine with energy [189]. In addition to an easier scaling of the battery system, the modular construction of the cell, module, and system can improve in-operation monitoring and reduce repairing efforts [21, 190, 191]. One often-mentioned example of modular battery system construction is the Modular Electrification Toolkit (MEB) by Volkswagen [192]. When developing new unified cell formats, it must be noted that the optimal battery module size may correlate with the chosen cell format and dimension [20]. While battery cell performance is usually measured using health, energy, and power indicators, performance rating on the pack level also includes optimized packaging, system integration, and topology [193, 194].

Various analyses of battery cells and their module and system integration have been presented in the literature. Thereby, several studies with individual cell formats or cell sizes focus on different objectives, such as electrical integration [51], aging [195–198], thermal management [199–201], or mechanical integration [202]. Löbberding et al. consolidate the energy densities of various cell formats at the different integration stages from the cell to the module to the system level [34]. Lensch-Franzen et al. report the challenges of cell integration on the system level [184]. Saw et al. additionally show the differences between various cell formats in system integration [22]. Large prismatic cells are found to be advantageous, especially for the utilization ratio within the module. Furthermore, their results also show that battery systems with high voltages and large cells can have advantages in assembly, thermal management, monitoring, controllability, as well as service, and maintenance [22]. Pierri et al. present a cell integration optimization into a given module size considering four different cells resulting in nine different configurations [177]. Reiter et al. use a framework for cell selection, modularization, and thermal management. Particular emphasis lies on the cell connection of serial and parallel connected cells without addressing the resulting achieved system energy density [203].

Previous studies often use only a few or even just one exemplary cell to draw conclusions regarding the entire cell format and its general performance in the battery system. Furthermore, module dimensions are usually considered fixed, and restrictions regarding, e.g., the module voltage or cell topology, are not being observed.

Aiming to bridge this research gap, this chapter sets the following summed objectives:

- How to optimize the battery module dimension given a fixed-sized cell and certain voltage restrictions (Chapter 3.4.1).

- How to optimize the battery cell dimension given a fixed-sized battery module (Chapter 3.4.2).

3.2 Model motivation

In order to meet the restrictive installation space limitations for battery systems, components must be selected optimally not only in terms of energy, performance, and costs but also geometrically. As the main component of battery systems, the battery cell geometry must be matched to the associated module configuration. The occurring problem can be stressed by stacking random cell geometries in different total module geometries. Figure 3.2 depicts the results of a 2D stacking model for different cell geometries within multiple module geometries. Three example cell sizes were assumed and stacked in the battery module without any restrictions regarding module energy or voltage. Different module sizes are depicted in the x- and y-axis of the figure. Based on the resulting utilization rate, the best cell geometry for the respective module size can be seen in the upper left part of the diagram. In the lower right part of the diagram, the actual corresponding utilization rates achieved by the best cell geometry are shown. This utilization rate is defined as the utilization space of the cells divided by the total module space. The z-axis was not considered for this illustration. A diagonal axis divides the two surfaces since the results are mirror-symmetric. The illustration emphasizes how the optimal cell format changes depending on the selected module size.

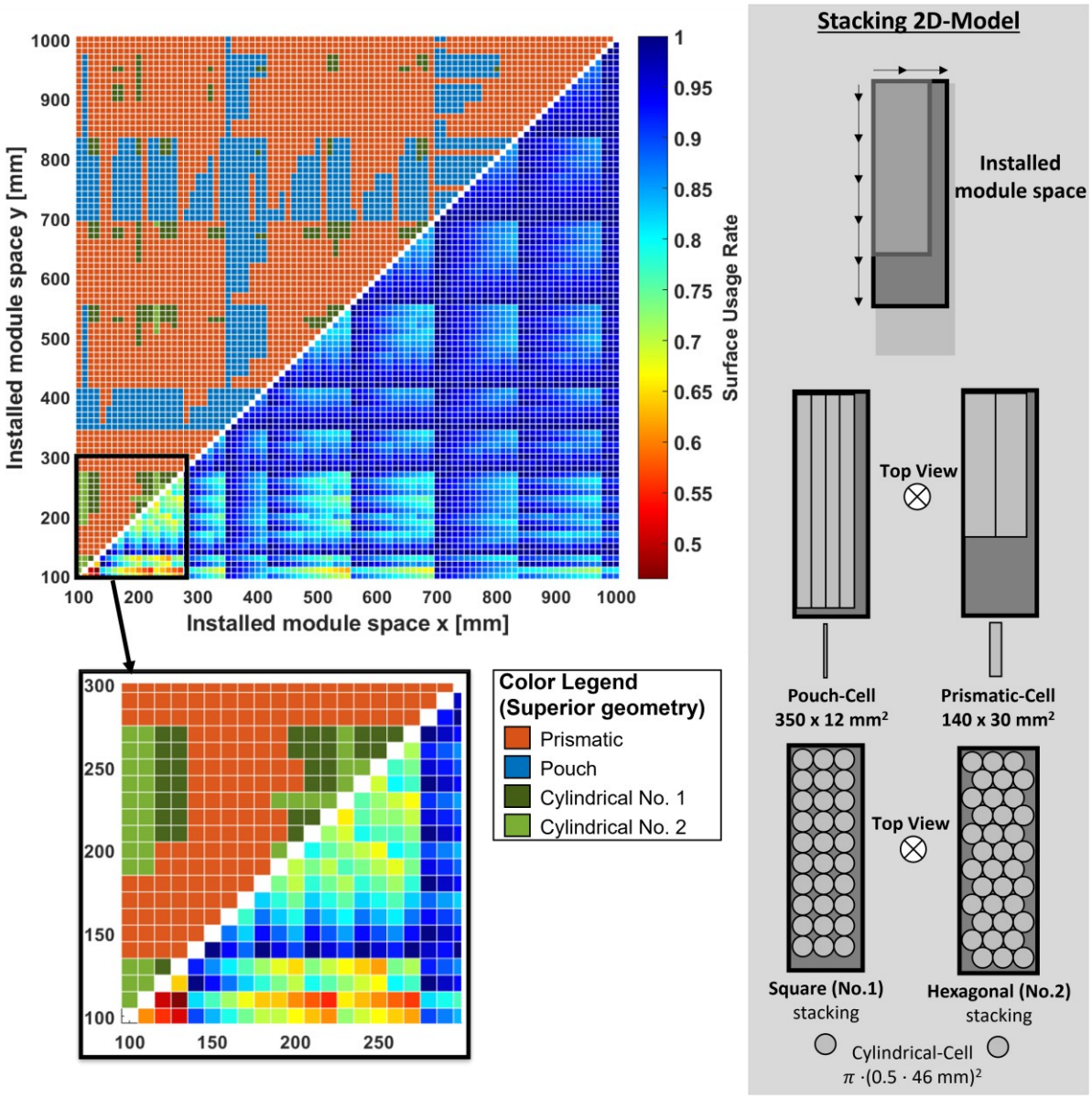

Figure 3.2: 2D stacking model results for comparison of different cell geometries depending on various module geometries.

Generally, utilization rates increase with larger module sizes. However, the figure shows that, given the three exemplary cell geometries, there are more and less advantageous module sizes. Moreover, different cells are rated optimal for different module installation space areas. Even the cylindrical cell is rated optimal in some areas, although literature often declares the cylindrical format as suboptimal for cellstacking [22, 179, 180]. Consequently, when only considering different cell geometries, no superior format can be determined without further analysis of cell format differences.

In Figure 3.3, two further factors are taken into account in addition to the pure cell geometrics. Firstly, a restrictive parameter that describes the ratio of usable and non-usable module space due to, e.g., passive components or packaging space. This non-usable space can be increased for pouch cells as they usually need to be framed due to their flexible casing and larger cell connectors [204, 205]. Equivalently, cellmodules with cylindrical cells use space-consuming spacers to form the cell package [206].

Secondly, the cell's volumetric energy density is modified between the different cell formats. Even though the actual value of the volumetric energy density varies significantly from cell to cell, literature considers cylindrical cells ahead of the pouch and prismatic cells [29, 34, 179, 207]. Figure 3.3, Figure 3.4, and Figure 3.5 depict different model results based on variations in the two restrictive stacking parameters mentioned above.

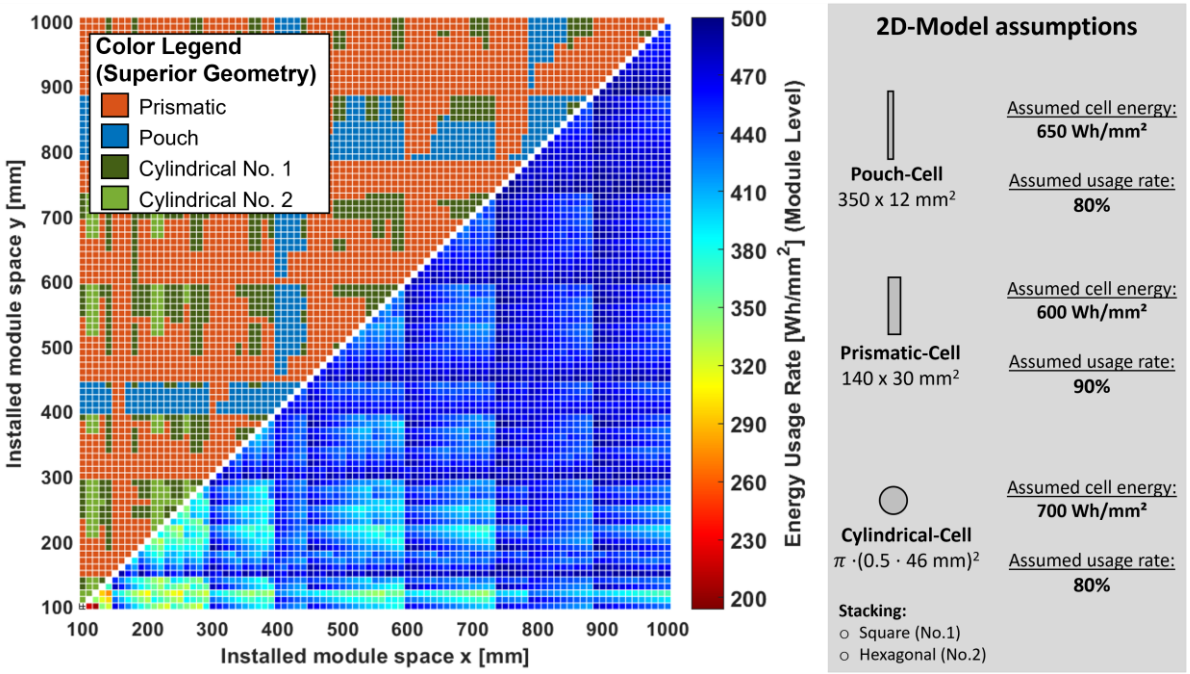

Figure 3.3: Trivial 2D stacking model for comparison of different cell geometries depending on module geometries. Assumption example 1.

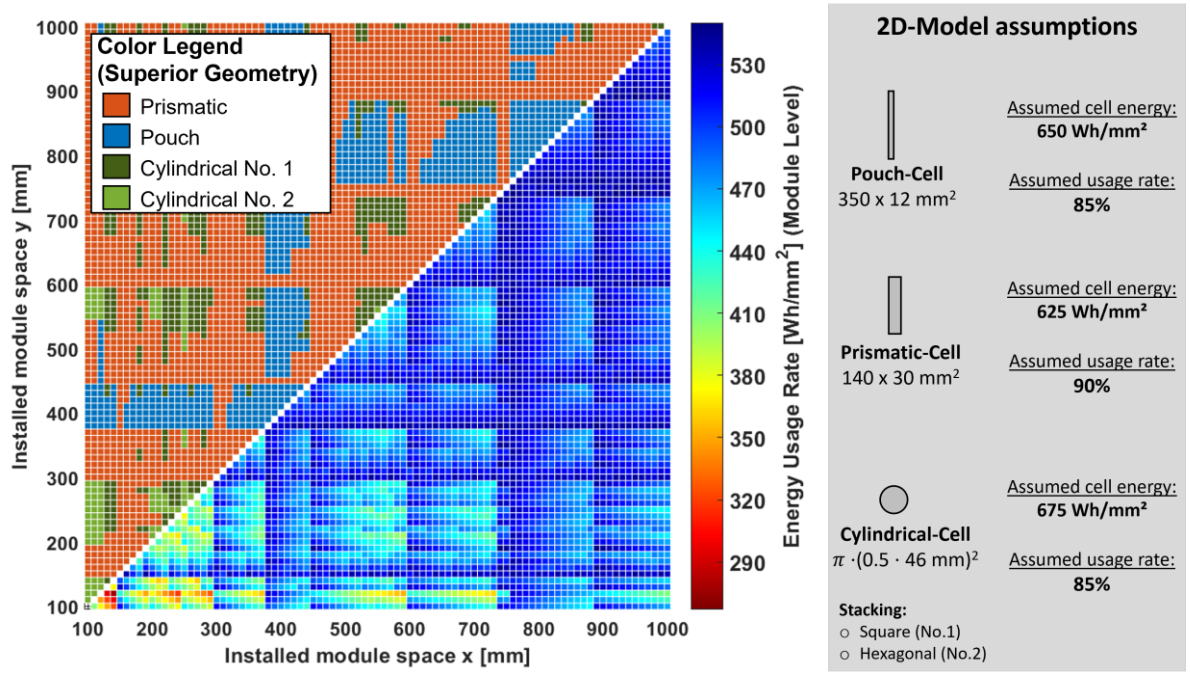

Figure 3.4: Trivial 2D stacking model for comparison of different cell geometries depending on module geometries. Assumption example 2.

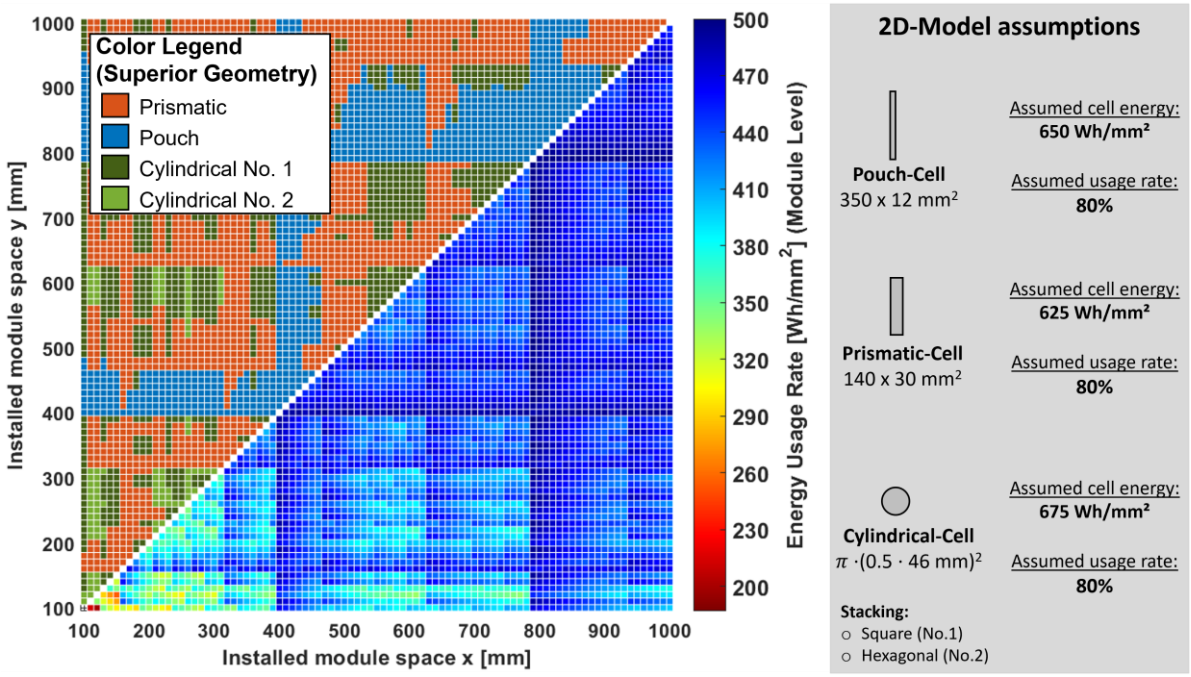

Figure 3.5: Trivial 2D stacking model for comparison of different cell geometries depending on module geometries. Assumption example 3.

The results generally show widely differing ratings of the three cell geometries depending on the model assumptions. In Figure 3.3 and Figure 3.4, the prismatic cell dominates in most module geometry regions. In Figure 3.5, especially the pouch cell shows advantages in larger and also quadratic-shaped module geometries. The phenomenon of application-dependent pros and cons of the different formats is one of the major reasons no unified cell format or geometry is declared superior. If anything, deciding on a format is a multicriteria optimization, in which the weighting of different technical aspects and further preferences play the decisive role. The illustrative examples above show that based on different assumptions, one or the other cell geometry is advantageous in certain module geometry regions. For this reason, automotive manufacturers are interested in a cell format that can serve a wide range of vehicles at an optimal cost for their portfolio of vehicles, specifications, and requirements.

In the following, a cellmodule model is presented that can generically combine and evaluate different module and cell geometry configurations. First, the geometric model is presented. Herein, a simplified base cell model is developed with included placeholders for, e.g., cell frames, connectors, and busbars. In addition, geometric models of the cell and associated production-related boundaries in cell sizing are derived and defined. Furthermore, external specifications, such as the cell-to-cell stacking distances, are included in a cell size-specific manner. This is followed by the electrical model, which also addresses the cellstacking procedure. A simplified cost reduction model also evaluates the observed cell dimensions cost-specifically. The combined model and the assumptions made are then summarized.

Figure 3.6 depicts an overview of the cellmodule model's workflow. This procedure and the working principle will be introduced for multiple scenarios. The model's applicability will be verified by analyzing the resulting optimized cell dimensions from different perspectives. Lastly, the model is validated based on real-world EV module packages.

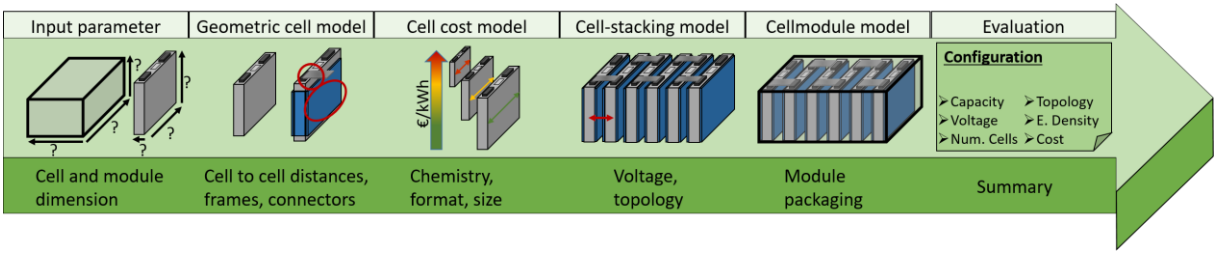

Figure 3.6: Basic procedure of cellmodule model. Figure adapted from [161].

3.3 Generic cellmodule model

Since battery modules within the battery system are usually equal in construction, this model operates based on one single module instead of the whole battery system. Furthermore, modules are assumed as cuboid formats maximizing flexibility and battery volume usage rates.

From the three commonly used cell formats, this chapter observes cell dimensioning of prismatic and pouch cells as cylindrical cells have so far only been used as small cells in EV applications which could lead to model biases. The cellmodule optimization model uses generic geometric assumptions to optimize cell and module dimensions given different initial requirements and parameters. Variables described in the following chapters may vary between applications and can therefore be easily adapted between individual optimizations.

3.3.1 Geometric model

As the first step, the initial geometric cell model with its corresponding limits and assumptions is derived. This model will be used to describe the stacking process when dimensioning a cellmodule. Generally, very different geometrically sized cells are being produced for EV applications. Yet, it is possible to assume some production-specific limits for cell sizing. Table 3.2 shows the assumed geometrical limits, cell- and module-specific sizes, as well as distance premises for cell-stacking. Spatial directions for the model parameters are given. Since cells are flexible in their stacking orientation, there are often multiple possibilities for the actual parameter's spatial direction. Figure 3.7 illustrates a detailed depiction of the different geometric model parameters and can be used to comprehend the base model with the parameters' spatial direction and orientation.

Geometric/model parameter	**Possible spatial direction (Figure 3.7): <u>and</u> → ' & ' <u>or</u> → ' | '**	**Identifier (Figure 3.7)**	**Prismatic cells [min., max.]**	**Pouch cells [min., max.]**
Cell limit thickness [mm] [20, 208–214]	x | y	(ID a1)	[20, 50]	[6, 18]
Cell limit length [mm] [20, 208–214]	x | y	(ID a2)	[80, 300]	[140, 550]
Cell height [mm]	z	(ID a3)	max. possible	max. possible

Cell terminals and busbar size [mm] [210, 213, 215]	x | y | z	(ID b)	15	30
Cell frame length and height [mm] [176, 204, 205, 214, 216]	(x & z) | (y & z)	(ID c) (1)	0	(ID a2) + 2·5 (ID a3) + 2·5
Cell frame additional thickness for cell-to-cell distance [mm] [184, 205, 214, 217–220]	x | y	(ID c) (2)	0	2-4 [a)]
Cell-to-cell distance [mm] [176, 184, 205, 214, 217–221]	x & y	(ID d)	1 - 3[b)]	contained in (ID c) (2)
Module housing thickness [mm] [176, 214, 222]	x & y & z	(ID e)	5	5
Volumetric energy density on cell level [Wh/l] [29, 34, 179, 207, 223, 224]	-	(ID f)	625	650

[a)] Linear interpolation: 4/3 mm + (60^{-1} Ah^{-1} mm) · ((cell capacity)) [Ah]
[b)] Linear interpolation: 2/3 mm + (60^{-1} Ah^{-1} mm) · ((cell capacity)) [Ah]

Table 3.2: Parametrization assumptions for the cellmodule optimization base model.

While predefining limits regarding thickness and length (ID a1, ID a2), state-of-the-art battery systems and prospects in production processes were carefully analyzed. The assumed limits depict a large geometric variability for prismatic and pouch cells. Yet, these limits in cell length and thickness may lead to unorthodox results in cell dimension since no further dependencies on length and thickness are implemented within the base model. When generating results, each optimized and calculated cell dimension must therefore be discussed for feasibility. The height of the cell (ID a3) corresponds to the maximum possible cell size in the z-direction, directly resulting from the module height. Therefore, it is cell-independent and assumed fixed for most of the analysis since the module height is often considered an exogenous size for battery module construction [176].

The spatial direction, as well as the width for cell terminals, connectors, and the corresponding busbars (ID b), can generally vary depending on different requirements. The exemplary dimensioning in Table 3.2 defines the terminals to be at the top of the cell for prismatic cells and on both the left and right sides for the pouch cell geometry. Additionally, the softer pouch cells are modeled with an included frame (ID c) to be stackable within the battery module [204, 205, 216]. The cell framing (ID c), which lies beyond the actual active part of the battery cell, is modeled as a placeholder. Thereby, the pouch foil cutting edge is to be assumed within this cell's frame (ID c(1)). Pressure and stiffness within and between cells and module housing can have different effects on the aging behavior of LIBs, like particle cracking in the active material, irreversible separator damage, or clogging of active material pores. Results from Deich et al. show that both too high and too low stiffness and compression can be unfavorable for the battery's aging behavior [225]. In a publication from Li et al. [218], the influences on swelling forces within a battery pack are discussed regarding lifetime and safety. The authors suggest enhancing cell-to-cell distance (ID 4) dependent on the cell capacity. For the pouch cell, this distance is calculated using the cell frame thickness (ID c(2)).

The distance range reflects the individual distances for different cell sizes and corresponding capacities. The space can be used for PET foils, aluminum sheet metal with thermal conductive pastes, compression, or thermal pads, and thermal propagation prevention with, e.g., mica sheets [184, 205, 217, 220, 221, 226]. Capacity-related cell spacing models are also consistent with the generally easier thermal management for geometrically smaller cells [227]. For thermal propagation prevention, 1 mm space for each cell is suggested for a 25 Ah pouch cell from Feng et al. in [219]. 2 mm - 2.4 mm is used in the analysis by Li et al. [218]. Cell-to-cell spacing from 1 mm - 10 mm is used in [202] by Coleman et al. Daubinger et al. found thickness changes of 17.5% for large 94 Ah aged prismatic cells [228]. Swelling space should also be modeled differently depending on the observed cell format and their corresponding packaging pattern. While the prismatic packaging material is usually an aluminum alloy, pouch cells are packaged with a flexible aluminum composite film [229].

This chapter's base model models cell-to-cell distance capacity-related from 1 mm – 3 mm for prismatic and from 2 mm - 4 mm for pouch cells, addressing additional risk prevention from swelling forces for pouch cells. The space varies linearly between a lower than 20 Ah to more than 140 Ah battery cell. It is important to note that if direct air-cooled systems are observed, spacing should be further increased [230–233].

The module housing thickness (ID e) may include the actual metal housing as well as possible mica sheets for thermal propagation protection [226]. It is assumed to be a fixed value for both the prismatic and pouch cells. Furthermore, the cell’s volumetric energy density (ID f) is being modified between the different cell formats. Out of the three commonly used cell formats, literature generally considers decreasing energy densities from cylindrical to pouch to prismatic cells [29, 34, 179, 207]. Furthermore, widely scattered values and ranges for volumetric energy densities are being cited [34, 207, 223]. In the VDMA Battery Production Report for 2020, prismatic cells are listed at 550 Wh/l, pouch at 600 Wh/l, and cylindrical at 850 Wh/l. For 2025 prismatic cells with 700 Wh/l, pouch cells with 800 Wh/l, and cylindrical cells with more than 950 Wh/l are expected. For 2030 the authors expect pouch and cylindrical cells to be almost equal in energy density [224]. For the following investigations, the energy density is assumed as 625 Wh/l for prismatic and 650 Wh/l for pouch cells.

The values shown in Table 3.2 represent the cellmodule basic model in which the geometric parameters can be adapted accordingly for various applications. The cell module model is built modular. Therefore, changes can be application-dependent applied to the model. However, unless otherwise stated, the above values are used as the default for the results of this chapter. Model variations are depicted in Chapter 3.4.2.4, investigating overall model robustness.

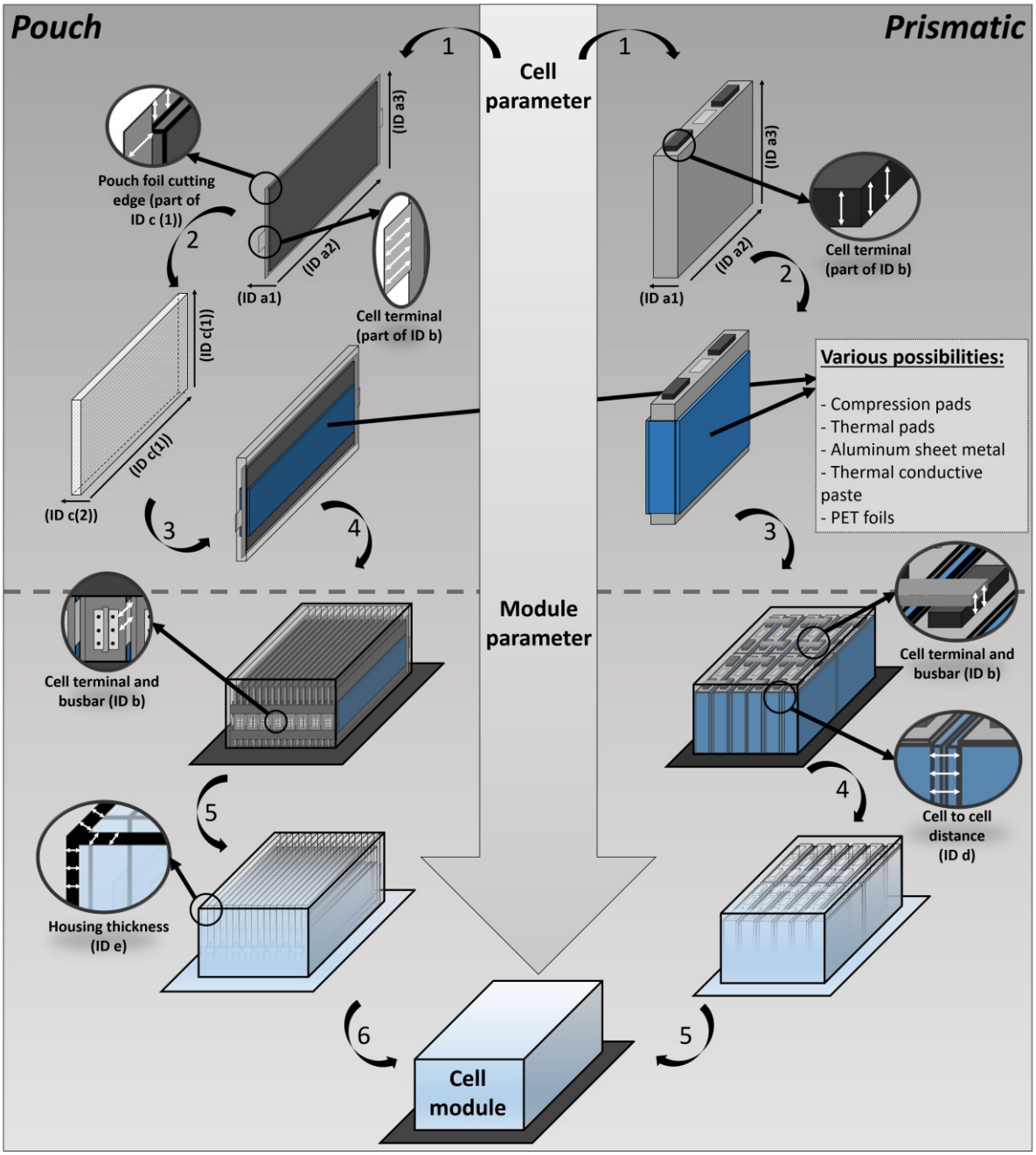

Figure 3.7: Schematic illustration and orientation of the cellmodule model parameters from Table 3.2.

3.3.2 Electrical model

In order to not exceed the component protection limits within the application and generate fewer losses, EVs are operated at high voltages. These are usually up to 400 V, and for some premium vehicles, even up to 800 V [234]. These voltages are generated by the serial connection of LIBs. The used nominal voltage for NMC-Type LIB with a graphite anode is set as 3.7 V. LFP, and LTO LIBs with lower voltages are not explicitly observed within this model yet could be analyzed using different initial parameters.

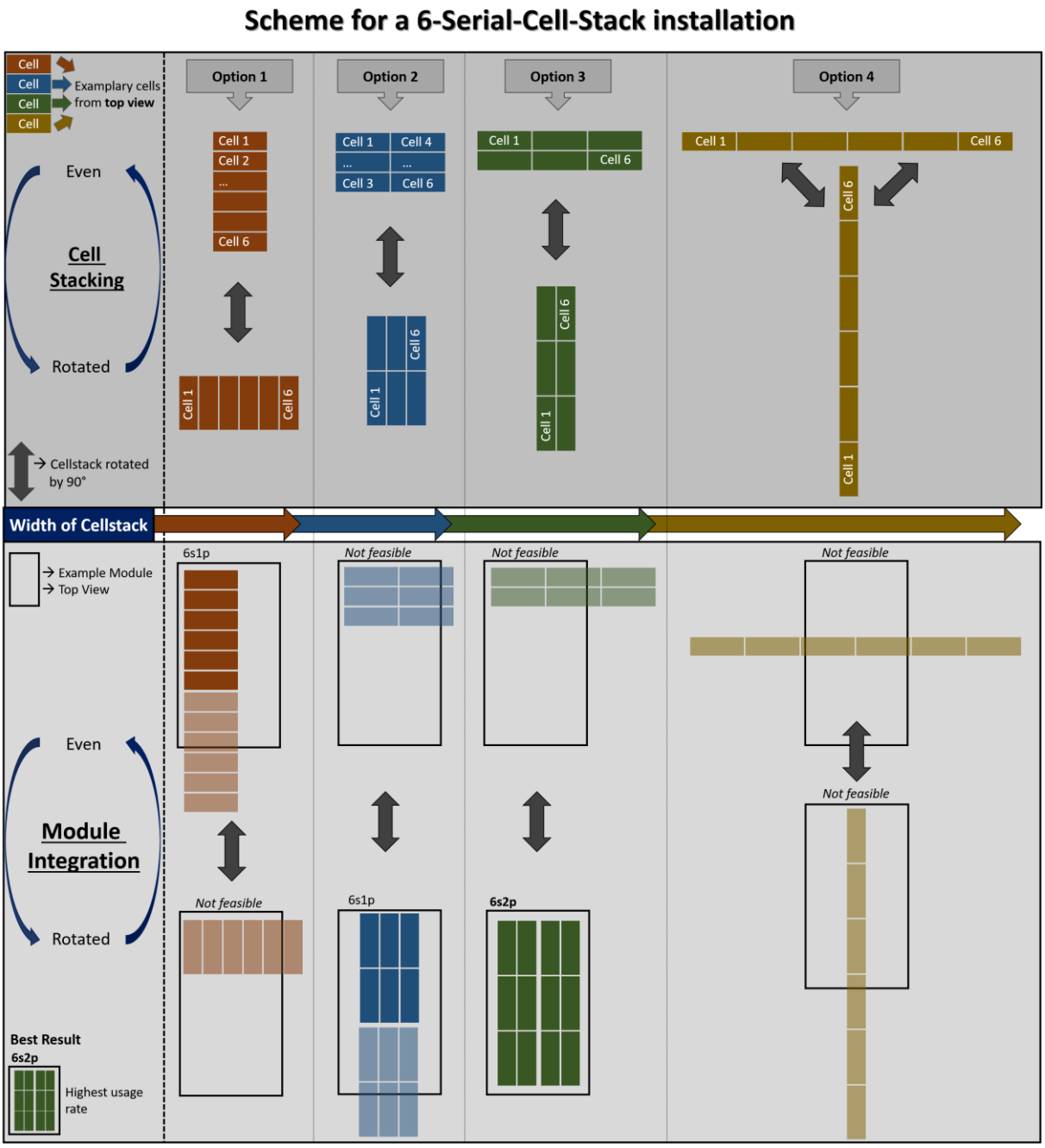

Figure 3.8: Scheme of the cellstacking process. At the top part, different stacking orientations for a 6-cellstack are depicted. The module integration for an exemplary module size is shown in the bottom part. Only identical cellstacks (cellstacks of one color and orientation) can be integrated in parallel into one module. The resulting utilization factor can be determined as the ratio of the used module area (red, blue, green, or yellow) divided by the initial module area (gray).

Figure 3.8 illustrates the scheme of the cellstacking model as well as the numerous possibilities in installing the 6-serial-cellstack ($6 \cdot 3.7\ V = 22.2\ V$) for one exemplary cell and module size. The model generally permits stacking cells along both the shorter or wider part of the module. Other stacking possibilities, such as stacking in the z-direction or mixed stacking of cells (stacks of different colors in Figure 3.8 within one module), are not being considered.

3.3.3 Cell cost and cell capacity correlation model

General cost reductions for LIBs are widely addressed in the literature [166, 186, 235–237]. The cost reduction model used for this chapter represents a qualitative analysis of cost reduction potential for cells of different sizes. It is intended to show how cost functions may influence the choice of the optimal cell format, depending on the available module space. While larger-format cells with higher capacities can offer significant cost reductions, smaller cells may lead to higher flexibility in module sizing and therefore achieve higher system energy densities. Consequently, an optimized cell format must achieve the ideal trade-off between specific cell costs and stacking density. While therefore modeling the cost reduction potential of the battery cells plays a major role within optimization models, the actual costs may vary significantly between manufacturers depending on multiple factors [238–241]. Significant manufacturing cost savings on the cell level have already been reported, especially due to less complexity for cutting and stacking steps in production [237, 240, 241]. For LIBs, thickening the electrode layer, and thus the energy storage capacity of each cell, favors the electrode-to-current collector ratio per stack and volume. In general, thicker electrodes, without changing the actual cell dimensions, increase energy densities and decrease power densities [242, 243]. In order to compensate for the loss of power, cell dimensions may be increased, leading to varying cost reduction potentials when scaling the overall cell size and capacity [186, 236].

Different cost reduction potentials from doubling the electrode coating thickness are being mentioned in recent literature articles. Patry et al. published an article that suggests about 25% reduction potential [235]. Wood et al. calculate cost savings of more than 30% [240]. Duffner et al. expect potential cost reductions of about 22% in a recently published study [242]. Ciez et al. additionally mentioned larger format cells are less expensive [186].

Furthermore, pouch cells can offer even lower production costs in comparison to solid-housed prismatic cells. Roughly 10% less has been reported by Schröder et al. [185].

Given this literature-based analysis, an initial prismatic reference cell with 25 Ah at 100 $\%_{€}/\mathrm{kWh}$ and a reference pouch cell with 25 Ah at 90 $\%_{€}/\mathrm{kWh}$ are assumed. Based on the literature analysis, the following cost reduction model is assumed to depict the cell capacity x_{capacity} dependent costs:

$$C_{\mathrm{prismatic}}\left(x_{\mathrm{capacity}}\right) = 70\,\frac{\%_{€}}{\mathrm{kWh}} + 30\,\frac{\%_{€}}{\mathrm{kWh}} \cdot \left(1-\alpha_{\mathrm{prismatic}}\right)^{\left(\left({}^{x}/_{C_{\mathrm{ref.prismatic}}}\right)-1\right)}, \tag{3.1}$$

$$C_{\mathrm{pouch}}\left(x_{\mathrm{capacity}}\right) = 70\,\frac{\%_{€}}{\mathrm{kWh}} + 20\,\frac{\%_{€}}{\mathrm{kWh}} \cdot \left(1-\alpha_{\mathrm{pouch}}\right)^{\left(\left({}^{x}/_{C_{\mathrm{ref.pouch}}}\right)-1\right)}. \tag{3.2}$$

With the reference cell capacities:

$$C_{\mathrm{ref.prismatic}} = C_{\mathrm{ref.pouch}} = 25\ \mathrm{Ah}. \tag{3.3}$$

A non-changeable material-based cost of 70 $\%_{€}/\mathrm{kWh}$ and a maximum cost reduction potential of 15% are assumed for doubling the cell capacity. This leads to a regressive strength of:

$$\alpha_{\mathrm{prismatic}} = \alpha_{\mathrm{pouch}} = 0.15. \tag{3.4}$$

This results in a non-linear cost decrease with increasing cell capacity. Figure 3.9 shows the qualitative dependence on cell cost reduction and cell capacity represented by Eqs. (3.1) and (3.2) for different regressive strengths.

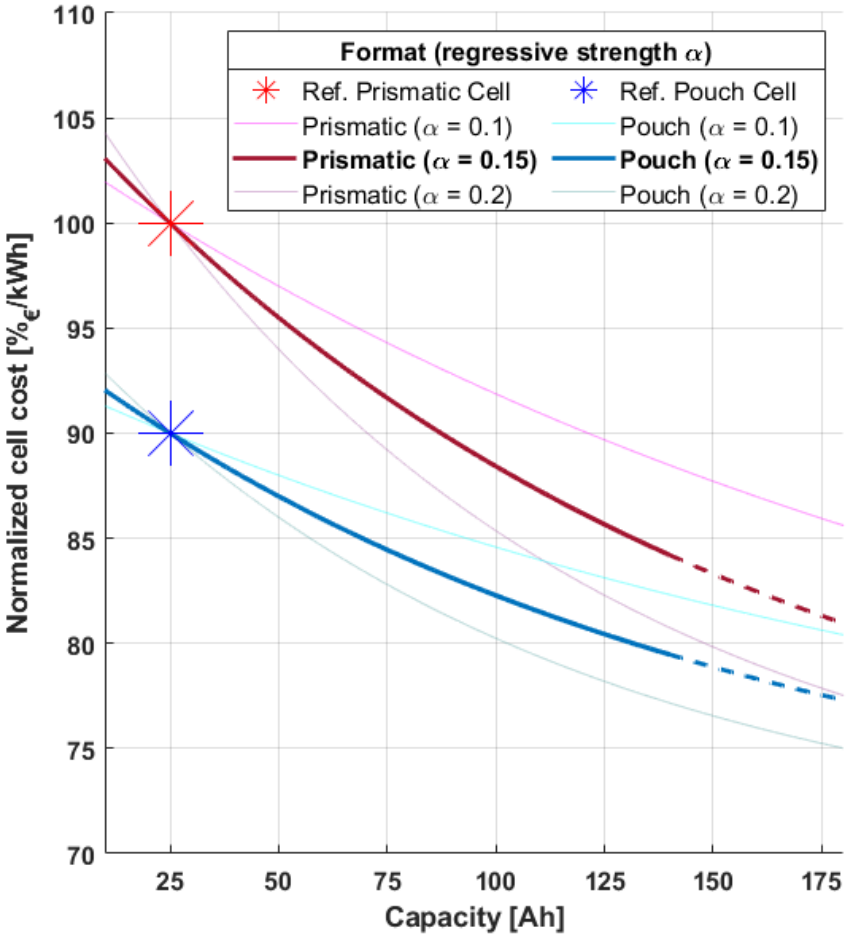

Figure 3.9: Illustration of the regressive qualitative cost reduction potential function depending on the cell capacity for different regressive strengths α. Bold blue and red lines are used for further analysis (α = 0.15). Reference cells: Prismatic 25 Ah at 100%; Pouch 25 Ah at 90%.

While this proposed cost model only compares cost reduction potentials for varying cell capacity and size, detailed holistic approaches to cell cost modeling, which take into account product, production, and economy-related parameters can be found in the work of Schünemann [244]. Another approach from Nelson et al., the “Battery Performance and Cost Model (BatPaC) evaluated costs for entire battery systems incorporating necessary cell specifications based on various EV requirements [187].

3.3.4 Model overview and summary

Figure 3.10 summarizes the presented cellmodule optimization tool with its submodels in their overall context. Input, modeling, and output variables, as well as sub-processes, are being illustrated and interconnected in a process-related manner.

In the input section, module space, the voltage restriction, and the observed cell format are determined. With the given voltage restriction, the minimum number of cells is defined. Both the module size and the cell size can be optimized iteratively depending on the optimization's objective (Chapter 3.4).

In the modeling section, the cell dimensions with their geometries and cell-to-cell distances are evaluated and summarized as the cell model. This cell model is used as input for the cellstacking and module integration (see Figure 3.8).

In the output section, the generated result for the observed module or cell size is evaluated. Achieved energy density, as well as the resulting cost reduction potential, are being calculated and stored for later comparison. This process has to be executed for each module and cell dimension setup.

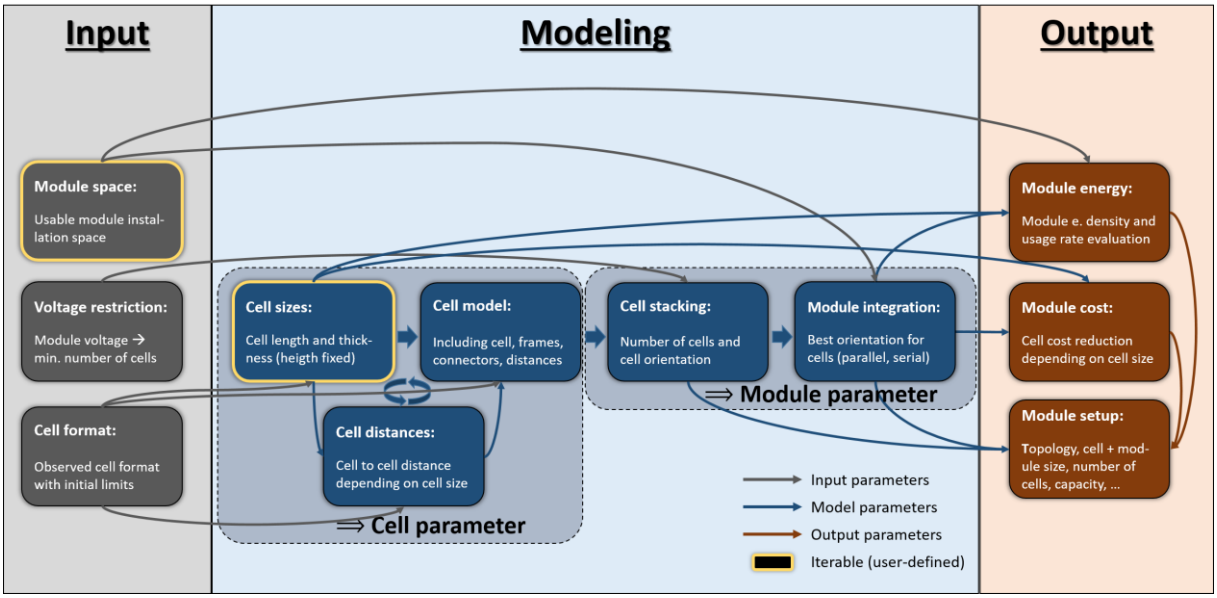

Figure 3.10: Flowchart of the cellmodule optimization model with an overview of input, output parameters, and dependencies.

3.4 Model results and discussion

This chapter emphasizes the results for two applications as examples of the presented model. Assumptions were mentioned and documented during model derivation. Major changes in both assumptions and inputparameters may change the results of the model optimization (see Chapter 3.4.2.4). A special focus of the result presentation is to evaluate both the energy and the cost perspective. This is especially emphasized in Chapter 3.4.2. The two examples of applications depict different settings in terms of degrees of freedom within the model. On the one hand, cell dimension optimization based on predefined cellmodules can be performed. On the other hand, module sizes

can be optimized around an exogenously defined cell dimension. The former is presented in Chapter 3.4.2, and the latter in the following Chapter 3.4.1.

3.4.1 Optimizing module size for different cell dimensions

In some application cases, a firmly defined battery cell with fixed dimensions may be exogenously optimal. This may be due to ongoing supply contracts, known failure behavior, and other predetermined reasons. Yet, dimensioning the module size around the cell remains to be optimized. Maximizing the module size may increase energy density on the module level since the amount of passive material can be minimized. However, large modules have to be operated with higher voltages to achieve the summed-up system voltage of up to 400 V or above. The required module voltage is a core value for the possible sizing of the module. In general, different module voltages are being used in the battery systems of EVs by different manufacturers. Often, battery modules are designed with voltages below 60 V, minimizing safety risks and ensuring handling without additional safety precautions [245]. Chapter 3.4.1.1 analyzes achievable module voltages depending on the module size for two different cell sizes. Chapter 3.4.1.2 focuses on achievable energy densities on the module level for various cell sizes.

3.4.1.1 Optimizing for module voltage

Two different cells are being compared for the exemplary analysis between the required module voltage and module space. Observed cell dimensions for the pouch and prismatic cell are given in Table 3.3. Also, the calculated cell capacity, as well as the resulting cell-to-cell distance, is shown. The module heights were assumed to be fixed at 100 mm. Using the cell model assumptions from Chapter 3.3.1 results in a cell height of 80 mm for the pouch and 75 mm for the prismatic cell.

Cell type	Cell length [mm]	Cell thickness [mm]	Cell height [mm]	Vol. energy density [Wh/l]	Resulting cell capacity [Ah]	Cell-to-cell distance [mm]
Cell 1 Pouch	360	10	80	650	50.6[a)]	2.18
Cell 2 Prismatic	134	28	75	600	45.66	1.43[b)]

[a)] (3.6 x 0.10 x 0.80) $dm^3 \cdot 650\ Wh\ l^{-1} \cdot (3.7\ V)^{-1} \approx 50.6\ Ah$

[b)] Linear interpolation, see Chapter 3.3.1: 2/3 mm + (60^{-1} mm Ah^{-1}) · 45.6 Ah = 1.43 mm

Table 3.3: Cell dimensions for two exemplary observed cells.

Figure 3.11 illustrates the differences in the required installed module space depending on the required module voltage for two cells using the optimization model. Results for the pouch format cell are depicted in the upper left area of the figure. The prismatic format cell can be found in the bottom right. A diagonal axis divides the two surfaces for the pouch and prismatic cell since the results are mirror-symmetric. Module voltage restrictions are depicted from a nominal module voltage of $3.7\ \mathrm{V} \leq U_{\mathrm{module}} < 22.2\ \mathrm{V}$ in yellow color (at least one serial connected cell) to $U_{\mathrm{module}} \geq 88.8\ \mathrm{V}$ in green color (at least 24 serial connected cells) in four steps. The gray areas are not feasible since the observed cell dimension cannot be placed within the corresponding module size.

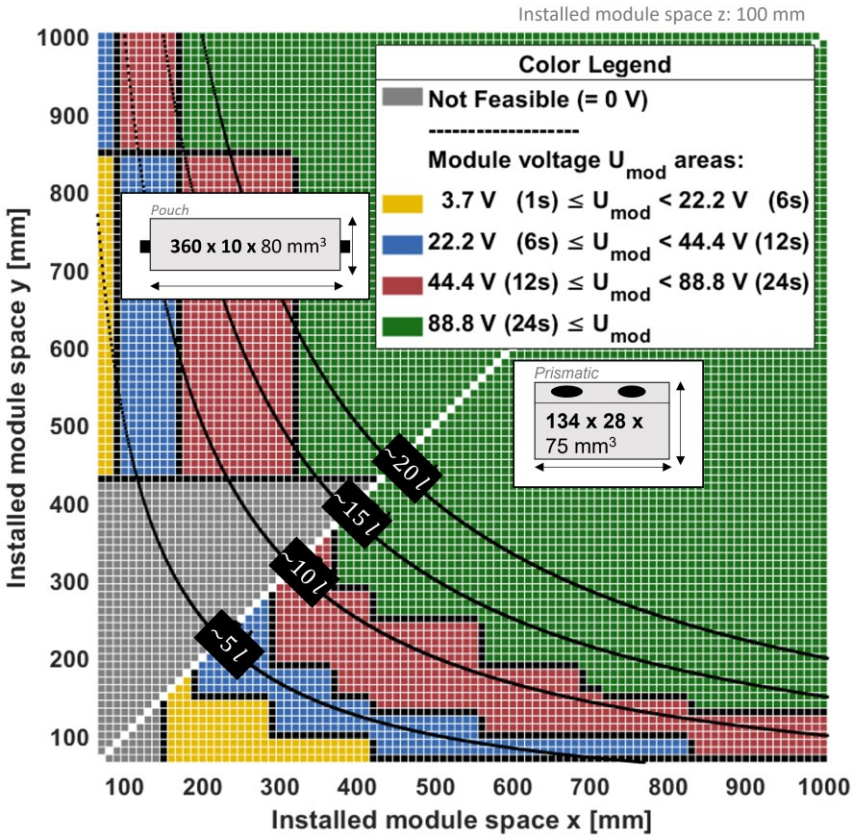

Figure 3.11: Achievable voltage level comparison. Results for the two exemplary cells from Table 3.3. A diagonal axis divides the two surfaces for the pouch and prismatic cell since the results are mirror-symmetric. Equivalent volume lines enable easier comparison at achievable module voltages at certain installed module spaces with corresponding volumes. The colors represent the different achievable voltage areas. The higher the voltage restriction, the larger the needed corresponding installed module space. The gray areas are not feasible since the observed cell dimension cannot be placed within the corresponding module size.

In general, optimal module sizes are illustrated by each edge of the left-sided outer line of any voltage area for both formats. Module dimensions situated on this edge offer the lowest space requirements within the observed voltage restriction. The comparison of the exemplary cells shows that although both cells have approximately the same capacity, more flexibility is achieved using the prismatic cell. Equivalent volume lines at 5 l, 10 l, 15 l, and 20 l help compare both cells distinctively. With the 10 l module, a nominal voltage of 88.8 V can already almost be achieved with the prismatic cell. In contrast, the pouch cell's minimum module dimension for this voltage restriction is at approx. 440 x 320 x 100 mm^3 and therefore roughly 14 l.

3.4.1.2 Model result: Volumetric energy density (module level)

For the analysis of achievable energy density on the module level, a total of eight different cells (four in each format) were examined. The module height was again set fixed at 100 mm. Furthermore, a commonly used nominal module voltage of 44.4 V was defined, which requires a serial cell connection of 12 cells for each optimization.

The results are shown in Figure 3.12. Each subplot (a-d) compares one specific pouch with one specific prismatic cell dimension. Results for pouch format cells are depicted in the upper left area of the figure. The respective prismatic format cells can be found in the bottom right. The calculated, achieved energy density on the module level is depicted at every feasible module size. The colors represent a range of 100 Wh/l - 550 Wh/l, from red (low energy density) to blue (high energy density) color. Average energy densities are around 350 Wh/l - 450 Wh/l for prismatic and around 250 Wh/l - 400 Wh/l for pouch cells. Similar energy densities at the module level can also be found in real-world field studies [29, 34]. The individual cell sizes of the observed cells increase in length (x-direction) and thickness (y-direction). The gray areas represent module dimensions where no configuration was found with the selected cell size because the required module voltage could not be accomplished. It can be seen that the gray, non-feasible area generally increases with larger cell sizes, especially with the length of the cells.

Various pareto-optima can be analyzed for each observed cell dimension. These are the blue (for prismatic) and light blue (for pouch) areas. Pareto-optimal areas depict the highest achieved energy densities on the module level at different module dimensions. Accordingly, from a system-specific point of view, every module dimension from the pareto-optimal areas can be rated equally regarding achievable energy density. Looking into more detail, a varying number of pareto-optima depending on the cell size can be observed. While the shorter cells (Figure 3.12a, c) achieve a large number of pareto-optima, the length of the cells causes a negative influence on the number of optima. As the number of pareto-optima decreases, the flexibility in the use of the cell also decreases, leading to a lower number of optimal module dimensions.

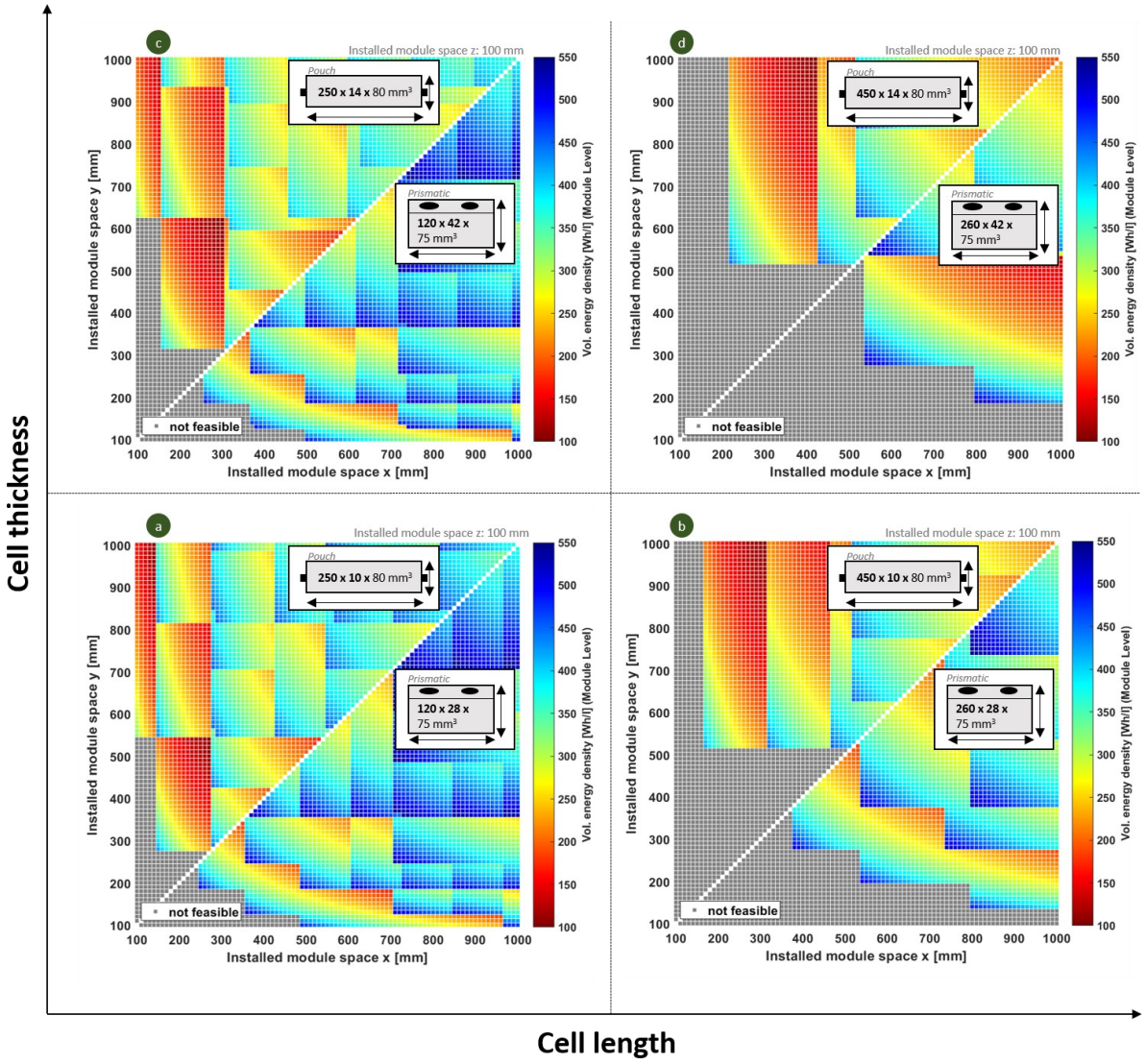

Figure 3.12: Comparison of achievable volumetric energy densities for eight different cell sizes in four sub-graphs (Figure 3.12a - Figure 3.12d). In each sub-graph, two cells of different formats are compared to each other. The x- and y-axis show the installed module space. A diagonal axis divides the two surfaces since the results are mirror-symmetric in the x- and y-direction. The colors represent the achieved volumetric energy density on the module level and correspond to the second y-axis. The bottom left sub-graph (Figure 3.12a) compares the two smallest cells. Cells grow in length to the right-handed side (Figure 3.12b) and in thickness to the top (Figure 3.12c). The top right sub-graph compares the two largest cells (Figure 3.12d). Different numbers of Pareto-optima can be observed. The gray area is not feasible since battery modules with the nominal voltage restriction of 44.4 V cannot be achieved.

3.4.2 Optimizing cell dimension for different module sizes

3.4.2.1 Derivation

The results of the previous chapter illustrate the multi-dimensional difficulties in defining advantageous module and cell dimensions. In addition to the energy-specific analysis, economic aspects must also be taken into account. This chapter aims to derive application-dependent cell dimensions. When optimizing cell dimensions, exogenously specified module configurations are required. A defined module volume of roughly 13 l was selected, on which three geometrically different module sizes were defined. Choosing the same volume for each module size maintains the highest degree of comparability. The module height is fixed at 100 mm for every configuration. Furthermore, the nominal module voltage of 44.4 V (12 serial cells) was applied to the model.

Table 3.4 sums up the three predefined module geometries used for the upcoming cell optimization. The defined module shapes can also be found in real-world applications: Module long could correspond to, e.g., the first generation Bolt from Chevrolet or models from Tesla, Module medium in Volkswagen's MEB Platform, and Module quadratic in BMW's i3.

Module	x-length [mm]	y-width [mm]	z-height [mm]
Module long	800	166	100
Module medium	550	241	100
Module quadratic	364	364	100

Table 3.4: Definition of the different module shapes (long, medium, quadratic).

Figure 3.13 shows the resulting cell dimensions obtained by the cellmodule optimization tool. A total of nine individual graphs are given. Each row, consisting of three graphs, corresponds to one module size (Module long, Module medium, or Module quadratic). On the x- and y-axis, different cell dimensions are observed and evaluated. The evaluation is differentiated into energy perspective in yellow and cost perspective in blue color. The energy perspective depicts the achievable volumetric energy density rating on the module level for the specific observed cell dimension. The cost perspective represents the corresponding normalized cell costs. In each graph, suitable cell dimensions for the pouch and the prismatic cell format can be seen. The summed perspective is depicted in green color on the right, adding up both perspectives and representing an overall evaluation. The brighter the yellow, blue, or green color, the better the specific perspective is evaluated. For each module configuration (long, medium, and quadratic), the evaluation/rating of the energy perspective, cost perspective as well as summed perspective is calculated as follows:

$$\begin{aligned}\psi_{\text{sum.persp.}} = {} & \omega_{\text{long}}[(\lambda_{\text{energy}} \cdot \varepsilon_{\text{long}}) + (\lambda_{\text{cost}} \cdot \varsigma_{\text{long}})] + \\ & \omega_{\text{medium}}(\lambda_{\text{energy}} \cdot \varepsilon_{\text{medium}}) + (\lambda_{\text{cost}} \cdot \varsigma_{\text{medium}})] + \\ & \omega_{\text{quad.}}([\lambda_{\text{energy}} \cdot \varepsilon_{\text{quad.}}) + (\lambda_{\text{cost}} \cdot \varsigma_{\text{quad.}})]\end{aligned} \tag{3.5}$$

With energy and cost perspective-specific weightings:

$$\sum_{i \in \{\text{energy,cost}\}} \lambda_i = 1. \tag{3.6}$$

And module-specific weightings:

$$\sum_{j\in\{\text{long,medium,quad.}\}} \omega_j = 1. \tag{3.7}$$

The energy perspective rating is defined as:

$$\varepsilon_{module} = \frac{e_{\text{x,y}} - e_{\text{min.}}}{e_{\text{max.}} - e_{\text{min.}}} \in [0,1];\ module \in \{\text{long, medium, quad.}\}. \tag{3.8}$$

With $e_{\text{x,y}}$ being the system energy density achieved with cell length x and thickness y.

Furthermore, the cost perspective rating is defined as:

$$\varsigma_{module} = \frac{c_{\text{max.}} - c_{\text{x,y}}}{c_{\text{max.}} - c_{\text{min.}}} \in [0,1];\ module \in \{\text{long, medium, quad.}\}. \tag{3.9}$$

With $c_{\text{x,y}}$ being normalized costs achieved with cell length x and thickness y.

The following simplification applies to the illustration of the summed perspective in Figure 3.13:

$$\omega_{\text{long}}, \omega_{\text{medium}}, \omega_{\text{quadratic}} \in \{0,1\}, \tag{3.10}$$

$$\lambda_{\text{energy}} = \lambda_{\text{cost}} = 0.5. \tag{3.11}$$

Resulting in individually observed module sizes with equally weighted energy and cost perspectives. Therefore, the summed perspective weighting function from Eq. (3.5) becomes simplified to:

$$\phi_{\text{sum.persp.},module} = 0.5 \cdot (\varepsilon_{module} + \varsigma_{module}),\quad module \in \{\text{long, medium, quad.}\}. \tag{3.12}$$

In addition, some data points are marked separately in each graph. The Top10 rated cell dimensions out of both the prismatic and pouch format are depicted in purple color. The very best-rated dimension is marked in red color. This particular cell size represents the optimum in the energy, cost, or the summed perspective.

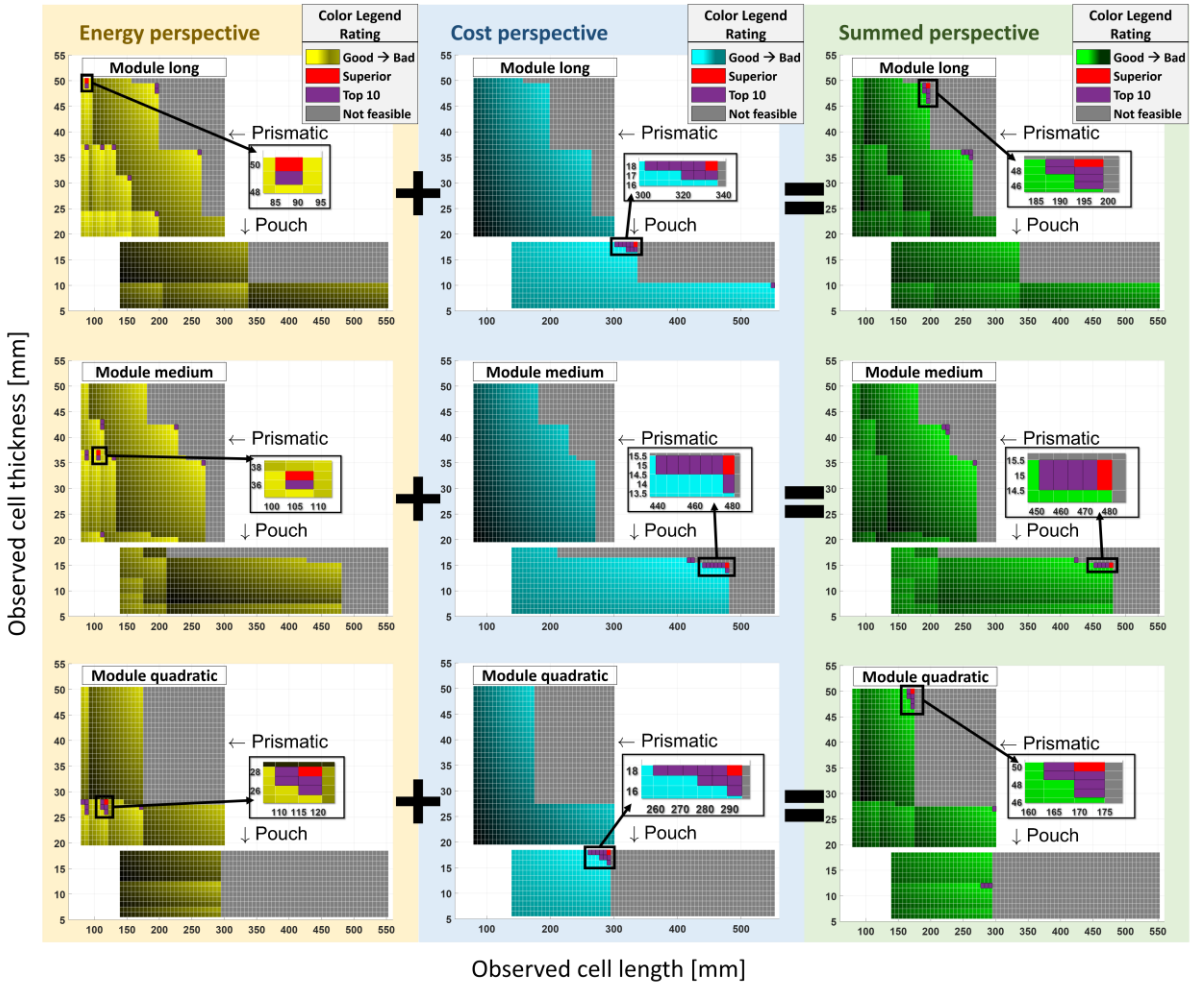

Figure 3.13: Results from the optimization of the cell dimension in nine individual graphs. The axes show the cell length (x-axis) and thickness (y-axis) for the pouch and prismatic format. Optimization in achievable energy density is depicted in the yellow graphs (energy perspective). Optimization in cell cost reduction potential is depicted in the blue graphs (cost perspective). The weighted result from the energy and cost perspective is depicted in the green graphs (summed perspective). The brighter the yellow, blue, or green color, the better the specific perspective is evaluated. Each graph additionally marks the best results found (red) and the 10 top-rated cell dimensions (purple). The gray areas are not feasible because the minimum requirement of 44.4 V nominal module voltage could not be achieved. Cell heights: Prismatic: 75 mm; Pouch 80 mm.

3.4.2.2 Model result and discussion: Optimizing cell dimension

For Module long, the results show the prismatic cell format as the overall best rated. While in the energy perspective, only prismatic cells appear in the Top10 rated cells, especially smaller cells with a size of up to approx. 90 mm x 50 mm are evaluated as superior. This cell dimension is uncharacteristic since it is rather thick with respect to its corresponding length. In real-world usage, this cell dimension should be carefully analyzed regarding its actual producibility. Furthermore, different other sizes are depicted within the Top10 rated geometries for the energy perspective. The cost

perspective results show pouch format cells as superior. Especially cells with approx. 340 mm x 18 mm are evaluated optimal. Yet, the summed perspective shows the optimum in medium-length but thick prismatic cells (approx. 195 mm x 49 mm).

For Module medium, prismatic cells with lengths of about 105 mm and thicknesses of about 37 mm are rated optimally. The cost optimum is again within the pouch format area with a length of 480 mm and a width of 15 mm. In contrast to the Module long results, the summed optimum for Module medium is the same pouch cell format as from the cost optimum.

For Module quadratic, smaller prismatic cells show the largest advantages in terms of energy perspective. Sizes of approx. 120 mm x 28 mm represent the best-rated result. From the cost perspective, rather small but thick pouch cells of up to 290 mm x 18 mm are determined optimally. Yet, in the summed perspective, large and thick prismatic cells at 170 mm x 50 mm are evaluated as superior. Within the Top10 rated results are also pouch cell dimensions at approx. 290 mm x 13 mm.

Summing up the results, the prismatic cells show to be better from an energy perspective, while the pouch cells offer advantages from the cost perspective. Although the prismatic cell format was rated superior in two of the three module sizes considered, the Top10 rated cell dimensions show balanced results for both the pouch and prismatic format. Especially the results from Module quadratic emphasize the need for trade-off analysis as the optimal summed perspective cell geometry was not rated optimally in either the energy or the cost perspective.

3.4.2.3 Further weighting model analysis

Mathematically, the weighting model from Eq. (3.5) is not associated with any restrictions. Yet, it is essential to consider if an actual weighting is reasonable.

In order to bring the technical and ecological requirements into a suitable trade-off relationship while maintaining the flexibility of the optimized battery cell, the weightings can be adapted to specific industry applications. Therefore, a weighting of only the energy or the cost perspective will not be sufficient in most cases. The same applies to module geometry factors. For example, a weighting of the Module quadratic geometry, even if only slightly, cuts off a larger part of the solution space, which can be seen in Figure 3.13.

Figure 3.14 depicts an exemplary application-related weighting, in which the energy perspective is weighted higher than the cost perspective. The Module medium geometry is to be optimized while securing the cell to also be applicable in the Module long variant. This was taken into account by weighting ω_{long} slightly above zero. Such weighting may be advantageous if the optimized cell geometry is intended to optimally serve one main vehicle with Module medium, while still being feasible in another smaller battery with Module long. The exact weightings can be seen in Figure 3.14.

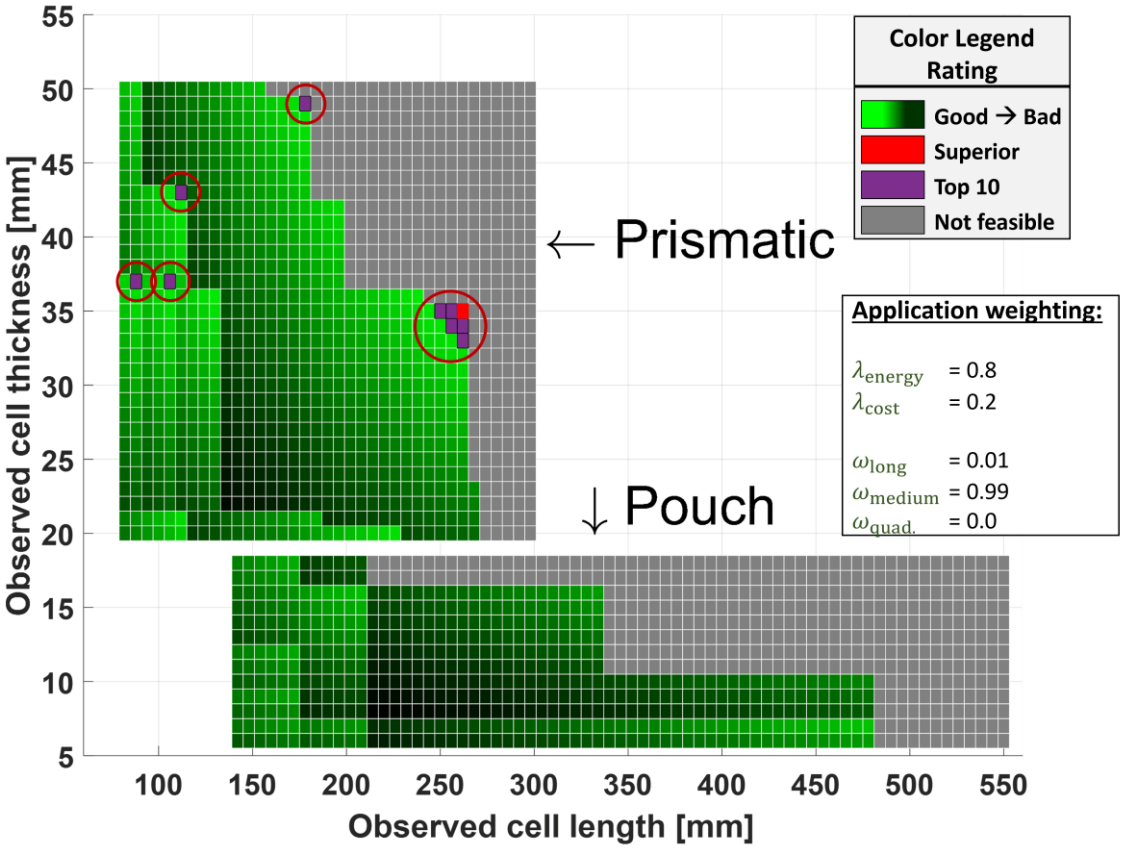

Figure 3.14: The summed perspective of cell dimension optimization for a specific application weighting. The brighter the color, the better the specific perspective is evaluated. Red circles mark the Top10 rated results. Cell heights: Prismatic: 75 mm; Pouch 80 mm.

The result shows that a prismatic cell with a length of approx. 260 mm and a width of 34 mm is optimal. Additional Top10 rated areas are at approx. 180 mm x 49 mm, 120 mm x 43 mm, 110 mm x 36 mm and 90 mm x 36 mm.

3.4.2.4 Result-robustness investigation

The above results show that given the derived model and weighting parameters, the prismatic cell geometries are superior in comparison to the pouch ones. In order to verify this in more detail, the model's robustness was analyzed in Figure 3.15 by changing the model parameters in favor of the pouch cell format. The changes in the model parameters refer to the cell connector size (ID b) as well as the cell's frame (ID c) and corresponding cell-to-cell distances of the pouch cell (see Chapter 3.3.1). For result generation, the same weightings used in Figure 3.14 were applied. The result shows that the pouch cell is now rated slightly better. However, among the Top10 rated resulting cell sizes, only one dimension is assigned to the pouch format. Moreover, the superior-rated prismatic cell geometry only slightly changed. The figure illustrates the general result robustness within the chosen model weightings.

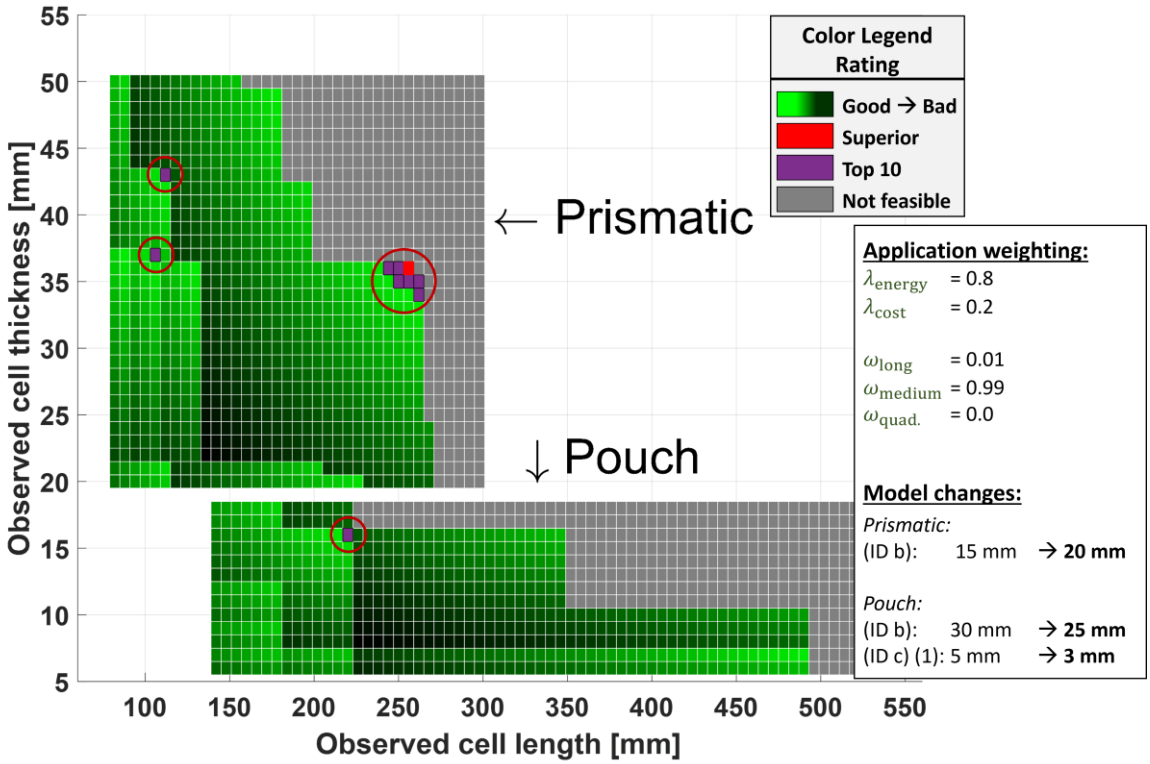

Figure 3.15: The summed perspective of cell dimension optimization for a specific application weighting with changed model parameters of the initial base model in favor of the pouch cell. The brighter the color, the better the respective cell size is evaluated. Red circles mark the Top10 rated results. Updated cell height: Prismatic 75 mm; Pouch 80 mm.

3.4.3 Model validation on real-world vehicle module and cell configurations

Multiple different application examples for the use of the cellmodule model have been shown in the last chapters. In the following, a real-world validation is carried out. Since cellmodule construction between different manufacturers is generally not uniform, has majorly evolved in recent years, and also depends on systemic variables, an evaluative validation of the results is only possible to a limited extent. Nevertheless, replicating real-world cellmodule configurations can provide a good benchmark for examining model accuracy. Thus, one cellmodule with prismatic cells and one cellmodule with pouch cells will be examined in more detail. The raw real-world module data and geometric dimensions are taken from the literature. The results will be used to review and verify the plausibility of the defined assumptions in the cellmodule model.

3.4.3.1 BMW i3 comparsion

The details of the battery system, including the system, module, and cell dimensions, are given in [48]. The described BMW i3 Mk1 22kWh battery system uses modules with dimensions of 360 x 311 x 150 mm³. These dimensions were used as input for the cell geometry optimization. The BMW i3 packs 12 cells in each module which equals a nominal cell voltage of 44.4 V (12 · 3.7 V).

Figure 3.16 shows the aggregated optimization results. The result generally shows that the prismatic cell format is optimal for the examined module geometry. The height of the cell geometries is fixed at 130 mm for each length and thickness. Three different regions can be identified among the Top10 cell geometries. The first region is located at about 150 mm in length and 50 mm in width. The second region is at about 300 mm in length and 25 mm in width. In between lies a region with several geometries within the top10 results. The best cell format found is also located in that third region. The optimum cell geometry is approximately 175 x 46 x 130 mm³. The cell used by BMW has dimensions of 173 x 45 x 123 mm³. The deviation is thus marginal and can be attributed, for example, to slightly different assumptions of module housing thicknesses. The cell height is overestimated by the cellmodule model by 7 mm. Additional module housing, space for cable routing, or increased space requirements for cell terminals and busbars may explain this difference.

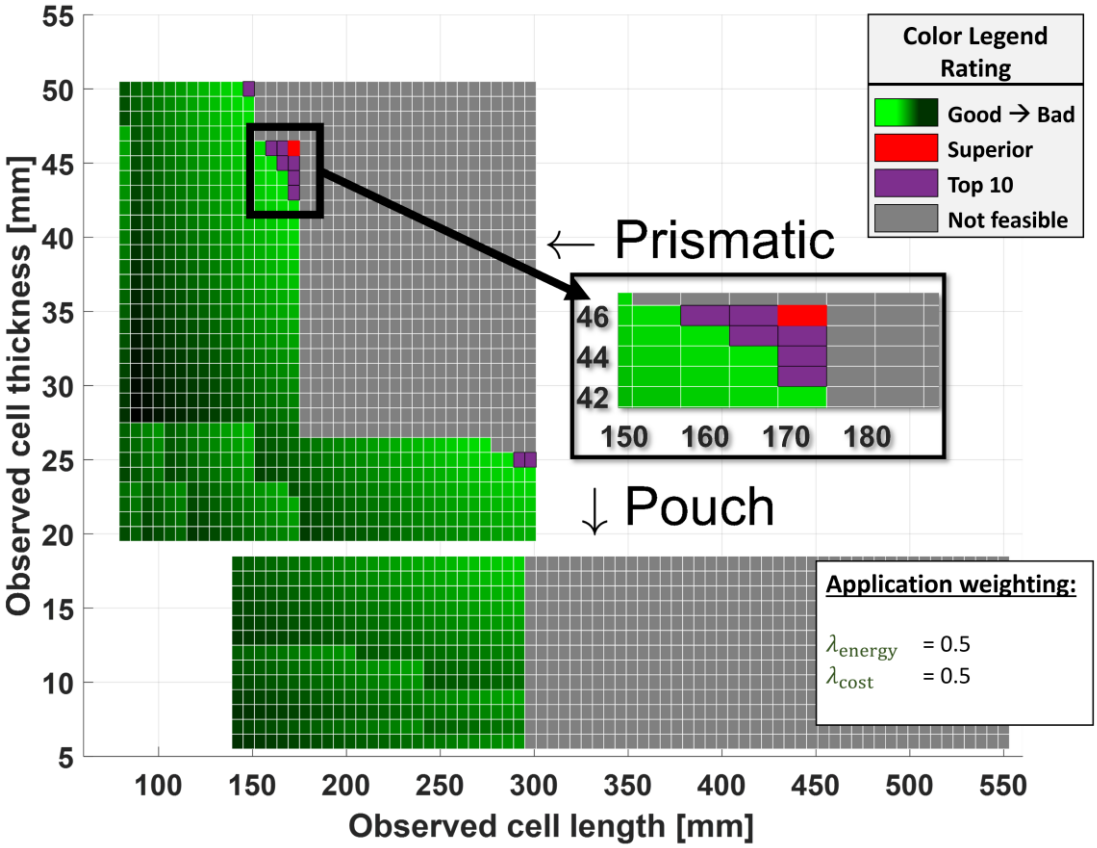

Figure 3.16: Cellmodule optimization validation with BMW i3 module size. Module size [48]: 360 x 311 x 150 mm³; Original cell configuration BMW i3 module [48]: Prismatic cell of 173 x 45 x 123 mm³ with 12 (12s1p) cells; Optimized cell dimensions ≈ 175 x 46 x 130 mm³. Cell height is not depicted in the graphic.

3.4.3.2 Renault Zoe comparison

The battery system, including the system, module, and cell dimensions, are described in [246]. The battery system of the Renault Zoe uses cellmodules with dimensions of 374 x 204 x 140 mm³. These dimensions were used as input for the cell geometry optimization. Furthermore, 16 cells per module were assumed.

Figure 3.17 shows the aggregated results. Since the battery modules in the Renault Zoe are not embedded in a separate housing (see [246]), the module housing thickness was set to 0 mm for cell geometry optimization. In general, the result shows that the pouch cell format is optimal for the examined module geometry. The height of the cell geometries is fixed at 130 mm for each length and thickness. Among the Top10 resulting cell geometries, a wide range of different cell lengths can be identified. The range shows cell lengths of approx. 265 mm to approx. 315 mm. In between lies the superior cell format. The optimum geometry is at approx. 285 x 10 x 130 mm³. The cell used by Renault has dimensions of 325 x 11.2 x 135 mm³. The slightly larger difference compared to the BMW results above can be attributed in particular to the modeled cell-to-cell distance. For larger cell lengths, the cell-to-cell distance becomes higher due to the increasing cell energy, resulting in a model-predicted possible cell thickness of only about 9 mm for a cell length of approx. 315 mm. Reducing the energy density from the base assumptions (Table 3.2) would reduce the cell-to-cell distance due to the resulting lower cell capacity and could bring the result closer to the cell geometry used by Renault. Nevertheless, the optimization shows promising results which compare well with the real-world design.

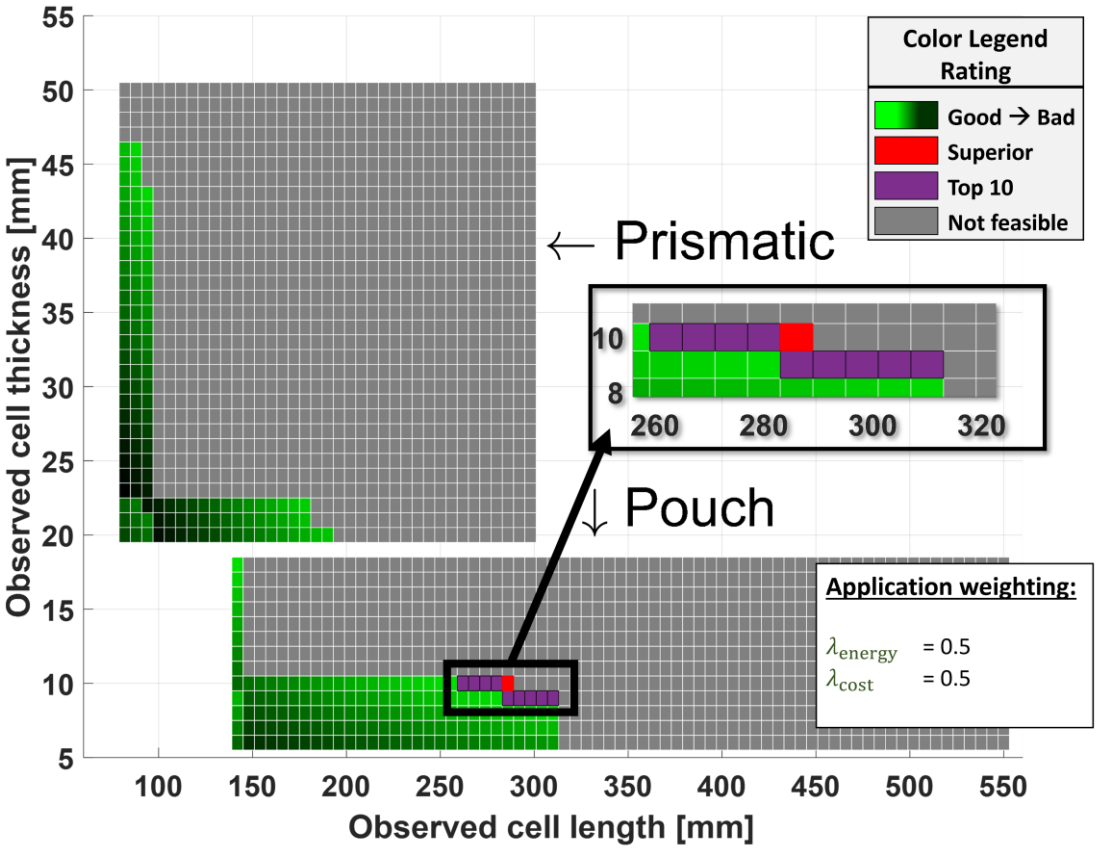

Figure 3.17: Cellmodule optimization validation with Renault Zoe module size. Module size [246]: 374 x 204 x 140 mm³; Original cell configuration in Renault Zoe module [246]: Pouch cell of 325 x 11.2 x 135 mm³ with 16 (8s2p) cells; Optimized cell dimensions ≈ 285 x 10 x 130 mm³. Cell height is not depicted in the graphic.

3.5 Model limitations

This chapter provides a model to systematically compare and evaluate cell formats and cellmodules with differing dimensions. Several assumptions and simplifications were described for this study. Geometric limits, as well as spatial directions for the different geometric sizes, like connectors, frames, or cell distances, may vary between different circumstances. Although cell height assumptions were considered, detailed analyses of different cell heights were not performed. It should be noted that for a definite application, specific design changes in the variables (e.g., different nominal voltage), as well as adding new variables, can easily be implemented. The validation results with real-world battery modules of different EVs confirmed the assumptions made to a large extent. In this chapter, generic assumptions regarding various parameters of the cell, the module, and the cellmodule package were collected and holistically modeled to derive application-related conclusions. Yet, specific changes to the model parameters, different weightings of cost and energy, adaptations in the model approach or variances in geometric shapes, and dependencies can lead to different results and conclusions.

3.6 Conclusive summary

A comparative evaluation of the pouch and prismatic cell formats was performed, analyzing the energy and cost perspective. For this purpose, a generic and geometry-related model was developed. On the one hand, this model allows the ideal module size to be calculated with a given cell format regarding the influence of energy and voltage level and, on the other hand, allows an optimal cell dimension to be evaluated for different module sizes and premises. The prismatic cell format showed particular advantages from the energy perspective, as it can be stacked well as a square robust body. The pouch cell may have advantages if the actual energy density on the module level is not the major optimization factor. Furthermore, specific module geometries like the Renault Zoe module also underlined the need for thinner pouch cells. Moreover, developments in cell formats and also in design technology could mitigate several advantages and disadvantages of both cell formats and change the results. Additionally, the analyses were performed purely on the module level and could be verified on the system level, including analysis of further possible influencing battery system components such as the cooling system, the electronics, and the mechanical construction in multiphysical battery system models. The presented cellmodule model can then be used as a subcomponent since it is built on modular submodels for cell geometry, cell stacking, and cell cost reduction, allowing individual adaptation as well as higher system integration.

4 Holistic battery system design analyses based on a generic tool with multiphysically coupled submodels

Parts of this chapter are published in a journal article [247] as part of this thesis. This chapter contains modifications and extensions with respect to the original publication. The use of the article content, including illustrations, is permitted with the consent of Elsevier.

Significant challenges appear in the multiphysical engineering process of battery systems for electric vehicles. Thereby, individual standalone simulation models offer essential opportunities to assist the development of components for the cellmodule, cooling, mechanics, and electronics. However, in order to address requirements in range, performance, and general installation space shortage for the battery system, interdependencies between the different components have to be considered.

This chapter presents a novel approach to a fully parametrized high-voltage battery optimization tool based on coupled simulation models for the battery system's main components. Thereby, several essential aspects of battery system engineering are first derived, then assigned and modeled in the submodels, and finally consolidated into an overall submodel-concept. Thus, the submodel-concept can both optimize each component individually and additionally perform an overall cost- or weight optimization in which components are designed, considering essential interdependencies.

The resulting observed battery system concepts are thoroughly determined in their physical (geometrical, electrical, thermal, mechanical) properties and also graphically described with millimeter accuracy. Comparisons between different concepts illustrate the cause-effect principles between multiple battery system components in great detail. Besides, integration repercussions for different lithium-ion cells are analyzed from the cell level to the system level. Thereby, in-depth evaluations of the cell, module, mechanical system frame design, cooling topology, and electronics integration are discussed. Lastly, battery systems from the field are used to validate the modeling approach and verify the plausibility of the weight prognosis.

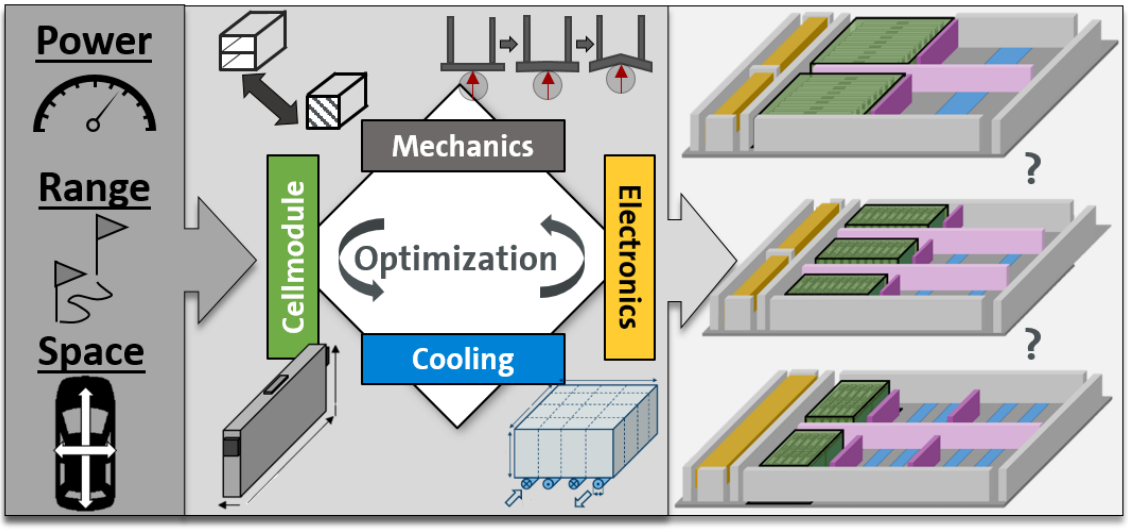

Figure 4.1: Graphical abstract for the holistic battery system optimization tool.

4.1 Introduction and scientific integration

As the most expensive component in electromobility, the lithium-ion battery plays a significant role in future vehicle development [31, 164, 248]. Usually, battery systems consist of connected battery modules containing numerous LIB cells in order to meet the EV's energy, power, and voltage level requirements [48, 249]. In addition, different types of electric vehicles have different requirements that greatly affect the design of a high-voltage battery system, including its internal components [250, 251]. Next to interior components, also size and shape requirements of components from cellmodule, mechanics, cooling, or electronics need to be adapted adequately. Figure 4.2 schematically depicts various influencing parameters from different components within the battery system. Major challenges must be addressed and consolidated in order to develop a cost- and weight-optimized battery system. Therefore, the coordination process for designing a battery system is an immense organizational effort associated with many iterative partial optimizations.

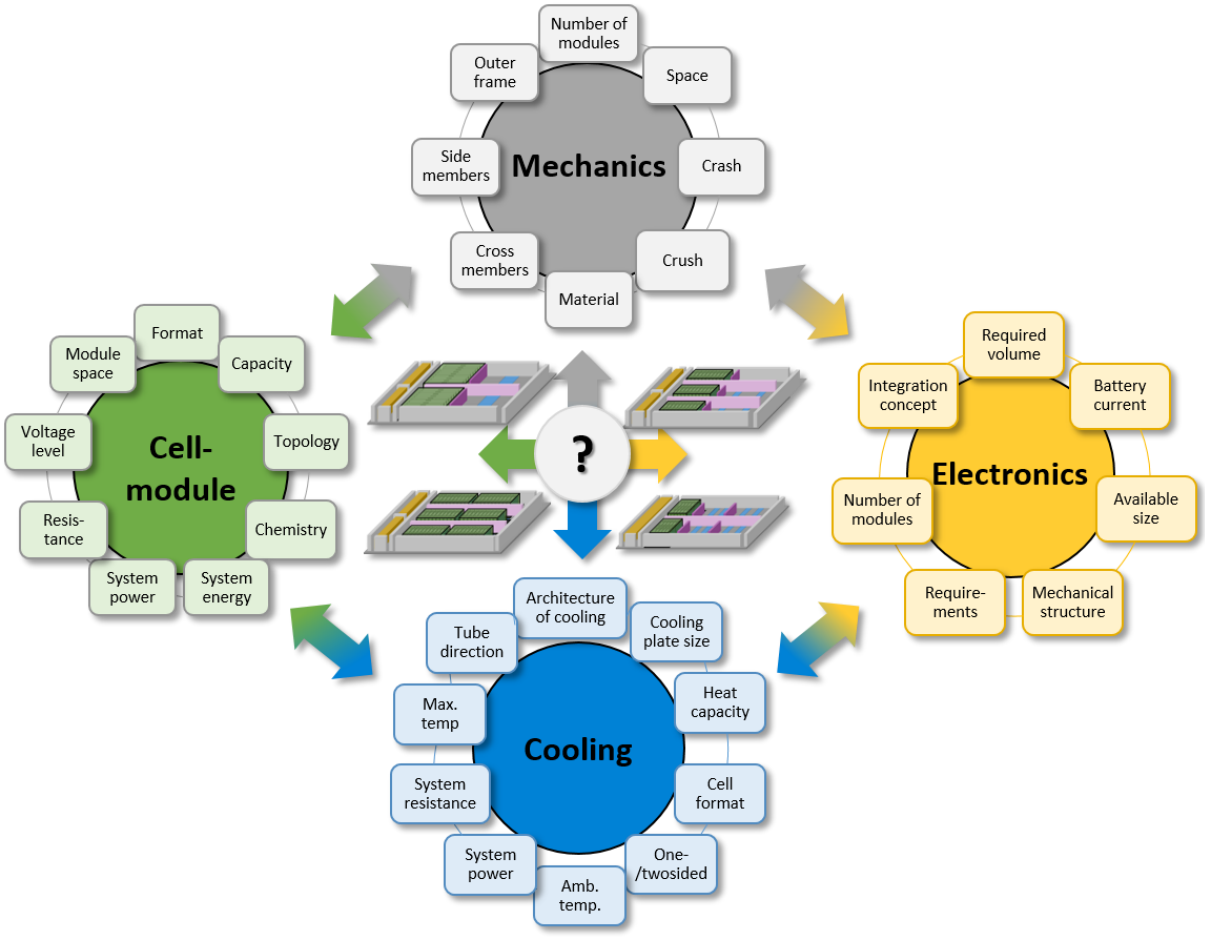

Figure 4.2: Overview of the main component groups cellmodule, mechanics, electronics, and cooling in battery system design. Each component has several dependent parameters. The components also depend on the parameters of the other components.

The literature proposes various reports, frameworks, and simulation models to delineate individual components in great detail. Dechent et al. report on battery cell lifetime for different cell formats, sizes, and chemistries [207]. Pierri et al. [177], Reiter et al. [203], and Saw et al. [22] propose cell integration frameworks and discuss

challenges in cell selection. Li et al. analyze thermal characteristics for different cooling specifications, including single and double-sided liquid cooling [252]. Chung et al. propose a thermal simulation model for a commercial pouch cell with various pack designs [216]. Kalnaus et al. report on the mechanical deformation of a large automotive pouch cell [253]. Uerlich et al. analyze battery pack packaging efficiency based on crash performance considering energy absorption from the cell level to the system level [123]. Arora et al. summarized mechanical design challenges and strategic placement techniques for optimal battery pack design [21]. The EV's battery junction box is generally only little addressed in the literature. However, analyses for a battery junction box testing the spring force of relays were, for example, executed by Carvou et al. [254].

In contrast to standalone simulation models, coupled models are, for example, performed by Zhao et al. [213]. Thereby, the cell geometry of a LIB pouch cell is optimized for a tab cooling strategy. Furthermore, Li et al. consider various components and propose a methodology for one whole battery pack design, focusing on cell selection and investigating the effects of different cell materials [255]. However, at the time of initial publication, no comparable work concerning combined battery system models that include all major components and ways to address EV-specific requirements was found in the literature. Nevertheless, in battery system engineering, the interdependencies of components are one of the biggest challenges, especially concerning installation space allocation. Therefore, coupled battery system design models must be developed to adequately represent the dependencies between the individual component simulation models while simultaneously performing technical and economic evaluations.

This chapter aims to bridge the aforementioned research gap and provide a novel model approach to optimize space allocation for battery systems using coupled simulation models of the main system components of cellmodule, cooling, mechanics, and electronics.

This chapter's major contributions are:

- A novel model approach to parametrize installation space allocation within a battery system using five independent superordinate design variables.

- Providing an innovative framework consisting of a holistic multiphysical approach to evaluate different components within the battery system from the cell level to the system level.

- Combining universal and fully parametrized submodels for each main system component, including multiple interdependencies between the technical submodels.

- Unique approaches for evaluating multiple battery system components with low computational time.

- Detailed comparison of multiphysical changes between different battery system concepts.

- Elaboration of holistic battery system designs based on exemplary battery systems from the field.

4.2 Introduction of HV-Battery-Optimization-Tool

4.2.1 Basics

The High-Voltage-Battery-Optimization-Tool (HV-BOT) is a software tool for optimizing HV battery systems within (hybrid) electric vehicles. The tool's main application is the optimization of battery system concepts given user-defined requirements. Different battery system concepts can be evaluated mutually with respect to feasibility, costs, and weight utilizing abstracted and fully parameterized technical submodels for the main component groups of cellmodule, mechanics, cooling, and electronics. Further applications include the evaluation of concept differences with regard to the total number of modules as well as the analysis of small differences, such as the stacking direction or size of battery cells, from an overall system-specific perspective.

The general procedure of the HV-BOT is depicted in Figure 4.3. The tool works based on the user-defined inputparameters describing the general requirements for the battery system. These are, for example, the overall installation space, the system energy, and power demand. By updating the design variables, which describe the space allocation for each component, different battery system designs can be evaluated. The submodel-concept, described in Chapters 4.2.2 and 4.3, evaluates the battery system given the specified space allocation.

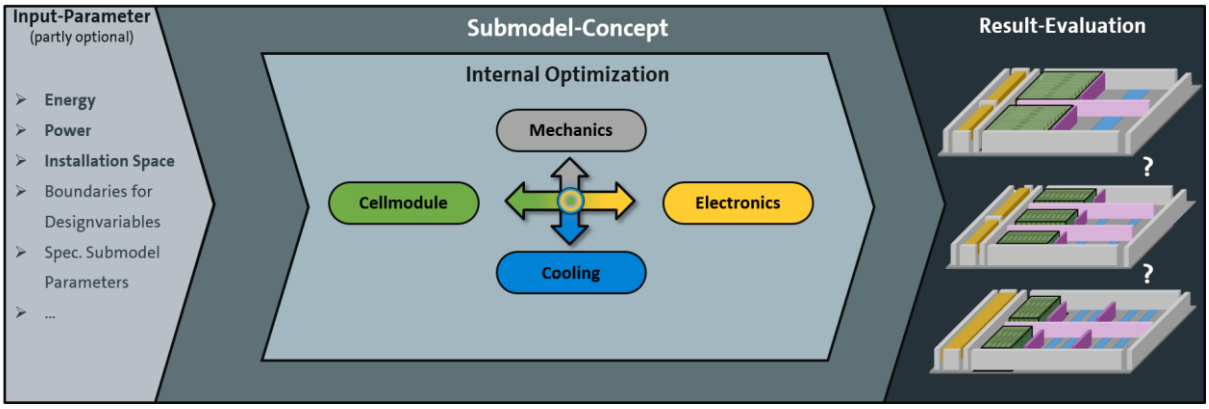

Figure 4.3: Flow diagram of the HV-BOT. Different inputparameters can be entered user-defined into the tool (e.g., energy, power, total installation space). A parameterization of the design variables $x_1, \dots, x_5$ is selected, representing space allocation for the different components. The respective submodels use the space allocation for cellmodule, mechanics, electronics, and cooling to evaluate the optimal configuration for the given inputparameters.

Five design variables are used to describe the battery system's space allocation, as exemplified in Figure 4.4. The design variables are mathematically defined as follows:

x_1 = Share of battery module installation space within the overall battery system installation space in the x-direction.

x_2 = Share of battery module installation space within the overall battery system installation space in the y-direction.

x_3 = Share of battery module installation space within the overall battery system installation space in the z-direction.

x_4 = Number of modules within the battery system in the x-direction.

x_5 = Number of modules within the battery system in the y-direction.

With $x_1, x_2, x_3 \in]0,1[;\ x_4, x_5 \in \mathbb{N}\backslash\{0\}$.

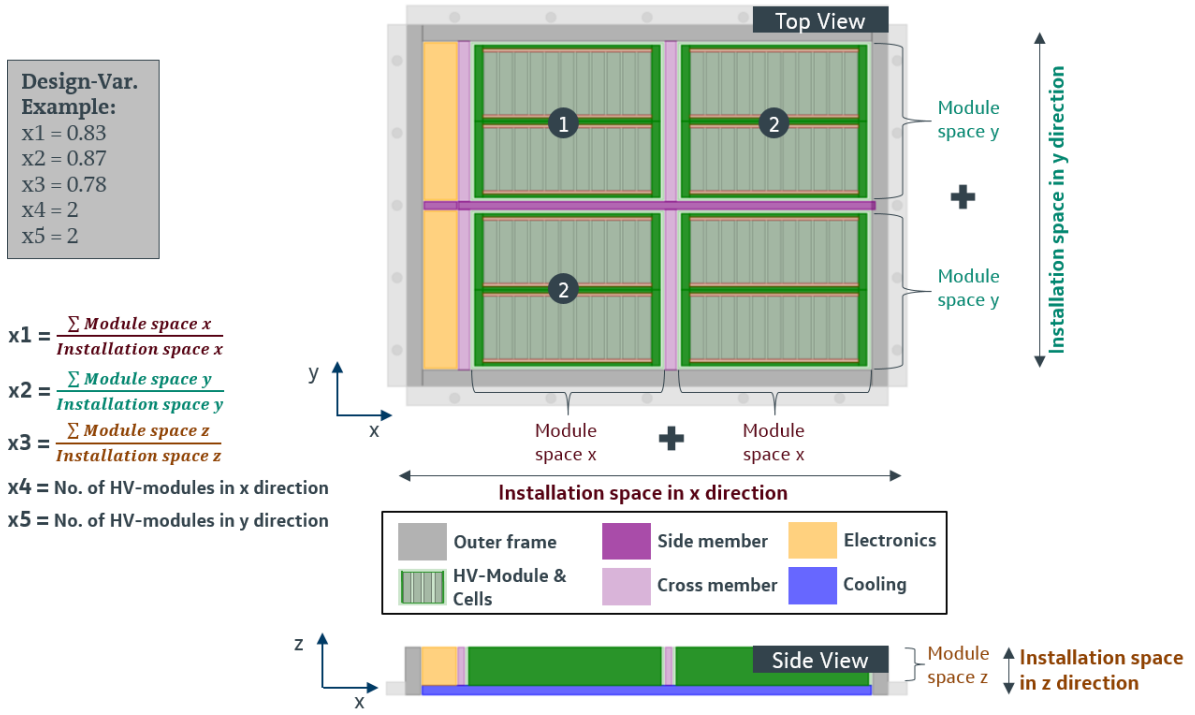

Figure 4.4: Exemplary HV-BOT parametrization for a fully evaluated battery system based on the five independent design variables x_1, x_2, x_3, x_4, x_5 from the top and the side view.

4.2.2 Mathematical model of the submodel-concept

The submodel-concept is based on four submodels $i \in \{1, 2, 3, 4\}$. The submodels are used to evaluate the technical specifications of the different components within the battery system design. The modular design of the submodel-concept enables the technical submodels to be updated frequently and, therefore, be adaptable to new developments in battery system engineering. Moreover, technical submodels can be individually elaborated from each other or even exchanged or added ($i \in \{1, \dots, n\}, n \in \mathbb{N}$). In addition to the technical specifications, each submodel returns a degree of feasibility (DOF) as output. The DOF is important as it may vary significantly based on the user-defined inputparameters. For each given design variable set $\mathbf{x}$ $(x_1, x_2, x_3, x_4, x_5)$, every submodel i returns the cost estimation $c_i(\mathbf{x}) \in \mathbb{R}^+$ of the corresponding technical component and the degree of feasibility $\mathrm{DOF} = \Phi_i(\mathbf{x}) \in \mathbb{R}^+$. A DOF of $\Phi_i(\mathbf{x}) \leq 1$ corresponds to a feasible solution for the submodel i, whereas values of $\Phi_i(\mathbf{x}) > 1$ describe an, at least partly, infeasible solution. The physical derivation for costs and DOF of each submodel is described in Chapter 4.3.

For each design variable set $\mathbf{x}$, the submodels' DOFs $\Phi_i(\mathbf{x})$ can be combined to infer the total feasibility $\mathcal{F}(\mathbf{x})$ of the evaluated battery system design, which is defined as:

$$\text{Feasibility } \mathcal{F}(\mathbf{x}) = \begin{cases} 1, & \text{for } \Phi_1(\mathbf{x}) \leq 1 \wedge \Phi_2(\mathbf{x}) \leq 1 \wedge \Phi_3(\mathbf{x}) \leq 1 \wedge \Phi_4(\mathbf{x}) \leq 1 \\ 0, & \text{for } \Phi_1(\mathbf{x}) > 1 \vee \Phi_2(\mathbf{x}) > 1 \vee \Phi_3(\mathbf{x}) > 1 \vee \Phi_4(\mathbf{x}) > 1 \end{cases}. \quad (4.1)$$

4.3 Physical models of the submodel-concept

In order to enable an iterative working procedure for the HV-BOT, the individual submodels have to run with low computation time. Internal optimizations of each submodel lead to an optimized concept for each component, given the available installation space allocation. Additionally, the HV-BOT submodel-concept has implemented interdependences between the individual submodels. Therefore, the chosen cell, its chemistry, or the mechanical battery structure directly influences other components like the cooling plate and its related costs. Figure 4.5 illustrates some major dependencies within the submodel-concept. The next chapters will introduce the different submodels from a technical perspective and describe how the different physics are implemented and abstracted. Further model descriptions, derivations, methodologies, references, and default assumptions for model parameters can be found in the appendix in Chapters 8.1 to 8.5.

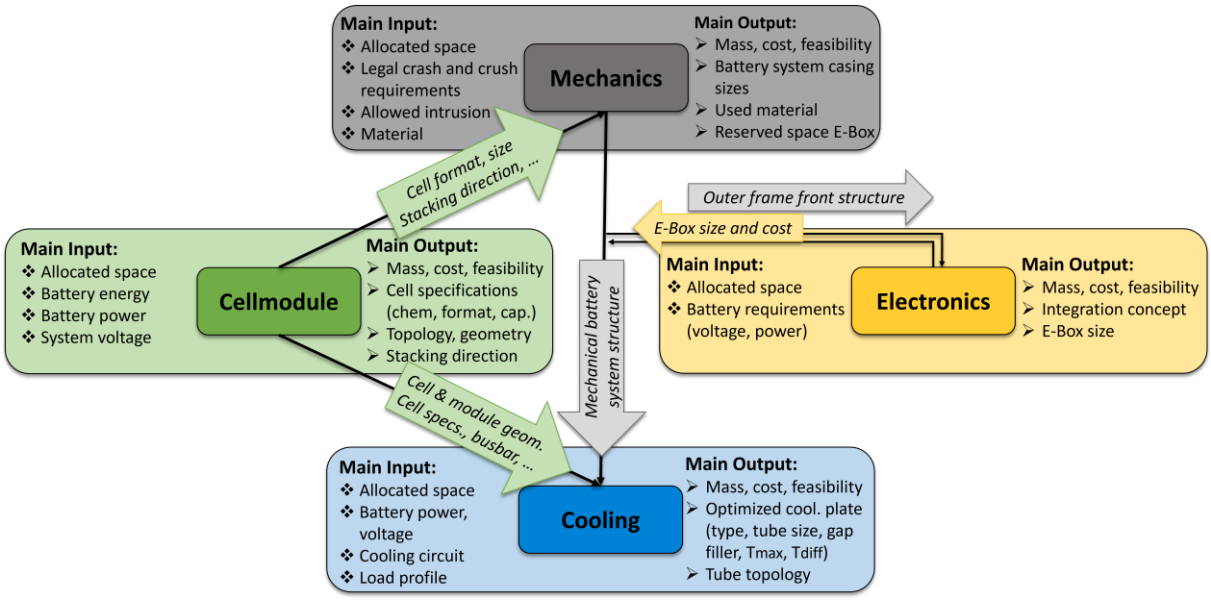

Figure 4.5: Schematic of the submodel-concept of cellmodule, mechanics, electronics, and cooling components. Main inputs and outputs are described for each submodel. Major implemented interdependencies are depicted on top of the arrow paths.

4.3.1 Submodel cellmodule

Cellmodule development is associated with multiple physics, resulting from its geometric, electrical, and thermal design. The main task is to design the battery module optimally for the respective application in terms of energy and power [189].

Furthermore, aspects of costs and other essential constraints regarding voltage, mechanical stability, electrical behavior, and thermal properties are design-relevant parameters [21, 190, 191].

In the following sections, the various aspects of modeling the cellmodule submodel are derived in different subchapters. First, the system-based stacking and packaging model is redescribed. Second, electrical and thermal modeling is defined. Third, the cellmodule cost model is derived. Lastly, aging-relevant packaging requirements are proposed.

4.3.1.1 Geometric stacking model

The HV-BOT cellmodule submodel uses a modified version of the stacking model described in Chapter 3. This chapter will briefly summarize the basic model and, in particular, describe the integration and extension used for this chapter.

In Chapter 3.3, the general procedure of the cellmodule model for stacking cells into the associated module geometry was already described. The cellmodule model used here also permits stacking cells along the module's shorter or wider side. Other stacking options (stacking in height and mixed stacking topologies) are not being considered. The overall available cellmodule space is defined given the global design variables x_1 to x_5 (see Chapter 4.2).

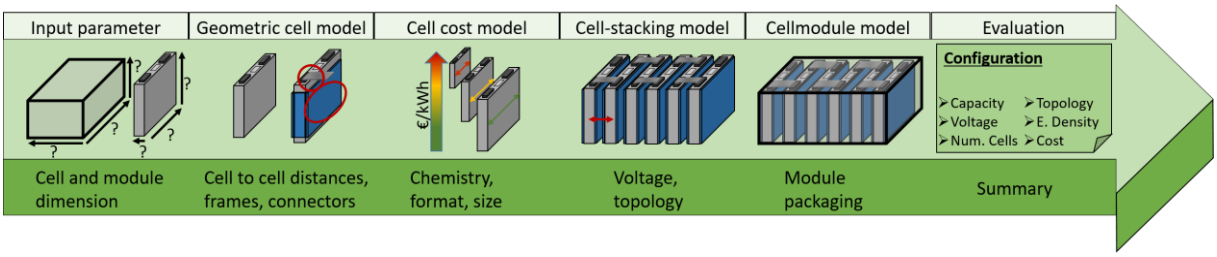

Figure 4.6: Schematic representation of the cellmodule submodel procedure. Illustration oriented to the original model from [161].

4.3.1.2 Cell topology requirement

System voltage results from the number of serially connected cells n_{serial} within the system and the cell chemistry-dependent maximum cell voltage $U_{\text{cell,max.ocv}}$. For this model approach, the cellmodules within the battery system are exclusively connected in series. Therefore, the necessary number of cells $n_{\text{CellsPerModule}}$ is based on the user-defined requirement of the system voltage $U_{\text{system,max.}}$ and the number of modules n_{modules} as follows:

$$n_{\text{CellsPerModule}e} \in \mathbb{N};\ n_{\text{CellsPerModule}} \approx \frac{U_{\text{system,max.}}}{U_{\text{cell,max.ocv}}} \cdot \frac{n_{\text{ParallelCells}}}{n_{\text{modules}}}. \tag{4.2}$$

Thereby, the number of parallel cells for each module $n_{\text{ParallelCells}}$ describes the degree of freedom in optimizing the cellmodule's electrical topology. Maximum cell open circuit voltage $U_{\text{cell,max.ocv}}$ is chemistry-dependent defined in the appendix in Chapter 8.1. Based on the total number of modules n_{modules}, some system configurations may contain more cells than others, although the same system voltage is required. This results from Eq. (4.2), as the number of cells in each module is rounded depending on

the system voltage and the total number of modules. After determining the number of cells for each module, a geometric, electrical, and thermal cellmodule model is built next. The deviation for these models is described in the following.

4.3.1.3 Geometric packaging properties

This section derives the geometric cellstack and module packaging properties for the different cell formats, sizes, and chemistries. First, the necessary cell-to-cell space is derived based on cell swelling and thermal propagation precautions. Second, methods for determining the frontplate and endplate thickness are developed. Third, spacing for the sideplates, coverplate, and bottomplate is defined.

Various studies in the literature are executed to describe reversible and non-reversible cell swelling. The work from Wünsch et al. in [215] showed cell swelling above 20% of the cell's thickness for an uncompressed pouch cell. Generally, cell swelling is directly influenced by the stacked electrode layers and, therefore, the corresponding cell thickness d_{cell}. In cellstack construction, cushion pads (also named compression pads) can be used to reduce cell swelling and thereby minimize specific aging effects [256, 257]. Thereby, cushion pads with compressive properties can be placed between the cells in the cellstack. The intrusion into the pad gradually increases the counterforce from the pad to the adjacent cells. Thus the thickness changes caused by cell swelling can be minimized. Figure 4.7 shows this behavior schematically for different exemplary cushion pads.

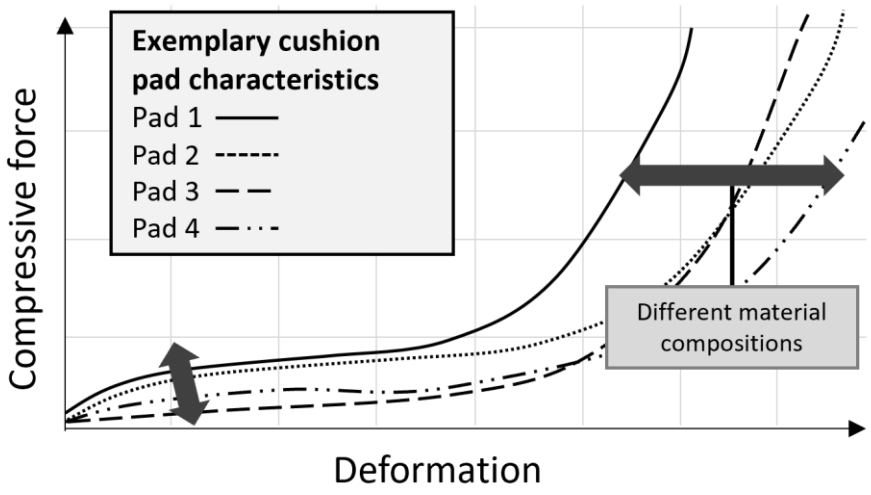

Figure 4.7: Exemplary cushion pad strain/force curve for different pad options.

By using different materials for the cushion pad, the deformation and force curve can be adjusted and thus be optimally adapted to the swelling behavior of the cell in use.

Space between individual cells within a module can also be reserved for other pads or materials to prevent cascading thermal runaway (see Chapter 2.2.1.6) [94]. As larger cells with higher capacities generally contain more potential thermal runaway energy, the cell-to-cell space should be correlated to the respective cell capacities C_{cell} (see Chapter 3.3.1). In order to combine both the effects of swelling influenced by the cell thickness [218] as well as cell energy-related thermal propagation cascading, a dynamic cell-to-cell space is used. For pouch cell packaging, the cell-to-cell space is defined as:

$$Cell - to - cell - space_{\text{pouch,NMC}} = \left(1.5\ \text{mm} + \frac{0.006\ \text{mm} \cdot C_{\text{cell}}}{\text{Ah}} + 0.08 d_{\text{cell}}\right). \quad (4.3)$$

The more robust internal housing of prismatic cells is generally advantageous for cell swelling [258]. Furthermore, the gassing vent in prismatic cells allows for a more controlled thermal runaway in the event of failure. Thus, the cell-to-cell space for prismatic cells is defined as:

$$Cell - to - cell - space_{\text{prismatic,NMC}} = \left(1\ \text{mm} + \frac{0.006\ \text{mm} \cdot C_{\text{cell}}}{\text{Ah}} + 0.04 d_{\text{cell}}\right). \quad (4.4)$$

For LFP-Type cells, a simplified approach is used. As LIBs with LFP chemistry are safer inherently [259] and thus less likely to run into unintended thermal runaway, the cell-to-cell space is defined smaller:

$$Cell - to - cell - space_{\text{pouch,LFP}} = 1.5\ \text{mm}, \quad (4.5)$$

$$Cell - to - cell - space_{\text{prismatic,LFP}} = 1\ \text{mm}. \quad (4.6)$$

Further important mechanical structure components in the cellmodule packaging are the frontplates and endplates. These plates are used to brace the stack of cells within the module and can also gather force occurring from cell swelling. Distances from cell to endplate and cell to frontplate are 50% of the previously defined cell-to-cell space values.

In order to better understand the direction of the forces within a cellstack, the occurring swelling forces in a cellmodule with stacked electrode layers are schematically depicted in Figure 4.8. Thereby, the cellstack-included cushion pads absorb the geometric swelling of the cells. With increasing intrusion into the compression pad, the counterforce on the cell also increases (see Figure 4.7 above). The compression pad is uniformly intruded and cannot move because the next adjacent cell in the cellstack pushes it in the opposing direction (see red arrows in Figure 4.8). This setup can ensure a homogeneous force distribution within the entire cellstack.

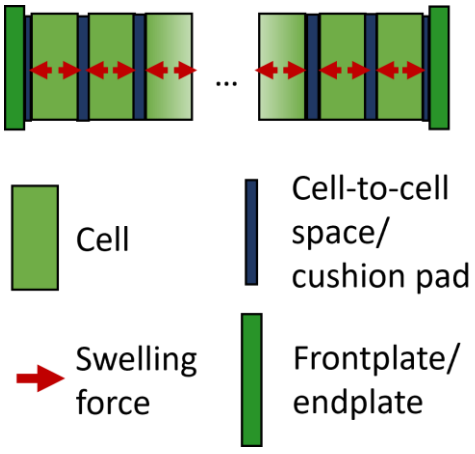

Figure 4.8: Cellstack setup and schematic swelling forces for a prismatic cellstack with frontplate and endplate.

However, the first cell and the last cell in a stack do not have two counterforce cells. The counterforce on the missing side can therefore be applied by using a rigid

frontplate and endplate. The plates must ensure a safe cellmodule construction throughout the entire lifetime of the battery. The literature has already analyzed the behavior of battery cells in varying mechanical conditions. For example, Müller et al. compare different compression forces for flexible and fixed (rigid throughout swelling) module compression [260]. Deich et al. furthermore vary the investigated module stiffnesses [225]. Extensive compression studies for larger automotive format pouch or prismatic cell sizes are not yet addressed in the literature. Therefore, this work uses a cell format-dependent but size-independent design area load force for the endplate design.

The Euler-Bernoulli beam theory is used to determine the necessary endplate thickness. For this purpose, the endplate's compression force is approximated as beam bending force. The endplate is assumed to be clamped at the left and right outer sides of the cellstack. The frontplate is assumed to be equally dimensioned and will thus not be explicitly described.

The endplate with the length l, has to withstand the pressure or the area load $\bar{q}$ within the cellstack throughout the lifetime. For the surrogate load case, a line load $q = \bar{q} * H$ can be calculated using the area load $\bar{q}$ and the endplate's height H. This results in a uniform line load on a two-sided-clamped beam. The maximum deflection $w_{\max.}$ is given by:

$$w_{\max.} = \frac{q \cdot l^4}{384 \cdot E \cdot I_\mathrm{y}}. \tag{4.7}$$

E represents the factor for the material-related modulus of elasticity. For aluminum, the modulus of elasticity equals $70\ \mathrm{GPa}$. I_y is the second moment of area of the endplate along the cellstacking. A derivation and in-depth investigation of the maximum deflection for different clamped and supported beams can be found in [261, 262]. For a rectangular hollow section profile with inner (hollow) height h and inner (hollow) thickness b, I_y can be determined by [263]:

$$I_\mathrm{y} = \frac{B^3 \cdot H - b^3 \cdot h}{12}. \tag{4.8}$$

A general simplification for the inner height h and thickness b is used according to:

$$\begin{aligned} b &= \alpha B, \\ h &= \beta H. \end{aligned} \tag{4.9}$$

Afterward, Eq. (4.8) can be redescribed as:

$$\begin{aligned} I_\mathrm{y} &= \frac{B^3 \cdot H - (\alpha B)^3 \cdot (\beta H)}{12} \\ \Leftrightarrow I_\mathrm{y} &= \frac{B^3 (H - \alpha^3 \beta \cdot H)}{12}. \end{aligned} \tag{4.10}$$

For the geometric design of the endplates, this work uses:

$$\alpha_{\text{prismatic,pouch}} = 0.7; \quad \beta_{\text{prismatic,pouch}} = 0.7. \tag{4.11}$$

By transforming Eqs. (4.7) and (4.8), the required endplate thickness is determined by:

$$B_{\text{opt}} = \sqrt[3]{\frac{q \cdot l^4 \cdot 12}{384 \cdot E \cdot w_{\text{max.}} \cdot (H - \alpha^3 \beta \cdot H)}} \cdot \alpha_{\text{safety}}. \tag{4.12}$$

For the safe and long-lasting operation of the battery cells, the endplates must hold the compression force while maintaining the maximum deflection $w_{\text{max.}}$. An assumed safety factor of $\alpha_{\text{safety}} = 1.3$ is intended to cover the uncertainty resulting from the assumed simplification by using the surrogate load case of beam bending. Generally, different endplate thicknesses can be determined, especially by changing the endplate material (modulus of elasticity) or structure (second moment of area). However, the endplate derivation by Eq. (4.12) gives a sufficient indication of the necessary installation space, which could be optimized with FEM simulations in future work.

In order to derive a cell size-dependent maximum endplate deflection $w_{\text{max.}}$ for Eq. (4.12), a maximum deflection angle $\alpha_{\text{max.deflection}}$ is set fixed according to:

$$\alpha_{\text{max.deflection}} = 0.5°. \tag{4.13}$$

Using the design angle $\alpha_{\text{max.deflection}}$ and simplified assumptions for the bending of the endplate, a maximum deflection $w_{\text{max.}}$ can be calculated using the formulas from trigonometry in the plane:

$$w_{\text{max.}} = \tan(\alpha_{\text{max.deflection}}) \cdot 0.5 l_{\text{plate}}. \tag{4.14}$$

The derivation of the design procedure and Eq. (4.14) is illustrated in Figure 4.9.

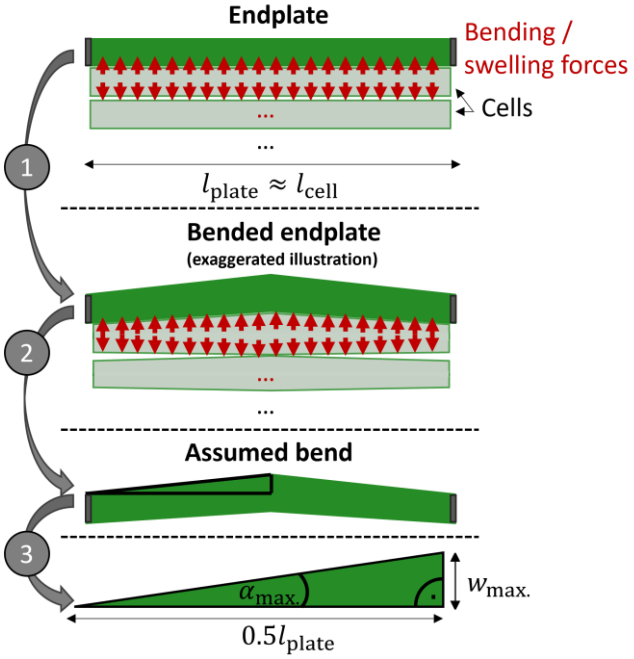

Figure 4.9: Schematic derivation of the maximum deflection for the endplate.

Lastly, the required design area force $\bar{q}$ has to be defined. The area force is defined differently depending on the cell format. For prismatic cells, the cell-to-cell distance was defined to be smaller than for pouch cells (see Eqs. (4.3) and (4.4)). Throughout the lifetime, the pressure within the prismatic cell stack will therefore be higher. The area forces are defined as:

$$\bar{q}_{\text{pouch}} = 300\ \text{kPa}, \qquad \bar{q}_{\text{prismatic}} = 700\ \text{kPa}. \tag{4.15}$$

The endplate for LFP-Type cellstacks is derived differently and based on a literature review regarding the LFP chemistry. Recent research stresses the potential of using LFP-Type cells as safer and more durable cell chemistry in battery system design [264–268]. Furthermore, the first cell to pack integration approaches, which use less module housing and safety provisions, show its realization with the LFP chemistry [259]. Derived from this, the endplate thickness for LFP-Type cells is dimensioned as fixed thickness:

$$Front/EndplateThickness_{\text{LFP}} = 5\ \text{mm}. \tag{4.16}$$

Future work could specify the design area force $\bar{q}$ as a function of cell housing, electrode chemistry, corresponding swelling behavior, and used cushion pad. Thus, a dynamically adapting force requirement could be derived.

In order to brace the cellstack with the frontplate and endplate, installation space is also required at the sides of the cellstack. This space is modeled as sideplate space. In general, the space provided for the sideplates can also be used for, e.g., tensioning straps. A thicker sideplate is used to provide additional protection for cells with side terminals. The sideplate thicknesses are defined as:

$$SideplateThickness_{\text{NMC,LFP}} = \begin{cases} 2.5\ \text{mm for side cell terminals} \\ 1\ \text{mm for top cell terminals} \end{cases}. \tag{4.17}$$

To connect the cellstack to the cooling plate and to compensate for tolerances, a thin coverplate and bottomplate with a connecting gap filler are additionally assumed:

$$Bottom/CoverplateThickness_{\text{NMC,LFP}} = 0.5\ \text{mm}, \tag{4.18}$$

$$CellToBottom/CoverplateGapFillerThickness_{\text{NMC,LFP}} = 0.5\ \text{mm}. \tag{4.19}$$

For glued systems, the mechanical packaging properties are reduced. The adapted packaging geometries can be found in the appendix.

The busbar thickness and width selection are derived according to DIN 43671 and based on the user-defined power requirements for charging and discharging (see Chapter 4.3.1.6). A summarizing default cellmodule packaging with the above-described components can be seen in Figure 4.10.

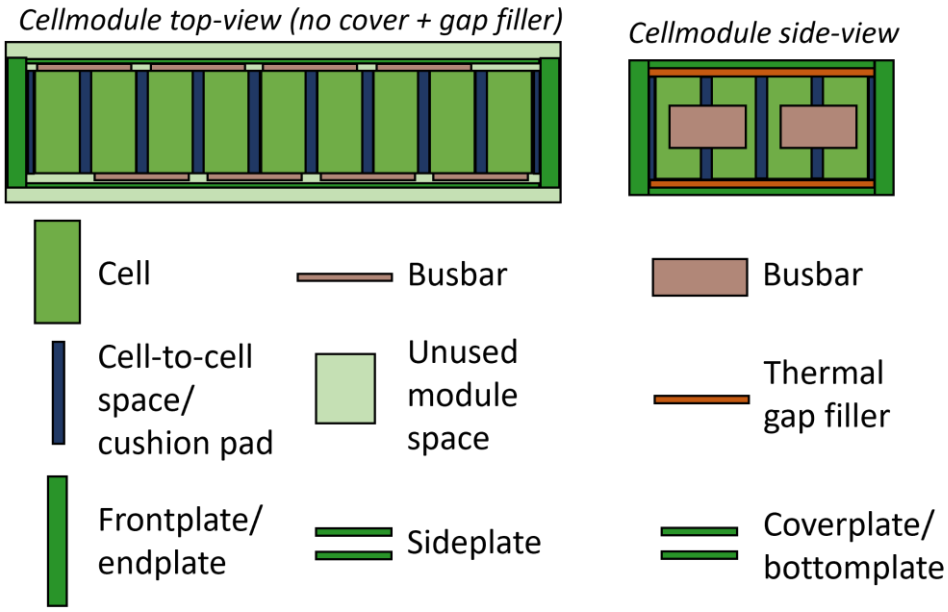

Figure 4.10: Schematic cellmodule packaging.

4.3.1.4 Electrical and thermal model

For further usage of the cellmodule in the other submodels, each cellstack is, next to geometrically, also modeled electrically and thermally. The modeling includes some simplifications and is intended to represent especially larger concept differences between different cell chemistries, formats, and sizes.

In order to maintain the generalizability of the model, reference data sheets with electrical and thermal data at the cell level are used. In particular, the cell data sheets describe the electrical resistances of the cells for different temperatures and SOCs. Additionally, a 2-RC model is used for describing the transient resistance behavior. Used data tables can be found in the appendix. Data sheets are selected depending on cell chemistry and format. Given the required cell size, energy, and power requirement, the electrical and thermal data are scaled using the resulting cell capacity, voltage, and power.

For the model's future viability, the existing reference data sheets can be easily adapted, and replaced, or new data sheets can be added for other cell chemistries (see Figure 4.11).

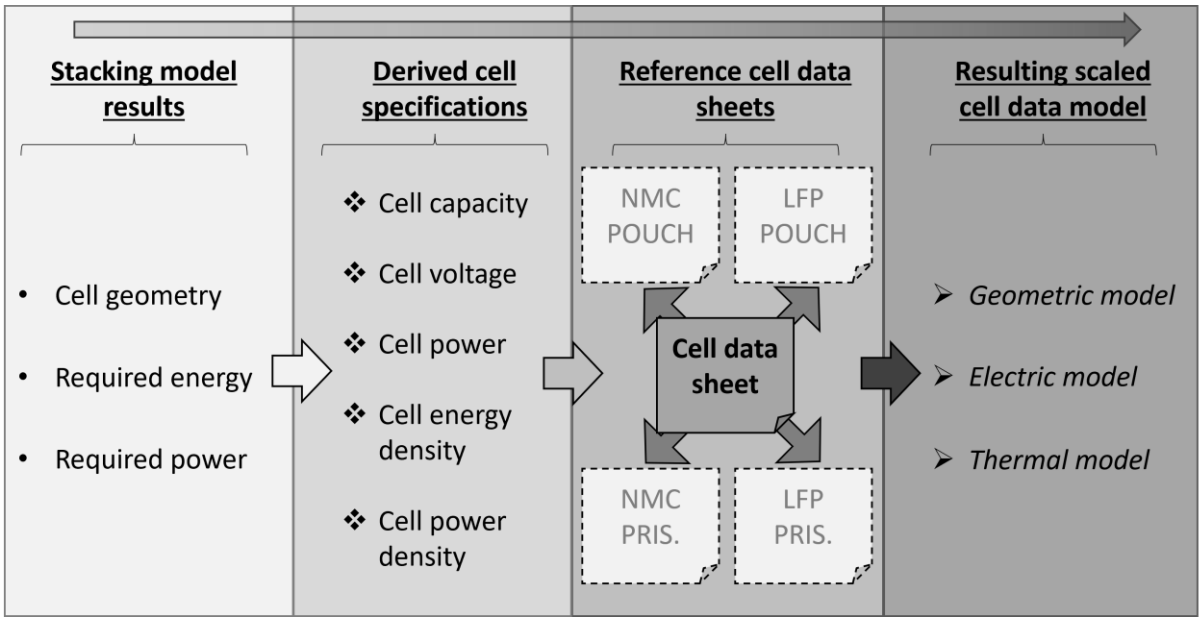

Figure 4.11: Schematic procedure from stacking model to the geometric, electrical, and thermal model of the used LIB cell and corresponding cellmodule.

4.3.1.5 Derivation of energy and power requirements

The initial energy and power requirements must be translated to the system, module, and cell level. For this purpose, a distinction is made between energy and power demand.

The user defines the system level energy requirement. However, for various safety and operational reasons, this energy requirement $E_{\text{system,usable}}$ is usually set lower than the actual energy E_{system} within the battery system (see Chapter 2.2.1.6). This limits the usable SOC window using the battery's static (relaxed) upper and lower cell voltage as follows:

$$\begin{aligned} &\text{SOC}_{\text{usable,lower lim.}} \Rightarrow U_{\text{usable,lower lim.}} > U_{\text{cell,min.ocv}}\,, \\ &U_{\text{cell,max.ocv}} > U_{\text{usable,upper lim.}} \Leftarrow \text{SOC}_{\text{usable,upper lim.}}. \end{aligned} \tag{4.20}$$

With a predefined usable SOC range ($\text{SOC}_{\text{usable,upper lim.}}$, $\text{SOC}_{\text{usable,lower lim.}}$) of the battery, the resulting usable energy at the system level $E_{\text{system,usable}}$ can be approximated as:

$$E_{\text{system,usable}} = E_{\text{system}} \cdot (\text{SOC}_{\text{usable,upper lim.}} - \text{SOC}_{\text{usable,lower lim.}}) \tag{4.21}$$

$$\Leftrightarrow E_{\text{system}} = \frac{E_{\text{system,usable}}}{\text{SOC}_{\text{usable,upper lim.}} - \text{SOC}_{\text{usable,lower lim.}}}. \tag{4.22}$$

Typical usable SOC ranges for EV battery systems are between 80% - 99%. The actual system energy E_{system} is afterward used to evaluate the required energy density at the cell level.

There are usually at least two design criteria for the power requirement. These are the power requirement for driving and the charging time requirement. Due to the lasting

high currents, the charging time requirement is, in many cases, significantly more critical for the battery system design in EVs (see Chapter 4.3.3).

For this work, a charge time requirement $t_{\text{charge req.}}$ for a SOC range of 5% - 75% is defined according to:

$$t_{\text{charge req.}} = \frac{C_{\text{system,5\%-75\%}}}{I_{\text{system}}(t)}. \tag{4.23}$$

A simplified two-stage quick charging (QC) design protocol is adopted for charging [98, 269, 270]. The protocol provides 50% of the charging time for the first charging stage and 50% for the second charging stage:

$$\begin{aligned} t_{\text{5\%-50\%}} &= 0.5 \cdot t_{\text{charge req.}}, \\ t_{\text{50\%-75\%}} &= 0.5 \cdot t_{\text{charge req.}}. \end{aligned} \tag{4.24}$$

Exemplary resulting C-rates (the rate at which the cell is charged relative to its capacity) for different charging times, using the quick charge protocol defined above, are shown in Table 4.1. These resulting C-rates are further used for aging-related module packaging properties and cell level cost evaluations.

Charge time requirement	C-rate for the first charging phase (SOC 5% - 50%)	C-rate for the second charging phase (SOC 50% - 75%)
60 minutes	0.9C	0.5C
30 minutes	1.8C	1C
20 minutes	2.7C	1.5C
10 minutes	5.4C	3C

Table 4.1: Examples of resulting C-rates for different charging time requirements following the previously defined quick charging protocol.

The quick charging protocol is intended to ensure that permissible system limits are not exceeded. For fast charging, crucial limits are:

- Comply with the maximum cell voltage limit: above the maximum permissible voltage, irreversible damage may occur due to the decomposition of the electrolyte and the cathode materials.

- Comply with the maximum cell temperature limit: above the maximum permissible cell temperature, the cell materials may decompose.

- Comply with the minimum anode surface potential: below the minimum anode surface potential, the cell may experience lithium plating.

A fast charging process is optimal if it charges the battery in the minimum time, taking into account the system limitations. Next to the above-mentioned static voltage limits (Eq. (4.20)), especially the global upper operating voltage limit $U_{\text{cell,max.cutoff}}$ of the cell has to be ensured throughout the battery's lifetime. Therefore, the begin-of-life internal cell resistances $R_{\text{cell}}(T, \text{SOC})$ are derived in simplified form using the charging current I_{charge} and the corresponding voltage response:

$$U_{\text{cell,max.cutoff}} - U_{\text{safety}}(\text{SOC}) = I_{\text{charge}}(t) \cdot (R_{\text{cell}}(T, \text{SOC}) \cdot \alpha_{\text{res.aging}}) + U_{\text{cell,ocv}}(T, \text{SOC}) \quad (4.25)$$

$$\Leftrightarrow R_{\text{cell}}(T, \text{SOC}) = \frac{U_{\text{cell,max.cutoff}} - U_{\text{safety}} - U_{\text{cell,ocv}}(T, \text{SOC})}{I_{\text{charge}}(t) \cdot \alpha_{\text{res.aging}}}. \quad (4.26)$$

$U_{\text{safety}}(\text{SOC})$ can be used to maintain a safety gap toward the cell's cutoff voltage $U_{\text{cell,max.cutoff}}$. The cell's resistance characteristics can, thus, be scaled to comply with the voltage limits described in Eq. (4.25). The chemistry-dependent voltage limits can be found in the appendix. The reserved resistance aging factor $\alpha_{\text{res.aging}}$ depends on the expected stress level and is therefore designed based on the charging requirements. This aging factor will be scenario-specifically defined in Chapter 4.3.1.8.

4.3.1.6 Electrical and thermal specifications on the module level

After determining the electrical resistances on the cell level. The module resistance is calculated using the serial and parallel connection topology within the cellmodule. Additionally, a resistance illustrating the contacting busbars is added. The busbar resistance is determined directly by using the cell's derived current requirement:

$$I_{\text{cell,max.}} = \max\left(I_{\text{cell,quick charge}}, I_{\text{cell,discharge}}\right). \quad (4.27)$$

The necessary cross-section A_{busbar} of the busbar is determined using DIN 43671. Using the length of the busbar per cell $l_{\text{busbar,cell}}$ and the specific resistance of copper ϱ_{copper}, the electrical busbar resistance can be described by:

$$R_{\text{busbar,cell}} = \varrho_{\text{copper}} \cdot \frac{l_{\text{busbar,cell}}}{A_{\text{busbar}}} \quad \text{with } \varrho_{\text{copper}} = \frac{1}{56}\,\Omega\,\frac{\text{mm}^2}{\text{m}}. \quad (4.28)$$

This results in the total module resistance:

$$R_{\text{module}}(\text{SOC}, T) = (R_{\text{busbar,cell}} + R_{\text{cell}}(\text{SOC}, T)) \cdot \frac{n_{\text{CellsPerModule}}}{n_{\text{ParallelCells}}}. \quad (4.29)$$

The thermal behavior of a LIB depends on a variety of factors. For considerations within the HV-BOT, constant values for the heat capacity $C_{\text{heat,cell}}$ and thermal conductivity λ_{cell} are used. Various literature articles discuss thermal differences between pouch and prismatic as well as NMC-Type and LFP-Type LIBs [271]. Results from Brdyden et al. [272] and Murashko et al. [273] compiled results indicating higher heat capacity for LFP-Type cells compared to NMC-Type cells. Sun [274] summarizes a generally higher heat capacity for pouch cells compared to prismatic format cells. Ziat et al. [275] confirm these trends with their results. A work from Steinhardt et al. [276] describes further detailed insights into the heat capacity and thermal conductivity of LIBs. Sun [274], Murashko et al. [273], and Yang et al. [277] also compare heat conductivity for different cell types. Findings from Wei et al. [278] show ranges from $10\ \frac{\text{W}}{\text{mK}}$ to $45\ \frac{\text{W}}{\text{mK}}$ for the in-plate conductivity and $0.66\ \frac{\text{W}}{\text{mK}}$ to $1.55\ \frac{\text{W}}{\text{mK}}$ for the through-plane or radial conductivity. Depending on the connection of the cellstack to the outer cell cup, the

thermal conductivity can change format-specifically. Christen et al. show temperature distribution experiments of a stacked prismatic cell [279]. Based on these literature findings, the heat conductivity on the cell level is defined in the appendix in Chapter 8.1 for the reference prismatic, pouch, LFP-Type, and NMC-Type cells.

Heat capacity on the module level is determined by additionally adding packaging materials M with weight m and specific heat capacity c_{p}:

$$C_{\mathrm{heat,module}} = C_{\mathrm{heat,cell}} \cdot n_{\mathrm{CellsPerModule}} + \sum_{i \in M} m_i \cdot c_{\mathrm{p},i} \,. \tag{4.30}$$

The anisotropic heat transfer conductivity on the module level is described by first determining the material-based specific heat resistances:

$$R_{\mathrm{th},i,\mathrm{x,y,z}} = \frac{l_{i,\mathrm{x,y,z}}}{\lambda_{i,\mathrm{x,y,z}} \cdot A_{\mathrm{yz,xz,xy}}} \tag{4.31}$$

with constant thermal conductivity $\lambda_{i,\mathrm{x,y,z}}$, constant material thickness $l_{i,\mathrm{x,y,z}}$ (path parallel to heat flow) and the cross-sectional area $A_{\mathrm{yz,xz,xy}}$ (perpendicular to the path of heat flux). For the module level analysis, a simplified average heat conductivity $\lambda_{\mathrm{module,avg.,x,y,z}}$ can be computed using the specific cell and module packaging topology consisting of the specific number of cells $n_{\mathrm{cells,x,y,z}}$ and packaging structure (for comparison, see Figure 4.10 above):

$$\lambda_{\mathrm{module,avg.,x,y,z}} = \frac{l_{\mathrm{module,x,y,z}}}{(n_{\mathrm{cells,x,y,z}} \cdot \; R_{\mathrm{th,cell,x,y,z}} + \sum_{i \in M} R_{\mathrm{th},i,\mathrm{x,y,z}}) \cdot A_{\mathrm{cell,yz,xz,xy}}}. \tag{4.32}$$

The cellmodule's thermal specifications are directly used in the cooling evaluations. Usage, model insights, and limitations from the submodel cooling are described in Chapter 4.3.3.

4.3.1.7 Cost model

The cost deviation for the cellmodule submodel is divided into two separate parts. On the one hand, the cell costs, and on the other hand, the module and packing costs. Both parts are relevant and can differ depending on the construction and requirements of the cellmodule.

Cell level costs:

Often, battery cell costs are quoted using a normalized cost per kWh. This allows easier comparability for different cell sizes or energies. Actual costs for lithium-ion cells are challenging to estimate in a general and definite way. The costs depend on the modeling approach, production location, production size, and many other factors. In order to still model cell costs at the module level, two key ratios are considered. Figure 4.12 gives an overview and shows the dimensions of the cell cost model used in this chapter.

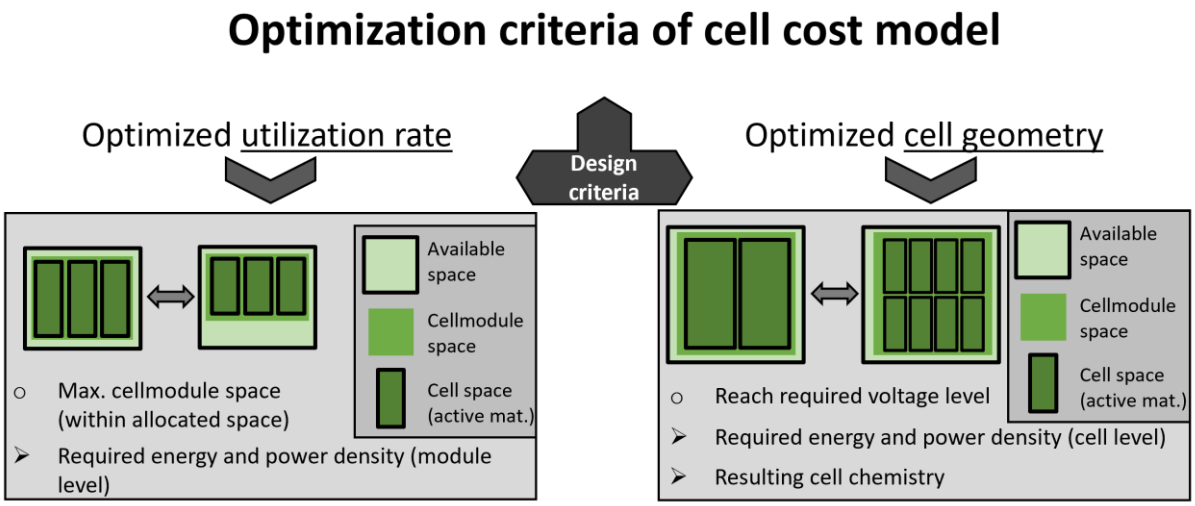

Figure 4.12: Schematic of used multi-criteria cell cost model.

First, the utilization on the cellmodule level is considered. It is defined as:

$$V_{\text{cellmodule space}} = V_{\text{available space}} - V_{\text{unused space}}. \tag{4.33}$$

This utilization describes the used cellmodule space based on the globally allocated available space subtracted by the non-usable (unused) space.

By generally maximizing $V_{\text{cellmodule space}}$, the needed energy and power density can be effectively minimized for a given energy or power requirement on the module level.

Secondly, the utilization and design of the cell space with actual cells are considered. Thereby, the cell size plays a decisive role. The cell size determines the ratio of active to passive material. Since only active material contributes to energy capability, the normalized cell cost per kWh increases when more passive material is used. However, if larger cells with a higher proportion of active material are used, the geometric flexibility of the cell is generally reduced. In addition, the requirement for module voltage, which is directly related to the number of cells and the cell chemistry, has to be considered.

In order to address both of the aforementioned cost design criteria, the cell costs for this work are defined based on a three-part cost model (see Table 4.2), which furthermore allows quantitative comparison between different cell types, sizes, or chemistries.

Cost part	Prismatic	Pouch
Fixed cost: gassing vent, production, welding, etc.	$1.5\ \frac{€}{\text{cell}}$	$1\ \frac{€}{\text{cell}}$
Outer material: cell shell (depending on cell geometry)	$2.5\ \frac{€}{\text{kg}}(\text{aluminum})$	$0.5\ \frac{€}{\text{kg}}(\text{pouch foil})$
Outer material: cell terminal/tab cost (see geometric details in the appendix, Chapter 8.1.3)	$2.5\ \frac{€}{\text{kg}}(\text{aluminum})$	Cathode: $2.5\ \frac{€}{\text{kg}}$ (aluminum) Anode: $10\ \frac{€}{\text{kg}}$ (copper)
Inner material: electrode stack, current collector, etc.	See Figure 4.13	See Figure 4.13

Table 4.2: Overview of cell level cost parts.

The fixed costs summarize any costs incurred for the production of each individual cell. Examples are the welding, electrode stacking, or cell closure process. The outer material for the cell shell and the cell terminal/tab is differentiated for prismatic and pouch cells. The actual shell/casing thickness is set as 1 mm for prismatic cells and 0.2 mm for pouch cells (see spatial details in the appendix in Chapter 8.1).

The largest share cost in LIBs takes the inner material-based costs. These costs include the total material of the cell's inner parts. Thus, different cell chemistries, electrolytes, electrode thicknesses, and other cell design parameters can majorly influence the inner cell material cost. Production-based cost model approaches (e.g., Schünemann [244], or Nelson et al. [187]) aim to determine the inner electrode stack costs by breaking down the costs for each production process and material used. However, the actual costs depend not only on the production equipment and machinery but are also globally time-volatile (see [280, 281]). This makes long-term cost forecasting for the time of the battery system's completion nearly impossible. Therefore, a less volatile, requirement-based cost model approach is used in this work. This approach especially prices the difficulty of fulfilling the energy and power/charging requirements. Thus, a lower energy or power electrode stack material is assumed with lower costs as it offers higher flexibility in material choice as well as electrode design.

The inner material costs used in this work are illustrated in Figure 4.13. The depicted range of possible volumetric electrode stack energy densities can be compared to values derived in [282]. Lower costs are represented in blue color and higher costs in red color. The color gray indicates unfeasible requirements that cannot be materialized due to cell chemistry-related boundaries. A reference charge C-rate of 1C was defined as the lower cost border. The upper border C-rate is 6C. Three different cell chemistry areas are marked within the graphic. The used requirement-based cost model approach does not initially assign specific cell chemistries to a required energy density. Rather, the NMC area, for example, could be served by a variety of different electrode chemistry variants. As an example, lower energy densities may use LMFP (see Chapter 2.2.1.4) or mixtures with high manganese while higher energy densities may need mixtures with higher nickel contents. Various exemplary costs are shown at the corner points in the graphic.

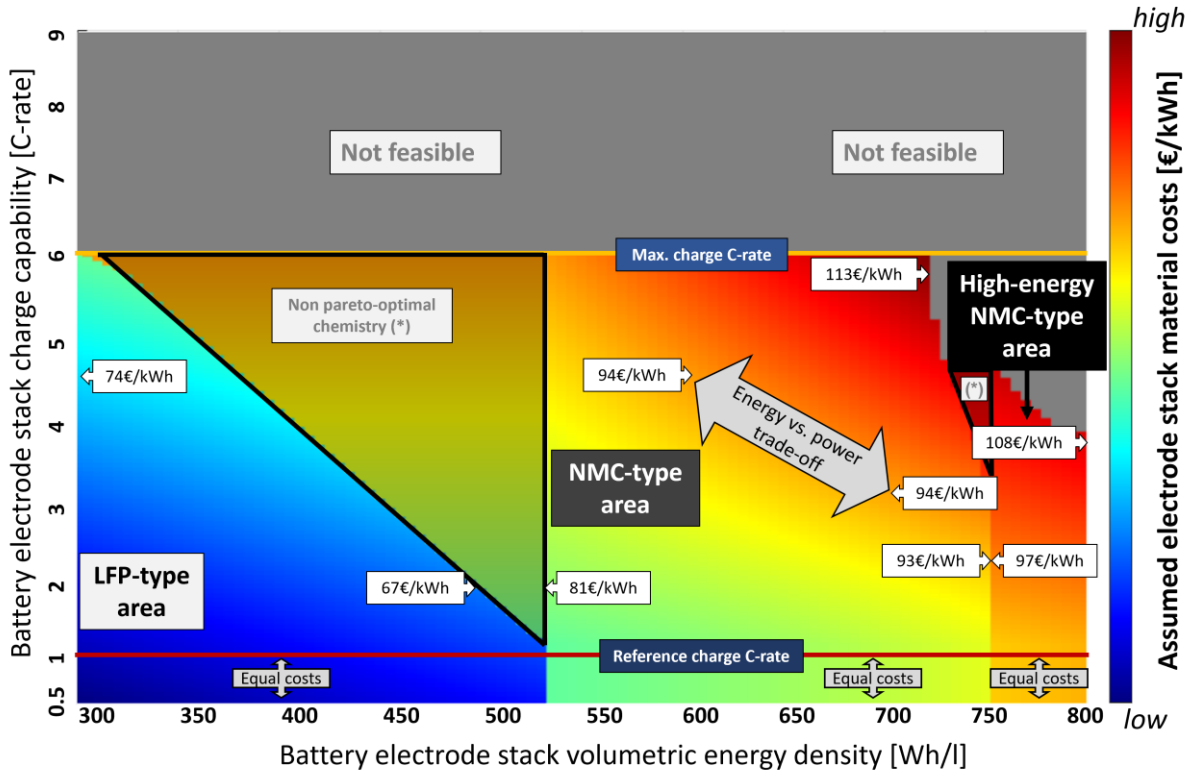

Figure 4.13: Assumed battery electrode stack costs dependent on volumetric energy and charge C-rate capability. Chemistry areas: LFP, NMC. Grayed-out area (*) = Non-pareto-optimal energy-to-charging-capability-ratio: other chemistry has to be used.

The visible color gradient greatly indicates the trade-off between energy and power, in which, e.g., the electrode thickness is varied. Generally, higher charge-capable cells can be designed by optimizing, e.g., anode, cathode, electrolyte, or the positive to negative-electrode ratio. For more insights, the review from Weiss et al. presents a holistic overview of fast-charging capable electrode design [283]. The perspective work from Masias et al. further illustrates energy versus power density trade-offs for different NMC-Type chemistries [284].

To graphically illustrate the above-derived cell cost modeling, some cost-course illustrations are presented below. Figure 4.14 shows the changing cell costs with increasing cell capacity. The resulting cost behaviors can be greatly compared to the simplified cost reduction model deduced in Chapter 3.3.3. For fixed energy densities, the resulting cost curves will shift higher or lower depending on the actual charge requirement. The observed cell geometry additionally influences the cost curve.

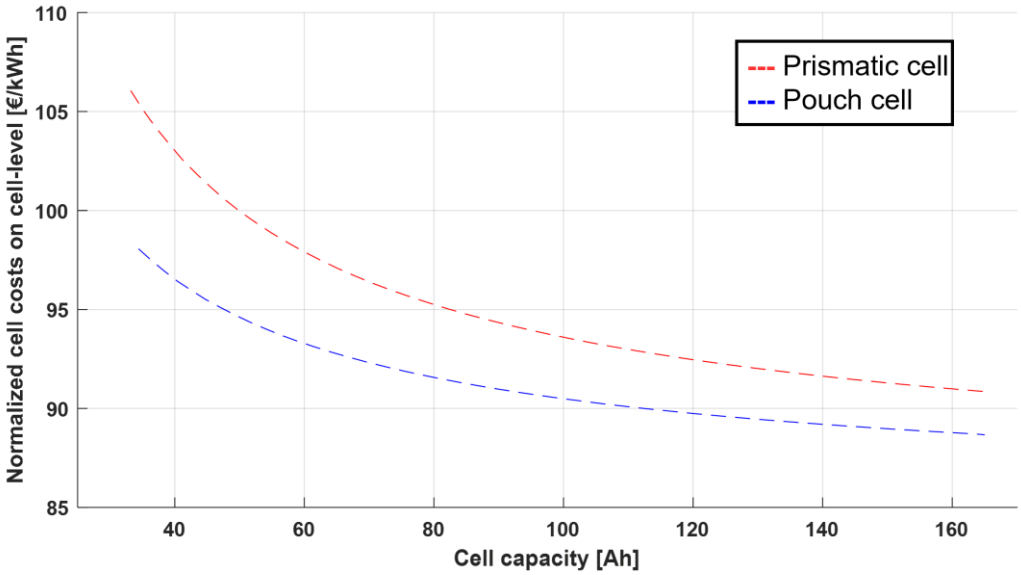

Figure 4.14: Cell cost comparison for various cell sizes and resulting cell capacities. (Charge requirement 2.4C, cell energy density 570 Wh/l).

Figure 4.15 is used to emphasize the general dependence of the cell costs on the energy density. Thereby, an exemplary prismatic cell geometry of 230 x 28 x 110 mm³ is assumed. The cost curve with the basic model assumptions from Table 4.2 is shown in red color (stated as default costs). The increasing costs with rising energy densities illustrate the working principle of the requirements-based cost model.

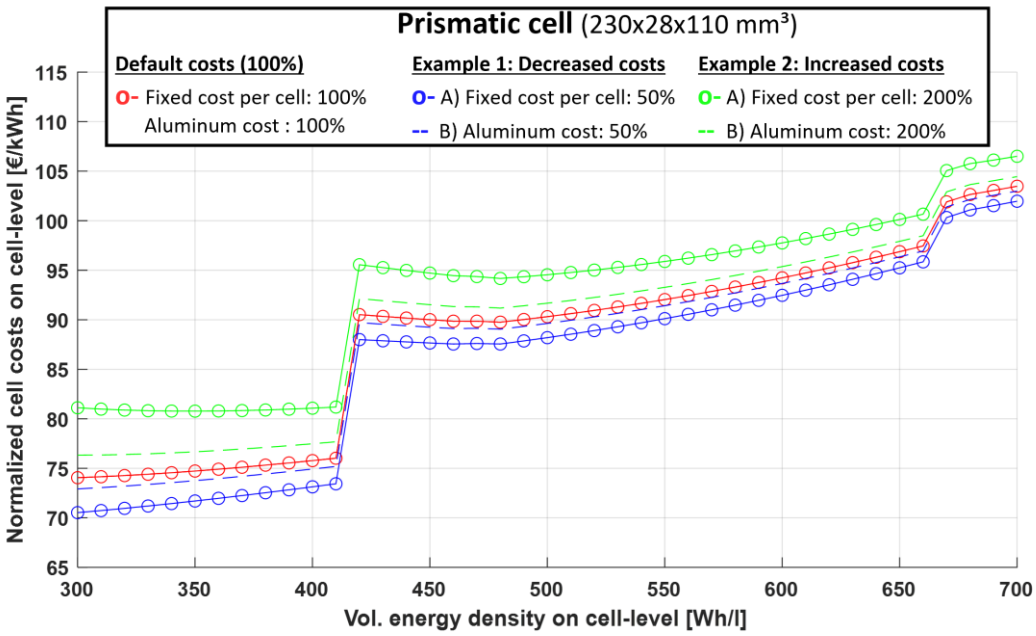

Figure 4.15: Cell cost comparison for one prismatic cell geometry with varying volumetric energy density. Fixed and outer material costs are varied with different colors (see default values in Table 4.2). (Charge requirement 2.4C).

Cost sensitivities for the fixed costs and the outer material costs are shown for reduced costs in blue (50% of default costs) and for increased costs in green (200% of default

costs) color. It is particularly noticeable that cost sensitivity is significantly greater for lower energy densities compared to high energy densities. The results emphasize that variations in fixed costs and costs of outer material affect cells with lower energy densities more, concluding that inner material costs dominate at high energy densities. This is because the total fixed and outer material costs decrease on normalized costs per kWh when higher energy densities are considered.

A concluding comparison of cell costs is shown in Figure 4.16. Here, the changing cell costs for one prismatic cell with two different volumetric energy densities are depicted depending on the required charge C-rate. The necessary charge C-rate is directly correlated to the charging performance (see Chapter 4.3.1.5). The x-axis represents the required charging capability in C-rate. The shape of both cost curves indicates that the costs of the lower energy density cells (blue) increase more slowly. This behavior stresses the typically opposing requirements in cell design for high power and high energy densities [68].

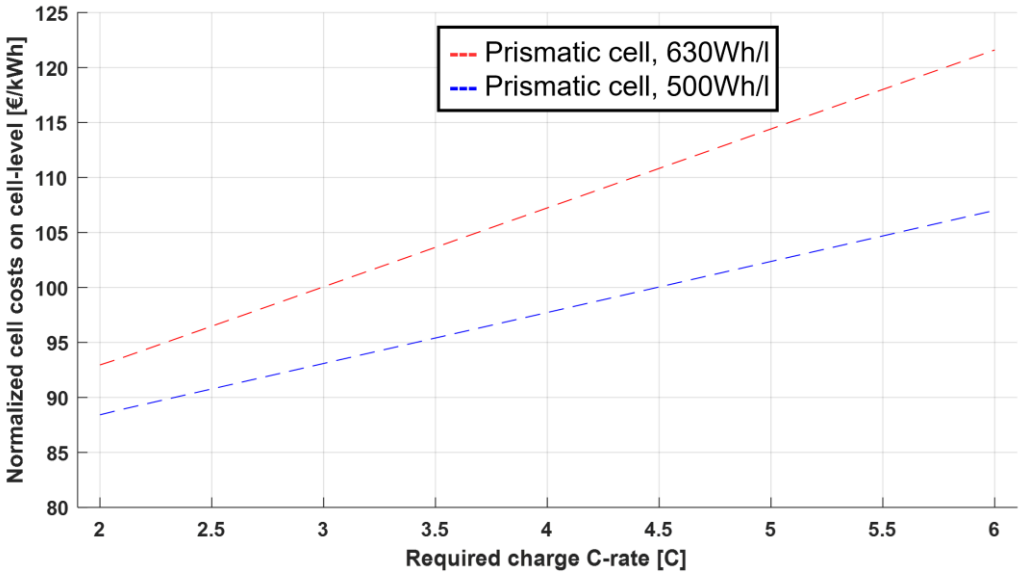

Figure 4.16: Cell cost comparison for one prismatic cell geometry with two different volumetric energy densities for varying charge requirements (cell size: 230 x 28 x 110 mm³).

Module- and packaging costs:

Module and packaging costs are modeled based on predefined material costs. The cost components and their corresponding material are summarized in Table 4.3. The actual costs are determined by the cellmodules' geometric properties described in Chapters 4.3.1.3, 4.3.1.6, and 8.1. Further packaging relevant components like busbars, cell compression pad material, and gap fillers costs are also gathered.

Component	Material	Default cost assumptions
Housing (frontplate, endplate, sideplates, coverplate, bottomplate)	Extruded aluminum	$5\ \frac{€}{kg}$

Busbar	Copper	$10\ \frac{€}{\mathrm{kg}}$
Stack packaging, cell-to-cell material	E.g., elastomeric or silicone and micro-cellular polyurethane foam with intrinsic heat resistance properties	$20\ \frac{€}{\mathrm{mm}^2} \cdot \frac{1}{\mathrm{mm}}$
Gap filler material	E.g., adhesive acrylic	$10\ \frac{€}{\mathrm{kg}}$
Unused space	E.g., polypropylene	$1\ \frac{€}{\mathrm{kg}}$

Table 4.3: Module and packaging parts and corresponding costs.

4.3.1.8 Aging requirement

Battery cell aging is a wide-ranging topic in lithium-ion battery technology. Many fundamentally different modeling approaches (physical, chemical, data-driven, mixed) are used to describe the change in cell capacity and internal resistance throughout usage. A large overview of usage-specific cyclic and calendar cell aging based on over 1000 cells with 1000 GB of data is combined in comprehensive ENPOLITE graphics and can be found in [207]. With the ENPOLITE graphics, cell aging test results can be compared in terms of energy, power, and temperature. The large comparison with more than 700 cylindrically and 300 calendar-aged cells is shown in the appendix in Chapter 8.8.

An aging analysis is often based on a stress current or power profile, which aims to test the actual behavior and thus predict the aging in the LIB as precisely as possible. Since HV-BOT is a physical-based battery system design tool, it does not represent any concrete usage scenarios of the battery system. One major stress factor for LIBs in the application is the charging power. Based on the charging requirement, a design-based approach to aging prevention is derived for this work. Depending on the charging requirement, changes in the cell package, thermal management design, and electrical cell design are considered. This approach aims to ensure that the requirements can be met throughout the battery's entire lifetime. The three different design scenarios are shown in Table 4.4.

Charging requirement: Scenario-based C-rates	**Cell package: Additional cell-to-cell space (see Chapter 4.3.1.3)**	**Thermomanagement: Characteristics for different analysis and design temperatures (Temperature value explanation see Chapter 8.3.1)**	**Resistance surcharge: Additional cell-aging resistance factor $\alpha_{\mathrm{res.aging}}$ (see Eqs. (4.25),(4.26))**
(Low QC priority) Scenario 1: $< 1.5\mathrm{C}$	-20%	$T_{\mathrm{cell}} \leq 55.0\ °\mathrm{C}$ $T_{\mathrm{diff.,module,QC}} \leq 17.5\ °\mathrm{C}$ $T_{\mathrm{diff.,fluid}} \leq 7\ °\mathrm{C}$	$+30\%$
(Medium QC priority) Scenario 2: $\geq 1.5\mathrm{C}$	0%	$T_{\mathrm{cell}} \leq 52.5\ °\mathrm{C}$ $T_{\mathrm{diff.,module,QC}} \leq 15.0\ °\mathrm{C}$ $T_{\mathrm{diff.,fluid}} \leq 5\ °C$	$+40\%$
(High QC priority) Scenario 3: $\geq 4\mathrm{C}$	$+20\%$	$T_{\mathrm{cell}} \leq 50.0\ °\mathrm{C}$ $T_{\mathrm{diff.,module,QC}} \leq 12.5\ °\mathrm{C}$ $T_{\mathrm{diff.,fluid}} \leq 3\ °\mathrm{C}$	$+50\%$

Table 4.4: Aging scenario lookup-table. Different aging-related design changes, depending on the charging requirement.

4.3.2 Submodel mechanics

4.3.2.1 Introduction

The safety of passengers in events of accidents is a crucial construction criterion for an electric vehicle and its battery system. Therefore, the functional integrity of the passenger compartment and the protection of sensitive components like the LIB cells are the main tasks of a car body structure. This includes the provision of sufficiently high stiffness to prevent the body from sagging and bending and, in case of an impact, the absorption of kinetic energy through controlled plastic deformation. Accordingly, two opposing requirements have to be addressed to design the battery system balancing both rigid and yielding structures. Thus, two load cases are primarily considered for designing the mechanical components within the mechanics' submodel. These are the side pole impact (crash) [285] as well as the mechanical integrity (crush) [286, 287]. Further country-specific automotive load cases can be found in [124, 288].

Within the HV-BOT, the mechanics' submodel is intended to ensure that the battery cells can be operated safely within the battery system. The main component of the mechanical battery system is the outer frame profile. An extruded aluminum profile is often used as the outer profile. One major advantage of extruded aluminum profiles is their variably in terms of height, width, and overall inner structure. Based on this variability, the corresponding requirements for the outer profile in terms of stiffness and energy absorbability can be perfectly met. The basis of the outer profile used in this work can be seen in Figure 4.17. Thereby, the outer profile is divided into two parts. Firstly, the fixed connection balcony, and secondly, a variable profile. The fixed connection balcony is used to connect the battery system via the vehicle rocker panel to the electric vehicle. Therefore, it is set geometrically fixed. The variable outer profile can be designed specifically for the requirements of the vehicle load cases (crash) and component load cases (crush). This process is derived and described in the following.

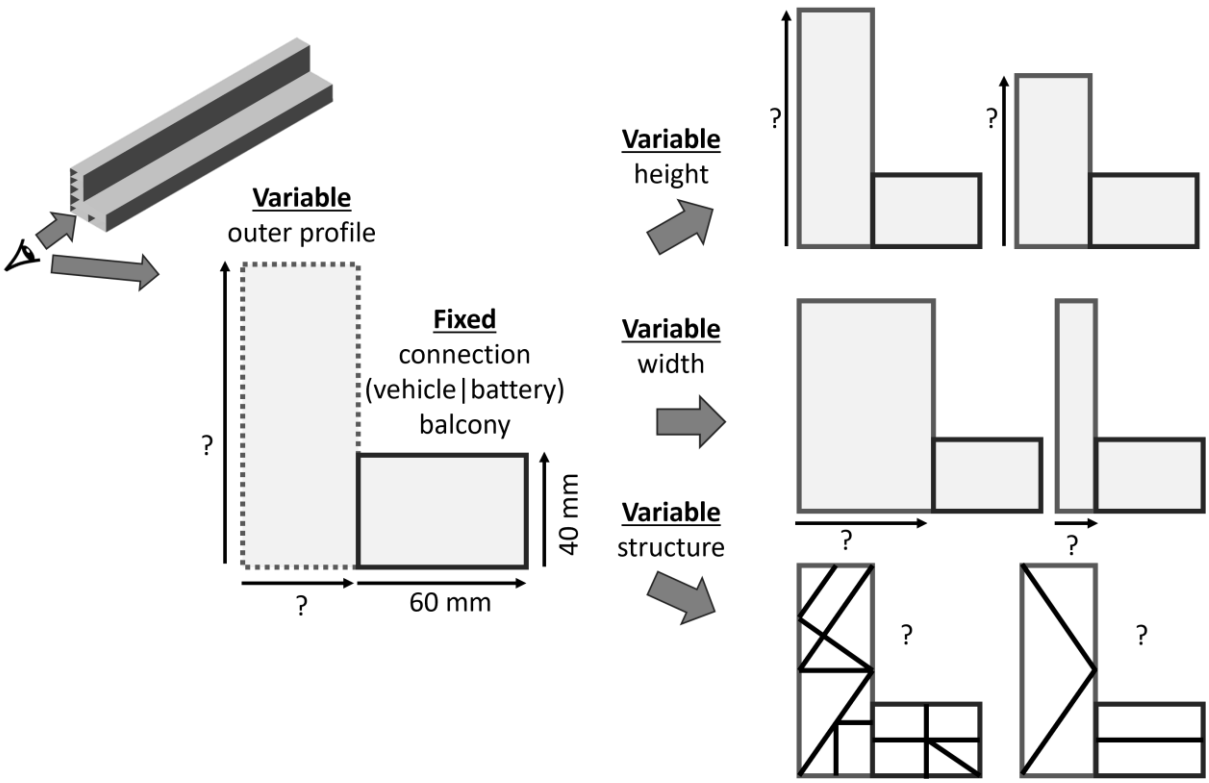

Figure 4.17: Variable design of an extruded outer profile.

4.3.2.2 Model

The testing scenario side pole impact simulates a car that crashes sideways against a roadside object like a tree or pole [285]. Herein, the vehicle's kinetic energy is mainly dissipated by the plastic deformation of structures like the battery system's outer frame. The left-handed side of Figure 4.18 illustrates the model approach to describe the crash event. The black-colored bar represents the rigid pole (together with a crashed/compressed vehicle rocker panel), and the gray-colored profile represents the battery frame's outer structure which protects the battery in green color. The kinetic energy dissipation process is depicted from left to right. The graphs below depict the contact force between the pole and the mechanical battery outer frame profile. An exemplary maximum contact force $F_{\max.}$ is reached close to the maximal intrusion $x_{\max.}$. The energy absorption E is described as the spatial integral of the axial impact force $F(x)$ over the deformation and displacement x:

$$E = \int_0^{\delta} F(x)\mathrm{d}x. \tag{4.34}$$

Here, δ denotes the effective deformation distance of the structure [123].

Next to the side pole test, the mechanical integrity (crush) also plays an essential role in the mechanical design of battery system structures. The test is also part of law requirements in several countries. A specified crush plate body intrudes the battery in serval positions. The right side of Figure 4.18 depicts the crush test schematically from a top view. In European regulations, the battery system must resist contact loads of at least 100 kN [286].

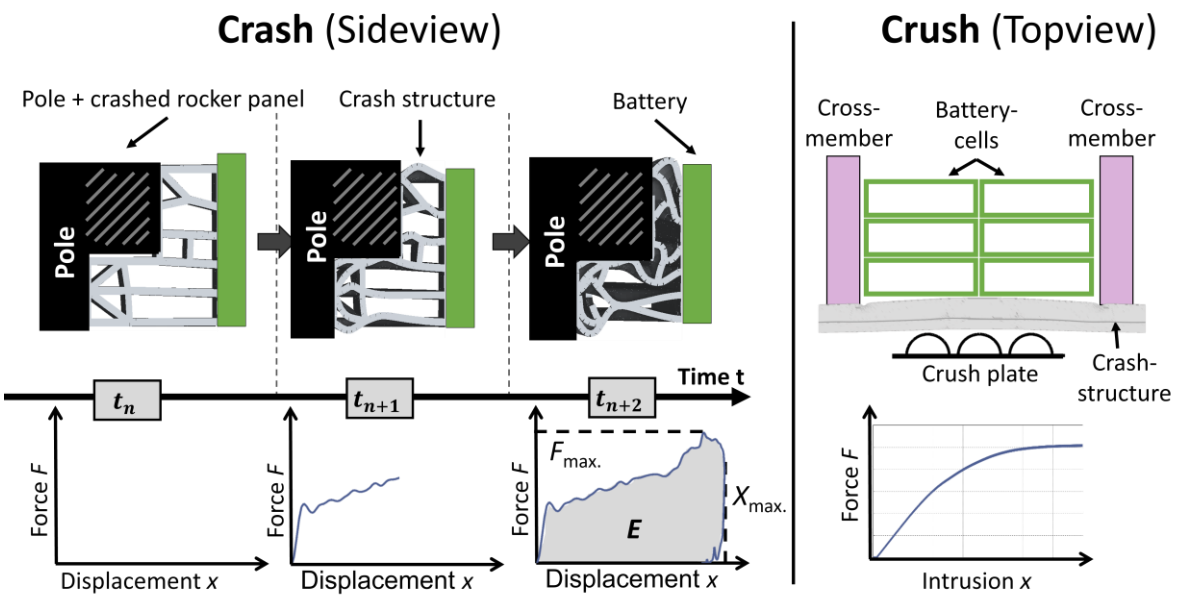

Figure 4.18: Left-handed side: schematic crash load model from the side view. Right-handed side: schematic crush load model from the top view.

Surrogate model

A surrogate model was developed to design the outer profile of the battery system within the HV-BOT. The model reduces the whole battery system depiction to the major parts for the two loads cases crash and crush. The surrogate model is depicted in Figure 4.19. Thereby, an outer profile is located in front of a crash body with a variable spring. Cross members support the outer profile with a prior defined span. This span is derived from evaluating the generic design variables x_1 to x_5 given the total installation space for the battery system.

Generally, the surrogate model can examine very different mechanical battery system designs with a wide range of cross member spans as well as outer profile shapes. The variable spring stiffness can be used to model the stiffness of different cell formats and different cell stacking directions. Moreover, the surrogate spring can be used to model the crash impact of rigid bodies (direct crash on cross beams). By additionally integrating bottom and cover plates in the surrogate model, an overall system stiffness is incorporated into the surrogate model. The bottom and cover plates can be either screwed or glued, which directly affects the system's rigidity. The surrogate model thus also allows the analysis of novel cell integration methods like cell to pack.

Next to the surrogate spring stiffness, the design-relevant intrusion of the crash bodies can be set. The intrusion defined here describes the allowed intrusion into the cellstack. Different cell formats and stacking direction-dependent intrusion depths are defined to test the load cases. For battery cells, a distinction was made between the cellstack design intrusion, which is used for the legal component load case crush, and a critical cellstack crash intrusion, which must never be exceeded due to, e.g., thermal runaway hazard.

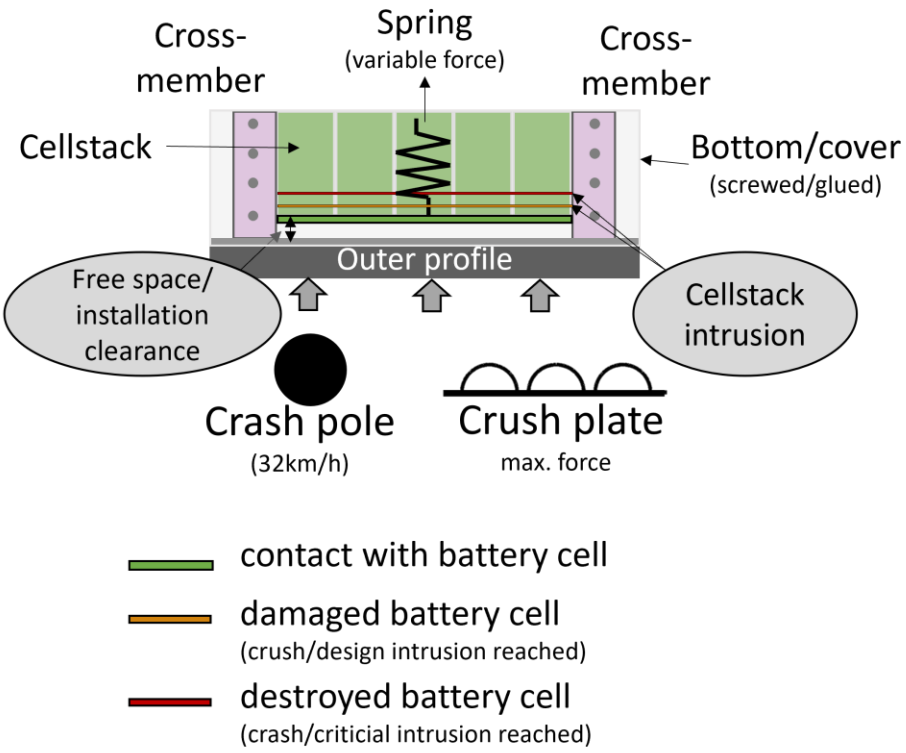

Figure 4.19: Surrogate model to test load cases crash and crush (top view).

With the surrogate model, the mechanical integrity of battery cells can be represented in a very variable way. In summary, the model allows the investigation of different span widths, spring forces, and intrusion depths. In addition to different cell formats, differences in stacking direction can also be considered. Table 4.5 summarizes the spring stiffnesses and stack intrusions for all different scenarios used in this work. The values were derived from numerous FEM-based investigations using different cell data. Thereby, a test specimen was pressed into a built-up cellstack in and against the cellstacking direction. The test ended when one cell reached its crucial intrusion. The resulting force response was used to define a normalized force value. This force is then used to define the spring stiffness within the surrogate model. The cellstack was constructed in the packaging manner equivalent to the model in Figure 4.10.

Investigations showed that more cellstack intrusion is possible when the test specimen is pressed in the stacking direction compared to pressing contrary to the stacking. This results from the deformable cushion pads. However, pressing in the stacking direction also showed lower forces. Both non-glued and glued cellstacks were investigated. For glued cellstacks, the cells were glued to both the bottom as well as the cover plate. Both quantities, the intrusion as well as the spring stiffness, can be variably changed within the surrogate model.

Default design model input data			**Prismatic**		**Pouch**	
			Alongside cellstacking	Contrary to cellstacking	Alongside cellstacking	Contrary to cellstacking
Glued cellstack package	Force	Spring stiffness [kN/mm]	2	12.5	1	1
		Design	5	5	5	5

	Intrusion [mm]	Critical	$10 + 0.1 \cdot d_{\text{cell}} \cdot n_{\text{cells,stack}}^{0.5}$	$10 + 0.1 \cdot l_{\text{cell}} \cdot n_{\text{cells,stack,side}}^{0.5}$	$10 + 0.04 \cdot l_{\text{stack}}$	$10 + 0.02 \cdot l_{\text{stack}}$
Screwed cellstack package	Force	Spring stiffness [kN/mm]	1	9.2	1	1
	Intrusion [mm]	Design	5	5	5	5
		Critical	$10 + 0.1 \cdot d_{\text{cell}} \cdot n_{\text{cells,stack}}$	$10 + 0.1 \cdot l_{\text{cell}} \cdot n_{\text{cells,stack,side}}$	$10 + 0.04 \cdot l_{\text{stack}}$	$10 + 0.02 \cdot l_{\text{stack}}$

d_{cell} = cell thickness, l_{cell} = cell length , l_{stack} = cellstack length, $n_{\text{cells,stack}}$ = number cells in cellstack
$n_{\text{cells,stack,side}}$ = number cells in cellstack contrary to cell stacking direction

Table 4.5: Allowed intrusion and stiffness data for the crash surrogate model.

FEM modeling methodology

Given the two major load cases and their corresponding surrogate models, multiple FEM simulations are used considering the non-linearities in geometry, material, and various boundary conditions. Herein, the dependency between the displacement vector $\vec{d}$ (Figure 4.18) and the linear dynamic response of a system can be described using the following equation of equilibrium as a second-order differential equation at time *t* [289]:

$$\underline{M}^{(t)}\left(\vec{d}^{(t)}\right) \cdot \vec{a}^{(t)} + \underline{D}^{(t)}\left(\vec{d}^{(t)}\right) \cdot \vec{v}^{(t)} + \underline{K}^{(t)}\left(\vec{d}^{(t)}\right) \cdot \vec{d}^{(t)} = \vec{f}^{(t)}\left(\vec{d}^{(t)}\right). \tag{4.35}$$

With $\underline{M}$ as mass-, $\underline{D}$ as damping-, $\underline{K}$ as stiffness matrix. $\vec{f}$ denotes the force-, $\vec{a}$ the acceleration- and $\vec{v}$ the velocity vector [290, 291]. The first term describes the inertia forces, the second term the damping forces, the third term represents the elastic forces, and the right-handed side shows the vector of the externally applied loads like gravity forces. Due to the highly non-linear behavior of the crash structures, small time steps are needed to capture the deformation accurately. Therefore, explicit time integration is used, as it generally offers higher efficiency in computation time. Derivations and further details can be found [289, 292].

Model integration

Within the HV-BOT, the mechanics' submodel is implemented as a fully parameterized model based on numerous prior executed FEM crash and crush simulations. Large multidimensional and coupled look-up tables of prior-executed simulations are used to evaluate different battery system concepts from a mechanical point of view. The usage of offline computations enables extensive in-depth comparisons in a short runtime. The design variables $(x_1, \dots, x_5)$ are used to determine the available installation space intended for the entire mechanical structure. It should be noted that the installation space for the electronics must be subtracted from the x-direction space if the electronics are to be integrated within the battery system (see Chapter 4.3.4). Given

the number of cellmodules (x_4, x_5) a general battery system topology consisting of the outer frame, cross- and side member is geometrically predefined. Afterward, each structure must be fully mass-related determined by following the next steps. This process is depicted in Figure 4.20.

Firstly, various outer profiles (OPs) were created using the graph and heuristics-based topology optimization (GHT) methods developed by Ortmann [292]. The method is used to find feasible outer frame profile structures balancing both the crash as well as the crush test requirements. While the crush requirement is defined in regional-specific regulations, the exact crash requirement for a battery system is dependent on further car topology specifications like the vehicle's rocker panel. Therefore, the crash energy requirement can be user-defined. To design the side crash profile, the crash test is first performed on a rigid structure (extremely high surrogate spring stiffness). The high spring stiffness demonstrates the crash impact directly into the rigid cross member. The result is a GHT-optimized outer profile that ensures optimum energy dissipation of the corresponding crash energy. The resulting outer profile is then also used to evaluate the side pole crash into the center of two crossbeams to determine the maximum cellstack intrusion (see Figure 4.19).

Secondly, a contact force $F_{\text{max.}}$, resulting from the performed rigid crash test with the GHT-created outer profile, is used to design the system's cross member rigidity. The rigidity determination uses previously defined bending simulations of various cross members with different widths, lengths, and types (full, strengthened, hollow). Hence, the resulting cross member structures are mass-optimized depending on the corresponding outer profile and the crash energy requirement.

Thirdly, the crush requirement is analyzed using again prior simulated results with multiple dependencies of the system's corresponding span between cross members as well as the observed outer frame profile, geometry, and material. The bending stiffness is tested both for the front and the lateral crush. If results are insufficient, heavier outer profiles will be chosen iteratively, starting again with the crash profile analysis.

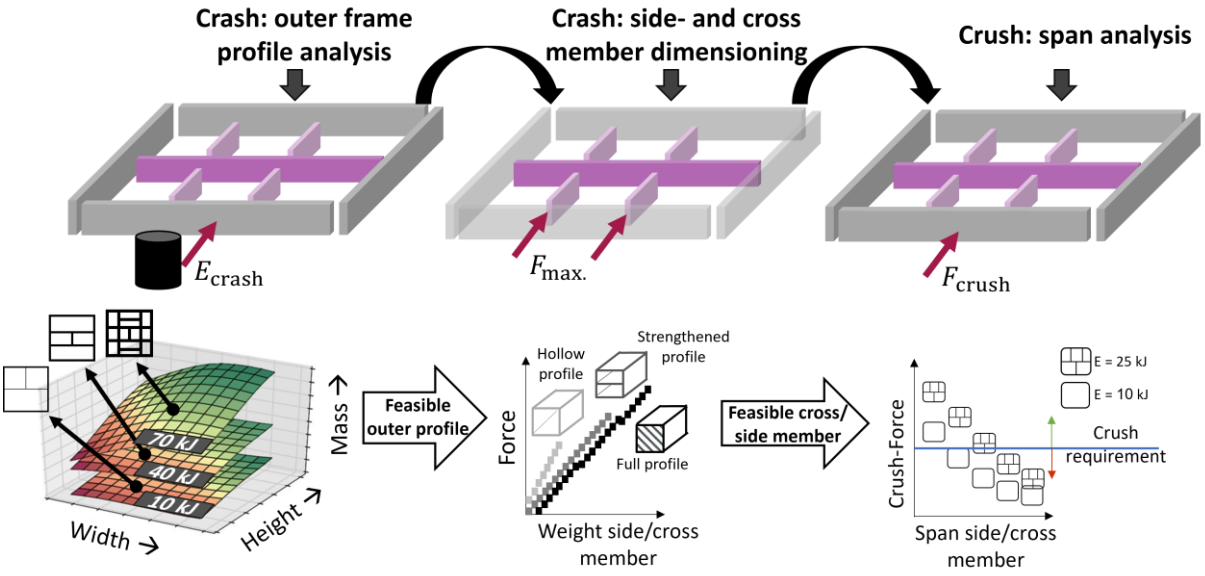

Figure 4.20: Schematic procedure of the submodel mechanics. Three main steps to evaluate the battery system frame topology.

4.3.2.3 Internal optimization

Since only the total space usable for the mechanical battery system is specified globally by the HV-BOTs design variables, the space allocation for the outer profile and the cross members can be designed variably. Therefore, the cross member cannot only be optimized regarding the structure (full, strengthened, hollow) but also the width can be optimally set to meet both the crash as well as bending requirements. The width for the cross members can thus be adjusted by shrinking the short outer profile width in an internal optimization. This trade-off is exemplarily illustrated in Figure 4.21.

The internal optimization can then also be used to find a cost- and mass-optimized design. The mass of the battery system mechanics results from the individual masses from the outer profile, the cross and side members, and the underride protection sheet. The bottom and cover plates are assigned to the submodel cooling as these mechanical structures are usually combined with the cooling plates. The cross member and outer profile are usually the most weight-intensive in the overall mechanics mass. Internal optimization is thus also used to optimize the mass by reallocating space between the shorter outer frame profile and the cross members. The flowchart of this design process is depicted in Figure 4.22.

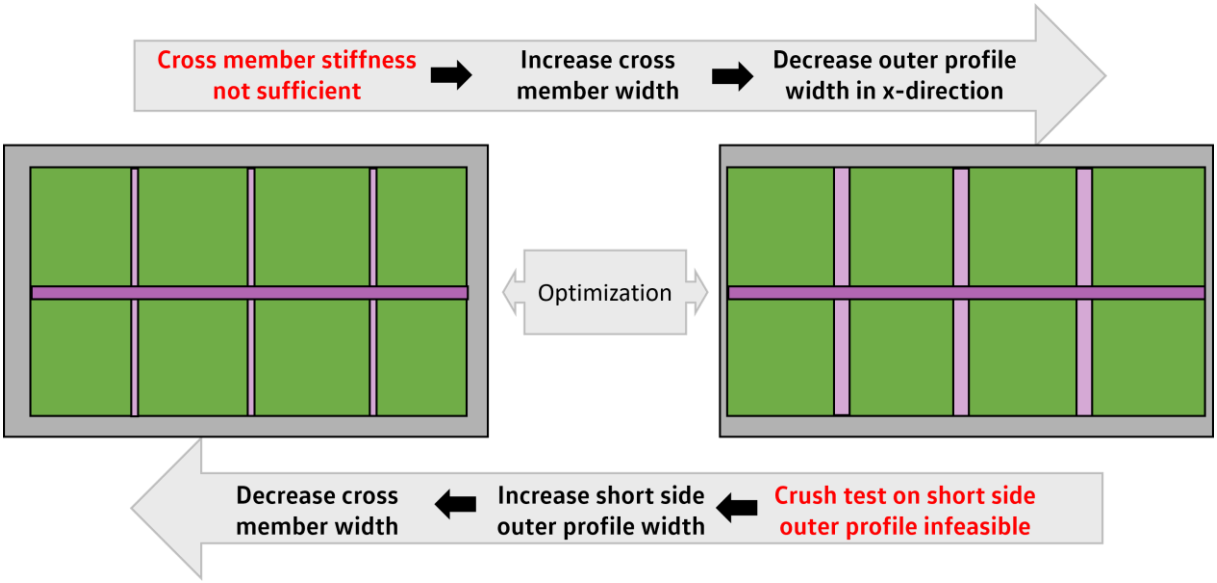

Figure 4.21: Space-neutral optimization of the cross member and outer profile.

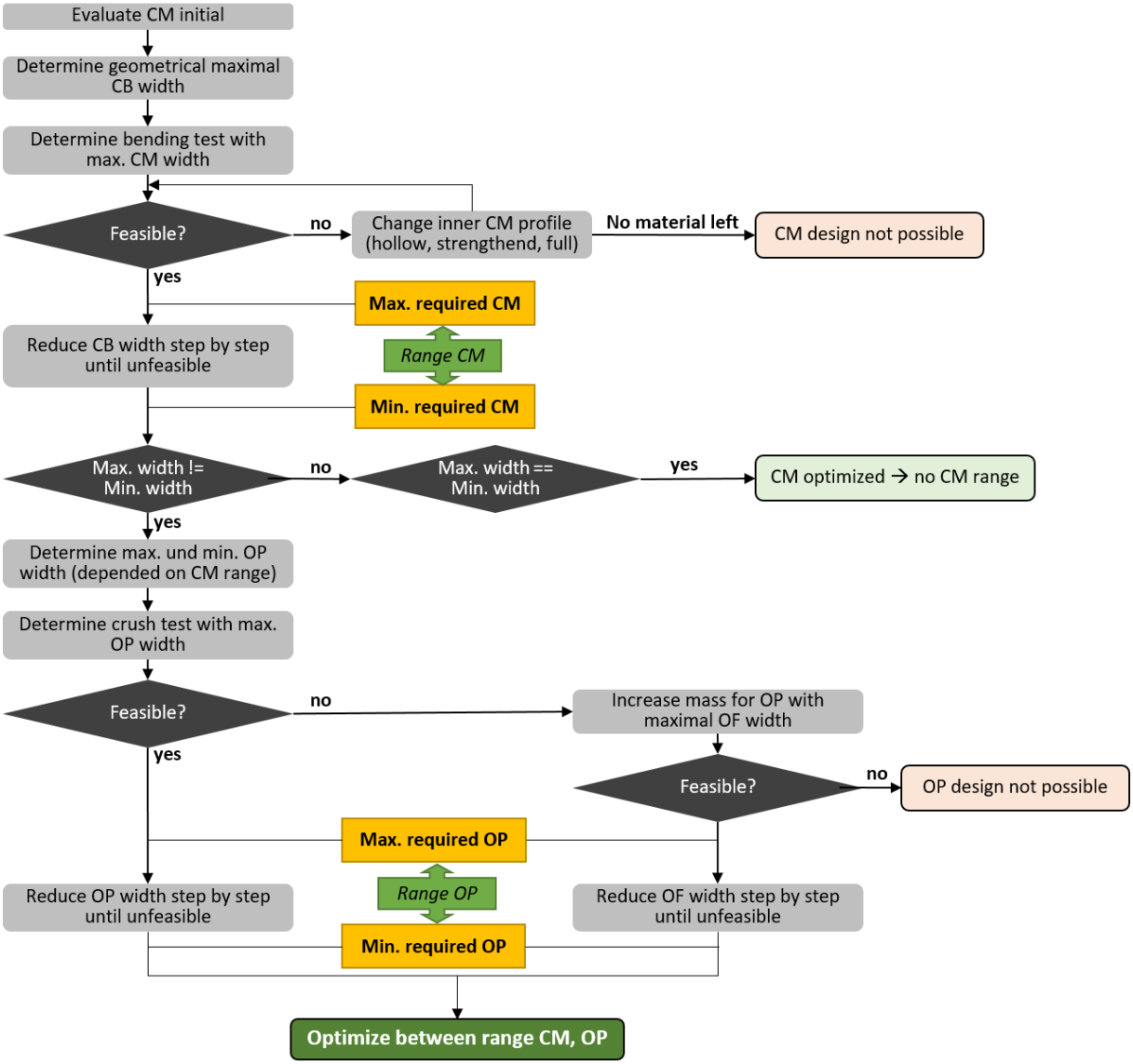

Figure 4.22: Flowchart optimization of outer profile (OP) and cross member (CM).

The major task in the internal optimization of the cross member and outer profile is the definition of the feasible geometric ranges for both subcomponents (OP and CM). The feasible geometric ranges for both components are defined by evaluating the load case feasibility within the geometrically feasible range. In Figure 4.23, the process of determining these ranges for both the cross member and the outer profile is graphically derived in six steps. The resulting bounded ranges can afterward be sampled to determine the cost or weight-optimized result.

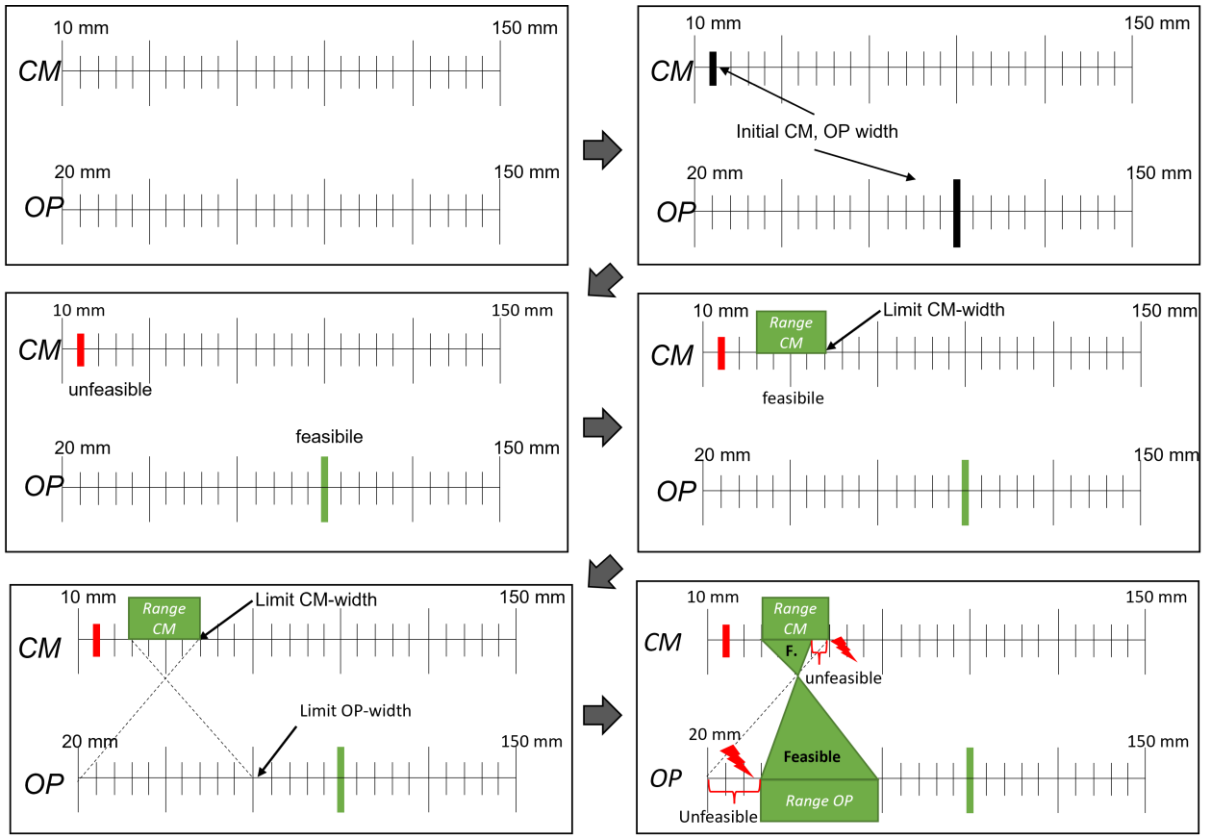

Figure 4.23: Schematic determination of the feasible geometric ranges for the cross members and the outer profile. The ranges are used in the internal optimization shown in Figure 4.22.

4.3.3 Submodel cooling

Major parts of Chapter 4.3.3 are published in a journal article [293] as part of this thesis with equal contribution of this thesis author, Sunny Rai, and Finn van Ginneken. This chapter contains minor modifications and extensions with respect to the original publication. The use of the article content, including illustrations, is permitted with the consent of Wiley-VCH.

Thermal management of LIBs plays a significant role in electric car behavior in terms of safety, available power, range, and aging. Therefore, a battery thermal management system has to be designed to be both efficient and reliable. HV-BOT uses a parameterized lumped mass model to optimize an active liquid cooling plate topology. The lumped masses model is based on multiple computational fluid dynamics (CFD) simulation investigations. The general advantage of lumped mass models lies in lower computation times and simple coupling of the energy balance with the model approach of equivalent electrical circuits.

The electrical, thermal, and geometrical design of the cellmodule and the overall mechanics of the battery system are used to determine the optimized cooling system design within the HV-BOT. Figure 4.24 shows a schematic cross-section of a cooling plate within the battery system. The arrangement and connection between the cooling plate and the cellmodule are depicted therein. Within the cooling submodel, the cooling

plate is optimally designed, taking into account the entire heat path from the cell to the module to the overall system.

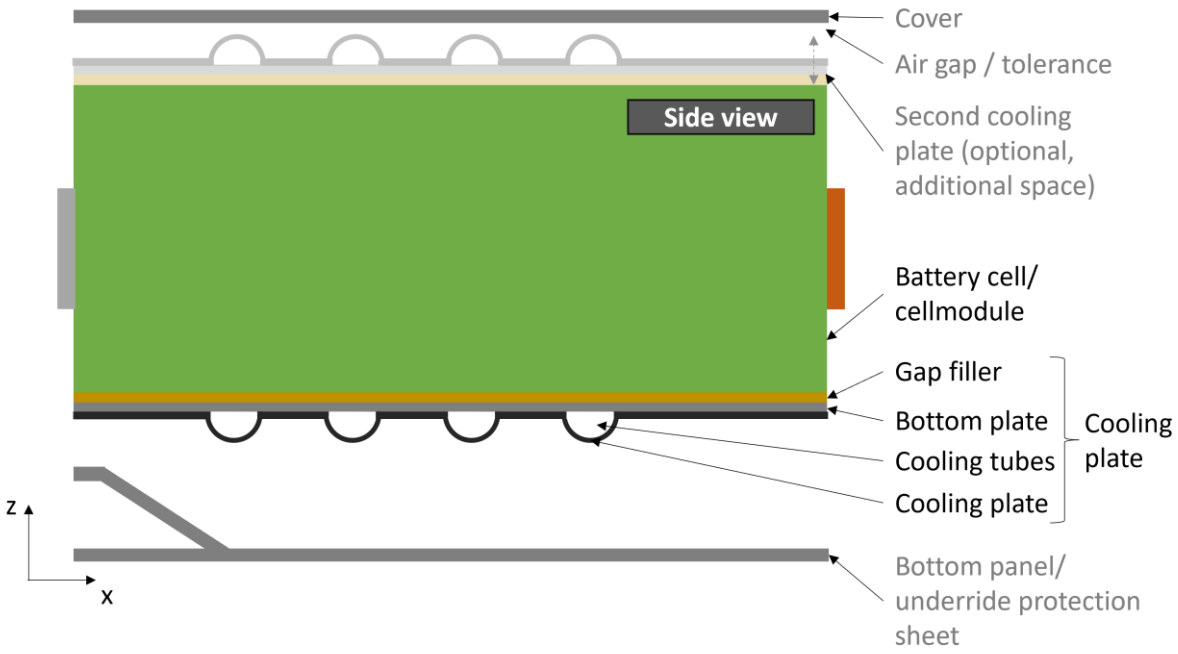

Figure 4.24: Schematic cross-section of a battery system with geometric construction principle of the cooling plate.

The following chapter describes the functionality and application of the simulation framework for optimized cooling plate design based on exemplary cellmodule geometries for a fast charging profile. Various model parameter assumptions and explanations are also given in the appendix in Chapter 8.3.

4.3.3.1 Introduction

To design an effective battery thermal management system (BTMS), multiple simulations with different levels of modeling, physics, and details are generally needed. However, complex and high-resolution models are time-consuming, both in terms of buildup and computation time. Especially the fast-moving early-stage development phases demand all-in-one model approaches allowing for quick and efficient concept evaluations. To meet these requirements, this chapter proposes a lumped-mass modeling approach and derives a methodology for evaluating various liquid cooling plate topologies. The framework is capable of optimizing cooling plate topologies within the HV-BOT based on differing geometric, electric, and thermal cell and cellmodule inputparameters. A novel modeling strategy preselects cooling plate parameters using a reduction procedure that couples the transient models' accuracy with the steady-state models' computation time advantages. This chapter’s results analyze different initial cellmodule geometries, indicating significant deviations in their optimized cooling plate properties. The cooling plate topologies are varied between two of their main construction design parameters: tube size and tube-to-tube distance. In addition to the battery’s mean temperature, further meaningful parameters like the resulting volume flow are evaluated, compared, and discussed for the entire set of observed cellmodule geometries. Subsequent sensitivity analyses show geometry-related optimal plate

topologies depending on the cooling circuit performance, stressing the capability of the model for usage within the HV-BOT.

The simulation model focuses on the design of the optimal cooling topology for different battery system sizes and provides a novel modeling approach to optimize the cooling plate design using coupled electrothermal simulation models.

Major contributions of the cooling plate optimization framework derived in this chapter are:

- Deriving a novel multi-parametric cooling plate simulation model for evaluating various cooling plate topologies at concept stages. Thereby, the entire cooling circuit and the corresponding pressure losses are generically parameterized. Thus, the coupled effects in the design of the cooling plate can be evaluated given various battery cooling requirements.

- Eliminating the use of detailed CAD models in the early design process through a multi-stage cooling plate optimization procedure for various design parameters.

- Cooling-specific evaluation of different cellmodule geometries with respect to their cooling plate capability based on aggressive fast charging requirements.

The remainder of this chapter is organized as follows. First, a description of the optimization process for the cooling plate will be presented, including the modeling approach used. This will be followed by a detailed account of the numerical optimization results of three geometrically different cellmodules in Chapter 4.3.3.4. The cooling plate model will then be concluded in Chapter 4.3.3.5, with an overview of the main findings and a discussion of potential areas for future research.

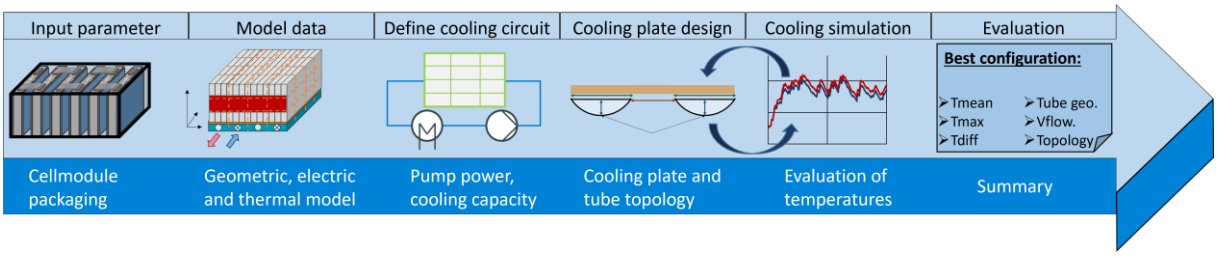

Figure 4.25: Schematic representation of the cooling submodel procedure.

4.3.3.2 Methods

In the following chapter, the optimization process for the cooling plate topology and the associated models are presented. First, the overall optimization process is described which is used to narrow down various cooling plate parameters until an optimal set of parameters is identified. Subsequently, the modeling approach for the battery modules and other components is described. The abstracted models in the respective optimization stage are then explained. Next, the modeling of heat sources and heat conduction is defined. Suiting assumptions for the entire battery, from the cell to the module to the system level, are then derived. Afterward, the heat conduction, the heat sources, and the modeling of the cooling plate, which represents the heat sink, are

described. Furthermore, the necessary symmetry assumptions, the modeling of pressure losses, and other components in the battery system are derived.

Optimization process and model input and output parameter

In order to determine the requirements for cooling plates, the irreversible heat losses within the battery cells and the heat transfer to the cooling system must be calculated. The irreversible heat losses can be described as a function of power or current using electrical equivalent circuit models (ECMs). ECMs with RC elements are often used to evaluate transient power profiles. However, transient evaluation combined with a large number of variable cooling plate parameters leads to a multidimensional solution space and, thus, to high computation times. A commonly used means of reducing the computational time of simulation models is to omit transient simulations by reproducing them based on appropriate steady-state or quasi-steady-state simulations. While this procedure effectively reduces computational time, it also has some drawbacks. The more the simulation is simplified, the more the model accuracy and corresponding validity of the simulation results may suffer. Therefore, an optimization process flow was developed for this model that uses parameter-specific partial evaluations from the steady-state, quasi-steady-state, or transient simulation and incorporates the partial solution into the rest of the workflow. Depending on the type of simulation, individual parameters are evaluated in the respective stage, while other parameters are not considered at first. Thereby, the advantages of accuracy are combined with those of computing speed. Figure 4.26 illustrates the procedure.

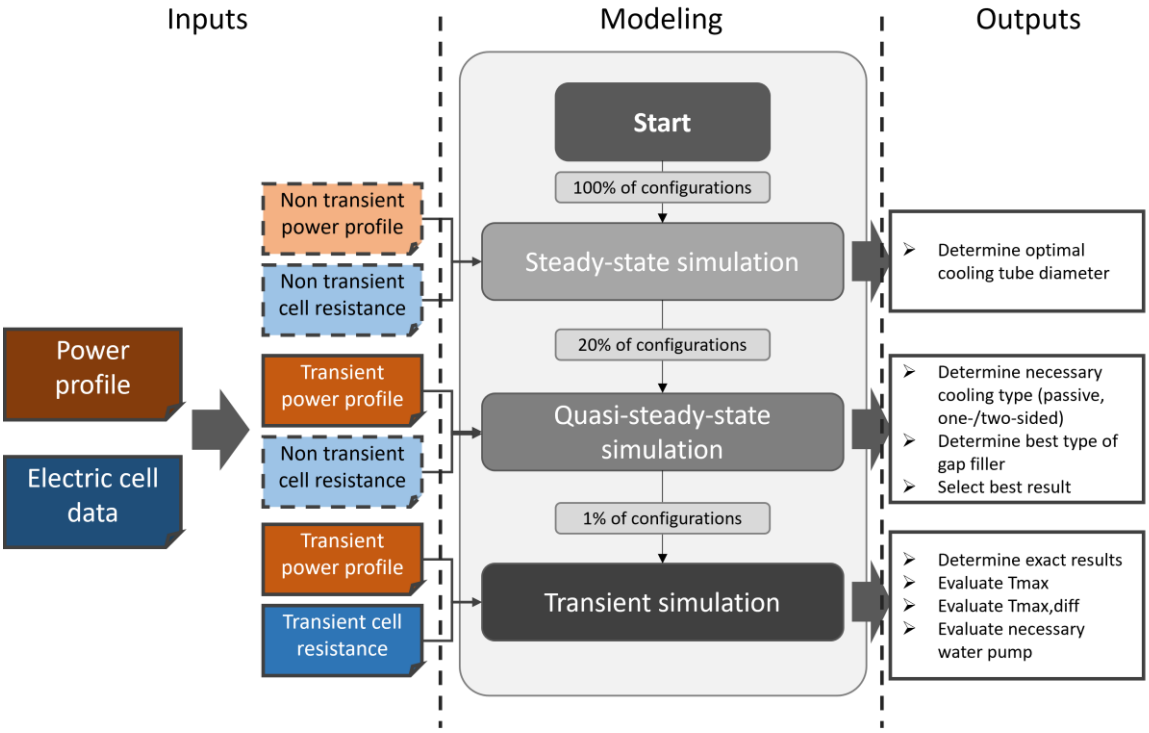

Figure 4.26: Flowchart diagram of the cooling plate optimization process. Different simulation types (steady-state, quasi-steady-state, and transient) are served by type-adjusted inputs for resistance and power. The determined outputs of each stage are based on the type of simulation. The individual

simulation stages reduce configurations starting from a large number of cooling plate possible variants.

On the left side in Figure 4.26, the inputs of the optimization process are shown. The inputs are adapted according to the model used. Each optimization step in the modeling section, except for the last one, is used to reduce possible cooling plate topologies. With the help of the last step, the parameters found for a topology are verified. Thus, the combinatorics of steady-state and quasi-steady-state models serve to identify optimal cooling plate topologies within the entire solution space.

In order to maintain the highest accuracy of the overall cooling system, the thermal network and the corresponding cooling circuit are calculated transiently in all three models. However, each of the three models is served with a different and stage-dependently designed ECM model and power profile. In the first step, the steady-state ECM model with a temperature-dependent voltage source and a temperature-dependent electrical resistance is assumed. This kind of ECM is named Rint-ECM in the following. The SOC is assumed to be constant in the steady-state model. The data for the electrical resistance and the voltage source is provided by the inputs. In addition, the inputs provide a current profile. From this current profile, a squared average C-rate is determined using Eq. (4.36):

$$\bar{c}_{\mathrm{Rate}} = \sqrt{\frac{\int_{t_0}^{t_{\mathrm{end}}} c_{\mathrm{Rate}}^2(t)\,\mathrm{d}t}{time}}. \tag{4.36}$$

The simplifications enable the computation of steady-state temperatures that generally have limited comparability with transient model results. However, a relative comparison between the results of the steady-state models is made possible. Thus, this comparison allows a selection of cooling channel heights, since it can be determined which configuration dissipates the most heat with the smallest possible temperature difference within the cellmodule. Therefore, the optimal outcome is identified using the maximum temperature and temperature difference within the corresponding cellmodule.

The quasi-steady-state also uses a Rint-ECM. However, the dependence of the voltage and the electrical resistance on the SOC is taken into account. Another difference from the steady-state model is that the current profile from the inputs is used directly. Electrical Rint parameters suitable for the current profile are derived with the transient equivalent circuit model. This allows comparability in terms of ohmic power loss between the quasi-stationary and the transient model. The found electrical parameters are multiplied by a safety factor to ensure that the quasi-stationary model has a slightly higher ohmic power loss than the transient model. This ensures that the quasi-steady-state model does not underestimate temperatures. Generally, to limit the risk of overestimation of the ohmic power losses, this safety factor has to be kept as small as possible. Thereby, the optimization of overly conservative cooling plate design can be prevented.

With the prior knowledge of the optimal cooling channel height, the number of cooling plate topologies is significantly reduced. The remaining cooling plate topologies are evaluated by using the efficient quasi-steady-state model.

In the final step of the optimization process, an impedance-based ECM consisting of a voltage source, electrical resistance, and two RC elements (see [293]) is used to verify the optimal parameter sets from the quasi-steady-state model with respect to the cooling system requirements. This type of ECM is called RC-ECM in the following.

The pre-selection of suitable cooling plate configurations in the proposed optimization process by stationary and quasi-stationary models is essential for a fast evaluation. Pre-selected configurations are finally evaluated with the transient model to be optimized with respect to the resulting cellmodule temperatures. This optimization process meets the requirements for the early development phases and thus aims for a conservative evaluation of different cooling plate concepts based on variable inputs. It allows the evaluation and comparison of cooling plate concepts regarding their general suitability for given battery specifications. General model limitations are discussed at the end of the following modeling approach section.

Modeling approach

The model presented here is based on the work of Wendland et al. in [294]. The cooling plate optimization process is capable of evaluating various cooling plate topologies combining serval design parameters and optimizing numerous variable combinations for the entire EV battery system within a few seconds. The simplified, parametrizable base model is composed of interconnected discrete point masses and is used to optimize the cooling plate topology with either indirect/passive air or active liquid cooling. For the modeling of the battery system and its components, Modelica with the MSL (Modelica Standard Library) 4.0.0 is used. Additionally, the base model is built with custom and already implemented models from the TIL library in Modelica [295, 296]. The parameterization and validation of the base model are based on various CFD simulations for different parts of the whole cooling plate topology. Furthermore, the modeling of the battery cells and the cooling plate was validated with a reference cellmodule by Wendland [153]. The reference module consisted of 24 pouch-shaped battery cells oriented parallel to the fluid flow in the cooling plate. The test was performed in an air-conditioned test chamber. In addition, the reference module was insulated on the non-cooled surfaces to minimize the influence of the environment. Current pulses with a duration of 30 s were used to achieve steady-state temperatures. In summary, simulation and measurement showed small deviations in the resulting temperatures. A detailed description of the validation process can be found in the work from Wendland [153].

To also evaluate the entire heat path from the generation of heat in the cellmodule module through heat transport into the coolant to heat exchange in the chiller, an almost entirely parameterizable approach was chosen. The assumed cellmodule can represent different cell sizes, chemistries, and cell-level interconnections. Dependencies are evaluated geometrically, electrically, and thermally by the cooling model. A heat transfer path from the module into the cooling plate was described using known equations. A distinction can be made between passive air cooling, one-sided and two-sided water/glycol cooling. Different gap filler thicknesses and types can be selected explicitly in an internal optimization for the necessary heat transfer. Different geometries of the cooling channels can be easily parameterized via the cross-sectional area and the perimeter. In addition, the number of passes (U/W-connections) can be parameterized. Pressure losses are calculated using multiple subdivisions inside and

outside the cooling plate. Thus, a pump capacity is derived using the necessary water/glycol flow rate calculated for an optimum cooling capability in the specific cooling plate configuration. Different dimensioning of the cooling circuit reflects different cooling capacities and thus directly influences the overall optimized result of the cooling plate configuration. The following section describes the individual parts and modeling approaches of the overall cooling plate optimization framework.

Modeling approach: modeling of cell, module, and battery system

The objective of thermally modeling the battery system is to describe the individual cellmodules and fluid flow in the cooling plate sufficiently accurately and efficiently in terms of its thermal behavior. Therefore, it is necessary to make abstractions for the model development.

The first abstraction comprises the battery system. The battery system is considered as a hydraulic and electrical interconnection of multiple cellmodules. Other components like the E-Box, are not considered. The second abstraction involves the module itself. It is considered as a homogeneous block with an anisotropic thermal conductivity in three spatial directions. According to Wendland [153], this abstraction admits that the temperature spread can be underestimated if contact resistances and insulation layers are neglected. Under the condition that the heat conduction path towards the cooling is calculated correctly, the maximum temperature in the range $T_{\mathrm{max.}} < 60\ °\mathrm{C}$ is represented sufficiently accurately. The third abstraction concerns the discretization. The discretization of a module depends on the discretization of the cooling channels and the cooling coils. Through this approach of discretization, individual cells in the module are not resolved and a discrete point mass can contain a part of a cell or several cells, depending on the discretization. It should be noted that the discretization in the height of the module can be freely chosen. Consequently, the module is modeled as a thermal network consisting of discrete point masses with a temperature state in the center (see Figure 4.27) and anisotropic heat transfers. For model development, it is also assumed that convective heat transfer with a constant coefficient to air exists on the side surfaces of the module. The cooling plate is always located on the bottom side of the module. Double-sided cooling is made possible by a symmetry plane in the height of the module.

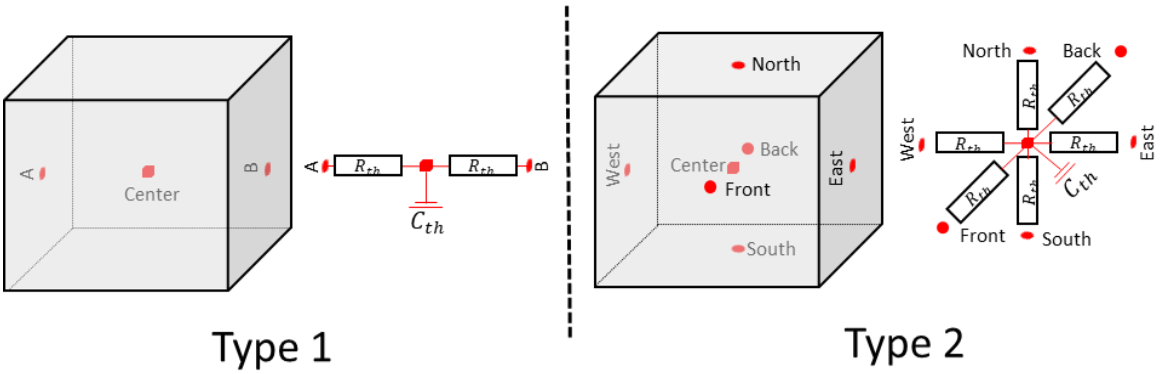

Figure 4.27: Schematic illustration of a discrete element divided into Type 1 and Type 2 elements. The thermal equivalent circuit is shown to the right of the respective element.

There are two types of discrete elements in the model. The Type 1 includes the one-dimensional transient heat conduction equation and is used to model the busbar system (consisting of tabs and busbars). The Type 2 is used to model the module itself. This type includes the three-dimensional transient heat conduction equation [297]. Thus, the anisotropic thermal conductivity of the active material of the battery cells can be considered. The elements of the Type 2 include not only the active material of the individual cells in the module but also all other installed materials and components in the module, for example, the battery module housing.

As shown in Figure 4.28, the cellmodule is discretized in three dimensions. The number of elements in length is denoted by the index i, those in width by the index j, and those in height by the index k. The heat flow rate $\dot{Q}_{i,j,k,surface}$ over the respective surface (see Figure 4.27) of each element can be determined as follows:

$$\dot{Q}_{i,j,k,\mathrm{surface}} = \frac{T_{i,j,k,surface} - T_{i,j,k}}{R_{\mathrm{th},i,j,k,\mathrm{surface\ to\ center}}}; \qquad (4.37)$$

$$\mathrm{surface} \in \{\mathrm{North}, \mathrm{South}, \mathrm{West}, \mathrm{East}, \mathrm{Front}, \mathrm{Back}\}.$$

The thermal resistance $R_{\mathrm{th},i,j,k,\mathrm{area\ to\ center}}$ between the respective surface and the center is determined by the geometry and thermal properties of each element representing the three-dimensional thermal resistance of the discrete element. The temperature state of each element can be determined using the first law of thermodynamics and the resulting heat conduction equation as follows [297]:

$$c_{\mathrm{p,heat,module}} \cdot V_{i,j,k} \cdot \rho_{\mathrm{module}} \cdot \frac{\mathrm{d}T_{i,j,k}}{\mathrm{d}t} = \sum_{\mathrm{surface}} \dot{Q}_{i,j,k,\mathrm{surface}} + \dot{Q}_{i,j,k,\mathrm{source}} \qquad (4.38)$$

The determination of the heat capacity and thermal conductivities for the corresponding cellmodule are derived in Chapter 4.3.1.6 in Eqs. (4.30) - (4.32).

For the calculation of the electrical resistance in each individual discrete element (see Figure 4.28 gray area), it is assumed that the resistance in one Type 2 element is equal to the electrical module resistance (see Eq. (4.39)). This assumption results from the different proportions of the discrete elements in the active material of the individual cells. Again, it should be noted that a discrete element can have shares in the active material of several cells.

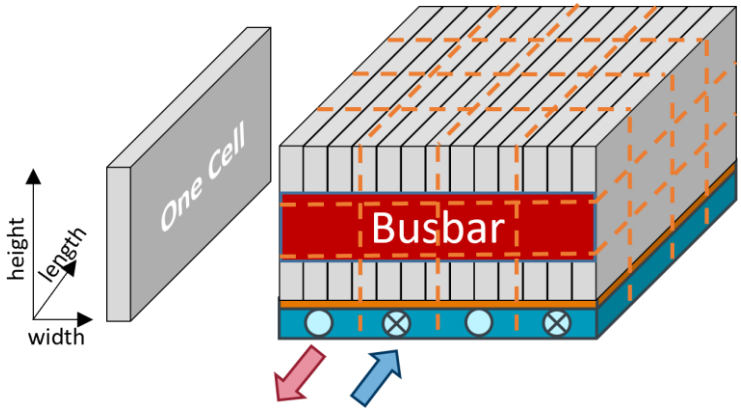

Figure 4.28: Schematic structure of the cellmodule.

Thus, the module's electrical resistance $R_{\mathrm{module}}(T, \mathrm{SOC})$ can be determined as follows:

$$R_{\mathrm{module}}(T,\mathrm{SOC}) = k_{\mathrm{scaled}} \frac{n_{\mathrm{series}} \cdot R_{\mathrm{cell}}(T,\mathrm{SOC})}{n_{\mathrm{parallel}}}. \tag{4.39}$$

The scaling factor k_{scaled} can be used to match the electrical resistance to other battery cells without affecting the influence of the temperature and state-of-charge dependent resistance field. k_{scaled} is the ratio of the electrical cell resistance to a given resistance at a specific SOC and temperature. For known electrical cell data the factor equals 1.

The current in each discrete element is equal to the module current I_{module}, so the irreversible heat for the steady-state and quasi-steady-state (see Figure 4.26) can be determined as follows:

$$\dot{Q}_{\mathrm{source,module}} = R_{\mathrm{module}}(T,\mathrm{SOC}) \cdot I_{\mathrm{module}}^2 . \tag{4.40}$$

For the RC-ECM, the irreversible heat is calculated from the ohmic losses via the internal resistance R_0, the first RC element $R_{\mathrm{RC},1}$, and the second RC element $R_{\mathrm{RC},2}$. Thus, the irreversible heat is described as follows:

$$\begin{aligned}\dot{Q}_{\mathrm{source,module}} = {} & R_{0,\mathrm{module}}(T,\mathrm{SOC}) \cdot I_{\mathrm{module}}^2 + \frac{U_{\mathrm{RC1}}^2}{R_{\mathrm{RC,1,module}}(T,\mathrm{SOC})} \\ & + \frac{U_{\mathrm{RC2}}^2}{R_{\mathrm{RC,2,module}}(T,\mathrm{SOC})}.\end{aligned} \tag{4.41}$$

$U_{\mathrm{RC},1}$ and $U_{\mathrm{RC},2}$ describe the voltage in the respective RC element. The voltage depends on the charge of the capacitance and can be described as follows:

$$\frac{\mathrm{d}U_{\mathrm{RC},i}}{\mathrm{d}t} = \frac{I_{\mathrm{module}}^2}{C_{\mathrm{RC},i(T,\mathrm{SOC})}} - \frac{U_{\mathrm{RC},i}}{R_{\mathrm{RC},i}(T,\mathrm{SOC}) \cdot C_{\mathrm{RC},i}(T,\mathrm{SOC})}. \tag{4.42}$$

The resistances ($R_{\mathrm{RC},0}(T,\mathrm{SOC})$, $R_{\mathrm{RC},1}(T,\mathrm{SOC})$ and $R_{\mathrm{RC},2}(T,\mathrm{SOC})$) are determined as in the steady-state case using Eq. (4.39). The capacitance $C_{\mathrm{RC},i}(T,\mathrm{SOC})$ of the respective RC element is determined with the help of the time constant $\tau_{\mathrm{RC},i}\,(T,\mathrm{SOC})$ and the resistance $R_{\mathrm{RC},i}(T,\mathrm{SOC})$. This ensures that the scaling factor k_{scaled} is also considered in the capacitance.

Since each discrete element represents only a portion of the module, the irreversible heat $\dot{Q}_{\mathrm{source,module}}$ is divided by the number of discrete elements, resulting in the following irreversible heat for each discrete element $\dot{Q}_{i,j,k,\mathrm{source}}$:

$$\dot{Q}_{i,j,k,\mathrm{source}} = \frac{\dot{Q}_{\mathrm{source,module}}}{n_{\mathrm{length}} \cdot n_{\mathrm{height}} \cdot n_{\mathrm{width}}}. \tag{4.43}$$

Besides the irreversible heat in the Type 2 elements, the busbar system (see Figure 4.28 red area) also plays a crucial role for edge elements. The busbar system has a 2D discretization with size $n_{\mathrm{width}} \cdot n_{\mathrm{height}}$. On the front and rear sides (given side terminals/tabs) of the cellmodule, one side of the Type 1 elements, representing the busbar system, is thermally connected to all Type 2 edge elements of the module. On the other side, the Type 1 elements are thermally connected to the environment.

For the busbar system, three heat sources are considered by ohmic resistances. The electrical contact resistance between the tab and the busbar $\dot{Q}_{\mathrm{Tab,Busbar}}$, the irreversible heat in the tabs $\dot{Q}_{\mathrm{Tab}}$ and that in the busbar itself ($\dot{Q}_{\mathrm{Busbar}}$). The heat sources are determined for each discrete element (index: j, k) as follows:

$$\dot{Q}_{j,k,\mathrm{Tab,Busbar}} = f_{j,k,\mathrm{distribution}} \cdot R_{\mathrm{Tab,Busbar}} \cdot I^2_{\mathrm{module}} \cdot n_{\mathrm{Tab,Busbar}}\,, \tag{4.44}$$

$$\dot{Q}_{j,k,\mathrm{Tab}} = f_{j,k,\mathrm{distribution}} * R_{\mathrm{Tab}} \cdot \left(\frac{I_{\mathrm{module}}}{n_{\mathrm{parallel}}}\right)^2 \cdot n_{\mathrm{Tabs}}\,, \tag{4.45}$$

$$\dot{Q}_{j,k,\mathrm{Busbar}} = f_{j,k,\mathrm{distribution}} \cdot R_{\mathrm{Busbar}} \cdot I^2_{\mathrm{module}} \cdot n_{\mathrm{Busbars}}\,. \tag{4.46}$$

In order to provide a local resolution of the heat contribution through the busbar system and for the scaling of the heat sources, a distribution matrix $f_{\mathrm{distribution}}$ is introduced. This matrix has the dimension n_{width} x n_{height}. The matrix entries zeros represent the areas of the module, which are not covered by the busbar system after parameterization. The remaining entries are determined by the area covered by the tabs in each discrete Type 2 element (see Figure 4.28). The sum of the matrix must be 1 so that the complete busbar system is represented. With the geometric properties of the busbar system and the discretization (defined by the cooling plate), the mass of each discrete Type 1 element can be determined. The electrical resistances (R_{Tab}, R_{Busbar}) are determined based on the geometry and the electrical conductivity of copper and aluminum. The electrical contact resistance $R_{\mathrm{Tab,Busbar}}$ is a settable parameter.

In addition to the heat sources in the busbar system, the heat flows across the balance volume of the busbar system must be determined. For this purpose, the thermal resistance R_{th} of the Type 1 element is determined based on the parameterized busbar system and the material properties. Thus, the heat flow rate to the Type 2 elements (index: type 2) and that to the environment (index: ambient) can be determined as follows:

$$\dot{Q}_{i,j,\mathrm{type\ 2}} = \frac{T_{i,j,\mathrm{active\ surface}} - T_{i,j}}{0.5 \cdot R_{\mathrm{th}} \cdot f_{i,j,\mathrm{distribution}}}\,, \tag{4.47}$$

$$\dot{Q}_{i,j,\mathrm{ambient}} = \frac{T_{i,j,\mathrm{ambient}} - T_{i,j}}{0.5 \cdot R_{\mathrm{th}} \cdot f_{i,j,\mathrm{distribution}}}\,. \tag{4.48}$$

The temperature $T_{i,j}$ of the respective element in the busbar system is determined as follows:

$$\begin{aligned} f_{i,j,\mathrm{distribution}} \cdot m_{\mathrm{module}} \cdot c_{\mathrm{p,heat,module}} \cdot \frac{\mathrm{d}T_{i,j,}}{\mathrm{d}t} \\ = \dot{Q}_{i,j,\mathrm{type\ 2}} + \dot{Q}_{i,j,\mathrm{ambient}} + \dot{Q}_{i,j,\mathrm{Tab,Busbar}} + \dot{Q}_{i,j,\mathrm{Tab}} + \dot{Q}_{i,j,\mathrm{Busbar}}\,. \end{aligned} \tag{4.49}$$

The influence of the environment is also considered. Convective heat transfer is assumed on all sides of the module except for the bottom and top in the case of double-sided cooling. The convective heat transfer is modeled using a heat transfer coefficient α. Different heat transfer coefficients can be found in [298–300]. For passive air cooling, the coefficient is vehicle type independent approximated as $\alpha = 5\ \frac{\mathrm{W}}{\mathrm{m^2K}}$. In the following, the modeling of the cooling plate, including the gap filler, is described.

Modeling approach: modeling of the cooling plate

The cooling plate geometry is crucial for the discretization of the module (see Figure 4.28). The number of cooling passes for one coil (see Figure 4.30) determines the discretization of the module width. Furthermore, the number of serial cooling channels in a coil determines the fluid paths. For example, two serial cooling channels in one coil result in a U-shaped fluid path, while three channels result in an S-shaped fluid path. The discretization is freely selectable along the cooling channels (in flow direction). The same applies to height discretization. The modeled cooling plate consists of the cooling channels and the gap filler (see Figure 4.29). The gap filler is modeled by a thermal resistance. Here, the mass and, thus, the thermal capacity are neglected due to the small thickness of the gap filler (~ 1 mm).

The cooling channels are parameterized using the length of the module and the height of the cooling channel, which results in a hydraulic cross-sectional area and a heat transfer area using the assumption of a circular segment and a height-to-width ratio (see Figure 4.29). The parameterization is done for each discrete element along the flow direction. Thereby several parallel cooling channels can be taken into account. For the calculation of the heat transfer coefficients between the fluid and tube wall as well as the pressure drop in the tubes, a 0D/1D approach is used for each discrete element in the tube. Rotating the cooling plate allows a fluid flow perpendicular to cell orientation. It should be noted that the discretization of the module length is then given by the topology of the cooling plate. A symmetry plane is used for double-sided cooling, assuming the same cooling mass flows and cooling plate geometry. Thus, the following cooling configurations can be investigated:

- Parallel – One-sided | Perpendicular – One-sided,
- Parallel – Double-sided | Perpendicular – Double-sided.

The cooling tubes are assumed as circular segments (see Figure 4.29). A similar shape is also described in [301]. An advantage of this form of cooling channels is the non-cutting and flexible production of the cooling plates. This work's assumed cooling plates consist of two parts. The cooling channels are formed in the lower part by deep drawing or cold extrusion. The cooling channels are then sealed with the upper part by roll seam welding or pressure welding.

The thermal capacity of the cooling plate is neglected. The distance from a module's border to the first tube is half of the tube-to-tube distance. The distance is used to determine the maximum number of cooling channels. It should be noted that the tube-to-tube distance only affects the maximum number of cooling channels but not the local change of heat sinks.

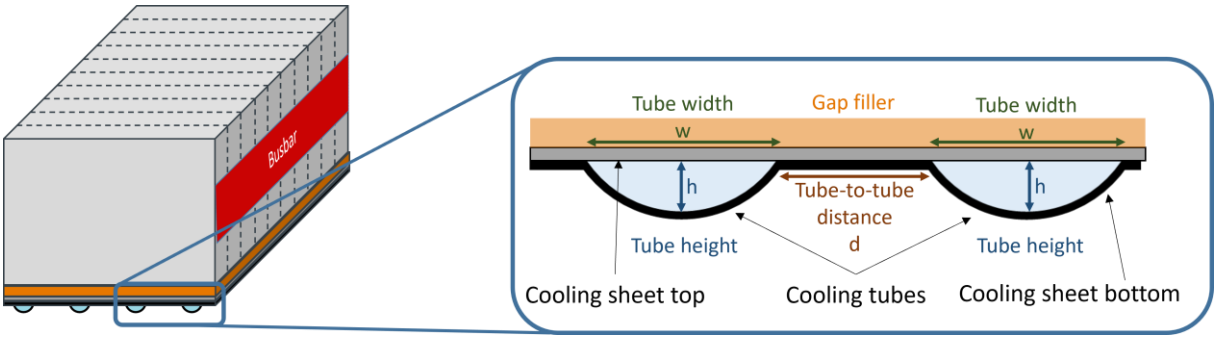

Figure 4.29: Schematic representation of the cooling plate with multiple geometric design parameters.

The proposed model aims to consider different cooling plate channel geometries and represent them sufficiently accurately. The following Eqs. (4.51) and (4.55) are generally valid for circular channels [297]. Nevertheless, to allow the mapping from the assumed cooling channel geometry (see Figure 4.29), which differs from the circular geometry, the hydraulic diameter is used. The use of the hydraulic diameter can lead to deviations in some cases, e.g. laminar flow or geometries that deviate from the circular shape [302]. For this reason, the model with this particular cooling channel geometry was verified with CFD simulations for pressure losses and heat transfer coefficient. It should be noted that deviations may occur for other cooling channel geometries. Therefore, the applicability of Eq. (4.51) and Eq. (4.55) should be reviewed for deviating cooling channel geometries.

The convective heat transfer for active liquid cooling within the system can be described using Nusselt number Nu for laminar and turbulent flows:

$$\alpha = k_{\text{passive}} \frac{Nu \cdot \lambda}{L} \; ; \qquad k_{\text{passive}} = \begin{cases} 1 \text{ for active cooling} \\ 0 \text{ for passive cooling} \end{cases} . \tag{4.50}$$

with α as the heat transfer coefficient, which describes the convective heat transfer between wall and fluid, λ the thermal conductivity of the fluid, and L the dimension governing the flow, which corresponds to the hydraulic cooling tube diameter d_{h}. For passive air cooling, heat transfer is prevented using the parameter k_{passive}, so that the heat can only be dissipated via the other surfaces cooled by the environment. In order to find suitable values for the convective heat transfer coefficient α for active liquid cooling, different equations for Nu depending on the fluid and the type of flow are considered.

For laminar flows ($Re < 2300$) the laminar Nusselt number $Nu_{\text{lam.}}$ is modeled by the following equations from Baehr et al. [297]:

$$Nu_{\text{lam.}} = \frac{3.657}{\tanh\left(2.264 \cdot [X^+]^{\frac{1}{3}} + 1.7 \cdot [X^+]^{\frac{2}{3}}\right)} + \frac{0.0499}{X^+} \cdot \tanh(X^+) \, . \tag{4.51}$$

The dimensionless length X^+ is defined by the following equation. It results from tube length l, hydraulic diameter d_{h} as well as the Péclet number Pe. The Péclet number is the product of Reynolds Re and Prandtl Pr number [297]:

$$X^{+} = \frac{l}{d_{\mathrm{h}} \cdot Pe} = \frac{l}{d_{\mathrm{h}} \cdot Re \cdot Pr}. \tag{4.52}$$

The Reynolds number Re in each discrete tube element is determined by Eq. (4.53). The substance-specific quantities, such as the density ρ_{fluid} and the dynamic viscosity η_{fluid} are calculated by TIL-Media [295, 296] for the incompressible fluid G12Evo. The fluid mass flow in each discrete tube element is determined using the fluid's routing and partitioning. Together with the fluid density ρ_{fluid}, the respective volume flow for the tube element is given. Flow velocity v_{fluid} is calculated using the volume flow in each tube element and the respective cross-sectional area.

$$Re = \frac{\rho_{\mathrm{fluid}} \cdot v_{\mathrm{fluid}} \cdot d_{\mathrm{h}}}{\eta_{\mathrm{fluid}}}. \tag{4.53}$$

For fully turbulent flows $(Re < 10000)$, the following equations from Gnielinski [303] are used in the model to calculate the turbulent Nusselt number $Nu_{\mathrm{turb.}}$:

$$Nu_{\mathrm{turb.}} = \frac{\left(\frac{\xi_{\mathrm{turb.flow}}}{8}\right) Re \cdot Pr}{1 + 12.7 \cdot \sqrt{\frac{\xi_{\mathrm{turb.flow}}}{8}} \cdot \left(Pr^{\frac{2}{3}} - 1\right)} + \left[1 + \left(\frac{d_{\mathrm{h}}}{l}\right)^{\frac{2}{3}}\right]. \tag{4.54}$$

The wall friction coefficient ξ can be described for the turbulent region using the following equation of Konakov (often also named Konakov equation [304, 305]) :

$$\xi_{\mathrm{turb.flow}} = (1.8 \cdot \log(Re) - 1.5)^{-2}. \tag{4.55}$$

For the transition region $(2300 < Re < 10000)$, linear interpolation is applied between the turbulent and laminar Nusselt numbers. The interpolation is done using the intermittency factor [306].

Modeling approach: use of symmetry

One elementary part of the proposed cooling model is the use of symmetries. As already mentioned above, a symmetry in height is assumed for double-sided cooling. This also guarantees the computational performance of the models for this cooling configuration. The discretization of the module width (see Figure 4.28) is based on the cooling channel passes (n_pass) of one coil in the module (see Figure 4.30). Figure 4.30 shows the second assumption regarding symmetry. Here the module is reduced to a coil assuming a symmetrical cooling plate. Adiabatic boundaries are assumed at the symmetry surfaces. Therefore, the surfaces on which convection is present must also be scaled. The scaling factor results from the number of coils. This approach massively reduced the computation time, which ultimately allows for a wider range of degrees of freedom for the optimization. The parameter for the number of passes can be used additionally to increase the degree of freedom in the cooling plate configuration. Depending on the topology, the pipe section at the end of each pass is connected to the next pipe section or the cooling plate's outlet. By this procedure, every second pass flows in the opposite direction to the first.

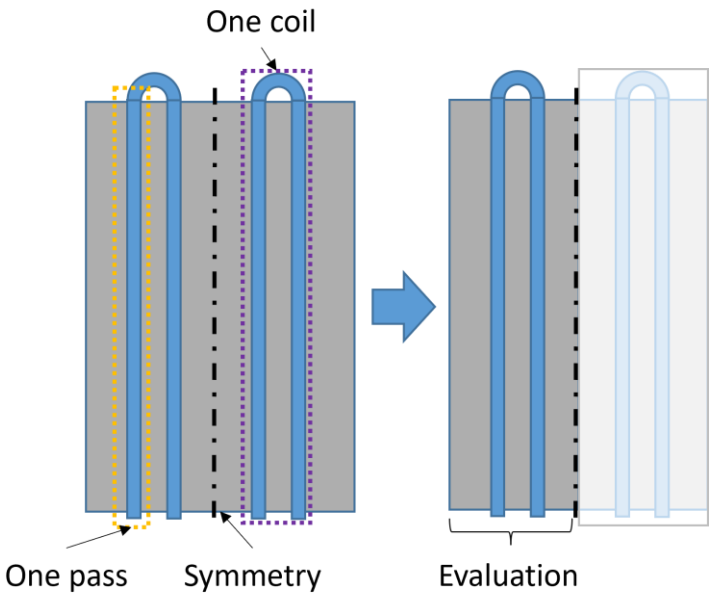

Figure 4.30: Schematic representation of the symmetry assumption used in the cooling plate optimization model.

Modeling approach: modeling of the pressure losses

Sufficient coolant flow in the cooling channels ensures that the cooling plate operates appropriately. A water pump in the circuit must therefore be dimensioned to compensate for occurring pressure losses inside and outside of the cooling plate.

Pressure losses inside and outside the cooling plate depend on various parameters like the cooling tube geometry as well as topology, the coolant temperature, and the volume flow rate. However, the overall objective of the pump design is to keep the difference between the inlet and outlet temperatures of the cooling water/glycol mixture relatively small. A homogeneous cooling of the cellmodules can only be achieved by a small difference within the coolant temperatures. A coolant temperature difference between the inlet and outlet of 5 K is used as the benchmark for the model. Scenario-dependent variations can be found in Chapter 4.3.1.8.

Pressure loss calculation is divided into multiple parts within the model. Figure 4.31 schematically divides the cooling system into different parts and depicts the differently evaluated pressure losses.

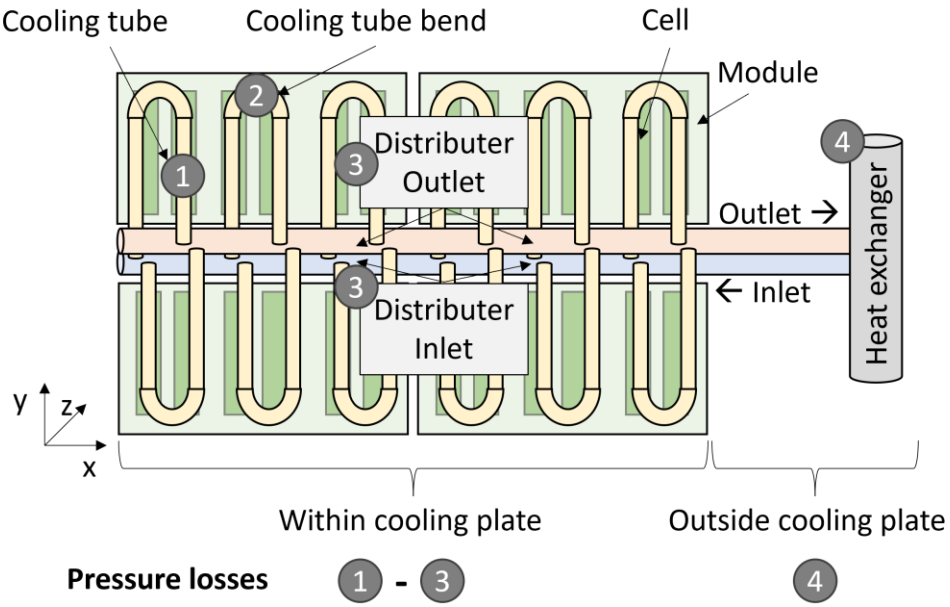

Figure 4.31: Overview and segmentation of different pressure losses within the entire battery cooling system.

Pressure drops within the tube's straight parts (see (1) in Figure 4.31) are determined by the following Darcy-Weisbach equation:

$$\Delta p = \lambda_{\text{flow}} \cdot \frac{\rho}{2} v^2 \cdot \frac{l}{d_{\text{h}}}. \tag{4.56}$$

The pressure drop depends on the velocity (v), the fluid's density (ρ), and the wall friction coefficient (ξ). The calculation of the wall friction coefficient ξ depends on the Reynolds number. For laminar flows, the Hagen-Poiseuille equation [303] is used.

$$\xi_{\text{laminar flow}} = \frac{64}{Re}. \tag{4.57}$$

For turbulent flows, the wall friction coefficient from Konakov [304, 305] is used (see Eq. (4.55)). For the transition region $(2300 < Re < 10000)$, linear interpolation is applied as described above.

Further pressure drops for cooling tube bends (see (2) in Figure 4.31), and the distribution of coolant into and from the tubes (see (3) in Figure 4.31) use an empirical approach with the form of:

$$\frac{\Delta p}{\Delta p_{\text{nominal}}} = \left(\frac{\eta}{\eta_{\text{nominal}}}\right)^x \left(\frac{\dot{m}}{\dot{m}_{\text{nominal}}}\right)^y. \tag{4.58}$$

Coefficients are evaluated and validated using various CFD simulation results of a cooling plate substitution model. η_{nominal} describes the reference coolant dynamic viscosity of the reference simulation. The parameter $\dot{m}_{\text{nominal}}$ is the reference mass flow rate.

In order to describe the pressure losses in the individual variables, suitable variable sizes for the exponents x and y were evaluated. The used coefficients for the different components are listed in the following Table 4.6.

Component	$\Delta p_{\text{nominal}}$ in mbar	η_{nominal} in Pa · s	$\dot{m}_{\text{nominal}}$ in kg/s	x	y
Single cooling tube bend	8.15	0.0044	0.026	0.5	1.45
Distribution of inlet and outlet for one-sided cooling	53.45	0.044	0.31	0.3	1.6
Distribution of the coolant for double-sided cooling	79.84	0.0044	0.63	0.3	1.6

Table 4.6: Used coefficients from an empirical approach to calculate the different pressure drops of the cooling plate components.

Pressure losses outside the cooling plate (see (4) in Figure 4.31) are caused by other operating components necessary for cooling the coolant, such as the chiller, valves, and the associated tubing. These pressure losses are strongly dependent on the individual components as well as their topology and can, thus, only be accurately calculated in dedicated pressure models. Therefore, this model uses an exemplary dependence for the pressure losses outside the cooling plate to describe its dependence on coolant temperature and volume flow rate. The pressure loss assumptions are shown graphically in Figure 4.32.

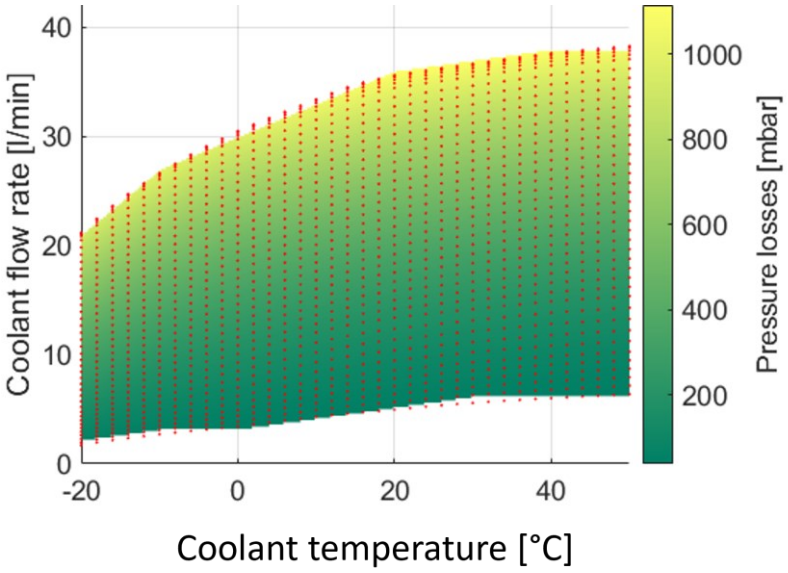

Figure 4.32: Data-based pressure losses outside the cooling plate depending on volume flow rate and coolant temperature extracted from representative vehicle concept simulations.

Modeling of the chiller, heat exchanger, and pump control:

As one of the last steps, the heat of the coolant must be dissipated. A simplified chiller stage model is assumed for this purpose. The maximum cooling capacity $\dot{Q}_{\text{cooling,max.}}$ is defined based on three chiller expansion stages using a linear dependence on volume flow (k_{V}) and fluid temperature (k_{T}) as well as a cooling capacity offset $(\dot{Q}_0)$, as follows:

$$\dot{Q}_{\text{cooling,max.}} = \dot{Q}_0 + k_{\text{V}} \cdot \dot{V}_{\text{flow}} + k_{\text{T}} \cdot T_{\text{fluid,in.}}\,. \tag{4.59}$$

The simplified approach allows a fast and sufficiently accurate mapping of the maximum transferable heat for a constant refrigerant inlet temperature of the chiller in the primary cooling circuit. The constants k_{V} and k_{T} allow a simplified consideration of the dependencies between maximum transferable heat, volume flow, and coolant inlet temperature in the battery-side coolant cooling $T_{\text{fluid,in.}}$.

The maximum cooling capacity depends on the chiller configuration (see Figure 4.33) and can easily be extended to other configurations. This simplification is used as it can enable a parameterizable cooling capacity with sufficient accuracy while still maintaining a short calculation time of the overall cooling plate optimization model.

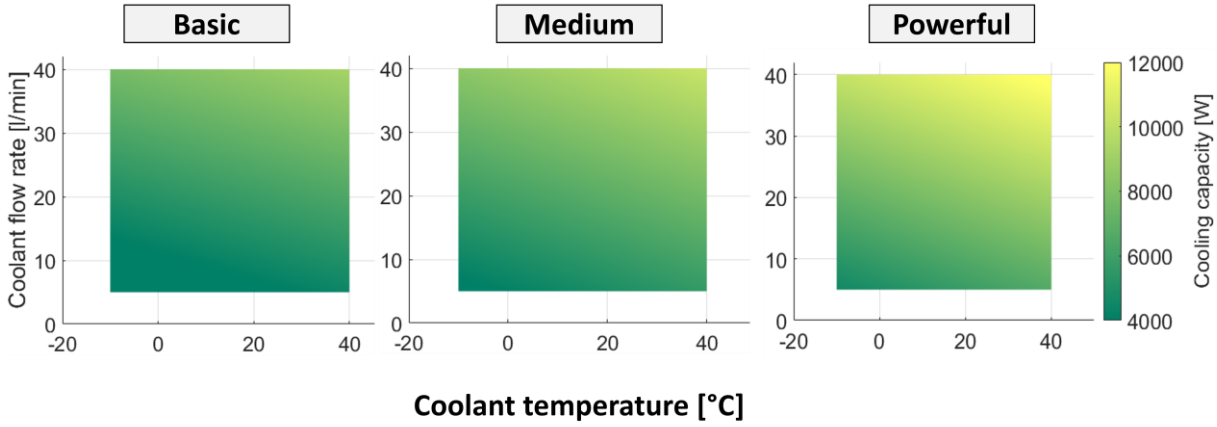

Figure 4.33: Comparison of three different data-based assumed cooling circuit configurations. Cooling capacities depend on coolant temperature and volume flow rate extracted from representative vehicle concept simulations.

Depending on the charge/discharge profile and ambient temperature, a different constant inlet temperature $T_{\text{fluid,out.,req.}}$ of the cooling plate can be specified. For driving and charging profiles, the target inlet temperature is set to 20 °C. This applies at an ambient temperature of 20 °C. At 40 °C, the inlet temperature is set to 15 °C. In between, linear interpolation is applied. Outside, a constant extrapolation is applied. Thus, the required heat $\dot{Q}_{\text{cooling,req.}}$ can be determined as follows:

$$\dot{Q}_{\text{cooling,req.}} = \dot{m}_{\text{fluid}} \cdot c_{\text{p}}(T) \cdot \left(T_{\text{fluid,in.}} - T_{\text{fluid,out.,req.}}\right). \tag{4.60}$$

In the case where the heat to be transferred is higher than the maximum cooling capacity, the maximum cooling capacity is used. Consequently, the inlet temperature can be determined with the following equation:

$$T_{\text{fluid,out.}} = \frac{\dot{Q}_{\text{poss.}}}{\dot{m}_{\text{fluid}} \cdot c_{\text{p}}(T)} + T_{\text{fluid,in.}};$$

$$\dot{Q}_{\text{poss.}} = \begin{cases} \dot{Q}_{\text{cooling,req.}} \text{ if } \dot{Q}_{\text{cooling,max.}} \geq \dot{Q}_{\text{cooling,req.}} \\ \dot{Q}_{\text{cooling,max.}} \text{ if } \dot{Q}_{\text{cooling,max.}} < \dot{Q}_{\text{cooling,req.}} \end{cases}. \tag{4.61}$$

The system level volume flow of the coolant is given by a controlled pump with a maximal hydraulic power of 45 W. If the temperature difference between the inlet and outlet in the battery system is above 5 K, the pulse duration modulation (PWM) signal of the pump is increased. If the difference is below, the PWM signal is reduced. The same applies to exceeding the permitted inlet temperature. Thus, the pump control can be used in the overall system optimization to optimize the pressure losses depending on the cooling plate topology. As the resulting volume flow depends on the pressure losses of the system, suitable cooling plate configurations can be derived by user-defined maximum pump power.

Model limitations

In this section, the model assumptions and the resulting limitations of the model are discussed. The objective and major advantage of the proposed optimization process is to quickly determine the suitability of the cooling plate topology based on a large set of parameters. In addition, sensitivities of different topology parameters can be discovered. For this reason and to increase the number of optimization degrees of freedom, the following assumptions were made:

- The battery module is assumed to have a constant homogeneous density and heat capacity.
- Double-sided cooling can be represented by symmetry in height.
- Only symmetrical cooling plates are considered to scale the number of cellmodules, according to Figure 4.30.
- A simplified refrigeration cycle with a data-based chiller and simplified pressure losses is used.

The framework presented here is used for the initial conception of a cooling plate topology. Thereby, non-standard processes/components that significantly influence the density or the heat capacity are not considered. Moreoever, constant component-dependent values are determined for the density and the heat capacity. It is assumed that these do not change significantly in the considered temperature range.

This framework is unsuitable for observing and evaluating asymmetries in the cooling plate, which result, for example, from non-equally distributed cooling channels. For this purpose, models with a higher discretization are required. However, higher discretization models cannot ensure fast evaluation of multiple different parameters and are thus unsuitable for higher-level cooling plate topology optimizations.

Moreover, a simplified approach for the cooling circuit was chosen as it is not the focus of this optimization. With the presented cooling circuit model, the dependencies between fluid temperature, pressure drop, and maximum transferable heat in the chiller are represented in a data-based manner. With these simplifications, the variables from CFD simulations could be mapped with sufficient accuracy. In addition, further conceptual cooling circuits can be mapped with little effort, which is one of the main advantages of the modular approach of the proposed framework. Therefore, this model

is suitable for evaluating and quantitively comparing conceptual states of cooling plate topologies within the HV-BOT.

4.3.3.3 Model summary and usage

The proposed cooling plate optimization model can be used to analyze the cooling capability of different cooling plate topologies based on numerous physical EV battery requirements. The framework evaluates the entire battery cooling process from the cellmodule to the cooling plate to the cooling circuit. A three-step workflow is used to evaluate the plate topologies with the above-described models. Figure 4.34 depicts these three steps schematically and also shows the major inputs, parameters, and outputs of the optimization framework. An extended list of all input and output parameters is given in the appendix in Chapter 8.3.

As the first step, the chosen cellmodule has to be electrically, thermally, and geometrically described and parameterized as the model's major inputparameter.

In the second step, the boundary conditions for the cooling circuit and plate are defined. Fixed model parameters (current profile, cooling chiller expansion stage, circular shape of cooling tube) are first specified. Additionally, variable cooling design parameters can be optionally set depending on the type of study. These include, e.g., the thickness and type of gap filler, the direction of the cooling channels, or the maximum PWM of the water pump.

In the last step, the results of the different parameter variations (e.g., cooling tube diameters and tube-to-tube distances) can be evaluated. Different temperatures (maximum, average, maximum difference) can thus be directly compared for the different cooling plate configurations. Since all other model parameters are fixed throughout the optimization, resulting temperature changes can be related directly to the changed parameter variations. Afterward, pareto-optimal design-relevant results can be derived. The model's runtime for optimizing the cooling tube diameter given one cellmodule geometry measures roughly 40 s - 50 s on a standard office notebook with an *Intel(R) Core(TM) i5-10310U* and 8 GB of RAM.

Generally, different feasibility limits are set within the HV-BOT depending on the application requirements (see Chapter 4.3.1.8). In any case, however, the cell temperature should not exceed 55 °C to prevent accelerated aging or safety-critical states [207, 307, 308].

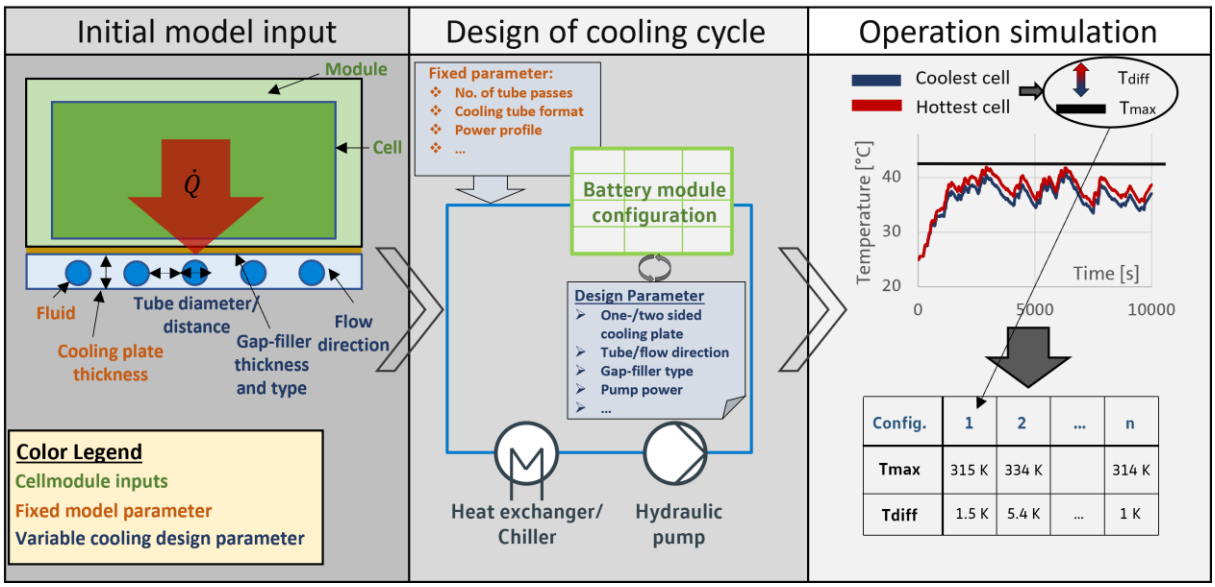

Figure 4.34: Three-part workflow of the cooling plate optimization model to evaluate different cooling plate topologies. First: determination of the initial inputs for the cellmodule and constraints for the cooling plate. Second: cooling cycle design by defining fixed parameters and setting changeable design parameters. Third: evaluation of each cooling plate configuration based on resulting temperatures. Figure adapted from [247].

4.3.3.4 Applicability results for the submodel cooling

The following chapter shows analyses and exemplary results with the proposed cooling model used as a standalone cooling plate optimization model. The applicability and optimization procedure describe the subsequent application in the holistic submodel-concept for the HV-BOT.

When designing a cooling plate for a battery system, the individual cooling plate tube topology must be optimized to efficiently cool the cellmodules with the included cells. Depending on the construction method used, the distances (tube-to-tube) between the cooling channels cannot be chosen arbitrarily. In addition, the size of the cooling tubes must be defined depending on the tube-to-tube distance. The size of the cooling tubes also influences the cooling capacity via the heat transfer area, the pressure losses, and the resulting volume flow. In this section, the above-described model will be used to optimally design the cooling plate for an exemplary battery system with specific requirements and with differing cellmodule geometry possibilities. Thus, three geometrically different cellmodules are predefined, stressing the applicability of the multi-parametric cooling plate simulation model. The geometric input properties of the cooling plate and the cellmodules can be found in Table 4.7.

Figure 4.35 describes the derivation of the cellmodule geometries from the same EV battery system. The dimension of the battery system allows the cellmodule to be variable in its geometry. The three cellmodules are divided geometrically into their naming pattern: long, medium, and quadratic. However, the electrical and thermal properties of all cellmodules are kept equal. Table 4.7 additionally provides a detailed physical description of the cellmodules and cooling plate as well as fundamental cooling model input specifications. The specifications are based on assumed values

for a mid-range vehicle and thus provide a holistic standard for a cooling plate and its cooling circuit.

Generally, various load profiles can be used as cooling plate design profiles. However, for the results shown in this chapter, a 25-minute constant current quick charging profile from 5% - 75% SOC was defined (see charging protocol in Chapter 4.3.1.5). The current profile is depicted in Figure 8.1 in the appendix. The high current generally ensures maximum cooling capacity from the cooling system in a short duration and is, therefore, particularly relevant for the cooling plate design in today's automotive battery development. In comparison, a 25-minute battery charge from 5% - 75% is a moderate to high quick charging time for modern EVs. Based on the maximum pump power (see above), a PWM signal of 30% is assumed for the following results. Since the battery system is rather small (51 kWh, see Table 4.7), it can be assumed that also a rather small water pump would be used for the battery cooling system. The sensitivity of the PWM signal will also be further discussed in the results to elaborate on the model's robustness.

Additionally, Figure 4.35 gives insights into the design possibilities of cooling plates using different cooling tube sizes as well as varying tube-to-tube distances. Based on this, the following chapter will introduce the graphical output scheme to examine and evaluate the differently designed cooling plates. Afterward, a variety of different cooling plate topologies will be investigated and evaluated in detail using the Module medium geometry. Thereby, different evaluation sizes will be examined to ultimately highlight and discuss the results from various perspectives. Then, the cooling plate topology evaluations are also carried out for the other module geometries long and quadratic. Lastly, the results are summarized, compared, and discussed from an overall view.

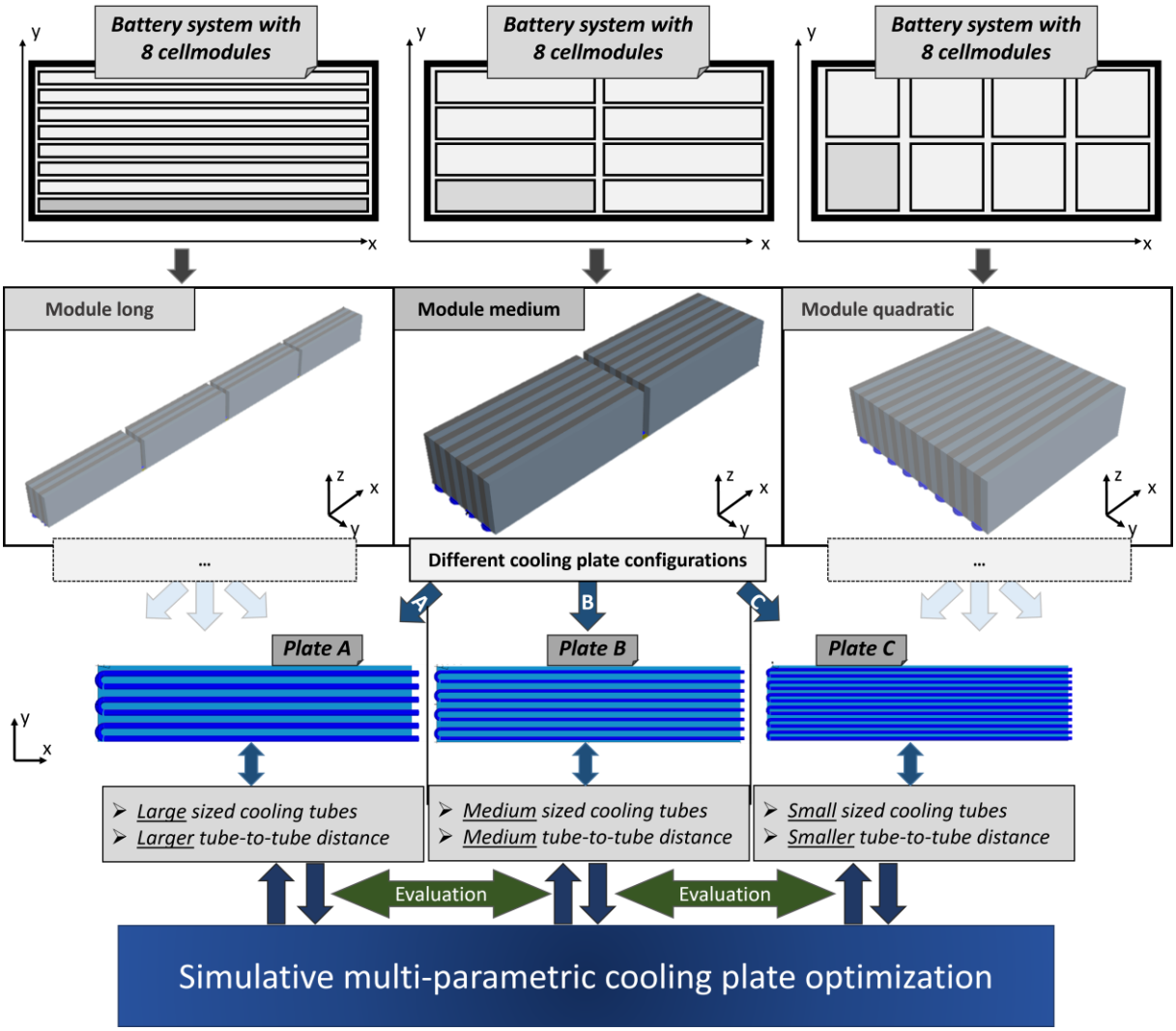

Figure 4.35: Derivation of the three geometrically different battery cellmodules. Each cellmodule's cooling plate can be optimized in terms of tube sizes and tube-to-tube distance.

Specification	Value
Cooling model	
Used cooling circuit stage	Basic, see Figure 4.33.
PWM pump power	PWM 30%
Cooling plate geometry and material properties	Two-part cooling plate (e.g. welded together) made of aluminum consisting of an upper base plate (2 mm) and a lower plate (1 mm) with deep drawn cooling channels (variable height).
Cooling type	One-sided bottom cooling.
Cooling design current profile and starting cell SOC	Quick charging protocol (constant current) for a 25-minute charge from 5% - 75% SOC (see visualization in appendix).
Cooling tube circle ratio	w/h = 3 (derivation and visualization in Figure 4.29).
Gap filler (thickness and heat conductivity)	Gap filler thickness (cooling plate to cellmodule): 1 mm Heat conductivity: 2 W/(m²·K)
Cooling tube direction	Parallel through the cellstacks (see Figure 4.30).
Number of passes for each tube	n_pass = 2 → u-shape tube.
Cooling plate	One-sided bottom cooling.

Battery model	
System level data	
Overall size of the cooling plate	1580 x 755 x 18 mm³ (optimized height can vary with tube size.)
Battery system energy	~ 51 kWh
Battery system topology	192s1p
Number of modules	8
Module level data	
Module size (length, width, height)	Long: 1440 x 90 x 120 mm³ Medium: 720 x 180 x 120 mm³ Quadratic: 360 x 360 x 120 mm³
Module topology	24 total cells; 24s1p interconnection
Module heat capacity and weight	Heat capacity: 1060 J/(kg·K) Weight: 31.1 kg (including 24 cells and aluminum housing shell.)
Module heat conductivity (x,y,z)	Along module (side to side): 30 W/(m² · K) Along module (bottom to top): 14 W/(m² · K) Through module (front to back): 1 W/(m² · K)
Cell level data	
Cell properties	Cell format: Pouch-Type Cell capacity: 72 Ah Cell voltage nominal: 3.7 V See [293] for details.
Busbar	Tab geometry (length, height, thickness): 40 x 30 x 0.3 mm³. Busbar (aluminum) geometry cell to cell (length, height, thickness): 36 x 30 x 3 mm³.

Table 4.7: Physical description of evaluated cellmodules and corresponding cooling model specifications.

Result evaluation of the Module medium geometry

In this chapter, results for the Module medium geometry are evaluated and discussed. Unless otherwise described, the assumptions from Table 4.7 apply. As a first step, results for the mean module temperature for a fixed tube-to-tube distance of 21 mm are depicted in Figure 4.36. This limits the parameter variation of the cooling plate to one only parameter, the cooling channel height. The following analyses assume that the width of the cooling tubes equals three times the tube's height. This was defined in Table 4.7 (see also the definition of the circular tube segments in Chapter 4.3.3.2). The average module temperature (y-axis) is depicted for different cooling tube heights (x-axis), resulting from fast-charging the defined battery module. Using the mean module temperature as the major evaluation variable offers advantages in comparing the total heat that can be dissipated depending on the cooling configuration. For an actual feasibility evaluation of a cooling topology, further quantities like the occurring maximum temperature and the maximum occurring temperature difference should be investigated. However, the absolute values of these quantities strongly depend on the current profile and the internal resistances of the cellmodule and can thus change application-dependent. Therefore, the mean module temperature is the most suitable parameter for the comparison of cooling plate configurations for a constant module geometry.

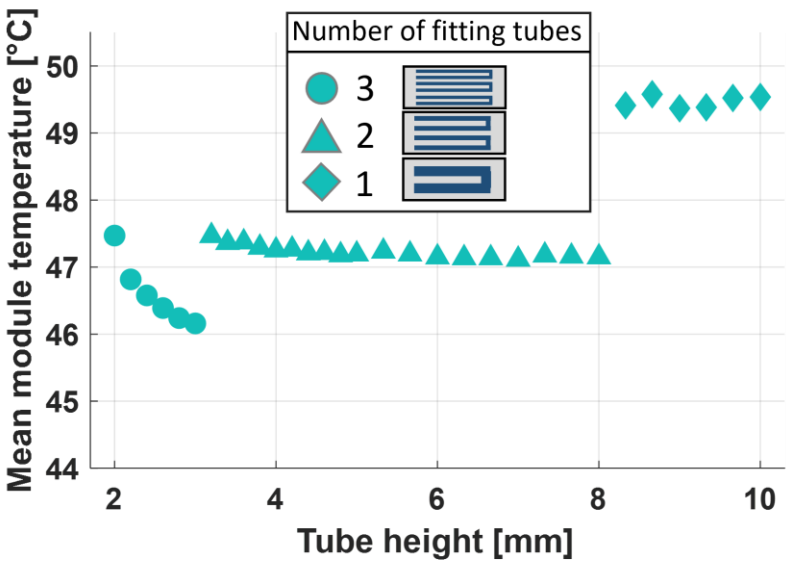

Figure 4.36: Resulting mean cellmodule temperature for a 25-minute quick charge with parallel cooling tube flow and a fixed tube-to-tube distance of 21 mm. Different tube heights influence the reached mean module temperature.

The results of the mean temperature depending on tube height show a three-part degressive course. The mean temperatures lie in a range from 46 °C to approx. 50 °C. In order to explain the three-part range, the number of tubes fitting underneath the module is represented by different symbols in the graph. Each tube has two passes (see Table 4.7).

The jumps between these tube-number-clusters are significant with approx. 1.5 °C and 2.2 °C. The degressive course results from the increasing pressure losses due to smaller cooling channel diameters. This effect will be discussed in more detail below. Due to the degressive course, the best cooling result is achieved with a tube height of roughly 3 mm.

However, this result is only evaluated as optimal for the considered tube-to-tube distance of 21 mm. In the following, this premise is removed, and a range of tube-to-tube distances from 11 mm - 25 mm is investigated. Figure 4.37 analyzes these results from different perspectives. The figure is divided into four individual graphs.

Figure 4.37 A shows the resulting reached mean temperatures (y-axis) within the Module medium geometry depending on the cooling tube height (x-axis). The color of the data points provides information regarding the evaluated tube-to-tube diameter (11 mm in blue to 25 mm in yellow). As already shown in Figure 4.36, degressive mean module temperature curves with jumps can be evaluated. These result from the number of geometrically suitable cooling tubes underneath the module geometry given the corresponding tube-to-tube distance as well as the size of the cooling tube. The size of the mapped data points varies slightly with the associated tube-to-tube distance. This ensures that data points with different tube-to-tube distances can visually lie on top of each other. The direct superposition of data points results from the modeling methodology and geometry assumptions described in Chapter 4.3.3.2.

Figure 4.37 B shows the dependence of the tube height (x-axis) and tube-to-tube distance (y-axis) with the achieved mean module temperature in a 2D contour plot. The color scale from blue to red provides information on the reached mean module

temperature. Lower temperatures are achieved with smaller tube diameters or smaller tube-to-tube distances.

Figure 4.37 C can be used to investigate the dependence of system coolant flow rate (y-axis), heat transfer area (x-axis), and mean module temperature (color). The heat transfer area is obtained by multiplying the width of the cooling channels by the number of tubes underneath the cellmodule. It should be noted that the heat transfer area depends on both the tube-to-tube distance and the size of the cooling tubes. A specific value can thus be obtained from different combinations of the two quantities, which explains the range of associated coolant flow rates in some values of the x-axis. The graphic underlines the complexity of the relationship between the heat transfer area and the reached module temperature.

Figure 4.37 D shows the geometrically suitable cooling tubes (y-axis) underneath the module geometry, given the corresponding tube height (x-axis) and tube-to-tube distance (color). The graph can be used to in-depth study the depicted results of graphics A - C.

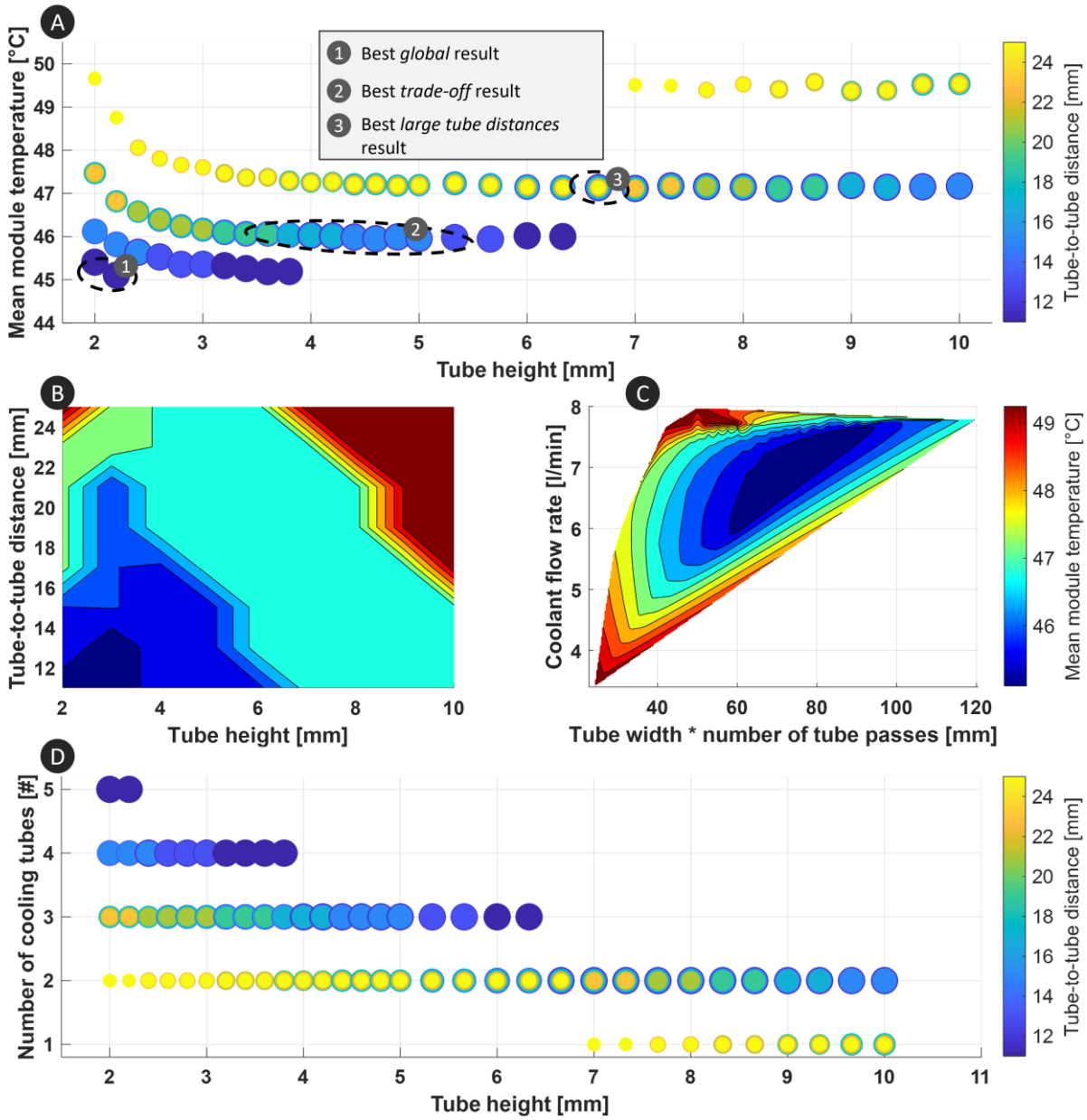

Figure 4.37: A) Resulting mean cellmodule temperature for a 25-minute quick charge with parallel cooling tube flow and variable tube-to-tube distance. Different tube heights and tube-to-tube distances influence the reached mean module temperature. B) In-depth view of the mean temperature areas for different geometric cooling tube configurations. C) Volume flow analysis depending on the heat transfer surface. D) Geometric derivation of the number of total fitting cooling tubes depending on the configuration parameters tube height and tube-to-tube distance.

The results can be evaluated on the basis of different quantities or perspectives. Therefore, three result perspective areas have been marked separately in Figure 4.37 A. The first area is the globally optimal result, which can be found in the lower left corner at small tube heights and smaller tube-to-tube distances. Here the lowest mean module temperatures are achieved. Since the producibility of several very small cooling channels can be complex, the best trade-off result marked with number 2 could also be application-dependent optimal. The range is intended to cover a selection of points between which the optimal combination of tube height and tube-to-tube distance

is mapped, depending on the manufacturability and the production technology of the cooling plate. The mean module temperatures are roughly 1 °C higher at approx. 46 °C. A third range has been marked to derive the best result with the maximum tube-to-tube distance. For cooling plate production using deep-drawing technology, the tube-to-tube distance parameter can be particularly relevant due to producibility-related boundaries and must therefore be carefully selected for some applications. The mean module temperature for the third area is roughly 47 °C.

Assisting the results of the three perspective areas, Figure 4.37 C illustrates generally lower mean module temperatures for medium to large heat transfer areas and coolant flow rates. However, the red surface in the upper left part of the graphic is particularly striking. Herein, comparatively high mean module temperatures are achieved despite a high coolant volume flow. This effect can be explained by considering the combination of a few large-sized cooling tubes. Thereby, a generally high coolant volume flow is achieved due to advantageous pressure losses in larger cooling tubes. However, the combination of only a few tubes leads to an insufficiently cooled cellmodule. Generally, the results in Figure 4.37 C underline the complexity of optimized cooling tube selection as high volume flows or heat transfer areas do not fully indicate the lowest mean module temperatures.

Results evaluation of the Module long and Module quadratic geometries

In this chapter, results for the Module long and Module quadratic geometry are evaluated and discussed. Unless otherwise described, the assumptions from Table 4.7 apply. The two module geometries long and quadratic considered here were shown graphically in Figure 4.35. Both module geometries do not differ in their physical properties (except geometrically) from the Module medium geometry evaluated in the last chapter. The changed cell arrangement and different space allocation resulting from the associated module geometry majorly change the demands for the optimized cooling plate. Figure 4.38 summarizes the results for both geometries. Thereby, Figure 4.38 A again shows different mean temperatures achieved for the Module long geometry. The mean module temperature (y-axis) is depicted depending on the cooling tube height (x-axis) for different tube-to-tube distances (color). Figure 4.38 B shows the associated coolant flow rate instead of the mean temperature on the y-axis. Figure 4.38 C and D are built in the same way and show the results for the quadratic geometry modules.

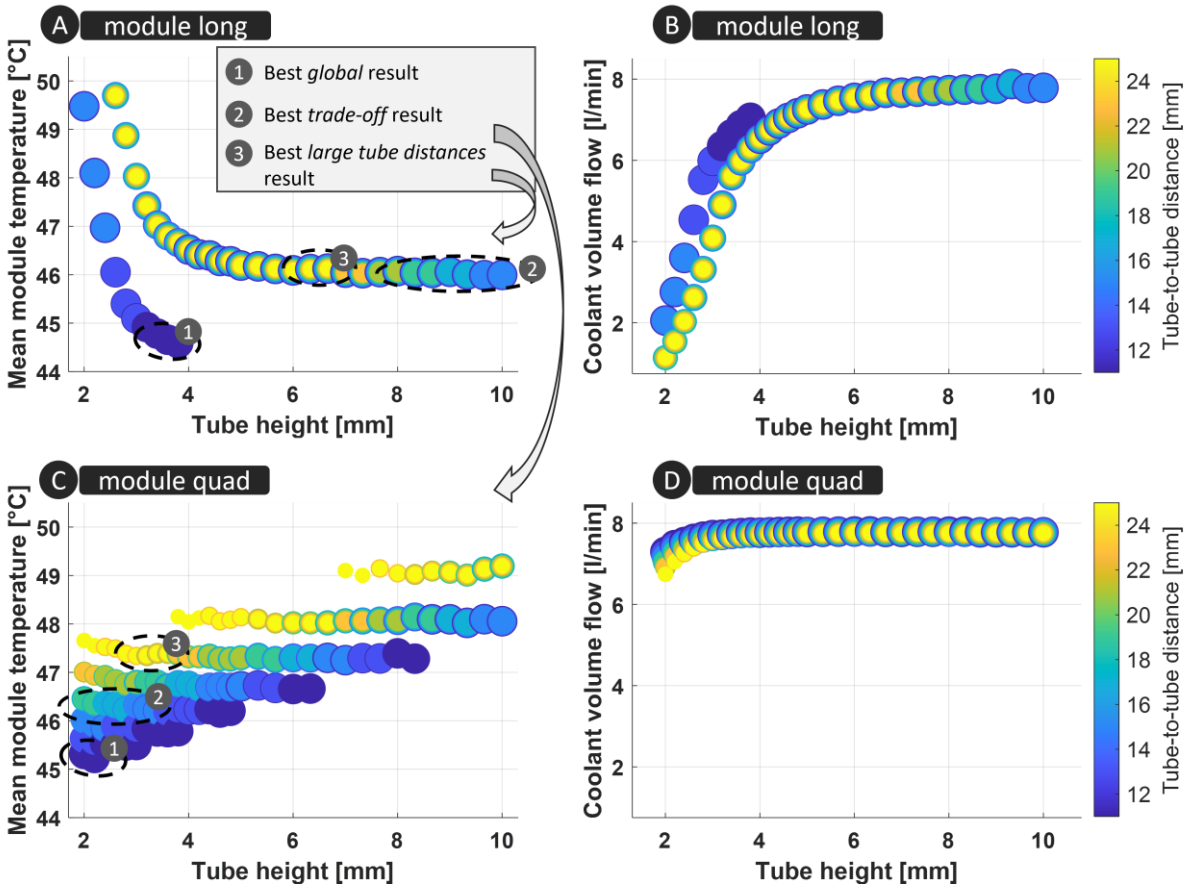

Figure 4.38: A) and C): Resulting mean cellmodule temperature for a 25-minute quick charge with parallel cooling tube flow and variable tube-to-tube distance. B) and D): Volume flow results.

The results in Figure 4.38 A and C are again evaluated with respect to three different perspectives. The first perspective is the best global result. The lowest temperature for Module long is roughly 44.5 °C and above 45 °C for Module quadratic. While the best global result for the Module quadratic can be found at very small tube heights with also small tube-to-tube diameters, the global best result for the Module long variant is at about 4 mm tube height. The reason for this lies in the geometry of the Module long. Due to the necessary longer cooling tubes, generally, high-pressure losses occur. Therefore, a globally optimal result requires a higher tube height in order to keep the pressure losses small and thus increase the volume flow. This phenomenon can be in-detail analyzed in the corresponding graphs in Figure 4.38 B and D. Herein, it can be seen that the coolant volume flow for the Module quadratic is above 7 l/min for every evaluated tube height, while for the Module long, larger tube heights are required to increase the volume flow and thus the heat that can be dissipated.

This trend can also be seen in the evaluation by the other evaluated perspectives. The best trade-off result (2) for the Module long variant shows a wide range with larger tube heights, while lower tube heights are needed for the quadratic module. Similar results are evaluated for the result with the largest tube-to-tube distance.

In summary, the Module long variant requires significantly greater tube heights than the Module quadratic geometry. This results, in particular, from the pressure losses occurring from the long cooling tubes required in the Module long geometry.

Summary and discussion

The optimization methodology developed in this chapter has allowed a variety of different cooling plate configurations to be investigated and evaluated. The results shown above have provided an overview of the evaluation possibilities with varying tube height and tube-to-tube distance for three different cellmodule geometries.

The different pressure losses, as well as corresponding coolant volume flow rates, resulted in degressive decreasing mean cellmodule temperatures depending especially on the cooling tube's height. This degressivity is directly related to the required length of the cooling channels. Therefore, the degressive course was particularly strong for Module long but almost not recognizable for Module quadratic.

For each of the investigated module geometries, results were clustered. Through the different clustering criteria (best global, best trade-off, best with maximized tube-to-tube-distance), individual cooling plate configurations were perspective-related and evaluated better or worse. In-detail investigations of the Module medium geometry underlined the model depth, thus, emphasizing the interaction between the geometrical quantities of tube height and tube-to-tube distance, as well as the necessary volume flow and the achieved mean module temperature.

Summary and discussion: PWM signal robustness

One relevant assumption made for the above-shown results was the pump power using the PWM signal in Table 4.7. The pump power was initially defined based on the rather small battery system size. However, in a real-world application, the actual pump size within the battery cooling system may depend on multiple other factors (cost, pressure losses outside the cooling plate, and coolant). Analyzing different PWM signals, thus, investigates the opportunities for larger or smaller dimensioning of the pump used in the final battery cooling system. In order to validate the robustness of the result, the PWM signal was varied, observing again the Module medium temperatures. Figure 4.39 summarizes these results.

The circle in gray color represents the results of the default pump assumptions from Figure 4.37. The squares represent results using a PWM signal of 50% with respect to the maximum pump power (see Chapter 4.3.3.2). The triangles correspond to the temperature results with a 20% PWM signal.

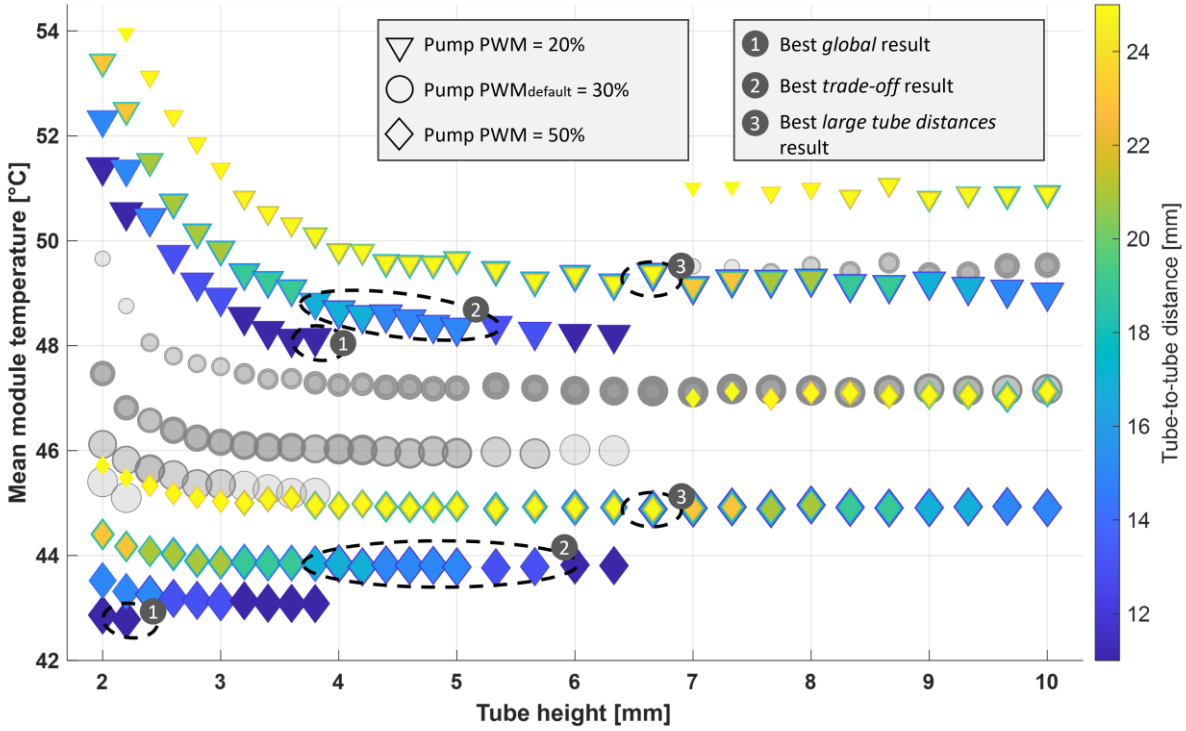

Figure 4.39: Comparison of three different PWM pump powers. Resulting mean cellmodule temperature for a 25-minute quick charge with parallel cooling tube flow and variable tube-to-tube distance. Gray dots replicate results from Figure 4.37 for a graphical comparison.

The results show that the mean temperature course remains largely the same with respect to the tube height and tube-to-tube distance. As expected, an increased PWM signal reduces the average temperature, while a lower PWM signal increases the mean module temperature. The explanation can be found in the increase or decrease of the resulting volume flow corresponding to the pump power. The resulting clustering (best global, best trade-off, best large tube distance) is almost not changing by the varied PWM signal. Only the best global result for the 20 % PWM results is shifted towards larger tube heights of almost 4 mm.

Larger changes can, however, be observed in the initial degressive drop in mean module temperature, especially at smaller tube heights. With a higher PWM signal, the temperature drop becomes less degressive. This could make smaller tube heights more attractive for the cooling plate design, as stronger pumps offer sufficient power for an increased volume flow even for more considerable pressure losses. In conclusion, the pump strength showed no significant influence on the distribution and shape of the results but had relevance in the detailed cooling plate design and especially the interpretation and conclusion of the results. Future work could further elaborate on this aspect and especially investigate it for the different module geometries.

Summary and discussion: overall comparison

A comparative and summarizing analysis between the module geometries considered in this chapter is depicted in Figure 4.40. The graphic depicts the collectively calculated mean module temperature for each module geometry with the default assumptions from Table 4.7. Thereby, Module long shows the lowest mean module temperatures, followed by Module medium and Module quadratic. Nevertheless, the highest temperature reached is also achieved by Module long, followed by Module medium and Module quadratic. A low tube-to-tube distance leads to the greatest advantages within the Module long geometry. This results in an optimal trade-off between heat transfer surface (4 mm tube height), high volume flow (> 7l/min), and high homogeneity (low tube-to-tube distance), which leads to an overall optimal cooling plate configuration due to the long-shaped geometry.

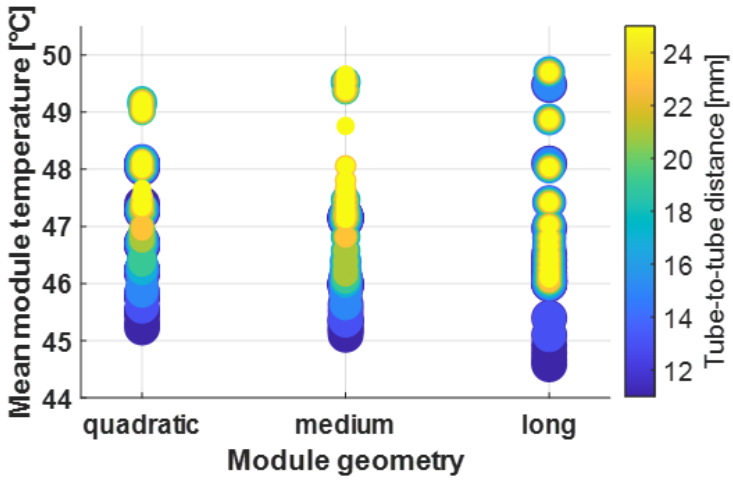

Figure 4.40: Comparison of all three different module geometries with varying tube-to-tube distances. Range of mean cellmodule temperature reached for a 25-minute quick charge.

4.3.3.5 Model conclusion

A comparative evaluation of various cooling plate designs was performed, analyzing the potential of different construction-relevant plate properties based on realistic EV battery requirements. The proposed cooling plate optimization model is fully parametrized using multiple individual submodels to present the entire battery cooling procedure from the cellmodule to the cooling plate to the cooling circuit. The model incorporates geometric limitations, occurring pressure losses, and operating point-specific cooling capacity.

Three exemplary cellmodules were derived from an EV battery system to examine the cooling plate optimization model. Based on the cellmodule geometries, various unique simulations with multiple tube diameters as well as tube-to-tube distances were conducted and analyzed. The results mainly emphasized:

- Optimized cooling plate topologies majorly differ depending on the cellmodule geometry: The three cellmodules were defined with equal electrical and thermal but different geometric properties. The results showed the smallest optimized cooling plate tube diameters for the quadratic module (2 mm height) and the largest tubes for the narrow module long (4 mm height).

- The lowest mean temperature for the narrow cellmodule long geometry: The module long variant showed an optimal trade-off between heat transfer surface, high volume flow, and high homogeneity. For otherwise equal conditions, the cooling plate of the module long could thus reach up to 1 °C lower average temperatures for a 25-minute constant current quick charging profile.

Different evaluation criteria helped to evaluate results from different perspectives and ultimately elaborate production-specific requirements for developing the cooling plate. Next to module temperatures, heat transfer areas, and resulting volume flows were also extracted from the results to stress the model's accuracy and highlight specific cooling configurations. The main findings are:

- Analysis of trade-offs in cooling plate design by using the proposed lumped mass model: The proposed lumped mass model was used to visually emphasize the complex trade-off between coolant volume flow and heat transfer area for multiple cooling plate topologies. The results suggested that only a simultaneous increase in both quantities can lead to an effective temperature decrease.

- Possibility of potential identification in early concept development phase: Results show the potential of lumped mass modeling to evaluate cooling plate topologies for early stage concept development stages of EV batteries. Thereby, the preselection of potential cooling plates can give a competitive starting point for the subsequent cooling plate concept detailing with more detailed CAD models.

- Future-proof modeling approach: The model is built modular and fully parameterized. The generically modeled individual submodels (pressure losses, cooling circuit, plate parametrization) of the cooling model use state-of-the-art data assumptions. Models can be changed, replaced, or extracted to be used in future cooling plate developments. Thereby future work can examine further related cooling methods, such as refrigerant cooling or novel approaches like immersion cooling, using the proposed model framework.

4.3.4 Submodel electronics

In the following chapter, the electronics submodel will be presented. Within the HV-BOT, the electronics need certain installation space depending on the system’s power requirement. Furthermore, different electronics integration concepts within or outside the battery system are presented and modeled. The objective of the electronics submodel is thus to quantify the influence of different vehicle performance classes on the electronics and the overall battery system.

A battery junction box serves as a switching unit for the battery in the electric vehicle. Various components like fuses, relays, switches, connectors, microcontrollers, or detection devices are used to enable charging, discharging, or seamless disconnection in the event of a technical error [309, 310]. The structure of the electronics in the battery system and the classification of the BJB were described in detail in Chapter 2.2.4. In the electronics submodel, the BJB is implemented as a 2D-black-box with outer space requirements depending on the battery system's power requirements. The available length in the y-direction for the BJB is given as input. As the BJB’s components can

generally be arranged flexibly, the actual width may be distributable depending on the available BJB length l_{Box}. In Figure 4.41, two exemplary BJB variants are illustrated with differing lengths and widths but equal performance.

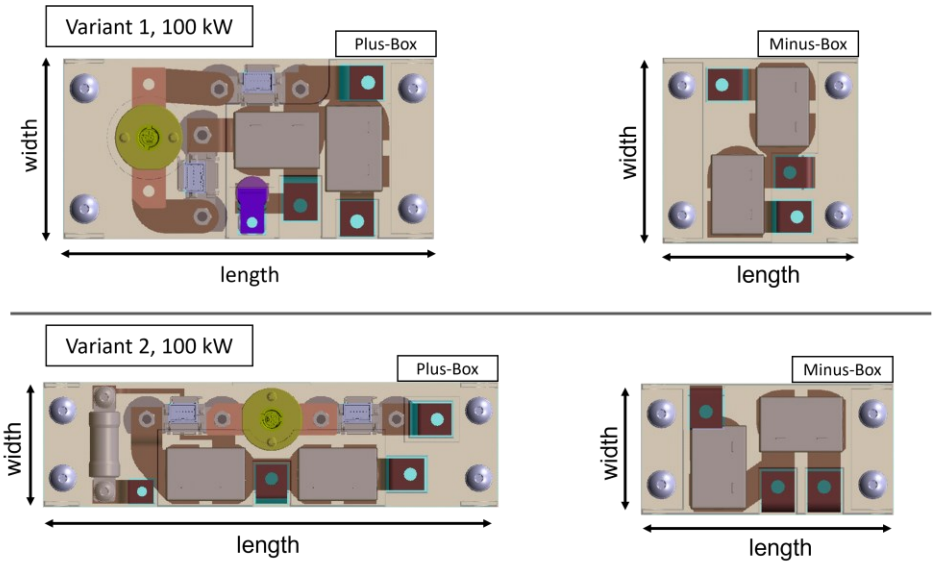

Figure 4.41: Different geometric variants of junction boxes.

For the BJB's width w_{Box} the following 2D assumption is used in this work:

$$w_{\mathrm{Box}}(l_{\mathrm{Box}}) = \left(\frac{A_{\mathrm{ref.Box}}}{l_{\mathrm{Box}}}\right)^{\left(\frac{l_{\mathrm{Box}}}{l_{\mathrm{ref.Box}}}\right)^{\delta}} \cdot \left(1 + \left(\rho_{\mathrm{scaling}} \cdot \frac{P_{\mathrm{system}} - P_{\mathrm{ref.system}}}{P_{\mathrm{ref.system}}}\right)\right). \tag{4.62}$$

This simplified model uses a reference BJB model to calculate the scaling width for other geometries. Area $A_{\mathrm{ref.Box}} \approx 70000\ \mathrm{mm}^2$; BJB's length (plus and minus box) $l_{\mathrm{ref.Box}} \approx 900\ \mathrm{mm}$, $\delta = 0.1$, $\rho_{\mathrm{scaling}} = 0.13$ and $P_{\mathrm{ref.system}} = 40\ \mathrm{kW}$ are used as reference data. The non-linear scaling assumes overall space advantages for wider, more compact BJBs. l_{Box} is defined between 400 mm and 1200 mm. Generally, an increased power demand P_{system} leads to larger-sized components. Two different BJB variants with 100 kW and 300 kW performance schematically illustrate this in Figure 4.42. As a subordinate aspect for space allocation in battery system design, detailed analyses of the BJB on a 3D component level are not part of the electronics submodel.

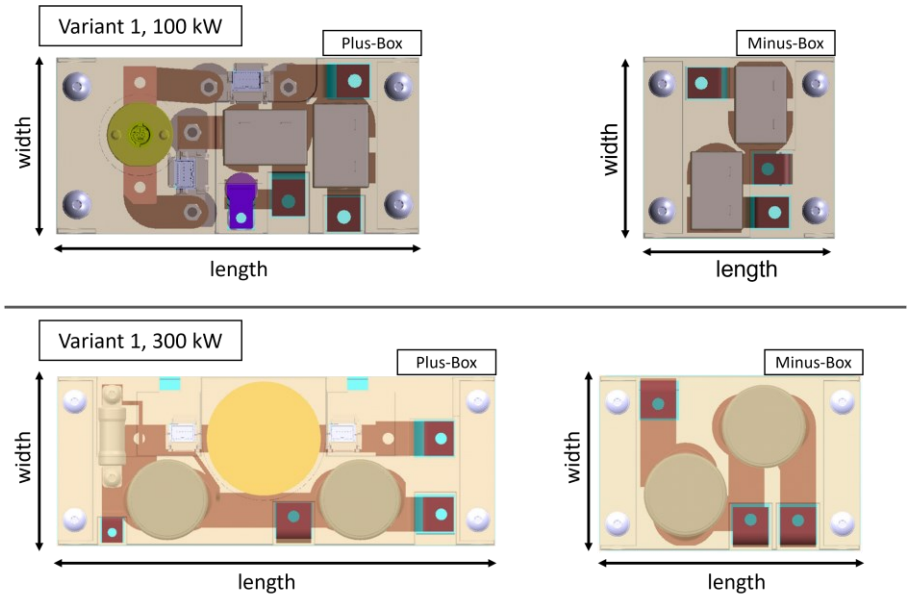

Figure 4.42: Different power requirement variants of junction boxes.

After defining the junction box's geometrical sizes, the actual integration within the battery system also has to be evaluated. For this, three different integration methods are implemented within the HV-BOT, which are depicted in Figure 4.43.

The *standard integration* is accompanied by at most one side member. The second integration concept, the *complex integration,* is accompanied by the number of side members already included within the battery systems. This may lead to increased complexity when designing the BJB since the inner parts of the box may be connected across the side members, leading to cost increases. The third integration is the *external integration* of the BJB. This concept does not include the BJB within the actual battery systems installation space. It would therefore be included in other parts of the vehicle. This integration concept is defined as the most expensive concept since complex requirements and development efforts accompany it. Different modes can be used to control HV-BOT using the different integrations. Mode 3 assumes high costs for external integration to ensure that it will only be used if no other integration concept is feasible.

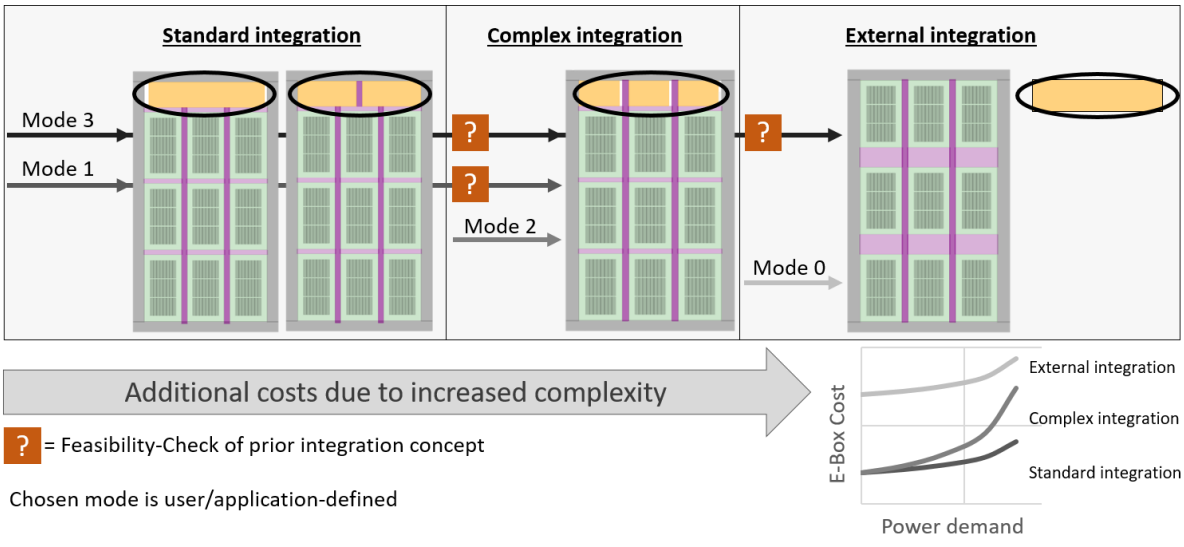

Figure 4.43: Schematic representation of the 2D electronics submodel procedure illustrating different modes of the electronic components integration process. Mode is settable from the user to control the electronics' target integration concept.

4.3.5 Objective function cost modeling

In this work, the cost modeling is performed as a user-defined framework. In Table 4.8, cost derivations used in this work are derived for each submodel. Actual costs may vary individually depending on various factors such as location, time, price or cost considerations, in-house production, or purchasing. The costs can, therefore, not be specified in a general and exogenous manner. An additional list of literature references for the different cost components is given in the appendix in Chapter 8.5.2.

It is also important to note that, next to the actual cost value, especially the variability in costs, is of major importance when optimizing space allocation within the battery system. Therefore any submodel's variable cost-share can be crucial, although the costs of the cellmodules are superior within battery systems [311]. General cost distributions will be compared with the literature in Chapter 4.4.3. Next to the cost, also a DOF term $\Phi_i(\mathbf{x}), i \in \{1,2,3,4\}$ is approximated using different physical relations within each submodel.

Submodel	**Cost derivation**	**Degree of feasibility (DOF) term derivation**
Cellmodule	The complex structure and different cost parts are fully described in Chapter 4.3.1.7.	Using a two-part penalty term: Firstly, the relative length/width that the cellstack exceeds the available module space. Secondly, the relative amount of energy density that the cell exceeds (due to its energy demand) with regard to the possible energy density.
Cooling	Using a two-part cost function consisting of plate volume and gap filler: Firstly, the deep-drawing process is used to generate the cooling channels inside the cooling plate. This process allows smooth surfaces to be preserved, which are crucial for subsequent pressure losses. Therefore, the costs are divided into pure material costs and deep-drawing process costs. These deep-drawing process costs are defined based on a reference cooling plate with 75 €/m². An overview of different influencing factors for cooling plate costs can be found in [312]. Based on literature findings for gap filler costs, the gap filler has costs C_{gf} depending on the thermal conductivity λ_{gf} with:	Using a two-part penalty term: Firstly, the relative proportion that cellmodule's temperature exceeds the specified $T_{\mathrm{max.}}$. Secondly, the relative proportion that the cellmodules' temperature difference exceeds the specified $\Delta T_{\mathrm{max.diff.}}$.

	$C_{\mathrm{gf}} = 0.515 \cdot \exp(0.976\,\lambda_{\mathrm{gf}}) \cdot \frac{€}{l} + 18\,\frac{€}{l}$ Secondly, the cost of the overall cooling circuit (chiller, compressor, piping) cannot be fully attributed to the battery system as it is also otherwise (e.g., passenger climate control) used in the car. Therefore, different cooling circuit stages are defined directly from the battery energy requirement (representing different vehicle classes). Assumed costs are 50 €, 75 €, and 100 € for the basic, medium, and high-end circuit. Three water pump costs are assumed with 10 €, 25 €, and 50 € for three pump strengths. See Chapter 4.3.3 for technical details for the cooling circuit and pump power.	
Mechanics	In mechanics, different types of profiles are used for the outer profile, side member, and cross member. The aluminum profiles are extruded profiles. Multiple cost-effecting factors are summarized in [313]. Besides, additional cost and weight result from the underride protection layer for bollard-type crashes (definition see Chapter 8.2). Based on the weight of the components, the material cost for extruded aluminum is assumed as 5 €/kg.	Using the best/lightest configuration out of all possible construction concepts: If no construction concept was feasible: DOF = 2. Additionally, added DOF is defined as the force the cross members have to withstand in the crash requirement relative to the force $F_{\mathrm{max.}}$ that the specified cross members are able to withstand.
Electronics	The electronics' costs are based on the integration of the geometry and power-dependent 2D junction box model. From this, a cost-relevant mass m_{Box} is derived. As multiple metals and metal compositions (copper, silver-nickel alloy, tin-lead,…) are used in the BJB, a BJB metal mix cost factor $c_{\mathrm{BJB-metal-mix}}$ = 40 €/kg is used for model simplification. The following costs are assumed: For standard integration: $C_{\mathrm{BJB}} = 200\,€ + m_{\mathrm{Box}} \cdot c_{\mathrm{BJB-metal-mix}} + n_{\mathrm{SM}} \cdot 10\,€$ For complex integration: $C_{\mathrm{BJB}} = 250\,€ + m_{\mathrm{Box}} \cdot c_{\mathrm{BJB-metal-mix}} + (n_{\mathrm{SM}} - 1)^2 \cdot 10\,€$ For external integration (2000 € *penalty cost term*): $C_{\mathrm{BJB}} = 200\,€ + m_{\mathrm{Box}} \cdot c_{\mathrm{BJB-metal-mix}} + 2000\,€$ Exemplary costs for converts and their cost scaling with increasing requirements can be found in [314].	The relative proportion of missing installation space in the integration concept. (Is never violated if the integration concept Mode = 3 since external integration is always possible.)

Table 4.8: Tabular overview for derivation and explanation of the cost modeling as well as the degree of feasibility for the submodels cellmodule, cooling, mechanics, and electronics.

4.4 Application, results, and validation

In this chapter, the HV-BOT's practical use is introduced. In particular, the applicability will be demonstrated by deriving designs of battery systems for different requirements. In addition, the interaction between the individual physical simulation models will be illustrated. Moreover, resulting cost and weight distributions will be validated with literature findings. Afterward, existing battery system concepts in the market will be rebuilt. The results of the HV-BOT will then be validated in order to discuss model limits.

Unless otherwise specified, default submodel specifications from Chapter 4.3, as well as the further detailed specifications in the appendix in Chapters 8.1 - 8.5, are used.

4.4.1 Analysis of space allocation variation

This chapter uses the combined submodel-concept from the presented submodels cellmodule, mechanics, cooling, and electronics to evaluate different battery system concepts. The battery system concepts are determined based on the list of inputparameters. Table 4.9 summarizes the exemplary defined inputparameters for one battery system. The parameters are separated into general parameters and submodel-specific parameters. Table 4.9 only mentions major design parameters. A comprehensive list of parameters can be found in the appendix. The parameters are fixed throughout the battery system optimization and thus represent the major requirements for the different design concepts.

Inputparameter (user-defined)	**Value**
General	
System installation space x,y,z	1800.0 x 1400.0 x 140.0 mm³
System energy demand	50 kWh
System power demand	140 kW
System charging time demand	20 min
System voltage demand	408 V
System usable battery DOD	96%
Cellmodule	
Cell geometry	Two possible cells: Prismatic: 160 x 18 x 105 mm³ Prismatic: 210 x 26 x 110 mm³
Maximum number of cellstacks per module	2
Cooling	
Ambient temperature	23.0 °C
Number of passes for cooling tube	2
Design current profile	Quick charging profile
Refrigeration circuit expansion stage	Basic
Mechanics	
Crashenergy requirement	20 kJ

Cellstack integration (only for prismatic cells)	Screwed cellstacks
Electronics	
Integration mode	3

Table 4.9: Exemplary user inputparameter for the battery system evaluation using the HV-BOT with the submodel-concept.

For an evaluation in the HV-BOT, an optimized battery concept can then be determined and evaluated on the basis of the design variables (see the definition in Chapter 4.2.1). Model and construction results for an exemplary set of design variables (*iteration n*: $x_1 = 0.8, x_2 = 0.73, x_3 = 0.78, x_4 = 3, x_5 = 5$) are summarized in Table 4.10. The list only extracts the most relevant result parameters. A comprehensive list of output parameters with explanations for each submodel can be found in the appendix.

Model	**Key inner-model parameters**		
Cellmodule	**System**		
	Energy = 52.1 kWh	Power = 140 kW	Charging Time = 20 min
	MaxVoltage = 441 V	Topology = 105s3p	Capacity = 134 Ah
	Cost = 5721.6 €	Mass = 273.9 kg	
	Module		
	Energy = 3.5 kWh	Power = 9.3 kW	Charging Time = 20 min
	MaxVoltage = 29.4 V	Topology = 7s3p	Capacity = 134 Ah
	FrontplateThickness = 9.5 mm	SideplateThickness = 2.5 mm	Cover/BottomplateThickness= 0.5 mm
	BusbarHeight = 30.0 mm	BusbarWidth = 15 mm	BusbarThickness = 5 mm
	StackingDirection = 'X'	CellsPerRow = 21	CellPerColumn = 1
	CellToCellDistance = 1.99 mm	CellToModuleGapFiller = 1.1 mm	Resis.Busbar(80%,20 °C) = 0.025 mOhm
	ThermalConductivityX = 1.06 W/(mK)	ThermalConductivityY= 20.57 W/(mK)	ThermalConductivityZ = 9.32 W/(mK)
	ModuleHeatCapacity = 923.8 J/(kgK)	HeatCapacity(no cells) = 710 J/(kgK)	
	CostCells = 352.38 €	ModuleCost = 29.09 €	CellMass = 15.4 kg
	MassBusbar = 842 g	MassCompressionPad = 210 g	MassHousing = 751 g
	MassGapFiller = 306 g	MassUnusedSpace = 742 g	MassPackaging = 2.85 kg
	CostBusbar = 8.42 €	CostCompressionPad = 14 €	ModuleHousing = 3.76 €
	CostGapFiller = 2.14 €	CostUnusedSpace = 0.74 €	
	Cell		
	CellX =160 mm	CellY = 18 mm	CellZ = 105 mm
	Energy = 165.4 Wh	Power = 444 W	Charging Time = 20 min
	NomVoltage = 3.7 V	MaxVoltage = 4.2 V	Capacity = 44.7 Ah
	VolEnergyDensity = 547 Wh/l	VolPowerDensity = 1469 W/l	CellFormat=prismatic
	ThermalConductivityX = 1.1 W/(mK)	ThermalConductivityY = 20 W/(mK)	ThermalConductivityZ = 10 W/(mK)
	HeatCapacity = 950 J/(kgK)	CellTerminalPosition = 'Side'	TerminalThickness = 10 mm
	TerminalWidth = 12.6 mm	TerminalHeight = 31.5 mm	FixCost = 1.5 €
	MassCell = 734 g	MassCellcup = 113 g	MassTerminal = 23 g
	CostCell = 16.78 €	CostCellcup = 0.28 €	CostTerminal = 0.19 €
	Inner-cellstack		
	StackX = 154 mm	StackY = 16 mm	StackZ = 103 mm
	MaxChargeContRate = 2.7C	VolEnergyDensity = 651.5 Wh/l	Chemistry = NMC-Type
	Mass = 598 g	Cost = 14.8 €	
	Other:		
	AgingScenario = 2		
Cooling	**Requirements:**		
	DesignProfile = Quick charging profile 20 min	Tmax = 52.5 °C	Tdelta = 15 °C

	LiquidDelta = 5 °C	NumPasses = 2	Cooling circuit = Basic
	Result:		
	Tmax = 47.1 °C	Tmean = 42.3 °C	TdeltaMax = 11.6 °C
	Vflow = 14.75 l/min	PWMpump = 44.2%	
	Construction:		
	FluidDirection = parallel	Gap filler height = 1 mm	LambdaGapFiller = 1 W/(mK)
	TubeHeight = 4 mm		
	Cost and weight		
	CostPump = 10 €	CostCoolingCircuit = 50 €	CostGapFiller = 23.4 €
	CostCoolingplate = 171 €	CostCoolingSystem = 254.4 €	MassTubes = 2.6 kg
	MassGapFiller = 2.8 kg	MassBottomPlate = 5.85 kg	MassCoverPlate = 5.85 kg
	MassLiquid = 3 kg	MassCooling = 20.1 kg	
Mechanics	**Requirements:**		
	Crashperformance = 20 kJ	NumCM = 3	NumSM = 4
	ElecMode = 3	WallThicknessSM = 2.5 mm	Material = Aluminum
	CrushForce = 120 kN		
	Result:		
	Feasible OP-range = 35 - 82.9 mm	Feasible CM-range = 20 - 51.9 mm	CrashForceOnCM = 450 N
	CrushForceLongSide = 202 kN	CrushForceShortSide = 121 kN	CrashInstrusionStack = 22 mm
	Construction:		
	CMspan = 490 mm	SMspan = 547.5 mm	OPwidthOpt. = 66.9 mm
	CMwidthOpt. = 30.6 mm	SMwidth = 35 mm	CMProfile = 'square' WallThicknessQT = 4 mm
	Cost and weight:		
	CostMechanics = 360.9 €	MassOP = 33.4 kg	MassBollardProtec. = 18.8 kg
	MassCM = 17.1 kg	MassSM = 12.3 kg	
Electronics	**Requirements:**		
	SystemNomVoltage = 389 V	PowerReq = 140 kW	CurrentDC = 362 A
	CurrentPowerReq = 359.9 A	ModuleY = 204.4 mm	NumModulesY = 5
	Results:		
	Imax = 362 A	WidthBox = 94.1 mm	LengthBox = 537.5 mm
	Cost and weight		
	CostBox = 508 €	MassBox = 7.7 kg	

Table 4.10: Key inner-model parameters from results of the different submodels. (Due to rounding, summed values may not equal the sum of the individual components.)

The results underline the level of detail of the individual simulation models. The list of parameters also indicates the suitability of the HV-BOT to describe battery systems as digital twins. Data from the cellmodule submodel greatly show how the electrical, thermal, and geometric specifications change over the individual integration stages (system, module, cell, and electrode stack). Next to the construction-relevant sizes and results, the cost assumptions can be monitored in great detail. For the cellmodule, the cost derivation is broken down from the inner-electrode level up to the system level.

A graphical illustration of the battery system design concept is given in the top part of Figure 4.44. In order to further emphasize dependencies between the individual component groups, a second set of design variables (iteration n+1) is used to evaluate a second battery system concept given the fixed inputparameters. Figure 4.44 depicts the changes and interdependencies for the two pairs of design variables based on the inputparameters from Table 4.9. Additionally, the cost breakdown and their changes are depicted on the right side of the figure. This system-to-system comparison starts with the change to fewer modules due to differences in variables x_4 and x_5 as well as more space for cellmodules in y- and z-direction resulting from changes in x_2 and x_3. This directly leads to larger cellmodules. Larger modules then lead to possible larger

cells, which change internal cell specifications and, thus, trigger further needed adaptations in the system design. The cell chemistry change from NMC-Type to LFP-Type particularly reduces the costs at the cell level. However, cost increases arise from the mechanical changes to the outer frame and the associated higher loads within the battery system. As a result, wider cross members become necessary. Furthermore, the cooling requirements change. Therefore, costs also rise due to a change to a gap filler with higher heat conductivity. Furthermore, the costs for the electronics increase, since on the one hand the available geometry changes, but on the other hand also the maximum current to provide the necessary power demand is slightly higher.

Nevertheless, since the cost savings occurring from the changed cell chemistry are large, the second configuration is significantly more cost-effective from an overall system cost perspective. However, this may change if the same cell chemistry is used between different battery system designs (see Chapter 6.3.2). The broken-down list of interdependencies delivers great insight into the complex repercussions of changes in space allocation and related costs. It further highlights the multitude of modeled interfaces between the individual submodels within the HV-BOT.

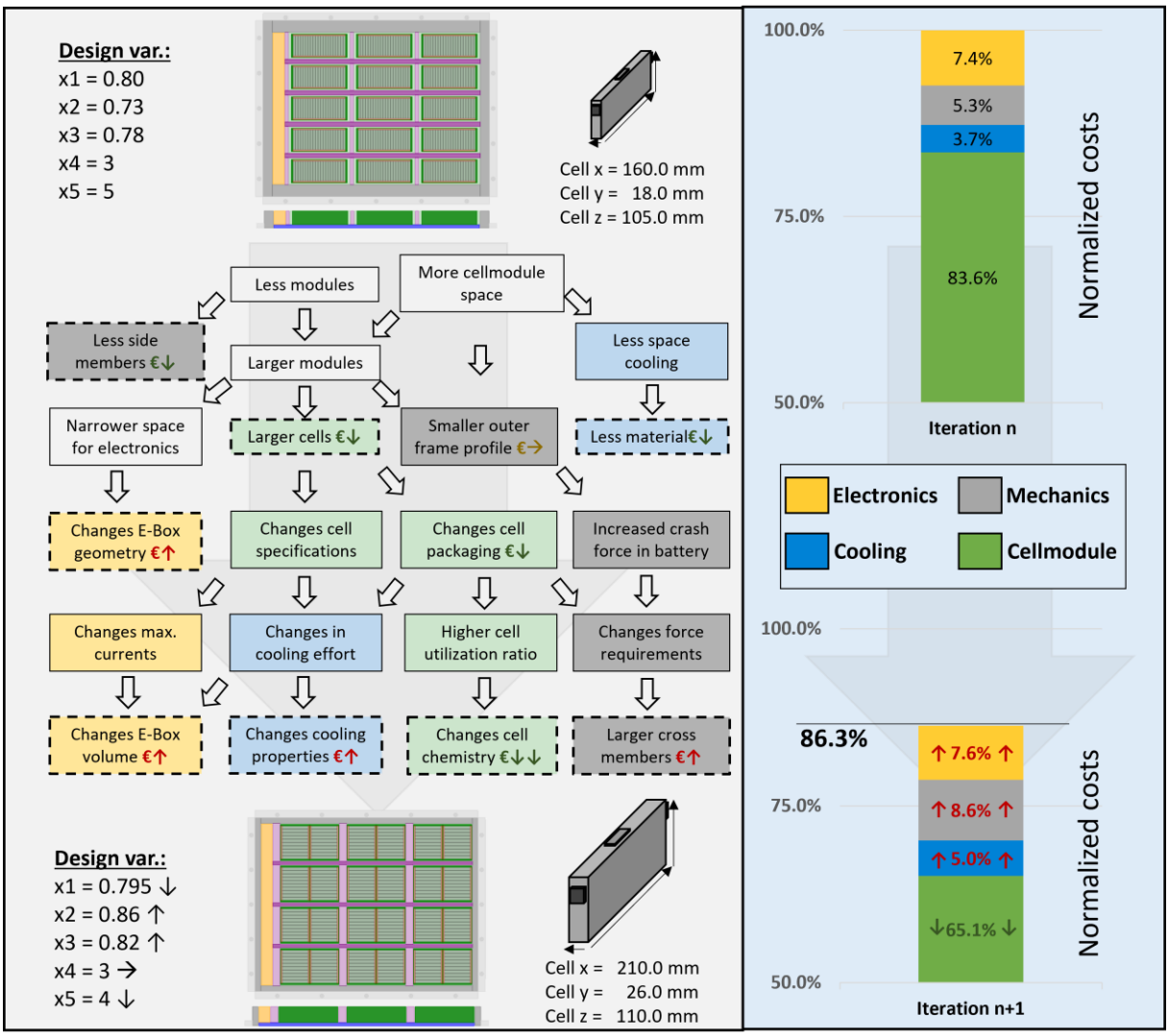

Figure 4.44: In-depth analysis of two exemplary results for inputparameters from Table 4.8.

The illustration above stresses the various dependencies of the change of installation space partitioning on all submodels. This underlines the advantageousness of coupled simulation models for designing battery systems. Furthermore, the insights into different cost changes enable weighing individual cost components against each other.

The cellmodule costs have by far the largest proportion in costs. However, the change in the cell costs in the figure above majorly arises from the change in cell chemistry. Within one cell chemistry, cost changes are much smaller and often result from the type of cell packaging resulting from the cellmodule geometry. Thus, only a small cell cost variance can be expected for a given energy requirement, resulting from the actual cell geometry or cellmodule packaging. This aspect will be further stressed in Chapter 6 by dividing cellmodule costs into cell level costs and packaging-related costs.

4.4.2 Cost sensitivity

In order to investigate the general cost sensitivity of the above-evaluated solutions, the assumed material-based packaging costs were varied.

Thereby, material-based costs for aluminum, steel, and copper, as well as their processing materials (extruded aluminum), were increased by 30%. Figure 4.45 depicts the relative costs compared to the costs evaluated in the upper part of Figure 4.44.

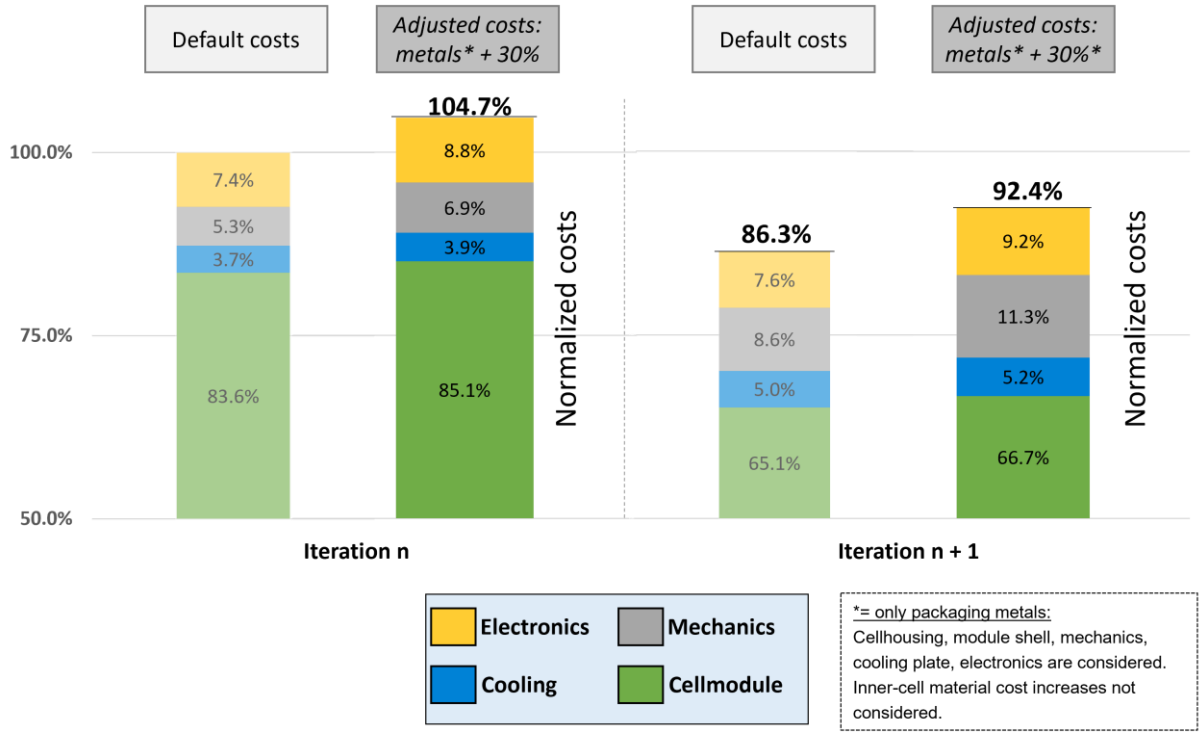

Figure 4.45: Cost sensitivity and comparison for increased metal costs. The graph illustrates the changing cost shares for varying metal cost assumptions. 100% corresponds to the default cost scenario.

Results show that the overall battery system cost increases by 4.7% and 6.1% relative to the outgoing 100% due to the metal material cost increase of 30%. A closer look at

the individual component groups shows that the mechanical costs have the largest relative increase in costs. This was to be expected as the mechanics cost modeling correlates directly with the metal material costs. On the other hand, cooling costs hardly increase as the main cost drivers are the plate production costs, the gap filler materials, and the overall cooling circuit (see Chapter 4.3.5). The rise of costs in the cellmodule is purely based on the cost increase for the cell housing shell, busbar, and terminal contacting material as well as the module packaging. Inner-cell material electrode stack costs were not increased due to the requirement cost-model approach described in Chapter 4.3.1.7. As a result of the high metal share, electronics costs also increase moderately.

4.4.3 Cost and weight validation

Literature findings are used to validate the resulting cost and weight distributions. Generally, very few analyses of total costs or weight shares at the component level for entire battery systems are described in the literature. One bigger compilation is given by Lutsey et al. in [315]. Herein, various literature reports are combined with data for Volkswagen, General Motors, and Tesla. The compilation states that 70% - 76% of battery system pack level costs can be attributed to cell costs. The cost range is consistent with the market analyses from Agarwal et al. performed in [316]. A report in BloombergNET evaluates volume-weighted average pack level costs of 138 $/kWh for BEVs in 2022 [317]. In [50], different summarized weight distributions for EVS varying between 60% and 80% for cells and 15% to 25% for mechanics can be found. This leaves the lowest weights for cooling and electronics. Further weight distributions can also be found in [190, 318–320]. In Figure 4.46, the cost and weight distributions derived by the battery system (Table 4.10) from the HV-BOT are shown graphically. The found distribution is consistent with the literature findings. It is important to note that cost and weight distributions will change depending not only on given model assumptions but also on the used-defined battery system requirements for energy, power, and overall installation space.

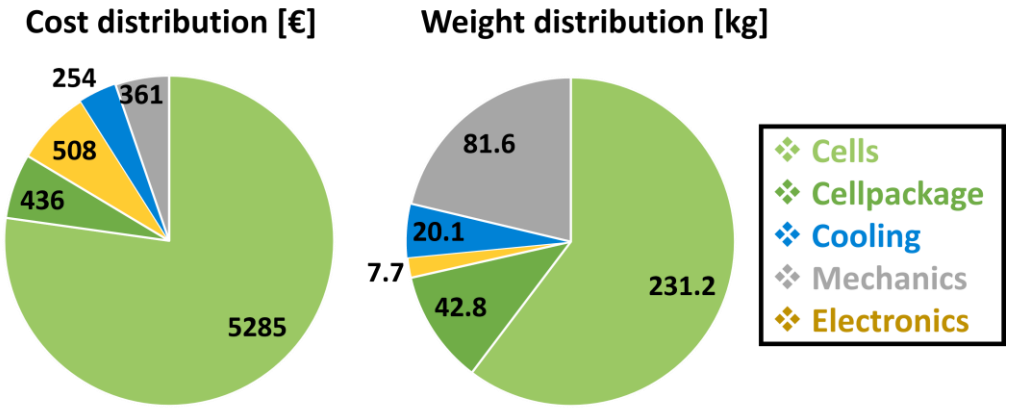

Figure 4.46: Resulting cost and weight distributions for the HV-BOT's optimized battery system design concept for inputparameters from Table 4.9.

4.5 Model comparison and concept validation with field data

Submodel derivations, result comparisons, and multiple plausibility checks have already been performed in the respective submodel-modeling Chapters 4.3.1 to 4.3.4 and Chapter 4.4. This chapter aims to illustrate the validity of the submodels' assumptions, their interaction, and the HV-BOT's basic installation space parametrization concept. Thus, the subsequent investigations examine the applicability of the HV-BOTs results to real-world battery systems. The inputparameters are set using researched data for the EV and its battery system. The space allocation is adjusted manually so that the resulting battery system corresponds closely to the actual system.

The system's reconstruction is based on the assumptions mentioned in the submodels' description and will, therefore, naturally differ from the actual system's construction. However, the resulting illustration of construction chains offers deep insights into battery system engineering.

4.5.1 Battery systems from the field

Two exemplary battery systems are reconstructed. First, a battery system with prismatic cells, and second, a battery system with pouch cells. Through literature research, data was collected to replicate the battery system. Missing data were assumed based on available illustrations and simplified derivations.

4.5.1.1 BMW i3 37.9 kWh

The battery system of the original first BMW i3 version was equipped with a 22 kWh battery system. An updated version in 2017 provided 33 kWh, and the latest update in 2019 brought 42.2 kWh into the system. The 2019 battery system for the BMW i3 has a usable energy of 37.9 kWh for about 250 km electric range. In Table 4.11, further HV-BOT-related inputparameters are defined. The data is based on [48], [321], [322], [323].

Inputparameter (user-defined)	**Value**
General	
System installation space x,y,z* *(assumed space without connection balcony)*	1540.0 x 843.0 x 173.0 mm³
System energy demand	37.9 kWh
System power demand*	75 kW
System charging time demand*	40 min
System voltage demand	400 V
System usable battery DOD	90%
Cellmodule	
Cell geometry	Prismatic: 173 x 45 x 123 mm³
Maximum number of cellstacks per module	2
Cooling	
Ambient temperature*	23.0 °C
Number of passes for cooling tube*	2
Design current profile*	Quick charging profile
Refrigeration circuit expansion stage*	Basic

Mechanics	
Crashenergy requirement *	5 kJ
Cellstack integration (only for prismatic cells)	Screwed cellstacks
Electronics	
Integration mode	3

* = assumed

Table 4.11: Exemplary BMW i3 42.2 kWh battery system user inputs for the HV-BOT.

Figure 4.47 shows the battery system design of the BMW i3 reconstructed by the HV-BOT. The top part of the figure shows the schematic battery system from the top view. The schematic side view is illustrated in the lower part of the figure. Generally, 12 cells are combined to form the eight cellmodules.

Construction chains are depicted below the top and side views of the battery system. The construction chains allow for analyzing the constructive setup of the battery system in great detail. The colored arrows at the top and side view of the battery systems mark the starting points of the construction chains. From there, the construction chains can be read from left to right. The individual used colors for the different parts can help to track the individual components within the schematic illustration of the battery system. Model-defined installation clearance is combined with unused space as tolerance space (Tol).

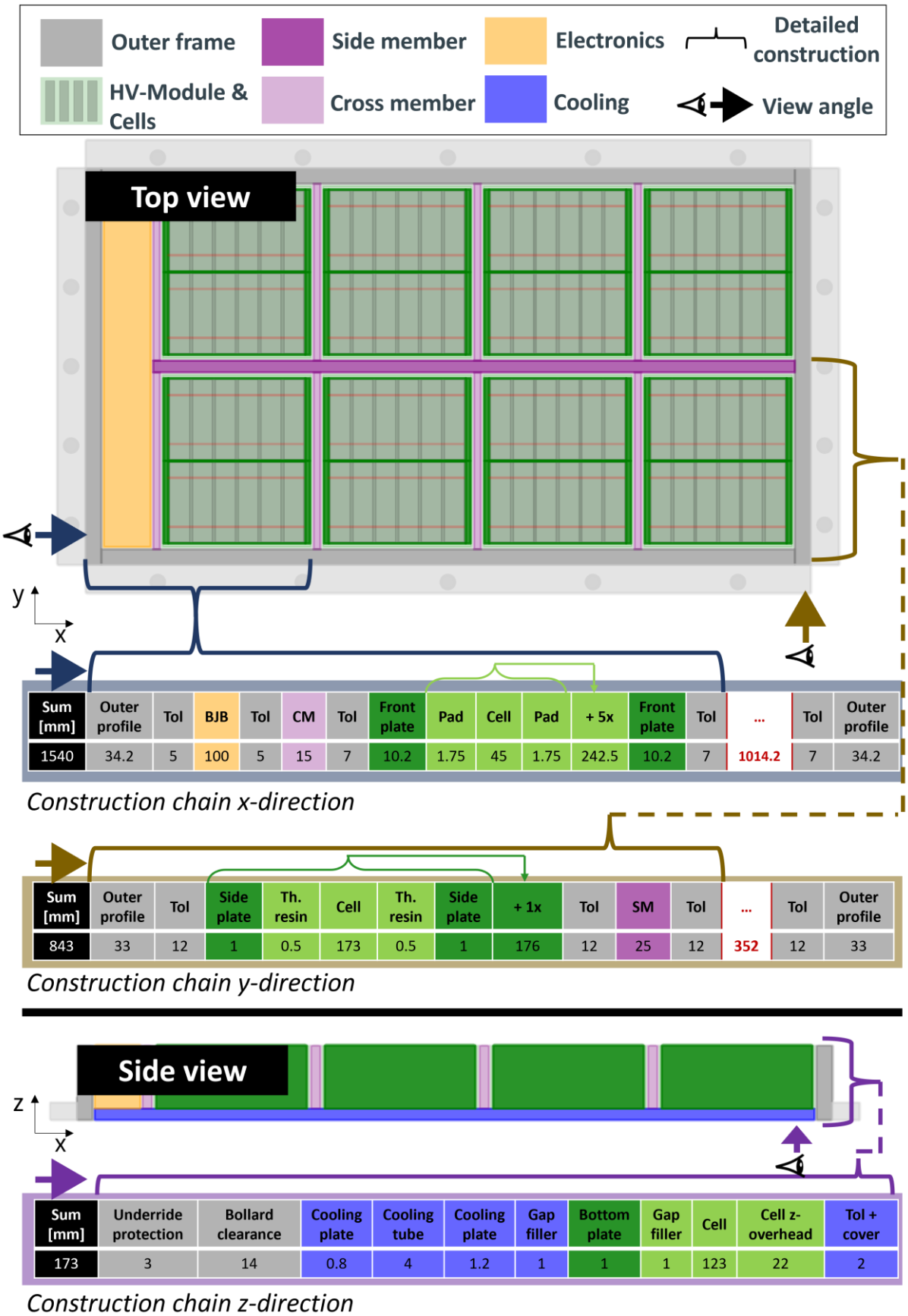

Figure 4.47: In-depth HV-BOT construction for BMW i3 battery system inputs.

The results validate the HV-BOT submodels and their interactive functionality in reconstructing the BMW i3's battery system concept. Furthermore, the feasible system underlines generally suitable assumptions in creating a feasible and realistic battery system with prismatic cells. A resulting 3D construction of the mechanical outer profile as well as the cellstack and cooling plate can be seen in Figure 4.48.

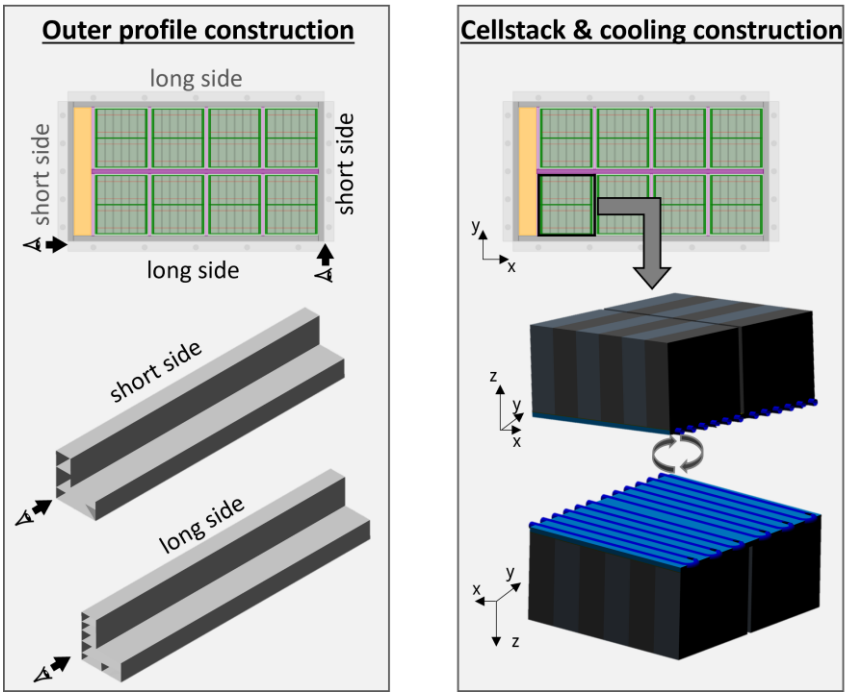

Figure 4.48: In-depth 3D view of optimized outer profile and cellstack cooling plate.

The corresponding weight distribution of the reconstructed battery system is illustrated in Figure 4.49. Thereby, the proportion of the cell's weight relative to the total battery system is roughly 70%. The actual weight distribution of the BMW i3 system is not publicly available in the literature for comparison.

No cross or side members are used in the original construction. Eliminating both would, therefore, further decrease the weight of the mechanics. As the i3 is a small vehicle with low weight, the necessary crash energy absorption of the battery system will generally be small. More vehicle data, especially regarding the rocker panel and position of the battery system in the overall vehicle topology, would be needed to set the exact crash energy requirement as input for the mechanics' submodel within the HV-BOT. Nevertheless, cross and side members are generally proven in battery system design to enhance the system's stiffness. Also, they are an essential component in modeling the mechanics and the fundamental concept of the design variables within the HV-BOT. HV-BOT modeled the cross members and the side member to be roughly 8 kg. The underride protection sheet accounts for roughly 12.5 kg. For larger and heavier vehicles, battery systems must also absorb higher crash forces and therefore need higher rigidity. An example of this is the BMW iX3 from 2020, which is also equipped with cross members in its battery systems [324].

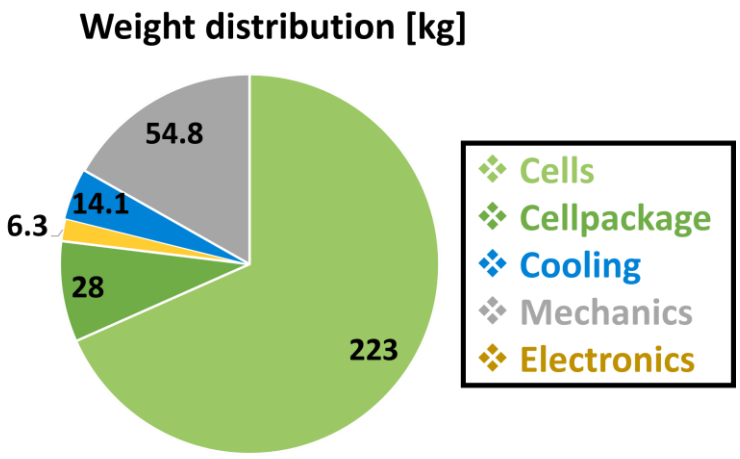

Figure 4.49: HV-BOT weight estimation and distribution for the BMW i3 37.9 kWh battery system.

4.5.1.2 Hyundai Kona Electric 39.2 kWh

The battery system of the Hyundai Kona electric with 39.2 kWh is from 2021. The battery system is developed for a sport utility vehicle type and serves about 300 km electric range. In Table 4.12, further relevant inputparameters are defined. As the vehicle is still new, most system specifications are not yet published in the literature. Therefore, most data result from internet specification sheet data, which can be found in [325], [326], and [327]. The larger Hyundai Kona battery system with 64 kWh can also be seen in [328]. The battery system design of the smaller variant is equal but does not use the front part for the battery system for batteries but for the engine. This can be seen in [329]. While the larger 64 kWh system is equipped with ten cellmodules, the smaller system comes with just six cellmodules. As the maximum system voltage is roughly 378 V, each of the six cellmodules must be connected in a 15s2p connection, leading to 90s2p for the entire system. In both system variants, in each case, two separate modules are combined to form one unified cellmodule

Inputparameter (user-defined)	Value
General	
System installation space x,y,z*	1260 x 1160 x 133 mm³
System energy demand	39.2 kWh
System power demand *	100 kW
System charging time demand*	50 min
System voltage demand	378 V
System usable battery DOD*	94%
Cellmodule	
Cell geometry*	Pouch: 280 x 100 x 14.3 mm³
Maximum number of cellstacks per module	2
Cooling	
Ambient temperature	23.0 °C
Number of passes for cooling tube*	2
Design current profile	Quick charging profile
Refrigeration circuit expansion stage	Basic
Mechanics	

Crashenergy requirement *	5 kJ
Cellstack integration (only for prismatic cells)	Not applicable due to cell format
Electronics	
Integration mode	3

* = assumed

Table 4.12: Exemplary Hyundai Kona electric 39.2 kWh battery system user inputs for the HV-BOT.

Figure 4.50 shows the battery system of the Hyundai Kona Electric 39 kWh reconstructed by the HV-Battery-Optimization-Tool. Equivalent to the analysis of the BMW i3 battery above, the top part of the figure shows the schematic battery system from the top view. The schematic side view is illustrated in the lower part of the figure. Thereby, 60 cells are combined to form the three cellmodules.

Construction chains are depicted below the top and side views of the battery system. The construction chains allow for analyzing the constructive setup of the battery system in great detail. The colored arrows at the top and side view of the battery systems mark the starting points of the construction chains. From there, the construction chains can be read from left to right. The individual used colors for the different parts can help to track the individual components within the schematic illustration of the battery system. Model-defined installation clearance is combined with unused space as tolerance space (Tol).

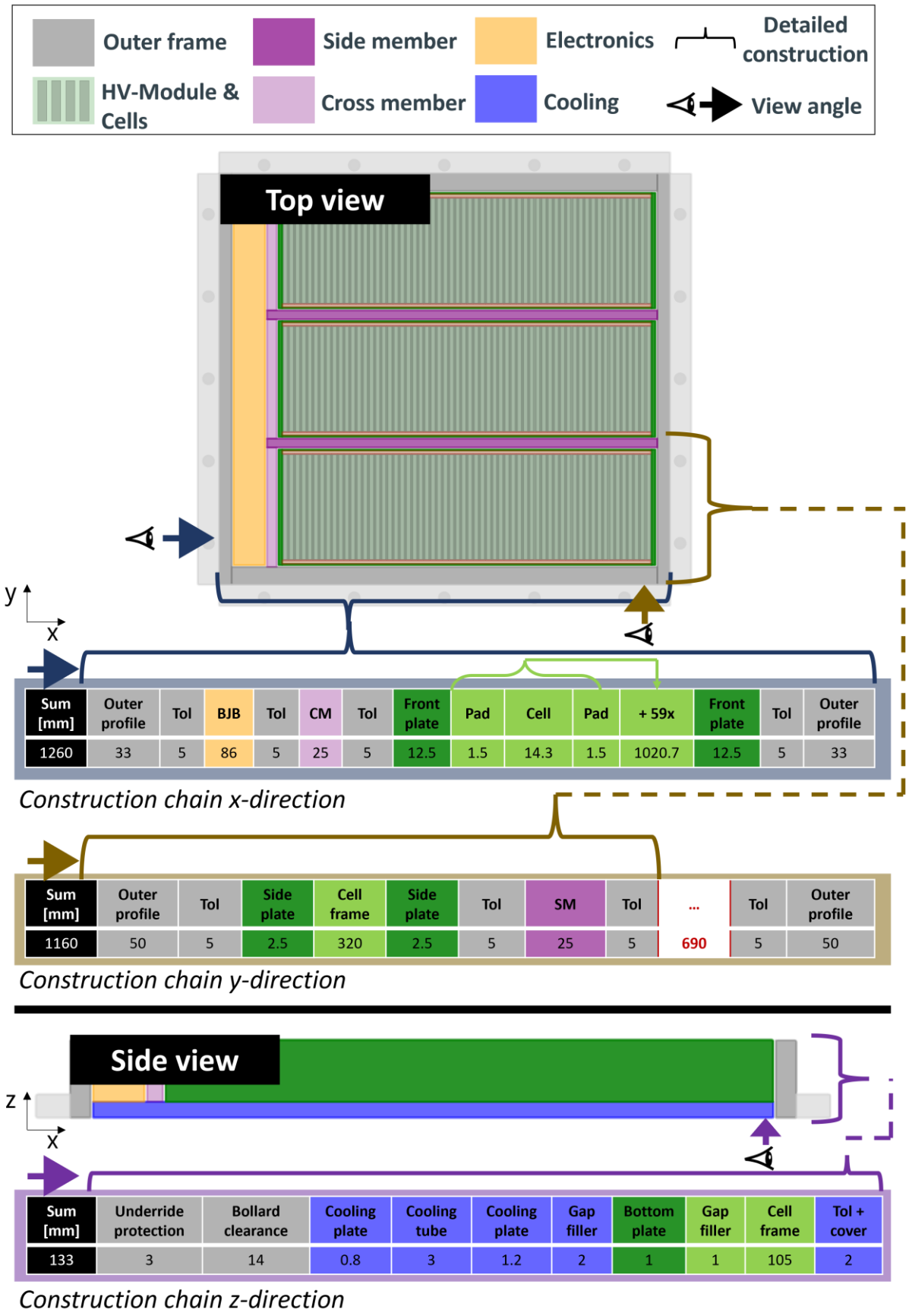

Sum [mm]	Outer profile	Tol	BJB	Tol	CM	Tol	Front plate	Pad	Cell	Pad	+ 59x	Front plate	Tol	Outer profile
1260	33	5	86	5	25	5	12.5	1.5	14.3	1.5	1020.7	12.5	5	33

Sum [mm]	Outer profile	Tol	Side plate	Cell frame	Side plate	Tol	SM	Tol	...	Tol	Outer profile
1160	50	5	2.5	320	2.5	5	25	5	690	5	50

Sum [mm]	Underride protection	Bollard clearance	Cooling plate	Cooling tube	Cooling plate	Gap filler	Bottom plate	Gap filler	Cell frame	Tol + cover
133	3	14	0.8	3	1.2	2	1	1	105	2

Figure 4.50: In-depth HV-BOT construction for Hyundai Kona 39.2 kWh battery system inputs.

Again, the results validate the HV-BOT submodels and their interactive functionality in reconstructing the Hyundai Kona's 39.2 kWh battery system concept. Furthermore, the feasible system underlines generally suitable assumptions in creating a feasible and realistic battery system with pouch cells. A resulting 3D construction of the mechanical outer profile as well as the cellstack and cooling plate can be seen in Figure 4.51.

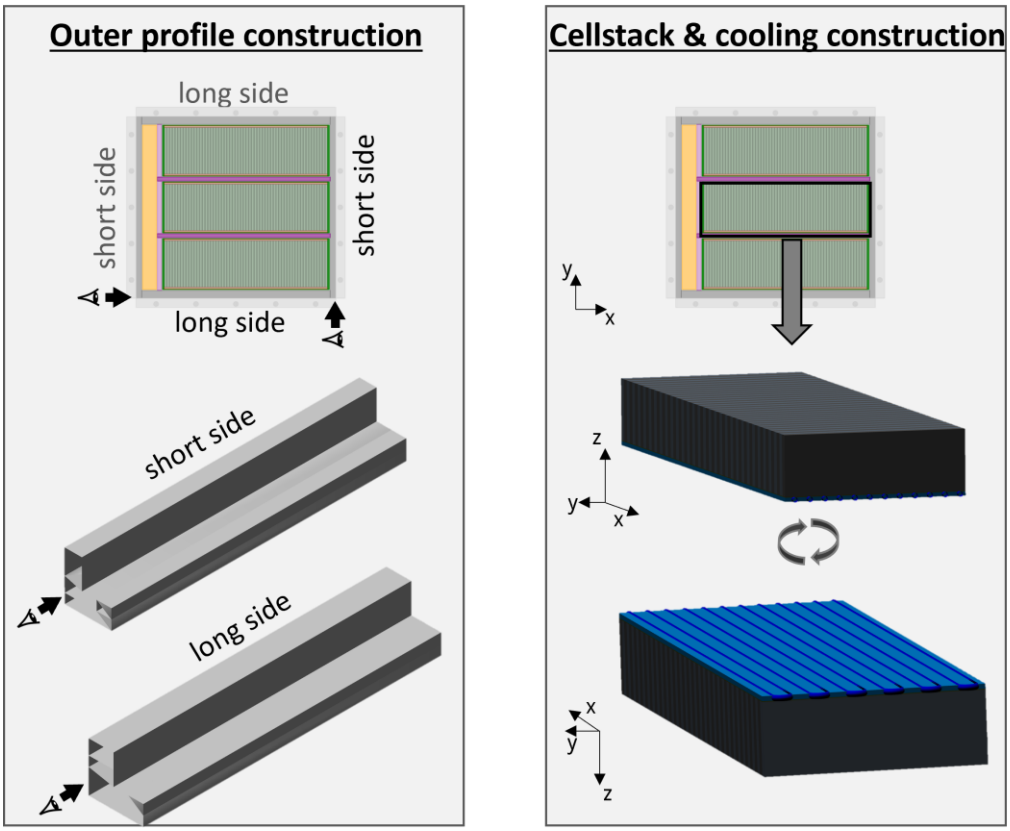

Figure 4.51: In-depth view of optimized outer profile and cellstack cooling plate.

The corresponding weight distribution of the reconstructed battery system is given in Figure 4.52. The proportion of cellpackging weight relative to the total battery system is roughly 15%. The high ratio of cellpackging weight underlines the extra weight needed for, e.g., the frames in a cellmodule construction with pouch cells. Also, the cooling shows higher costs, resulting from the thicker gap filler needed for the larger cellmodules (see derivation in Chapter 8.3).

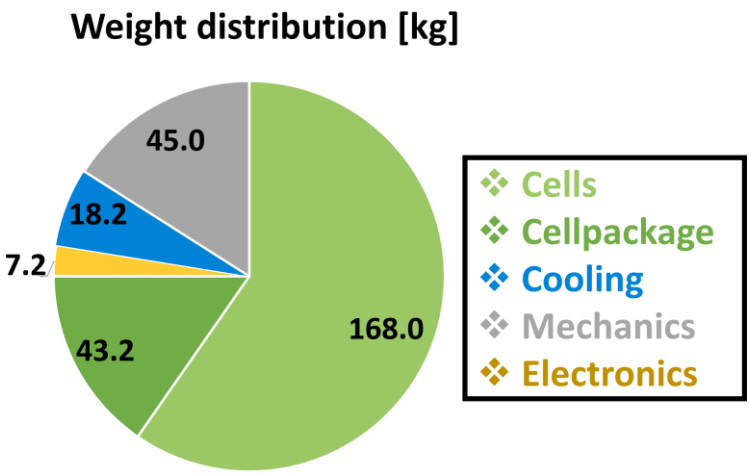

Figure 4.52: HV-BOT weight estimation and distribution for the Hyundai Kona 39.2 kWh battery system.

4.6 Limitations

The exemplary reconstruction of actual battery systems from the field emphasized the HV-BOT's functionality in analyzing different system designs. The construction chains stressed the detailed modeling and verified the usage of the HV-BOT to create digital battery system twins.

Beforehand, the multiphysically of the interfaces was demonstrated by comparing two different battery system designs with equal inputparameters in a broken-down in-depth investigation. The results suggest that the HV-BOT can model, design, and optimize battery system concepts with varying requirements. Special emphasis has been placed on illustrating the resulting interdependencies between the major battery system components of cellmodule, mechanics, cooling, and electronics. Furthermore, trade-off relationships between subcomponents were derived to demonstrate the importance of holistic simulation models for battery system design. The following restrictions and limitations, among others, apply to the usage and further tool development:

Due to the modular structure of the submodel-concept, further design relevant technical simulation models may be easily integrated into the submodel-concept, enabling, for example, the possibility to specifically evaluate a thermal propagation hazard level. Additionally, the existing submodels could be extended to increase the range of analysis possibilities. In this context, the submodel cellmodule could be expanded to include other cell chemistries, such as sodium ion or the cylindrical cell format (see the study in Chapter 6.7). For submodel cooling, direct refrigerant cooling could be addressed. In the submodel mechanics, further load cases, like the z-shock or the front crash, could also be evaluated to determine the optimized battery frame from an even more holistic perspective. The submodel electronics could benefit from switching from a 2D to a requirements-based 3D model.

Additionally, the following general adaptations could be especially beneficial:

- Cost models could be further detailed, and effort-dependent manufacturing costs could also be taken into account. This would allow weighing up battery designs in even greater detail.

- Recyclability is only minor addressed in the submodel-concept in observing the battery system’s weight estimation. New approaches could give each material a recycling factor, allowing recyclability optimization and general life cycle analyses.

- With the current submodel-concept, the connection of individual cells via the busbar is modeled. However, no electrical connections between individual stacks, modules, and the BJB are addressed. Therefore, no differences between stacking directions are given from an electrical point of view. This factor can influence the cellstacking direction in actual applications because long wiring is usually avoided. These can affect the total weight, costs as well as electromagnetic compatibility.

4.7 Conclusive summary

This chapter included modeling a framework to compile, analyze, and evaluate different battery system concepts, focusing on the functional chain of changes in space allocation for different major component groups. The battery system components' space allocation was fully parametrized using five interdependent design variables. Four different simulation models were abstracted to depict the battery system’s main component groups: cellmodule, cooling, mechanics, and electronics. The individual submodels were created for holistic design options. Special emphasis was given to making comprehensible assumptions that can be adapted to specific scenarios. For the cellmodule submodel, the reference look-up data sheets for the different cell formats and cell chemistries can be easily entered or changed within the tool. This enables future battery cell technologies to be easily integrated into the framework.

Interdependently coupling the submodels formed a novel approach to battery system design modeling. The concluding submodel-concept internally optimized the battery system based on the design variables for space allocation and user-defined EV requirements like energy, power, and voltage level. Different sets of requirements and real-world battery systems were evaluated, representing the diversity of battery system design for electric vehicles. The interaction of the submodels offers to analyze small design details (e.g., cooling tube height, the wall thickness of cross members, or size of busbars) as well as systemic variables (e.g., necessary water pump power, crashperformance on battery frame, cellstacking direction). This enables the creation of digital battery systems twin using the HV-BOT, which can be used in even higher integrated advanced full-vehicle models.

The results of this chapter indicate the great potential of coupled battery simulation models for future battery system design. In addition to pure feasibility observations of the individual components within battery systems, coupled model frameworks are also able to reveal neglected interdependencies between components and thus unleash the unseen potential in both cost and weight.

It is a significant challenge to precisely condition each model and its interdependencies individually to generate optimized statements reliably. In order to be able to make

adaptations within the models at later stages, a modular structure for the tool was chosen. The validation with real-world EVs and their corresponding battery systems showed overall promising results for the generic modeling approach and its assumptions.

5 Optimization strategy for coupled battery system design models

Parts of this chapter are published in journal articles [330] and [247] as part of this thesis. The work in [330] is elaborated with equal contribution of this thesis author and Johannes Christofer Hahn. This chapter contains minor modifications and extensions with respect to the original publication. The use of the article content, including illustrations, is permitted with the consent of Elsevier.

In the development of battery systems for electric vehicles, numerous components from different physical subareas must be harmonized with each other. Automotive engineers already use extensive simulation models to optimize individual components satisfying increasing demands of EV range and power. However, at the time of initial publication, no comparable work concerning strategies for the combined optimization of battery systems was found in the literature. Therefore, this chapter presents an optimization strategy for the holistic design of battery systems, which utilizes coupled simulation models of the battery system's technical subcomponents representing cellmodules, mechanics, cooling, and electronics. Given user-specified battery system requirements, methods of Gaussian process regression and Classification are combined to determine the optimal battery system design in terms of costs and feasibility. An inherited mixed-integer problem is addressed by using discretization of the solution space and refinement strategies in likely optimal regions. Moreover, the information gained per iteration is maximized by means of predictive calculations and parallelization methods. Testing the presented optimization strategy in different scenarios gives promising results, showcasing its robustness towards different technical requirements for battery systems. Also, exemplary analyses regarding the impact of the total installation space on costs and feasibility are conducted.

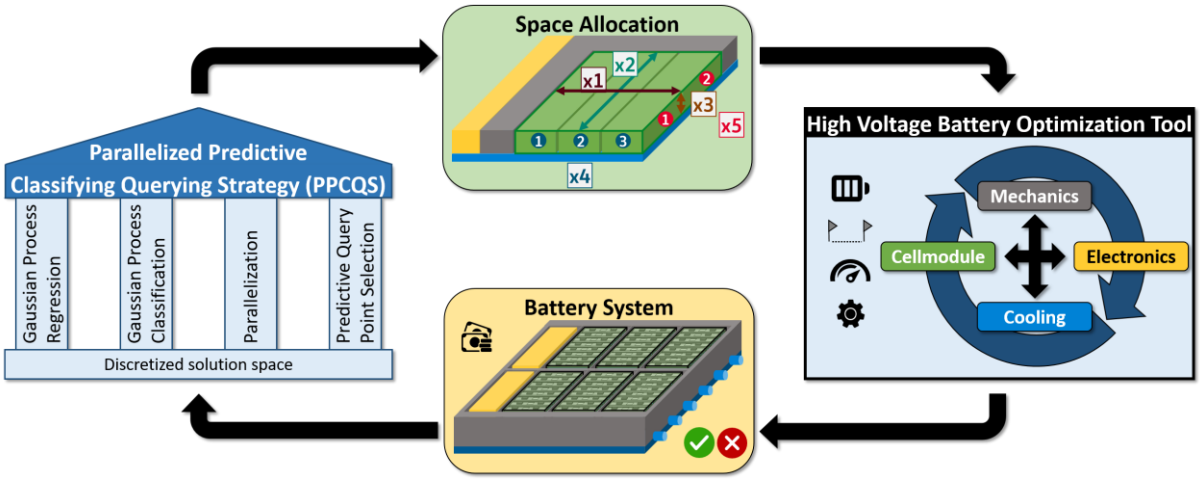

Figure 5.1: Graphical abstract of the optimization presented in this chapter.

5.1 Introduction and scientific integration

Electric vehicles are a widely accepted means on the path to future mobility. As an essential part of bringing CO_2-emissions to lower levels, EVs achieve already recurring record sales [28, 164–166]. The lithium-ion battery plays a major role within the vehicle's battery system [284]. In EVs, multiple LIBs are interconnected in series and

parallel, forming the battery module. Multiple battery modules are used to build the battery system to serve the EV's engine with energy and power [48, 249]. The modular structure of the cell, the module, and the system brings advantages in operation, maintenance, and repair while also making the battery system easier to scale, which is widely used by EV car manufacturers [190, 191]. Yet, EVs are still rather expensive, especially due to the cost-intensive battery cells [31, 167]. Multiple studies are performed in the literature stressing the cost distributions for different component groups within battery systems [315]. Although cell costs make up the majority of costs in battery systems, cost savings lie in each component and, in particular, in the optimized alignment of the system design [316, 331]. Therefore to develop a battery system, major challenges from various fields of technology must be reconciled with each other. Individual components are already widely addressed in the literature. Multiple simulation models, procedures, studies, and reviews for battery cells and modules [22, 34, 161, 177, 184, 194, 203, 207, 332], thermal management [51, 171, 199–202, 216, 333–339], mechanical design [21, 123, 124, 288, 340–342], or different electrical behavior [343–345] are extensively discussed. While standalone models represent specific effects in great detail and accuracy, external factors and interdependencies between different components and their physics must also be considered for the design of battery systems. Due to the complexity and individuality of technical simulation models, holistic optimization frameworks for designing battery systems that combine the individual components are rarely addressed in the literature. One of the few existing frameworks has been proposed by Li et al. [255], where various components are considered for an advanced battery pack design. A series of optimizations are used to determine one optimized system in their study. Yet, no restrictions regarding the generic applicability of the optimization for different battery system models or general changes to the base model are discussed. However, in the rapidly changing world of battery system technology [346–350], this aspect is a major prerequisite for optimization frameworks as individual simulation models may change due to technical innovations resulting in high demands on the versatility and robustness of the optimization. Thus, a generic optimization framework needs to be developed that can be used for coupled and individually interchangeable battery component simulations.

In this context, machine learning algorithms may play a promising role. Different supervised [351–354], unsupervised [355], and reinforcement learning [356] strategies have already been addressed in the fields of individual battery system components. Yu [357] and Li et al. [358] propose prognostic state-of-health frameworks using Gaussian process regression. Battery thermal systems with optimized cooling are discussed by Li et al. [359], also utilizing GPR. Generally, Gaussian process regression, including various search strategies, is widely used to solve black-box optimization [360, 361], proving its flexibility and adaptability to diverse optimization problems. Different approaches in literature try to preserve the critical balance between exploration and exploitation of the design space [362]. However, proposed battery-related optimization methods are often either quite complex to control or not generally applicable to other optimization problems.

This chapter aims to bridge the aforementioned research gap of generic optimization frameworks for coupled battery system design simulations. Thereby, a machine learning methodology is proposed for efficiently optimizing parametrized battery systems utilizing coupled simulation models for holistic evaluations in terms of costs and feasibility. This chapter combines established methods of Gaussian process regression and classification and uses coupling of information about both the feasibility

and cost of individual components to identify and afterward specify globally optimal solution spaces in a five-dimensional mixed-integer solution space. Great emphasis was placed on the generality of the optimization strategy in order to gain generic applicability to various similar optimization problems. Examples are the variable number of simulation models, the discretization level of the optimization variables, the available computing speed, or the number of the CPU's logical cores.

The proposed optimization strategy comprises a combination of three main features forming its novelty:

- The optimization strategy enables finding the global cost optimum with respect to a mandatory condition, i.e., the feasibility of the solution. This is achieved by using both Gaussian process regression and Gaussian process classification. Consequently, the total solution space is split into three fundamental regions: feasible, infeasible, and uncertain.

- The optimization strategy is suitable for mixed-integer problems. A uniform grid is used to discretize the solution set and refine areas where the solutions are of higher interest, i.e., where the global optimal battery system is most likely to be located.

- The optimization strategy utilizes parallelization methods to maximize the total information gain in every iteration. Multiple query points are chosen sequentially to maximize the information gain for every query point using predictive means and standard deviations.

Regarding the predevelopment of battery systems for electric vehicles, the presented optimization strategy offers two novel application possibilities:

- Given a set of user-defined technical battery system parameters like total energy, or power demand, the optimization strategy allows finding the optimal battery system design using the parametrization from the high-voltage battery optimization tool described in Chapter 4.

- Parameter studies analyzing the impact of different technical requirements on the cost and feasibility of the optimal battery system are conducted.

This chapter is structured as follows: In Chapter 5.2, the optimization problem within HV-BOT is derived and defined. Chapter 5.3 introduces the fundamentals of the used methods of Gaussian process regression and classification. In Chapter 5.4, the optimization strategy is explained extensively. Chapter 5.5 presents the results of conducted performance tests and analyses as well as a parameter study. Conclusions are drawn in Chapter 5.6.

5.2 Methods of the optimization problem

In this chapter, the basics of the optimization problem are described. Thereby, the optimization problem within the HV-BOT is first motivated. From this, the optimization problem is derived and defined.

5.2.1 High-voltage battery optimization tool as black-box

In Chapters 4.2 and 4.3, the methodology, functionality, physical interactions, and internal optimization of the submodel-concept of the HV-BOT were derived, explained, and illustrated in detail. In addition, various studies were conducted for user-specified design variables to illustrate the optimization in the submodel-concept and to illustrate the chains of effects of various components within HV battery systems.

While the space allocation of the main components is already known when rebuilding battery system concepts from real-world EVs, this allocation is unknown for new projects. Thereby, an optimal configuration of design variables must be found that allows, for example, the lowest cost given the battery requirements specified by the user. While submodel optimization is a search for a local optimum of the individual component, searching for optimal design variables and corresponding space allocation for each component is a global optimization. For the further derivation of the global optimization in this chapter, the submodel-concept is assumed to be a black-box. Reasons for this are given in Chapter 5.4. The black-box model structure is depicted in Figure 5.2. The technical parameters, such as total space, power, or energy content, are set as the fixed inputs for the black-box. The second input is the varying set of design variables. As the black-box output, only the costs and the feasibility of the considered design variable configuration will be evaluated.

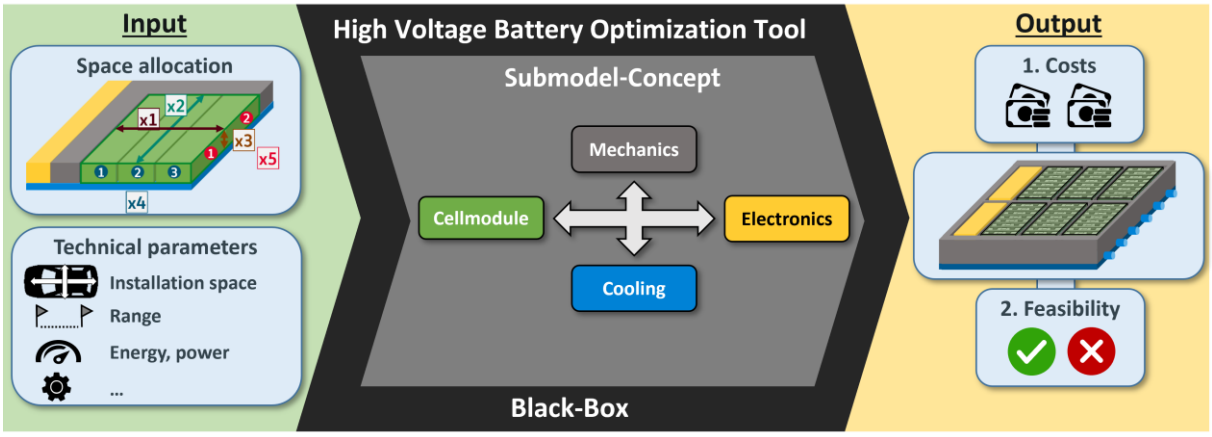

Figure 5.2: Schematic black-box HV-BOT model assumed for the optimization framework.

5.2.2 Definition and analysis of the optimization problem

The HV-BOT evaluates a battery system design (= space allocation $(x_1, \dots, x_5)$) for given technical parameters and returns a concrete battery system with optimal costs and feasibility for that supplied space allocation. Consequently, the optimization of battery systems can be reduced to the optimization of the space allocation. In order to search for a battery system with minimal costs and secured feasibility, the optimization problem is defined as:

$$\text{minimize } c(\mathbf{x}) = c_1(\mathbf{x}) + c_2(\mathbf{x}) + c_3(\mathbf{x}) + c_4(\mathbf{x}) \tag{5.1}$$

$$\begin{aligned} &\text{subject to } \mathcal{F}(\mathbf{x}) = 1 \\ &\mathbf{x} = (x_1, \dots, x_5) \quad \text{with} \quad x_1, x_2, x_3 \in]0{,}1[;\ x_4, x_5 \in \mathbb{N}\backslash\{0\}. \end{aligned} \tag{5.2}$$

With $c_i(\mathbf{x})$ being the cost estimation of submodels i and $\mathcal{F}(\mathbf{x})$ the combined feasibility for all submodels (see Chapter 4).

Trying to solve this optimization problem leads to a number of challenges. An obvious method to find the global optimum is to check every possible solution manually. However, if the actual possible solution space is large and the time needed for evaluations is long, this procedure may lead to unacceptable durations, as shown in Table 5.1.

Domain $x_1, x_2, x_3 \in$	**Domain** $x_4, x_5 \in$	**Sample distance for** x_1, x_2, x_3	**Sample distance for** x_4, x_5	**Total number of possible solutions**	**Assumed time per evaluation of objective function**	**Total examination time**
[0.7,0.9]	[2,6]	0.1	2	3·3·3·3·3 = 243	1 minute	243 minutes
[0.6,0.9]	[2,6]	0.1	2	4·4·4·3·3 = 576	2 minutes	19.2 hours
[0.6,0.9]	[2,6]	0.05	1	7·7·7·5·5 = 8575	4 minutes	23.8 days
[0.5,0.95]	[1,10]	0.005	1	91·91·91·10·10 = 75357100	10 minutes	1433.7 years

Table 5.1: Comparison of total examination times for varying scenarios motivating the need for an optimization algorithm.

Given the definition of the design variables, the HV-BOT operates based on the class of mixed-integer problems (MIPs). MIPs are missing continuity which eliminates the usage of numerous optimization strategies using the objective functions' derivation or gradient as the source of information [363–365]. Due to the strong nonlinearity in the submodels, a non-convex optimization problem can be assumed. This eliminates the possibility of deterministic algorithms and optimization approaches. Alternative methods, such as genetic and evolutionary algorithms, like the Firefly algorithm (FA) heuristic, are able to generate solutions that satisfy the integer constraints. Yet, these solutions are usually far from optimal and often lead to locally optimized results. Therefore, further investigations using, for example, Monte-Carlo-Simulation approaches are often necessary [366, 367]. However, heuristics often need specific settings in their degrees of freedom in order to perform satisfactorily. Since the implementation and, thus, response function of each submodel may change in the future to incorporate new research results or improvements of the used simulations, choosing universally optimal settings may not be possible. Consequently, the development of the optimization strategy aims to achieve robustness that allows the HV-BOT to cope with arbitrary submodel implementations and user-defined technical parameters, always finding solutions close to the global optimum.

To further stress the problem's complexity, 1400 sets of design variables were evaluated, given an exemplary set of technical parameters. The results returned by the submodels are illustrated as a flowchart in Figure 5.3. The sets of design variables were carefully chosen using equidistant sampling. Sensitivity analyses were performed based on these sample results to conceive the submodels' behavior. The top part of

Figure 5.3 shows the flow of the 1400 sets along their inputs and outputs. Controllers within the graph were used to constrict certain input variables. In both of the bottom graphs, $x_1$is the free variable while x_3, x_4 and x_5 are set exemplary fix at $x_3 = 0.75$; $x_4 = 3$; $x_5 = 5$ for the following analysis. The difference between the bottom left (Example 1) and right (Example 2) graphic is illustrated by the fixed values for the variable x_2. For the left graph, x_2 is fixed at $x_2 = 0.81$, and for the right graph, $x_2 = 0.87$. This leads to only five of 1400 samples being left to observe. It can then be seen that every set of variables for x_1 ($x_1 = 0.65, \dots, 0.81$) follows a similar output-path. While the cost shares still vary for both graphs, the actual feasibility is either constant at 1, meaning feasible, or 0, meaning not feasible.

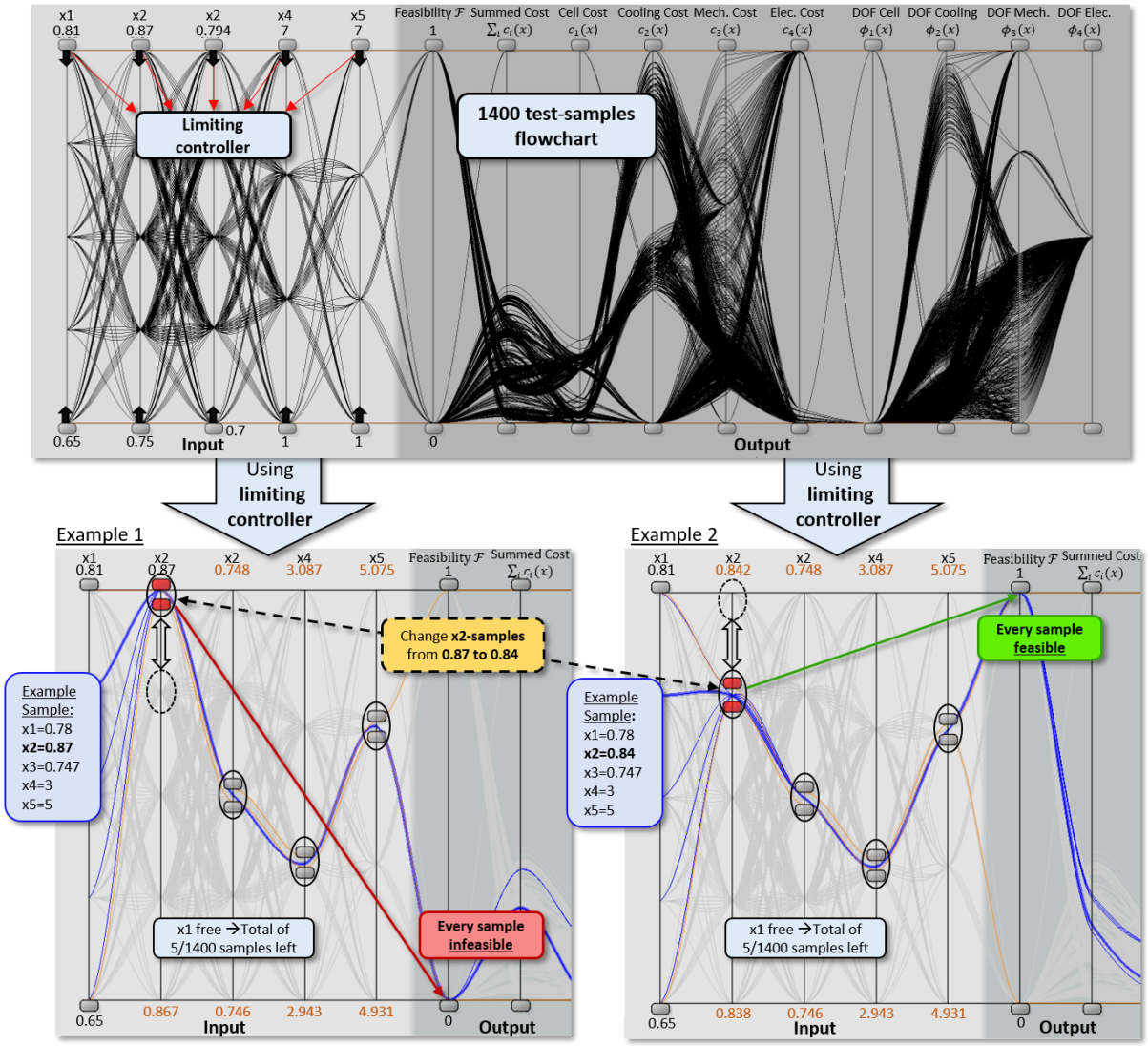

Figure 5.3: Effects of parameter changes on the feasibility. The upper graph shows a flowchart of 1400 evaluated battery system designs. A light grey background indicates the design variables. Results of the evaluations using the HV-BOT are depicted in the dark grey area. The lower two extracts each depict five filtered samples. For both graphs x_1 is free and x_3, x_4 and x_5 are constant. On the left, x_2 is fixed at 0.87, whereas on the right x_2 is fixed at 0.84.

It can be summarized that although highly non-linear and non-convex submodels are coupled with each other, correlations can be observed, at least for small design

variable changes. It may therefore be possible to define feasible solution regions in which it is promising to search for the global optimum, while other regions may be largely ignored due to their infeasibility. As the distribution of feasible regions and the total costs of a set of design variables can differ drastically depending on the model's technical parameters, the optimization strategy has to find ways to identify the general proportion of feasible and infeasible regions.

5.3 Machine learning methods for battery system optimization

In Chapter 5.2.1, the HV-BOT was redescribed as black-box structure. Inputs are the technical parameters and varying space allocation. Outputs are the costs and feasibility of the evaluated battery system designs. In Section 5.2.2, the optimization problem was defined, which reduces the optimization of battery systems to the optimization of the space allocation. Consequently, the optimization problem described in Eqs. (5.1) and (5.2) consists of a regression problem (the costs) and a classification problem (the feasibility). In order to address both problems, the optimization methodology utilizes both Gaussian process regression and Gaussian process classification (GPC) methods. Based on a comparison of different packages for modeling Gaussian processes presented in [368], the classes *GaussianProcessRegressor* and *GaussianProcessClassifier* of the scikit-learn package [369] are selected for the implementation of the optimization algorithm. The scikit-learn package provides easy-to-use functionalities and mostly outperforms other packages in modeling quality and speed. Fundamentals about Gaussian process regression and classification and their transfer to the used scikit-learn package functions are presented in the following. Detailed derivations can be found in [370].

5.3.1 Gaussian process regression

A Gaussian process is a method to model an unknown function f, that can only be evaluated pointwise and can be understood as a distribution over functions. For this chapter, only the noise-free description of Gaussian processes is considered, meaning that the observation y for an input $\mathbf{x}$ and the corresponding function evaluation $f(\mathbf{x})$ are equal: $y = f(\mathbf{x})$.

Like other modeling methods, a GP allows interpolating known training points $\mathcal{D} = (\boldsymbol{X}, \mathbf{y}) = \{(\mathbf{x}_j, y_j) | j = 1, \dots, n\}$ and predicting values of unknown test points $\boldsymbol{X}_*$. However, a key advantage is that it also provides a statement about the certainty of a prediction by placing a Gaussian distribution over the output value y of a test point $\mathbf{x}$. This distribution is entirely described by a mean (the prediction) and a variance. Analog, a Gaussian process is fully specified by a mean function $m(\mathbf{x})$ and a covariance function $k(\mathbf{x}, \mathbf{x}')$, which are defined as:

$$m(\mathbf{x}) = \mathbb{E}[f(\mathbf{x})], \tag{5.3}$$

$$k(\mathbf{x}, \mathbf{x}') = \mathbb{E}[(f(\mathbf{x}) - m(\mathbf{x}))(f(\mathbf{x}') - m(\mathbf{x}'))\,]. \tag{5.4}$$

Together, Eqs. (5.3) and (5.4) specify a prior distribution over functions, which incorporates prior knowledge or assumptions about the modeled function f. For

simplicity, the mean function is assumed to be zero. However, within the HV-BOT, the modeled cost function takes values roughly in the range of [3000, 20000]. Using the scikit-learn package, this can be taken into account by setting the *normalize_y* parameter of the *GaussianProcessRegressor* class to *True*, which normalizes the training data by removing its mean and scaling to unit variance. The covariance $k(\mathbf{x}, \mathbf{x}')$ is given by a kernel function, which determines the strength of dependency between the output values $f(\mathbf{x})$ and $f(\mathbf{x}')$ of two points $\mathbf{x}$ and $\mathbf{x}'$. The scikit-learn package provides a broad set of different kernel functions, which can also be combined by addition or multiplication. Further information on different kernels can be found in [145, 369–371]. This framework uses a constant kernel multiplied with the radial basis function (RBF), also known as the squared exponential kernel. The kernel is defined as:

$$k(\mathbf{x}, \mathbf{x}') = c \cdot \exp\left(-\frac{\|\mathbf{x} - \mathbf{x}'\|^2}{2l^2}\right). \tag{5.5}$$

where $\|\cdot\|$ denotes the Euclidean distance. The free parameters $c \in \mathbb{R}^+$ (constant) and $l \in \mathbb{R}^+$ (length-scale) are called hyperparameters $\theta = (c, l)$. These determine how the GP interpolates available training data.

Calling the *fit* function of the *GaussianProcessRegressor* class, which expects the training data $\mathcal{D}$ with length *n* as a parameter, triggers the optimization of the hyperparameters. This is done by maximizing the log marginal likelihood with respect to the hyperparameters θ. The log marginal likelihood is defined as:

$$\log p(\mathbf{y}|\boldsymbol{X}, \theta) = -\frac{1}{2}\mathbf{y}^{\mathrm{T}} K(\boldsymbol{X}, \boldsymbol{X})^{-1}\mathbf{y} - \frac{1}{2}\log|K(\boldsymbol{X}, \boldsymbol{X})| - \frac{n}{2}\log 2\pi. \tag{5.6}$$

$K(\boldsymbol{X}, \boldsymbol{X})$ is the matrix of covariances calculated by evaluating the kernel function $k(\mathbf{x}, \mathbf{x}')$ at all pairs of training points. As there may be multiple local optima, an object of the *GaussianProcessRegressor* class is initialized with an additional parameter *n_restarts_optimizer*, which states how many optimization reruns are carried out starting from different initial hyperparameters that are distributed log-uniform in the space of allowed hyperparameters.

Once the kernel function is fitted to the training data $\mathcal{D} = (\boldsymbol{X}, \mathbf{y})$, the predicted Gaussian distributions of outputs $\mathbf{f}_*$ for a set of test points $\boldsymbol{X}_*$ are given by:

$\mathbf{f}_*|\boldsymbol{X}_*, \mathbf{y}, \boldsymbol{X} \sim \mathcal{N}\left(\bar{\mathbf{f}}_*,\ \mathrm{cov}(\mathbf{f}_*)\right)$, where

$$\bar{\mathbf{f}}_* \coloneqq \mathbb{E}[\mathbf{f}_*|\boldsymbol{X}, \mathbf{y}, \boldsymbol{X}_*] = K(\boldsymbol{X}_*, \boldsymbol{X})K(\boldsymbol{X}, \boldsymbol{X})^{-1}\mathbf{y}, \tag{5.7}$$

$$\mathrm{cov}(\mathbf{f}_*) = K(\boldsymbol{X}_*, \boldsymbol{X}_*) - K(\boldsymbol{X}_*, \boldsymbol{X})K(\boldsymbol{X}, \boldsymbol{X})^{-1}K(\boldsymbol{X}, \boldsymbol{X}_*). \tag{5.8}$$

$\mathcal{N}(\boldsymbol{\mu}, \Sigma)$ denotes a Gaussian distribution with mean vector $\boldsymbol{\mu}$ and covariance matrix Σ. Eqs. (5.7) and (5.8) are derived by conditioning the prior distribution in Eqs. (5.3) and (5.4) on the training data $\mathcal{D}$. Further details can be found in [370]. The matrices $K(\boldsymbol{X}, \boldsymbol{X}_*)$, $K(\boldsymbol{X}_*, \boldsymbol{X})$ and $K(\boldsymbol{X}_*, \boldsymbol{X}_*)$ are determined equivalently to $K(\boldsymbol{X}, \boldsymbol{X})$. Using the scikit-learn package, the predictive mean values and covariances of a set of test points in Eqs. (5.7) and (5.8) can be calculated by the function *predict* of the

GaussianProcessRegressor class. As an alternative to the vector of covariances, it can also return the vector of standard deviations. This is set by the two inputparameters *return_cov* and *return_std* of the function call.

5.3.2 Gaussian process classification

Generally, Gaussian process classification is capable of performing multi-class classification. However, for the present purposes, binary classification is sufficient, as only a distinction between the feasibility and infeasibility of a battery system is needed. Let $y = 1$ denote feasibility and $y = 0$ infeasibility (see Chapter 5.2). The basic idea is to fit a latent function $f(\mathbf{x}) \in \mathbb{R}$ to the training data, which is then mapped to the probability domain $[0, 1]$ using a sigmoid-function $\sigma(z)$, so that a probabilistic prediction about the classification of a point $\mathbf{x}$ is obtained. Consequently, the values of $f(\mathbf{x})$ are not observed and not of any relevance. The only essential requirement on f is that the values of $\sigma\big(f(\mathbf{x})\big) \in [0, 1]$ lead to the correct classification of $\mathbf{x}$. The probability of feasibility for a given test point $\mathbf{x}$ is then described by:

$$\pi(\mathbf{x}) \coloneqq p(y = 1|\mathbf{x}) = \sigma\big(f(\mathbf{x})\big) \tag{5.9}$$

with $\sigma(z)$ mapping from $\mathbb{R}$ to $[0, 1]$. As only binary classification is considered, the probability of the other class (infeasibility) is given by $p(y = 0|\mathbf{x}) = 1 - p(y = 1|\mathbf{x})$. The scikit-learn package uses the logistic function $\lambda(z)$ as sigmoid-function:

$$\sigma(z) = \lambda(z) = \frac{1}{1 + \exp(-z)}. \tag{5.10}$$

Like in GPR, the latent function $f(\mathbf{x})$ is modeled by a Gaussian process with zero mean and a covariance specified by a kernel function. The hyperparameters of the kernel function are tuned by optimizing the log marginal likelihood in Eq. (5.6) analog to regression.

The prediction of the class probability of a test point $\mathbf{x}_*$ conditional to the training points $\mathcal{D} = (\boldsymbol{X}, \mathbf{y})$ is then computed in two steps:

The distribution of the latent variable is determined by:

$$p(f_*|\boldsymbol{X}, \mathbf{y}, \mathbf{x}_*) = \int p(f_*|\boldsymbol{X}, \mathbf{x}_*, \mathrm{f}) p(f|\boldsymbol{X}, \mathbf{y}) d\mathrm{f}. \tag{5.11}$$

The probabilistic prediction is derived by:

$$\bar{\pi}_* \coloneqq p(y_* = +1|\boldsymbol{X}, \mathbf{y}, \mathbf{x}_*) = \int \sigma(f_*) p(f_*|\boldsymbol{X}, \mathbf{y}, \mathbf{x}_*) d\mathrm{f}_*. \tag{5.12}$$

As the posterior $p(f|\boldsymbol{X}, \mathbf{y})$ is non-Gaussian for classification, the integral in Eq. (5.11) is not analytically tractable. Different approximations for this likelihood have been presented and evaluated [370, 372]. The scikit-learn package implements the Laplace Approximation. A short overview of the calculation of this approximation can be found in the appendix in Chapter 8.7.

Using the scikit-learn package, the probabilistic prediction in Eq. (5.12) can be calculated by calling the function *predict_proba* of the *GaussianProcessClassifier* class, which expects a set of test points as a parameter. The predicted classification is determined based on the predicted probabilities by choosing the class (feasible or infeasible) with the higher probability. Alternatively, the predictive classification can be computed directly by using the function *predict*. The essential functions of the scikit-learn package with their inputs, outputs, and corresponding equations are summarized in Table 5.2.

Scikit-learn function	Input	Output	Equation
*GaussianProcessRegressor**	kernel, *n_restarts_optimizer*, *normalize_y*	initialized prior GP (object)	(5.3), (5.4)
*GaussianProcessClassifier**	kernel, *n_restarts_optimizer*	initialized prior GP (object)	(5.3), (5.4)
fit	training data $\mathcal{D}$	-	(5.6)
predict (for GPR)	test data $\boldsymbol{X}_*$, *return_std*, *return_cov*	predicted means and either standard deviations or covariances	(5.7), (5.8)
predict_proba	test data $\boldsymbol{X}_*$	predicted class probabilities	(5.12)
predict (for GPC)	test data $\boldsymbol{X}_*$	predicted classification	decision based on the result of (5.12)
*ConstantKernel**	*constant_value*, *constant_value_bounds*	constant kernel (object)	(5.5)
*RBF**	*length_scale*, *length_scale_bounds*	radial-basis function (object)	(5.5)

* = This call creates and initializes a new object of a class and is therefore not a typical function.

Table 5.2: Allocation of scikit-learn functions to the corresponding mathematical equation.

5.4 Integrating machine learning methods in battery system optimization

The presented methods of Gaussian process regression and classification have been used for the implementation of an optimization strategy for battery system designs utilizing the HV-BOT. Although its technical submodels are practically known, the HV-BOT is treated like a black-box, where only the inputs and outputs are observed. This approach was chosen to ensure that the submodels can be developed further in the future without affecting the optimization. The optimization variables are given by the five design variables determining the space allocation of the battery system, as presented in Chapter 4.2. The user-defined technical parameters are set once for a complete run of the optimization. The unknown cost function is modeled with a GPR. Four different GPCs are used for modeling the individual feasibilities of the four

technical submodels, as the feasibilities of all four submodels are mandatory for the location of the global cost optimum. Thus, a total number of five Gaussian processes is needed for this optimization problem.

As stated in Section 5.2.2, the design variables of the HV-BOT implicate a mixed-integer problem. The optimization framework uses coarse uniform discretization of the entire solution domain and a strong refinement in potentially optimal regions to still model the problem close to continuously. Consequently, the solution space is always represented by a finite number of five-dimensional points, where every point defines one battery system design. In the following, the terms point and battery system design are used equivalently for the explanation of the optimization strategy. Discretization and refinement are discussed in more detail in Section 5.4.1.

In order to increase the overall computational speed of the algorithm, test point evaluations using the HV-BOT are parallelized. Hence, multiple query points have to be selected for evaluation in every iteration. For this work, the machine used comprised eight logical cores. Thus, eight battery system designs are evaluated in parallel in each iteration.

The complete optimization loop is depicted in Figure 5.4.

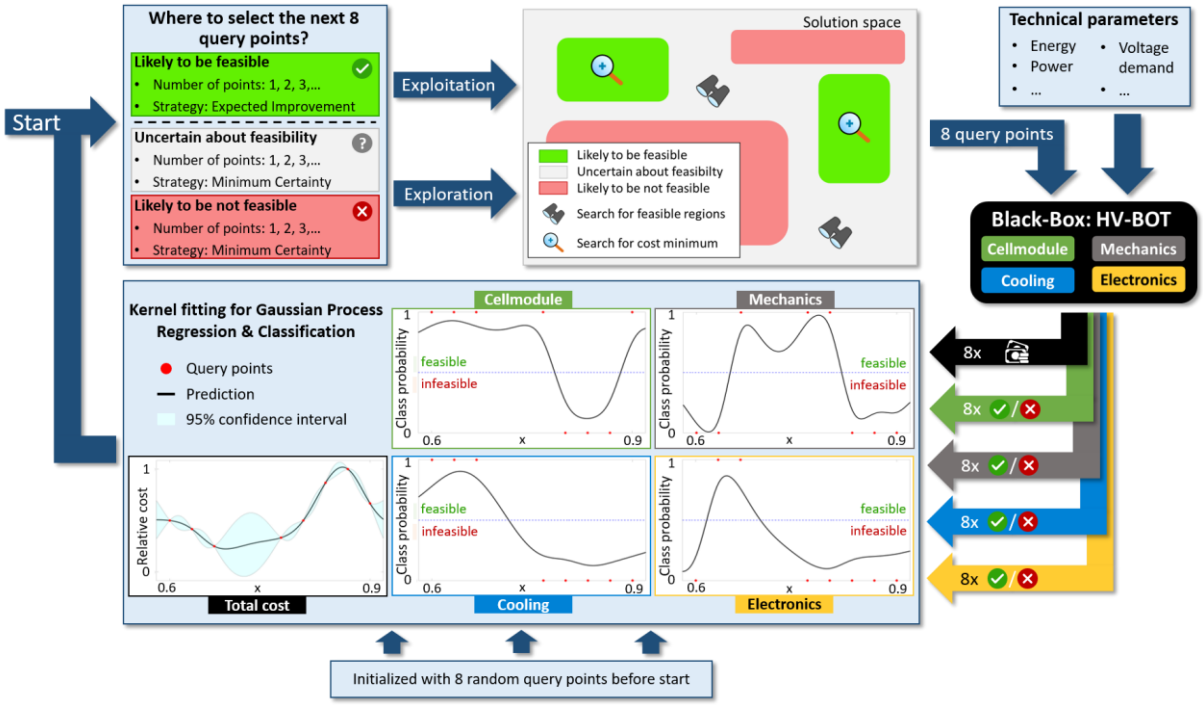

Figure 5.4: Gaussian process based optimization algorithm PPCQS (Parallelized Predictive Classifying Querying Strategy). Depicted are the main steps of the optimization loop starting in the top left corner.

Before the main algorithm starts, eight query points are selected randomly from within the uniform grid and evaluated by the HV-BOT black-box. These initial evaluations are used to train the GPs before any predictions about unknown battery system designs are made. Afterward, the optimization loop is actuated.

Firstly, eight new query points are chosen. A querying strategy divides the points of the uniform grid into three groups and applies different acquisition functions to these

groups for the selection of the next battery system designs to evaluate. The goal is to maximize the information gain on both the location of regions with feasible battery system designs and simultaneously find the location of the global cost optimum within these regions. Moreover, query points are selected based on predictive calculations conditional to the already chosen query points to maximize the information gain for every query point. This querying strategy is explained extensively in Section 5.4.2.

Secondly, the selected query points are fed to the HV-BOT black-box. Each query point is evaluated by one logical core of the CPU, each returning the total costs $c(\mathbf{x})$ as well as the feasibilities $\Phi_i(\mathbf{x})$ of every submodel i.

Thirdly and lastly, the returned results are added to the training data, which is then used to refit the GPs to incorporate the gained knowledge for the selection of query points in the next iteration. This optimization framework is denoted as *Parallelized Predictive Classifying Querying Strategy (PPCQS)*.

5.4.1 Uniform grid and refinement

As a battery system design is defined by three real numbers (x_1,x_2, x_3) and two integers (x_4, x_5), a mixed-integer problem has to be addressed. This difficulty is addressed by placing a uniform grid over the complete solution space in which each dimension is discretized equidistantly. Consequently, the precision of the position of the global optimum is limited to the fineness of the grid. In order to increase the accuracy of the grid, a refinement strategy is applied to regions of higher interest, i.e., where the global optimum will most likely be located. Due to the fact that the feasibility of a solution is mandatory for the location of the global optimum, the refinement is applied in regions where all GPCs modeling the feasibility of the submodels predict feasibility. This will be further explained in Section 5.4.2. Only the first three dimensions of the grid need to be refined, as the last two dimensions are limited to integers. Thus, the accuracy of these dimensions is already maximum. For every of the first three dimensions and all combinations of these, a new point is added in the middle between two already existing points of the grid. Hence, for every existing point at most 26 new points $(3 \cdot 3 \cdot 3 - 1)$ are added to the grid, resulting in a division of the maximum error of the location of the global optimum by half with every applied refinement.

For optimization results in this chapter, the HV-BOT's design variable limits of x_1, x_2 and x_3 are defined to be $x_1 \in [0.65, 0.85], x_2 \in [0.75, 0.90]$ and $x_3 \in [0.70, 0.85]$. Six discretization levels for every dimension of the grid are chosen, leading to maximum relative errors of 1%, 0.75%, and 0.75% regarding the location of the global optimum caused by discretization with one applied refinement. Assuming a battery system with dimensions of 1800 x 1200 x 150 mm³, the maximum absolute errors are 18 mm, 9 mm, and 1.125 mm, respectively. Generally, the refinement could be further increased, yet this accuracy is sufficient for the purposes of the HV-BOT in the predevelopment of battery systems. Figure 5.5 shows an example of discretization and refinement for x_1 and x_2.

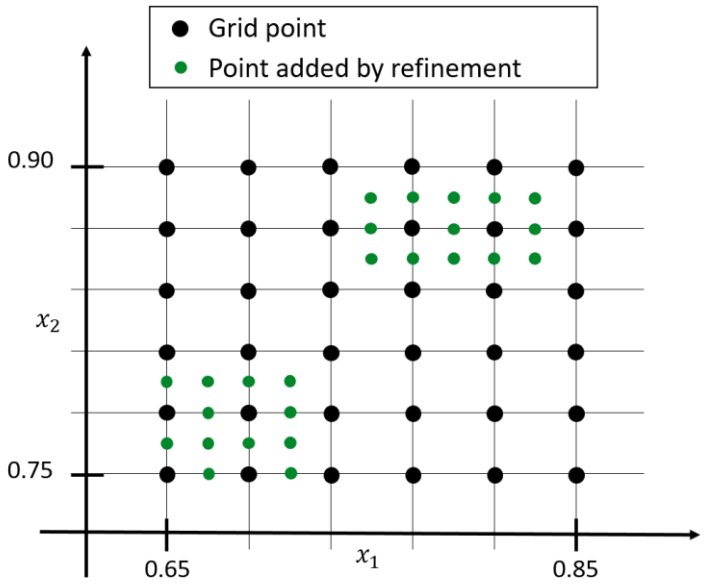

Figure 5.5: Discretization of the solution space. Depicted is the uniform grid in the directions of x_1 and x_2. The green points illustrate the functioning of the refinement strategy.

5.4.2 Querying strategy

An essential challenge in developing optimization algorithms is deciding which query point should be evaluated next. This question intensifies for a parallelized querying strategy as not one, but multiple points (for this work eight) have to be selected in one iteration. Due to the continuity of the used Gaussian processes, at least a few of the selected query points will likely be located close to each other if all query points are selected according to the same acquisition function. Consequently, the optimization algorithm will perform poorly, as the information gain in every iteration is very low, weakening the advantages of parallelization. Therefore, a predictive querying strategy is implemented, meaning that query points are selected sequentially and conditionally to query points that have already been chosen in the current iteration. If m query points $\{\mathbf{x}_1, \dots, \mathbf{x}_m\}$ with predicted values $\{\hat{y}_1, \dots, \hat{y}_m\}$ have already been selected, the GPs are refitted according to a temporary predictive training set $\widehat{\mathcal{D}} = \mathcal{D} \cup \{(\mathbf{x}_1, \hat{y}_1), \dots, (\mathbf{x}_m, \hat{y}_m)\}$ before the predictions for all points of the uniform grid are recalculated. Based on this predictive calculation, the next query point is chosen, and the whole process of fitting and predicting repeats. A detailed overview of predictive optimization using differential entropy can be found in [145].

Another major challenge of many optimization problems is the balance between the exploration and the exploitation of the design space. Emphasizing exploration may cause the optimization algorithm to jump from one local optimum to another, never staying at one very promising local optimum and thus never finding the global optimum. In contrast, if exploitation is predominant, the algorithm may get stuck in a local optimum, which can also lead to insufficient results as the global optimum may be located somewhere else.

Utilizing all available logical cores of a computer by means of parallelization methods, the optimization framework proposes a querying strategy that uses a few logical cores for exploitation and the rest for exploration. Thus, a mixture of both is achieved in every

iteration. This is done by dividing all points of the uniform grid into three groups (see Figure 5.6):

- points, that are likely feasible F,
- points, that are likely not feasible N,
- points, where the feasibility is uncertain U.

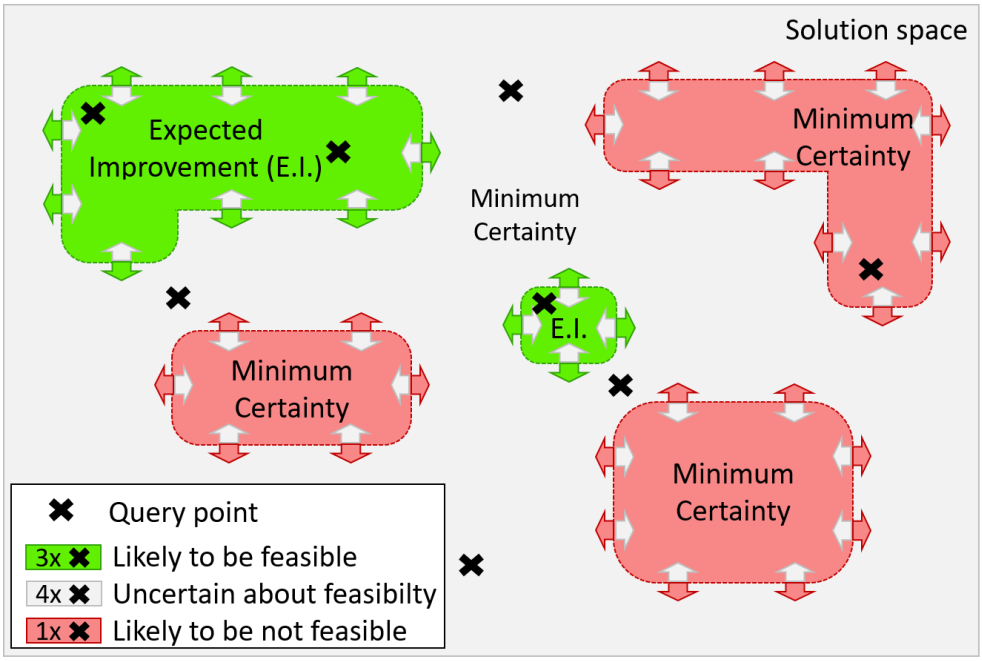

Figure 5.6: Dissection of solution space and selection of query points. The solution space is divided into three possibly disjoint regions for the distinction between likely feasible, likely not feasible points and points, where the feasibility is uncertain. In an exemplary machine with eight logical cores, three query points are taken from the set of likely feasible points, four points from the set of uncertain points, and one point from the set of likely infeasible points. The borders of the three regions may change over time.

This allocation is done using the probabilistic predictions $p(y_i|\mathbf{x})$ of the GPCs, modeling the feasibilities of the four technical submodels. The condition for an assignment to F can be written as:

$$p(y_i = 1|\mathbf{x}) \geq \alpha \; \forall i \in \{1,2,3,4\}, \tag{5.13}$$

the condition for an assignment to N as:

$$\exists i \in \{1,2,3,4\} \text{ so that } p(y_i = 0|\mathbf{x}) \geq \beta, \tag{5.14}$$

with i indicating the submodel. Every point that does not comply with one of these two conditions is allocated to U. The two thresholds α and β can be chosen by the user of this querying strategy. Note that if just one submodel is likely not feasible, the point itself is likely not feasible, whereas all submodels have to be likely feasible for a point

to be likely feasible in total. Therefore, the threshold for the allocation to N should be chosen higher compared to the threshold for the allocation to F. For the generation of the results presented in Chapter 5.5, the thresholds were set to $\alpha = 0.635$ and $\beta = 0.9$.

As stated in Chapter 5.4, the sections of the uniform grid underlying F are refined before points are chosen for evaluation. If possible, query points are selected as shown in Figure 5.6: Three points are taken from F, four points from U and one point from N. As implied by Figure 5.6, the size and shape of the individual groups can change over time. If F becomes larger than U, their ratio of selected query points is inverted ($F{:}\,4$ and $U{:}\,3$). Moreover, it is a deliberate decision to always evaluate one point of N, in order to punctually validate the classification of likely not feasible points.

In order to find regions of feasible solutions as well as solutions with minimal costs, different acquisition functions are applied to the three groups. For the selection of query points from U and N, a new acquisition function named Minimum Certainty (MC) is proposed, which combines the probabilistic predictions of the GPCs and aims at maximizing the information gain on the location of feasible solutions. It is defined as follows:

$$a_{\mathrm{MC}}(\mathbf{x}) = \frac{1}{1 + \gamma \cdot m(\mathbf{x})} \prod_{i=1}^{4} (p(y_i = 1|\mathbf{x}) - 0.5)^2. \tag{5.15}$$

Here, $m(\mathbf{x}) \in \{0,1,2,3,4\}$ denotes the count of submodels that are predicted feasible. The parameter $\gamma \in \mathbb{R}^+$ can be chosen by the user and determines the impact of predicted feasibility. In Figure 5.7 the acquisition function is depicted for a two-dimensional example (= only two submodels) and different choices of γ. The undefined areas are the regions where a point is assigned to the set of likely feasible points F. The results presented in Chapter 5.5 were achieved using a value of $\gamma = 1$. The minimum of the acquisition function is found where the certainty about the classification of at least one submodel is at minimum, corresponding to a predicted probability of $p(y_i = 1|\mathbf{x}) = 0.5$. The next query point $\mathbf{x}_*$ from the set of uncertain points U is then given by:

$$\mathbf{x}_* = \underset{\mathbf{x} \in U}{\operatorname{argmin}}\ a_{\mathrm{MC}}(\mathbf{x}). \tag{5.16}$$

The next query point from the set of likely not feasible points N is chosen analogously.

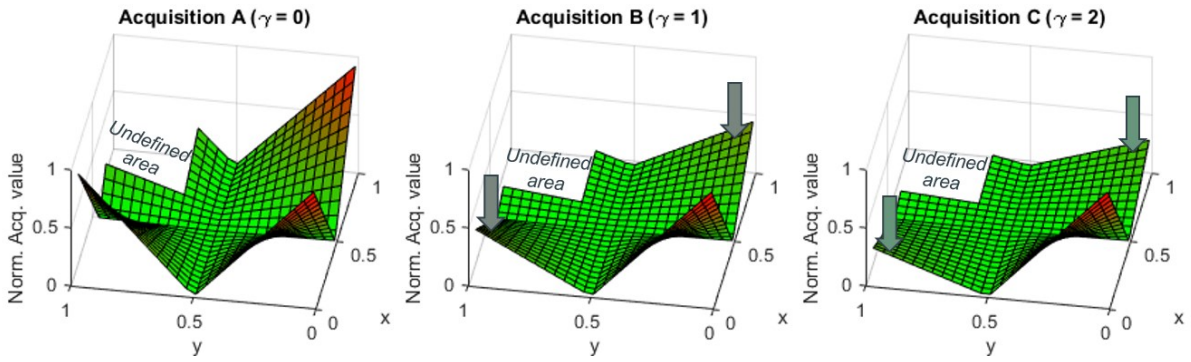

Figure 5.7: Illustration of the acquisition function named Minimum Certainty. The acquisition function is depicted for a two-dimensional example and different choices of the free parameter γ.

In contrast, the query points from the set of likely feasible points F are selected using the GPR, which models the cost function. As a well-evaluated querying strategy, Expected Improvement (EI) is used as the acquisition function for the GPR [373]. It is defined as:

$$a_{\mathrm{EI}}(\mathbf{x}) = \sigma(\mathbf{x}) \cdot \Big(\gamma(\mathbf{x}) \cdot \Phi\big(\gamma(\mathbf{x})\big) + \mathcal{N}(\gamma(\mathbf{x})|0,1)\Big) \quad \text{with } \gamma(\mathbf{x}) = \frac{f(\mathbf{x}_{\mathrm{best}}) - \mu(\mathbf{x})}{\sigma(\mathbf{x})}. \tag{5.17}$$

Here, $\Phi(\cdot)$ denotes the cumulative distribution function of the standard distribution, $\mathbf{x}_{\mathrm{best}}$ is the best point found so far and $\mu(\mathbf{x})$ and $\sigma(\mathbf{x})$ are the predicted mean and standard deviation of the Gaussian distribution over $f(\mathbf{x})$. The next query point is then determined by:

$$\mathbf{x}_* = \underset{\mathbf{x}\in F}{\operatorname{argmax}}\ a_{\mathrm{EI}}(\mathbf{x}). \tag{5.18}$$

In Algorithm 1 the complete algorithm for the optimization of battery systems using PPCQS is summarized in pseudo-code.

Algorithm 1 Parallelized Predictive Classifying Querying Strategy (PPCQS)

Initialization of the GPs with RBF kernel
Initialization of the uniform grid $\boldsymbol{S}$
Choose eight random query points $\boldsymbol{X}$ from $\boldsymbol{S}$
Evaluate $\boldsymbol{X}$ parallelized with HV-BOT black-box → $\mathbf{y}$
for $\mathrm{i} = 1 \ldots \mathrm{N}$ **do**
    Optimize hyperparameters of GPs: $fit(\boldsymbol{X}, \mathbf{y})$
    Predict probabilistic classification for $\boldsymbol{S}$: $predict\_proba(\boldsymbol{S})$
    Allocate points of $\boldsymbol{S}$ to the three groups $\boldsymbol{F}$, $\boldsymbol{U}$ and $\boldsymbol{N}$ using Eqs. (5.13), (5.14)
    Determine the distribution of query points: A points in $\boldsymbol{F}$, B points in $\boldsymbol{N}$ and C points in $\boldsymbol{U}$
    Apply refinement to the set of likely feasible points $\boldsymbol{F}$
    Initialize predictive training sets $\widehat{\boldsymbol{X}} \leftarrow \boldsymbol{X}, \hat{\mathbf{y}} \leftarrow \mathbf{y}$
    for $\mathrm{j} = 1 \ldots \mathrm{A}$ **do**
        Predict costs for likely feasible points: $predict(\boldsymbol{F}, return\_std = True)$
        Determine query point $\mathbf{x}_* = \underset{\mathbf{x}\in F}{\operatorname{argmax}}\ a_{\mathrm{EI}}(\mathbf{x})$ using Eq. (5.17)
        Add query point and its predictions to predictive training data:
        $\widehat{\boldsymbol{X}} \leftarrow \widehat{\boldsymbol{X}} \cup \mathbf{x}_*,\ \hat{\mathbf{y}} \leftarrow \hat{\mathbf{y}} \cup \boldsymbol{y}(\mathbf{x}_*)$
        Optimize hyperparameters of GPs with predictive training set: $fit(\widehat{\boldsymbol{X}}, \hat{\mathbf{y}})$
    end for
    for $\mathrm{j} = 1 \ldots \mathrm{B}$ **do**
        Predict probabilistic classification for likely not feasible points: $predict\_proba(\boldsymbol{N})$
        Determine query point $\mathbf{x}_* = \underset{\mathbf{x}\in N}{\operatorname{argmin}}\ a_{\mathrm{MC}}(\mathbf{x})$ using Eq. (5.15)
        Add query point and its predictions to predictive training data:

$\widehat{\boldsymbol{X}} \leftarrow \widehat{\boldsymbol{X}} \cup \mathbf{x}_*,\ \hat{\mathbf{y}} \leftarrow \hat{\mathbf{y}} \cup \boldsymbol{y}(\mathbf{x}_*)$

Optimize hyperparameters of GPs with predictive training set: $fit(\widehat{\boldsymbol{X}}, \hat{\mathbf{y}})$

end for

for $\mathrm{j} = 1 \ldots \mathrm{C}$ **do**

Predict probabilistic classification for uncertain points: $predict\_proba(\boldsymbol{U})$

Determine query point $\mathbf{x}_* = \underset{\mathbf{x} \in U}{\operatorname{argmin}}\ a_{\mathrm{MC}}(\mathbf{x})$ using Eq. (5.15)

Add query point and its predictions to predictive training data:

$\widehat{\boldsymbol{X}} \leftarrow \widehat{\boldsymbol{X}} \cup \mathbf{x}_*,\ \hat{\mathbf{y}} \leftarrow \hat{\mathbf{y}} \cup \boldsymbol{y}(\mathbf{x}_*)$

Optimize hyperparameters of GPs with predictive training set: $fit(\widehat{\boldsymbol{X}}, \hat{\mathbf{y}})$

end for

Evaluate all query points $\boldsymbol{X}_*$ parallelized with HV-BOT black-box → $\mathbf{y}_*$

Add query points and results to training set: $\boldsymbol{X} \leftarrow \boldsymbol{X} \cup \boldsymbol{X}_*,\ \mathbf{y} \leftarrow \mathbf{y} \cup \mathbf{y}_*$

end for

5.5 Model results and discussion

This chapter presents the applicability of the proposed optimization methodology. The results are based on the state of the HV-BOT at the time of the first publication [247, 330]. The results of the optimization strategy presented are applicable to further developments of the HV-BOT (see Chapter 6).

This chapter presents results using the PPCQS optimization for different technical requirements on the battery system and varying limitations on the battery cell using the HV-BOT black-box model. Particular emphasis is placed on depicting the functionality, robustness, and applicability in battery system engineering.

5.5.1 Scenario-dependent optimization results

Different user-defined requirement scenarios are used to examine a wide range of difficulties for the optimization. PPCQS will be compared to other state-of-the-art optimization algorithms to stress the differences in the optimization logic and underline the advantages of using the presented optimization in coupled battery simulation models like the HV-BOT black-box model.

5.5.1.1 Scenario definition

Three very different optimization scenarios are constructed. Table 5.3 describes the three predefined scenarios with their different initial inputs. Next to the installation space, the different scenarios differ in system energy and voltage demand as well as the mechanics material and especially the integrated cell specifications.

Scenario 1 *flexible* is characterized by cellmodule specifications using a variable prismatic cell format with specified cell borders, offering large flexibility regarding length, thickness, and height of the corresponding cell and thus also general, flexible

integration possibilities. Scenario 2 *restricted* is limited to four different cells, two for prismatic and two for pouch format, offering generally less flexibility in its integration. Scenario 3 *concentrated* is fixed to one prismatic cell format leading to a generally narrowed feasible solution space.

Furthermore, four different algorithms are tested in each scenario against each other. These are the metaheuristic Firefly algorithm as well as Gaussian process regression using Expected Improvement as the acquisition function and the Newton algorithm as the acquisition function solver. Also, random algorithm is used as a benchmark result. The Firefly algorithm metaheuristic uses a trade-off between randomness and knowledge of existing solutions to sample the solution space. Firefly algorithm setting parameters used in this analysis can be found in the footnotes of Table 5.3. The operation and choice of hyperparameters of the Firefly algorithm are derived in Chapter 5.5.1.2. As scenarios 2 and 3 already feature larger non-feasible regions due to the restricted cell integration, the Firefly algorithm was replaced with Gaussian process regression using the Firefly algorithm as the acquisition function for comparison.

Technical parameters for the battery system	**Scenario 1 *flexible***	**Scenario 2 *restricted***	**Scenario 3 *concentrated***
Overall installation space (x,y,z) [mm³]	1850 x 1440 x 150	1850 x 1240 x 150	2050 x 1540 x 150
System energy demand [kWh]	80	60	90
System power demand [kW]	175	175	175
System voltage demand [V]	500	400	550
Specified cell format and geometry [mm³]	*Prismatic cells* Cell sizes in the range [min., max.]: Cell length: [100,300] Cell thickness: [15,50] Cell height: [100,120]	*Prismatic cells* Cell size 1: 210 x 25 x 110 Cell size 2: 230 x 35 110 *Pouch cells* Cell size 3: 300 x 8 x 110 Cell size 4: 420 x 12 x 110	*Prismatic cell* Cell size 1: 220 x 30 x 110
Ambient temperature [°C]	20	20	20
Mechanics material	Aluminum or Steel	Aluminum	Aluminum
Tested optimization algorithms	Firefly[1] GPR[4] Newton (EI) Random PPCQS	GPR[4] Newton (EI) GPR[4] Firefly[2] (Par.[3]) Random PPCQS	GPR[4] Newton (EI) GPR[4] Firefly[2] (Par. [3]) Random PPCQS

[1] Parameter: $\alpha = 1; \beta = 0.2\,, \gamma = 0.5, \delta = 0.98, \text{flies} = 5$

[2] Used as acquisition function with parameter:

$\alpha = 1, \beta = 0.6\,, \gamma = 20, \delta = 0.95, \text{flies} = 30, \text{internal iterations} = 30$

[3] Greedy parallelization strategy: Taking maximum number of most promising data points

[4] Used kernel described in Chapter 5.3 and Eq. (5.5)

Table 5.3: Definition of three scenarios for testing. The scenarios differ in the technical parameters for the battery system and in the geometric limitations of the battery cell format.

5.5.1.2 Firefly algorithm and sensitivity analysis for hyperparameter selection

Before evalution the scenarios mentioned above, the following chapter derives the basics of the Firefly algorithm and validates the hyperparameter selection used in Chapter 5.5.1.1.

Basics of the Firefly algorithm

The Firefly algorithm was initially developed by Yang [374] as a nature-inspired algorithm emulating the behavior of fireflies. It is widely developed, and multiple variations have been proposed in the literature [375–382]. The algorithm samples the solution space towards favorable regions and simultaneously uses random sampling to prevent finding only a local optimum. Monte-Carlo-Simulation approaches can additionally be used to minimize the risk of premature convergence within a local optimum. The Firefly algorithm is controlled using three main parameters. Firstly, the attractiveness parameter indicates the speed or width of movement to the next brighter firefly. Secondly, the absorption coefficient, which depicts the distance-related reduction in light intensity of fireflies. And thirdly, the random walk parameter. In order to control the movement of one set of optimization variables $\mathbf{x}_i$ at time step $t+1$ to another set $\boldsymbol{x}_j$, the following equation is used:

$$\mathbf{x}_i^{t+1} = \mathbf{x}_i^t + \beta \cdot \exp\left(-\gamma D_{i,j}^2\right)\left(\mathbf{x}_j^t - \mathbf{x}_i^t\right) + \alpha^t \cdot \varepsilon_i \tag{5.19}$$

with β as the parameter to control the attractiveness, γ the absorption coefficient, and D the Euclidean distance. α^t depicts the random walk using a randomly generated number from the interval [-0.5, 0.5] and ε_i is a vector of random numbers drawn from different distributions such as the uniform distribution, Gaussian distribution, and Lévy flight [383, 384]. Figure 5.8 illustrates the flowchart of the Firefly algorithm. Performance evaluations can, for example, be found in [385]. For further evaluations, $\alpha^t = \alpha_0 * \delta^n$ is used with $\alpha_0 = 1$ and the random walk cooling factor δ^n for each iteration n. ε_i is defined using the optimization design variable's boundaries. For design variables x_4 and x_5, Eq. (5.19) is rounded to integer. The choice of β, δ and γ is analyzed in a sensitivity analysis below.

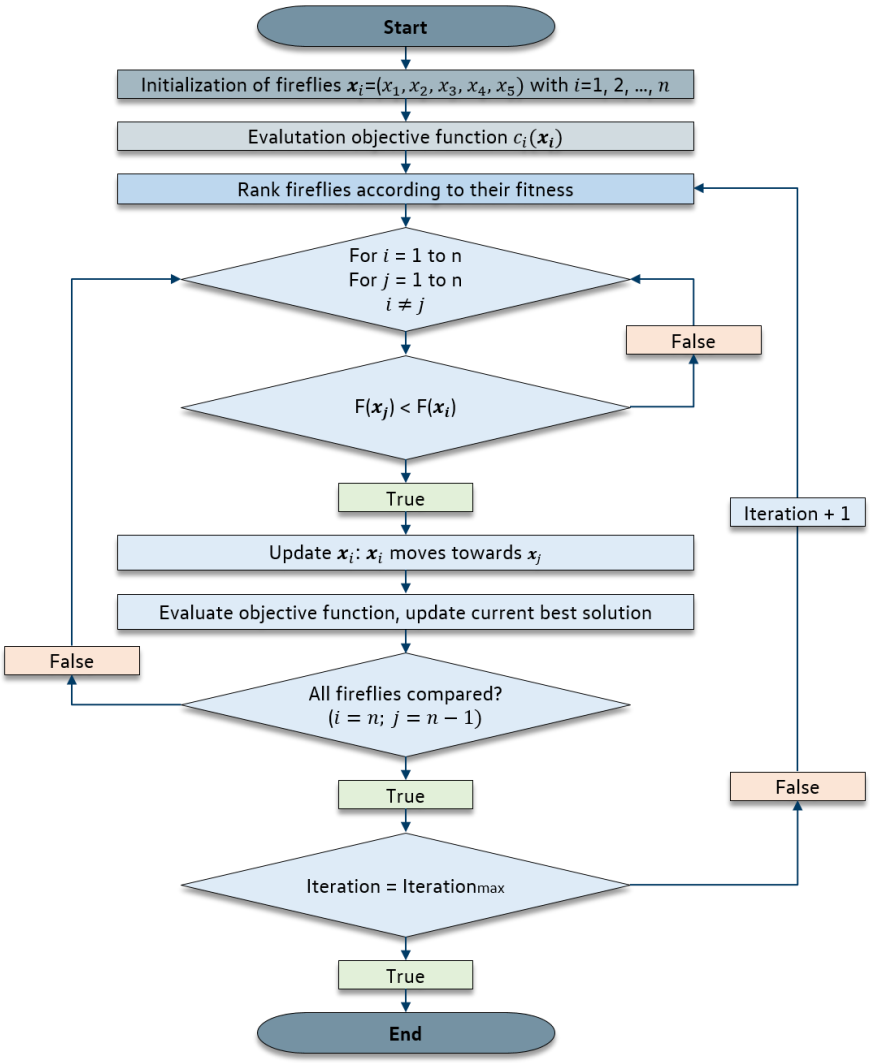

Figure 5.8 Flowchart diagram of the Firefly algorithm.

Analysis of hyperparameters

The following analyzes the optimal choice of FA hyperparameters for both of the used FA variants within this chapter. First, as a standalone optimization algorithm for finding cost minima. Second, as an acquisition algorithm to find the minimum on the metamodel of the objective function created by the GPR algorithm.

In order to optimally select the hyperparameters, a one-factor-at-a-time (OFAT) sensitivity analysis was performed. For this purpose, several optimizations were executed with the HV-BOT. The study design was defined so that each hyperparameter combination was performed a total of five times. Subsequently, the optima found were averaged using the median to measure the performance of the parameter combination. This procedure was executed for a wide range of parameter combinations, which are also typically used in the literature. For computation time reasons, the use of exactly five flies was specified for the sensitivity analysis of the pure Firefly algorithm. A total of 100 FA iterations were executed for each parameter set. The sensitivity of the three hyperparameters for the pure Firefly algorithm is shown in Figure 5.9.

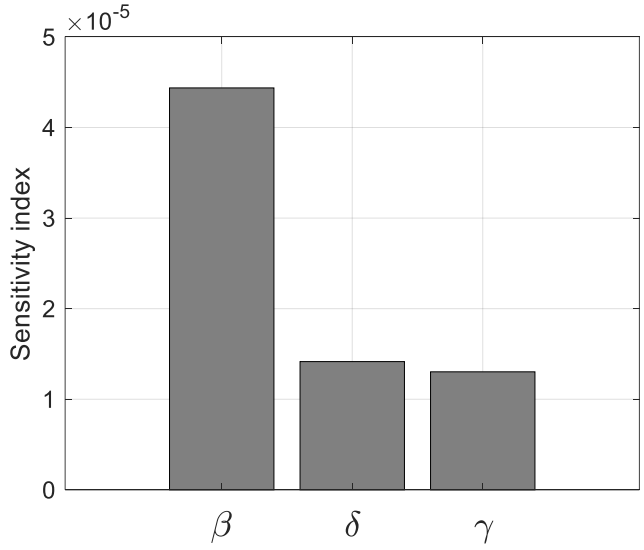

Figure 5.9: Result overview of the one-at-a-time sensitivity analysis for the Firefly algorithm used in the HV-BOT.

The results show the strongest sensitivity for the attractiveness parameter β. In order to select the optimal value for all hyperparameters, further in-depth analyses were performed. These can be found in the appendix in Chapter 8.6.1. Additional figures provide a more detailed resolution of the cause-effect relationship of the different parameter combinations. To account for multiplicative effects, a regression analysis was used to examine correlations between parameters in order to derive advantageous hyperparameter combinations.

For the analysis of the FA as an acquisition function, 30 flies were used. A total of 30 internal iterations were then executed on the GPR's meta-model for each of the total 100 outer GPR optimization iterations. The results of the sensitivity analysis using the FA for the acquisition function in the GPR are shown in Figure 5.10. Again, the attractiveness parameter β shows the highest sensitivity. However, parameters δ and γ also show higher sensitivity compared to the results of the pure FA above. The regression analysis results can be found in the appendix in Chapter 8.6.2.

The summarized results confirm a suitable hyperparameter choice for both FA applications from Table 5.3.

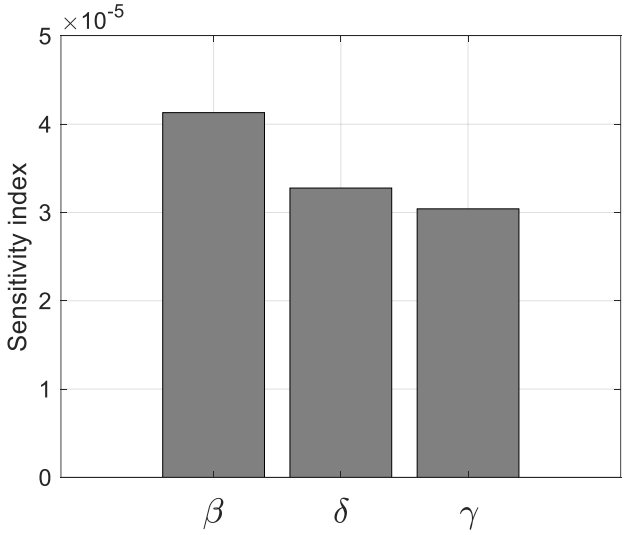

Figure 5.10: Results overview of the one-at-a-time sensitivity analysis when using the Firefly algorithm as an acquisition function within the GPR.

5.5.1.3 Penalty cost model

The following comparisons between the algorithm performances will be based on cost minimization. In order to ensure that the optimal solution is also a feasible solution $\mathcal{F}(\mathbf{x}) \leq 1$, the costs must reflect that these feasible solutions are more advantageous compared to the non-feasible solution $\mathcal{F}(\mathbf{x}) > 1$. As only PPCQS can consider further information regarding feasibility in its querying strategy, additional penalty cost models were integrated that artificially increase each submodel's total cost to ensure fair comparability.

The penalty cost model provides that for each DOF $\Phi_i(\mathbf{x}) > 1$ a penalty cost term $\zeta_i(\mathbf{x}) \in \mathbb{R}^+$ is added to the submodel's costs $c_i(\mathbf{x})$, leading to summed costs $\kappa_i(\mathbf{x}) \in \mathbb{R}^+$ for each submodel i defined as follows:

$$\kappa_i(\mathbf{x}) = c_i(\mathbf{x}) + \zeta_i(\mathbf{x}), \quad i \in \{1, 2, 3, 4\}, \tag{5.20}$$

in which the penalty cost term $\zeta_i(\mathbf{x})$ is defined as:

$$\zeta_i(\mathbf{x}) = \min(C, \ln(\Phi_i(\mathbf{x})) \cdot 5000), i \in \{1, 2, 3, 4\}. \tag{5.21}$$

Thereby, the logarithm ensures that a cost-optimal result is also a feasible one, as it penalizes small DOFs significantly greater compared to a linear relation. As the DOF terms Φ_i appear to be between 0 and 10, an upper boundary of $C = 5000$ is defined.

5.5.2 Results analysis and discussion

Figure 5.11 and Figure 5.12 show the current cost optimum with respect to the number of iterations for every algorithm tested in each of the three defined scenarios. Furthermore, the battery system schematic from each optimized result is depicted below each graph from the top and side view. The costs are normalized to the maximum temporary optimum that has been observed in a scenario. A wide range of

resulting relative costs is evaluated during the optimization process. For the detailed algorithm comparison, only an adjusted range is depicted. Furthermore, it should be noted that only feasible temporary cost optimums are depicted in the graphs for the first two scenarios. As PPCQS was the only optimization to find feasible solutions in the third scenario, the infeasible cost evaluations from the other algorithms are also depicted as diamond-formed points. Moreover, the consumed computational times are shown.

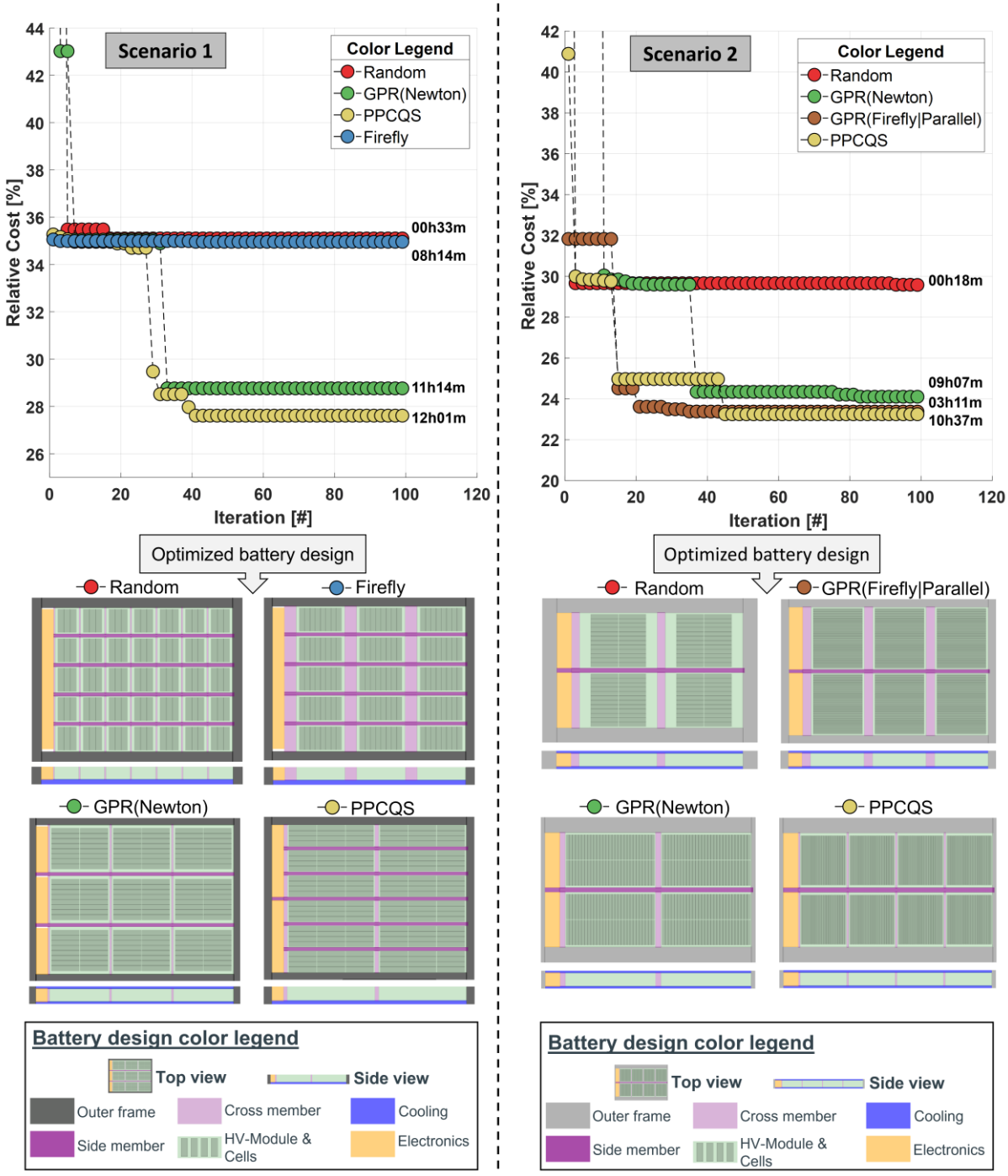

Figure 5.11: Comparison of optimization algorithms for scenario 1, and 2.

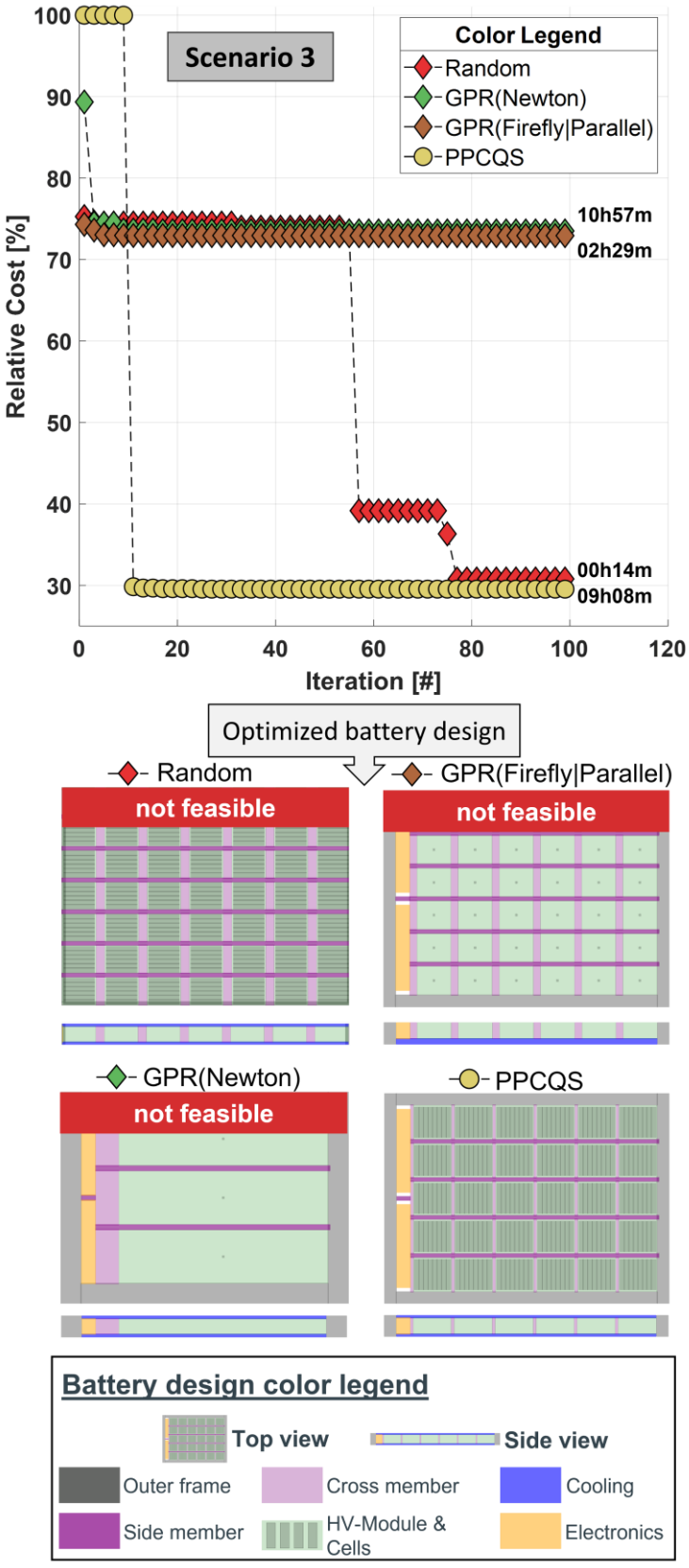

Figure 5.12: Comparison of optimization algorithms, scenario 3. Herein, also infeasible solutions are considered, as all algorithms except PPCQS did not find any feasible solutions.

Results show that the PPCQS algorithm finds the best solution in every scenario. This is especially stressed by the third scenario, where the other algorithms do not even find a feasible battery system design. Choosing points randomly performs poorly in all three scenarios. Considering that the final solution from the random algorithm for the third scenario is infeasible despite its low costs indicates possible weaknesses of the penalty cost model. Firefly algorithm was only used in the first scenario and found a feasible solution there. However, the depicted optimization process indicates that it got stuck in a local optimum. Using Firefly as the acquisition function in GPR performs very well in the second scenario, where it found the second-best solution with costs very close to the best solution. The GPR with Newton algorithm provides good results in scenarios one and two, finding the second- and third-best solutions, respectively.

From a technical perspective, the fact that PPCQS always finds the best solution is of even higher relevance, as the final battery system designs vary significantly between both the scenarios and the different algorithms within one scenario. The differences in the technical requirements of the battery system and the limitations on the cell format result in completely unlike optimal designs. Furthermore, even within one scenario, a slight improvement in costs can be achieved by substantially changing the battery system design, which can be observed in scenario 2. Here, GPR with Firefly and PPCQS both found systems with low costs, yet the number of cellmodules and the orientation of the stacks are unequal. This stresses the importance of robustness and showcases the advantages of the proposed optimization strategy combined with the HV-BOT in the design of battery systems.

The runtimes were measured on a standard office notebook with an *Intel(R) Core(TM) i5-10310U* and 8 GB of RAM. Although the runtime for PPCQS surpasses every other algorithm, it is not expected that any other algorithm would find any better solution as the result trend shows convergence within the 100 iterations.

To further analyze the algorithm's behavior and affirm the convergence trend towards the end of the iterations, each algorithm's exploration and exploitation balance is depicted in-depth in Figure 5.13. For this analysis, the solution space was divided into 108 equally sized areas (five-dimensional cuboids). For each algorithm, the amount of exploration was then measured by counting the areas where a test point had been taken from with respect to the iteration. In contrast, the amount of exploitation was determined by counting how many times a query point was selected from the area where the algorithm located its best solution.

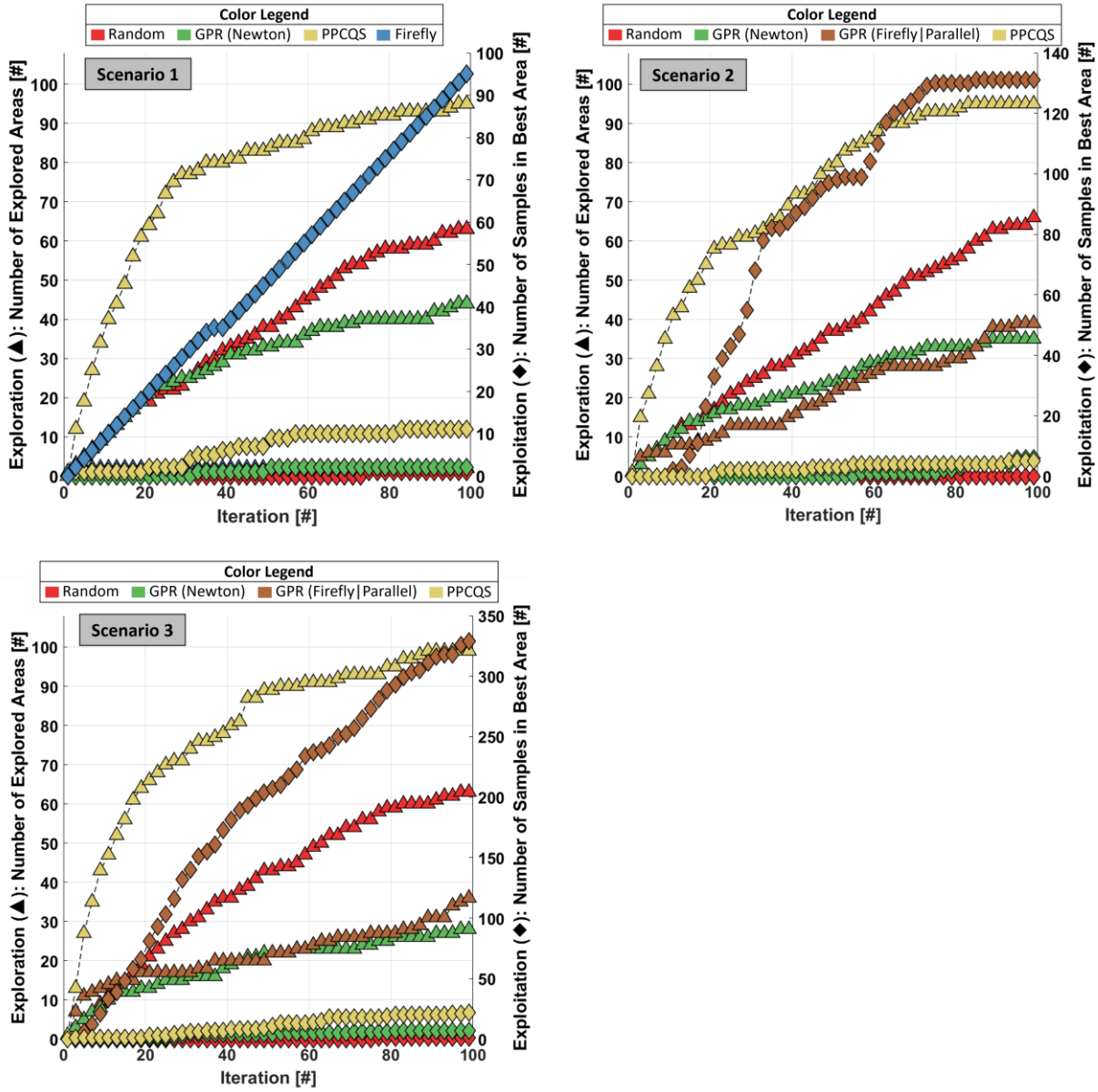

Figure 5.13: Balance of exploration and exploitation for scenario 1, 2, and 3.

It can be seen that PPCQS quickly explores different areas of the solution space, evaluating various battery system designs, which allows the algorithm to achieve a basic overview of the location of feasible solutions and the cost function. Considering the aforementioned variety of optimal battery system designs depending on the technical requirements, this fast and effective exploration of the complete solution space seems essential. At the same time, a sufficient amount of exploitation in the search for the cost optimum is conducted, leading to the observed promising results. On the contrary, all other tested algorithms show a disadvantageous relation between exploration and exploitation. Firefly performs almost no exploration, confirming that it got stuck in a local minimum. GPR with Firefly and GPR with Newton conduct a similar, relatively low amount of exploration. Interestingly, the first-mentioned focuses extensively on exploitation, whereas the last-mentioned exploits way less.

In conclusion, only the PPCQS algorithm was able to find a feasible battery system design for every scenario defined in Table 5.3. Furthermore, the final solution is always the best regarding the costs compared to all other algorithms, as seen in Figure 5.11

and Figure 5.12. Therefore, for the design of battery systems, PPCQS provides strong robustness that other algorithms were not able to offer. This is mainly achieved by the combined use of regression and classification methods, leading to an effective balance of exploration and exploitation, which can be observed in Figure 5.13.

5.5.3 Comparison and sensitivity of optimized battery systems for various installation spaces

In order to stress the relevance of a robust optimization methodology using the HV-BOT model, this chapter will perform a sensitivity analysis with respect to the total volume of the system and its geometry. For this purpose, five different volume sizes with four different geometries each were defined, as shown in Table 5.4. Other technical parameters were set fixed to values listed in Table 5.5. The PPCQS optimization strategy within the HV-BOT was then used to determine the optimal battery system and its costs for every installation space configuration.

Volume	**1.7 m² x 0.15 m**	**1.9 m² x 0.15 m**	**2.1 m² x 0.15 m**	**2.3 m² x 0.15 m**	**2.5 m² x 0.15 m**
Geometry 1 (x,y)[mm²]	1300 x 1308	1400 x 1357	1500 x 1400	1600 x 1438	1700 x 1471
Geometry 2 (x,y)[mm²]	1400 x 1214	1500 x 1267	1600 x 1313	1700 x 1353	1800 x 1389
Geometry 3 (x,y)[mm²]	1500 x 1133	1500 x 1188	1700 x 1235	1800 x 1278	1900 x 1318
Geometry 4 (x,y)[mm²]	1600 x 1063	1600 x 1118	1800 x 1167	1900 x 1211	2000 x 1250

Table 5.4: Definition of the testing matrix for installation space analysis. The scenarios differ in the geometric format as well as overall installation volume. Only values of x- and y-dimensions were altered. The height of the systems (z-direction) was set fixed to 0.15 m.

Technical parameters for the battery system	**Values**
System energy demand	60 kWh
System power demand	140 kW
System voltage demand	400 V
Specified cell format and geometry	*Prismatic cell* Cell size: 220 x 25 x 110 mm³
Ambient temperature	20 °C
Mechanics material	Aluminum

Table 5.5: Fixed technical specifications for the installation space analysis.

The results are depicted in Figure 5.14. The left side of the figure shows optimized results for the 20 different geometries. Therein, the x- and y-axes show the corresponding geometry. Equivalent volume lines mark the four different geometry configurations tested for each of the five different volumes. Based on the color of the individual bubbles, the achieved relative costs of the best-found result within the optimization are depicted. The costs are illustrated from green-colored low costs to

red-colored high costs. In addition, infeasible solutions are marked as bubbles without color. A strong color gradient from red to green is clearly visible and separately framed with a dotted line. This area describes the possibility of changing the cell chemistry and, thus, the resulting abrupt decrease in total system costs. This change, however, does not simply occur between two volume lines. This can be seen well in volume 2.1 m² x 0.15 m, in which two geometries with red and two geometries with green costs are shown. This phenomenon is caused by the predefined cell geometry and thus underlines the complexity of the integration capability of different cell geometries at the system level. To further analyze smaller cost differences in the light green area, this area is depicted in more detail in the right part of Figure 5.14. The overall cost optimum is reached at a geometry of 1700 mm x 1353 mm. Surrounding system configurations are associated with higher costs. Unfavorable installation space geometries or the general under- or oversizing of the system lead to increased costs in cooling, mechanics, or electronic components.

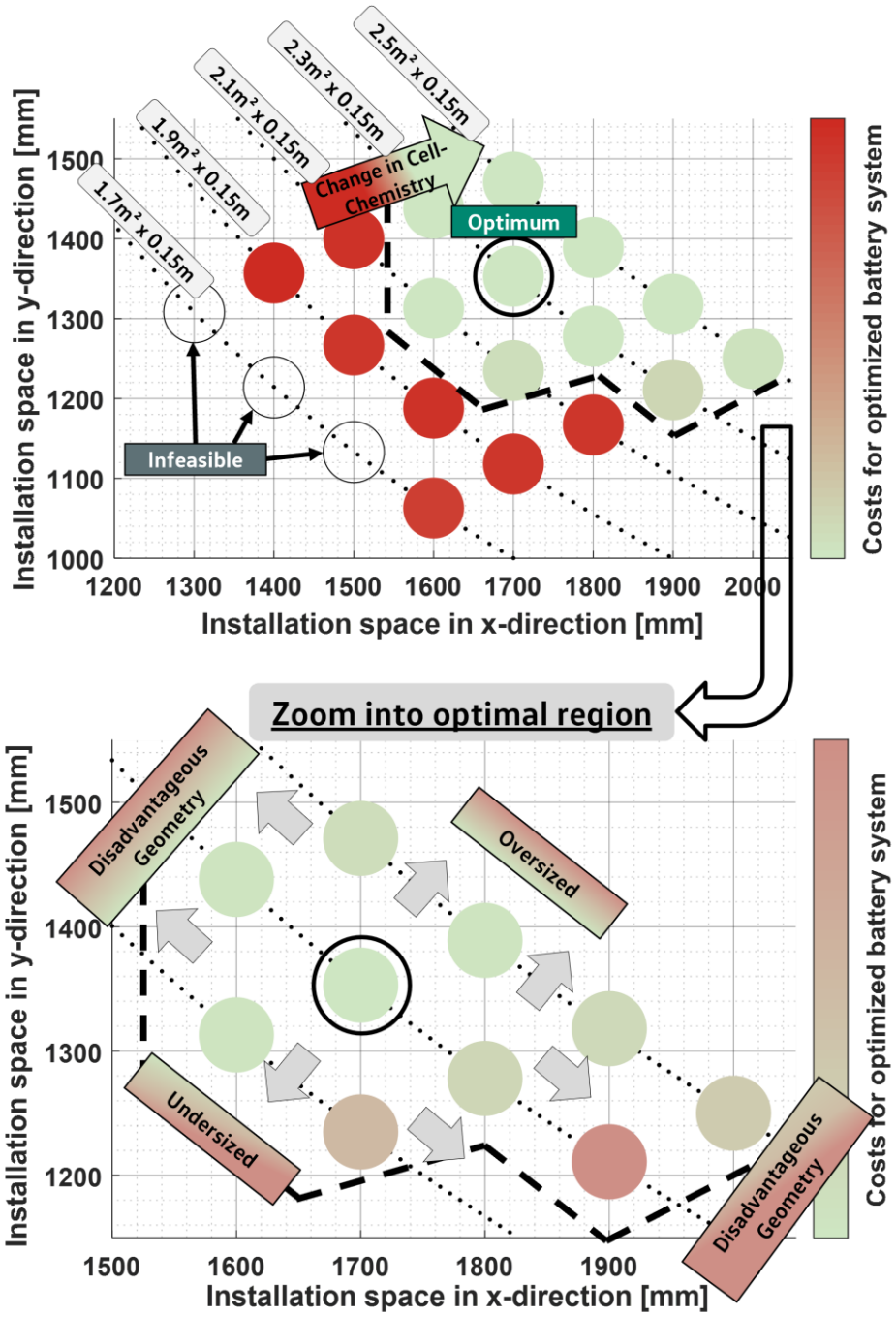

Figure 5.14: Summarized results of optimized costs for different battery system installation spaces for a sensitivity analysis.

The sensitivity analysis presented here can be of enormous importance for battery system manufacturers when installation space decisions have to be analyzed. In this context, a reliable and robust optimization strategy is indispensable as it enables revealing the optimal simulation result and cost-related tipping points. Through the installation space analysis, particularly cost-intensive areas can be precisely identified.

In summary, the sensitivity analysis for different installation spaces and geometries with PPCQS stresses the extreme and cost-sensitive dependencies in the complex environment of battery system development. For this reason, it is of particular importance to optimize the battery systems with a robust and safe optimization

algorithm to ensure the model's accuracy as well as the validity and reliability of simulation results.

5.5.4 Benchmark results for PPCQS in other optimization problems

PPCQS was further benchmarked by optimizing the Rastrigin function and comparing the results to an optimization using basic GPR acquisition strategies. Chapter 5.5 showed convincing results for the proposed optimization framework PPCQS. Next to the actual best objective cost value, the convergence was also generally faster compared to the other algorithms. In order to provide a more general goodness analysis for PPCQS, the strategy was applied to an optimization of the strongly non-convex and non-linear Rastrigin function. Figure 5.15 summarizes the results and comparisons. Strategy 1 and 2 use Gaussian process regression with the widely accepted Expected Improvement method as an acquisition function in order to find the most promising next query points. The Gaussian process was defined analogously to Chapter 5.3. As PPCQS uses parallelization in its querying strategy, Strategies 1 and 2 also chose eight individual test points per iteration. Strategy 1 selects the points of the evaluated goodness from the Expected Improvement in descending order. Strategy 2 uses the predictive goodness by refitting the Gaussian process after each point selection. Strategy 3 represents the optimization strategy PPCQS as described in Chapter 5.4. Since the Rastrigin function, by definition, has no DOF, the DOF $\phi_i(\boldsymbol{x})$ for x_1 and x_2 was additionally defined as:

$$\Phi_i(x_i) = \begin{cases} 1, & \text{for } -1 \leq x_i \leq 1 \\ 0, & \text{for } (x_i < -1) \ \vee (x_i > 1) \end{cases} \tag{5.22}$$

with $i \in \{1,2\}$.

Figure 5.15 additionally shows for Strategy 3 how the points are divided into the three defined regions (feasible F, not feasible N, uncertain U). Furthermore, the results show that PPCQS finds the global optimum at (0,0) quickly and effectively while simultaneously, a large solution range of the function is sampled. In addition, the global optimum region around (0,0) is sampled in great detail, underlining the functionality of the grid refinement. In the resulting plot at the bottom of Figure 5.15, the three optimization strategies are depicted for comparison, given the current best objective value subjected to the number of observed samples. The promising results indicate that the optimization strategy PPCQS can also be applied to other optimization problems besides the HV-BOT.

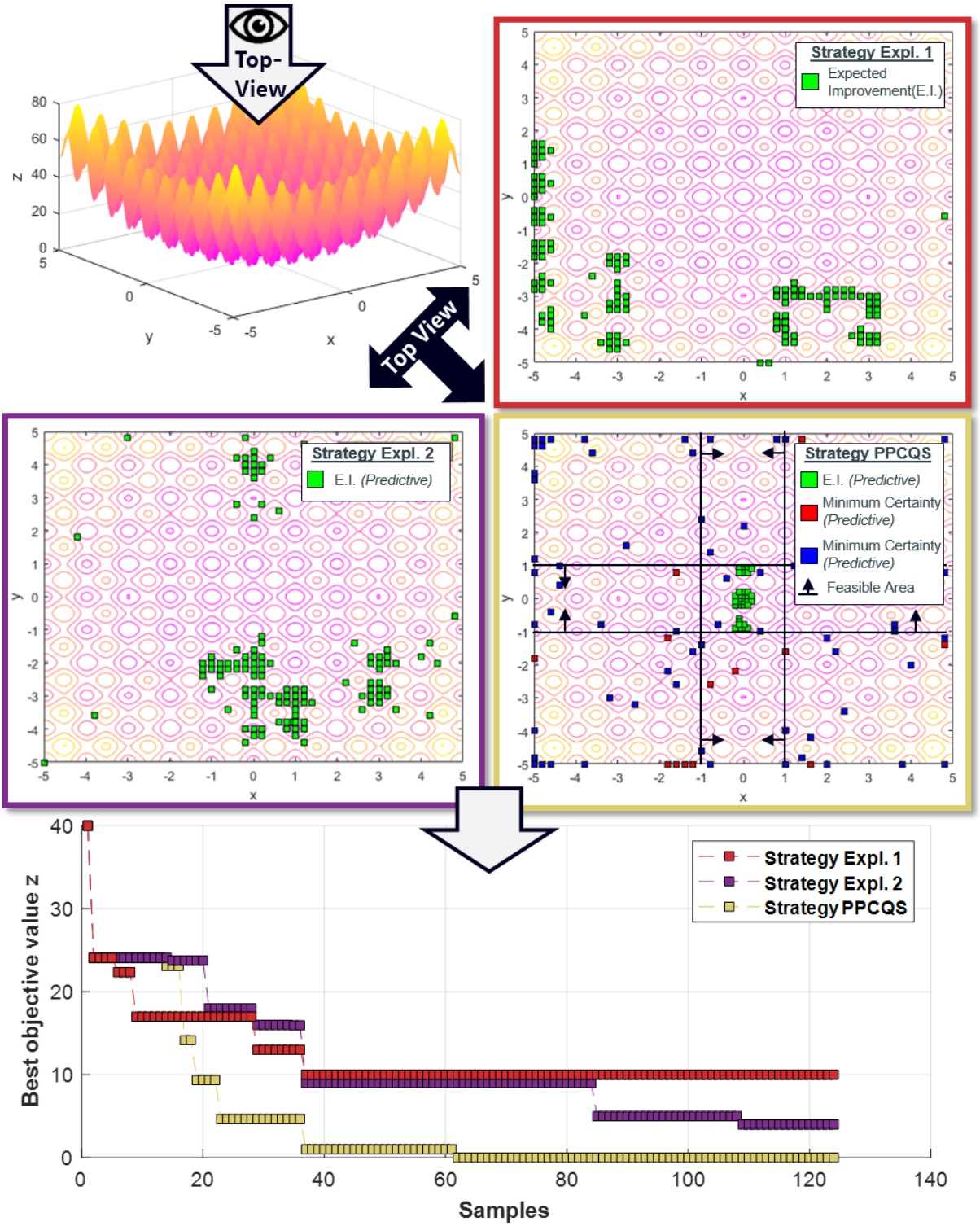

Figure 5.15: Result summary of an optimization of the Rastrigins function. Two strategies are compared with the proposed PPCQS. Both strategies use GPR optimization and compute the acquisition function by maximizing the Expected Improvement. Strategy 1 selects the eight most promising points in descending order. Strategy 2 uses the predictive method in which the model is refitted after each point selection.

5.6 Conclusive summary

This chapter introduced a novel optimization strategy for coupled battery system design simulations named Parallelized Predictive Classifying Querying Strategy (PPCQS). PPCQS was developed to handle the optimization for different conditions of battery-related black-box optimization models. Thereby, the simulation submodels in the HV-BOT were treated as a black-box emphasizing the algorithm's robustness. This adaptability of the algorithm is crucial because simulation models are constantly evolving.

PPCQS comprises both regression and classification methods based on Gaussian processes to determine the global cost optimum subject to a mandatory feasibility condition. Furthermore, coupled classification splits the total solution space into three fundamental regions: feasible, infeasible, and uncertain. Parallelization methods are used to decrease runtime and to increase information gain in every iteration by conducting multiple black-box evaluations simultaneously. This is enhanced by using different acquisition functions for querying multiple test points in order to gain information on both battery system designs that comply with the feasibility condition and designs with minimal costs. A new acquisition function named Minimum Certainty is introduced to search for feasible solutions. Afterward, the Expected Improvement function is used to find the cost minimum. Moreover, the query points are selected predictively to maximize the information gain for every single query point.

Testing PPCQS in three scenarios defined by different technical requirements for battery systems and comparing it to three established algorithms showed that PPCQS outperforms the other algorithms in terms of robustness and accuracy in determining the global cost optimum. An efficient mixture of exploration and exploitation ensures that a wide range of different battery system designs is evaluated and, at the same time, slight variations of promising solutions are investigated in the search for the cost minimum. Additionally, sensitivity analyses regarding the impact of the total installation space on costs and feasibility showcased exemplary use cases of the presented optimization strategy. They also emphasize the complexity of integrating battery cells at the system level as well as the importance of a robust optimization strategy for achieving valid and reliable simulation results.

Thus, PPCQS offers a favorable optimization strategy for the design of battery systems using the HV-BOT. In future work, the optimization strategy could be analyzed in various other technical battery system or component simulation models that have similarly challenging optimization problem requirements as the HV-BOT. Furthermore, sensitivity analyses could show which values of the parameters in the used classification methods and acquisition functions are scenario-dependent optimal. Additional runtime improvements could also be analyzed using a high computational cluster with numerous logical cores.

6 Applicative optimization of battery systems and derivation of conclusive design guidelines

Parts of this chapter are published in a journal article [247] as part of this thesis. The use of the article content, including illustrations, is permitted with the consent of Elsevier.

This chapter aims to merge the methodology of multiphysical models for the battery system principal components from Chapter 4 with combined regression and classification optimization from Chapter 5. This chapter aims to discuss different fundamental battery system design questions and highlight physical sensitivities. Unless otherwise stated, model assumptions derived in Chapters 4, 5, and 8 apply.

6.1 Merging battery system design models and optimization methodology

Merging the submodel-concept with the Gaussian process optimization procedure enables the HV-BOT to optimize battery system designs based on a system perspective. Thereby, the HV-BOT iteratively tries to find better solutions by updating the design space allocation variables. Figure 6.1 illustrates the working principle schematically.

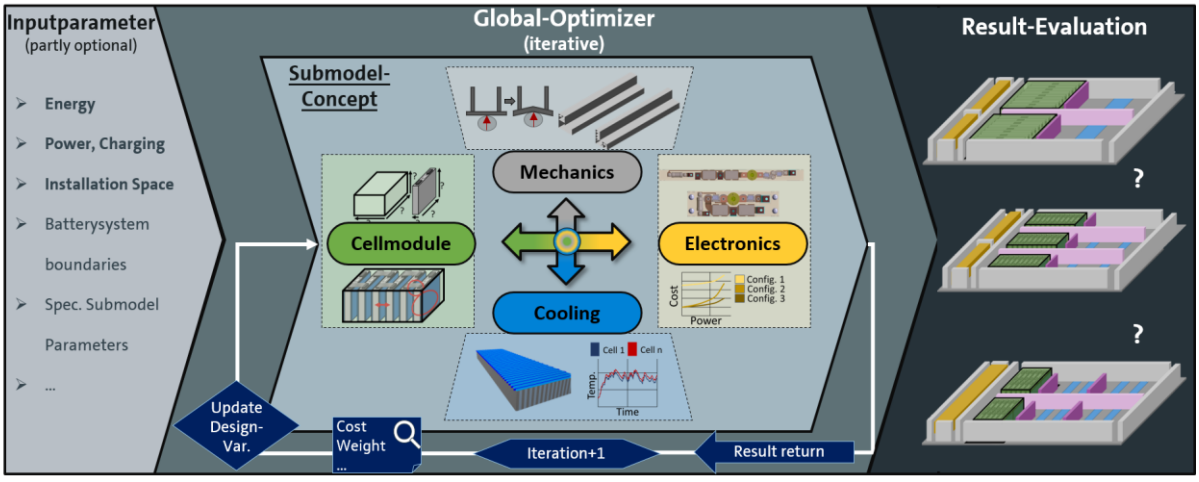

Figure 6.1: Flow diagram of the HV-BOT. Different inputparameters can be entered user-defined into the tool (e.g., energy, power, total installation space). A starting parameterization of the design variables $x_1, \dots, x_5$ is selected, representing space allocation for the different components. The respective submodels use the space allocation for cellmodule, mechanics, electronics, and cooling to evaluate the optimal configuration for the given inputparameters. The result is evaluated, and the design variables are adjusted for the next iteration. The procedure is executed for a predefined number of iterations.

6.1.1 Discussion of global objective value

In the following optimizations, different installation space allocations are sampled, tested, and subsequently evaluated, as described above. Generally, different output variables result from the simulation models, as described in Chapter 4.3. Two main result variables are the weight and the cost estimation of the tested battery system design concept.

However, the global optimization algorithm is only capable of optimizing on the basis of one objective value. In this respect, a discussion of the more suitable and advantageous objective value between weight and costs is given below.

6.1.1.1 Manufacturing and engineering perspective

From a manufacturing and engineering perspective, the overall battery system weight plays a crucial role. With lower weight, resources can be saved, and the efficiency of the overall electric vehicle can be increased. In addition, there can be advantages in production speed, machine load, and general work processes.

However, the total direct material costs of the battery system are the basis for the profitability and the ultimate profit of the vehicle manufacturer. In order to compete in the electric vehicle market, the battery system costs and the directly associated EV manufacturing costs play a decisive role. Since the battery system is the most cost-relevant component in the electric vehicle, it is also directly reflected in the total price of the final product. In addition, it can be argued that, to a certain extent, an increase in the weight of the battery system may be accepted, provided that the resulting high cost savings can be used elsewhere in the EV or as a price advantage for the consumer.

6.1.1.2 Modeling perspective

From the modeling perspective, both weight and cost in the HV-BOT are fundamentally based on several assumptions and estimations. In addition, a number of costs, particularly mechanical structures, are derived directly from the estimated weight and a material unit cost. This work did not model the actual material mix of the different cell electrode chemistries. While modeling cell electrode stack cost based on a requirements-based approach allows for manufacturer variability in the final chemistry of the battery cell, the actual cell chemistry will have a large impact on the overall weight of the battery system due to the gravimetric energy density of the cell chemistry. Accordingly, this work's actual modeled cell weight gives only a rough indication of possible cell chemistry. In a pure weight optimization, this could then lead to incorrect optima.

6.1.1.3 Decision derivation

Costs for mechanical structures, parts of cooling plate design, and the electronics integration are derived linearly from their estimated weight or volume. In pure weight optimization, however, the actual cost-related significance of one unit of weight is not evaluated. In an exaggerated example, this would mean that one kilogram of rather cheap aluminum would have the same significance on the overall result as one kilogram of rather expensive cell cushion pad material. Although partially estimated

costs may increase the dispersion of results due to cost uncertainties, a valuation-relevant distinction between weights of different components can still be performed.

This enables an optimization result that balances particularly sensitive and high-cost parts. In addition, parts that can not be independently weighted, such as the refrigeration circuit or the required coolant-water pump, can be included in an evaluation. Through individual, time- as well as view-dependent determination of the costs, optimal results can thus also be derived for specific applications. For the reasons mentioned above, the final results should also be evaluated regarding the total weight (see Chapter 6.3.1).

In summary, the cost estimation from the simulation models derived in Chapter 4.3 is used as the global optimization objective value in the chapters below.

6.2 Working principle of system optimization with detailed cost progression

In order to better describe the optimization principle in the HV-BOT, an exemplary set of inputparameters will be iteratively optimized in the following. The parameters are fixed throughout the optimization and thus represent the main requirements for the final battery system design. Table 4.8 summarizes the user-defined inputparameters for the to-be-optimized battery system.

Inputparameter (user-defined)	**Value**
General	
System installation space x,y,z	1800.0 x 1400.0 x 150.0 mm³
System energy demand	50 kWh
System power demand	140 kW
System charging time demand	20 min
System voltage demand	408 V
System usable battery DOD	96%
Cellmodule	
Cell geometry	Two possible cells (internal optimization): Prismatic: 160 x 18 x 105 mm³ Prismatic: 210 x 26 x 110 mm³
Maximum number of cellstacks per module	1
Cooling	
Ambient temperature	23.0 °C
Number of passes for cooling tube	2
Design current profile	Quick charging profile
Refrigeration circuit expansion stage	Basic
Mechanics	
Crashenergy requirement	20 kJ
Cellstack integration (only for prismatic cells)	Screwed cellstacks
Electronics	
Integration mode	3

Table 6.1: Exemplary HV-BOT inputparameters for the to-be-optimized battery system.

Figure 6.2 shows the optimization procedure, which lasted about 600 minutes for 100 iterations. The runtimes were measured on an office notebook with an *Intel(R) Core(TM) i5-10310U* and 8GB of RAM. Four exemplary battery system designs are depicted at the top of the figure from a 2D top and side view, indicating the variability of tested configurations throughout the optimization process. Each resulting bar represents the cost distribution of the current best solution. At roughly 400 minutes, the solution slowly converges.

In the lower part of the graphic, the first 350 minutes of the optimization are illustrated in more detail. Herein, the proportional components' cost changes during optimization are indicated within each bar cost. Furthermore, the change from the NMC-Type battery cell with higher energy densities to the LFP-Type cell with lower energy densities is marked separately. The change in cell chemistries results from achieving a higher cell-packaging density to compensate for the lower individual cell voltage. The cost drop is distinctly visible within the cellmodule costs. Next to the cellmodule, also the mechanics show considerable variability in their costs. The costs for electronics and cooling generally indicate less variability. One considerable cooling cost shift can be observed in the change from NMC-Type to LFP-Type cells. The changed cell specifications and corresponding cooling efforts may cause this change. The significant cost leap in the electronics' costs at the beginning of the optimization is caused by the change between external and internal electronics integration (see Chapter 4.3.5).

In general, the illustrative optimization underlines the mutual dependencies of the individual component groups and emphasizes the variability in battery system concepts for a fixed set of inputparameters. Furthermore, it can be seen that the cost of the cellmodule varies significantly less within one cell chemistry, resulting in a similar relevance of the costs of the other main component groups.

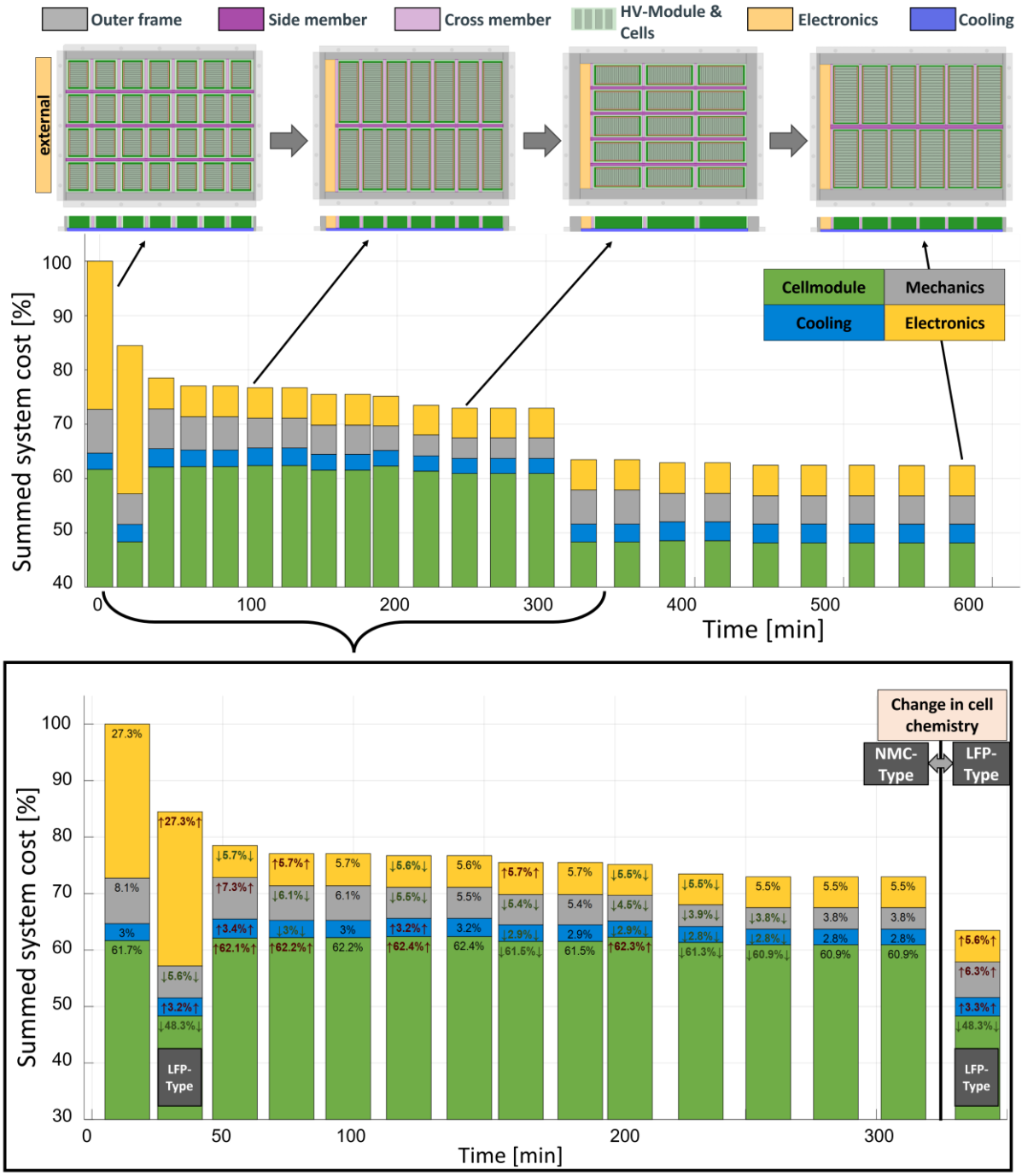

Figure 6.2: Cost optimization results of the HV-BOT for inputs from Table 4.9, including exemplary illustrated battery systems from the top and side view. Cost distributions are depicted for each submodel. 100% is defined from the first found feasible configuration. The change from NMC-Type cell chemistry to LFP-Type cell chemistry is marked. The sample rate of the top and bottom plots equals four.

6.3 Cell integration analysis at the system level

A cell and module geometry trade-off in cellmodule packaging has been executed and discussed in detail in Chapter 3. In addition, this chapter examines cell integration capability at the system level. For this purpose, prior-defined cell geometries are first

integrated into a fixed overall system design space. The graphical output, as well as the cost and weight comparisons, allow for an in-depth comparison of the integration capability.

In the second part of this chapter, one cell is set geometrically fixed. Subsequently, a cost sensitivity for varying overall system installation spaces is investigated. Thereby, the phenomenon of undersized and oversized systems will be stressed and quantified.

6.3.1 Cell integration analysis for different cell formats

This chapter analyzes the cell integration capability for two different battery cells. The evaluation compares the cost shares for the corresponding system integrations. The two different cells and further inputparameters are defined in Table 6.2.

Inputparameter (user-defined)	Value
General	
System installation space x,y,z	1800.0 x 1400.0 x 150.0 mm³
System energy demand	74.0 kWh
System power demand	150 kW
System charging time demand	25 min
System voltage demand	400 V
System usable battery DOD	96%
Cellmodule	
Cell geometry	Two observed cells: Prismatic: 200 x 30 x 117 mm³ Pouch: 450 x 12.5 x 113 mm³
Maximum number of cellstacks per module	1
Cooling	
Ambient temperature	23.0 °C
Number of passes for cooling tube	2
Design current profile	Quick charging profile
Refrigeration circuit expansion stage	Medium
Mechanics	
Crashenergy requirement	15 kJ
Cellstack integration (only for prismatic cells)	Screwed cellstacks
Electronics	
Integration mode	3

Table 6.2: HV-BOT inputparameters for analyzing the system integration capability of two different battery cells.

The resulting battery system integrations for both cells are depicted in Figure 6.3. Additional information is illustrated describing the profile cross-sections of the outer profiles as well as the cooling plate topology.

The prismatic cell integration shows a system with a total of ten cellstacks. Two stacks along the long battery side and five stacks along the short battery system side. The electrical system interconnection is 100s2p. A much wider outer profile was used for the short battery side than for the long battery side. A one-sided bottom cooling was determined for the system.

The pouch cell integration shows nine larger cellstacks, with three stacks along both the long and short sides of the system. The electrical interconnection is 99s2p. In contrast to the prismatic cell system, the outer profile (cross-section) of the long side is significantly wider than on the short battery side. A two-sided cooling plate is derived from the solution. This two-sided cooling plate results from, e.g., the higher energy density on the cell level and, thus, higher current and local heating losses. The pouch cell has a geometrically smaller volume than the prismatic cell (roughly 10%). However, both systems fulfill the energy requirement of 77 kWh, and the number of cells is almost equal. Therefore, the pouch cell needs higher energy density to fulfill the energy requirement.

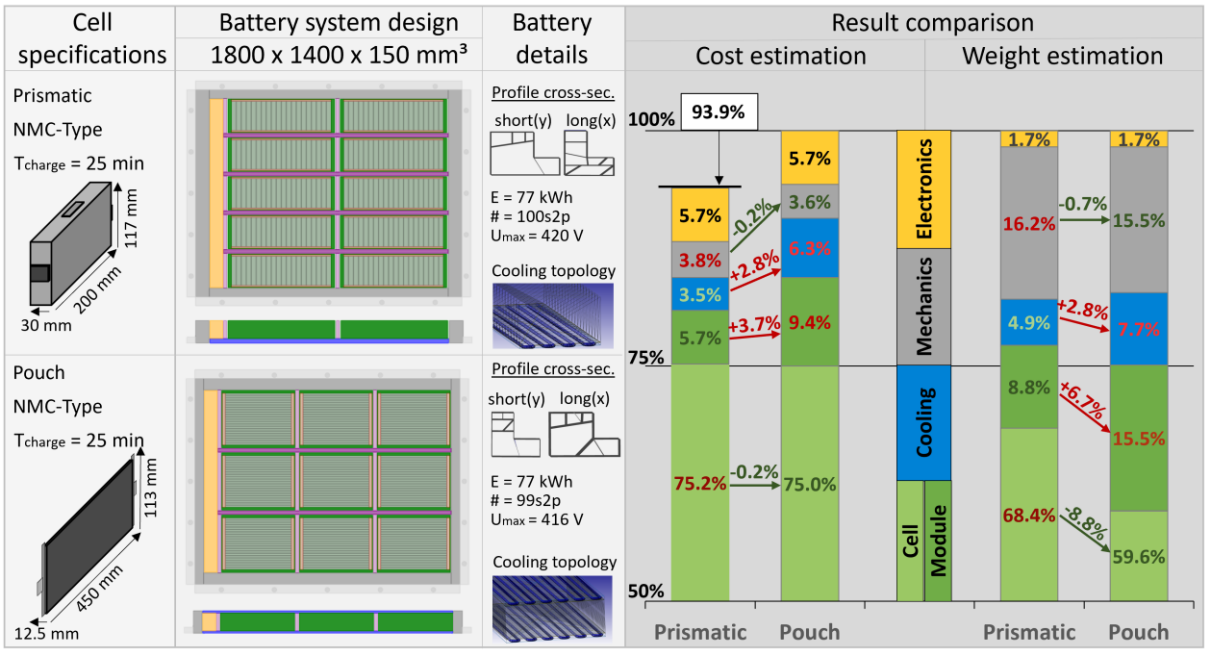

Figure 6.3: Result comparison of the system integration for two different cell formats and geometries (see Table 6.2).

In order to compare the optima of configurations, a cost and weight share breakdown is depicted on the graphic's right side. In this comparison, the prismatic cell configuration on the left-handed side shows small disadvantages in the costs on the cell level. However, module packaging costs are increased for the pouch cell. The main reason is the more complex structure of the pouch cellstacks, for example, due to the geometrically larger cell-to-cell spacing areas. While the larger cellstacks require less mechanical structure within the battery frame and thus show lower costs in the mechanics, there are high additional costs associated with double-sided cooling for the pouch system. The electronics costs are equal.

The weight comparison shows an equal summarized weight for both configurations. The lower overall weight of the pouch cell system mainly results from the weight advantages on the cell level. As the volumetric and gravimetric energy densities are modeled in relation to each other, the increased energy density leads to the weight advantages for the pouch cell. However, this weight advantage on the cell level is compensated by heavier packaging as well as extra weight for the double-sided cooling plates. The system's mechanics are heavier for the prismatic cell configuration, leading to an equal weight comparison.

The material aluminum cost plays a significant role in almost every component group. Examples are the cell cup of the prismatic cells, the front, end, side, and cover plates in cell packaging, the cooling plate, or the mechanical inner and outer profile structure. Therefore, a change in the cost of materials may significantly impact the overall cost distribution. To investigate sensitivities in system costs, the assumed costs for all metals were varied in Figure 6.4.

The comparison shows that the cost variations only slightly change the overall result. Increasing the metal costs lowers the total cost differences between the two system integrations slightly while decreasing the metal cost increases the cost differences. The reason for this is the higher total mass of the system with prismatic cells. In particular, the cost differences for the mechanics, module packaging, and overall electronics costs show a larger sensitivity to the metal cost variations. However, the integration with prismatic cells remains overall advantageous from a cost perspective.

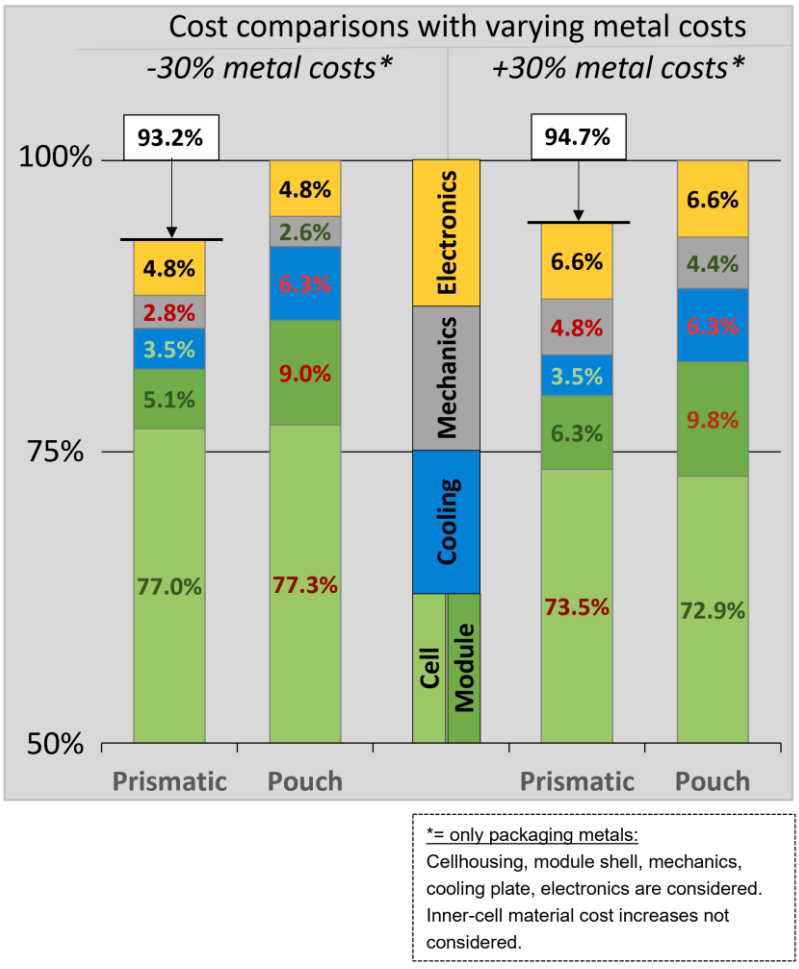

Figure 6.4: Cost comparison for varying assumptions in metal costs. The graph illustrates the comparison of prismatic versus pouch configuration for varying costs. 100% corresponds to the more expensive configuration in both scenarios (prismatic versus pouch).

6.3.2 Comparison of variable installation volumes

This chapter stresses the sensitivity of the overall battery system installation space given one predefined prismatic battery cell geometry. Next to the internal optimization of the submodel-concept (first layer optimization, see Chapter 4.4) and the optimization of the space allocation using the design variables (second layer optimization, Chapter 6.1.1), the overall available installation space is optimized in this chapter (third layer optimization). The individual optimization layers are shown schematically in Figure 6.5.

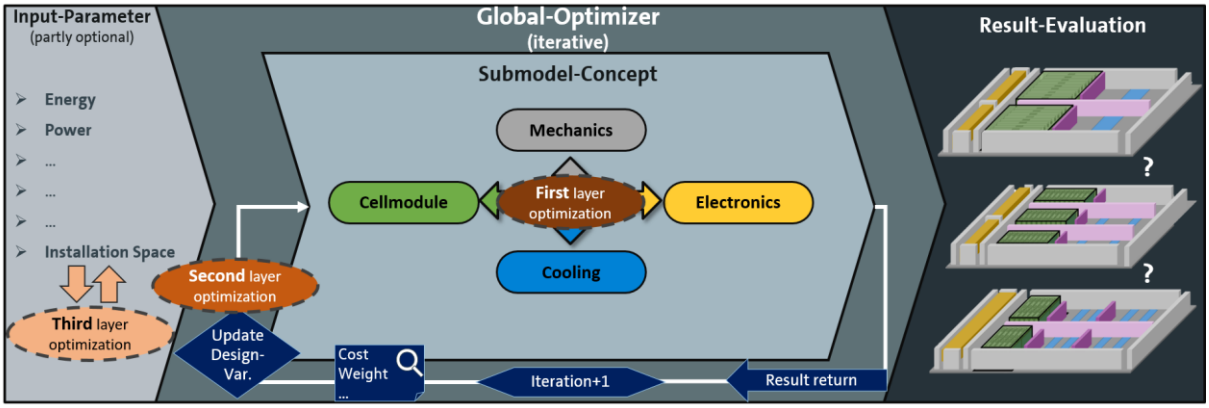

Figure 6.5: Flow diagram of the HV-BOT. The three layers of optimization are marked.

The installation space distribution is optimized by sampling through a wide range of installation spaces. The range includes 17 installation spaces from 1400.0 x 1000.0 x 150 mm³ up to 2200.0 x 1400.0 x 150.0 mm³. The inputparameters are set fixed for each installation space. The comprehensive list of inputparameters is given in Table 6.3.

Inputparameter (user-defined)	Value
General	
System installation space x,y,z	Variable, see Figure 6.6
System energy demand	50.0 kWh
System power demand	140 kW
System charging time demand	25 min
System voltage demand	300 V
System usable battery DOD	98%
Cellmodule	
Cell geometry	Prismatic: 170 x 25 x 115 mm³
Maximum number of cellstacks per module	2
Cooling	
Ambient temperature	23.0 °C
Number of passes for cooling tube	2
Design current profile	Quick charging profile
Refrigeration circuit expansion stage	Basic
Mechanics	
Crashenergy requirement	15 kJ
Cellstack integration (only for prismatic cells)	Screwed cellstacks
Electronics	

Integration mode	3

Table 6.3: HV-BOT inputparameters for total installation space analysis with cost comparisons.

Figure 6.6 shows the different installation space configurations, excluding the constant height, on the x-axis. The y-axis represents the normalized costs of the configurations. Thereby, the most expensive configuration represents 100%. The graphic can be divided into three areas. The areas are separated by different cell chemistry clusters. Each cluster has constant costs at the cell level (light green color). Furthermore, the same cell with identical properties and equal electrical module topology is installed in each configuration within one cluster. Cell level requirements (and thus cell chemistry) can only change if a further p-connection of cells fits into the respective module installation space considering the system voltage requirement. Thus, the built clusters are the NMC-Type area, the high power (low energy) optimized NMC-Type area, and the LFP-Type area. Each area shows a parabolically-formed total cost course around the optimal installation space. The NMC-Type optimum is at the configuration of 1600 mm x 1000 mm. Smaller systems resulted in extensively higher costs for mechanics resulting from the usage of massive materials or profiles as most of the space has been used for the cellmodules. For the smallest possible configuration at 1400 mm x 1000 mm, external electronics are needed, which is assumed with high additional costs (see Chapter 4.3.4), leading to high overall costs. For geometrically larger systems, the costs for mechanics and cooling increase again, indicating partly oversized system spaces.

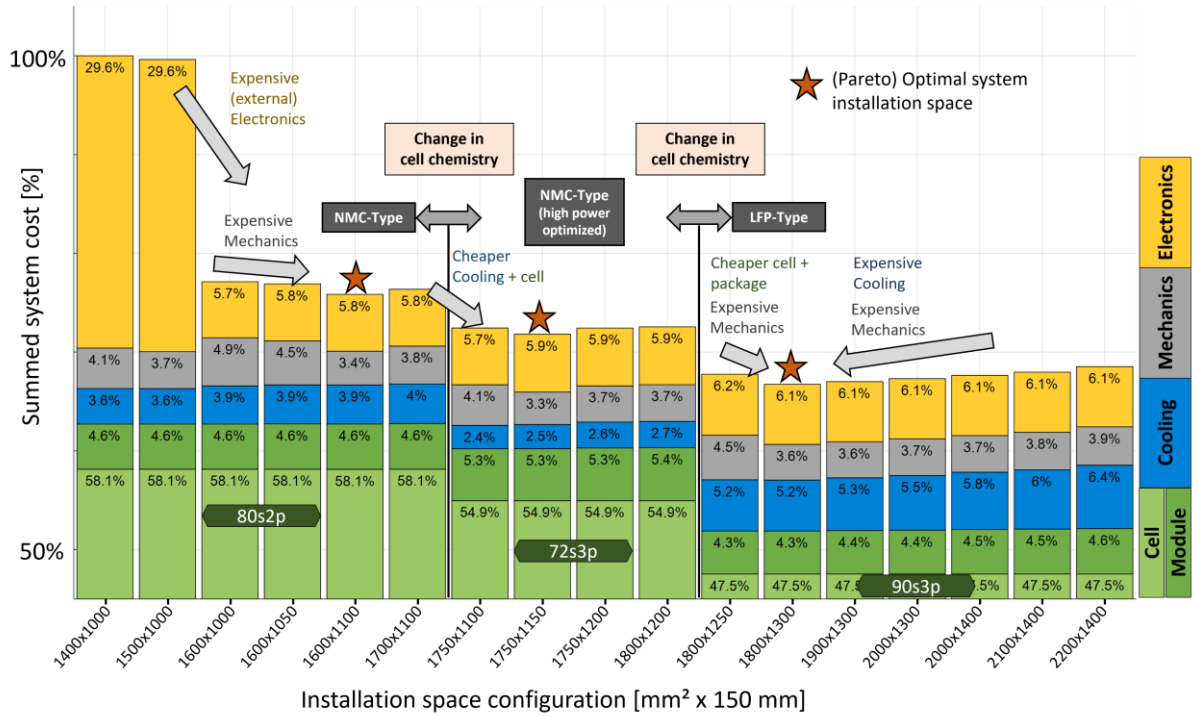

Figure 6.6: Result representation for total installation space cost comparisons. The cost distribution per submodel is given for different installation spaces. Each installation space was separately optimized, given user inputs from Table 6.3.

The same phenomenon can be seen for the optimum in the high power NMC-Type and LFP-Type areas. The former especially shows advantages in cooling costs, indicating the sufficiency of a one-sided cooling plate for the optimized NMC-Type cell. The latter also includes the global optimum, as the cell costs are evaluated as significantly lower.

In summary, a pareto-optimal installation space can be found for each cell chemistry area. In real-world usage, the optimal system installation could then be selected on the basis of the actual vehicle and its available installation space for the battery system.

6.4 Cell optimization for different geometric battery system design spaces

The last chapter investigated the integration capability of fixed cell formats and sizes. In this chapter, the cell geometry is defined variable and will be optimized based on the given requirements at the system level. Three vehicle classes (small, medium, and large) were defined to derive a spot-on optimized battery cell. An overall optimization was performed for each of the systems. A distinction is made between prismatic and pouch cell format results.

6.4.1 Prismatic cell optimization

The prismatic cell results are shown in Figure 6.7, focusing on the optimal cell size. Furthermore, the resulting cost shares are compiled for comparison.

The resulting three battery systems for the three vehicle classes look similar in packaging. Furthermore, each system is equipped with a 1p interconnection emphasizing large cells to be generally cost-optimal. Nevertheless, some significant differences between the three configurations can be identified. Three different prismatic cell geometries are determined for each of the three vehicles. The cell geometries depend, in particular, on the selected voltage level and, therefore, on the minimum number of cells required. The small system is equipped with an LFP-Type cell.

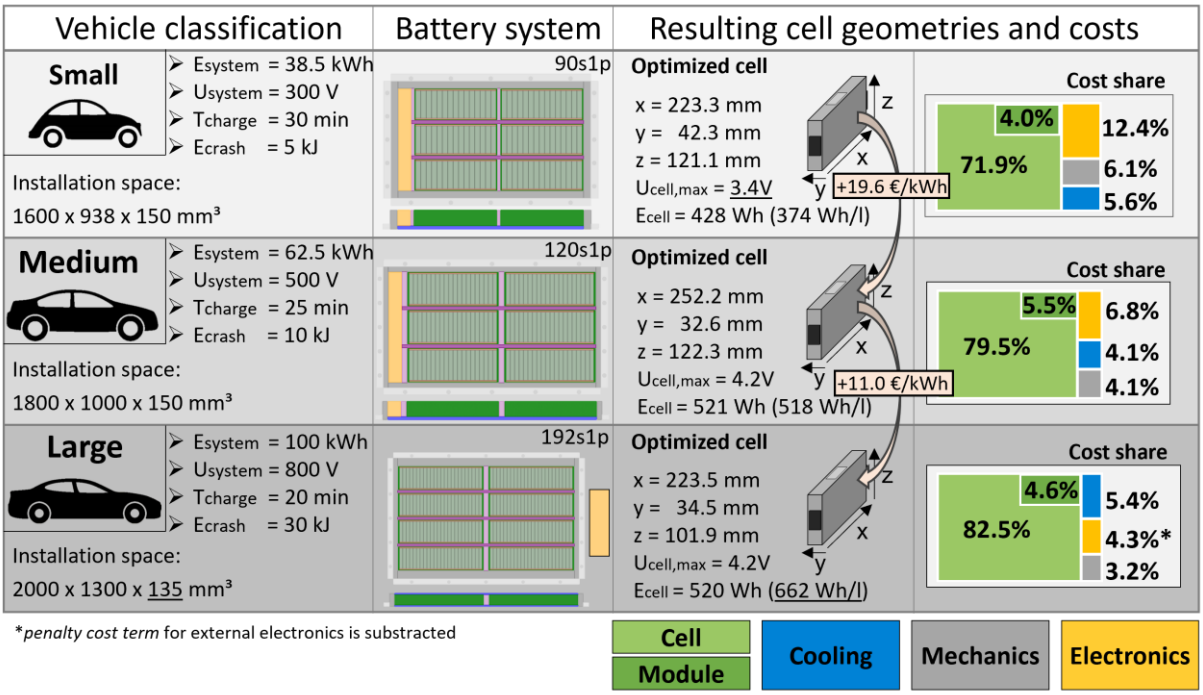

Figure 6.7: System level prismatic cell geometry optimization for different exemplary vehicle classes.

For the small battery system, the cell costs account for roughly 72% of the total costs. Therefore, major cost optimization potential can be found in the other main component groups. For example, the system's relatively wide outer frame profile emphasizes that the outer profile was optimized using additional installation space to be lighter while still fulfilling the crash requirements.

The medium system's share of cell costs is almost 80%. Due to the single-sided cooling and the simple system design, further component costs are kept low. Compared to the small system above, the module packaging costs are significantly higher since the NMC-Type battery cells require more complex and, therefore, weight- and cost-intensive packaging.

More than 80% of the costs for the large system are attributable to the cell costs. The cell costs are increased because the cell has to offer high power/charging and energy requirements. Additionally, the cell is geometrically significantly smaller. Due to the resulting high cooling requirements, the cost share of cooling is also significantly increased. This results from a stronger cooling circuit capacity, stronger water pumps, and a double-side cooling plate.

6.4.2 Pouch cell optimization

The pouch cell results are shown in Figure 6.8. Furthermore, the resulting cost shares are again compiled for comparison.

The resulting three battery systems for the three vehicle classes again look similar in packaging. However, compared to the results with prismatic cell format, the pouch cells are rotated by 90°. Due to the high length flexibility of the pouch cell, rotating the cell can be particularly advantageous for the mechanical design to fulfill the crash

requirement. Three different pouch cell geometries are determined for each of the three configurations. The cell geometries depend, in particular, on the selected voltage level and, therefore, on the minimum number of cells required. The small system is again equipped with an LFP-Type cell.

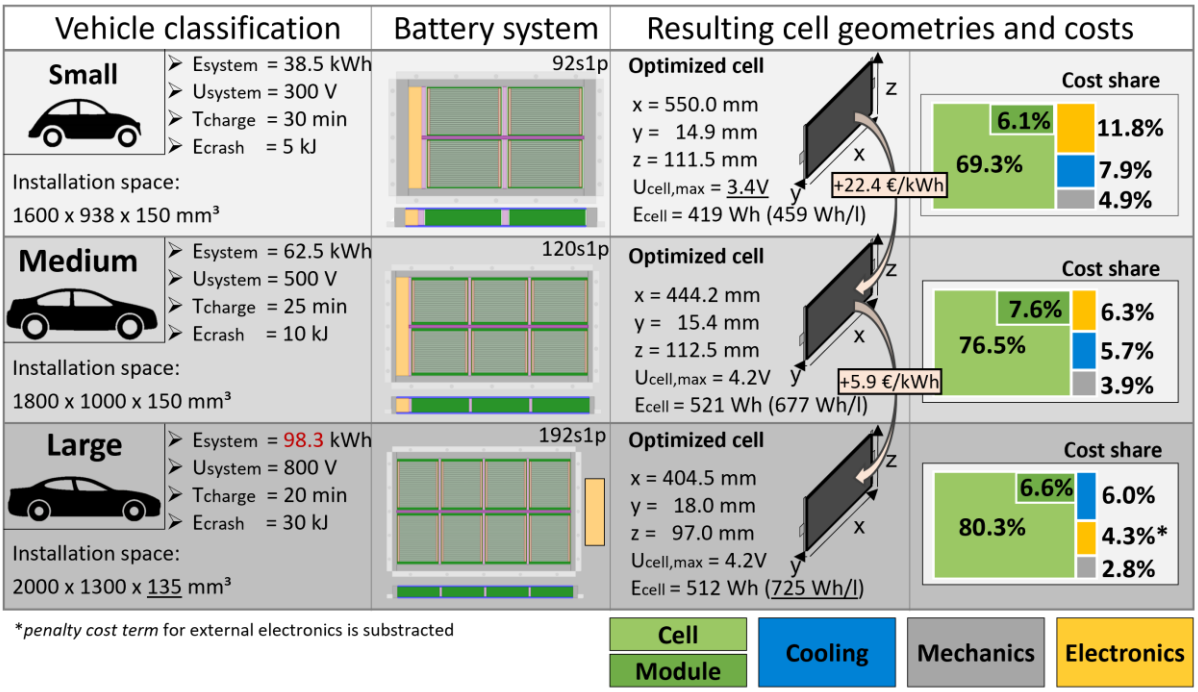

Figure 6.8: System level pouch cell geometry optimization for different exemplary vehicle classes.

For the small battery system, the cell costs account for less than 70% of the total costs. The large size of the cell allows the use of only four cellstacks. Moreover, the system is optimized with a double-sided cooling plate. In-depth results analysis showed that the global optimizer also found results with a one-sided cooling plate but did not evaluate it as optimal due to the higher cost of the other components, especially the module packaging, and mechanics. The results with a one-sided cooling plate showed multiple smaller cellstacks, offering a more distributed heat exchange.

For the medium system, the share of cell costs is roughly 76%. A double-sided cooling plate is evaluated as optimal again. Compared to the small system, the module packaging costs are significantly higher since the NMC-Type battery cells require more complex and, therefore, weight- and cost-intensive packaging.

For the large system, roughly 80% of the costs are attributable to the cell costs. The cell costs are increased because the cell has to offer high power/charging and energy requirements. The energy requirement of 100 kWh could not be achieved by the pouch cell, as the volumetric energy density on the cell level is limited to a maximum of 725 Wh/l (see Chapter 8.1.3). Therefore, the system large has roughly 98 kWh.

In summary, the results also emphasize large cells to be cost-optimal, as each system is equipped with a 1p interconnection. Additionally, pouch cell systems show smaller spans between the cross members. This results from their lower inherent stiffness for the crash load case. Stacking the pouch cells across the system can help fulfill the crash requirement. One resulting conclusion from using smaller cellstacks is that an

overall larger number of cellstacks is required. This leads to more packaging and may reduce the degree of utilization. An overall comparison of the pouch cell results with those of the prismatic cell stresses this aspect.

6.5 Comparison of installation space sizes for optimized battery systems

The last chapter has shown that optimal cell geometries depend on the system geometry and the corresponding system requirements. In this chapter, variable prismatic cell geometries will be additionally investigated on the basis of variable total installation spaces.

6.5.1 Comparisons in large-area installation spaces

This chapter will perform a sensitivity analysis with respect to the total volume of the system and its geometric shape. For this purpose, eight different volume sizes with five different geometries were defined, as shown in Table 6.4. Other technical parameters were set fixed to values listed in Table 6.5. Afterward, costs for the optimal battery system for every installation space configuration are compared.

Volume Geometry	**A: 1.5 m² x 0.15 m**	**B: 1.7 m² x 0.15 m**	**C: 1.9 m² x 0.15 m**	**D: 2.1 m² x 0.15 m**	**E: 2.3 m² x 0.15 m**	**F: 2.5 m² x 0.15 m**	**G: 2.7 m² x 0.15 m**	**H: 2.9 m² x 0.15 m**
Geom. 1 (x,y)[mm²]	1200 x 1250	1300 x 1308	1400 x 1357	1500 x 1400	1600 x 1438	1700 x 1471	1800 x 1500	1900 x 1526
Geom. 2 (x,y)[mm²]	1300 x 1154	1400 x 1214	1500 x 1267	1600 x 1313	1700 x 1353	1800 x 1389	1900 x 1421	2000 x 1450
Geom. 3 (x,y)[mm²]	1400 x 1071	1500 x 1133	1600 x 1188	1700 x 1235	1800 x 1278	1900 x 1318	2000 x 1350	2100 x 1381
Geom. 4 (x,y)[mm²]	1500 x 1000	1600 x 1063	1700 x 1118	1800 x 1167	1900 x 1211	2000 x 1250	2100 x 1286	2200 x 1318
Geom. 5 (x,y)[mm²]	1600 x 938	1700 x 1000	1800 x 1056	1900 x 1105	2000 x 1150	2100 x 1900	2200 x 1227	2300 x 1261

Table 6.4: Definition of the testing matrix for installation space analysis. The scenarios differ in the geometric format as well as overall installation volume. Only values of x- and y-dimensions were altered. The height of the systems (z-direction) was set fixed to 0.15 m.

Inputparameter (user-defined)	**Value**
General	
System energy demand	60.0 kWh
System power demand	100 kW
System charging time demand	20 min
System voltage demand	400 V
System usable battery DOD	96%
Cellmodule	
Cell geometry	Flexible prismatic geometry [min., max.]: Length: [80, 280] Thickness: [20, 35]

	Height: max. possible
Maximum number of cellstacks per module	2
Cooling	
Ambient temperature	23.0 °C
Number of passes for cooling tube	2
Design current profile	Quick charging profile
Refrigeration circuit expansion stage	Basic
Mechanics	
Crashenergy requirement	20 kJ
Cellstack integration (only for prismatic cells)	Screwed cellstacks
Electronics	
Integration mode	3

Table 6.5: HV-BOT inputparameters for the installation space analysis.

The results are depicted in Figure 6.9. The top side of the figure shows the geometric system configurations. Thereby, the x- and y-axes show the corresponding installation space size. Equivalent volume lines mark the set of geometric shapes within one system installation space volume. Each system installation space configuration is indicated with a letter from A to H and a number from 1 to 5. The letter describes the corresponding system installation space volume. The number defines the observed installation space geometry. The configuration number can also be found in Table 6.4. A line divides the optimized cell chemistry areas of NMC-Type and LFP-Type configurations.

The bottom side shows the corresponding cost-optimized results in a bar graph. Each bar depicts the optimized resulting overall costs for one geometric system installation space configuration. Within each bar, the cell costs are individually marked in green color. The NMC-Type and LFP-Type areas are divided by a line. In both areas, the optimal results from an overall cost perspective as well as the cell cost perspective are marked with a green (cell costs) or black (overall costs) star symbol. Some configurations were not observed as they had optimized results with external electronics, which this chapter will not discuss.

In the NMC-Type area, a general decreasing course in overall costs from smaller to larger systems can be observed. This results from the summarized costs for mechanics, cooling, electronics, and the cellmodule. Larger systems also lead to the possibility of using larger cell sizes. The larger cell sizes can further lead to decreased system costs. However, compared to the overall system costs, it can be seen that the cell costs do not follow the same strict decrease of costs. Therefore, the lowest cell costs are achieved within configuration C2 (see Table 6.4). The global cost optimum for the NMC-Type area is located at configuration D5. Generally, the smaller volumes B and C show larger cost differences within one volume. Thereby, geometries lying at the outer borders show slightly higher costs. Unfavorable installation space geometries or the general under- or oversizing of the system lead to increased costs in cooling, mechanics, or electronic components.

The cost in the LFP area is significantly flatter. While cost differences within a volume become smaller with rising system volume, the cell costs show a strictly decreasing trend. Thus, the lowest cell costs can be found in configuration H3. However, since the effects of over-dimensioning appear, the overall optimal system costs are not located in this configuration but in configuration F5.

Since the battery system space in EVs is severely limited, those configurations with lower system costs and smaller installation space volume represent likely superior overall results than low-cost configurations in larger volumes. However, specific vehicle restrictions can often limit the possible battery installation length or width. In these cases, a geometry with higher volume and the same cost can be advantageous from the overall vehicle perspective.

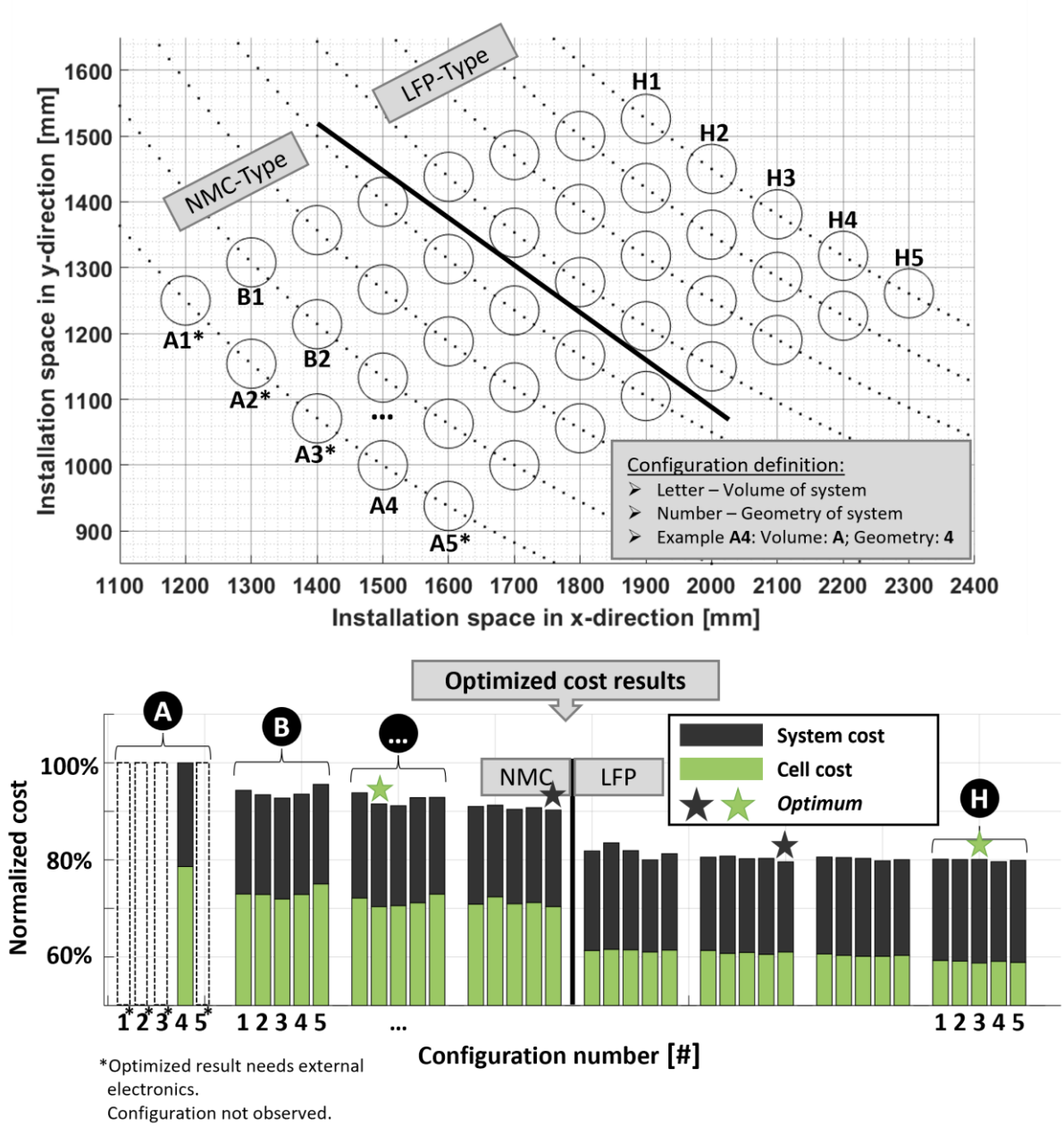

Figure 6.9: Summarized results of optimized costs for different battery system installation spaces for a sensitivity analysis.

Given the inputparameters from Table 6.5, a large number of partially pareto-optimal results were derived and analyzed based on overall and cell level costs. The results stress that the HV-BOT effectively identifies promising installation spaces. It was shown that the optimal design space selection is not trivial, especially when using a variable prismatic cell format. In a second step, each of the pareto-optimal results could

be evaluated in a detailed analysis to observe the actual packaging with the corresponding mechanical design and, furthermore, compare the system's weights.

6.6 Cell design for different stages of battery cell to pack integration

To simultaneously increase EV performance while further reducing overall costs, the components besides the cellmodule must be spot-on optimized. Novel cell integration methods like cell to pack, cell to chassis, or cell to car promise the extensive potential to reduce both the battery system's weight and costs. In simple terms, cell to pack describes the engineering to integrate the battery cells directly into the battery housing without being bundled into separately housed modules. Cell to car means that the cells are even deeper integrated and inserted directly into the vehicle floor and thus become an integral part of the chassis construction (which can be the battery frame). The gained installation space from reducing mechanical structures can be used to bring more energy and power into the battery system using larger cell formats [386].

Due to the variable parameterization of the submodels presented in Chapter 4.3, the HV-BOT can evaluate major changes in the cell packaging. This chapter is intended to stress the differences between the different integration levels and compare and ultimately quantify the evaluated battery systems in terms of weight distribution and possible cell size.

Changes to multiple boundary conditions and model assumptions are used to depict the integration stages of the battery cells within the EV. A comprehensive summary of the six evaluable integration stages is given in Table 6.6. Since no formal definition of the terms cell to module, cell to pack, or cell to car exists, the individual stages are defined based on the corresponding assumptions and further subdivided into partial integration stages by the additional terms basic, advanced, and holistic. After definition, each stage is evaluated and compared quantitatively (see Figure 6.10).

Stage	Naming	Submodel and parameter assumptions	Description, derivation, evaluation
1	Cell to module	Module housing: Front/Back = default Sideplates = 5 mm Cover/ Bottomplate = 5 mm No. stacks per module = 1 Crashenergy = 15 kJ No intrusion of cellmodule Number of modules: Nx = 4 Ny = 4	Individual module units for high modularity. Modules often with thicker housing. Cellmodules only used for energy and power providence, not as mechanical components of the battery system. Ideal for simple battery system construction with varying system energy options. Good recyclability. Good repairability.
2a	Cell to pack (basic)	Module housing: Default: see Chapter 4.3.1.3	Cellstacks integrated directly into battery system. Remaining battery cell "boxes" but with less overall cellstack housing.

		No. stacks per module = 1 Crashenergy = 15 kJ Intrusion of cells allowed. Number of modules: Nx = 2 Ny = 4	Cellstacks are used for energy and power providence, additionally for mechanical stiffness of the battery system. Ideal for novel battery system construction with less weight/ more space for larger cell geometries. Medium modularity. Good recyclability. Medium repairability.
2b	Cell to pack (advanced)	Module housing: Default: see Chapter 4.3.1.3 No. stacks per module = 2 Crashenergy = 15 kJ Intrusion of cells allowed. Number of modules: Nx = 2 Ny = 2	Multiple cellstacks integrated directly into battery system. Remaining battery cell “boxes” but with less overall cellstack housing. Cellstacks are used for energy and power providence, additionally for mechanical stiffness of the battery system. Ideal for novel battery system construction with lower weight and more space for larger cell geometries. Low modularity. Good recyclability. Medium repairability.
2c	Cell to pack (holistic)	Module housing: Default: see Chapter 4.3.1.3 No. stacks per module = 2 Highly integrated cross members into the cellstack. Crashenergy = 15 kJ Intrusion of cells allowed. Number of modules: Nx = 2 Ny = 2	Multiple cellstacks integrated directly into the battery system. Unifying of cellstacks in which the inner mechanical structure is partly integrated. The remaining cellstacks have less overall housing. Cellstacks are used for energy and power providence, additionally for mechanical stiffness of the battery system. Ideal for novel battery system construction with lower weight and more space for larger cell geometries. Low to no modularity. Medium recyclability. Difficult repairability.
3a	Cell to car (basic)	Module housing: Glued cellstacks (no bottom, cover): see Chapter 8.1.3 No. stacks per module = 2 Highly integrated cross members into the cellstack.	Multiple cellstacks integrated directly into vehicle floor. This enables the vehicle floor to also function as a battery system. This eliminates the need for a dedicated battery cover. Unifying of cellstacks in which the inner mechanical structure is partly integrated. Through glued cellstacks into the overall

		Crashenergy = 10kJ (due to the cell to car approach, crash load partially transferred to further vehicle components) Intrusion of cells allowed. Number of modules: Nx = 2 Ny = 2	vehicle, less energy absorption is necessary on the battery level (increased overall stiffness). The remaining cellstacks have less overall housing. Cellstacks are used for energy and power providence, additionally for mechanical stiffness of the battery system. The battery system is spot-on designed for the required energy requirement. No modularity. Ideal for novel battery system construction with minimum weight and maximum space for larger cell geometries. Difficult recyclability. Difficult repairability.
3b	Cell to car (advanced)	Module housing: Glued cellstacks (no bottom, cover): see Chapter 8.1.3 No. stacks per module = 4 Highly integrated cross members into the cellstack. Crashenergy = 10 kJ (due to the cell to car approach, crash load partially transferred to further vehicle components) Intrusion of cells allowed. Number of modules: Nx = 2 Ny = 1	Multiple cellstacks integrated directly into vehicle floor. This enables the vehicle floor to also function as a battery system. This eliminates the need for a dedicated battery cover. Almost no mechanical structures within the battery system. Through glued cellstacks into the overall vehicle, less energy absorption is necessary on the battery level (increased overall stiffness). The remaining cellstacks have less overall housing. Cellstacks are used for energy and power providence, additionally for mechanical stiffness of the battery system. The battery system is spot-on designed for the required energy requirement. No modularity. Ideal for novel battery system construction with minimum weight and maximum space for larger cell geometries. Difficult recyclability. Difficult repairability.

Table 6.6: Overview of different battery cell-to-system integration stages with different packaging assumptions and derivation.

From the overview above, a variety of challenges with higher levels of integration can already be identified. Deeper cell integration stages offer possible battery system designs with less passive/packaging material. Generally, larger modules contribute to this effect. However, when removing module housing in cell to pack approaches to use the space with energy-storing battery cells, the occurring mechanical loads from, e.g.,

the crash, must be assured partly by the battery cells. The cells then also need to contribute to the mechanical stiffness of the overall battery system.

Cell to car represents an extension of this approach. In cell to car systems, the battery cover can, for example, no longer be required, as the passenger compartment floor replaces it. Structure-maintaining packaging parts or mechanical battery system elements can also be omitted and replaced by, for example, connection parts for the vehicle seats that are available in any case. The integration of several functions on one component generally makes battery systems less complex in their basic structure. However, interfaces are added in vehicle-level development as some existing components are given more functionality. Gluing the cellstacks with the vehicle housing ensures that crash loads can be transferred over the entire vehicle to relieve the load from the battery system and, thus, the battery cell. While these measures are able to increase the system's stiffness overall, they can also significantly reduce recyclability and reparability.

In Table 6.6, inputparameters are defined to evaluate changing battery system energy and corresponding cell geometries depending on the system integration level.

Inputparameter (user-defined)	**Value**
General	
System installation space x,y,z	1600.0 x 1200.0 x 150.0 mm³
System energy demand	Output parameter with fixed cell level energy density of 650 Wh/l
System power demand	160 kW
System charging time demand	Not considered
System voltage demand	800 V (192s1p)
System usable battery DOD	100 %
Cellmodule	
Cell geometry	Variable prismatic cell
Maximum number of cellstacks per module	Variable
Cooling	Not considered
Mechanics	See Table 6.6
Electronics	
Integration mode	0

Table 6.7: HV-BOT inputparameters for the comparative evaluation of different cell-to-system integration stages.

Figure 6.10 shows the results. Thereby, the resulting battery system concept for each of the six integration stages, described in Table 6.6, is illustrated from the top view. In addition, a weight distribution between the components of the cells, module packaging, and system housing is given for each integration stage. Furthermore, the resulting cell geometry and system energy are derived for each result.

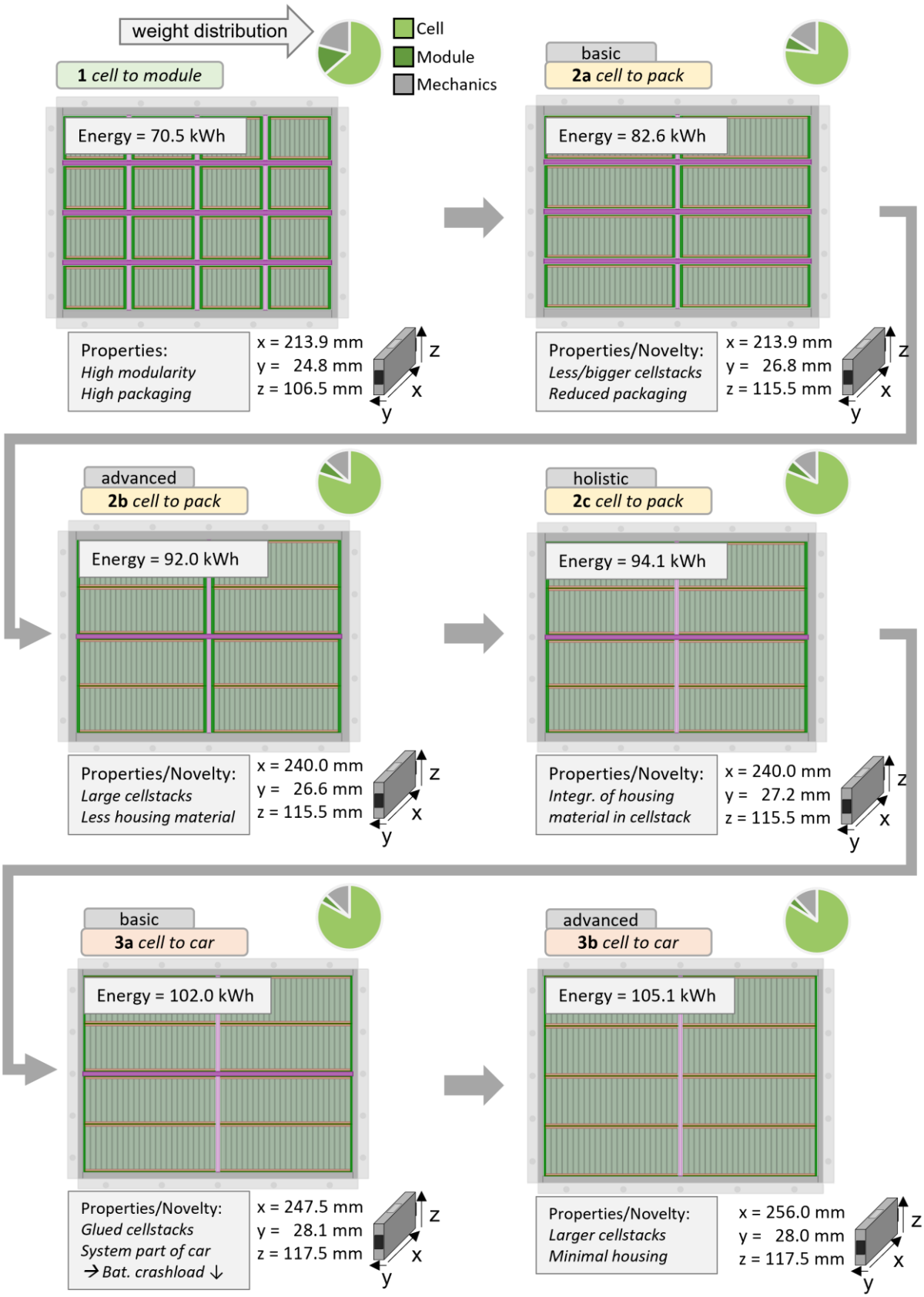

Figure 6.10: Battery system energy and cell geometry comparison of different cell integration stages with inputparameters from Table 6.6 and Table 6.7. System energies are based on 650 Wh/l on the cell level.

The resulting system energy is based on a cell with an energy density of 650 Wh/l. For each stage, properties and novelties of the integration stage are described. Each successive integration level also has properties of the last integration level.

The results show significantly differing battery system designs. In particular, the achieved system energies differ majorly. Particularly striking are the changes from the cell to module to the cell to pack (basic) system. This change is accompanied by the greatest advantages in terms of energy (+17%). Deeper integration steps further increase the energy and, in particular, also reduce the proportion of packaging material. This reduction could transition to a reduction in normalized system costs. The level of savings will be determined, in particular, by the complexity of the production process. However, by ranking the results in terms of repairability and recyclability factors, car manufacturers must make complex strategic decisions to decide for or against a specific level of cell to system integration.

6.7 Investigation of packaging density for different cell formats

This chapter investigates packing density comparisons at the battery system level for different cell formats. Chapter 4.3.1 has derived the geometric stacking for prismatic and pouch cells in detail. For a comprehensive comparison, cylindrical cells are also evaluated in this chapter. Thereby, the basics of cylindrical packaging are briefly described. Specific model and parameter assumptions can be found in the appendix.

6.7.1 Stacking derivation for cylindrical cells

Similar to prismatic and pouch cells, cylindrical cells can be stacked square in the module or system. Due to the cylindrical shape, square stacking results in larger gaps between the individual cells. This aspect was explained and exemplarily quantified in Chapter 3.2. Hexagonal packing is usually used as an efficient stacking method for cylindrical battery cells. Thereby, the stacking logic can be represented in a simplified way using the tessellation of hexagons. From a top view, the cylindrical cells appear as a circle. The “circular” cells are then approximated as hexagons to be volume-efficiently stacked. Figure 6.11 explains this method and derives the resulting maximum number of cells in each direction.

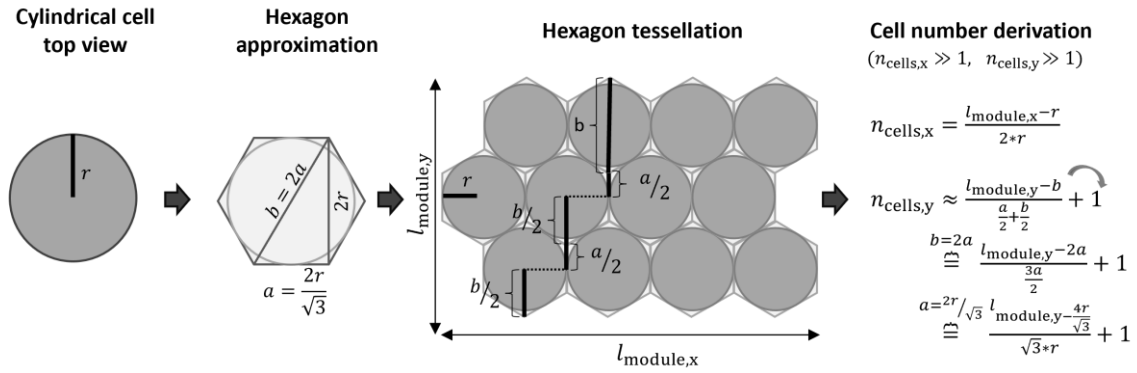

Figure 6.11: Derivation of hexagonal stacking of cylindrical battery cells.

Radius r includes the initial cell radius r_{cell}, and reserved space $\rho_{\text{isolation,swelling}}$ for the cell's isolation, and reserved space for volumetric cell changes (e.g., swelling):

$$r = r_{\text{cell}} + \rho_{\text{isolation,swelling}} \tag{6.1}$$

For this chapter, a reserved space of $\rho_{\text{isolation,swelling}} = 0.1 \cdot r_{\text{cell}}$ is assumed.

6.7.2 Comparison of packaging densities

The following chapter will compare different packing densities for the three established cell formats: prismatic, pouch, and cylindrical. A battery system with 78 kWh, 800V, and a total of eight individual modules is to be built. Further inputparameters are specified in Table 6.8. The respective cell geometry is optimized for each cell format and thus spot-on optimized for the respective system geometry. No cooling or electronics configuration is evaluated for the following analyses.

Inputparameter (user-defined)	**Prismatic**	**Pouch**	**Cylindrical**
General			
System installation space x,y,z	1800.0 x 1200.0 x 130.0 mm³		
System energy demand	78 kWh		
System power demand	150 kW		
System charging time demand	Not considered		
System voltage demand	800 V		
System usable battery DOD	100%		
Number of modules	8		
Cellmodule			
Cell geometry	Cost-optimized variable [min., max.]: length: 80 – 300 mm thickness: 20 – 50 mm	Cost-optimized variable [min., max.]: length: 6 – 18 mm thickness: 140 – 550 mm	Cost-optimized variable [min., max.]: radius: 7.5 – 23 mm
Maximum number of cellstacks per module	2	1	variable
Module packaging	See Chapter 4.3.1		See appendix
Cooling	Not considered		
Mechanics	See Chapter 4.3.2		Same as prismatic
Crashenergy	10 kJ		
Electronics			
Integration mode	0		

Table 6.8: HV-BOT inputparameters for packaging density comparison.

The results of the investigation are summarized in Figure 6.12. The left side shows the resulting battery system with a cylindrical cell format. The system contains a 192s7p topology with a cylindrical cell with a diameter of 32.8 mm and a height of 95.3 mm. By

using the geometric dimensions of the modules and the system, a volumetric efficiency of 59.2% at the module level (mod. dens.) and 38.6% at the system level (sys. dens.) can be derived. The maximum theoretical packaging density for cylindrical cells of $\frac{\pi}{2\sqrt{3}} \approx 0.91$ [387] is reduced due to the reserved space (Eq. (6.1)), the module housing, and the unused space in both the front and end of the cellmodule (see Figure 6.12).

The results for the pouch cell format (top) and prismatic cell format (bottom) are shown on the right side of the graph. The achieved packaging densities at the module level are 63.3% and 74.1%, respectively, and at the system level, 41.3% and 48.4%, respectively.

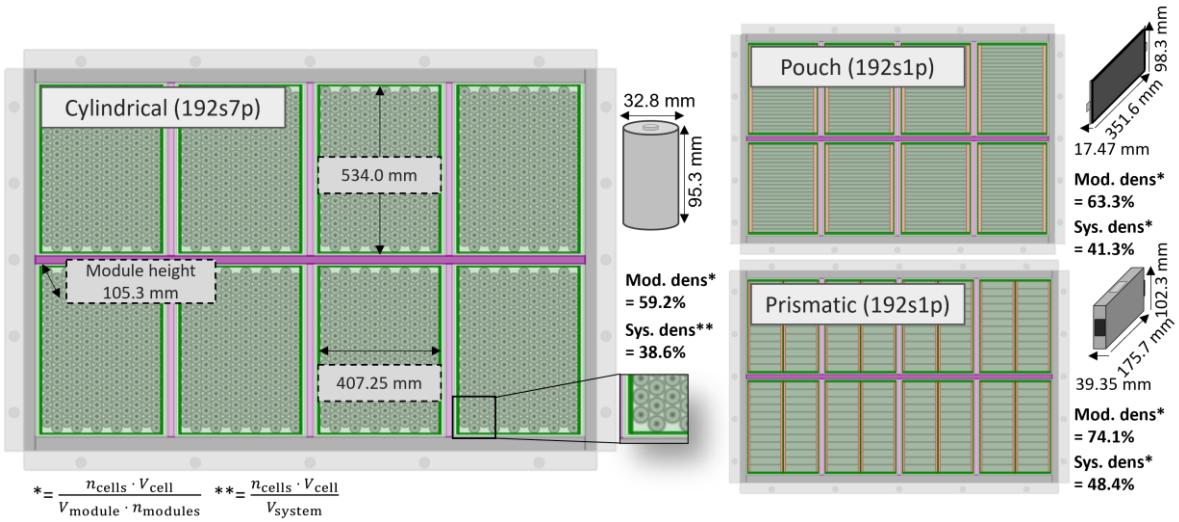

Figure 6.12: Top view on battery system design configurations for each cell format with optimized cell geometry.

A direct comparison of the systems shows a significantly increased number of total cells for the system with cylindrical cells. As a result, the cylindrical configuration has a parallel connection of 7 cells. For the pouch and prismatic cell configurations, the cell size is optimized so that a 1p interconnection can be achieved. This also leads to generally large cell geometries for both formats.

In a direct comparison of packing densities, the prismatic cell format shows significant advantages over the pouch and cylindrical formats. However, it is important to note that these packing densities only measure the cell utilization rate but do not consider that different energy densities can be achieved at the cell level. Therefore, evaluating the global best result depends also on cell level energy densities and the resulting cell costs.

Novel developments in the automotive industry show the industrial-setting larger cylindrical cell formats like the 4680 format established by Tesla. Larger optimal cylindrical cell geometries can be obtained by softening certain system requirements like system voltage, module geometry, or system energy. Battery systems with larger cylindrical cells are depicted in Figure 6.13. Thereby, the battery system concepts are again evaluated based on the inputparameters defined in Table 6.8. However, changes in voltage, module geometry, or energy are examined to stress the changing optimized cell size. For each graphic, the changed parameter from Table 6.8 for each concept is described in the top left corner.

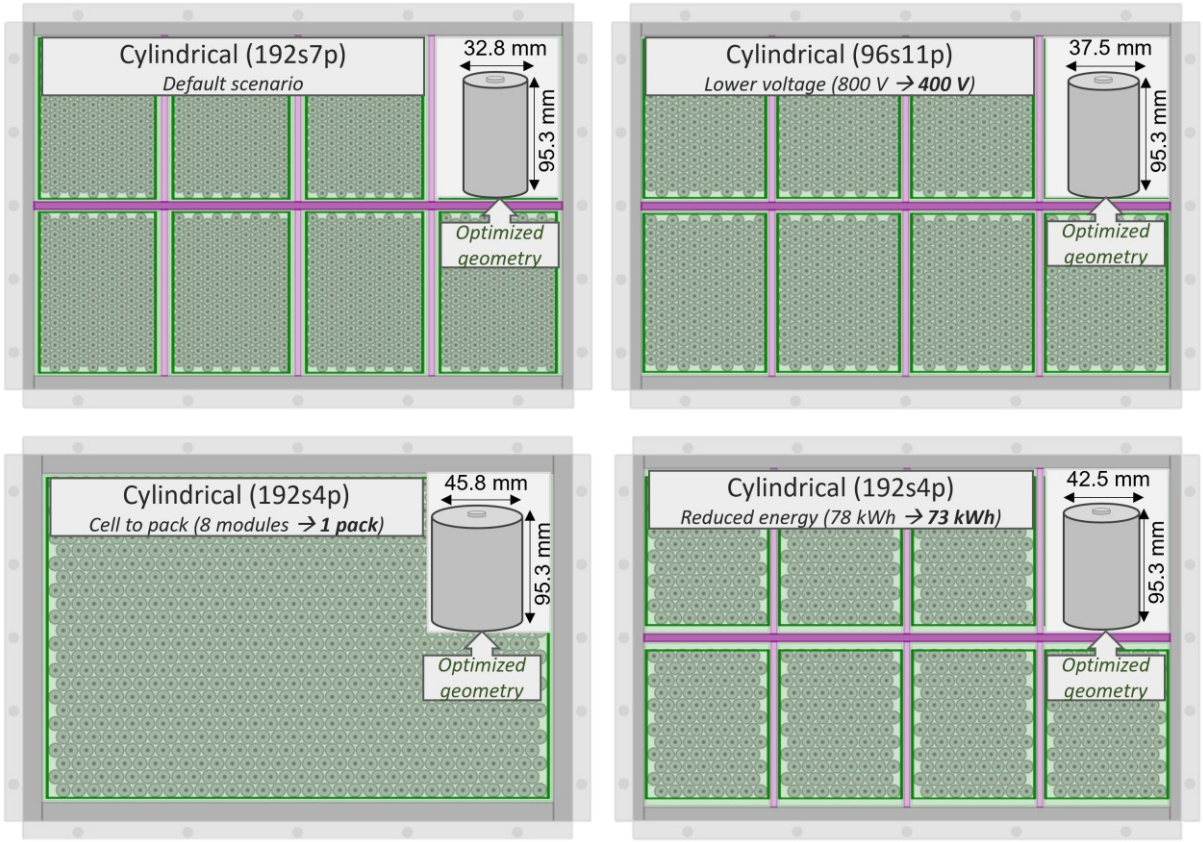

Figure 6.13: Changing optimized cylindrical cell geometries for varying system requirements. Three options for larger optimized cylindrical cell geometries by changing the battery system's structure and requirements.

The results confirm the availability of using larger cell geometries given the softened system requirements. In particular, the cell to pack approach allows the use of large cell formats, as the increased unusable space (due to the larger cell) at the front and end of each module is minimized by using only one module/pack of cells.

6.8 Limitations

This chapter contains a wide range of results with different analysis focuses. The generation of results with the HV-BOT is also associated with several limitations. Direct model-related limitations were addressed in Chapter 4.6. In addition, further advice for the interpretation of results can be given.

The results shown above are based on the assumptions and modeling approaches of the physical simulation models described in Chapter 4. In particular, the different cost assumptions of the individual submodels directly influence the results marked as optimal within this chapter. Sensitivities of cost components were therefore varied in Chapter 6.3.1. While optimal battery system design may slightly change for varying cost assumptions, comparative analyses with different inputparameters, as shown in Chapters 6.3.2 and 6.6, will be largely unaffected. These results are more related to the physical assumptions of battery system modeling. Since the HV-BOT submodels are based on several geometric, electrical, thermal, and mechanical assumptions described in Chapter 4, even small changes in the modeling may influence the final results. Therefore, the assumptions were precisely conditioned based on the latest

literature findings and actual production procedures. Finally, the results also depend directly on the prior-defined inputparameters. Therefore, it is also essential to conscientiously determine the inputparameters used in each analysis.

6.9 Conclusive summary

This study presented multiple usage scenarios, analyses, and potential investigations with regard to optimal battery system design. First, the optimization from Chapter 5 was integrated into the overall HV-BOT framework from Chapter 4. The optimization procedure was then exemplarily presented. Moreover, the selection of the appropriate objective function was also discussed on the basis of different perspectives and then determined for the purposes of this thesis.

Afterward, an in-depth system-oriented analysis of different cell geometry integration as well as optimization of the overall installation space for battery systems with given user-defined and battery system-related requirements, was executed. The cell geometry analysis showed relevant and quantitive differences between the pouch and prismatic cell to system integration capability. Cost and weight comparisons demonstrated the advantages and disadvantages of both formats in system integration. Additional variation in cost assumptions further underlined the differences found. The higher packaging utilization rate from prismatic cells was shown in the cell geometry optimization for different scenarios. The significance of the other battery system components was also emphasized based on the proportional cost distribution. The results indicated that cooling, mechanics, and electronics cost components are highly relevant for entry-level battery systems and tend to decrease for larger battery systems.

The trade-off relationship between the individual main component groups was graphically represented with installation space variation analyses. Furthermore, it was shown that minimizing the cell costs within one cell chemistry does not necessarily lead to the globally optimal result. The aspect of over- and underdimensioning of battery systems was also addressed.

In addition, the novel integration methods of battery cells in the form of cell to pack were discussed and quantitatively evaluated at different stages. Different integration levels were defined on the basis of changing model assumptions. Subsequent evaluations were able to quantify the increase in storable energy through growing cell geometry.

Afterward, cylindrical cell integration within the HV-BOT was derived. The resulting packaging utilization rates for each cell format were compared at the module and system level. Lastly, conditions for the usage of large cylindrical cells were analyzed.

7 Conclusion and outlook

In order to meet rising EV requirements and develop a safe, durable, ecological, and economical battery system, multiple groups of components have to be holistically combined. The system's main components of cellmodule, cooling, mechanics, and electronics already have an inherently high level of complexity. As the battery system's central component, the battery cells show variances and dependencies in performance, size, weight, and cost. Thus, integrating a specific cell within the battery system emerges geometrical, electrical, thermal, and mechanical restrictions and interdependencies within the entire system. This complex coordination process can be supported by holistic simulations, which are capable of evaluating battery system concepts from the cell to the system level.

In this work, a multiphysical simulation-based framework for the design, analysis, and evaluation of high-voltage battery systems was developed. Based on varying EV battery requirements, the framework provides the ability to create digital twins of current and future generations of battery systems. The HV-Battery-Optimization-Tool was used to conduct generic investigations addressing recent battery system design issues. The modeling results and major contributions are summarized below.

7.1 Summary and contribution

Firstly, a generic cellmodule model was conducted, which can be used to evaluate different battery modules based on variable package specifications. The model parameterization represents a range of pooled data from the literature to geometrically model the cell, the cellstack, cell-to-cell distances, module housings, and further sizes. Applicability is presented by contrasting different pouch and prismatic cells at the module level. The resulting energy densities stress the trade-off between cell size and flexibility in battery module packaging. Next to module design, optimized cell selection is also a complex task. Therefore, cell geometry optimizations were illustrated in a differentiated evaluation from an energy and cost perspective. A weighting model was used to consolidate both perspectives. Validation was executed using actual cellmodule configurations from two different EVs in the field.

Secondly, in order to investigate entire battery systems, the cellmodule model was coupled with further battery system-related submodels creating an interconnected framework. Thus, in addition to the cellmodule, also the mechanical system integration, the design of the electronics, and the cooling capability of the battery can be investigated. A novel parameterization of the overall system installation space allocates each major component fixed space in which it can optimize itself depending on the outcomes of the other components. By changing the space allocation iteratively, different battery system concepts can be evaluated and compared to each other. Given specified battery requirements, the framework thus offers the generation of interconnected digital battery system twins with individual specifications.

In order to develop the framework's component-submodel-concept, the geometric cellmodule model was first extended by a cell-specific electrical and thermal model. Thereby, the specified battery cell is designed based on the battery system requirements like installation space, energy, voltage, and charging power. Furthermore, the compatibility of energy and power was evaluated at the cell level from

different perspectives leading to changing aging-scenario-dependent packaging requirements.

Next, a mechanical model designs the battery system's frame based on crucial EV homologation requirements. Thereby, evaluations are based on the exact mechanical properties derived from the optimized cellmodule. Additionally, an internal mechanical optimization distributes the available installation space to minimize both weight and costs. Multiple surrogate load cases were developed to represent the dependencies of the mechanical outer and inner structure. Thus, novel cell integration approaches like cell to pack can be analyzed and quantified. Similarly, the electronics' integrability in the system was evaluated as a function of system power and voltage. Also, a thermal cooling plate model evaluates the cooling capability of the cellmodule based on demanding load profiles. The internal cooling optimization varies the cooling plate's tube sizes, gap fillers, and required coolant flow rates to derive a cooling circuit that meets the requirement while simultaneously optimizing costs. The chosen modeling approach allows quick evaluation of several cooling plate topologies using a novel reduction procedure that couples the transient models' accuracy with the steady-state models' computation time advantages.

After deriving the main component's simulation models, a multitude of interfaces was specified to consolidate all models with each other and ensure a mutual evaluation of battery system concepts. Illustrative examples stressed component sensitivities between changing battery system concepts. To validate the framework approach, real-world battery systems were reconstructed and analyzed in-depth.

Thirdly, an optimization methodology was developed incorporating both the information about the feasibility of a battery system as well as the cost or weight estimation. The combination of the classification and regression problem was modeled using multidimensional Gaussian processes. Thereby, the total solution space is divided into several areas. The different areas are predictively sampled using area-targeted search criteria to either find additional promising solution areas or to improve already found results. This optimization methodology enables the overall design space to be optimized within a few millimeters. Method validations also showed promising results for other non-linear optimization problems.

Lastly, several applicative optimizations and conclusive battery system design guidelines were derived. Thus, the integration capability for different cell formats and sizes was deeply investigated at the cell, module, and system levels. Moreover, subsequent optimizations of the installation space with a fixed prismatic cell underlined the aspect of undersized and oversized battery systems. Thereby, a cost trade-off balancing between individual component groups was graphically demonstrated. Pareto-optimal system installation spaces were identified for different cell chemistry clusters. The results also illustrated the cost relevance of the other main component groups besides the cellmodule. Afterward, cell geometry optimizations were performed for three different classes of battery systems. Besides the changing spot-on optimized cell geometries, the results especially indicated the changing relevance of the other component groups. Next, different cell integration stages were discussed. Thereby, cell to pack was analyzed by defining different stages with varying cell packaging assumptions. For this, a comprehensive overview of the properties of various levels of integration was first compiled. The influence on the cell size and the resulting system energy was then extracted and quantified for the prismatic cell format. Lastly,

packaging investigations for the cylindrical cell format were conducted to compare utilization ratios for all three cell formats at the module and system levels.

7.2 Outlook

This thesis aims to address optimizations of battery system design for different major component groups based on vehicle-specific inputparameters. The modeled framework can already be used to emulate battery systems as digital twins. This feature may enable reaching an even higher simulative integration state in the form of a holistic EV optimization framework, in which the HV-BOT could be used as a subunit for the vehicle's optimized battery system. Additionally, the modular approach of the HV-BOT offers an ideal workspace for further improvements. Thus, to selectively detail the battery system design on a simulation basis, additional work could be taken in developing the simulation models. Suggested enhancements are:

- Extending the overall framework/submodels for the cylindrical cell format (intercell cooling, mechanics)
- Adding cell data of additional cell chemistries (e.g., sodium-ion)
- Modeling of other battery cooling concepts (refrigerant cooling, immersive cooling)
- Addressing further vehicle load cases (e.g., vehicle front crash) and component load cases (e.g., z-shock)
- Depicting the battery electronics as a 3D volume model
- Derivation of a simulation model for thermal propagation evaluation
- Elaboration and extension of the cost and weight models
- Adding recyclability as an essential design premise

With these model improvements, battery systems could be analyzed in even greater detail and accuracy. Adding recyclability and general economic factors will further enhance the level of the evaluability of battery systems.

By recognizing design potentials affecting the environment as well as weight and costs at an early stage, the development of battery systems can become more efficient and, at the same time, more cost-effective. Through industrial competition, this cost reduction will eventually also reach the end customer, making battery-powered mobility overall more accessible. The speed of these advances may have a lasting impact on the progression of climate change and, thus, the resulting impacts on planet Earth.

8 Appendix

8.1 Submodel cellmodule

Exemplary battery cell resistance characteristics can be found in [388]. Temperature dependencies of internal resistances are, e.g., shown in [389].

Cell data is assumed generically and cell-type-dependent (chemistry, format) and, thus, does not describe a specific cell's behavior. In order to evaluate a specific cell, cell type, or cell chemistry, the cell data can be individually exchanged. Resistance values are normalized to a reference resistance $R_{\mathrm{ref.}}$. The reference resistance $R_{\mathrm{ref.}}$ is scaled considering the cell's capacity (see Chapter 4.3.1.4), the aging factor $\alpha_{\mathrm{res.aging}}$, and the quick charging time requirement (see Chapter 4.3.1.5).

8.1.1 NMC-Type reference data

8.1.1.1 Electrical resistance

The values below are factors related to a reference charge resistance $R_{\mathrm{ref.}}(50\%, 25\ °\mathrm{C})$.

$\boldsymbol{R_{\mathrm{ref.charge}}/R_{\mathrm{ref.}}}$										
T\SOC	0%	5%	10%	20%	35%	50%	65%	80%	95%	100%
-25 °C	…									
-20 °C										
-10 °C	3.6	3.6	3.6	3.6	3.8	4.1	4.1	5.7	11.3	-
0 °C	2.0	2.0	2.0	2.0	2.2	2.2	2.2	3.1	5.8	-
10 °C	1.2	1.2	1.2	1.2	1.3	1.4	1.4	1.8	3.9	-
25 °C	0.9	0.9	0.9	0.9	1.0	$R_{\mathrm{ref.}}$	1.0	1.3	2.3	-
40 °C	0.7	0.7	0.7	0.7	0.8	0.8	0.8	1.0	1.5	-
50 °C	…									
55 °C										

Table 8.1: Scaled electrical charge resistance data for NMC reference cell.

The values below are factors related to a reference discharge resistance $R_{\mathrm{ref.}}(50\%, 25\ °\mathrm{C})$.

$\boldsymbol{R_{\mathrm{ref.discharge}}/R_{\mathrm{ref.}}}$										
T\SOC	0%	5%	10%	20%	35%	50%	65%	80%	95%	100%
-25 °C	…									
-20 °C										
-10 °C	-	23.0	14.0	4.3	3.3	3.0	2.9	2.9	2.9	2.9
0 °C	-	14.0	10.0	2.4	2.1	1.9	1.9	1.9	1.9	1.9
10 °C	-	6.3	4.3	1.6	1.5	1.3	1.3	1.3	1.3	1.3
25 °C	-	7.3	2.3	1.1	1.1	$R_{\mathrm{ref.}}$	1.0	1.0	1.0	1.0
40 °C	-	2.8	1.6	0.9	0.9	0.8	0.8	0.8	0.8	0.8
50 °C	…									
55 °C										

Table 8.2: Scaled electrical discharge resistance data for NMC reference cell.

8.1.1.2 Open circuit voltage

The reference NMC OCV data is listed below.

SOC	OCV@25 °C
0%	3.35 V
5%	3.38 V
10%	3.42 V
15%	3.46 V
20%	3.51 V
25%	3.56 V
30%	3.59 V
35%	3.62 V
40%	3.64 V
45%	3.66 V
50%	3.72 V
55%	3.74 V
60%	3.8 V
65%	3.85 V
70%	3.9 V
75%	3.95 V
80%	4 V
85%	4.05 V
90%	4.1 V
95%	4.15 V
100%	4.2 V

Table 8.3: OCV data for NMC reference cell.

8.1.1.3 Thermal data

Cell format	Heat capacity $[\frac{\mathrm{J}}{\mathrm{kg \cdot K}}]$	Th. conductivity in x-direction (side to side) $[\frac{\mathrm{W}}{\mathrm{m \cdot K}}]$	Th. conductivity in y-direction (front to back) $[\frac{\mathrm{W}}{\mathrm{m \cdot K}}]$	Th. conductivity in z-direction (top to bottom) $[\frac{\mathrm{W}}{\mathrm{m \cdot K}}]$
Prismatic	950	20	1.1	10
Pouch	960	20	1.1	10

Table 8.4: Thermal data for NMC reference cell.

8.1.2 LFP-Type reference data

8.1.2.1 Electrical resistance

Charge resistance:

The values below are factors related to a reference charge resistance $R_{\mathrm{ref.}}(50\%, 25\ °\mathrm{C})$.

$R_{\mathrm{ref.charge}}/R_{\mathrm{ref.}}$										
T\SOC	0%	5%	10%	20%	35%	50%	65%	80%	95%	100%
-25 °C										
-20 °C	…									
-10 °C	4.2	4.3	4.4	4.5	4.5	6.0	6.6	9.6	12.6	-
0 °C	2.2	2.2	2.3	2.3	2.2	2.6	2.8	3.8	4.3	-
10 °C	1.4	1.4	1.4	1.4	1.4	1.6	1.6	2.0	2.4	-
25 °C	1.0	1.0	1.0	1.0	1.0	$R_{\mathrm{ref.}}$	1.1	1.3	1.4	-
40 °C	0.9	0.9	0.9	0.9	0.9	1.0	1.1	1.3	1.4	-
50 °C										
55 °C	…									

Table 8.5: Scaled electrical charge resistance data for LFP reference cell.

Discharge resistance:

The values below are factors related to a reference discharge resistance $R_{\mathrm{ref.}}(50\%, 25\ °\mathrm{C})$.

$R_{\mathrm{ref.discharge}}/R_{\mathrm{ref.}}$										
T\SOC	0%	5%	10%	20%	35%	50%	65%	80%	95%	100%
-25 °C										
-20 °C	…									
-10 °C	-	5.2	4.2	3.7	3.6	3.5	3.5	3.3	3.1	3.1
0 °C	-	3.5	2.7	2.2	2.3	2.1	2.1	2.0	1.9	1.9
10 °C	-	2.4	1.8	1.6	1.6	1.5	1.5	1.4	1.3	1.3
25 °C	-	1.2	1.2	1.1	1.1	$R_{\mathrm{ref.}}$	1.0	1.0	0.9	0.9
40 °C	.	1.0	1.0	1.0	1.0	0.9	0.9	0.9	0.8	0.8
50 °C										
55 °C	…									

Table 8.6: Scaled electrical discharge resistance data for LFP reference cell.

8.1.2.2 Open circuit voltage

The reference LFP OCV data is listed below.

SOC	OCV@25 °C
0%	2.7 V
5%	3.15 V
10%	3.2 V
15%	3.21 V
20%	3.24 V
25%	3.28 V
30%	3.30 V
35%	3.30 V
40%	3.30 V
45%	3.30 V
50%	3.31 V
55%	3.32 V
60%	3.33 V
65%	3.34 V
70%	3.34 V

75%	3.35 V
80%	3.35 V
85%	3.36 V
90%	3.36 V
95%	3.37 V
100%	3.4 V

Table 8.7: OCV data for LFP reference cell.

8.1.2.3 Thermal data:

Cell format	**Heat capacity** $[\frac{J}{kg \cdot K}]$	**Th. conductivity in x-direction (side to side)** $[\frac{W}{m \cdot K}]$	**Th. conductivity in y-direction (front to back)** $[\frac{W}{m \cdot K}]$	**Th. conductivity in z-direction (top to bottom)** $[\frac{W}{m \cdot K}]$
Prismatic	1020	18	0.9	8
Pouch	1030	18	0.9	8

Table 8.8: Thermal data for LFP reference cell.

8.1.3 List of model parameters

Main Inputs	**Description | Derivation | Method**
Installation space (x_1, x_2, x_3)	Used to determine the outer dimensions of each module geometry.
Number of modules (x_4, x_5)	Used to determine the number of modules and the required voltage level, energy, and power for each module.
System energy requirement	Used for energy demand on the module level and corresponding energy density of cell level.
System power requirement	Used for power demand on the module level and corresponding power density of cell level.
System charging time requirement	Used for power demand on the module level and corresponding power density of cell level.
System voltage requirement	Used to determine the minimum number of cells for each module. Defined as $U_{system,max.} = n_{serial} \cdot U_{cell,max.}$ with $U_{cell,max.ocv,NMC-Type}(100\%, 25\,°C) \approx 4.2\,V$ and $U_{cell,max.ocv,LFP-Type}(100\%, 25\,°C) \approx 3.4\,V$
Cell size, cell type, cell chemistry	Optional setting to specify a prior-defined cell format, size, and type. The cell size can be set to a user-defined range in which the best (default: cost-optimized) cell will be chosen in the internal optimization process. See Chapter 3 for details.
Geometric cell properties	Geometry properties for cell model. The properties are used for constructing the cell shell model. Cell terminal connection space is modeled as a placeholder for both the cell terminals/tabs as well as the busbar. Prismatic cell side terminals (default): Terminal placeholder in terminal direction = 10 mm (each side).

	Terminal dimension: 5 mm (thickness), 0.7 · $l_{cell,y}$ (width), 0.3 · $l_{cell,z}$ (height) Pouch cell side terminals/tabs (default): Terminal placeholder in terminal direction = 20 mm (each side). Terminal dimension: 20 mm (length), 0.05 · $l_{cell,y}$ (width), 0.3 · $l_{cell,z}$ (height) Cylindrical cell: Terminal placeholder in terminal direction = 8 mm. Terminal dimension: 4 mm (height), 0.8 · $A_{cell,top}$(area) Cell housing material default values: ➢ 1 mm of aluminum on all cell sides for prismatic cell ➢ 0.2 mm pouch foil on all cell sides for pouch cells ➢ 0.3 mm aluminum for cylindrical cells The cell electrode (stack) volume results from subtracting the housing thicknesses from the cell size. For prismatic cells, an additional 2 mm of installation space is deducted on the side of the tabs (current collector) for connecting the electrode layers/tabs to the cell terminal.
Cellstacking properties	The properties are used for constructing the cellmodule. Properties can be defined differently depending on different cell shapes, formats, or sizes. Default: ➢ Cell-to-cell distance (dependent on cell capacity. Reserved space for cell terminals, busbars, or frames is excluded) • Along short cell side (e.g.: cushion pad, see Chapter 4.3.1) • Along long cell side: 0 mm • Along height of cell: 0 mm • 10% of cell diameter for cylindrical cells ➢ Space around cell housing (e.g. for isolation, cell framing, tolerance) • Along short cell side: none • Along height of cell (can be compensated by the cell terminal/busbar size): →1 mm for prismatic cells →5 mm for pouch cells →1 mm for cylindrical cells • Along long cell side (can be compensated by the cell terminal/busbar size): →1 mm for prismatic cells →5 mm for pouch cells ➢ At least 0.5 mm space is used for gap filler between cells and module bottom and cover plate (needed tolerance space). ➢ Number of allowed stacks next to each other = 2 (default). ➢ Busbar modeling based on DIN 43671 (copper).
Geometric module properties	Geometric module packaging properties. Dimensioning for screwed cellmodules (prismatic, pouch) see Chapter 4.3.1.

	Cylindrical modules: $Front/EndplateThickness_{\text{cylindrical}} = 5\ \text{mm}$ $SideplateThickness_{\text{cylindrical}} = 5\ \text{mm}$ For glued cellmodules (all cell types): $Front/EndplateThickness_{\text{glued}} = 0.5 \cdot Front/EndplateThickness_{\text{screwed}}$ $SideplateThickness_{\text{glued}} = 0\ \text{mm}$ $CoverplateThickness_{\text{glued}} = 0\ \text{mm}$ $Bottom/CoverplateThicknesss_{\text{glued}} = 0\ mm$ $CellToCoverplateGapFillerThickness_{\text{glued}} = 0\ \text{mm}$
Cell voltage charging limitations	For this work, a charge time requirement is defined for a charging SOC range of 5% - 75%. The following voltage limits are used for the cell resistance design (see Chapter 4.3.1.5). For NMC-Type cells: $U_{\text{cell,max.cutoff}} - U_{\text{safety}}(\text{SOC} = 5\% - 50\%) = 4\ \text{V}$ $U_{\text{cell,max.cutoff}} - U_{\text{safety}}(\text{SOC} = 50\% - 75\%) = 4.25\ \text{V}$ For LFP-Type cells: $U_{\text{cell,max.cutoff}} - U_{\text{safety}}(\text{SOC} = 5\% - 75\%) = 3.8\ \text{V}$
Main Outputs	
Feasibility	Feasible: <= 1; Infeasible > 1
Mass (module level or cell level)	Module mass is dependent on geometric module properties (thickness) and the specific weight of the module's material (see Chapter 4.3.1.7). Cell mass is derived using the cell size (for determination of cell housing weight), cell design properties (for determination of cell terminal weight), and the required energy density (for determination of electrode stack weight).
Cost	See Chapter 4.3.1.7.
Cell size (x,y,z)	Prior-defined or optimized cell geometry.
Constructed cell model	Including calculated prior-defined cellstacking properties, e.g., gap filler, compression pad, and cell frames.
Cell chemistry	Type of chemistry for optimized cell geometry (NMC-Type, LFP-Type).
Cell format	Type of format for optimized or prior-defined cell geometry (prismatic, pouch, cylindrical).
Cell topology	Electrical cell connection on the module level.
Cell orientation and assembly	Geometric assembly of individual cells. Including the number of cells in each spatial direction and the stacking direction.
Cell energy density	Needed energy density to fulfill the system energy requirements. Energy density on cellstack level is defined by using the inner-cell electrode stack volume. Energy density borders for prismatic, pouch, NMC, and LFP-Type are defined as: Prismatic: <= 437 Wh/l for LFP-Type <= 688 Wh/l for NMC-Type

	Pouch : <= 460 Wh/l for LFP-Type <= 725 Wh/l for NMC-Type Cylindrical: <= 470 Wh/l for LFP-Type <= 750 Wh/l for NMC-Type See, e.g., [207, 224, 259] for further different energy density analyses and compilations.
Cell capacity	Derived from the observed cell geometry energy density, and nominal voltage.
Module thermal properties (Heat capacity, thermal conductivity)	Derived from the cell and packaging properties (see Chapter 4.3.1).
Module electrical resistance	Derived from the properties of the cells and module busbar (see Chapter 4.3.1).

Table 8.9: Tabular overview for the explanation, derivation, methodology, or reference for the cellmodule model inputs and outputs.

8.2 Submodel mechanics

8.2.1 List of model parameters

Main Input	Description | Derivation | Method | Reference
Installation space (x_1, x_2, x_3)	Used to determine the installation space available for the inner and outer mechanical structure (installation space not used from the cellmodule is available for other components).
Number of modules (x_4, x_5)	Used to determine the general structure and number of side and cross members. Used for span deviation between cross- and side members for crush load case.
Free space/ installation clearance	Necessary free space (installation clearance) between different components within the battery system for tolerances, and assembly. Default: 5 mm.
Crush force requirement	Force for load crush test (e.g., according to legal European regulations [286]). Default: 120 kN.
Crash energy requirement	Crash energy requirement that the battery system must be able to safely absorb (design value depends on the vehicle weight, vehicle rocker panel, material, ...).
Material	Mode 1 (Default): aluminum. Mode 2: steel. Mode 3: Internal optimization (cost or weight) between aluminum and steel.
Thickness of underride protection sheet	Thickness of underride protection, see [390] for more details. Default: 3 mm (aluminum).
Bollard clearance	Free space (placeholder) and unusable installation space in z-direction to protect the battery cells in the event of a bollard crash. See [390] for more details. Default 14 mm.
Inputs (Cellmodule)	
Cellstacking direction	Used for the evaluation of the load crush test.

Cell format	Used for the evaluation of the load crush test.
Design cellmodule intrusion	See Chapter 4.3.2.2.
Inputs (Electronics)	
E-Box size (x-direction)	E-Box geometry is subtracted from the available installation space (in x-direction) for mechanical structures (front and back outer profile, cross member).
E-Box integration mode	See Chapter 4.3.4.
Main Outputs	
Feasibility	Feasible: <= 1; Infeasible > 1
Mass	Based on volume estimation, material and inner structure of the outer frame, cross member, and side member.
Cost	See Chapter 4.3.5.
Used Material	Depending on chosen mode: (best) used material for the mechanical components in the battery system.
Outer frame sizes (x,y,z) and structure	The profile width and structure (from the extruded profiles) are internally optimized through the crash and crush load case results. (The length and height are fixed by the total system size.) Long (side parts) and short (front and back) outer frame sizes may be different from each other.
Cross member sizes (x,y,z)	Internally optimized through crash and crush test results.
Side member sizes (x,y,z)	Internally optimized through space requirements of the outer frame.
Number of side members and cross members	Depending on the total number of modules and the E-Box integration mode.
Updated E-Box integration mode	May be changed during mechanical optimization when optimizing the outer frame sizes (see Chapter 4.3.4).
Updated E-Box size (x,y,z)	May be changed during mechanical optimization when optimizing the outer frame sizes (see Chapter 4.3.4).

Table 8.10: Tabular overview for the explanation, derivation, methodology, or reference for the mechanics model inputs and outputs.

8.3 Submodel cooling

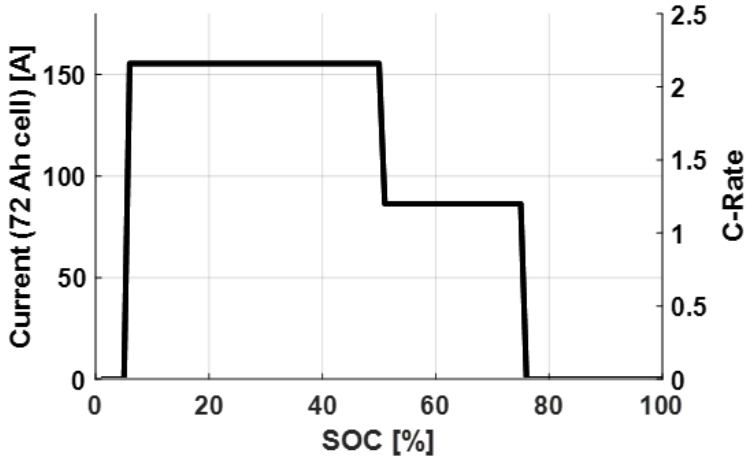

Figure 8.1: Two-stage design quick charging current profile for a 25-minute 5% - 75% SOC charge for a 72 Ah cell.

8.3.1 List of model parameters

Main Inputs	Description | Derivation | Method
Installation space (x_1, x_2, x_3)	Used to determine the outer dimensions of each module geometry. This allows the installation space for the cooling plate to be determined.
Number of modules (x_4, x_5)	Used to determine the number of modules.
Ambient temperature	Used for heat exchange determination (e.g.: cooling capacity of the chiller).
Cooling design profile	Load profile used for the cooling plate and cooling circuit design (driving and/or charging profile). Default: User specified time for a fast charging current profile.
Cooling model specifications and setup	Cooling model specifications, e.g.: ➢ T_{cell}: border for maximum cell temperature for cooling design Default: see Chapter 4.3.1.8 ➢ $T_{\text{diff.,module,QC}}$: border for maximum delta of cell temperatures in a cellmodule (while quick charging) for cooling design Default: see Chapter 4.3.1.8 ➢ $T_{\text{diff.,fluid}}$: border for maximum delta water (inlet and outlet) temperature for cooling (water pump) design; Default: see Chapter 4.3.1.8 ➢ PWM signal: border for power of hydraulic water pump power (for active water/glycol cooling) (can be internally optimized). The PWM refers to a maximal hydraulic power of 45 W. Default: internal optimization ➢ heat transfer coefficients to ambient; Default: see Chapter 4.3.3 ➢ cooling circuit model (basic, medium, powerful); Default: depending on battery system energy E_{system}: - $E_{\text{system}} \leq 65\ \text{kWh} \rightarrow$ basic

	- $65\ \text{kWh} < E_{\text{system}} \leq 85\ \text{kWh} \rightarrow \text{medium}$ - $E_{\text{system}} > 85\ \text{kWh} \rightarrow \text{powerful}$ ➢ number of passes per module for cooling tubes Default: n_pass = 2 ➢ cooling tube topology (parallel and/or perpendicular) (can be internally optimized) Default: internally optimized ➢ range of gap filler heat conductivities (can be internally optimized) Default: $\lambda \in \{1,2,3,4\}\frac{\text{W}}{\text{m}\cdot\text{K}}$ with internal optimization
Geometric cooling specifications	Geometric sizing of: ➢ the battery system's cover and bottom plate, as well as the thickness of the cooling plate; Default 1.2 + 0.8 mm (for each side, one plain plate, one deep-drawn for cooling tubes) ➢ possible height of cooling tubes (can be optimized). Default: [3, 4, 5, 6, 7, 8, 9, 10] mm with internal optimization. ➢ length to height ratio of circle selection (cooling tube format); Default: 3, see Chapter 4.3.3 for derivation. ➢ distance between two cooling tubes. Default: 18 mm ➢ thickness of gap filler (used also for tolerance compensation). Default: assumed variable depending on the cellmodule size: $d_{\text{gap filler}} = 0.5\ \text{mm} + 4.5 \cdot l_{\text{module,x}} \cdot l_{\text{module,y}} \cdot 10^{-6}\ \text{mm}^{-1}$ with $d_{\text{gap filler}} \in [1\ \text{mm}, 3\ \text{mm}]$ see Chapter 4.3.3 for illustrations.
Inputs (Cellmodule)	
Cell geometry	Used to determine the geometric module configuration.
Cell voltage $U_{\text{cell}}(\text{SOC}, T)$	Used to determine the electrical circuit model of the module.
Cell resistance $R_{\text{cell}}(\text{SOC}, T)$	Used to determine the electrical circuit model of the module.
Cell capacity	Used to scale normalized load profiles.
Number of cells $n_{\text{CellsPerModule}}$	Used to determine the electrical circuit model of the module.
Cellmodule topology ('x's 'y'p)	Used to determine the electrical circuit model of the module.
Cellstacking direction (x|y)	Used to determine the geometric module configuration.
Cellmodule thermal data	Used to determine the thermal model of the module (heat capacity, thermal conductivity).
Cellmodule busbar	Geometry: used to determine the geometric module configuration. Resistance: used to determine the electrical circuit model of the module.
Inputs (Mechanics)	
Free space in the z-direction	Used for bollard crash load case clearance. The used space is subtracted from the available cooling plate thickness. Default space for underride protection layer thickness and bollard clearance: 3 mm + 14 mm.
Main Outputs	
Feasibility	Feasible: <= 1; Infeasible > 1.
Mass	Based on volume estimation and material / inner structure.
Cost	See Chapter 4.3.5.
Thickness gap filler	Determined using the cellmodule geometry.

Type/ conductivity of gap filler	Gap filler heat conductivity (can be internally optimized).
Height of cooling tubes	Cooling tube height based on available installation space (can be internally optimized).
Max. temperature reached	The maximum temperature reached within the cellmodule in the overall best simulation setup.
Mean temperature reached	The mean (derived from the timestep of the maximum temperature) temperature reached within the cellmodule in the overall best simulation setup.
Max. temperature difference	The maximum temperature difference (derived from the timestep of the maximum temperature) reached within the cellmodule in the overall best simulation setup.
Cooling architecture	Internally optimized: - active water/glycol one-sided → Default: considered - active water/glycol two-sided → Default: considered - passive air cooling → Default: not considered
Cooling tube topology	Parallel or perpendicular (can be internally optimized).
Water pump power, coolant water flow	Necessary water pump power (and corresponding coolant volume flow) to reach the requirement regarding the maximum water inlet and outlet temperature (can be internally optimized).

Table 8.11: Tabular overview for the explanation, derivation, methodology, or reference for the cooling model inputs and outputs.

8.4 Submodel electronics

8.4.1 List of model parameters

Main Inputs	Description | Derivation | Method | Reference
Installation space (x_1, x_2)	Used to calculate available installation space for the battery junction box.
Number of modules (x_4, x_5)	Used for 'complex' integration evaluation (see Figure 4.43).
System power requirement	Used to determine the design system current in order to evaluate the resulting BJB size.
System voltage requirement	Used to determine the design system current in order to evaluate the resulting BJB size.
Mode	The junction box can be integrated differently into the system. See Chapter 4.3.4.
Input (Mechanic)	
Reserved E-box space (y-direction)	Used to calculate available installation space for the battery junction box. Installation space along the front (or back) side of the battery system is determined by the total installation space in y-direction and the outer profile (long side) thickness (as well as any side members). Afterward, the BJB space in the x-direction can be evaluated to meet specific space/volume requirements.
Front crush evaluation	Used to evaluate the necessary BJB integration concept.
Main Outputs	
Feasibility	Feasible: <= 1; Infeasible > 1

Mass	Based on BJB black-box volume estimation.
Cost	See Chapter 4.3.5.
E-Box sizes x,y,z	Installation space reserved for components of the BJB.
Integration concept	Depending on front crush evaluation, see Figure 4.43.

Table 8.12: Tabular overview for the explanation, derivation, methodology, or reference for the electronics model inputs and outputs.

8.5 General design variable assumptions and cost references

8.5.1 Design variables

For the high-voltage battery system optimizations in this work, the design variables (see Chapter 4.2) were restricted between the following borders (unless otherwise mentioned):

$$x_1 \in [0.7, 0.95]$$

$$x_2 \in [0.7, 0.95]$$

$$x_3 \in [0.7^*, 0.85^*]$$

$$*= \text{borders are adapted depending on geometric properties.}$$

$$x_4 \in \{2, 3, 4, 5, 6, 7\}$$

$$x_5 \in \{2, 3, 4, 5, 6, 7\}$$

8.5.2 Reference list for cost components and materials

The following table summarizes numerous references for different costs, cost estimations, or cost suggestions. It is important to note that different costs can be highly volatile. Factors for volatility are: market price development, political development, market trends, economies of scale, and many others. The references below were used in addition to those mentioned directly in the derivation of the cost parts.

Submodel	Cost parts	References
Cellmodule	Cell, module, and system integration costs.	Cell: [284, 391–394] Module/system integration: [22, 167, 281, 317, 393, 395]
Cooling	The deep-drawing process of aluminum plates, gap filler, water/coolant pump, and cooling circuit costs.	General/ Cooling circuit: [315, 316, 396] Cooling plate: [312, 397–400] Water/coolant pump: [401–403] Aluminum: [404] Extruding process [405–408]
Mechanics	Material-based costs for extruded aluminum and processed steel.	General: [21, 22] Aluminum: [404]

		Extruding process: [405–408]
Electronics	Cost for electronics in EVs for different power levels. Cost for different integration difficulties of the electronics.	General/junction box components: [315, 316, 409]

Table 8.13: Compilation of references for component cost derivations.

8.6 Firefly algorithm sensitivity analysis in the HV-BOT environment

8.6.1 Analysis of the pure optimization algorithm

One-at-a-time sensitivity analysis for each of three Firefly algorithm parameters: the attractiveness parameter β, the absorption coefficient γ, and the random walk parameter α, consisting of the initial random factor α_0 $(= 1)$ and the random walk cooling factor δ^n. The sensitivity was measured by the normalized objective cost function resulting from the simulation models von the HV-BOT.

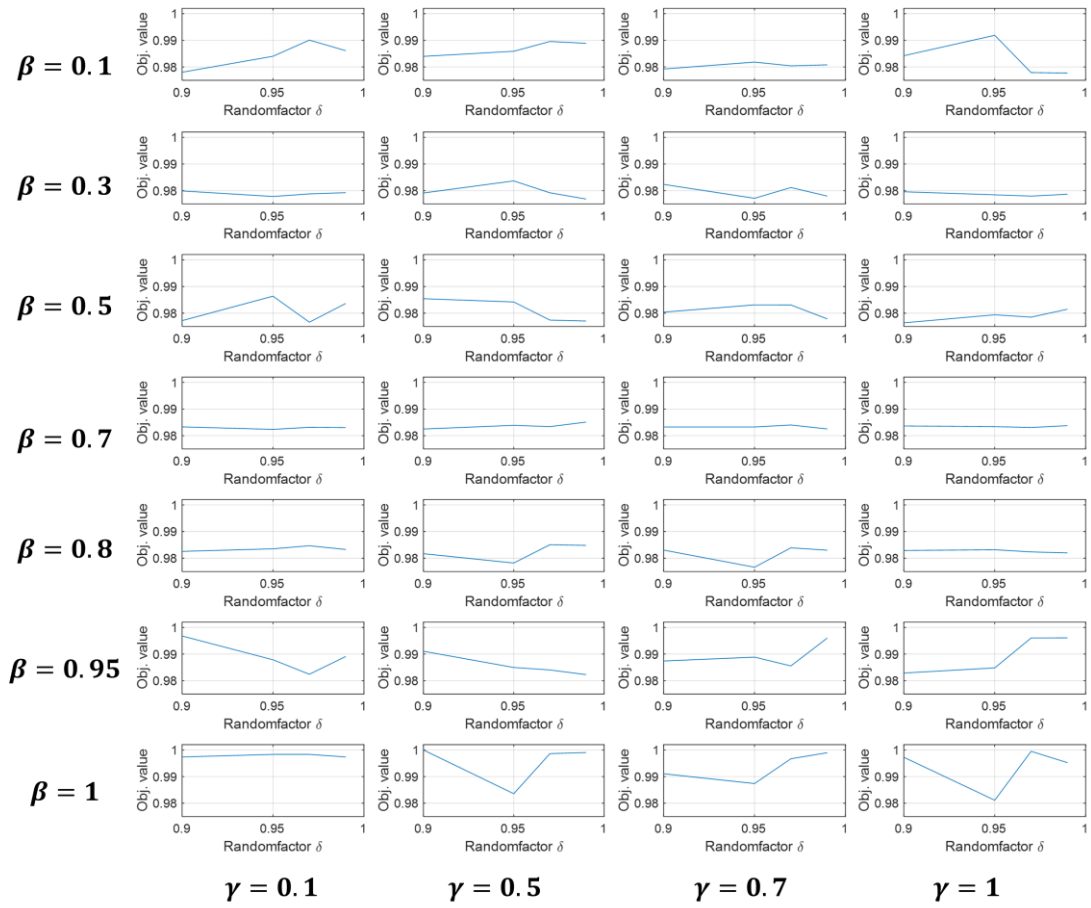

Figure 8.2: Results from one-at-a-time sensitivity analysis of the Firefly algorithm in the HV-BOT.

The results generally indicate the growing influence of the random factor α with increasing β.

Additionally, a regression model was used to determine the statistical strength and impact of each parameter. An assumed linear and quadratic relation of attractiveness parameter β led to a generally high coefficient of determination. Thereby, $\beta_{\text{opt.}} = \frac{210.48}{2 \cdot 242.42} \approx 0.434$ (for objective function minimization).

```
Linear regression model:
    norm_cost ~ 1 + beta + gamma + delta + beta^2

Estimated Coefficients:
                   Estimate      SE       tStat       pValue
                   ________    ______    _______    ___________

    (Intercept)      5581.3     63.601     87.755    1.6235e-101
    beta            -210.48     32.678     -6.441     3.4695e-09
    gamma           -8.0544     6.7666    -1.1903        0.23655
    delta            36.394     66.136    0.55028        0.58327
    beta^2           242.42     28.383     8.5409     9.9624e-14


Number of observations: 112, Error degrees of freedom: 107
Root Mean Squared Error: 23.4
R-squared: 0.585,  Adjusted R-Squared: 0.569
F-statistic vs. constant model: 37.7, p-value = 1.2e-19
```

Figure 8.3: Regression analysis results for Firefly algorithm within HV-BOT.

8.6.2 Analysis of Firefly algorithm as acquisition function in GPR optimization

In this sensitivity analysis, the Firefly algorithm is used as an acquisition function for a GPR optimization. Again, the one-at-a-time sensitivity analysis is used for each of the three Firefly algorithm parameters for the attractiveness parameter β, the absorption coefficient γ, and the random walk parameter α, consisting of the initial random factor α_0 $(= 1)$ and the random walk cooling factor δ^n. The sensitivity was measured by the normalized objective cost function resulting from the simulation models von the HV-BOT.

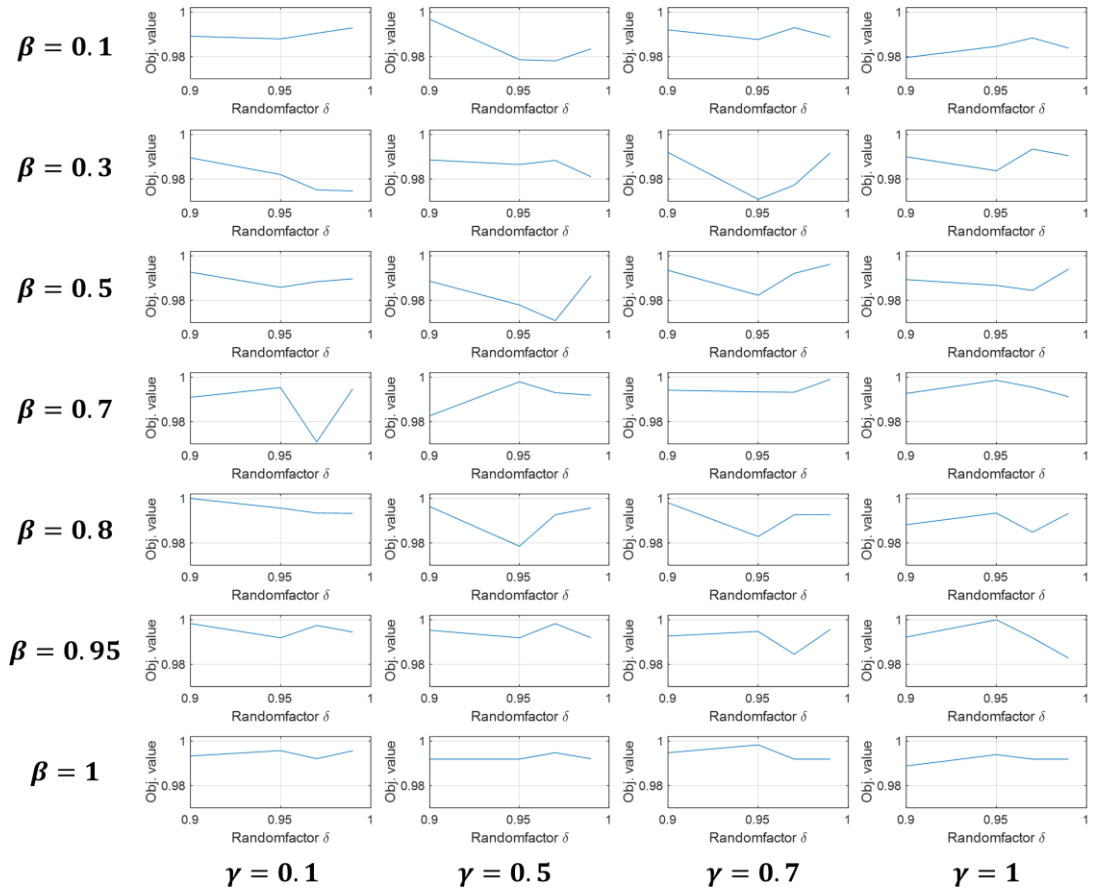

Figure 8.4: Results from one-at-a-time sensitivity analysis of the Firefly algorithm within GPR optimization in the HV-BOT.

Higher random walk factors δ show generally lower objective values. To further emphasize this observation, a regression model was used to determine the statistical strength and impact of each parameter.

```
Linear regression model:
    norm_cost ~ 1 + beta + gamma + delta + delta^2

Estimated Coefficients:
                   Estimate      SE       tStat       pValue
                   ________    _______    _________    __________

    (Intercept)      12591      3127.1      4.0265     0.00010602
    beta            53.381      9.9937      5.3415     5.2323e-07
    gamma          0.20027      9.3051    0.021523        0.98287
    delta           -14768      6640.7     -2.2239       0.028254
    delta^2          7774.7     3521.4      2.2079       0.029389


Number of observations: 112, Error degrees of freedom: 107
Root Mean Squared Error: 32.2
R-squared: 0.246,  Adjusted R-Squared: 0.217
F-statistic vs. constant model: 8.7, p-value = 4.02e-06
```

Figure 8.5: Regression analysis results for Firefly algorithm within GPR in HV-BOT.

In Figure 8.5, the results show a generally lower coefficient of determination. Nevertheless, an assumed linear and quadratic relation of random walk parameter δ showed statistical significance. Thereby, $\delta_{\text{opt.}} = \frac{14768}{2 \cdot 7774.7} \approx 0.95$ (for objective function minimization).

8.7 Laplace Approximation

The Laplace Approximation approaches the posterior $p(f|\boldsymbol{X}, \boldsymbol{y})$ with a Gaussian by doing a second-order Taylor expansion of $\log p(f|\boldsymbol{X}, \boldsymbol{y})$ around the maximum of the posterior. The approximation $q(\mathbf{f}|\boldsymbol{X}, \mathbf{y})$ of $p(f|\boldsymbol{X}, \boldsymbol{y})$ is then given by:

$$q(\mathbf{f}|\boldsymbol{X}, \mathbf{y}) = \mathcal{N}\left(\mathbf{f}\middle|\hat{\mathbf{f}}, A^{-1}\right) \propto \exp\left(-\frac{1}{2}\left(\mathbf{f} - \hat{\mathbf{f}}\right)^{\mathrm{T}} A \left(\mathbf{f} - \hat{\mathbf{f}}\right)\right), \tag{8.1}$$

where $\hat{\mathbf{f}} = \operatorname{argmax}_{\mathbf{f}} p(\mathbf{f}|\boldsymbol{X}, \mathbf{y})$ is the position of the maximum of the posterior, which poses as the mean of the Gaussian distribution, and $A = -\nabla\nabla \log p(\mathbf{f}|\boldsymbol{X}, \mathbf{y})|_{\mathbf{f}=\hat{\mathbf{f}}}$ is the Hessian of the negative log posterior at that maximum, whose inverse is used as the covariance matrix.

According to Bayes' theorem, the posterior is given by:

$$p(\mathbf{f}|\boldsymbol{X}, \mathbf{y}) = \frac{p(\mathbf{y}|\mathbf{f}) p(\mathbf{f}|\boldsymbol{X})}{p(\mathbf{y}|\boldsymbol{X})}. \tag{8.2}$$

As $p(\mathbf{y}|\boldsymbol{X})$ is independent of $\mathbf{f}$, the maximum posterior is then determined by maximizing:

$$\begin{aligned} \Psi(\mathbf{f}) &\coloneqq \log p(\mathbf{y}|\mathbf{f}) + \log p(\mathbf{f}|\boldsymbol{X}) \\ &= \log p(\mathbf{y}|\mathbf{f}) - \frac{1}{2}\mathbf{f}^{\mathrm{T}} K(\boldsymbol{X}, \boldsymbol{X})^{-1}\mathbf{f} - \frac{1}{2}\log|K(\boldsymbol{X}, \boldsymbol{X})| - \frac{n}{2}\log 2\pi, \end{aligned} \tag{8.3}$$

where the definition of the log marginal likelihood from Eq. (5.6) has been applied. Differentiating two times with respect to $\mathbf{f}$ gives:

$$\nabla\Psi(\mathbf{f}) = \nabla \log p(\mathbf{y}|\mathbf{f}) - K(\boldsymbol{X}, \boldsymbol{X})^{-1}\mathbf{f}, \tag{8.4}$$

$$\nabla\nabla\Psi(\mathbf{f}) = \nabla\nabla \log p(\mathbf{y}|\mathbf{f}) - K(\boldsymbol{X}, \boldsymbol{X})^{-1} = -W - K(\boldsymbol{X}, \boldsymbol{X})^{-1} \tag{8.5}$$

with $W \coloneqq -\nabla\nabla \log p(\mathbf{y}|\mathbf{f})$. Using the logistic function as sigmoid function, the condition for a maximum $\nabla\Psi = 0$ leads to $\hat{\mathbf{f}} = K(\boldsymbol{X}, \boldsymbol{X})\left(\nabla \log p\left(\mathbf{y}\middle|\hat{\mathbf{f}}\right)\right)$, which is solved using Newton's method to obtain $\hat{\mathbf{f}}$.

The covariance matrix A^{-1} can then be expressed by:

$$A^{-1} = (-\nabla\nabla \log p(\mathbf{f}|\boldsymbol{X}, \mathbf{y})|_{\mathbf{f}=\hat{\mathbf{f}}})^{-1} = (W + K(\boldsymbol{X}, \boldsymbol{X})^{-1})^{-1}. \tag{8.6}$$

Having determined $q(f|\boldsymbol{X}, \mathbf{y})$, the posterior mean and variance of f_* are derived by:

$$\mathbb{E}_q[f_*|\boldsymbol{X},\mathbf{y},\mathbf{x}_*] = \mathbf{k}(\mathbf{x}_*)^{\mathrm{T}} K(\boldsymbol{X},\boldsymbol{X})^{-1}\hat{\mathbf{f}} = \mathbf{k}(\mathbf{x}_*)^{\mathrm{T}}\,\nabla \log p\big(\mathbf{y}\big|\hat{\mathbf{f}}\big), \tag{8.7}$$

$$\begin{aligned}\mathbb{V}_q[f_*|\boldsymbol{X},\mathbf{y},\mathbf{x}_*] &= \mathbb{E}_{p(f_*|\boldsymbol{X},\mathbf{x}_*,\mathrm{f})}[(f_* - \mathbb{E}[f_*|\boldsymbol{X},\mathbf{x}_*,\mathrm{f}])^2] \\ &\quad + \mathbb{E}_{q(\mathbf{f}|\boldsymbol{X},\mathbf{y},)}[(\mathbb{E}[f_*|\boldsymbol{X},\mathbf{x}_*,\mathrm{f}] - \mathbb{E}[f_*|\boldsymbol{X},\boldsymbol{y},\boldsymbol{x}_*])^2] \\ &= k(\mathbf{x}_*,\mathbf{x}_*) - \mathbf{k}(\mathbf{x}_*)^{\mathrm{T}}(K(\boldsymbol{X},\boldsymbol{X}) + W^{-1})^{-1}\mathbf{k}(\mathbf{x}_*).\end{aligned} \tag{8.8}$$

Here, $\mathbf{k}(\mathbf{x}_*)$ denotes the vector of covariances between the test point and the training points. The derivations of Eqs. (8.7) and (8.8) can be found in [370]. They give rise to a Gaussian approximation of the posterior distribution of the latent variable in Eq. (5.11):

$$p(f_*|\boldsymbol{X},\mathbf{y},\mathbf{x}_*) \simeq q(f_*|\boldsymbol{X},\mathbf{y},\mathbf{x}_*) = \mathcal{N}\big(f_*|\mathbb{E}_q[f_*|\boldsymbol{X},\mathbf{y},\mathbf{x}_*],\mathbb{V}_q[f_*|\boldsymbol{X},\mathbf{y},\mathbf{x}_*]\big). \tag{8.9}$$

The approximation of the probabilistic prediction in Eq. (5.12) is then derived by:

$$p(f_*|\boldsymbol{X},\mathbf{y},\mathbf{x}_*) \simeq q(f_*|\boldsymbol{X},\mathbf{y},\mathbf{x}_*) = \mathcal{N}\big(f_*|\mathbb{E}_q[f_*|\boldsymbol{X},\mathbf{y},\mathbf{x}_*],\mathbb{V}_q[f_*|\boldsymbol{X},\mathbf{y},\mathbf{x}_*]\big). \tag{8.10}$$

8.8 Enpolite: Comparing Lithium-Ion cells across Energy, Power, Lifetime, and Temperature

The Enpolite graphics below are published in a journal article [207] with equal contribution of this thesis author and Philipp Dechent. Additional information and an interactive version can also be found on the website enpolite.org.

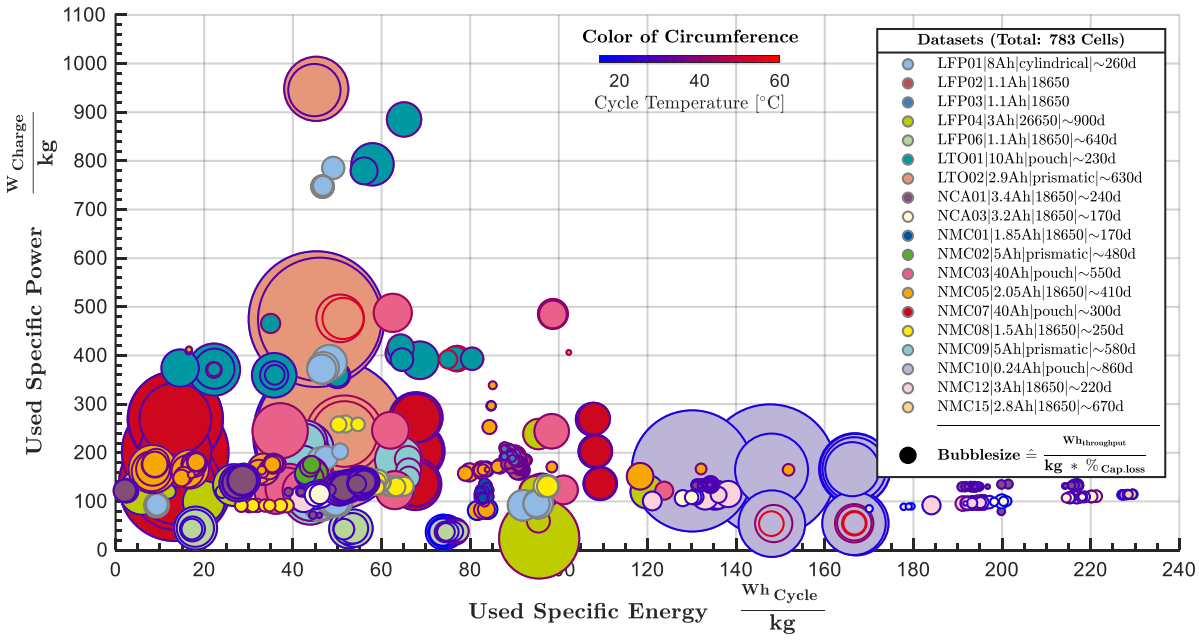

Figure 8.6: Cyclic ENPOLITE plot representing 783 cells.

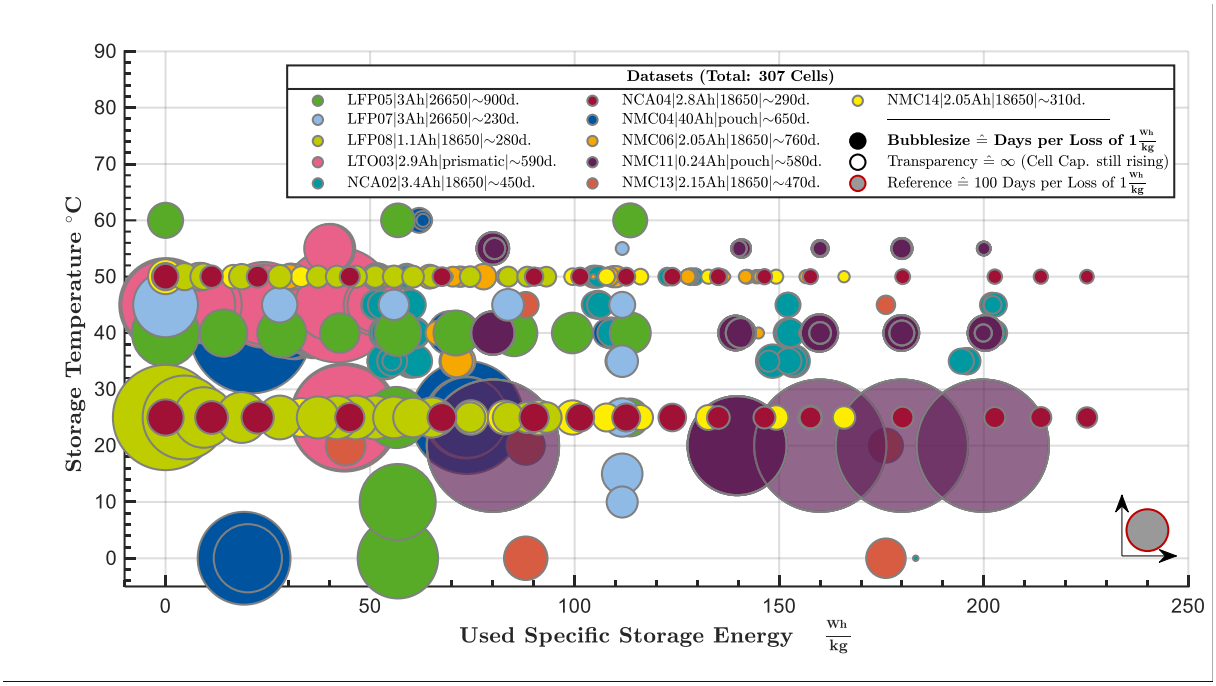

Figure 8.7: Calendar ENPOLITE plot representing 307 cells.

9 List of Abbreviations

BEV	Battery electric vehicle
BJB	Battery junction box
BMC	Battery management controller
BMS	Battery management system
BOL	Begin of life
BTMS	Battery thermal management system
CAD	Computer-aided design
CARB	California Air Resources Board
CFD	Computational fluid dynamics
CM	Cross member
CMC	Cell management controller
COP	Carry-over-part
DIFF	Difference
DOD	Depth of discharge
DOF	Degree of feasibility
ECM	Equivalent circuit model
EI	Expected Improvement
EIS	Electrochemical impedance spectroscopy
ENPOLITE	Energy, Power, Lifetime, and Temperature plot of aged battery cells
EOL	End of life
EU	European Union
EV	Electric vehicle
FA	Firefly algorithm
FCV	Fuel cell vehicle
FEM	Finite element method
GER	Germany
GHG	Greenhouse gas
GHT	Graph and heuristics-based topology optimization
GP	Gaussian process
GPC	Gaussian process classification
GPR	Gaussian process regression
HEV	Hybrid electric vehicle
HV	High-voltage
HV-BOT	High-Voltage-Battery-Optimization-Tool

LAM	Loss of active material
LFP	Lithium iron phosphate (cathode material)
LIB	Lithium-ion battery
LLI	Loss of lithium inventory
LMFP	Lithium manganese iron phosphate (cathode material)
LTO	Lithium titanate oxide (anode material)
MC	Minimum certainty
MEB	Modular electrification toolkit from Volkswagen
MIP	Mixed-integer problem
MMC	Module management controller
MSL	Modelica standard library
NCA	Lithium nickel cobalt aluminum oxide (cathode material)
NMC	Lithium nickel manganese cobalt oxide (cathode material)
OCV	Open circuit voltage
OEM	Original equipment manufacturer
OFAT	One factor at a time
OP	Outer profile
PAR	Parallel
PDP	Product development process
PET	Polyethylene terephthalate
PHEV	Plug-in hybrid electric vehicle
PPCQS	Parallelized Predictive Classifying Querying Strategy
PRIS	Prismatic
PTC	Positive temperature coefficient
PWM	Pulse duration modulation
QC	Quick charging
RBF	Radial basis function
SEI	Solid electrolyte interface
SM	Side member
SOC	State of charge
SOP	Start of production
TOL	Tolerance

10 Bibliography

[1] United States Environmental Protection Agency, *Overview of Greenhouse Gases*, 2022. [Online]. Available: https://www.epa.gov/ghgemissions/overview-greenhouse-gases (accessed: 05/2023).

[2] Die Bundesregierung, *Bis 2030 die Treibhausgase halbieren*, 2019. [Online]. Available: https://www.bundesregierung.de/breg-de/themen/klimaschutz/klimaziele-und-sektoren-1669268 (accessed: 05/2023).

[3] worldometer, *Germany CO2 Emissions.* [Online]. Available: https://www.worldometers.info/co2-emissions/germany-co2-emissions/ (accessed: 05/2023).

[4] Umwelt Bundesamt, *Greenhouse gas emissions rose by 4.5 percent in 2021*, 2022. [Online]. Available: https://www.umweltbundesamt.de/en/press/pressinformation/greenhouse-gas-emissions-rose-45-percent-in-2021 (accessed: 05/2023).

[5] T. Haasz, J. J. Gómez Vilchez, R. Kunze, P. Deane, D. Fraboulet, U. Fahl, and E. Mulholland, “Perspectives on decarbonizing the transport sector in the EU-28,” *Energy Strategy Reviews*, vol. 20, 124–132, 2018.

[6] S. Solaymani, “CO2 emissions patterns in 7 top carbon emitter economies: The case of transport sector,” *Energy*, vol. 168, 989–1001, 2019.

[7] European Parliament, *CO2 emissions from cars: facts and figures (infographics)*, 2019. [Online]. Available: https://www.europarl.europa.eu/news/en/headlines/society/20190313STO31218/co2-emissions-from-cars-facts-and-figures-infographics (accessed: 05/2023).

[8] European Parliament, *CO_2-Emissionen des Luft- und Schiffsverkehrs: Zahlen und Fakten (Infografik)*, 2019. [Online]. Available: https://www.europarl.europa.eu/news/de/headlines/society/20191129STO67756/co2-emissionen-des-luft-und-schiffsverkehrs-zahlen-und-fakten-infografik (accessed: 05/2023).

[9] European Environment Agency, *EEA greenhouse gases - data viewer*, 2021. [Online]. Available: https://www.eea.europa.eu/data-and-maps/data/data-viewers/greenhouse-gases-viewer (accessed: 02/2023).

[10] European Commission, *CO_2 emission performance standards for cars and vans.* [Online]. Available: https://climate.ec.europa.eu/eu-action/transport-emissions/road-transport-reducing-co2-emissions-vehicles/co2-emission-performance-standards-cars-and-vans_en (accessed: 01/2023).

[11] IEA, *The role of CCUS in low-carbon power systems*, 2020. [Online]. Available: https://www.iea.org/reports/the-role-of-ccus-in-low-carbon-power-systems (accessed: 05/2023).

[12] H. Ritchie, M. Roser, and P. Rosado, *Emissions by sector*, 2020. [Online]. Available: https://ourworldindata.org/emissions-by-sector (accessed: 05/2023).

[13] H. Ritchie, M. Roser, and P. Rosado, *CO_2 and Greenhouse Gas Emissions*, 2020. [Online]. Available: https://ourworldindata.org/co2-emissions (accessed: 05/2023).

[14] IEA, *Transport: Improving the sustainability of passenger and freight transport*, 2023. [Online]. Available: https://www.iea.org/topics/transport (accessed: 05/2023).

[15] Agora Energiewende, *Die Energiewende in Deutschland: Stand der Dinge 2022. Rückblick auf die wesentlichen Entwicklungen sowie Ausblick auf 2023*, 2023. [Online]. Available: https://static.agora-energiewende.de/fileadmin/Projekte/2022/2022-10_DE_JAW2022/A-EW_283_JAW2022_WEB.pdf (accessed: 01/2023).

[16] Umwelt Bundesamt, *Indicator: Greenhouse gas emissions*, 2022. [Online]. Available: https://www.umweltbundesamt.de/en/data/environmental-indicators/indicator-greenhouse-gas-emissions (accessed: 05/2023).

[17] Federal Ministry for the Environment, Nature Conservation, Building and Nuclear Safety, *Climate Action Plan 2050: Principles and goals of the German government's climate policy*, 2016. [Online]. Available: https://www.bundesregierung.de/breg-en/service/information-material-issued-by-the-federal-government/climate-action-plan-2050-728890 (accessed: 05/2023).

[18] G. Bieker, *A global comparison of the life-cycle greenhouse gas emissions of combustion engine and electric passenger cars*, 2021. [Online]. Available: https://theicct.org/sites/default/files/publications/Global-LCA-passenger-cars-jul2021_0.pdf (accessed: 05/2023).

[19] V. Nimesh, R. Kumari, N. Soni, A. K. Goswami, and V. Mahendra Reddy, “Implication viability assessment of electric vehicles for different regions: An approach of life cycle assessment considering exergy analysis and battery degradation,” *Energy Conversion and Management*, vol. 237, 114104, 2021.

[20] M. Zwicker, M. Moghadam, W. Zhang, and C. V. Nielsen, “Automotive battery pack manufacturing – a review of battery to tab joining,” *Journal of Advanced Joining Processes*, vol. 1, 100017, 2020.

[21] S. Arora, W. Shen, and A. Kapoor, “Review of mechanical design and strategic placement technique of a robust battery pack for electric vehicles,” *Renewable and Sustainable Energy Reviews*, vol. 60, 1319–1331, 2016.

[22] L. H. Saw, Y. Ye, and A. A. Tay, “Integration issues of lithium-ion battery into electric vehicles battery pack,” *Journal of Cleaner Production*, vol. 113, 1032–1045, 2016.

[23] H. Wang, S. Wang, X. Feng, X. Zhang, K. Dai, J. Sheng, Z. Zhao, Z. Du, Z. Zhang, K. Shen, C. Xu, Q. Wang, X. Sun, Y. Li, J. Ling, J. Feng, H. Wang, and M. Ouyang, “An experimental study on the thermal characteristics of the Cell-To-Pack system,” *Energy*, vol. 227, 120338, 2021.

[24] K. Shen, J. Sun, Y. Zheng, C. Xu, H. Wang, S. Wang, S. Chen, and X. Feng, “A comprehensive analysis and experimental investigation for the thermal management of cell-to-pack battery system,” *Applied Thermal Engineering*, vol. 211, 118422, 2022.

[25] F. Pampel, S. Pischinger, and M. Teuber, “A systematic comparison of the packing density of battery cell-to-pack concepts at different degrees of implementation,” *Results in Engineering*, vol. 13, 100310, 2022.

[26] J. Warner, “Lithium-Ion Battery Applications,” in *The Handbook of Lithium-Ion Battery Pack Design*, Munich: Elsevier, 2015, 177–209.

[27] R. Irle, *Global EV Sales for 2021.* [Online]. Available: https://www.ev-volumes.com/news/ev-sales-for-2021/ (accessed: 10/2022).

[28] N. Rietmann, B. Hügler, and T. Lieven, “Forecasting the trajectory of electric vehicle sales and the consequences for worldwide CO2 emissions,” *Journal of Cleaner Production*, vol. 261, 121038, 2020.

[29] A. König, L. Nicoletti, D. Schröder, S. Wolff, A. Waclaw, and M. Lienkamp, “An Overview of Parameter and Cost for Battery Electric Vehicles,” *WEVJ*, vol. 12, no. 1, 21, 2021.

[30] N. Rietmann and T. Lieven, “How policy measures succeeded to promote electric mobility – Worldwide review and outlook,” *Journal of Cleaner Production*, vol. 206, 66–75, 2019.

[31] H. L. Breetz and D. Salon, “Do electric vehicles need subsidies? Ownership costs for conventional, hybrid, and electric vehicles in 14 U.S. cities,” *Energy Policy*, vol. 120, 238–249, 2018.

[32] R. Logtenberg, J. Pawley, and B. Saxifrage, *Comparing Fuel and Maintenance Costs of Electric and Gas Powered Vehicles in Canada*, 2018. [Online]. Available: https://www.2degreesinstitute.org/reports/comparing_fuel_and_maintenance_costs_of_electric_and_gas_powered_vehicles_in_canada.pdf (accessed: 07/2022).

[33] California Air Resources Board, *Advanced Clean Cars (ACC) II Workshop*, 2021. [Online]. Available: https://ww2.arb.ca.gov/sites/default/files/2021-05/acc2_workshop_slides_may062021_ac.pdf (accessed: 07/2022).

[34] H. Löbberding, S. Wessel, C. Offermanns, M. Kehrer, J. Rother, H. Heimes, and A. Kampker, “From Cell to Battery System in BEVs: Analysis of System Packing Efficiency and Cell Types,” *WEVJ*, vol. 11, no. 4, 77, 2020.

[35] M. Fischer, M. Werber, and P. V. Schwartz, “Batteries: Higher energy density than gasoline?,” *Energy Policy*, vol. 37, no. 7, 2639–2641, 2009.

[36] A. Fill and K. P. Birke, “Impacts of cell topology, parameter distributions and current profile on the usable power and energy of lithium-ion batteries,” in *2019 International Conference on Smart Energy Systems and Technologies (SEST)*, Porto, Portugal, 2019, 1–6.

[37] I. Aretxabaleta, I. M. de Alegria, J. Andreu, I. Kortabarria, and E. Robles, “High-Voltage Stations for Electric Vehicle Fast-Charging: Trends, Standards, Charging Modes and Comparison of Unity Power-Factor Rectifiers,” *IEEE Access*, vol. 9, 102177–102194, 2021.

[38] I. Aghabali, J. Bauman, P. J. Kollmeyer, Y. Wang, B. Bilgin, and A. Emadi, “800-V Electric Vehicle Powertrains: Review and Analysis of Benefits, Challenges, and Future Trends,” *IEEE Trans. Transp. Electrific.*, vol. 7, no. 3, 927–948, 2021.

[39] S. Rothgang, T. Baumhöfer, H. van Hoek, T. Lange, R. W. de Doncker, and D. U. Sauer, “Modular battery design for reliable, flexible and multi-technology energy storage systems,” *Applied Energy*, vol. 137, 931–937, 2015.

[40] S. Neupert and J. Kowal, “Inhomogeneities in Battery Packs,” *WEVJ*, vol. 9, no. 2, 20, 2018.

[41] B. Wang, C. Ji, S. Wang, J. Sun, S. Pan, D. Wang, and C. Liang, “Study of non-uniform temperature and discharging distribution for lithium-ion battery modules

in series and parallel connection," *Applied Thermal Engineering*, vol. 168, 114831, 2020.

[42] N. Ganesan, S. Basu, K. S. Hariharan, S. M. Kolake, T. Song, T. Yeo, D. K. Sohn, and S. Doo, "Physics based modeling of a series parallel battery pack for asymmetry analysis, predictive control and life extension," *Journal of Power Sources*, vol. 322, 57–67, 2016.

[43] Z. Song, X.-G. Yang, N. Yang, F. P. Delgado, H. Hofmann, and J. Sun, "A study of cell-to-cell variation of capacity in parallel-connected lithium-ion battery cells," *eTransportation*, vol. 7, 100091, 2021.

[44] L. Zhong, C. Zhang, Y. He, and Z. Chen, "A method for the estimation of the battery pack state of charge based on in-pack cells uniformity analysis," *Applied Energy*, vol. 113, 558–564, 2014.

[45] M. Dubarry, C. Pastor-Fernández, G. Baure, T. F. Yu, W. D. Widanage, and J. Marco, "Battery energy storage system modeling: Investigation of intrinsic cell-to-cell variations," *Journal of Energy Storage*, vol. 23, 19–28, 2019.

[46] N. Wassiliadis, M. Steinsträter, M. Schreiber, P. Rosner, L. Nicoletti, F. Schmid, M. Ank, O. Teichert, L. Wildfeuer, J. Schneider, A. Koch, A. König, A. Glatz, J. Gandlgruber, T. Kröger, X. Lin, and M. Lienkamp, "Quantifying the state of the art of electric powertrains in battery electric vehicles: Range, efficiency, and lifetime from component to system level of the Volkswagen ID.3," *eTransportation*, vol. 12, 100167, 2022.

[47] M. Lelie, T. Braun, M. Knips, H. Nordmann, F. Ringbeck, H. Zappen, and D. U. Sauer, "Battery Management System Hardware Concepts: An Overview," *Applied Sciences*, vol. 8, no. 4, 534, 2018.

[48] G. Harper, R. Sommerville, E. Kendrick, L. Driscoll, P. Slater, R. Stolkin, A. Walton, P. Christensen, O. Heidrich, S. Lambert, A. Abbott, K. Ryder, L. Gaines, and P. Anderson, "Recycling lithium-ion batteries from electric vehicles," *Nature*, vol. 575, no. 7781, 75–86, 2019.

[49] H.-K. Kim, J. H. Choi, and K.-J. Lee, "A Numerical Study of the Effects of Cell Formats on the Cycle Life of Lithium Ion Batteries," *J. Electrochem. Soc.*, vol. 166, no. 10, A1769-A1778, 2019.

[50] T. Hettesheimer, A. Thielmann, C. Neef, and A. Durand, *Preparatory Study on Ecodesign and Energy Labelling of Batteries under FWC ENER/C3/2015-619-Lot 1: TASK 4 : Technologies –For Ecodesign and Energy Labelling*, 2019. [Online]. Available: https://publica.fraunhofer.de/entities/publication/dad22037-0b4a-436d-a2bf-0e50b49c0754/details (accessed: 01/2023).

[51] A. Rheinfeld, J. Sturm, A. Frank, S. Kosch, S. V. Erhard, and A. Jossen, "Impact of Cell Size and Format on External Short Circuit Behavior of Lithium-Ion Cells at Varying Cooling Conditions: Modeling and Simulation," *J. Electrochem. Soc.*, vol. 167, no. 1, 13511, 2019.

[52] J. Li, J. Fleetwood, W. B. Hawley, and W. Kays, "From Materials to Cell: State-of-the-Art and Prospective Technologies for Lithium-Ion Battery Electrode Processing," *Chemical reviews*, vol. 122, no. 1, 903–956, 2022.

[53] A. Das, D. Li, D. Williams, and D. Greenwood, "Joining Technologies for Automotive Battery Systems Manufacturing," *WEVJ*, vol. 9, no. 2, 22, 2018.

[54] A. Abdellahi, S. Atalay, and A. Rajan, “Impact of cell variability on pack statistics for different vehicle segments,” *Journal of Power Sources*, vol. 508, 230246, 2021.

[55] H. Budde-Meiwes, J. Drillkens, B. Lunz, J. Muennix, S. Rothgang, J. Kowal, and D. U. Sauer, “A review of current automotive battery technology and future prospects,” *Proceedings of the Institution of Mechanical Engineers, Part D: Journal of Automobile Engineering*, vol. 227, no. 5, 761–776, 2013.

[56] J. Xie and Y.-C. Lu, “A retrospective on lithium-ion batteries,” *Nature communications*, vol. 11, no. 1, 2499, 2020.

[57] P. Zhu, D. Gastol, J. Marshall, R. Sommerville, V. Goodship, and E. Kendrick, “A review of current collectors for lithium-ion batteries,” *Journal of Power Sources*, vol. 485, 229321, 2021.

[58] Y. Chen, Y. Kang, Y. Zhao, L. Wang, J. Liu, Y. Li, Z. Liang, X. He, X. Li, N. Tavajohi, and B. Li, “A review of lithium-ion battery safety concerns: The issues, strategies, and testing standards,” *Journal of Energy Chemistry*, vol. 59, 83–99, 2021.

[59] T. Nemeth, P. Schröer, M. Kuipers, and D. U. Sauer, “Lithium titanate oxide battery cells for high-power automotive applications – Electro-thermal properties, aging behavior and cost considerations,” *Journal of Energy Storage*, vol. 31, 101656, 2020.

[60] J. Lu, Z. Chen, F. Pan, Y. Cui, and K. Amine, “High-Performance Anode Materials for Rechargeable Lithium-Ion Batteries,” *Electrochem. Energ. Rev.*, vol. 1, no. 1, 35–53, 2018.

[61] Z.-y. Feng, W.-j. Peng, Z.-x. Wang, H.-j. Guo, X.-h. Li, G.-c. Yan, and J.-x. Wang, “Review of silicon-based alloys for lithium-ion battery anodes,” *Int J Miner Metall Mater*, vol. 28, no. 10, 1549–1564, 2021.

[62] Z. Yang, Y. Dai, S. Wang, and J. Yu, “How to make lithium iron phosphate better: A review exploring classical modification approaches in-depth and proposing future optimization methods,” *J. Mater. Chem. A*, vol. 4, no. 47, 18210–18222, 2016.

[63] T. Wang, K. Ren, M. He, W. Dong, W. Xiao, H. Pan, J. Yang, Y. Yang, P. Liu, Z. Cao, X. Ma, and H. Wang, “Synthesis and Manipulation of Single-Crystalline Lithium Nickel Manganese Cobalt Oxide Cathodes: A Review of Growth Mechanism,” *Frontiers in chemistry*, vol. 8, 747, 2020.

[64] A. Manthiram, “An Outlook on Lithium Ion Battery Technology,” *ACS central science*, vol. 3, no. 10, 1063–1069, 2017.

[65] J. Jiang, S. Liu, Z. Ma, Y. Le Wang, and K. Wu, “Butler-Volmer equation-based model and its implementation on state of power prediction of high-power lithium titanate batteries considering temperature effects,” *Energy*, vol. 117, no. 1, 58–72, 2016.

[66] L. Yang, W. Deng, W. Xu, Y. Tian, A. Wang, B. Wang, G. Zou, H. Hou, W. Deng, and X. Ji, “Olivine LiMn x Fe 1−x PO 4 cathode materials for lithium ion batteries: Restricted factors of rate performances,” *J. Mater. Chem. A*, vol. 9, no. 25, 14214–14232, 2021.

[67] J. Li, Z. Du, R. E. Ruther, S. J. AN, L. A. David, K. Hays, M. Wood, N. D. Phillip, Y. Sheng, C. Mao, S. Kalnaus, C. Daniel, and D. L. Wood, “Toward Low-Cost,

High-Energy Density, and High-Power Density Lithium-Ion Batteries," *JOM*, vol. 69, no. 9, 1484–1496, 2017.

[68] M. J. Lain, J. Brandon, and E. Kendrick, "Design Strategies for High Power vs. High Energy Lithium Ion Cells," *Batteries*, vol. 5, no. 4, 64, 2019.

[69] L. Zolin, M. Chandesris, W. Porcher, and B. Lestriez, "An Innovative Process for Ultra-Thick Electrodes Elaboration: Toward Low-Cost and High-Energy Batteries," *Energy Technol.*, vol. 7, no. 5, 1900025, 2019.

[70] Y. Kuang, C. Chen, D. Kirsch, and L. Hu, "Thick Electrode Batteries: Principles, Opportunities, and Challenges," *Adv. Energy Mater.*, vol. 9, no. 33, 1901457, 2019.

[71] P. Dechent, E. Barbers, A. Epp, D. Jöst, W. Li, D. U. Sauer, and S. Lehner, "Correlation of Health Indicators on Lithium-Ion Batteries," *Energy Technol.*, vol. 11, no. 7, 2201398, 2023.

[72] K. A. Severson, P. M. Attia, N. Jin, N. Perkins, B. Jiang, Z. Yang, M. H. Chen, M. Aykol, P. K. Herring, D. Fraggedakis, M. Z. Bazant, S. J. Harris, W. C. Chueh, and R. D. Braatz, "Data-driven prediction of battery cycle life before capacity degradation," *Nat Energy*, vol. 4, no. 5, 383–391, 2019.

[73] P. Fermín-Cueto, E. McTurk, M. Allerhand, E. Medina-Lopez, M. F. Anjos, J. Sylvester, and G. dos Reis, "Identification and machine learning prediction of knee-point and knee-onset in capacity degradation curves of lithium-ion cells," *Energy and AI*, vol. 1, 100006, 2020.

[74] A. Aitio and D. A. Howey, "Predicting battery end of life from solar off-grid system field data using machine learning," *Joule*, vol. 5, no. 12, 3204–3220, 2021.

[75] P. M. Attia, A. Bills, F. Brosa Planella, P. Dechent, G. dos Reis, M. Dubarry, P. Gasper, R. Gilchrist, S. Greenbank, D. Howey, O. Liu, E. Khoo, Y. Preger, A. Soni, S. Sripad, A. G. Stefanopoulou, and V. Sulzer, "Review—"Knees" in Lithium-Ion Battery Aging Trajectories," *J. Electrochem. Soc.*, vol. 169, no. 6, 60517, 2022.

[76] Y. Li, K. Liu, A. M. Foley, A. Zülke, M. Berecibar, E. Nanini-Maury, J. van Mierlo, and H. E. Hoster, "Data-driven health estimation and lifetime prediction of lithium-ion batteries: A review," *Renewable and Sustainable Energy Reviews*, vol. 113, 109254, 2019.

[77] A. Barré, B. Deguilhem, S. Grolleau, M. Gérard, F. Suard, and D. Riu, "A review on lithium-ion battery ageing mechanisms and estimations for automotive applications," *Journal of Power Sources*, vol. 241, 680–689, 2013.

[78] C. Reiter, N. Wassiliadis, L. Wildfeuer, T. Wurster, and M. Lienkamp, "Range Extension of Electric Vehicles through Improved Battery Capacity Utilization: Potentials, Risks and Strategies," *2018 21st International Conference on Intelligent Transportation Systems (ITSC)*, 321–326, 2018.

[79] J. Liu, Z. Wang, J. Bai, T. Gao, and N. Mao, "Heat generation and thermal runaway mechanisms induced by overcharging of aged lithium-ion battery," *Applied Thermal Engineering*, vol. 212, 118565, 2022.

[80] X.-L. Gao, X.-H. Liu, W.-L. Xie, L.-S. Zhang, and S.-C. Yang, "Multiscale observation of Li plating for lithium-ion batteries," *Rare Met.*, vol. 40, no. 11, 3038–3048, 2021.

[81] X. Feng, M. Ouyang, X. Liu, L. Lu, Y. Xia, and X. He, “Thermal runaway mechanism of lithium ion battery for electric vehicles: A review,” *Energy Storage Materials*, vol. 10, 246–267, 2018.

[82] P. V. Chombo and Y. Laoonual, “A review of safety strategies of a Li-ion battery,” *Journal of Power Sources*, vol. 478, 228649, 2020.

[83] X. Feng, L. Lu, M. Ouyang, J. Li, and X. He, “A 3D thermal runaway propagation model for a large format lithium ion battery module,” *Energy*, vol. 115, no. 1, 194–208, 2016.

[84] Z. M. Konz, E. J. McShane, and B. D. McCloskey, “Detecting the Onset of Lithium Plating and Monitoring Fast Charging Performance with Voltage Relaxation,” *ACS Energy Lett.*, vol. 5, no. 6, 1750–1757, 2020.

[85] R. Xiong, Y. Pan, W. Shen, H. Li, and F. Sun, “Lithium-ion battery aging mechanisms and diagnosis method for automotive applications: Recent advances and perspectives,” *Renewable and Sustainable Energy Reviews*, vol. 131, 110048, 2020.

[86] M. Lewerenz, G. Fuchs, L. Becker, and D. U. Sauer, “Irreversible calendar aging and quantification of the reversible capacity loss caused by anode overhang,” *Journal of Energy Storage*, vol. 18, 149–159, 2018.

[87] F. B. Spingler, M. Naumann, and A. Jossen, “Capacity Recovery Effect in Commercial LiFePO4 / Graphite Cells,” *J. Electrochem. Soc.*, vol. 167, no. 4, 40526, 2020.

[88] T. Ohzuku, N. Matoba, and K. Sawai, “Direct evidence on anomalous expansion of graphite-negative electrodes on first charge by dilatometry,” *Journal of Power Sources*, 97-98, 73–77, 2001.

[89] Q. Xiao, M. Gu, H. Yang, B. Li, C. Zhang, Y. Liu, F. Liu, F. Dai, L. Yang, Z. Liu, X. Xiao, G. Liu, P. Zhao, S. Zhang, C. Wang, Y. Lu, and M. Cai, “Inward lithium-ion breathing of hierarchically porous silicon anodes,” *Nature communications*, vol. 6, no. 1, 8844, 2015.

[90] L. de Biasi, A. O. Kondrakov, H. Geßwein, T. Brezesinski, P. Hartmann, and J. Janek, “Between Scylla and Charybdis: Balancing Among Structural Stability and Energy Density of Layered NCM Cathode Materials for Advanced Lithium-Ion Batteries,” *J. Phys. Chem. C*, vol. 121, no. 47, 26163–26171, 2017.

[91] B. Rowden and N. Garcia-Araez, “A review of gas evolution in lithium ion batteries,” *Energy Reports*, vol. 6, no. 5, 10–18, 2020.

[92] J. Schmitt, B. Kraft, J. P. Schmidt, B. Meir, K. Elian, D. Ensling, G. Keser, and A. Jossen, “Measurement of gas pressure inside large-format prismatic lithium-ion cells during operation and cycle aging,” *Journal of Power Sources*, vol. 478, 228661, 2020.

[93] A. Barai, R. Tangirala, K. Uddin, J. Chevalier, Y. Guo, A. McGordon, and P. Jennings, “The effect of external compressive loads on the cycle lifetime of lithium-ion pouch cells,” *Journal of Energy Storage*, vol. 13, 211–219, 2017.

[94] C. Yang, N. Sunderlin, W. Wang, C. Churchill, and M. Keyser, “Compressible battery foams to prevent cascading thermal runaway in Li-ion pouch batteries,” *Journal of Power Sources*, vol. 541, 231666, 2022.

[95] A. S. Mussa, M. Klett, G. Lindbergh, and R. W. Lindström, “Effects of external pressure on the performance and ageing of single-layer lithium-ion pouch cells,” *Journal of Power Sources*, vol. 385, Part 3, 18–26, 2018.

[96] M. Steinhardt, E. I. Gillich, M. Stiegler, and A. Jossen, “Thermal conductivity inside prismatic lithium-ion cells with dependencies on temperature and external compression pressure,” *Journal of Energy Storage*, vol. 32, 101680, 2020.

[97] X. Han, L. Lu, Y. Zheng, X. Feng, Z. Li, J. Li, and M. Ouyang, “A review on the key issues of the lithium ion battery degradation among the whole life cycle,” *eTransportation*, vol. 1, 100005, 2019.

[98] A. Tomaszewska, Z. Chu, X. Feng, S. O'Kane, X. Liu, J. Chen, C. Ji, E. Endler, R. Li, L. Liu, Y. Li, S. Zheng, S. Vetterlein, M. Gao, J. Du, M. Parkes, M. Ouyang, M. Marinescu, G. Offer, and B. Wu, “Lithium-ion battery fast charging: A review,” *eTransportation*, vol. 1, 100011, 2019.

[99] Y. Hu and S.-Y. Choe, “Simultaneous and continuous characterization of reversible and irreversible heat of lithium-ion battery using wavelet transform technique,” *Electrochimica Acta*, vol. 375, 137973, 2021.

[100] L. Zhang, H. Peng, Z. Ning, Z. Mu, and C. Sun, “Comparative Research on RC Equivalent Circuit Models for Lithium-Ion Batteries of Electric Vehicles,” *Applied Sciences*, vol. 7, no. 10, 1002, 2017.

[101] X. Hu, S. Li, and H. Peng, “A comparative study of equivalent circuit models for Li-ion batteries,” *Journal of Power Sources*, vol. 198, 359–367, 2012.

[102] X. Lai, W. Gao, Y. Zheng, M. Ouyang, J. Li, X. Han, and L. Zhou, “A comparative study of global optimization methods for parameter identification of different equivalent circuit models for Li-ion batteries,” *Electrochimica Acta*, vol. 295, 1057–1066, 2019.

[103] M. Keyser, A. Pesaran, Q. Li, S. Santhanagopalan, and K. Smith *et al.,* “Enabling fast charging – Battery thermal considerations,” *Journal of Power Sources*, vol. 367, 228–236, 2017.

[104] A. S. Kumar, T. Satyavani, and M. Senthilkumar, “Effect of temperature and charge stand on performance of lithium-ion polymer pouch cell,” *Journal of Energy Storage*, vol. 6, 239–247, 2016.

[105] J. Lin, X. Liu, S. Li, C. Zhang, and S. Yang, “A review on recent progress, challenges and perspective of battery thermal management system,” *International Journal of Heat and Mass Transfer*, vol. 167, 120834, 2021.

[106] N. Wassiliadis, J. Schneider, A. Frank, L. Wildfeuer, X. Lin, A. Jossen, and M. Lienkamp, “Review of fast charging strategies for lithium-ion battery systems and their applicability for battery electric vehicles,” *Journal of Energy Storage*, vol. 44, B, 103306, 2021.

[107] K. Monika, C. Chakraborty, S. Roy, S. Dinda, S. A. Singh, and S. P. Datta, “Parametric investigation to optimize the thermal management of pouch type lithium-ion batteries with mini-channel cold plates,” *International Journal of Heat and Mass Transfer*, vol. 164, 120568, 2021.

[108] W. Wu, S. Wang, W. Wu, K. Chen, S. Hong, and Y. Lai, “A critical review of battery thermal performance and liquid based battery thermal management,” *Energy Conversion and Management*, vol. 182, 262–281, 2019.

[109] C. White and L. G. Swan, “Pack-level performance of electric vehicle batteries in second-life electricity grid energy services,” *Journal of Energy Storage*, vol. 57, 106265, 2023.

[110] A. Jarrett and I. Y. Kim, “Influence of operating conditions on the optimum design of electric vehicle battery cooling plates,” *Journal of Power Sources*, vol. 245, 644–655, 2014.

[111] X. Li, J. Zhao, J. Duan, S. Panchal, J. Yuan, R. Fraser, M. Fowler, and M. Chen, “Simulation of cooling plate effect on a battery module with different channel arrangement,” *Journal of Energy Storage*, vol. 49, 104113, 2022.

[112] T. Deng, G. Zhang, Y. Ran, and P. Liu, “Thermal performance of lithium ion battery pack by using cold plate,” *Applied Thermal Engineering*, vol. 160, 114088, 2019.

[113] Y. Chen, K. Chen, Y. Dong, and X. Wu, “Bidirectional symmetrical parallel mini-channel cold plate for energy efficient cooling of large battery packs,” *Energy*, vol. 242, 122553, 2022.

[114] L. Ma, D. Hansen, L. Durfee, and G. Becker, “Thermo-Mechanical Modeling of a Representative Battery Pack for Electric Vehicles,” *2021 20th IEEE Intersociety Conference on Thermal and Thermomechanical Phenomena in Electronic Systems (iTherm)*, 2021.

[115] Y. Deng, C. Feng, J. E, H. Zhu, J. Chen, M. Wen, and H. Yin, “Effects of different coolants and cooling strategies on the cooling performance of the power lithium ion battery system: A review,” *Applied Thermal Engineering*, vol. 142, 10–29, 2018.

[116] X. Zhang, Z. Li, L. Luo, Y. Fan, and Z. Du, “A review on thermal management of lithium-ion batteries for electric vehicles,” *Energy*, vol. 238, A, 121652, 2022.

[117] Z. Wang, Y. Wang, Z. Xie, H. Li, and W. Peng, “Parametric investigation on the performance of a direct evaporation cooling battery thermal management system,” *International Journal of Heat and Mass Transfer*, vol. 189, 122685, 2022.

[118] G. Xia, L. Cao, and G. Bi, “A review on battery thermal management in electric vehicle application,” *Journal of Power Sources*, vol. 367, 90–105, 2017.

[119] M. Akbarzadeh, T. Kalogiannis, J. Jaguemont, J. He, L. Jin, M. Berecibar, and J. van Mierlo, “Thermal modeling of a high-energy prismatic lithium-ion battery cell and module based on a new thermal characterization methodology,” *Journal of Energy Storage*, vol. 32, 101707, 2020.

[120] B. Shabani and M. Biju, “Theoretical Modelling Methods for Thermal Management of Batteries,” *Energies*, vol. 8, no. 9, 10153–10177, 2015.

[121] eSafety, *Making Europe’s roads safer for everyone*, 2006. [Online]. Available: https://www.ttsitalia.it/file/Libreria/Europe/eSafety_brochure.pdf (accessed: 10/2022).

[122] J. Magliaro, W. Altenhof, and A. T. Alpas, “A review of advanced materials, structures and deformation modes for adaptive energy dissipation and structural crashworthiness,” *Thin-Walled Structures*, vol. 180, 109808, 2022.

[123] R. Uerlich, K. Ambikakumari Sanalkumar, T. Bokelmann, and T. Vietor, “Finite element analysis considering packaging efficiency of innovative battery pack

designs," *International Journal of Crashworthiness*, vol. 25, no. 6, 664–679, 2020.

[124] EVERSAFE, *Recommendations and Guidelines for Battery Crash Safety and Post-Crash Safe Handling*, 2014. [Online]. Available: https://www.diva-portal.org/smash/get/diva2:1367933/FULLTEXT01.pdf (accessed: 03/2023).

[125] L. Berzi, N. Baldanzini, D. Barbani, M. Delogu, R. Sala, and M. Pierini, "Simulation of crash events for an electric four wheel vehicle," *Procedia Structural Integrity*, vol. 12, 249–264, 2018.

[126] G. Zhang, H. Lu, D. Yu, Z. Bao, and H. Wang, "A node-based partly smoothed point interpolation method (NPS-PIM) for dynamic analysis of solids," *Engineering Analysis with Boundary Elements*, vol. 87, 165–172, 2018.

[127] G. R. Liu, T. Nguyen-Thoi, H. Nguyen-Xuan, and K. Y. Lam, "A node-based smoothed finite element method (NS-FEM) for upper bound solutions to solid mechanics problems," *Computers & Structures*, vol. 87, 1-2, 14–26, 2009.

[128] BYD, *BYD's new blade battery set to redefine EV safety standards.* [Online]. Available: https://en.byd.com/news/byds-new-blade-battery-set-to-redefine-ev-safety-standards/ (accessed: 07/2022).

[129] CATL, *CATL launches CTP 3.0 battery "Qilin," achieves the highest integration level in the world*, 2022. [Online]. Available: https://www.catl.com/en/news/958.html (accessed: 07/2022).

[130] S. Link, C. Neef, and T. Wicke, "Trends in Automotive Battery Cell Design: A Statistical Analysis of Empirical Data," *Batteries*, vol. 9, no. 5, 261, 2023.

[131] C. Yang, "Running battery electric vehicles with extended range: Coupling cost and energy analysis," *Applied Energy*, vol. 306, B, 118116, 2022.

[132] EUR-Lex, *Proposal for a REGULATION OF THE EUROPEAN PARLIAMENT AND OF THE COUNCIL concerning batteries and waste batteries, repealing Directive 2006/66/EC and amending Regulation (EU) No 2019/1020*, 2020. [Online]. Available: https://eur-lex.europa.eu/legal-content/EN/TXT/?uri=CELEX%3A52020PC0798 (accessed: 07/2022).

[133] L. Jin, J. Tian, S. Gao, P. Xie, M. Akbarzadeh, T. Kalogiannis, M. Berecibar, Y. Lan, D. Hu, Y. Ding, and G. Qiao, "A novel hybrid thermal management approach towards high-voltage battery pack for electric vehicles," *Energy Conversion and Management*, vol. 247, 114676, 2021.

[134] J. Warner, "Battery Management System Controls," in *The Handbook of Lithium-Ion Battery Pack Design*, Munich: Elsevier, 2015, 91–101.

[135] A. Osyczka, "An approach to multicriterion optimization problems for engineering design," *Computer Methods in Applied Mechanics and Engineering*, vol. 15, no. 3, 309–333, 1978.

[136] F. Peres and M. Castelli, "Combinatorial Optimization Problems and Metaheuristics: Review, Challenges, Design, and Development," *Applied Sciences*, vol. 11, no. 14, 6449, 2021.

[137] J. S. Arora, O. A. Elwakeil, A. I. Chahande, and C. C. Hsieh, "Global optimization methods for engineering applications: A review," *Structural Optimization*, vol. 9, 3-4, 137–159, 1995.

[138] J. D. Pintér, “How difficult is nonlinear optimization? A practical solver tuning approach, with illustrative results,” *Ann Oper Res*, vol. 265, no. 1, 119–141, 2018.

[139] C. Gambella, B. Ghaddar, and J. Naoum-Sawaya, “Optimization problems for machine learning: A survey,” *European Journal of Operational Research*, vol. 290, no. 3, 807–828, 2021.

[140] I. H. Sarker, “Machine Learning: Algorithms, Real-World Applications and Research Directions,” *SN computer science*, vol. 2, no. 3, 160, 2021.

[141] J. McCarthy, M. Minsky, N. Rochester, and C. E. Shannon, “A Proposal for the Dartmouth Summer Research Project on Artificial Intelligence,” in *Dartmout Summer Research Project on Artificial Intelligence*, 1956.

[142] K. P. Murphy, *Machine learning: Machine Learning: A Probabilistic Perspective*. Cambridge: MIT Press, 2012.

[143] R. Nian, J. Liu, and B. Huang, “A review On reinforcement learning: Introduction and applications in industrial process control,” *Computers & Chemical Engineering*, vol. 139, 106886, 2020.

[144] S. Marsland, *Machine learning: An algorithmic perspective*. Boca Raton: CRC Press, 2014.

[145] E. Schulz, M. Speekenbrink, and A. Krause, “A tutorial on Gaussian process regression: Modelling, exploring, and exploiting functions,” *Journal of Mathematical Psychology*, vol. 85, 1–16, 2018.

[146] P. I. Frazier, *A Tutorial on Bayesian Optimization*, 2018. [Online]. Available: https://doi.org/10.48550/arXiv.1807.02811 (accessed: 01/2023).

[147] H. Wang, B. van Stein, M. Emmerich, and T. Back, “"A new acquisition function for Bayesian optimization based on the moment-generating function,” *2017 IEEE International Conference on Systems, Man, and Cybernetics (SMC)*, 507–512, 2017.

[148] J. M. Hernández-Lobato, M. W. Hoffman, and Z. Ghahramani, *Predictive Entropy Search for Efficient Global Optimization of Black-box Functions*, 2014. [Online]. Available: https://arxiv.org/abs/1406.2541 (accessed: 07/2022).

[149] R. B. Schnabel, “A view of the limitations, opportunities, and challenges in parallel nonlinear optimization,” *Parallel Computing*, vol. 21, no. 6, 875–905, 1995.

[150] B. M. Assran, A. Aytekin, H. R. Feyzmahdavian, M. Johansson, and M. G. Rabbat, “Advances in Asynchronous Parallel and Distributed Optimization,” *Proc. IEEE*, vol. 108, no. 11, 2013–2031, 2020.

[151] G. Schryen, “Parallel computational optimization in operations research: A new integrative framework, literature review and research directions,” *European Journal of Operational Research*, vol. 287, no. 1, 1–18, 2020.

[152] U. Ibusuki and P. C. Kaminski, “Product development process with focus on value engineering and target-costing: A case study in an automotive company,” *International Journal of Production Economics*, vol. 105, no. 2, 459–474, 2007.

[153] R. Wendland, *Ein Beitrag zur thermischen Auslegung von Fahrzeug-Batteriesystemen*. Braunschweig: Technische Universität Braunschweig, 2021.

[154] H.-H. Braess and U. Seiffert, “Produktentstehungsprozess,” in *Vieweg Handbuch Kraftfahrzeugtechnik*, H.-H. Braess and U. Seiffert, Eds., Wiesbaden: Vieweg+Teubner Verlag, 2012, 881–948.

[155] M. Held, D. Weidmann, D. Kammerl, C. Hollauer, M. Mörtl, M. Omer, and U. Lindemann, “Current challenges for sustainable product development in the German automotive sector: A survey based status assessment,” *Journal of Cleaner Production*, vol. 195, 869–889, 2018.

[156] G. Michalos, S. Makris, N. Papakostas, D. Mourtzis, and G. Chryssolouris, “Automotive assembly technologies review: Challenges and outlook for a flexible and adaptive approach,” *CIRP Journal of Manufacturing Science and Technology*, vol. 2, no. 2, 81–91, 2010.

[157] G. Canuto da Silva and P. C. Kaminski, “Proposal of framework to managing the automotive product development process,” *Cogent Engineering*, vol. 4, no. 1, 1317318, 2017.

[158] C. Frank, L. Holsten, T. Şahin, and T. Vietor, “How to manage vehicle platform variants? A method to assess platform variance through competitive analysis,” *Procedia CIRP*, vol. 109, 598–603, 2022.

[159] D. Doran, S. Ben Mahmoud-Jouini, and S. Lenfle, “Platform re-use lessons from the automotive industry,” *International Journal of Operations & Production Management*, vol. 30, no. 1, 98–124, 2010.

[160] S. Bondar, J. Stjepandić, and A. Pfouga, “Supplier Collaboration in Development of Product Platforms,” *2018 IEEE International Conference on Engineering, Technology and Innovation (ICE/ITMC)*, 1–7, 2018.

[161] A. Epp and D. U. Sauer, “Multiperspective Optimization of Cell and Module Dimensioning for Different Lithium-Ion Cell Formats on Geometric and Generic Assumptions,” *Energy Technol.*, vol. 10, no. 3, 2100874, 2022.

[162] X. He, S. Zhang, Y. Wu, T. J. Wallington, X. Lu, M. A. Tamor, M. B. McElroy, K. M. Zhang, C. P. Nielsen, and J. Hao, “Economic and Climate Benefits of Electric Vehicles in China, the United States, and Germany,” *Environmental science & technology*, vol. 53, no. 18, 11013–11022, 2019.

[163] S.-C. Kang and H. Lee, “Economic appraisal of implementing electric vehicle taxis in Seoul,” *Research in Transportation Economics*, vol. 73, 45–52, 2019.

[164] Z. P. Cano, D. Banham, S. Ye, A. Hintennach, J. Lu, M. Fowler, and Z. Chen, “Batteries and fuel cells for emerging electric vehicle markets,” *Nat Energy*, vol. 3, no. 4, 279–289, 2018.

[165] J. Zheng, X. Sun, L. Jia, and Y. Zhou, “Electric passenger vehicles sales and carbon dioxide emission reduction potential in China’s leading markets,” *Journal of Cleaner Production*, vol. 243, 118607, 2020.

[166] S. Ding and R. Li, “Forecasting the sales and stock of electric vehicles using a novel self-adaptive optimized grey model,” *Engineering Applications of Artificial Intelligence*, vol. 100, 104148, 2021.

[167] G. Berckmans, M. Messagie, J. Smekens, N. Omar, L. Vanhaverbeke, and J. van Mierlo, “Cost Projection of State of the Art Lithium-Ion Batteries for Electric Vehicles Up to 2030,” *Energies*, vol. 10, no. 9, 1314, 2017.

[168] C. Hampel, *Opel Mokka-e prices are out and order books open*, 2020. [Online]. Available: https://www.electrive.com/2020/09/22/opel-mokka-e-prices-start-at-32990-euros/ (accessed: 03/2021).

[169] P. Lyu, X. Liu, J. Qu, J. Zhao, Y. Huo, Z. Qu, and Z. Rao, "Recent advances of thermal safety of lithium ion battery for energy storage," *Energy Storage Materials*, vol. 31, 195–220, 2020.

[170] Y. Ma, H. Mou, and H. Zhao, "Cooling optimization strategy for lithium-ion batteries based on triple-step nonlinear method," *Energy*, vol. 201, 117678, 2020.

[171] F. Bai, M. Chen, W. Song, Q. Yu, Y. Li, Z. Feng, and Y. Ding, "Investigation of thermal management for lithium-ion pouch battery module based on phase change slurry and mini channel cooling plate," *Energy*, vol. 167, 561–574, 2019.

[172] A. Sauer, A. Thielmann, and R. Isenmann, "Modularity in Roadmapping – Integrated foresight of technologies, products, applications, markets and society: The case of "Lithium Ion Battery LIB 2015"," *Technological Forecasting and Social Change*, vol. 125, 321–333, 2017.

[173] Q. Wang, B. Mao, S. I. Stoliarov, and J. Sun, "A review of lithium ion battery failure mechanisms and fire prevention strategies," *Progress in Energy and Combustion Science*, vol. 73, 95–131, 2019.

[174] Tesla, *2020 Annual Meeting of Stockholders and Battery Day*, 2020. [Online]. Available: https://www.tesla.com/2020shareholdermeeting (accessed: 06/2023).

[175] Volkswagen Group News, *Power Day: Volkswagen presents technology roadmap for batteries and charging up to 2030*, 2021. [Online]. Available: https://www.volkswagen-newsroom.com/en/press-releases/power-day-volkswagen-presents-technology-roadmap-for-batteries-and-charging-up-to-2030-6891 (accessed: 05/2021).

[176] G. Pistoia and B. Liaw, Eds., *Behaviour of Lithium-Ion Batteries in Electric Vehicles: Battery Health, Performance, Safety, and Cost*. Cham: Springer, 2018.

[177] E. Pierri, V. Cirillo, T. Vietor, and M. Sorrentino, "Adopting a Conversion Design Approach to Maximize the Energy Density of Battery Packs in Electric Vehicles," *Energies*, vol. 14, no. 7, 1939, 2021.

[178] D. Bhattacharjya, D. Carriazo, J. Ajuria, and A. Villaverde, "Study of electrode processing and cell assembly for the optimized performance of supercapacitor in pouch cell configuration," *Journal of Power Sources*, vol. 439, 227106, 2019.

[179] J. W. Choi and D. Aurbach, "Promise and reality of post-lithium-ion batteries with high energy densities," *Nat Rev Mater*, vol. 1, no. 4, 359, 2016.

[180] E. Maiser, "Battery packaging - Technology review," in *AIP Conference Proceedings 16 June 2014*, Freiberg, 2014, 204–218.

[181] R. Wagner, N. Preschitschek, S. Passerini, J. Leker, and M. Winter, "Current research trends and prospects among the various materials and designs used in lithium-based batteries," *J Appl Electrochem*, vol. 43, no. 5, 481–496, 2013.

[182] Z. Gao, C. Chin, J. Chiew, J. Jia, and C. Zhang, "Design and Implementation of a Smart Lithium-Ion Battery System with Real-Time Fault Diagnosis Capability for Electric Vehicles," *Energies*, vol. 10, no. 10, 1503, 2017.

[183] T. G. Tranter, R. Timms, P. R. Shearing, and D. J. L. Brett, “Communication—Prediction of Thermal Issues for Larger Format 4680 Cylindrical Cells and Their Mitigation with Enhanced Current Collection,” *J. Electrochem. Soc.*, vol. 167, no. 16, 160544, 2020.

[184] C. Lensch-Franzen, M. Gohl, M. Schmalz, and T. Doguer, “From Cell to Battery System - Different Cell Formats and their System Integration,” *MTZ Worldw*, vol. 81, no. 11, 68–73, 2020.

[185] R. Schröder, M. Aydemir, and G. Seliger, “Comparatively Assessing different Shapes of Lithium-ion Battery Cells,” *Procedia Manufacturing*, vol. 8, 104–111, 2017.

[186] R. E. Ciez and J. F. Whitacre, “Comparison between cylindrical and prismatic lithium-ion cell costs using a process based cost model,” *Journal of Power Sources*, vol. 340, 273–281, 2017.

[187] P. A. Nelson, S. Ahmed, K. G. Gallagher, and D. W. Dees, *Modeling the Performance and Cost of Lithium-Ion Batteries for Electric-Drive Vehicles"*. Third Edition, ANL/CSE-19/2, 2019. [Online]. Available: https://www.anl.gov/cse/batpac-model-software (accessed: 05/2021).

[188] F. Duffner, M. Wentker, M. Greenwood, and J. Leker, “Battery cost modeling: A review and directions for future research,” *Renewable and Sustainable Energy Reviews*, vol. 127, 109872, 2020.

[189] J. Warner, “Battery Pack Design Criteria and Selection,” in *The Handbook of Lithium-Ion Battery Pack Design*, Munich: Elsevier, 2015, 35–49.

[190] C. Yuan, Y. Deng, T. Li, and F. Yang, “Manufacturing energy analysis of lithium ion battery pack for electric vehicles,” *CIRP Annals*, vol. 66, no. 1, 53–56, 2017.

[191] T. Lange, H. van Hoek, C. Schäper, and R. W. de Doncker, “Advanced Modular Drive Train Concepts for Electric Vehicles,” in *Lecture Notes in Mobility, Advanced Microsystems for Automotive Applications 2013*, J. Fischer-Wolfarth and G. Meyer, Eds., Heidelberg: Springer, 2013, 223–232.

[192] Volkswagen Group News, *Modular electric drive matrix (MEB)*, 2023. [Online]. Available: https://www.volkswagen-newsroom.com/en/modular-electric-drive-matrix-meb-3677 (accessed: 05/2023).

[193] Z. B. Omariba, L. Zhang, and D. Sun, “Review of Battery Cell Balancing Methodologies for Optimizing Battery Pack Performance in Electric Vehicles,” *IEEE Access*, vol. 7, 129335–129352, 2019.

[194] M. Ye, X. Song, R. Xiong, and F. Sun, “A Novel Dynamic Performance Analysis and Evaluation Model of Series-Parallel Connected Battery Pack for Electric Vehicles,” *IEEE Access*, vol. 7, 14256–14265, 2019.

[195] D. E. Demirocak and B. Bhushan, “Probing the aging effects on nanomechanical properties of a LiFePO4 cathode in a large format prismatic cell,” *Journal of Power Sources*, vol. 280, 256–262, 2015.

[196] M. Dubarry, B. Y. Liaw, M.-S. Chen, S.-S. Chyan, K.-C. Han, W.-T. Sie, and S.-H. Wu, “Identifying battery aging mechanisms in large format Li ion cells,” *Journal of Power Sources*, vol. 196, no. 7, 3420–3425, 2011.

[197] W. Shi, X. Hu, J. Wang, J. Jiang, Y. Zhang, and T. Yip, “Analysis of Thermal Aging Paths for Large-Format LiFePO4/Graphite Battery,” *Electrochimica Acta*, vol. 196, 13–23, 2016.

[198] M. Storch, S. L. Hahn, J. Stadler, R. Swaminathan, D. Vrankovic, C. Krupp, and R. Riedel, “Post-mortem analysis of calendar aged large-format lithium-ion cells: Investigation of the solid electrolyte interphase,” *Journal of Power Sources*, vol. 443, 227243, 2019.

[199] T. Grandjean, A. Barai, E. Hosseinzadeh, Y. Guo, A. McGordon, and J. Marco, “Large format lithium ion pouch cell full thermal characterisation for improved electric vehicle thermal management,” *Journal of Power Sources*, vol. 359, 215–225, 2017.

[200] O. Elsewify, M. Souri, M. N. Esfahani, E. Hosseinzadeh, and M. Jabbari, “A new method for internal cooling of a large format lithium-ion battery pouch cell,” *Energy*, vol. 225, 120139, 2021.

[201] H. Lundgren, P. Svens, H. Ekström, C. Tengstedt, J. Lindström, M. Behm, and G. Lindbergh, “Thermal Management of Large-Format Prismatic Lithium-Ion Battery in PHEV Application,” *J. Electrochem. Soc.*, vol. 163, no. 2, A309-A317, 2015.

[202] B. Coleman, J. Ostanek, and J. Heinzel, “Reducing cell-to-cell spacing for large-format lithium ion battery modules with aluminum or PCM heat sinks under failure conditions,” *Applied Energy*, vol. 180, 14–26, 2016.

[203] C. Reiter, X. Lin, L.-E. Schlereth, and M. Lienkamp, “Finding the ideal automotive battery concept,” *Forsch Ingenieurwes*, vol. 83, no. 4, 817–830, 2019.

[204] G. Kovachev, H. Schröttner, G. Gstrein, L. Aiello, I. Hanzu, H. M. Wilkening, A. Foitzik, M. Wellm, W. Sinz, and C. Ellersdorfer, “Analytical Dissection of an Automotive Li-Ion Pouch Cell,” *Batteries*, vol. 5, no. 4, 67, 2019.

[205] A. Kampker, S. Wessel, F. Fiedler, and F. Maltoni, “Battery pack remanufacturing process up to cell level with sorting and repurposing of battery cells,” *Jnl Remanufactur*, vol. 11, no. 1, 1–23, 2021.

[206] E. Gerlitz, M. Greifenstein, J. Hofmann, and J. Fleischer, “Analysis of the Variety of Lithium-Ion Battery Modules and the Challenges for an Agile Automated Disassembly System,” *Procedia CIRP*, vol. 96, 175–180, 2021.

[207] P. Dechent, A. Epp, D. Jöst, Y. Preger, P. M. Attia, W. Li, and D. U. Sauer, “ENPOLITE: Comparing Lithium-Ion Cells across Energy, Power, Lifetime, and Temperature,” *ACS Energy Lett.*, vol. 6, no. 6, 2351–2355, 2021.

[208] X.-G. Yang, T. Liu, and C.-Y. Wang, “Innovative heating of large-size automotive Li-ion cells,” *Journal of Power Sources*, vol. 342, 598–604, 2017.

[209] L. Wuschke, H.-G. Jäckel, T. Leißner, and U. A. Peuker, “Crushing of large Li-ion battery cells,” *Waste management*, vol. 85, 317–326, 2019.

[210] S. Jung and D. Kang, “Multi-dimensional modeling of large-scale lithium-ion batteries,” *Journal of Power Sources*, vol. 248, 498–509, 2014.

[211] S. U. Kim, P. Albertus, D. Cook, C. W. Monroe, and J. Christensen, “Thermoelectrochemical simulations of performance and abuse in 50-Ah automotive cells,” *Journal of Power Sources*, vol. 268, 625–633, 2014.

[212] M. Keppeler, S. Roessler, and W. Braunwarth, “Production Research as Key Factor for Successful Establishment of Battery Production on the Example of Large-Scale Automotive Cells Containing Nickel-Rich LiNi 0.8 Mn 0.1 Co 0.1 O 2 Electrodes,” *Energy Technol.*, vol. 8, no. 6, 2000183, 2020.

[213] Y. Zhao, L. B. Diaz, Y. Patel, T. Zhang, and G. J. Offer, “How to Cool Lithium Ion Batteries: Optimising Cell Design using a Thermally Coupled Model,” *J. Electrochem. Soc.*, vol. 166, no. 13, A2849-A2859, 2019.

[214] S. H. Hong, D. S. Jang, S. Park, S. Yun, and Y. Kim, “Thermal performance of direct two-phase refrigerant cooling for lithium-ion batteries in electric vehicles,” *Applied Thermal Engineering*, vol. 173, 115213, 2020.

[215] M. Wünsch, J. Kaufman, and D. U. Sauer, “Investigation of the influence of different bracing of automotive pouch cells on cyclic liefetime and impedance spectra,” *Journal of Energy Storage*, vol. 21, 149–155, 2019.

[216] Y. Chung and M. S. Kim, “Thermal analysis and pack level design of battery thermal management system with liquid cooling for electric vehicles,” *Energy Conversion and Management*, vol. 196, 105–116, 2019.

[217] X. Rui, X. Feng, H. Wang, H. Yang, Y. Zhang, M. Wan, Y. Wei, and M. Ouyang, “Synergistic effect of insulation and liquid cooling on mitigating the thermal runaway propagation in lithium-ion battery module,” *Applied Thermal Engineering*, vol. 199, 117521, 2021.

[218] Y. Li, C. Wei, Y. Sheng, F. Jiao, and K. Wu, “Swelling Force in Lithium-Ion Power Batteries,” *Ind. Eng. Chem. Res.*, vol. 59, no. 27, 12313–12318, 2020.

[219] X. Feng, X. He, M. Ouyang, L. Lu, P. Wu, C. Kulp, and S. Prasser, “Thermal runaway propagation model for designing a safer battery pack with 25 Ah LiNixCoyMnzO2 large format lithium ion battery,” *Applied Energy*, vol. 154, 74–91, 2015.

[220] K. F. Yeow and H. Teng, “Characterizing Thermal Runaway of Lithium-ion Cells in a Battery System Using Finite Element Analysis Approach,” *SAE Int. J. Alt. Power.*, vol. 2, no. 1, 179–186, 2013.

[221] M. V. Rajasekhar and P. Gorre, “High voltage battery pack design for hybrid electric vehicles,” in *2015 IEEE International Transportation Electrification Conference (ITEC)*, Chennai, India, 1–7.

[222] A. Kulkarni, A. Kapoor, and S. Arora, “Battery Packaging and System Design for an Electric Vehicle,” in *18th Asia Pacific Automotive Engineering Conference*, 2015.

[223] J. B. Quinn, T. Waldmann, K. Richter, M. Kasper, and M. Wohlfahrt-Mehrens, “Energy Density of Cylindrical Li-Ion Cells: A Comparison of Commercial 18650 to the 21700 Cells,” *J. Electrochem. Soc.*, vol. 165, no. 14, A3284-A3291, 2018.

[224] S. Michaelis, E. Rahimzei, A. Kampker, H. Heimes, C. Offermanns, M. Locke, H. Löbberding, S. Wennemar, A. Thielmann, T. Hettesheimer, C. Neef, A. Kwade, W. Haselrieder, S. Blömeke, S. Doose, N. von Drachenfels, R. Drees, A. Fröhlich, L. Gottschalk, and Z. Huang, *Roadmap Battery Production Equipment 2030: Update 2020*, 2021. [Online]. Available: https://www.vdma.org/viewer/-/v2article/render/4761196 (accessed: 03/2022).

[225] T. Deich, M. Storch, K. Steiner, and A. Bund, “Effects of module stiffness and initial compression on lithium-ion cell aging,” *Journal of Power Sources*, vol. 506, 230163, 2021.

[226] X. Lai, S. Wang, H. Wang, Y. Zheng, and X. Feng, “Investigation of thermal runaway propagation characteristics of lithium-ion battery modules under different trigger modes,” *International Journal of Heat and Mass Transfer*, vol. 171, 121080, 2021.

[227] A. A. Pesaran, G.-H. Kim, and M. Keyser, “Integration issues of cells into battery packs for plug-in and hybrid electric vehicles: Preprint,” *EVS-24 International Battery, Hybrid and Fuel Cell Electric Vehicle Symposium*, 2009.

[228] P. Daubinger, M. Schelter, R. Petersohn, F. Nagler, S. Hartmann, M. H. Herrmann, and G. A. Giffin, “Mechanical Effects Occurring inside Large Format 94 Ah Prismatic Lithium-Ion Cells at Different Bracing during Aging,” *ECS Meeting Abstracts*, 2022, 436, 2022.

[229] Y. Sun, H. Lu, and Y. Jin, “Experimental and Numerical Study on Mechanical Deformation Characteristics of Lithium Iron Phosphate Pouch Battery Modules under Overcharge Conditions,” *Energy Fuels*, vol. 35, no. 18, 15172–15184, 2021.

[230] H. Wang, F. He, and L. Ma, “Experimental and modeling study of controller-based thermal management of battery modules under dynamic loads,” *International Journal of Heat and Mass Transfer*, vol. 103, 154–164, 2016.

[231] T. Wang, K. J. Tseng, J. Zhao, and Z. Wei, “Thermal investigation of lithium-ion battery module with different cell arrangement structures and forced air-cooling strategies,” *Applied Energy*, vol. 134, 229–238, 2014.

[232] W. Tong, K. Somasundaram, E. Birgersson, A. S. Mujumdar, and C. Yap, “Thermo-electrochemical model for forced convection air cooling of a lithium-ion battery module,” *Applied Thermal Engineering*, vol. 99, 672–682, 2016.

[233] K. Kirad and M. Chaudhari, “Design of cell spacing in lithium-ion battery module for improvement in cooling performance of the battery thermal management system,” *Journal of Power Sources*, vol. 481, 229016, 2021.

[234] C. Jung, “Power Up with 800-V Systems: The benefits of upgrading voltage power for battery-electric passenger vehicles,” *IEEE Electrification Magazine*, vol. 5, no. 1, 53–58, 2017.

[235] G. Patry, A. Romagny, S. Martinet, and D. Froelich, “Cost modeling of lithium-ion battery cells for automotive applications,” *Energy Sci Eng*, vol. 3, no. 1, 71–82, 2015.

[236] M. Singh, J. Kaiser, and H. Hahn, “Thick Electrodes for High Energy Lithium Ion Batteries,” *J. Electrochem. Soc.*, vol. 162, no. 7, A1196-A1201, 2015.

[237] T. Danner, M. Singh, S. Hein, J. Kaiser, H. Hahn, and A. Latz, “Thick electrodes for Li-ion batteries: A model based analysis,” *Journal of Power Sources*, vol. 334, 191–201, 2016.

[238] G. E. Blomgren, “The Development and Future of Lithium Ion Batteries,” *J. Electrochem. Soc.*, vol. 164, no. 1, A5019-A5025, 2017.

[239] P. Nelson, D. Santini, and J. Barnes, “Factors Determining the Manufacturing Costs of Lithium-Ion Batteries for PHEVs,” *WEVJ*, vol. 3, no. 3, 457–468, 2009.

[240] D. L. Wood, J. Li, and C. Daniel, “Prospects for reducing the processing cost of lithium ion batteries,” *Journal of Power Sources*, vol. 275, 234–242, 2015.

[241] A. Sakti, J. J. Michalek, E. R. Fuchs, and J. F. Whitacre, “A techno-economic analysis and optimization of Li-ion batteries for light-duty passenger vehicle electrification,” *Journal of Power Sources*, vol. 273, 966–980, 2015.

[242] F. Duffner, L. Mauler, M. Wentker, J. Leker, and M. Winter, “Large-scale automotive battery cell manufacturing: Analyzing strategic and operational effects on manufacturing costs,” *International Journal of Production Economics*, vol. 232, 107982, 2021.

[243] H. Zheng, J. Li, X. Song, G. Liu, and V. S. Battaglia, “A comprehensive understanding of electrode thickness effects on the electrochemical performances of Li-ion battery cathodes,” *Electrochimica Acta*, vol. 71, 258–265, 2012.

[244] J.-H. Schünemann, *Modell zur Bewertung der Herstellkosten von Lithiumionenbatteriezellen*. Göttingen: Sierke Verlag, 2015.

[245] C. Linse and R. Kuhn, “Design of high-voltage battery packs for electric vehicles,” in *Advances in Battery Technologies for Electric Vehicles*: Elsevier, 2015, 245–263.

[246] K. Benabdelaziz, B. Lebrouhi, A. Maftah, and M. Maaroufi, “Novel external cooling solution for electric vehicle battery pack,” *Energy Reports*, vol. 6, no. 3, 262–272, 2020.

[247] A. Epp, R. Wendland, J. Behrendt, R. Gerlach, and D. U. Sauer, “Holistic battery system design optimization for electric vehicles using a multiphysically coupled lithium-ion battery design tool,” *Journal of Energy Storage*, vol. 52, A, 104854, 2022.

[248] A. Kwade, W. Haselrieder, R. Leithoff, A. Modlinger, F. Dietrich, and K. Droeder, “Current status and challenges for automotive battery production technologies,” *Nat Energy*, vol. 3, no. 4, 290–300, 2018.

[249] J. Deng, C. Bae, J. Marcicki, A. Masias, and T. Miller, “Safety modelling and testing of lithium-ion batteries in electrified vehicles,” *Nat Energy*, vol. 3, 261–266, 2018.

[250] J. A. Sanguesa, V. Torres-Sanz, P. Garrido, F. J. Martinez, and J. M. Marquez-Barja, “A Review on Electric Vehicles: Technologies and Challenges,” *Smart Cities*, vol. 4, no. 1, 372–404, 2021.

[251] S. Verma, S. Mishra, A. Gaur, S. Chowdhury, S. Mohapatra, G. Dwivedi, and P. Verma, “A comprehensive review on energy storage in hybrid electric vehicle,” *Journal of Traffic and Transportation Engineering (English Edition)*, vol. 8, no. 5, 621–637, 2021.

[252] J. Li and H. Zhang, “Thermal characteristics of power battery module with composite phase change material and external liquid cooling,” *International Journal of Heat and Mass Transfer*, vol. 156, 119820, 2020.

[253] S. Kalnaus, H. Wang, T. R. Watkins, S. Simunovic, and A. Sengupta, “Features of mechanical behavior of EV battery modules under high deformation rate,” *Extreme Mechanics Letters*, vol. 32, 100550, 2019.

[254] E. Carvou, N. Ben Jema, B. Mitchell, C. Gautherot, J. Rivenc, and L. Colchen, “Contact behavior of electrical vehicle-battery junction box under high shorting and breaking current,” in *26th International Conference on Electrical Contacts (ICEC 2012)*, Beijing, 2012, 151–155.

[255] W. Li, A. Garg, M. Xiao, X. Peng, M. L. Le Phung, M. van Tran, and L. Gao, “Intelligent optimization methodology of battery pack for electric vehicles: A multidisciplinary perspective,” *Int J Energy Res*, vol. 44, no. 12, 9686–9706, 2020.

[256] S. Niu, S. heng, G. Zhu, J. Xu, Q. Qu, K. Wu, and H. Zheng, “Analysis on the effect of external press force on the performance of LiNi0.8Co0.1Mn0.1O2/Graphite large pouch cells,” *Journal of Energy Storage*, vol. 44, B, 103425, 2021.

[257] P. Daubinger, M. Schelter, R. Petersohn, F. Nagler, S. Hartmann, M. Herrmann, and G. A. Giffin, “Impact of Bracing on Large Format Prismatic Lithium-Ion Battery Cells during Aging,” *Advanced Energy Materials*, vol. 12, no. 10, 2102448, 2022.

[258] Saint-Gobain Tape Solutions, *Innovative Compression Pads for Maximum EV Battery Cell Performance*, 2022. [Online]. Available: https://www.tapesolutions.saint-gobain.com/sites/hps-mac3-composites-tapesolutions/files/assetbank_media/Compression-Pads-Max-EV-Battery-Cell-Performance-O-1638_65.pdf (accessed: 11/2022).

[259] X.-G. Yang, T. Liu, and C.-Y. Wang, “Thermally modulated lithium iron phosphate batteries for mass-market electric vehicles,” *Nat Energy*, vol. 6, no. 2, 176–185, 2021.

[260] V. Müller, R.-G. Scurtu, K. Richter, T. Waldmann, M. Memm, M. A. Danzer, and M. Wohlfahrt-Mehrens, “Effects of Mechanical Compression on the Aging and the Expansion Behavior of Si/C-Composite|NMC811 in Different Lithium-Ion Battery Cell Formats,” *J. Electrochem. Soc.*, vol. 166, no. 15, A3796-A3805, 2019.

[261] X. Zhu and L. Li, “A well-posed Euler-Bernoulli beam model incorporating nonlocality and surface energy effect,” *Appl. Math. Mech.-Engl. Ed.*, vol. 40, no. 11, 1561–1588, 2019.

[262] R. Gentle, P. Edwards, and B. Bolton, “Statics,” in *Mechanical Engineering Systems*, Munich: Elsevier, 2001, 204–294.

[263] D. Pasini, “Shape transformers for material and shape selection of lightweight beams,” *Materials & Design*, vol. 28, no. 7, 2071–2079, 2007.

[264] M. Fichtner, “Recent Research and Progress in Batteries for Electric Vehicles,” *Batteries & Supercaps*, vol. 5, no. 2, e202100224, 2022.

[265] Z. Zhou, X. Zhou, B. Cao, L. Yang, and K. M. Liew, “Investigating the relationship between heating temperature and thermal runaway of prismatic lithium-ion battery with LiFePO4 as cathode,” *Energy*, vol. 256, 124714, 2022.

[266] L. Wang, J. Qiu, X. Wang, L. Chen, G. Cao, J. Wang, H. Zhang, and X. He, “Insights for understanding multiscale degradation of LiFePO4 cathodes,” *eScience*, vol. 2, no. 2, 125–137, 2022.

[267] P. Qin, Z. Jia, J. Wu, K. Jin, Q. Duan, L. Jiang, J. Sun, J. Ding, C. Shi, and Q. Wang, “The thermal runaway analysis on LiFePO4 electrical energy storage

packs with different venting areas and void volumes," *Applied Energy*, vol. 313, 118767, 2022.

[268] Y. Shi, "Feasibility of BYD blade batteries in electric vehicles," *HSET*, vol. 32, 193–198, 2023.

[269] M. Xu, R. Wang, B. Reichman, and X. Wang, "Modeling the effect of two-stage fast charging protocol on thermal behavior and charging energy efficiency of lithium-ion batteries," *Journal of Energy Storage*, vol. 20, 298–309, 2018.

[270] J. Liang, Y. Gan, W. Song, M. Tan, and Y. Li, "Thermal–Electrochemical simulation of electrochemical characteristics and temperature difference for a battery module under two-stage fast charging," *Journal of Energy Storage*, vol. 29, 101307, 2020.

[271] X. Zhang, R. Klein, A. Subbaraman, S. Chumakov, X. Li, J. Christensen, C. Linder, and S. U. Kim, "Evaluation of convective heat transfer coefficient and specific heat capacity of a lithium-ion battery using infrared camera and lumped capacitance method," *Journal of Power Sources*, vol. 412, 552–558, 2019.

[272] T. S. Bryden, B. Dimitrov, G. Hilton, C. Ponce de León, P. Bugryniec, S. Brown, D. Cumming, and A. Cruden, "Methodology to determine the heat capacity of lithium-ion cells," *Journal of Power Sources*, vol. 395, 369–378, 2018.

[273] K. A. Murashko, J. Pyrhönen, and J. Jokiniemi, "Determination of the through-plane thermal conductivity and specific heat capacity of a Li-ion cylindrical cell," *International Journal of Heat and Mass Transfer*, vol. 162, 120330, 2020.

[274] Y. Sun, *Characterization of thermal conductivity and thermal transport in lithium-ion battery: Thermal & Fluids Analysis Workshop, TFAWS 2018*, 2018. [Online]. Available: https://tfaws.nasa.gov/wp-content/uploads/TFAWS18-PT-11.pdf (accessed: 06/2022).

[275] K. Ziat, H. Louahlia, and H. Gualous, "A comparative study of Li-ion batteries thermal behavior with different geometries,capacities,cathode materials," in *IEECP 2021: International Conference On Innovations in Energy Engineering & Cleaner Production*, Silicon Valley, 2021.

[276] M. Steinhardt, J. V. Barreras, H. Ruan, B. Wu, G. J. Offer, and A. Jossen, "Meta-analysis of experimental results for heat capacity and thermal conductivity in lithium-ion batteries: A critical review," *Journal of Power Sources*, vol. 522, 230829, 2022.

[277] H. Yang, C. N. Savory, B. J. Morgan, D. O. Scanlon, J. M. Skelton, and A. Walsh, "Chemical Trends in the Lattice Thermal Conductivity of Li(Ni, Mn, Co)O 2 (NMC) Battery Cathodes," *Chem. Mater.*, vol. 32, no. 17, 7542–7550, 2020.

[278] L. Wei, Z. Lu, F. Cao, L. Zhang, X. Yang, X. Yu, and L. Jin, "A comprehensive study on thermal conductivity of the lithium-ion battery," *Int J Energy Res*, vol. 44, no. 12, 9466–9478, 2020.

[279] R. Christen, G. Rizzo, A. Gadola, and M. Stöck, "Test Method for Thermal Characterization of Li-Ion Cells and Verification of Cooling Concepts," *Batteries*, vol. 3, no. 1, 3, 2017.

[280] IEA, *Global EV Outlook 2023*, 2023. [Online]. Available: https://www.iea.org/reports/global-ev-outlook-2023 (accessed: 05/2023).

[281] M. Philippot, G. Alvarez, E. Ayerbe, J. van Mierlo, and M. Messagie, “Eco-Efficiency of a Lithium-Ion Battery for Electric Vehicles: Influence of Manufacturing Country and Commodity Prices on GHG Emissions and Costs,” *Batteries*, vol. 5, no. 1, 23, 2019.

[282] Roland Berger, *Battery Monitor 2022: The value chain in the field of tension between economoy and ecology*, 2022. [Online]. Available: https://www.rolandberger.com/en/Insights/Publications/Battery-Monitor-2022-Technology-and-sustainability-in-the-battery-market.html (accessed: 11/2022).

[283] M. Weiss, R. Ruess, J. Kasnatscheew, Y. Levartovsky, N. R. Levy, P. Minnmann, L. Stolz, T. Waldmann, M. Wohlfahrt-Mehrens, D. Aurbach, M. Winter, Y. Ein-Eli, and J. Janek, “Fast Charging of Lithium-Ion Batteries: A Review of Materials Aspects,” *Advanced Energy Materials*, vol. 11, no. 33, 2101126, 2021.

[284] A. Masias, J. Marcicki, and W. A. Paxton, “Opportunities and Challenges of Lithium Ion Batteries in Automotive Applications,” *ACS Energy Lett.*, vol. 6, no. 2, 621–630, 2021.

[285] EURO NCAP, *Oblique pole side impact testing protocol*, 2015. [Online]. Available: https://cdn.euroncap.com/media/20874/oblique-pole-side-impact-test-protocol-v702.pdf (accessed: 02/2022).

[286] EUR-Lex, *UN Regulation No 100 – Uniform provisions concerning the approval of vehicles with regard to specific requirements for the electric power train [2021/2190]*, 2021. [Online]. Available: http://data.europa.eu/eli/reg/2021/2190/oj (accessed: 12/2021).

[287] B. Kotak, Y. Kotak, K. Brade, T. Kubjatko, and H.-G. Schweiger, “Battery Crush Test Procedures in Standards and Regulation: Need for Augmentation and Harmonisation,” *Batteries*, vol. 7, no. 3, 63, 2021.

[288] European Commission, *OSTLER: Optimised Storage Integration for the Electric Car*, 2014. [Online]. Available: https://trimis.ec.europa.eu/project/optimised-storage-integration-electric-car (accessed: 11/2021).

[289] K.-J. Bathe, *Finite element procedures*. Upper Saddle River: Prentice Hall, 1996.

[290] K. Schrader and M. Schauer, “Multi-directional design control of plastic crash components by means of domain-predictive feed-forward neural networks,” *Struct Multidisc Optim*, vol. 64, no. 6, 4115–4128, 2021.

[291] A. Schumacher, “Grundwissen zur Entwicklung mechanischer Systeme,” in *Optimierung mechanischer Strukturen: Grundlagen und industrielle Anwendungen*, Berlin, Heidelberg: Springer Berlin Heidelberg, 2020, 9–48.

[292] C. Ortmann, *Entwicklung eines graphen- und heuristikbasierten Verfahrens zur Topologieoptimierung von Profilquerschnitten für Crashlastfälle*. Aachen: Shaker, 2015.

[293] A. Epp, S. Rai, F. van Ginneken, A. Varchmin, J. Köhler, and D. U. Sauer, “Simulative Investigation of optimal Multiparameterized Cooling Plate Topologies for different Battery System Configurations,” *Energy Technol.*, vol. 11, no. 9, 2300405, 2023.

[294] R. Wendland, P. Padberg, W. Tegethoff, and J. Köhler, “Dynamic Optimization of Thermal Management and Cooling Plate Design for Battery Systems,” in vol.

1, *27th Aachen Colloquium Automobile and Engine Technology 2018*, Lutz Eckstein und Stefan Pischinger, Ed., Aachen, 2018, 335–357.

[295] C. Richter, *Proposal of New Object-Oriented Equation-Based Model Libraries for Thermodynamic Systems*. Braunschweig: Technische Universität Braunschweig, 2008.

[296] C. W. Schulze, *A Contribution to Numerically Efficient Modelling of Thermodynamic Systems*. Braunschweig: Technische Universität Braunschweig, 2013.

[297] H. D. Baehr and K. Stephan, *Wärme- und Stoffübertragung,* 9th ed. Berlin, Heidelberg: Springer Vieweg Berlin, 2016.

[298] G. Cerbe and G. Wilhelms, *Technische Thermodynamik: Theoretische Grundlagen und praktische Anwendungen,* 15th ed. München: Carl Hanser Verlag, 2008.

[299] L. Cheng, G. Ribatski, and J. R. Thome, “New prediction methods for CO2 evaporation inside tubes: Part II—An updated general flow boiling heat transfer model based on flow patterns,” *International Journal of Heat and Mass Transfer*, vol. 51, 1-2, 125–135, 2008.

[300] S. Jeong, E. Cho, and H.-k. Kim, “Evaporative Heat Transfer and Pressure Drop of CO2 in a Microchannel Tube,” in *Proceedings of the ASME 3rd International Conference on Microchannels and Minichannels: ASME 3rd International Conference on Microchannels and Minichannels, Part B cont’d*, Toronto, 2015, 103–108.

[301] J. Meintschel, D. Schröter, and V. Keck, “Verfahren zur Herstellung einer Kühlplatte mit einem integrierten Kühlkanal für eine Batterie und Verwendung einer Kühlplatte,” DE102008059955B4.

[302] A. C. Benim and S. B. Maddala, “Numerical investigation of friction laws for laminar and turbulent flow in undulated channels,” *HFF*, vol. 31, no. 6, 1837–1856, 2021.

[303] V. Gnielinski, “On heat transfer in tubes,” *International Journal of Heat and Mass Transfer*, vol. 63, 134–140, 2013.

[304] P. Konakov, *A New Correlation for the Friction Coefficient in Smooth Tubes,* 7th ed. Moscov: Report of the Academic Society for Science of the UDSSR, 1946.

[305] D. Taler, “Determining velocity and friction factor for turbulent flow in smooth tubes,” *International Journal of Thermal Sciences*, vol. 105, 109–122, 2016.

[306] VDI e. V., *VDI heat atlas,* 2nd ed. Berlin, Heidelberg: Springer, 2010.

[307] F. Leng, C. M. Tan, and M. Pecht, “Effect of Temperature on the Aging rate of Li Ion Battery Operating above Room Temperature,” *Scientific reports*, vol. 5, no. 1, 12967, 2015.

[308] D. Ren, H. Hsu, R. Li, X. Feng, D. Guo, X. Han, L. Lu, X. He, S. Gao, J. Hou, Y. Li, Y. Wang, and M. Ouyang, “A comparative investigation of aging effects on thermal runaway behavior of lithium-ion batteries,” *eTransportation*, vol. 2, 100034, 2019.

[309] H. Lim, D.-H. Jung, G. Kwon, Y. J. Lee, and J. S. Park, “Downsizing an automotive junction box based on large current-carrying printed-circuit board

optimization," *Proceedings of the Institution of Mechanical Engineers, Part D: Journal of Automobile Engineering*, vol. 231, no. 2, 267–278, 2017.

[310] S. W. Lee and S.-W. Baek, "Implementation and Experimental Verification of Smart Junction Box for Low-Voltage Automotive Electronics in Electric Vehicles," *Applied Sciences*, vol. 10, no. 7, 2214, 2020.

[311] J. Deng, C. Bae, A. Denlinger, and T. Miller, "Electric Vehicles Batteries: Requirements and Challenges," *Joule*, vol. 4, no. 3, 511–515, 2020.

[312] BOYD, *Liquid Cold Plate Manufacturing Cost Drivers: The Impact of Using Different Technologies in Liquid Cold Plate Fabrication*, 2020. [Online]. Available: https://www.boydcorp.com/resources/temperature-control/liquid-cold-plate-cost-drivers.html (accessed: 10/2022).

[313] Gabrian, *5 Important Factors That Impact the Cost of Custom Aluminum Extrusions.* [Online]. Available: https://www.gabrian.com/cost-of-custom-aluminum-extrusions/ (accessed: 10/2022).

[314] G. Domingues-Olavarria, P. Fyhr, A. Reinap, M. Andersson, and M. Alakula, "From Chip to Converter: A Complete Cost Model for Power Electronics Converters," *IEEE Trans. Power Electron.*, vol. 32, no. 11, 8681–8692, 2017.

[315] N. Lutsey and M. Nicholas, "Update on Electric Vehicle Costs in the United States through 2030," *International Council on Clean Transportation (ICCT)*, 2019.

[316] S. Agarwal and M. Rosina, *LI-ION BATTERY PACKS FOR AUTOMOTIVE AND STATIONARY STORAGE APPLICATIONS 2020*, 2020. [Online]. Available: https://s3.i-micronews.com/uploads/2020/03/YDR20068_Li-ion-Battery_Packs_for_Automotive_and_Stationary_Storage_Applications_2020_flyer.pdf (accessed: 09/2021).

[317] V. Henze, *Lithium-ion Battery Pack Prices Rise for First Time to an Average of $151/kWh*, 2022. [Online]. Available: https://about.bnef.com/blog/lithium-ion-battery-pack-prices-rise-for-first-time-to-an-average-of-151-kwh/ (accessed: 04/2023).

[318] H. C. Kim, T. J. Wallington, R. Arsenault, C. Bae, S. Ahn, and J. Lee, "Cradle-to-Gate Emissions from a Commercial Electric Vehicle Li-Ion Battery: A Comparative Analysis," *Environmental science & technology*, vol. 50, no. 14, 7715–7722, 2016.

[319] L. A.-W. Ellingsen, G. Majeau-Bettez, B. Singh, A. K. Srivastava, L. O. Valøen, and A. H. Strømman, "Life Cycle Assessment of a Lithium-Ion Battery Vehicle Pack," *Journal of Industrial Ecology*, vol. 18, no. 1, 113–124, 2014.

[320] G. Majeau-Bettez, T. R. Hawkins, and A. H. Strømman, "Life cycle environmental assessment of lithium-ion and nickel metal hydride batteries for plug-in hybrid and battery electric vehicles," *Environmental science & technology*, vol. 45, no. 10, 4548–4554, 2011.

[321] H. Becker, *BMW i3 Charging – The Charging Guide*, 2019. [Online]. Available: https://www.bmwblog.com/2019/11/15/bmw-i3-charging-the-charging-guide/ (accessed: 07/2022).

[322] plugin magazine, *BMW i3 (22 kWh).* [Online]. Available: https://plugin-magazine.com/electric-vehicles/bmw-i3/ (accessed: 07/2022).

[323] evspecifications.com, *2019 BMW i3 42 kWh - Specifications and price.* [Online]. Available: https://www.evspecifications.com/en/model/cd6382 (accessed: 07/2022).

[324] M. Rutten, *TEST DRIVE: BMW iX3 – A Competent Electric SUV Based Upon a Winning Formula*, 2020. [Online]. Available: https://www.bmwblog.com/2020/11/05/test-drive-bmw-ix3-electric-suv/ (accessed: 01/2023).

[325] Electric Vehicle Database, *Hyundai Kona Electric 39 kWh.* [Online]. Available: https://ev-database.uk/car/1239/Hyundai-Kona-Electric-39-kWh (accessed: 07/2022).

[326] evspecifications.com, *2019 Hyundai KONA Electric 39 kWh - Specifications and price.* [Online]. Available: https://www.evspecifications.com/en/model/42546b (accessed: 09/2022).

[327] J. Nisewanger, *Exclusive: details on Hyundai's new battery thermal management design*, 2018. [Online]. Available: https://electricrevs.com/2018/12/20/exclusive-details-on-hyundais-new-battery-thermal-management-design/ (accessed: 09/2022).

[328] ericy, *Kona Battery Pack*, 2020. [Online]. Available: https://www.insideevsforum.com/community/index.php?threads/kona-battery-pack.9750/ (accessed: 07/2022).

[329] Popular Hyundai, *Electric car battery assembly dismantled*, 2020. [Online]. Available: https://www.youtube.com/watch?v=CAFme0KAXXI (accessed: 07/2022).

[330] A. Epp, J. C. Hahn, and D. U. Sauer, "Optimization strategy for coupled battery system design models using Gaussian Process Regression and Classification," *Journal of Energy Storage*, vol. 52, B, 104998, 2022.

[331] B. Nykvist and M. Nilsson, "Rapidly falling costs of battery packs for electric vehicles," *Nature Clim Change*, vol. 5, no. 4, 329–332, 2015.

[332] J. Li and M. S. Mazzola, "Accurate battery pack modeling for automotive applications," *Journal of Power Sources*, vol. 237, 215–228, 2013.

[333] D. Werner, S. Paarmann, A. Wiebelt, and T. Wetzel, "Inhomogeneous Temperature Distribution Affecting the Cyclic Aging of Li-Ion Cells. Part I: Experimental Investigation," *Batteries*, vol. 6, no. 1, 13, 2020.

[334] J. Jaguemont, L. Boulon, and Y. Dubé, "A comprehensive review of lithium-ion batteries used in hybrid and electric vehicles at cold temperatures," *Applied Energy*, vol. 164, 99–114, 2016.

[335] S. Paul, C. Diegelmann, H. Kabza, and W. Tillmetz, "Analysis of ageing inhomogeneities in lithium-ion battery systems," *Journal of Power Sources*, vol. 239, 642–650, 2013.

[336] S. Al Hallaj, H. Maleki, J. S. Hong, and J. R. Selman, "Thermal modeling and design considerations of lithium-ion batteries," *Journal of Power Sources*, vol. 83, 1-2, 1–8, 1999.

[337] L. Raijmakers, D. L. Danilov, R.-A. Eichel, and P. Notten, "A review on various temperature-indication methods for Li-ion batteries," *Applied Energy*, vol. 240, 918–945, 2019.

[338] K. Uddin, A. Picarelli, C. Lyness, N. Taylor, and J. Marco, “An Acausal Li-Ion Battery Pack Model for Automotive Applications,” *Energies*, vol. 7, no. 9, 5675–5700, 2014.

[339] C. Zhu, X. Li, L. Song, and L. Xiang, “Development of a theoretically based thermal model for lithium ion battery pack,” *Journal of Power Sources*, vol. 223, 155–164, 2013.

[340] S. Wu, G. Sun, X. Wu, G. Li, and Q. Li, “Crashworthiness analysis and optimization of fourier varying section tubes,” *International Journal of Non-Linear Mechanics*, vol. 92, 41–58, 2017.

[341] J. Kukreja, T. Nguyen, T. Siegmund, W. Chen, W. Tsutsui, K. Balakrishnan, H. Liao, and N. Parab, “Crash analysis of a conceptual electric vehicle with a damage tolerant battery pack,” *Extreme Mechanics Letters*, vol. 9, no. 3, 371–378, 2016.

[342] J. Zhu, T. Wierzbicki, and W. Li, “A review of safety-focused mechanical modeling of commercial lithium-ion batteries,” *Journal of Power Sources*, vol. 378, 153–168, 2018.

[343] M. Shen and Q. Gao, “A review on battery management system from the modeling efforts to its multiapplication and integration,” *Int J Energy Res*, vol. 43, no. 10, 5042–5075, 2019.

[344] Y. Wang, J. Tian, Z. Sun, L. Wang, R. Xu, M. Li, and Z. Chen, “A comprehensive review of battery modeling and state estimation approaches for advanced battery management systems,” *Renewable and Sustainable Energy Reviews*, vol. 131, 110015, 2020.

[345] L. Zhou, L. He, Y. Zheng, X. Lai, M. Ouyang, and L. Lu, “Massive battery pack data compression and reconstruction using a frequency division model in battery management systems,” *Journal of Energy Storage*, vol. 28, 101252, 2020.

[346] R. M. Salgado, F. Danzi, J. E. Oliveira, A. El-Azab, P. P. Camanho, and M. H. Braga, “The Latest Trends in Electric Vehicles Batteries,” *Molecules (Basel, Switzerland)*, vol. 26, no. 11, 3188, 2021.

[347] Y. Zhao, O. Pohl, A. I. Bhatt, G. E. Collis, P. J. Mahon, T. Rüther, and A. F. Hollenkamp, “A Review on Battery Market Trends, Second-Life Reuse, and Recycling,” *Sustainable Chemistry*, vol. 2, no. 1, 167–205, 2021.

[348] M. Lu, X. Zhang, J. Ji, X. Xu, and Y. Zhang, “Research progress on power battery cooling technology for electric vehicles,” *Journal of Energy Storage*, vol. 27, 101155, 2020.

[349] H. Dai, B. Jiang, X. Hu, X. Lin, X. Wei, and M. Pecht, “Advanced battery management strategies for a sustainable energy future: Multilayer design concepts and research trends,” *Renewable and Sustainable Energy Reviews*, vol. 138, 110480, 2021.

[350] B. Liu, Y. Jia, C. Yuan, L. Wang, X. Gao, S. Yin, and J. Xu, “Safety issues and mechanisms of lithium-ion battery cell upon mechanical abusive loading: A review,” *Energy Storage Materials*, vol. 24, 85–112, 2020.

[351] A. Obeid, U. Tariq, and S. Mukhopadhyay, “Supervised learning for early and accurate battery terminal voltage collapse detection,” *IET Circuits, Devices & Systems*, vol. 14, no. 3, 347–356, 2020.

[352] W. Li, N. Sengupta, P. Dechent, D. Howey, A. Annaswamy, and D. U. Sauer, “One-shot battery degradation trajectory prediction with deep learning,” *Journal of Power Sources*, vol. 506, 230024, 2021.

[353] W. Li, N. Sengupta, P. Dechent, D. Howey, A. Annaswamy, and D. U. Sauer, “Online capacity estimation of lithium-ion batteries with deep long short-term memory networks,” *Journal of Power Sources*, vol. 482, 228863, 2021.

[354] X. Cui, S. Chen, M. Xiao, and W. Li, “A Computational Fluid Dynamics Coupled Multi-Objective Optimization Framework for Thermal System Design for Li-Ion Batteries With Metal Separators,” *Journal of Electrochemical Energy Conversion and Storage*, vol. 18, no. 3, 30903, 2021.

[355] S. Li, H. He, C. Su, and P. Zhao, “Data driven battery modeling and management method with aging phenomenon considered,” *Applied Energy*, vol. 275, 115340, 2020.

[356] W. Li, H. Cui, T. Nemeth, J. Jansen, C. Ünlübayir, Z. Wei, L. Zhang, Z. Wang, J. Ruan, H. Dai, X. Wei, and D. U. Sauer, “Deep reinforcement learning-based energy management of hybrid battery systems in electric vehicles,” *Journal of Energy Storage*, vol. 36, 102355, 2021.

[357] J. Yu, “State of health prediction of lithium-ion batteries: Multiscale logic regression and Gaussian process regression ensemble,” *Reliability Engineering & System Safety*, vol. 174, 82–95, 2018.

[358] X. Li, C. Yuan, and Z. Wang, “Multi-time-scale framework for prognostic health condition of lithium battery using modified Gaussian process regression and nonlinear regression,” *Journal of Power Sources*, vol. 467, 228358, 2020.

[359] W. Li, A. Garg, M. Xiao, and L. Gao, “Optimization for Liquid Cooling Cylindrical Battery Thermal Management System Based on Gaussian Process Model,” *Journal of Thermal Science and Engineering Applications*, vol. 13, no. 2, 21015, 2021.

[360] R. Meka, A. Alaeddini, S. Oyama, and K. Langer, “An Active Learning Methodology for Efficient Estimation of Expensive Noisy Black-Box Functions Using Gaussian Process Regression,” *IEEE Access*, vol. 8, 111460–111474, 2020.

[361] B. Berger, F. Rauscher, and B. Lohmann, “Analysing Gaussian Processes for Stationary Black-Box Combustion Engine Modelling,” *IFAC Proceedings Volumes*, vol. 44, no. 1, 10633–10640, 2011.

[362] P. M. Attia, A. Grover, N. Jin, K. A. Severson, T. M. Markov, Y.-H. Liao, M. H. Chen, B. Cheong, N. Perkins, Z. Yang, P. K. Herring, M. Aykol, S. J. Harris, R. D. Braatz, S. Ermon, and W. C. Chueh, “Closed-loop optimization of fast-charging protocols for batteries with machine learning,” *Nature*, vol. 578, no. 7795, 397–402, 2020.

[363] M. Mansour and J. E. Ellis, “Comparison of methods for estimating real process derivatives in on-line optimization,” *Applied Mathematical Modelling*, vol. 27, no. 4, 275–291, 2003.

[364] J. J. Gorgoso-Varela, F. N. Ogana, and P. O. Ige, “A comparison between derivative and numerical optimization methods used for diameter distribution estimation,” *Scandinavian Journal of Forest Research*, vol. 35, 3-4, 156–164, 2020.

[365] Y. Bard, “Comparison of Gradient Methods for the Solution of Nonlinear Parameter Estimation Problems,” *SIAM J. Numer. Anal.*, vol. 7, no. 1, 157–186, 1970.

[366] Y. Zhang, R. Xiong, H. He, and M. G. Pecht, “Lithium-Ion Battery Remaining Useful Life Prediction With Box–Cox Transformation and Monte Carlo Simulation,” *IEEE Trans. Ind. Electron.*, vol. 66, no. 2, 1585–1597, 2019.

[367] H. Hoseinzadeh, A. Kasaeian, and M. Behshad Shafii, “Geometric optimization of parabolic trough solar collector based on the local concentration ratio using the Monte Carlo method,” *Energy Conversion and Management*, vol. 175, 278–287, 2018.

[368] C. B. Erickson, B. E. Ankenman, and S. M. Sanchez, “Comparison of Gaussian process modeling software,” *European Journal of Operational Research*, vol. 266, no. 1, 179–192, 2018.

[369] *scikit-learn: Machine Learning in Python.* [Online]. Available: https://scikit-learn.org/ (accessed: 01/2022).

[370] C. E. Rasmussen and C. K. I. Williams, *Gaussian processes for machine learning*. Cambridge: The MIT Press, 2006.

[371] D. Duvenaud, *Automatic model construction with Gaussian processes*. Cambridge: University of Cambridge, 2014.

[372] H. Nickisch and C. Rasmussen, “Approximations for Binary Gaussian Process Classification,” *Journal of Machine Learning Research*, vol. 9, 2035–2078, 2008.

[373] J. Snoek, H. Larochelle, and R. P. Adams, “Practical Bayesian Optimization of Machine Learning Algorithms,” in *Proceedings of the 25th International Conference on Neural Information Processing Systems - Volume 2*, Red Hook: Curran Associates Inc., 2012, 2951–2959.

[374] X.-S. Yang, “Firefly Algorithms for Multimodal Optimization,” in *Stochastic Algorithms: Foundations and Applications. SAGA 2009. Lecture Notes in Computer Science*, O. Watanabe and T. Zeugmann, Eds., Berlin, Heidelberg: Springer, 2009.

[375] H. Wang, W. Wang, X. Zhou, H. Sun, J. Zhao, X. Yu, and Z. Cui, “Firefly algorithm with neighborhood attraction,” *Information Sciences*, 382-383, 374–387, 2017.

[376] A. H. Gandomi, X.-S. Yang, S. Talatahari, and A. H. Alavi, “Firefly algorithm with chaos,” *Communications in Nonlinear Science and Numerical Simulation*, vol. 18, no. 1, 89–98, 2013.

[377] A. H. Gandomi, X.-S. Yang, and A. H. Alavi, “Mixed variable structural optimization using Firefly Algorithm,” *Computers & Structures*, vol. 89, 23-24, 2325–2336, 2011.

[378] I. Fister, I. Fister, JR., X.-S. Yang, and J. Brest, “A comprehensive review of firefly algorithms,” *Swarm and Evolutionary Computation*, vol. 13, 34–46, 2013.

[379] W. Alomoush, K. Omar, A. Alrosan, Y. M. Alomari, D. Albashish, and A. Almomani, “Firefly photinus search algorithm,” *Journal of King Saud University - Computer and Information Sciences*, vol. 32, no. 5, 599–607, 2020.

[380] L. d. S. Coelho and V. C. Mariani, “Improved firefly algorithm approach applied to chiller loading for energy conservation,” *Energy and Buildings*, vol. 59, 273–278, 2013.

[381] N. J. Cheung, X.-M. Ding, and H.-B. Shen, “Adaptive firefly algorithm: parameter analysis and its application,” *PloS one*, vol. 9, no. 11, e112634, 2014.

[382] W. A. Khan, N. N. Hamadneh, S. L. Tilahun, and J. M. Ngnotchouye, “A Review and Comparative Study of Firefly Algorithm and its Modified Versions,” in *Optimization Algorithms - Methods and Applications*, O. Baskan, Ed.: InTech, 2016.

[383] L. Zhang, L. Liu, X.-S. Yang, and Y. Dai, “A Novel Hybrid Firefly Algorithm for Global Optimization,” *PloS one*, vol. 11, no. 9, e0163230, 2016.

[384] S. Yu, S. Zhu, Y. Ma, and D. Mao, “A variable step size firefly algorithm for numerical optimization,” *Applied Mathematics and Computation*, vol. 263, C, 214–220, 2015.

[385] A. J. Umbarkar, U. T. Balande, and P. D. Seth, “Performance evaluation of firefly algorithm with variation in sorting for non-linear benchmark problems,” in *APPLIED MATHEMATICS AND COMPUTER SCIENCE: Proceedings of the 1st International Conference on Applied Mathematics and Computer Science*, Rome, Italy, 2017, 20032.

[386] J. T. Frith, M. J. Lacey, and U. Ulissi, “A non-academic perspective on the future of lithium-based batteries,” *Nature communications*, vol. 14, no. 1, 420, 2023.

[387] M. Agranovsky, M. Ben-Artzi, G. Galloway, L. Karp, D. Khavinson, S. Reich, G. Weinstein, and L. Zalcman, *Complex Analysis and Dynamical Systems VI: Part 2: Complex Analysis, Quasiconformal Mappings, Complex Dynamics*. Providence: American Mathematical Society, 2016.

[388] L. Chen, M. Zhang, Y. Ding, S. Wu, Y. Li, G. Liang, H. Li, and H. Pan, “Estimation the internal resistance of lithium-ion-battery using a multi-factor dynamic internal resistance model with an error compensation strategy,” *Energy Reports*, vol. 7, 3050–3059, 2021.

[389] A. Lebkowski, “Temperature, Overcharge and Short-Circuit Studies of Batteries used in Electric Vehicles,” *Przeglad Elektrotechniczny*, vol. 1, no. 5, 69–75, 2017.

[390] Y. Xia, T. Wierzbicki, E. Sahraei, and X. Zhang, “Damage of cells and battery packs due to ground impact,” *Journal of Power Sources*, vol. 267, 78–97, 2014.

[391] M. S. E. Houache, C.-H. Yim, Z. Karkar, and Y. Abu-Lebdeh, “On the Current and Future Outlook of Battery Chemistries for Electric Vehicles—Mini Review,” *Batteries*, vol. 8, no. 7, 70, 2022.

[392] H. Bajolle, M. Lagadic, and N. Louvet, “The future of lithium-ion batteries: Exploring expert conceptions, market trends, and price scenarios,” *Energy Research & Social Science*, vol. 93, 102850, 2022.

[393] V. Henze, *Battery Pack Prices Cited Below $100/kWh for the First Time in 2020, While Market Average Sits at $137/kWh*, 2020. [Online]. Available: https://about.bnef.com/blog/battery-pack-prices-cited-below-100-kwh-for-the-first-time-in-2020-while-market-average-sits-at-137-kwh/ (accessed: 01/2023).

[394] G. Bhutada, *Breaking Down the Cost of an EV Battery Cell*, 2022. [Online]. Available: https://www.visualcapitalist.com/breaking-down-the-cost-of-an-ev-battery-cell/ (accessed: 01/2023).

[395] H. Berg and M. Zackrisson, “Perspectives on environmental and cost assessment of lithium metal negative electrodes in electric vehicle traction batteries,” *Journal of Power Sources*, vol. 415, 83–90, 2019.

[396] G. Zhao, X. Wang, M. Negnevitsky, and H. Zhang, “A review of air-cooling battery thermal management systems for electric and hybrid electric vehicles,” *Journal of Power Sources*, vol. 501, 230001, 2021.

[397] BOYD, *Electric Vehicle Liquid Cold Plate Case Study.* [Online]. Available: https://www.boydcorp.com/resources/resource-center/case-studies/ev-battery-liquid-cold-plate-weight-reduction-design.html (accessed: 01/2023).

[398] SOGEFI Group, *EV BATTERY COOLING PLATES.* [Online]. Available: https://www.sogefigroup.com/en/products/air-cooling-business-unit/ev-battery-cooling-plates.html (accessed: 01/2023).

[399] BOYD, *Liquid Cooling Solutions in Electric Vehicles: Creating Competitive Advantage in eMobility Applications*, 2022. [Online]. Available: https://info.boydcorp.com/hubfs/Resources/Resource-Center/Boyd-Liquid-Cooling-for-EV.pdf (accessed: 01/2023).

[400] R. Singh, G. Lapp, J. Velardo, P. Thanh Long, M. Mochizuki, A. Akbarzadeh, A. Date, K. Mausolf, and K. Busse, “BATTERY COOLING OPTIONS IN ELECTRIC VEHICLES WITH HEAT PIPES,” *Frontiers in Heat and Mass Transfer*, vol. 16, no. 2, 2021.

[401] M. Sellén, *Water Pump Replacement Cost (2022 Prices & Guide)*, 2022. [Online]. Available: https://mechanicbase.com/estimator/water-pump-replacement-cost/ (accessed: 01/2023).

[402] costaide.com, *How Much Does a Water Pump Cost.* [Online]. Available: https://costaide.com/water-pump-cost/ (accessed: 01/2023).

[403] Vovyo pump, *Automotive Electric Water Pump.* [Online]. Available: https://www.vovyopump.com/automotive-electric-water-pump/ (accessed: 01/2023).

[404] boerse.de, *Aluminium cost*. [Online]. Available: https://www.boerse.de/rohstoffe/Aluminiumpreis/XC0009677839 (accessed: 01/2023).

[405] Gabrian, *5 Important Factors That Impact the Cost of Custom Aluminum Extrusions.* [Online]. Available: https://www.gabrian.com/cost-of-custom-aluminum-extrusions/ (accessed: 01/2023).

[406] IQS Directory, *Aluminum Extrusion Manufacturers and Companies.* [Online]. Available: https://www.iqsdirectory.com/aluminum-extrusions/ (accessed: 01/2023).

[407] Brightstar Aluminum Machinery, *What is the cost of setting up an aluminum extrusion factory?*, 2020. [Online]. Available: https://www.machine4aluminium.com/what-is-the-cost-of-setting-up-an-aluminum-extrusion-factory/ (accessed: 01/2023).

[408] Metal supermarktes, *The Aluminium Extrusion Process*, 2015. [Online]. Available: https://www.metalsupermarkets.co.uk/the-aluminium-extrusion-process/ (accessed: 01/2023).

[409] C. Whaling, *EV Power Electronics Cost Analysis*, 2014. [Online]. Available: https://tec.ieee.org/newsletter/may-june-2014 (accessed: 01/2023).

11 List of Publications

Within the course of this dissertation, several publications have been prepared, which are listed below. Content from these publications is used for this dissertation. This is in line with the rules for dissertation of the faculty for Electrical Engineering and Information Technology at RWTH Aachen University and has been agreed with Prof. Dirk Uwe Sauer, the major supervisor of this dissertation. Text elements, graphs, pictures, or tables from these publications are not explicitly cited within the dissertation as far as they are mainly created by me. If such elements in the listed publications are mainly created by the co-authors, a direct link to the publication is given.

Scientific Journals

[1] **A. Epp***, S. Rai*, F. van Ginneken*, A. Varchmin, J. Köhler, and D. U. Sauer, “Simulative Investigation of optimal Multiparameterized Cooling Plate Topologies for different Battery System Configurations,” Energy Technol., vol. 11, no. 9, 2300405, 2023. https://doi.org/10.1002/ente.202300405. **equal contribution*

[2] **A. Epp***, J. C. Hahn*, and D. U. Sauer, “Optimization strategy for coupled battery system design models using Gaussian Process Regression and Classification,” Journal of Energy Storage, vol. 52, B, 104998, 2022. https://doi.org/10.1016/j.est.2022.104998. **equal contribution*

[3] **A. Epp**, R. Wendland, J. Behrendt, R. Gerlach, and D. U. Sauer, “Holistic battery system design optimization for electric vehicles using a multiphysically coupled lithium-ion battery design tool,” Journal of Energy Storage, vol. 52, A, 104854, 2022. https://doi.org/10.1016/j.est.2022.104854.

[4] **A. Epp** and D. U. Sauer, “Multiperspective Optimization of Cell and Module Dimensioning for Different Lithium-Ion Cell Formats on Geometric and Generic Assumptions,” Energy Technol., vol. 10, no. 3, 2100874, 2022. https://doi.org/10.1002/ente.202100874.

[5] P. Dechent*, **A. Epp***, D. Jöst, Y. Preger, P. M. Attia, W. Li, and D. U. Sauer, “ENPOLITE: Comparing Lithium-Ion Cells across Energy, Power, Lifetime, and Temperature,” ACS Energy Lett., vol. 6, no. 6, 2351–2355, 2021. https://doi.org/10.1021/acsenergylett.1c00743. **equal contribution*

[6] P. Dechent, E. Barbers, **A. Epp**, D. Jöst, W. Li, D. U. Sauer, and S. Lehner, “Correlation of Health Indicators on Lithium-Ion Batteries,” Energy Technol., vol. 11, no. 7, 2201398, 2023. https://doi.org/10.1002/ente.202201398.

Conference Proceedings

[1] **A. Epp** and D. U. Sauer, Optimized battery system design for different stages of cell to pack integration, Lecture, Advanced Power Conference, Aachen, Germany, 2023.

[2] **A. Epp** and D. U. Sauer, Lithium-ion cell format and geometry optimization based on system integration capability and requirements for electric vehicles, Poster, International Battery Production Conference, Braunschweig, Germany, 2022.

Patent Applications

[1] **A. Epp**, R. Wendland, R. Gerlach, J. Behrendt, L. M. Subke, T. Franke, S. Fiebig, Verfahren und Vorrichtung zum Bestimmen von Konfigurationsparametern zur Auslegung einer Hochvoltbatterie für ein Fahrzeug, DE Application No. DE 10 2022 200 930 A1, dated 27 January 2022.

12 Curriculum Vitae

Personal Information:

Name	Alexander Epp
Date of birth	February 18th, 1997
Place of birth	Lübbecke, Germany

Education:

12/2020 – Current	PhD candidate, Electrical Engineering and Information Technology, RWTH Aachen University, Aachen, Germany
10/2018 – 09/2020	Master of Science, Business Administration and Engineering: Electrical Power Engineering, RWTH Aachen University, Aachen, Germany
10/2015 – 09/2018	Bachelor of Science, Business Administration and Engineering: Electrical Energy Technology, RWTH Aachen University, Aachen, Germany
08/2007 – 07/2015	Abitur, Söderblom-Gymnasium, Espelkamp, Germany

Work Experience:

12/2020 – Current	Volkswagen AG, Technical Development, Wolfsburg, Germany
11/2018 – 03/2020	Research assistant, Institute for Power Electronics and Electrical Drives (ISEA), RWTH Aachen University, Aachen, Germany
04/2018 – 07/2018	Volkswagen AG, Production and Logistics, Wolfsburg, Germany

ABISEA Band 1
Eßer, Albert
Berührungslose, kombinierte Energie- und Informations-übertragung für bewegliche Systeme
1. Aufl. 1992, 129 S.
ISBN 3-86073-046-0

ABISEA Band 2
Vogel, Ulrich
Entwurf und Beurteilung von Verfahren zur Hochausnutzung des Rad-Schiene-Kraftschlusses durch Triebfahrzeuge
1. Aufl. 1992, 131 S.
ISBN 3-86073-060-6

ABISEA Band 3
Reckhorn, Thomas
Stromeinprägendes Antriebssystem mit fremderregter Synchron-maschine
1. Aufl. 1992, 128 S.
ISBN 3-86073-061-4

ABISEA Band 4
Ackva, Ansgar
Spannungseinprägendes Antriebssystem mit Synchronmaschine und direkter Stromregelung
1. Aufl. 1992, 137 S.
ISBN 3-86073-062-2

ABISEA Band 5
Mertens, Axel
Analyse des Oberschwingungsverhaltens von taktsynchronen Delta - Modulationsverfahren zur Steuerung von Pulsstrom-richtern bei hoher Taktzahl
1. Aufl. 1992, 178 S.
ISBN 3-86073-069-X

ABISEA Band 6
Geuer, Wolfgang
Untersuchungen über das Alterungsverhalten von Blei-Akkumulatoren
1. Aufl. 1993, 97 S.
ISBN 3-86073-097-5

ABISEA Band 7
Langheim, Jochen
Einzelradantrieb für Elektrostraßenfahrzeuge
1. Aufl. 1993, 213 S.
ISBN 3-86073-123-8
(vergriffen)

ABISEA Band 8
Fetz, Joachim
Fehlertolerante Regelung eines Asynchron-Doppelantriebes für ein Elektrospeicherfahrzeug
1. Aufl. 1993, 136 S.
ISBN 3-86073-124-6
(vergriffen)

ABISEA Band 9
Schülting, Ludger
Optimierte Auslegung induktiver Bauelemente für den Mittelfrequenzbereich
1. Aufl. 1993, 126 S.
ISBN 3-86073-174-2
(vergriffen)

ABISEA Band 10
Skudelny, H.-Ch.
Stromrichtertechnik
4. Aufl. 1997, 259 S.
ISBN 3-86073-189-0

ABISEA Band 11
Skudelny, H.-Ch.
Elektrische Antriebe
3. Aufl. 1997, 124 S.
ISBN 3-86073-231-5

ABISEA Band 12
Schöpe, Friedhelm
Batterie-Management für Nickel-Cadmium Akkumulatoren
1. Aufl. 1994, 148 S.
ISBN 3-86073-232-3
(vergriffen)

ABISEA Band 13
v. d. Weem, Jürgen
Schmalbandige aktive Filter für Schienentriebfahrzeuge am Gleichspannungs-fahrdraht
1. Aufl. 1995, 126 S.
ISBN 3-86073-233-1

ABISEA Band 14
Backhaus, Klaus
Spannungseinprägendes Direktantriebssystem mit schnelllaufender geschalteter Reluktanzmaschine
1. Aufl. 1995, 146 S.
ISBN 3-86073-234-X
(vergriffen)

ABISEA Band 15
Reinold, Harry
Optimierung dreiphasiger Pulsdauermodulations-verfahren
1. Aufl. 1996, 107 S.
ISBN 3-86073-235-8

ABISEA Band 16
Köpken, Hans-Georg
Regelverfahren für Parallelschwingkreis-umrichter
1. Aufl. 1996, 125 S.
ISBN 3-86073-236-6

ABISEA Band 17
Mauracher, Peter
Modellbildung und Verbundoptimierung bei Elektrostraßenfahrzeugen
1. Aufl. 1996, 192 S.
ISBN 3-86073-237-4

ABISEA Band 18
Protiwa, Franz-Ferdinand
Vergleich dreiphasiger Resonanz-Wechselrichter in Simulation und Messung
1. Aufl. 1997, 178 S.
ISBN 3-86073-238-2

ABISEA Band 19
Brockmeyer, Ansgar
Dimensionierungswerkzeug für magnetische Bau-elemente in Stromrichter-anwendungen
1. Aufl. 1997, 175 S.
ISBN 3-86073-239-0

ABISEA Band 20
Apeldoorn, Oscar
Simulationsgestützte Bewertung von Steuerverfahren für netzgeführte Stromrichter mit verringerter Netzrückwirkung
1. Aufl. 1997, 134 S.
ISBN 3-86073-680-9

ABISEA Band 21
Lohner, Andreas
Batteriemanagement für verschlossene Blei-Batterien am Beispiel von Unterbrechungsfreien Stromversorgungen
1. Aufl. 1998, 126 S.
ISBN 3-86073-681-7

ABISEA Band 22
Reinert, Jürgen
Optimierung der Betriebseigenschaften von Antrieben mit geschalteter Reluktanzmaschine
1. Aufl. 1998, 153 S.
ISBN 3-86073-682-5

ABISEA Band 23
Nagel, Andreas
Leitungsgebundene Störungen in der Leistungselektronik: Entstehung, Ausbreitung und Filterung
1. Aufl. 1999, 140 S.
ISBN 3-86073-683-3

ABISEA Band 24
Menne, Marcus
Drehschwingungen im Antriebsstrang von Elektrostraßenfahrzeugen - Analyse und aktive Dämpfung
1. Aufl. 2001, 169 S.
ISBN 3-86073-684-1

ABISEA Band 25
von Bloh, Jochen
Multilevel-Umrichter zum Einsatz in Mittelspannungs-Gleichspannungs-Übertragungen
1. Aufl. 2001, 137 S.
ISBN 3-86073-685-X

ABISEA Band 26
Karden, Eckhard
Using low-frequency impedance spectroscopy for characterization, monitoring, and modeling of industrial batteries
1. Aufl. 2002, 137 S.
ISBN 3-8265-9766-4

ABISEA Band 27
Karipidis, Claus-Ulrich
A Versatile DSP/ FPGA Structure optimized for Rapid Prototyping and Digital Real-Time Simulation of Power Electronic and Electrical Drive Systems
1. Aufl. 2001, 164 S.
ISBN 3-8265-9738-9

ABISEA Band 28
Kahlen, Klemens
Regelungsstrategien für permanentmagnetische Direktantriebe mit mehreren Freiheitsgraden
1. Aufl. 2002, 154 S.
ISBN 3-8322-1222-1

ABISEA Band 29
Inderka, Robert B.
Direkte Drehmomentregelung Geschalteter Reluktanzantriebe
1. Aufl. 2003, 182 S.
ISBN 3-8322-1175-6

ABISEA Band 30
Schröder, Stefan
Circuit-Simulation Models of High-Power Devices Based on Semiconductor Physics
1. Aufl. 2003, 123 S.
ISBN 3-8322-1250-7

ABISEA Band 31
Buller, Stephan
Impedance-Based Simulation Models for Energy Storage Devices in Advanced Automotive Power Systems
1. Aufl. 2003, 138 S.
ISBN 3-8322-1225-6

ABISEA Band 32
Schönknecht, Andreas
Topologien und Regelungsstrategien für das induktive Erwärmen mit hohen Frequenz-Leistungsprodukten
1. Aufl. 2004, 157 S.
ISBN 3-8322-2408-4

ABISEA Band 33
Tolle, Tobias
Konvertertopologien für ein aufwandsarmes, zweistufiges Schaltnetzteil zum Laden von Batterien aus dem Netz
1. Aufl. 2004, 148 S.
ISBN 3-8322-2676-1

ABISEA Band 34
Götting, Gunther
Dynamische Antriebsregelung von Elektrostraßenfahrzeugen unter Berücksichtigung eines schwingungsfähigen Antriebsstrangs
1. Aufl. 2004, 157 S.
ISBN 3-8322-2804-7

ABISEA Band 35
Dieckerhoff, Sibylle
Transformatorlose Stromrichterschaltungen für Bahnfahrzeuge am 16 2/3Hz Netz
1. Aufl. 2004, 147 S.
ISBN 3-8322-3094-7

ABISEA Band 36
Hu, Jing
Bewertung von DC-DC-Topologien und Optimierung eines DC-DC-Leistungsmoduls für das 42-V-Kfz-Bordnetz
1. Aufl. 2004, 148 S.
ISBN 3-8322-3201-X

ABISEA Band 37
Detjen, Dirk-Oliver
Characterization and Modeling of Si-Si Bonded Hydrophobie Interfaces for Novel High-Power BIMOS Devices
1. Aufl. 2004, 135 S.
ISBN 3-8322-2963-9

ABISEA Band 38
Walter, Jörg
Simulationsbasierte Zuverlässigkeitsanalyse in der modernen Leistungselektronik
1. Aufl. 2004, 121 S.
ISBN 3-8322-3481-0

ABISEA Band 39
Schwarzer, Ulrich
IGBT versus GCT in der Mittelspannungsanwendung - ein experimenteller und simulativer Vergleich
1. Aufl. 2005, 170 S.
ISBN 3-8322-4489-1

ABISEA Band 40
Bartram, Markus
IGBT-Umrichtersysteme für Windkraftanlagen: Analyse der Zyklenbelastung, Modellbildung, Optimierung und Lebensdauervorhersage
1. Aufl. 2006, 185 S.
ISBN 3-8322-5039-5

ABISEA Band 41
Ponnaluri, Srinivas
Generalized Design, Analysis and Control of Grid side converters with integrated UPS or Islanding functionality
1. Aufl. 2006, 163 S.
ISBN 3-8322-5281-9

ABISEA Band 42
Jacobs, Joseph
Multi-Phase Series Resonant DC-to-DC Converters
1. Aufl. 2006, 185 S.
ISBN 3-8322-5532-X

ABISEA Band 43
Linzen, Dirk
Impedance-Based Loss Calculation and Thermal Modeling of Electrochemical Energy Storage Devices for Design Considerations of Automotive Power Systems
1. Aufl. 2006, 185 S.
ISBN 3-8322-5706-3

ABISEA Band 44
Fiedler, Jens
Design of Low-Noise Switched Reluctance Drives
1. Aufl. 2007, 176 S.
ISBN 978-3-8322-5864-1

ABISEA Band 45
Fuengwarodsakul, Nisai
Predictive PWM-based Direct Instantaneous Torque Control for Switched Reluctance Machines
1. Aufl. 2007, 141 S.
ISBN 978-3-8322-6210-5

ABISEA Band 46
Meyer, Christoph
Key Components for Future Offshore DC Grids
1. Aufl. 2007, 187 S.
ISBN 978-3-8322-6571-7

ABISEA Band 47
Fujii, Kansuke
Characterization and Optimization of Soft-Switched Multi-Level Converters for STATCOMs
1. Aufl. 2008, 199 S.
ISBN 978-3-8322-6981-4

ABISEA Band 48
Carstensen, Christian
Eddy Currents in Windings of Switched Reluctance Machines
1. Aufl. 2008, 179 S.
ISBN 978-3-8322-7118-3

ABISEA Band 49
Bohlen, Oliver
Impedance-based battery monitoring
1. Aufl. 2008, 190 S.
ISBN 978-3-8322-7606-5

ABISEA Band 50
Thele, Marc
A contribution to the modelling of the charge acceptance of lead-acid batteries - using frequency and time domain based concepts
1. Aufl. 2008, 165 S.
ISBN 978-3-8322-7659-1

ABISEA Band 51
König, Andreas
High Temperature DC-to-DC Converters for Downhole Applications
1. Aufl. 2009, 154 S.
ISBN 978-3-8322-8489-3

ABISEA Band 52
Dick, Christian Peter
Multi-Resonant Converters as Photovoltaic Module-Integrated Maximum Power Point Tracker
1. Aufl. 2010, 182 S.
ISBN 978-3-8322-9199-0

ABISEA Band 53
Kowal, Julia
Spatially resolved impedance of nonlinear inhomogeneous devices: using the example of lead-acid batteries
1. Aufl. 2010, 203 S.
ISBN 978-3-8322-9483-0

ABISEA Band 54
Roscher, Michael Andreas
Zustandserkennung von LiFeP04-Batterien für Hybrid- und Elektrofahrzeuge
1. Aufl. 2011, 186 S.
ISBN 978-3-8322-9738-1

ABISEA Band 55
Hirschmann, Dirk
Highly Dynamic Piezoelectric Positioning
1. Aufl. 2011, 146 S.
ISBN 978-3-8322-9746-6

ABISEA Band 56
Rigbers, Klaus
Highly Efficient Inverter Architectures for Three-Phase Grid Connection of Photovoltaic Generators
1. Aufl. 2011, 244 S.
ISBN 978-3-8322-9816-9

ABISEA Band 57
Kasper, Knut
Analysis and Control of the Acoustic Behavior of Switched Reluctance Drives
1. Aufl. 2011, 205 S.
ISBN 978-3-8322-9869-2

ABISEA Band 58
Köllensperger, Peter
The Internally Commutated Thyristor - Concept, Design and Application
1. Aufl. 2011, 214 S.
ISBN 978-3-8322-9909-5

ABISEA Band 59
Schoenen, Timo
Einsatz eines DC/DC-Wandlers zur Spannungsanpassung zwischen Antrieb und Energiespeicher in Elektro-und Hybridfahrzeugen
1. Aufl. 2011, 128 S.
ISBN 978-3-8440-0622-3

ABISEA Band 60
Hennen, Martin
Switched Reluctance Direct Drive with Integrated Distributed Inverter
1. Aufl. 2012, 141 S.
ISBN 978-3-8440-0731-2

ABISEA Band 61
van Treek, Daniel
Position Sensorless Torque Control of Switched Reluctance Machines
1. Aufl. 2012, 144 S.
ISBN 978-3-8440-1014-5

ABISEA Band 62
Bragard, Michael
The Integrated Emitter Turn-Off Thyristor. An Innovative MOS-Gated High-Power Device
1. Aufl. 2012, 164 S.
ISBN 978-3-8440-1152-4

ABISEA Band 63
Gerschler, Jochen B.
Ortsaufgelöste Modellbildung von Lithium-Ionen-Systemen unter spezieller Berücksichtigung der Batteriealterung
1. Aufl. 2012, 334 S.
ISBN 978-3-8440-1307-8

ABISEA Band 64
Neuhaus, Christoph R.
Schaltstrategien für Geschaltete Reluktanzantriebe mit kleinem Zwischenkreis
1. Aufl. 2012, 133 S.
ISBN 978-3-8440-1487-7

ABISEA Band 65
Butschen, Thomas
Dual-ICT- A Clever Way to Unite Conduction and Switching Optimized Properties in a Single Wafer
1. Aufl. 2012, 168 S.
ISBN 978-3-8440-1771-7

ABISEA Band 66
Plum, Thomas
Design and Realization of High-Power MOS Turn-Off Thyristors
1. Aufl. 2013, 113 S.
ISBN 978-3-8440-1884-4

ABISEA Band 67
Kiel, Martin
Impedanzspektroskopie an Batterien unter besonderer Berücksichtigung von Batteriesensoren für den Feldeinsatz
1. Aufl. 2013, 226 S.
ISBN 978-3-8440-1973-5

ABISEA Band 68
Brauer, Helge
Schnelldrehender Geschalteter Reluktanzantrieb mit extremem Längendurchmesserverhältnis
1. Aufl. 2013, 192 S.
ISBN 978-3-8440-2345-9

ABISEA Band 69
Thomas, Stephan
A Medium-Voltage Multi-Level DC/DC Converter with High Voltage Transformation Ratio
1. Aufl. 2014, 226 S.
ISBN 978-3-8440-2605-4

ABISEA Band 70
Richter, Sebastian
Digitale Regelung von PWM Wechselrichtern mit niedrigen Trägerfrequenzen
1. Aufl. 2014, 126 S.
ISBN 978-3-8440-2641-2

ABISEA Band 71
Bösing, Matthias
Acoustic Modeling of Electrical Drives - Noise and Vibration Synthesis based on Force Response Superposition
1. Aufl. 2014, 188 S.
ISBN 978-3-8440-2752-5

ABISEA Band 72
Waag, Wladislaw
Adaptive algorithms for monitoring of lithium-ion batteries in electric vehicles
1. Aufl. 2014, 232 S.
ISBN 978-3-8440-2976-5

ABISEA Band 73
Sanders, Tilman
Spatially Resolved Electrical In-Situ Measurement Techniques for Fuel Cells
1. Aufl. 2014, 126 S.
ISBN 978-3-8440-3121-8

ABISEA Band 74
Baumhöfer, Thorsten
Statistische Betrachtung experimenteller Alterungsuntersuchungen an Lithium-Ionen Batterien
1. Aufl. 2015, 157 S.
ISBN 978-3-8440-3423-3

ABISEA Band 75
Andre, Dave
Systematic Characterization of Ageing Factors for High-Energy Lithium-Ion Cells and Approaches for Lifetime Modelling Regarding an Optimized Operating Strategy in Automotive Applications
1. Aufl. 2015, 196 S.
ISBN 978-3-8440-3587-2

ABISEA Band 76
Merei, Ghada
Optimization of off-grid hybrid PV-wind-diesel power supplies with multi-technology battery systems taking into account battery aging
1. Aufl. 2015, 184 S.
ISBN 978-3-8440-4148-4

ABISEA Band 77
Schulte, Dominik
Modellierung und experimentelle Validierung der Alterung von Blei-Säure Batterien durch inhomogene Stromverteilung und Säureschichtung
1. Aufl. 2016, 165 S.
ISBN 978-3-8440-4216-0

ABISEA Band 78
Schenk, Mareike
Simulative Untersuchung der Wicklungsverluste in Geschalteten Reluktanzmaschinen
1. Aufl. 2016, 126 S.
ISBN 978-3-8440-4282-5

ABISEA Band 79
Wang, Yu
Development of Dynamic Models with Spatial Resolution for Electrochemical Energy Converters as Basis for Control and Management Strategies
1. Aufl. 2016, 188 S.
ISBN 978-3-8440-4303-7

ABISEA Band 80
Ecker, Madeleine
Lithium Plating in Lithium-Ion Batteries:
An Experimental and Simulation Approach
1. Aufl. 2016, 154 S.
ISBN 978-3-8440-4525-3

ABISEA Band 81
Zhou, Wei
Modellbasierte Auslegungsmethode von Temperierungssystemen für Hochvolt-Batterien in Personenkraftfahrzeugen
1. Aufl. 2016, 175 S.
ISBN 978-3-8440-4589-5

ABISEA Band 82
Lunz, Benedikt
Deutschlands Stromversorgung im Jahr 2050
Ein szenariobasiertes Verfahren zur vergleichenden Bewertung von Systemvarianten und Flexibilitätsoptionen
1. Aufl. 2016, 187 S.
ISBN 978-3-8440-4627-4

ABISEA Band 83
Hofmann, Andreas G.
Direct Instantaneous Force Control: Key to Low-Noise Switched Reluctance Traction Drives
1. Aufl. 2016, 228 S.
ISBN 978-3-8440-4715-8

ABISEA Band 84
Budde-Meiwes, Heide
Dynamic Charge Acceptance of Lead-Acid Batteries for Micro-Hybrid Automotive Applications
1. Aufl. 2016, 157 S.
ISBN 978-3-8440-4733-2

ABISEA Band 85
Engel, Stefan P.
Thyristor-Based High-Power On-Load Tap Changers Control under Harsh Load Conditions
1. Aufl. 2016, 156 S.
ISBN 978-3-8440-4986-2

ABISEA Band 86
Van Hoek, Hauke
Design and Operation Considerations of Three-Phase Dual Active Bridge Converters for Low-Power Applications with Wide Voltage Ranges
1. Aufl. 2017, 231 S.
ISBN 978-3-8440-5011-0

ABISEA Band 87
Diekhans, Tobias
Wireless Charging of Electric Vehicles - a Pareto-Based Comparison of Power Electronic Topologies
1. Aufl. 2017, 151 S.
ISBN 978-3-8440-5048-6

ABISEA Band 88
Lehner, Susanne
Reliability Assessment of Lithium-Ion Battery Systems with Special Emphasis on Cell Performance Distribution
1. Aufl. 2017, 184 S.
ISBN 978-3-8440-5090-5

ABISEA Band 89
Käbitz, Stefan
Untersuchung der Alterung von Lithium-Ionen-Batterien mittels Elektroanalytik und elektrochemischer Impedanzspektroskopie
1. Aufl. 2016, 258 S.
DOI: 10.18154/RWTH-2016-12094

ABISEA Band 90
Witzenhausen, Heiko
Elektrische Batteriespeichermodelle: Modellbildung, Parameteridentifikation und Modellreduktion
1. Aufl. 2017, 266 S.
DOI: 10.18154/RWTH-2017-03437

ABISEA Band 91
Münnix, Jens
Einfluss von Stromstärke und Zyklentiefe auf graphitische Anoden
1. Aufl. 2017, 171 S.
DOI: 10.18154/RWTH-2017-01915

ABISEA Band 92
Pilatowicz, Grzegorz
Failure Detection and Battery Management Systems of Lead-Acid Batteries for Micro-Hybrid Vehicles
1. Aufl. 2017, 212 S.
DOI: 10.18154/RWTH-2017-09156

ABISEA Band 93
Drillkens, Julia
Aging in Electrochemical Double Layer Capacitors: An Experimental and Modeling Approach
1. Aufl. 2017, 179 S.
DOI: 10.18154/RWTH-2018-223434

ABISEA Band 94
Magnor, Dirk
Globale Optimierung netzgekoppelter PV-Batteriesysteme unter besonderer Berücksichtigung der Batteriealterung
1. Aufl. 2017, 210 S.
DOI: 10.18154/RWTH-2017-06592

ABISEA Band 95
Iliksu, Merve
Elucidation and Comparison of the Effects of Lithium Salts on Discharge Chemistry of Nonaqueous Li-O_2 Batteries
1. Aufl. 2018, 160 S.
DOI: 10.18154/RWTH-2018-223782

ABISEA Band 96
Schmalstieg, Johannes
Physikalisch-elektrochemische Simulation von Lithium-Ionen-Batterien: Implementierung, Parametrierung und Anwendung
1. Aufl. 2017, 168 S.
DOI: 10.18154/RWTH-2017-04693

ABISEA Band 97
Soltau, Nils
High-Power Medium-Voltage DC-DC Converters: Design, Control and Demonstration
1. Aufl. 2017, 176 S.
DOI: 10.18154/RWTH-2017-04084

ABISEA Band 98
Stieneker, Marco
Analysis of Medium-Voltage Direct-Current Collector Grids in Offshore Wind Parks
1. Aufl. 2017, 144 S.
DOI: 10.18154/RWTH-2017-04667

ABISEA Band 99
Masomtob, Manop
A New Conceptual Design of Battery Cell with an Internal Cooling Channel
1. Aufl. 2017, 167 S.
DOI: 10.18154/RWTH-2018-223281

ABISEA Band 100
Marongiu, Andrea
Performance and Aging Diagnostic on Lithium Iron Phosphate Batteries for Electric Vehicles and Vehicle-to-Grid Strategies
1. Aufl. 2017, 222 S.
DOI: 10.18154/RWTH-2017-09944

ABISEA Band 101
Gitis, Alexander
Flaw detection in the coating process of lithium-ion battery electrodes with acoustic guided waves
1. Aufl. 2017, 109 S.
DOI: 10.18154/RWTH-2017-099519

ABISEA Band 102
Neeb, Christoph
Packaging Technologies for Power Electronics in Automotive Applications
1. Aufl. 2017, 132 S.
DOI: 10.18154/RWTH-2018-224569

ABISEA Band 103
Adler, Felix
A Digital Hardware Platform for Distributed Real-Time Simulation of Power Electronic Systems
1. Aufl. 2017, 156 S.
DOI: 10.18154/RWTH-2017-10761

ABISEA Band 104
Becker, Jan
Flexible Dimensionierung und Optimierung hybrider Lithium-Ionenbatterie-speichersysteme mit verschiedenen Auslegungs-zielen
1. Aufl., 2017, 157 S.
DOI: 10.18154/RWTH-2017-09278

ABISEA Band 105
Warnecke, Alexander J.
Degradation Mechanisms in NMC Based Lithium-Ion Batteries
1. Aufl. 2017, 158 S.
DOI: 10.18154/RWTH-2017-09646

ABISEA Band 106
Taraborrelli, Silvano
Bidirectional Dual Active Bridge Converter using a Tap Changer for Extended Voltage Ranges
1. Aufl. 2017, 94 S.
DOI: 10.18154/RWTH-2018-228242

ABISEA Band 107
Sarriegi, Garikoitz
SiC and GaN Semiconductors: The Future Enablers of Compact and Efficient Converters for Electromobility
1. Aufl. 2017, 106 S.
DOI: 10.18154/RWTH-2018-227548

ABISEA Band 108
Senol, Murat
Drivetrain Integrated Dc-Dc Converters utilizing Zero Sequence Currents
1. Aufl. 2017, 134 S.
DOI: 10.18154/RWTH-2018-226170

ABISEA Band 109
Kojima, Tetsuya
Efficiency Optimized Control of Switched Reluctance Machines
1. Aufl. 2017, 142 S.
DOI: 10.18154/RWTH-2018-226697

ABISEA Band 110
Lewerenz, Meinert
Dissection and Quantitative Description of Aging of Lithium-Ion Batteries Using Non-Destructive Methods Validated by Post-Mortem-Analyses
1. Aufl. 2018, 139 S.
DOI: 10.18154/RWTH-2018-228663

ABISEA Band 111
Büngeler, Johannes
Optimierung der Verfügbarkeit und der Lebensdauer von Traktionsbatterien für den Einsatz in Flurförderfahrzeugen
1. Aufl. 2018, 171 S.
DOI: 10.18154/RWTH-2018-226569

ABISEA Band 112
Wegmann, Raphael
Betriebsstrategien und Potentialbewertung hybrider Batteriespeichersysteme in Elektrofahrzeugen
1. Auflage 2018, 184 S.
DOI: 10.18154/RWTH-2018-228833

ABISEA Band 113
Nordmann, Hannes
Batteriemanagementsysteme unter besonderer Berücksichtigung von Fehlererkennung und Peripherieanalyse
1. Aufl. 2018, 222 S.
DOI: 10.18154/RWTH-2018-228763

ABISEA Band 114
Engelmann, Georges
Reducing Device Stress and Switching Losses Using Active Gate Drivers and Improved Switching Cell Design
1. Aufl. 2018, 195 S.
DOI: 10.18154/RWTH-2018-228973

ABISEA Band 115
Klein-Heßling, Annegret
Active DC-Power Filters for Switched Reluctance Drives during Single-Pulse Operation
1. Aufl. 2018, 166 S.
DOI: 10.18154/RWTH-2018-231030

ABISEA Band 116
Burkhart, Bernhard
Switched Reluctance Generator for Range Extender Applications - Design, Control and Evaluation
1. Aufl. 2018, 194 S.
DOI: 10.18154/RWTH-2019-00025

ABISEA Band 117
Biskoping, Matthias
Discrete Modeling and Control of a versatile Power Electronic Test Bench with Special Focus on Central Photovoltaic Inverter Testing
1. Aufl. 2018, 236 S.
DOI: 10.18154/RWTH-2019-03346

ABISEA Band 118
Schubert, Michael
High-Precision Torque Control of Inverter-Fed Induction Machines with Instantaneous Phase Voltage Sensing
1. Aufl. 2019, 221 S.
DOI: 10.18154/RWTH-2018-231364

ABISEA Band 119
Van der Broeck, Christoph
Methodology for Thermal Modeling, Monitoring and Control of Power Electronic Modules
1. Aufl. 2019, 290 S.
DOI: 10.18154/RWTH-2019-01370

ABISEA Band 120
Hust, Friedrich Emanuel
Physico-chemically motivated parameterization and modelling of real-time capable lithium-ion battery models – a case study on the Tesla Model S battery
1. Aufl. 2019, 203 S.
DOI: 10.18154/RWTH-2019-00249

ABISEA Band 121
Ralev, Iliya
Accurate Torque Control of Position Sensorless Switched Reluctance Drives
1. Aufl. 2019, 154 S.
DOI: 10.18154/RWTH-2019-03071

ABISEA Band 122
Ayeng'o, Sarah Paul
Optimization of number of PV cells connected in series for a direct-coupled PV system with lead-acid and lithium-ion batteries
1. Aufl. 2019, 114 S.
DOI: 10.18154/RWTH-2019-01843

ABISEA Band 123
Koschik, Stefan Andreas
Permanenterregte Synchronmaschinen mit verteilter Einzelzahnsteuerung - Regelkonzepte und Betriebsstrategien für hochintegrierte Antriebssysteme
1. Aufl. 2019, 158 S.
DOI: 10.18154/RWTH-2019-03446

ABISEA Band 124
Farmann, Alexander
A comparative study of reduced-order equivalent circuit models for state-of-available-power prediction of lithium-ion batteries in electric vehicles
1. Aufl. 2019, 214 S.
DOI: 10.18154/RWTH-2019-04700

ABISEA Band 125
Mareev, Ivan
Analyse und Bewertung von batteriegetriebenen, oberleitungsversorgten und brennstoffzellengetriebenen Lastkraftwagen für den Einsatz im Güterfernverkehr in Deutschland
1. Aufl. 2019, 158 S.
DOI: 10.18154/RWTH-2019-04698

ABISEA Band 126
Qi, Fang
Online Model-predictive Thermal Management of Inverter-fed Electrical Machines
1. Aufl. 2019, 154 S.
DOI: 10.18154/RWTH-2019-08304

ABISEA Band 127
Kairies, Kai-Philipp
Auswirkungen dezentraler Solarstromspeicher auf Netzbetreiber und Energieversorger
1. Aufl. 2019, 140 S.
DOI: 10.18154/RWTH-2019-06706

ABISEA Band 128
Fleischer, Michael
Traction control for Railway Vehicles
1. Aufl. 2019, 162 S.
DOI: 10.18154/RWTH-2019-10570

ABISEA Band 129
Teuber, Moritz
Lifetime Assessment and Degradation Mechanisms in Electric Double-Layer Capacitors
1. Aufl. 2019, 150 S.
DOI: 10.18154/RWTH-2019-10071

ABISEA Band 130
Bußar, Christian
Investigation of Optimal Transformation Pathways towards 2050 for the Successful Implementation of a Sustainable Reduction of Carbon Emissions from Power Generation
1. Aufl. 2019, 204 S.
DOI: 10.18154/RWTH-2019-09975

ABISEA Band 131
Wienhausen, Arne Hendrik
High Integration of Power Electronic Converters enabled by 3D Printing
1. Aufl. 2019, 146 S.
DOI: 10.18154/RWTH-2019-08746

ABISEA Band 132
Kwiecien, Monika
Electrochemical Impedance Spectroscopy on Lead-Acid Cells during Aging
1. Aufl. 2019, 138 S.
DOI: 10.18154/RWTH-2019-09480

ABISEA Band 133
Titiz, Furkan Kaan
A Three-phase Low-voltage Grid-connected Current Source Inverter
1. Aufl. 2019, 128 S.
DOI: 10.18154/RWTH-2020-00458

ABISEA Band 134
Wünsch, Martin
Separation der Kathoden-alterung in Lithium-Ionen-Batteriezellen mittels elektrochemischer Impedanzspektroskopie
1. Aufl. 2019, 177 S.
DOI: 10.18154/RWTH-2019-11017

ABISEA Band 135
Badeda, Julia
Modeling and Steering of Multi-Use Operation with Uninterruptible Power Supply Systems - utilizing the example of lead-acid batteries
1. Aufl. 2020, 282 S.
DOI: 10.18154/RWTH-2020-05456

ABISEA Band 136
Kleinsteinberg, Björn
Energy Efficiency Increase of a Vanadium Redox Flow Battery with a Power-Based Model
1. Aufl. 2020, 163 S.
DOI: 10.18154/RWTH-2020-06092

ABISEA Band 137
Cai, Zhuang
Optimization of dimension and operation strategy for a wind-battery energy system in German electricity market under consideration of battery ageing process
1. Aufl. 2020, 144 S.
DOI: 10.18154/RWTH-2020-06525

ABISEA Band 138
Sabet, Pouyan Shafiei
Analysis of Predominant Processes in Electrochemical Impedance Spectra and Investigation of Aging Processes of Lithium-Ion Batteries with Layered Oxide Cathodes and Graphitic Anodes
1. Aufl. 2020, 136 S.
DOI: 10.18154/RWTH-2020-07683

ABISEA Band 139
Angenendt, Georg
Operation, Optimization and Additional Market Participation of Households with PV Battery Storage System and Power-to-Heat Application
1. Aufl. 2020, 221 S.
DOI: 10.18154/RWTH-2020-05200

ABISEA Band 140
Oberdieck, Karl Friedrich
Measurement and Mitigation of Electromagnetic Emissions of Propulsion Inverters for Electric Vehicles
1. Aufl. 2020, 181 S.
DOI: 10.18154/RWTH-2020-09215

ABISEA Band 141
Bubert, Andreas Martin
Optimierung des elektrischen Antriebsstrangs von Elektrofahrzeugen mit Betrachtung parasitärer Ströme innerhalb der elektrischen Maschine
1. Aufl. 2020, 215 S.
DOI: 10.18154/RWTH-2020-09556

ABISEA Band 142
Fleischer, Christian Georg
Model-Driven Software Development and Verification Solutions for Safety Critical Battery Management Systems
1. Aufl. 2021, 356 S.
DOI: 10.18154/RWTH-2021-00436

ABISEA Band 143
Arzberger, Arno
Thermografische Methoden zur zerstörungsfreien Messung der anisotropen Wärmeleitfähigkeit von Lithium-Ionen Zellen
1. Aufl. 2020, 131 S.
DOI: 10.18154/RWTH-2021-00479

ABISEA Band 144
Lange, Tobias
Oberwellenbasierte Modellierung, Regelung und Auslegung von Permanentmagnet- und Reluktanz-Synchronmaschinen
1. Aufl. 2020, S.
DOI: 10.18154/RWTH-2021-02537

ABISEA Band 145
Weiss, Claude
Fault Tolerant Switched Reluctance Machines with Distributed Inverters – Modeling and Control
1. Aufl. 2020, S.
DOI: 10.18154/RWTH-2021-02327

ABISEA Band 146
Huck, Moritz
Modelling the Transient Behaviour of Lead-Acid Batteries: Electrochemical Impedance of Adsorbed Species
1. Aufl. 2020, 151 S.
DOI: 10.18154/RWTH-2020-08362

ABISEA Band 147
Willenberg, Lisa
Volumenausdehnung und ihre Auswirkungen auf die Alterung einer zylindrischen Lithium-Ionen-Batterie
1. Aufl. 2020, S.
DOI: 10.18154/RWTH-2021-01906

ABISEA Band 148
Rogge, Matthias
Electrification of Public Transport Bus Fleets with Battery Electric Busses
1. Aufl. 2020, 161 S.
DOI: 10.18154/RWTH-2021-02146

ABISEA Band 149
Münderlein, Jeanette
Numerische Methodik zur Auslegung eines Hybriden Speichersystems mit Multinutzen“
1. Aufl. 2020, 221 S.
DOI: 10.18154/RWTH-2021-00867

ABISEA Band 150
Merten, Michael
Participation of Battery Storage Systems in the Secondary Control Reserve Market
1. Aufl. 2020, 187 S.
DOI: 10.18154/RWTH-2021-01029

ABISEA Band 151
Ge, Lefei
Performance Enhancement of Switched Reluctance Machines for High-speed Back-up Generators
1. Aufl. 2020, 152 S.
DOI: 10.18154/RWTH-2020-11546

ABISEA Band 152
Neubert, Markus
Modeling, Synthesis and Operation of Multiport-Active Bridge Converters
1. Aufl. 2020, 227 S.
DOI: 10.18154/RWTH-2020-10814

ABISEA Band 153
Schülting, Philipp
Optimierte Auslegung von hochintegrierten und bidirektionalen Onboard GaN-Ladegeräten
1. Aufl. 2020, 158 S.
DOI: 10.18154/RWTH-2020-09771

ABISEA Band 154
Sewergin, Alexander
Design Challenges and Solutions for the Practical Application of SiC Power Moduls – Exemplified by an Automotive DC-DC Converter. 1. Aufl. 2021, 154 S.
DOI: 10.18154/RWTH-2021-04498

ABISEA Band 155
Stippich, Alexander
Exploiting the Full Potential of Silicon Carbide Devices via Optimized Highly Integrated Power Modules
1. Aufl. 2021, 188 S.
DOI: 10.18154/RWTH-2021-08122

ABISEA Band 156
Gottschlich, Jan
Hilfsspannungsversorgungskonzepte für Mittelspannungs-DC/DC-Wandler
1. Aufl. 2021, 178 S.
DOI: 10.18154/RWTH-2021-11881

ABISEA Band 157
Hollstegge, Philipp
Injektion raumzeigerzerlegter Stromharmonischer zur Minderung tonaler Geräuschanteile in asymmetrisch sechsphasigen Permanentmagnetsynchronmaschinen
1. Aufl. 2021, 191 S.
DOI: 10.18154/RWTH-2021-11040

ABISEA Band 158
Grau, Vivien
Development of a Test Bench to Investigate the Impact of Steep Voltage Slopes on the Lifetime of Insulation Systems for Coil Windings
1. Aufl. 2021, 182 S.
DOI: 10.18154/RWTH-2021-09577

ABISEA Band 159
Ringbeck, Florian
Optimized Charging of Lithium-Ion Batteries with Physico-Chemical Models
1. Aufl. 2021, 174 S.
DOI: 10.18154/RWTH-2021-11038

ABISEA Band 160
Bank, Thomas
Performance and Aging Analysis of High-Power Lithium Titanate Oxide Cells for Low-Voltage Vehicle Applications
1. Aufl. 2021, 148 S.
DOI: 10.18154/RWTH-2021-10369

ABISEA Band 161
Aupperle, Felix
Realizing High-Performance Silicon-Based Lithium-Ion Batteries
1. Aufl. 2022, 138 S.
DOI: 10.18154/RWTH-2022-05155

ABISEA Band 162
Schröer, Philipp A.
Entwicklung einer adaptiven Leistungsprognosefunktion für Starterbatterien mit Lithium-Titanat-Oxid-Anode als Grundlage zur sicheren Energieversorgung im Fahrzeug
1. Aufl. 2021, 187 S.
DOI: 10.18154/RWTH-2021-10819

ABISEA Band 163
Dechent, Philipp
Simulation and Real-Life assessment of cell-to-cell variation of ageing lithium-ion batteries
1. Aufl. 2022, 149 S.
DOI: 10.18154/RWTH-2022-09298

ABISEA Band 164
Li, Weihan
Battery Digital Twin with Physics-Based Modeling, Battery Data and Machine Learning
1. Aufl. 2022, 234 S.
DOI: 10.18154/RWTH-2022-02292

ABISEA Band 165
Thien, Tjark G. C.
Optimaler Betrieb von stationären Hybrid-Batteriespeichern am Beispiel des Projekts M5BAT
1. Aufl. 2022, 172 S.
DOI: 10.18154/RWTH-2022-00997

ABISEA Band 166
Lüdecke, Christoph
Compensating Asymmetries of Parallel-Connected SiC MOSFETs Using Intelligent Gate Drivers
1. Aufl. 2022, 166 S.
DOI: 10.18154/RWTH-2022-09587

ABISEA Band 167
Rahe, Christiane
Untersuchung von Batterieelektroden mit optischen Verfahren
1. Aufl. 2022, 214 S.
DOI: 10.18154/RWTH-2022-08794

ABISEA Band 168
Weber, Felix Martin
Stability of lithium electrolyte interphase enabling rechargeable lithium-metal batteries
1. Aufl. 2023, 168 S.
DOI: 10.18154/RWTH-2023-03565

ABISEA Band 169
Henn, Jochen
Gate Driver Integrated Closed-Loop Control for Electromagnetic Emissions and Switching Losses of Wide Bandgap Power Electronic Converters
1. Aufl. 2023, 169 S.
DOI: 10.18154/RWTH-2023-07726

ABISEA Band 170
Quabeck, Stefan
Modeling of Parasitic Currents and Fault Detection in Electrical Traction Drives
1. Aufl. 2023, S.
DOI: 10.18154/RWTH-2023-10920

ABISEA Band 171
Hecht, Christopher
Usage overview, prediction, and siting optimization for electric vehicles public charging infrastructure with machine learning and big data methods
1. Aufl. 2023, S.
DOI:

ABISEA Band 172
Kuipers, Matthias L. U.
Development of a Virtual Cell Design Tool for Objective Comparisons between State-of-the-Art Battery Cells and Next Generation Technologies
1. Aufl. 2023, S.
DOI:

ABISEA Band 173
Brieske, Daniel Martin
Anwendungsbezogene Modellierung und Zustandsbestimmung von Lithium-Schwefel-Batterien
1. Aufl. 2023, S.
DOI:

ABISEA Band 174
Teichert, Philipp
Einfluss der Degradation von nickelreichen $Li[Ni_xMn_yCo_z]O_2$ (NMC) Elektroden (mit $x \geq 0.6$) auf Vollzellalterung von Lithium-Ionen-Zellen
1. Aufl. 2023, S.
DOI:

ABISEA Band 175
Kühnle, Hannes Sebastian
Optical and electrochemical investigations of fundamental lithium metal deposition processes on lithium surfaces
1. Aufl. 2023, S.
DOI:

The lithium-ion battery is the most expensive and weight-intensive component in electric vehicles (EVs). Therefore, in the development of new EVs, the battery is often the focus of optimization. In addition to the actual battery cell design, the serial and parallel cell connection, the cooling capability, the battery's mechanical integration, and the electronics play a decisive role in a battery system. There are also major direct dependencies between the optimal battery system and the necessary EV requirements regarding energy, power, and system voltage. Moreover, fundamental guidelines with regard to durability, safety, and general lifetime must be met and thus taken into account in the battery system package design.

This thesis aims to combine the multitude of interfaces within battery system development using a multiphysical framework capable of holistically evaluating, comparing, and optimizing battery system concepts. The framework consists of interconnected simulation models representing each major component group within the battery system. Machine learning optimization is used to derivate globally optimized battery system design concepts. Using combined Gaussian process regression and classification methods, the solution space is divided into multiple areas in which area-targeted search criteria are used.

Finally, novel EV battery-related issues are discussed from the cell to the module to the system level. Findings underline the imperative need for component-coupled simulation models when evaluating battery system designs.

ISSN 1437-675X